Annual Research Briefs – 1990

Center for Turbulence Research

February 1991

NASA

Ames Research Center

Stanford University

CONTENTS

Preface

This report contains the 1990 annual progress reports of the Research Fellows and students of the Center for Turbulence Research. It is intended primarily as a contractor report to the National Aeronautics and Space Administration, Ames Research Center. Another report entitled, "Studying turbulence using numerical simulation databases -III," covering the 1990 CTR Summer Program research activities was released earlier this year. In addition, numerous CTR Manuscript Reports were published last year. The purpose of the CTR Manuscript Series is to expedite the dissemination of research results by the CTR staff.

The Center for Turbulence Research is devoted to the fundamental study of turbulent flows; its objectives are to produce advances in physical understanding of turbulence, in turbulence modeling and simulation, and in turbulence control. The CTR staff study a wide range of problems in turbulence; they together with the NASA-Ames scientific staff and Stanford faculty members have formed a critical mass for the study of turbulence.

Last year, in its fourth operational year, CTR had twenty two resident Postdoctoral Fellows and two Sr. Research Fellows, and it supported seven doctoral students and eight short term visitors with stays of one month or longer. Several other doctoral students who are supported by grants from the Air Force Office of Scientific Research and the Office of Naval Research also conduct their research at the CTR. The 1990 CTR Summer Program had twenty seven guest participants from seven countries. Three of the visiting Fellows offered formal courses at Stanford during the academic year. These were *Mixing and Chaos* (J. Ottino), *Hydrodynamic Stability* (W. Criminale), and *Advanced Topics in Turbulence* (J. Mathieu). All were well attended by CTR Fellows, staff, and students.

The reports appearing in the following pages are a brief account of the accomplishments of the CTR Fellows in 1990. They are grouped in the general areas of modeling, combustion, flow physics, experimental studies, turbulence theory, and simulation. The CTR roster for 1990 is provided in the Appendix. Also listed are the members of the Advisory Committee which meets annually to review the Center's Program and the Steering Committee which acts on Fellowship applications.

Special thanks are due to Debra Spinks, the Center's Administrative Assistant, for her skillful compilation and processing of this report.

Parviz Moin
William C. Reynolds
John Kim

Turbulence closure modeling near rigid boundaries

By P. A. Durbin

1. Motivation and objectives

The near-wall region plays an essential role in turbulent boundary layers: it is a region of high shear; the peak rate of production and peak intensity of turbulence occurs there; and the peak rate of dissipation occurs right at the wall. Nevertheless, this region has received less attention from modelers than have more nearly homogeneous flows. One reason for this is that when the boundary layer is near equilibrium, experimental data can be used to prescribe the flow in the wall layer. Another reason is that most turbulence models are developed under assumptions of near homogeneity. This is a poor approximation in the wall region. My objective has been to develop a single-point moment closure model for the strongly non-homogeneous A turbulent flow near a rigid boundary.

All the previous work in this area has used an eddy viscosity 'damping function' (this is true of second order closures as well as of k–ϵ models). The need for a damping function in k–ϵ models is explained by figure 1. The solid curve is the exact eddy viscosity

$$\nu_t = -\overline{uv}/\partial_y U \tag{1}$$

evaluated from DNS data. The dotted curves are the k–ϵ viscosity

$$\nu_t = C_\mu k T \tag{2}$$

where $T = k/\epsilon$ (see §2.3 below). The standard value of $C_\mu = 0.09$ is used in the upper curve while $C_\mu = 0.075$ in the lower. One sees that in the wall region ($y_+ < 100$) the k–ϵ viscosity has the wrong profile. A damping function is commonly used to correct this fundamentally wrong behavior; the damping function is simply defined as the ratio of the solid to the dotted curve.

Tensoral considerations (Lumley 1978) suggest that

$$\nu_t = C_\mu \overline{v^2} T \tag{3}$$

might be a more basically correct form. The dashed line shows that this, with $C_\mu = 0.2$, is a good approximation when $y_+ < 100$. Of course, figure 1 was constructed using DNS data for k, ϵ and $\overline{v^2}$; what is required is a model which can predict these quantities.

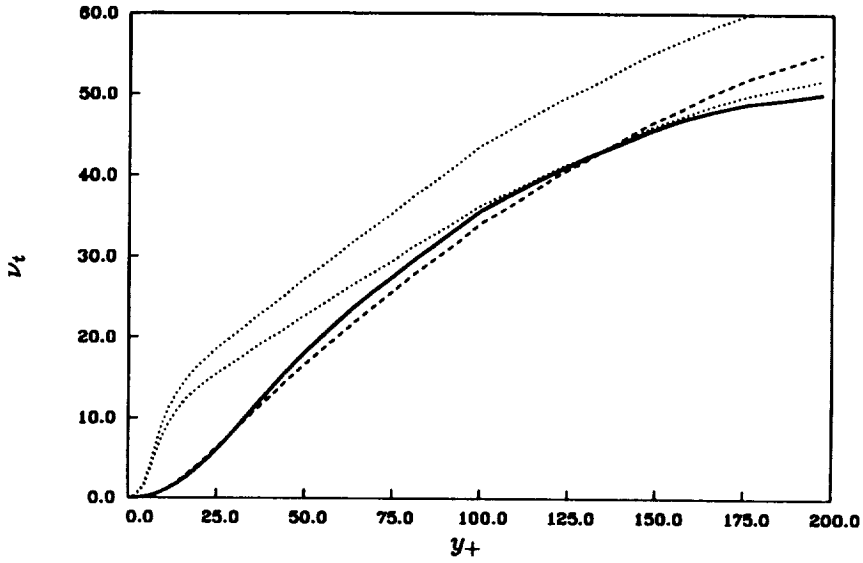

FIGURE 1. Exact eddy viscosity (solid) compared to k–ϵ (dotted, $C_\mu = 0.09$ upper, $C_\mu = 0.075$ lower) and k–ϵ–v (dashed) formulas. These curves were computed from DNS data.

2. Accomplishments

2.1. Near wall model

Such a model has been developed and is described in Durbin (1990). In this section, the model will be described very briefly.

Boundary conditions are important in near wall modeling. The no-slip and no-normal flux conditions lead to

$$\begin{aligned} k &= \partial_y k = 0 \\ \overline{v^2} &= O(y^4) \end{aligned} \tag{4}$$

at the boundary, $y = 0$. In order to satisfy these conditions at the two boundaries to a channel, the model equations must be fourth order. The standard k–ϵ system has this property. In the thin-layer approximation with an eddy viscosity model for turbulent transport, the standard k–ϵ system is

$$\begin{aligned} \partial_y(\nu + \nu_t/\sigma_k)\partial_y k &= \epsilon - \nu_t(\partial_y U)^2 \\ \partial_y(\nu + \nu_t/\sigma_\epsilon)\partial_y \epsilon &= [C_{\epsilon_2}\epsilon - C_{\epsilon_1}\nu_t(\partial_y U)^2]/T \ . \end{aligned} \tag{5}$$

$C_{\epsilon_1}, C_{\epsilon_2}, \sigma_k$ and σ_ϵ are constants. The left sides of (5) represent turbulent diffusion of energy and dissipation, and the right sides represent the imbalance between destruction and production of energy and dissipation. T is a time-scale, which we take to be

$$T = \max(k/\epsilon, C_T(\nu/\epsilon)^{1/2}) \tag{6}$$

with $C_T = 6$, from DNS data. Away from the wall ($y_+ > 5$ or so), this becomes the Lagrangian decorrelation scale k/ϵ. Because this Lagrangian time-scale tends to zero at the wall, the Kolmogorov scale has been used as a lower bound on T.

A $\overline{v^2}$ model based on usual modeling procedures would be

$$\partial_y(\nu + \nu_t/\sigma_k)\partial_y\overline{v^2} = \frac{\overline{v^2}}{k}\epsilon - \wp_{22}, \tag{7}$$

where $\wp_{22}$ represents the velocity-pressure gradient correlation combined with part of the dissipation. The first term on the right side is an anisotropic contribution to dissipation of $\overline{v^2}$ (see Durbin 1990 for more discussion).

The suppression of $\overline{v^2}$ by the no-normal flux condition (4) is quite important. It is responsible for the behavior shown in figure 1. In order to introduce this boundary condition and the associated homogeneous solutions, we propose an elliptic model for $\wp_{22}$:

$$\begin{aligned} L^2\partial_y^2 f_{22} - f_{22} &= -\Pi_{22} - (\frac{\overline{v^2}}{k} - \frac{2}{3})/T \\ \wp_{22} &= k f_{22} \ . \end{aligned} \tag{8}$$

The second term on the right side of the first equation is associated with dissipation rate. In the homogeneous limit, it will make the dissipation rate isotropic in (7). Π_{22} is a homogeneous pressure strain model. Thus (8) provides for elliptic relaxation to the homogeneous limit. We use the Launder, Reece,& Rodi (1975) form for Π_{22}

$$\Pi_{22} = \frac{C_1}{T}(\frac{2}{3} - \frac{\overline{v^2}}{k}) + C_2\frac{\nu_t}{k}(\partial_y U)^2. \tag{9}$$

L is the length scale

$$L = C_L \max(k^{3/2}/\epsilon, C_\eta(\nu^3/\epsilon)^{1/4}). \tag{10}$$

The elliptic relaxation model is largely justified by the fact that the wall causes irrotational fluctuations in the interior of the flow when the no-normal flux condition is imposed (Hunt and Graham 1978). This is a kinematic effect which cannot be associated with any terms in the Reynolds stress budget. The present representation of these irrotational fluctuations is quite indirect.

Predictions by this model are compared to DNS channel flow data in figures 2 ($R_\tau = 395$) and 3 ($R_\tau = 180$). The predictions are certainly as good or better than those obtained using a damping function to correct the k–ϵ formula (2) (Shih 1990). My hope is that the present approach is more sound.

2.2. Local anisotropy in strained turbulence

In order to obtain the predictions in figure 2, it was necessary to use a higher than usual value of C_{ϵ_1}; in other words, the production of dissipation was higher than in quasi-homogeneous models. A possible source of this extra production of

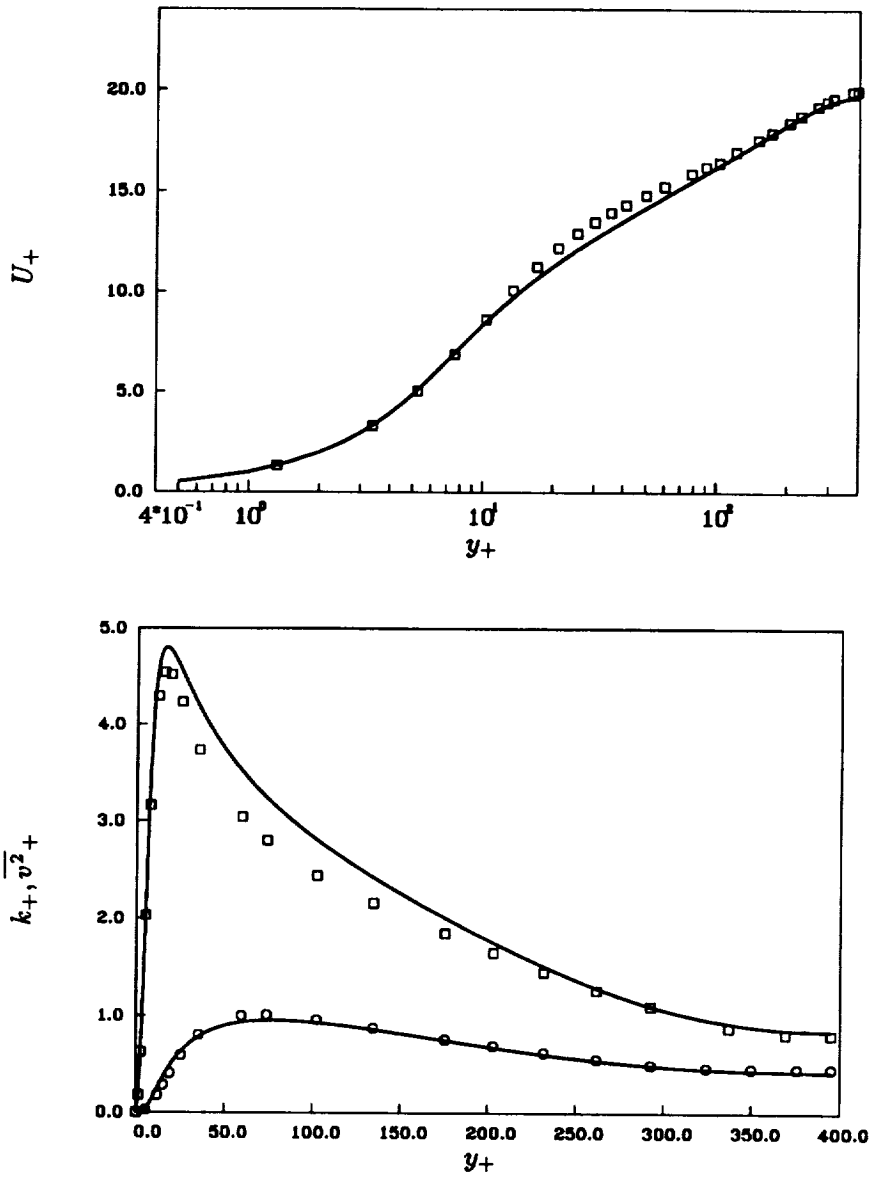

FIGURE 2. $R_\tau = 395$. Comparison of present model (line) to DNS data (symbols): (a) mean flow; (b) k (upper curve) and $\overline{v^2}$ (lower curve).

dissipation is anisotropy of the vorticity tensor. The exact equation for dissipation contains the term

$$(\epsilon_{ij} + d_{ij})S_{ij} \tag{11}$$

with the convention of summation on repeated indices, and where S_{ij} is the mean rate of strain tensor and

$$\epsilon_{ij} = 2\nu\overline{\partial_k u_i \partial_k u_j}, \quad d_{ij} = 2\nu\overline{\partial_i u_k \partial_j u_k}. \tag{12}$$

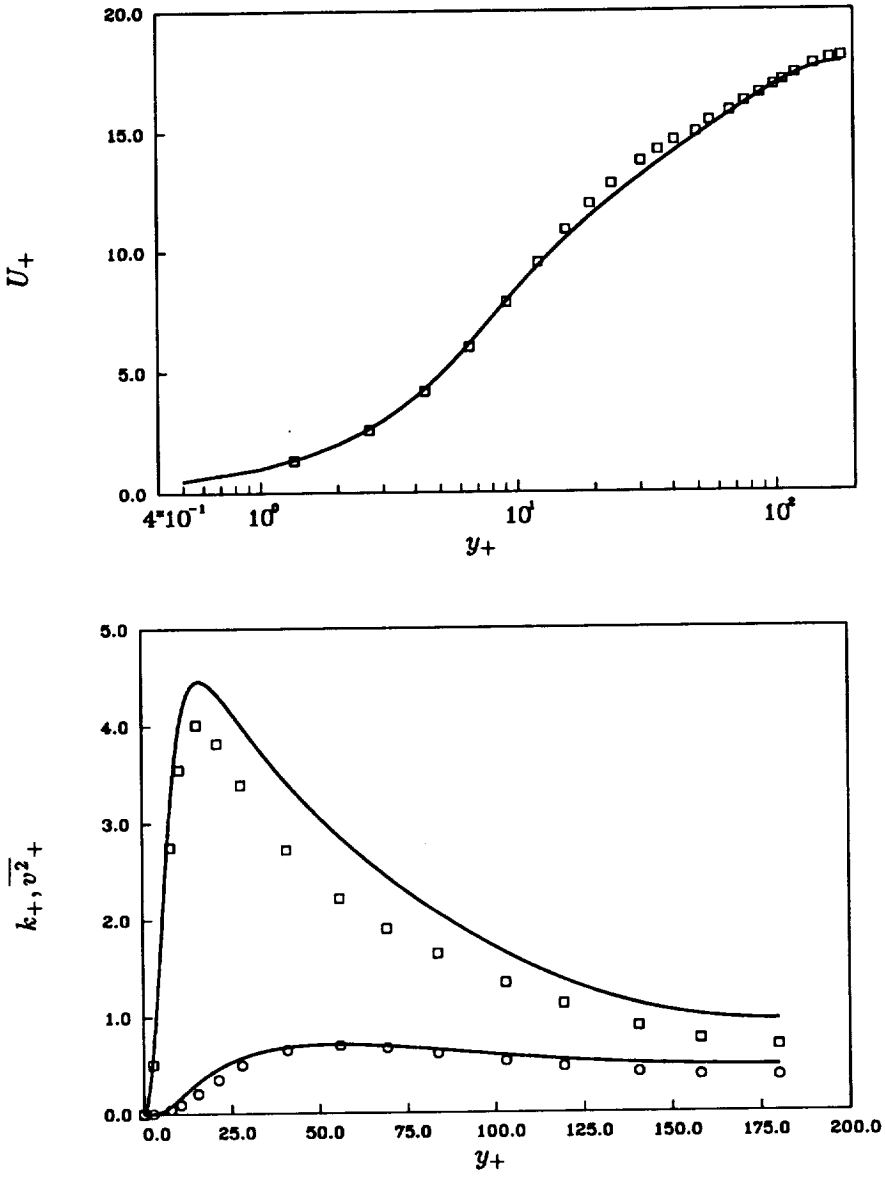

FIGURE 3. $R_\tau = 180$. Comparison of present model to DNS data.

In homogeneous flow

$$\epsilon_{ij} + d_{ij} = -2\nu(\overline{\omega_i\omega_j} - \frac{2}{3}\delta_{ij}\overline{\omega_k\omega_k}). \tag{13}$$

A corollary to the hypothesis of local (or small-scale) isotropy is that $\epsilon_{ij} + d_{ij} = 4\epsilon\delta_{ij}/3$, so that (11) vanishes in incompressible flow ($S_{ii} = 0$).

Although the hypothesis of local isotropy is usually understood to depend on a condition of high Reynolds number, it would also seem restricted to low mean rates

of strain. To see this, one notes that in homogeneous turbulence, the equation for ϵ_{ij} is

$$d_t\epsilon_{ij} = N_{ij} + 2(d_{ikjl} + d_{jkil})\partial_l U_k - \epsilon_{ik}\partial_k U_j - \epsilon_{jk}\partial_k U_i - 2d_{klij}\partial_k U_l \tag{14}$$

where

$$N_{ij} \equiv 2\nu\overline{(\partial_i u_j + \partial_j u_i)\partial_k u_l \partial_l u_k} - \overline{\epsilon'_{ik}\partial_k u_j} - \overline{\epsilon'_{jk}\partial_k u_i} - 4\nu^2\overline{\partial^2_{km}u_i\partial^2_{km}u_j}$$

contains the non-linear and dissipative terms and

$$d_{ijkl} = 2\nu\overline{\partial_i u_k \partial_j u_l}.$$

Equation (14) contains only statistics of the velocity gradient tensor, so the hypothesis of local isotropy should apply term by term. Therefore,

$$\begin{aligned} \epsilon_{ij} &= \frac{2}{3}\epsilon\delta_{ij};\ N_{ij} = \frac{2}{3}N\delta_{ij} \\ d_{ijkl} &= \frac{4}{15}\epsilon\delta_{ij}\delta_{kl} - \frac{1}{15}\epsilon(\delta_{ik}\delta_{jl} + \delta_{jk}\delta_{il}) \end{aligned} \tag{15}$$

in which $\epsilon_{ii} = 2\epsilon$ is twice the rate of kinetic energy dissipation, $N_{ii} = 2N$, and $d_{kkij} = \epsilon_{ij}$ has been used. On substituting (15) into (14), one finds

$$\frac{2}{3}\delta_{ij}d_t\epsilon = \frac{2}{3}\delta_{ij}N - \frac{4}{15}\epsilon S_{ij}. \tag{16}$$

Because $S_{ii} = 0$, (16) can only be satisfied if $S_{ij} = 0$; conversely, local isotropy is inconsistent with the Navier-Stokes equations if $S_{ij} \neq 0$. With the conventional estimate $N = O(\epsilon/T)$, the condition for local isotropy to be a valid approximation is that $ST \ll 1$. In the wall region, ST reaches values of about 16. DNS computations show significant local anisotropy in that region.

The ϵ model (5) is not justified by reference to the exact terms which the model replaces; instead, it is based on a loose notion that the difference between production and dissipation of ϵ can be modeled as a function of the production and dissipation of energy. Thus one writes

$$N = \frac{\epsilon}{T}F(P/\epsilon) \tag{17}$$

(N is as in (16) and P means rate of turbulent kinetic energy production). The standard model (5) amounts to assuming a linear form for F; thus

$$N = \frac{\epsilon}{T}[C_{\epsilon_1}P/\epsilon - C_{\epsilon_2}]. \tag{18}$$

The additional production of dissipation by local anisotropy might be incorporated by letting C_{ϵ_1} depend on P/ϵ. Assuming that dependence to be linear amounts to including a quadratic term in F:

$$N = \frac{\epsilon}{T}[C_{\epsilon_1}P/\epsilon\frac{(1 + a_1P/\epsilon)}{(1 + a_1)} - C_{\epsilon_2}]. \tag{19}$$

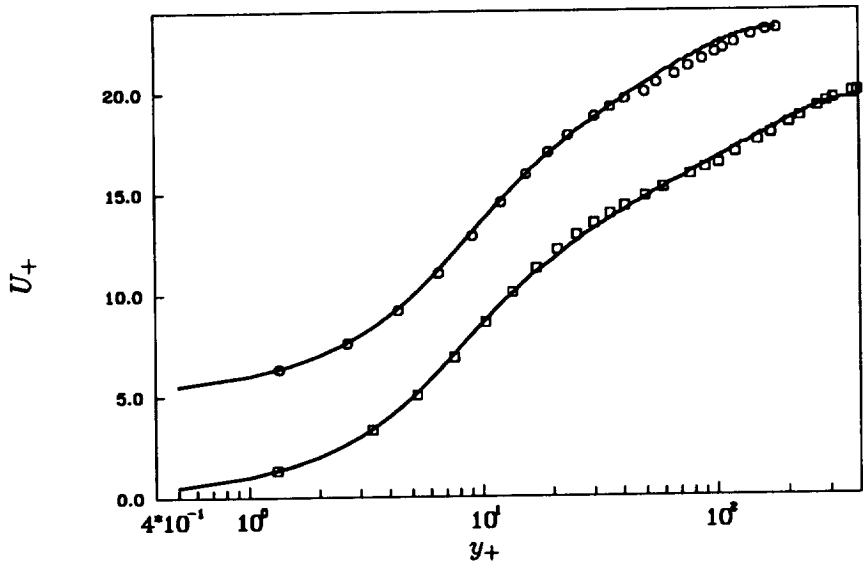

FIGURE 4. Mean velocity profiles with anisotropy term. $R_\tau = 395$ and 180. The upper curve, for which $R_\tau = 180$, has been displaced up by 5 units.

This reduces to (18) when $P = \epsilon$. A computation using (19) in the present near wall model is included in figure 4. Here $a_1 = 0.1$. While one might find this inclusion of an extra constant dissatisfying, the fact is that local anisotropy does contribute significantly to dissipation in the part of the near wall region in which $P/\epsilon > 1$. Thus (19) was chosen because it enhances production of dissipation in the right region and reduces to the standard model in the outer region, where $P \approx \epsilon$.

2.3. k/ϵ is a Lagrangian time-scale

It is useful to have some understanding of the time-scale which enters turbulence models. While $T = k/\epsilon$ might be justified solely on dimensional grounds, I wish to point out that it is also a Lagrangian decorrelation time-scale. Comparison of (3) to the Markovian limit of Lagrangian dispersion theory suggests that it may indeed be appropriate to regard T as a Lagrangian time-scale (after invoking Reynolds' analogy).

When the turbulence is non-homogeneous, Lagrangian statistics are non-stationary so T cannot be an integral scale. Rather, it is a local decorrelation scale in the following sense: The Lagrangian auto-correlation for an ensemble of trajectories originating at y is

$$R_L(y) = \frac{\overline{\mathbf{u}(t;y) \cdot \mathbf{u}(t+\tau;y)}}{(\overline{|\mathbf{u}(t;y)|^2}\ \overline{|\mathbf{u}(t+\tau;y)|^2})^{1/2}}. \tag{20}$$

By Kolmogorov scaling

$$R_L = 1 - c\epsilon\tau/k + O(\epsilon\tau/k)^2, \quad \tau_\eta \ll \tau \ll T$$

where c is a constant. Define T by

$$\frac{1}{T(y)} = \lim_{\tau/T \to 0} \frac{1 - R_L}{\tau}. \tag{21}$$

(The limit is asymptotically equivalent to $\tau/\tau_\eta \to \infty$.) One finds that $T \propto k/\epsilon$. Hence, k/ϵ is a Lagrangian decorrelation time-scale.

3. Future plans

A primary motivation for developing near wall models is the need to predict non-equilibrium boundary layers, especially those approaching separation. My hope is to extend the present efforts into that direction. Such work on boundary layers has already begun. The present near wall model appears to be satisfactory. However, the rotational-irrotational interface seems to be a source of difficulty. Irrotational fluctuations contribute to the turbulent energy in the outer part of the boundary layer. Again, the irrotational 'action at a distance' cannot be identified with any term in the Reynolds stress budget (it is *not* an effect of pressure-strain correlation). Near the wall, the dominant effect of these irrotational fluctuations was to suppress the normal velocity. In the outer half of the boundary layer, they contribute to the total kinetic energy. This problem is under investigation. A parabolic code with an expanding grid was written for this work. Ultimately, it will be necessary to write a fully elliptic code. Use can be made of DNS techniques.

REFERENCES

DURBIN, P. A. 1990 Near wall turbulence closure modeling without 'damping functions'. *CTR Manuscript 112,* Center for Turbulence Research, Stanford University.

HUNT, J. C. R. & GRAHAM, J. M. R. 1978 Free-stream turbulence near plane boundaries. *J. Fluid Mech.* **84**, 209-235.

LUMLEY, J. L. 1978 Computational modeling of turbulent flows. *Adv. Appl. Mech.* **18**, 126-176.

LAUNDER, B. E., REECE, G. J. & RODI, W. 1975 Progress in the development of a Reynolds-stress turbulence closure. *J. Fluid Mech.* **68**, 537-566.

SHIH, T.-S. 1990 An improved k–ϵ model for near wall turbulence and comparison with direct numerical simulations. Unpublished.

Compressible turbulent flows: modeling and similarity considerations

By O. Zeman

1. Motivations and objectives

With the recent revitalization of high speed flow research, compressibility presents a new set of challenging problems to turbulence researchers. Questions arise as to what extent compressibility affects turbulence dynamics, structures, the Reynolds stress-mean velocity (constitutive) relation, and the accompanying processes of heat transfer and mixing. In astrophysical applications, compressible turbulence is believed to play an important role in intergalactic gas cloud dynamics and in accretion disk convection.

Our work is principally directed toward understanding and modeling of the compressibility effects in free shear flows, boundary layers, and boundary layer/shock interactions.

2. Introduction

Compressibility effects in turbulent flows depend mainly on the r.m.s. fluctuating Mach number M_t, defined as the ratio of the r.m.s. fluctuating velocity to the mean field sonic velocity. Direct numerical simulations (DNS) of homogeneous turbulence indicate that when $M_t \leq 0.1$, the turbulence dynamics is generally unaffected by compressibility. It means that the vortical (solenoidal) and the compressive (acoustic) modes of the fluctuating field are virtually decoupled (Kovásznay, 1953). Only when M_t exceeds a value of about 0.3 does compressibility begin to noticeably influence turbulence dynamics and structure. Further increase in M_t may lead to the formation of shock-like structures, or turbulent shocklets. Shocklet formation has been recently detected in the DNS of decaying turbulence by Lee, Lele, and Moin (1990). In the DNS of homogeneous shear turbulence, Blaisdell (1990) detected the shocklets for $M_t \geq 0.7$. Zeman (1990) suggested that weak shocklets may be responsible for the growth rate attenuation in shear layers and proposed a physical model for shocklet formation and the associated (dilatation) dissipation. On the basis of the DNS results and experimental evidence in mixing layers (e.g. Papamoschou and Roshko 1988), compressibility effects may be broadly classified by the magnitude of M_t. Thus we shall refer to the range $0.3 < M_t < 0.6$ as moderate Mach numbers whereby the compressibility effects are observable but with shock-like occurrences being statistically insignificant. At large Mach numbers $M_t > 0.6$, a full scope of compressibility-induced effects may be expected, such as shocklet and baroclinic vorticity generation and significant solenoidal/compressive mode interactions.

3. Accomplishments

The accomplishments described in the following subsections consist of: The study of similarity in supersonic mixing layers (2.1), description of the new proposed

model for the pressure-dilatation term and its application in decaying turbulence (2.2), the study of constitutive relations in compressible shear-driven turbulence (2.3), and current work concerning the effect of mean compression on turbulence as in the turbulence/shock interactions (2.4).

3.1. Similarity in supersonic mixing layers

The most prominent effect of compressibility on mixing layers is inhibition of the layer growth as observed in experiments e.g. by Bogdanoff (1983), Papamoschou and Roshko (1988), and Samimy and Elliott (1990) among others. These findings have been unified by the concept of the so-called convective Mach number (M_c) introduced by Bogdanoff and Papamoschou & Roshko, wherein properly normalized growth rates are expected to be solely a function of M_c. The experimental data suggest that the growth rate decreases appreciably for convective Mach numbers in the range between 0.3 and 1.2; beyond $M_c = 1.5$ the growth rates level off at about 30% of the low speed value.

Zeman (1990a) (hereafter referred to as Z90) suggested that growth inhibition in mixing layers is related to dilatation dissipation, ϵ_d. Dilatation dissipation occurs in regions where fluid elements acquire supersonic relative speeds and form shock-like structures called shocklets. These structures generate high levels of ϵ_d. In mixing layers, the shocklet contribution to dilatation dissipation is expected to become important when the Mach number M (based on the relative velocity difference $\Delta U = U_1 - U_2$ of the free streams) is about one (or $M_c \approx 0.5$). This value appears to coincide with the onset of growth rate reduction.

There is so far no satisfactory physical explanation for the leveling of the growth rates at large convective Mach numbers ($M_c > 1.2$). As shown in Z90, a second-order closure model which accounts for shocklet dissipation predicts this leveling reasonably well, and one could argue that for larger Mach numbers (say $M_c > 1.5$), the velocity fluctuations are controlled (through the shocklet dissipation) by the local sonic velocity and not by the velocity difference ΔU. Evidence of this effect is shown in Fig. 5 of Z90, where the modeled r.m.s. Mach number at the mixing layer centerline is plotted vs. $M = 2M_c$. As M increases beyond a value of 3, M_t approaches an asymptotic (saturation) limit $M_t \to M_{t\infty} \approx 0.5$, suggesting that r.m.s. turbulent fluctuations are determined by the local sonic speed, $q \propto a(T)$. This result forms the starting point and basis for a similarity theory for supersonic mixing layers. The theory has been described in Zeman (1990b), and the following is its brief summary.

3.1.1 Outline of the similarity theory

In shear layers of practical interest, the turbulent Reynolds number $R_e = u'\ell/\nu$ is sufficiently large so that terms of order $O(R_e^{-1})$ or smaller can be neglected (here, u', ℓ are, respectively, the turbulence velocity and length scales). Furthermore, because the value of the layer growth rate $d\delta/dx$ is a small number (for $M_c > 1$, $d\delta/dx < 0.03$), it is permissible to invoke the thin-layer approximation and the Favre-averaged equations for mean density, velocity, enthalpy, and pressure

$(\rho,\ U_i\ H,\ P)$, then reduce to

$$\frac{\partial \overline{\rho}\widetilde{U}_j}{\partial x_j} = 0 \tag{1}$$

$$\overline{\rho}\widetilde{U}_j\frac{\partial \widetilde{U}_1}{\partial x_j} = -\frac{\partial \overline{\rho u_1 u_2}}{\partial x_2} \tag{2}$$

$$c_p\overline{\rho}\widetilde{U}_j\frac{\partial \widetilde{T}}{\partial x_j} = -\frac{\partial \overline{\rho h u_2}}{\partial x_2}\frac{1}{\gamma} + \rho\epsilon_{tot} - \overline{pu_{j,j}} \tag{3}$$

$$\overline{\rho} = \frac{p_o}{RT + \overline{u_2^2}} \tag{4}$$

The axes $x_1 \equiv x,\ x_2 \equiv y$ are oriented in the streamwise and transverse directions respectively; the factor $1/\gamma$ in (3) stems from absorption of the pressure flux $\overline{pu_2}$ into the enthalpy flux. As shown in Z90, ϵ_{tot} consists of solenoidal and dilatation contributions and can be expressed as $\epsilon_{tot} = \epsilon_s(1 + F(M_t))$. For the purpose of similarity analysis, it is more convenient to deal with energy production; in the turbulence energy budget of mixing layers about 90 percent of the turbulence (shear) production is dissipated; we make a convenient approximation $\rho\epsilon_{tot} - pu_{j,j} \approx -\overline{\rho u_1 u_2}\widetilde{U}_{1,2}$. Seeking the similarity solutions to (1)-(4), we assume possible similarity functions for mean velocity and temperature as follows

$$\widetilde{U}(x,y) = U_c + \Delta U f(\eta) \tag{6}$$

$$\widetilde{T}(x,y) = T_o + \Delta T\theta(\eta) \tag{7}$$

The subscript 'c' designates variables at the mixing layer centerline $y = y_c$; $\eta = (x - y_c)/\delta_\omega$ is the similarity variable where $\delta_\omega = \Delta U/(\partial U/\partial y)_c$, and $\Delta T = T_c - T_o$ is the temperature excess. The appropriate boundary values are $f = 0,\ \theta = 1$ at $\eta = 0$, and $f = 1/2,\ \theta = 0$ at $\eta = \infty$.

Similarity solutions exist only if the differential equations for functions $f(\eta)$ and $\theta(\eta)$ are independent of the parameters of the flow, the Mach number $M = \Delta U/a_o = 2M_c$, and the ratio $\Delta U/U_c$. By scaling argument, it can be inferred from (4)-(8) that

$$\Delta T/T_o = \alpha M^2, \tag{8}$$

where the empirical constant α has been determined from the modeling results as $\alpha \approx 0.05$ (Zeman, 1990a). Finally, assuming that the concept of eddy viscosity (K) and diffusivity (K_h) remains valid in compressible regime, we obtain

$$-\frac{\delta'_\omega U_c}{\Delta U}f'\int_0^\eta \overline{\rho}(1 + \frac{\Delta U}{U_c}f)d\eta = \frac{K_c}{\Delta U\delta_\omega}(\frac{K}{K_c}\overline{\rho}f')', \tag{9}$$

and

$$-\frac{\delta'_\omega U_c}{\Delta U}\theta'\int_0^\eta \overline{\rho}(1 + \frac{\Delta U}{U_c}f)d\eta = \frac{K_c}{\Delta U\delta_\omega}[(\gamma P_{rt})^{-1}(\frac{K}{K_c}\overline{\rho}\theta')' + \beta\overline{\rho}\frac{K}{K_c}(f')^2]. \tag{10}$$

The constant $\beta = \alpha^{-1}R/c_p$ is associated with the heating term in the energy equation (10); this term is responsible for the density variation and coupling of the energy and momentum equations. In view of the similarity analysis, it is important to note that: i) according to the experimental evidence, the growth rate parameter $\delta'_\omega U_c/\Delta U$ appearing in (9) and (10) is dependent on M; ii) the turbulence Reynolds number $R_T = \Delta U \delta_\omega / K_c$ is also a function of M, since by definition

$$R_T^{-1} = \frac{K_c}{\Delta U \delta_\omega} = \frac{u_*^2}{\Delta U^2}, \tag{11}$$

where u_*^2 designates the centerline Reynolds shear stress $-\widetilde{uv}_c$. The ratio $u_*/\Delta U$ decreases with M as shown experimentally by Samimy and Elliott (1990). Without loss of generality, we shall assume that $\Delta U/U_c << 1$ so that this parameter may be eliminated from similarity consideration.

The density $\overline{\rho}/\rho_o = (1+\alpha M^2 \theta(\eta))^{-1}$ cannot be expressed as a similarity function and, therefore, in principle the proposed similarity functions $f(\eta)$, $\theta(\eta)$ do not exist unless $M \to \infty$. However, an approximate similarity will always be possible near the core of the layer where $\theta(\eta) \approx 1$. Then, the standard similarity requirements to be satisfied are

1) Eddy viscosity profiles in (9), (10) be selfsimilar, i.e. $K/K_c = \kappa(\eta)$ and
2) The coefficients in the differential equations (9), (10) be proportional, i.e.

$$C_\delta \equiv \frac{\delta'_\omega U_c}{\Delta U} \propto \frac{1}{R_T} = \frac{u_*^2}{\Delta U^2}, \tag{13}$$

Now, as mentioned earlier, the (centerline) r.m.s. Mach number approaches for $M \geq 3$ a saturation limit $M_{t\infty}$, and all Reynolds stress components must be proportional to the square of the sonic speed a_c; i.e., $\widetilde{u_i u_j}_c \propto u_*^2 \propto a_c^2$ where $a_c = a_o\sqrt{1+\alpha M^2}$. Then, according to (13), we obtain the principal result of the similarity analysis—that the nondimensional growth rate C_δ is related to M through the relation

$$C_\delta \propto \frac{u_*^2}{\Delta U^2} \propto \frac{1+\alpha M^2}{M^2}. \tag{14}$$

A comparison between the parametric formula (14), experiments, and the Z90 model results are shown in Fig. 1. We remark that the experimental growth rates in Fig. 1 are inferred from a momentum or Pitot probe thickness; these, in general, differ from the growth rates based on the vorticity thickness δ_ω. The plots of functions $f(\eta)$, $\theta(\eta)$ (shown in Zeman, 1990b) indicate that both the computed mean temperature and velocity profiles converge to selfsimilar shape for $M \geq 3$. Zeman (1990b) has also shown that the normalized stresses follow the similarity law

$$\frac{\widetilde{u_i u_j}}{\Delta U^2} \propto \frac{1+\alpha M^2}{M^2} g_{ij}(\eta). \tag{15}$$

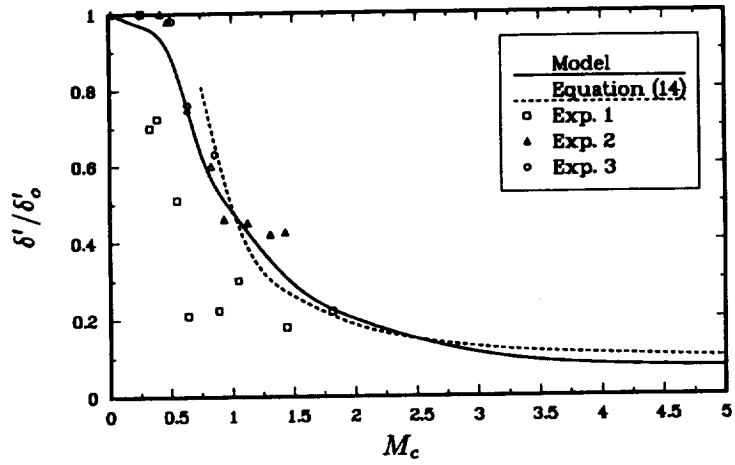

FIGURE 1. Normalized growth rate vs. $M_c = \frac{1}{2}M$. Exp. 1 and 2 denote data from Papamoschou and Roshko (1988), 3 are data of Samimy and Elliott (1990)

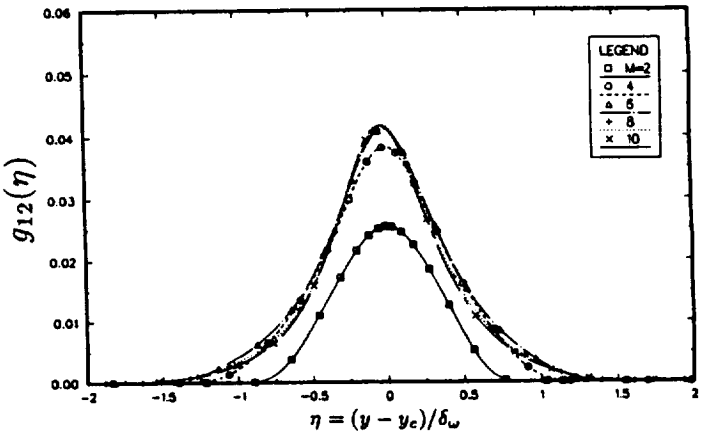

FIGURE 2. Shear stress similarity function $g_{12}(\eta) = -\frac{\widetilde{u_1 u_2}}{\Delta U^2}\frac{M^2}{1+\alpha M^2}$.

The function $g_{12}(\eta)$ corresponding to the shear stress $\widetilde{u_1 u_2}$ is shown in Fig. 2. The function g_{12} is seen to collapse to a self-similar form for $M \geq 4$.

In conclusion, it is evident that although the similarity requirements in compressible mixing layers are incomplete, the proposed similarity laws represented by equations (13)-(15) yield, for all practical purposes, useful estimates of expected temperatures and turbulence quantities in high Mach number shear layers.

3.2. Pressure-dilatation and compressible turbulence decay

It has been shown in Z90 that in the Reynolds stress equations for homogeneous turbulence, one can identify two principal compressible terms: the dilatation dissipation ϵ_d and the pressure-dilatation correlation $\overline{pu_{j,j}}$. In equilibrium mixing layers, the pressure-dilatation was estimated as negligible (Z90); however, in temporally

evolving flows, this is not so, and $\overline{pu_{j,j}}$ has to be considered. For convenience, we shall hereafter use the identity $\overline{pu_{j,j}} = \bar{\rho}\Pi_d$, where Π_d has the same dimension as ϵ_d (rate of energy per unit mass).

The following two findings were described in Zeman (1990c), and in Zeman and Blaisdell (1990). First, considering shockless turbulence, Zeman (1990c) inferred an approximation

$$\Pi_d \approx -\frac{1}{2}\frac{D\overline{p^2}}{Dt}\frac{1}{(\bar{\rho}a)^2}. \tag{16}$$

According to the Blaisdell DNS results, the above approximation is well satisfied at Mach numbers as high as $M_t = 0.7$ both in decaying and shear-driven turbulence (see Fig. 3). Equation (16) is exact in linear acoustics. Second, in order to close (16), Zeman (1990c) suggested that the pressure variance will tend to relax to its equilibrium value (p_e^2) on the time scale (τ_a) associated with the propagation speed of pressure perturbations,

$$\frac{D\overline{p^2}}{Dt} = -\frac{\overline{p^2} - p_e^2}{\tau_a}. \tag{17}$$

By means of scaling arguments, the equilibrium pressure has been related to q^2 and M_t by the parametric relation

$$\frac{p_e^2}{\bar{\rho}^2 q^2 a^2} = P_e(M_t) = \frac{\alpha M_t^2 + \beta M_t^4}{1 + \alpha M_t^2 + \beta M_t^4}. \tag{18}$$

Optimal values of the adjustable constants in (18) are $\alpha = 0.8$, $\beta = 1.0$. Chandrasekhar (1952) showed that the propagation speed of density (or pressure) perturbations in isotropic turbulence is $c = a\sqrt{2 + \frac{2}{3}M_t^2}$, which yields with certain approximations $\tau_a \approx 0.13\tau M_t$. The turbulence time scale is, as usual, related to the solenoidal field, which dominates the turbulence dynamics even in the compressible regime, i.e., $\tau = q^2/\epsilon_s$. Also, the model equation for the solenoidal dissipation ($D\epsilon_s/Dt \propto -\epsilon_s/\tau$) remains independent of compressibility, i.e. of M_t.

A model-DNS comparison of the decay of compressible turbulence with initial $M_{to} = 0.7$ and $(\overline{p^2}/\bar{p}^2)_o = 0.045(\gamma M_{to})^2$, is displayed in Figs. 3 and 4 (see also Zeman and Blaisdell, 1990). Fig. 3 shows the evolution of the pressure dilatation term normalized by the initial (solenoidal) dissipation, Π_d/ϵ_{so}. The evolution time t is normalized by half the initial time scale $\tau_o = (q^2/\epsilon_s)_o$. Fig. 3 also displays the validation of (16): the dashed and dotted lines are, respectively, DNS computed data of the left-, and right-hand sides of (16). Fig. 4 presents a similar graph for the pressure variance normalized by mean pressure. Important properties of the present model are that

1) it is capable of predicting a correct magnitude of Π_d/ϵ_{so} which may vary, depending on initial conditions, by an order of 100 (see Zeman and Blaisdell, 1990);

2) as indicated in Fig. 4, the Π_d-model provides a correct amount of energy transfer to the fluctuating pressure field, including the time scale of the transfer. Overall, although the Π_d-model does not agree with the DNS data in every detail, its integral effect, which dictates the overall energy transfer, is physically correct. Another

example of compressible decay (given in Zeman and Blaisdell, 1990) involves initial conditions when $M_t < 0.1$ is very small but the pressure fluctuation content is high, i.e., $\overline{p^2}/\overline{p}^2 > (\gamma M_t)^2$. In that case, the initial energy transfer is reversed and the potential energy residing in the pressure field is converted into kinetic energy. This causes an initial rapid increase in q^2. Again, the present model is capable of capturing the basic physics of this process.

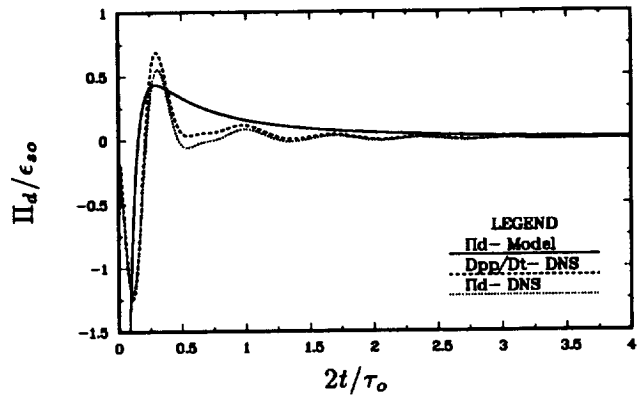

FIGURE 3. Model-DNS comparison: pressure-dilatation evolution.

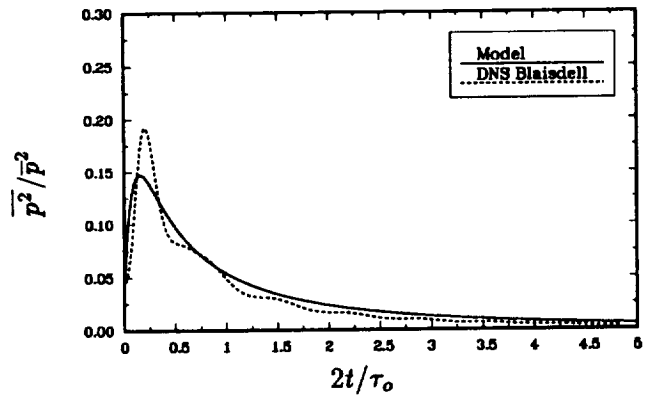

FIGURE 4. Model-DNS comparison: pressure variance evolution.

3.3. Compressible shear turbulence

To the first order approximation, the compressibility terms inferred for decaying turbulence are unaffected by the presence of mean shear, and the pressure-dilatation model outlined in the previous section remains the same for the homogeneous shear turbulence. Furthermore, on the basis of the differential equations for fluctuating pressure, one can argue that the slow and rapid pressure terms in the Favre-averaged setting will retain their incompressible forms so that the direct compressibility contributions in the Reynolds stress equations will be again the dilatation dissipation and pressure dilatation terms.

With the mean shear $dU_1/dx_2 = S$, the actual set of equations needed to compute the (Favre-averaged) stress components $R_{ij} = \overline{\rho u_i u_j}/\overline{\rho} = \widetilde{u_i u_j}$ are (Zeman, 1991)

$$1/2\frac{\partial q^2}{\partial t} = P_s - (\epsilon_s + \epsilon_d - \Pi_d), \tag{19}$$

$$\frac{\partial R_{12}}{\partial t} + C\frac{R_{12}}{\tau} = -0.4R_{22}S, \tag{20}$$

$$\frac{\partial R_{22}}{\partial t} + C\frac{R_{22}}{\tau} = 0.4P_s - \frac{C - 2(1 + (\epsilon_d - \Pi_d)/\epsilon_s)}{3}\epsilon_s, \tag{21}$$

$$\frac{\partial \epsilon_s}{\partial t} = -C_\epsilon\frac{(\epsilon_s - 0.75P_s)}{\tau}, \; \epsilon_d/\epsilon_s = F(M_t). \tag{22}$$

The above equations are based on the Z90 version of a compressible turbulence model. Here the return-to-isotropy constant is $C = 3.25$, $C_\epsilon = 3.7$, $\tau = q^2/\epsilon_s$, and $P_s = -R_{12}S$ is the rate of turbulence production by shear. The closure equations for the dilatation terms Π_d and ϵ_d are as outlined in Section 2.2.

As alluded to in Zeman and Blaisdell (1990) and shown in Figs 5 and 6, the model equations (11)-(14) possess two asymptotic solutions depending on the initial Mach number M_t. If M_t is identically zero, the solution agrees with the incompressible DNS and experimental data (Tavoularis 1985, Rogers *et al.* 1986). The kinetic energy and R_{ij} grow exponentially, i.e. $q^2 \propto R_{ij} \propto exp\{\lambda_o St\}$, and the turbulent time scale approaches a constant value dictated by the shear, i.e. $S\tau \approx 11.7$. If, on the other hand, M_t is initially finite, the model solutions asymptote to a new state characterized by $M_t = M_{t\infty} \approx 0.62$ and $S\tau \approx 7.3$. The energy growth is again exponential but with a smaller growth parameter $\lambda < \lambda_o$. Both the model and DNS data suggest that before the asymptotic state is reached, $\lambda = \lambda(M_t)$ decreases with increasing M_t, although the DNS data exhibit rather different transient behavior due likely to low DNS Reynolds numbers. The model-computed evolutions of M_t shown in Fig. 6 also include DNS data with the initial $M_{to} = 0.4$ (in order to match the initial behavior of the DNS-computed M_t, the model initial value of $S\tau$ was 3 rather than 5.9 used in the DNS computations). The general result of the asymptotic behavior is independent of the form of dilatation dissipation function. For example, using the relation $\epsilon_d/\epsilon_s \approx M_t^2$, the solutions approached almost the same asymptotic state as with the shocklet dissipation assumption. As evident from Fig. 6, the DNS data of M_t do not show any sign of converging toward an asymptote; however, this may be due to the lack of shock wave resolution.

3.3.1 Pressure-dilatation effects in shear turbulence.

The pressure-dilatation Π_d plays, in the shear-turbulence dynamics, an equally important role as ϵ_d, but its effect on turbulence is rather subtle. As turbulence approaches equilibrium (for $St > 5$), the average Π_d becomes a negative constant fraction of the local solenoidal dissipation. The model predicts $\Pi_d/\epsilon_s \approx -0.07$, while the DNS yields a somewhat smaller value (-0.05). The agreement between the DNS and model is surprisingly close considering the fact that in the model Π_d

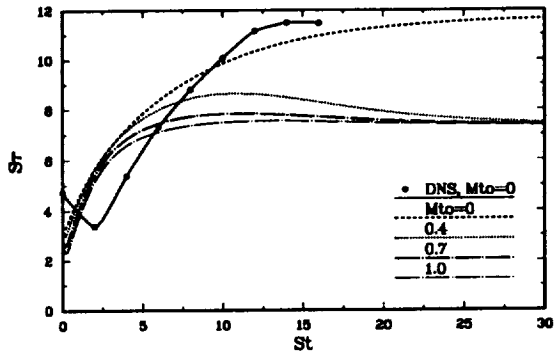

FIGURE 5. Evolution of turbulence time scale in shear turbulence.

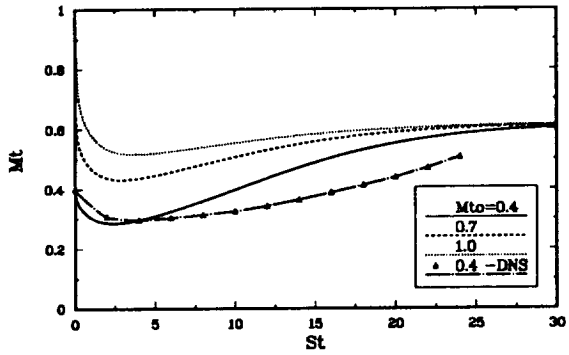

FIGURE 6. Evolution of r.m.s. Mach number M_t.

depends on the subtle difference between the current value of $\overline{p^2}$ and the equilibrium value p_e^2 in the pressure-relaxation model (17). Evidently, $\overline{p^2}$ always lags behind the equilibrium value which is continually growing with q^2 and M_t. Physically this means that as the kinetic energy is produced by shear, a fraction of it is transferred to the potential energy ($\propto \overline{p^2}$). The transfer is mediated by Π_d, and thus in the kinetic energy balance (19), $\Pi_d < 0$ represents a loss of the same order as ϵ_d.

The second, important aspect of the pressure-relaxation model is the capability to predict the pressure variance $\overline{p^2}$. This is demonstrated in Fig. 7, where $\overline{p^2}/\overline{\rho}^2$ is plotted vs. M_t; the cross-hatched area represents the spread of DNS data (Blaisdell, 1990), and full circles are the model results. The model-DNS agreement is satisfactory, and if necessary, further improvement could be made by adjusting the constant α in (18). It is noted that since the acoustic time scale τ_a is small compared with the time scale of evolution, it follows, according to (17), that $|\overline{p^2} - p_e^2|/\overline{\rho}^2 << 1$, and therefore, $\overline{p^2}/\overline{\rho}^2 \approx \gamma^2 M_t^2 P_e(M_t)$. The DNS data favor the M_t^2 -dependence in the equilibrium function P_e in (18).

In view of the above arguments and comparison with the DNS results, it is evident that the combined model for the pressure dilatation and pressure variance (in (17) and (18)) represents the essential physics of compressive-solenoidal field interactions

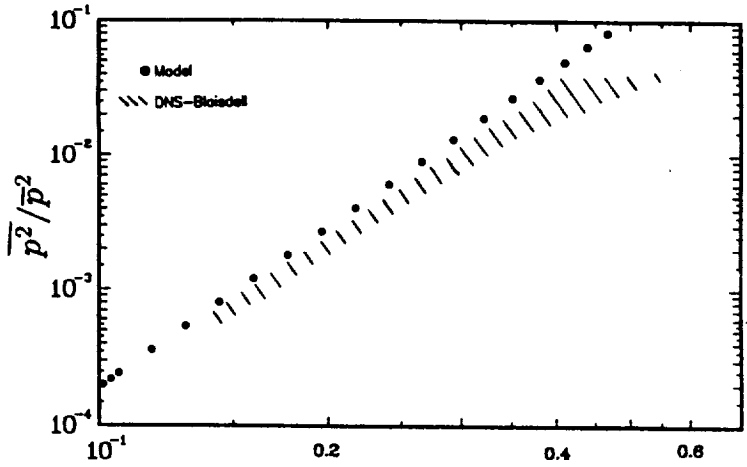

FIGURE 7. Normalized pressure variance in shear turbulence vs M_t.

in quasi-equilibrium shear turbulence.

4. Future plans

We plan to investigate the effect of mean compression (or expansion) on the structure of compressible decaying or shear-driven turbulence. In the presence of nonzero mean divergence $\nabla \cdot \mathbf{U}$, the pressure variance equation will contain a source term, i.e.,

$$\frac{1}{2}\frac{D\overline{p^2}}{Dt} = -(\bar{\rho}a)^2\Pi_d - \overline{p^2}\nabla \cdot \mathbf{U} + \textit{other terms}$$

This suggests that the pressure-dilatation term should have a form

$$\Pi_d = \frac{1}{2(\bar{\rho}a)^2}\left[\frac{\overline{p^2} - p_e^2}{\tau_a} + c_p\overline{p^2}\nabla \cdot \mathbf{U}\right] + \ldots$$

Hence, in analogy with the pressure-strain terms in incompressible turbulence, the first part of Π_d is the return-to-equilibrium term, and the second is a rapid term depending on the mean distortion $\nabla \cdot \mathbf{U}$. In the case of isotropic, homogeneous compression, the process of (rapid) compression can be treated by linear, rapid-distortion theory, and the unknown constant c_p associated with the rapid term in the Π_d-model above can be determined.

The future work will focus on the inhomogeneous rapid compression taking place when turbulence passes through a shock or a succession of shocks. Preliminary results indicate that one-dimensional compression has considerable influence on the structural parameters of shear-maintained turbulence.

REFERENCES

BLAISDELL, G. A. 1990 Numerical simulations of compressible homogeneous turbulence. *Ph. D. Thesis.* Mechanical Engineering Dept., Stanford University.

CHANDRASEKHAR, S. 1952 The fluctuations of density in isotropic turbulence. *Proc. Roy. Soc. A.* **210**, 18.

KOVÁSZNAY, L. S. G. 1953 Turbulence in supersonic flow. *J. Aeronaut. Sci.* **20**, 657.

LEE, S., LELE, S., & MOIN, P. 1990 Eddy-shocklets in decaying compressible turbulence. CTR Report No. 110, Stanford University (to be published in *Phys. Fluids*).

PAPAMOSCHOU, D., & ROSHKO, A. 1988 The compressible turbulent shear layer: an experimental study. *J. Fluid Mech.* **197**, 453.

ROGERS, M. M., MOIN, P., & REYNOLDS, W. C. 1986 Report No. TF-25, Stanford University.

SAMIMY, M. & ELLIOTT, G. S. 1990 The effects of compressibility on the characteristics of free shear layers. *AIAA J.* **28**, 429.

TAVOULARIS, S. 1985 Asymptotic laws for transversely homogeneous turbulent shear flows. *Phys. Fluids.* **28**, 999.

ZEMAN, O. 1990a Dilatation dissipation: The concept and application in modeling compressible mixing layers. *Phys. Fluids A.* **2**, 178.

ZEMAN, O. 1990b Similarity in supersonic mixing layers. submitted to *AIAA J.*

ZEMAN, O. 1990c On the decay of compressible isotropic turbulence. CTR Report No. 115, Stanford University (submitted to *Phys. Fluids*).

ZEMAN, O., & BLAISDELL, G. A. 1990 New physics and models for compressible turbulence. In *Advances of Turbulence 3.* Springer-Verlag.

ZEMAN, O. 1991 Toward a constitutive relation in compressible turbulence. Proceedings of the Lumley's 60th Birthday Symposium.

Single and double point modeling of homogeneous turbulence

By C. Cambon[1]

1. Introduction

Investigations carried out for revisiting homogeneous turbulent flows in the presence of mean shear, rotation, or external compression are summarized in this report. The simplest and most concise RDT (Rapid Distortion Theory) formulation, which includes a comprehensive linear stability analysis, is used for this purpose. Such a linear approach could be extended by a generalized EDQNM (Eddy Damped Quasi-Normal Markovian, Orszag, 1970) to two point closure in order to model non-linear interactions, especially when pure Coriolis effects are present. The results are discussed in connection with databases obtained by DNS (Direct Numerical Simulations), including previous CTR results and new calculations in progress. The main goal is to contribute to and significantly improve on the rational one-point closure models in progress at the CTR and at ECL.

In the case of a mean planar flow, including arbitrary rate of strain and rotation, previous studies suggest that the products of the spanwise (normal to the plane of the mean flow) integral length scales by associated Reynolds stress components $\mathcal{E}^l_{ij} = \overline{u_i u_j} L^l_{ij}$ are relevant quantities to be examined. Such quantities, referred to as *Quasi-2D energy components* are shown to have a very simple behavior in the inviscid RDT limit. Moreover, they play an important role for the study of streaks, or *jet structures*, predicted by Lee, Kim and Moin (1990) in the case of pure shear flows. Simple RDT solutions and non-linear effects exhibited by DNS could be used for developing transport equation models for the spanwise Quasi-2D energy components. The validation of this model will be done in the case of pure rotation (see Jacquin *et al.*, 1990, for example) and pure shear.

More generally, all of these works could support a one-point closure model recently proposed by Reynolds (1989, 1990), which includes transport equations for both the Reynolds stress tensor and the *structure tensor*. This model could complement a proposal by Cambon, Jacquin and Lubrano (1990) based upon splitting the Reynolds stress tensor anisotropy b_{ij} into a part unaffected by the "rapid" background rotation b^e_{ij} and a complementary part b^z_{ij}. The latter was shown to be damped by a strong system rotation.

Additional works concern the non-linear effects of the Coriolis force. New DNS (Mansour, Cambon and Speziale, 1990) are in progress in order to achieve comparisons with the generalized EDQNM model and the experiment (Cambon and Jacquin, 1989, Jacquin *et al.*, 1990). Good agreement is obtained for predicting

1 Ecole Centrale de Lyon (France)

the *non-linear non-isotropic* behavior of the integral length scales in an intermediary range of Rossby numbers (from 0.01 to 1). These results also complement our knowledge of the behavior of the Quasi-2D energy components, mentioned above. Speziale, who is also interested in these studies, proposed, moreover, to revisit the case of pure shear flow in a rotating frame. By looking only at RDT, we selected very simple cases for challenging the one-point closure models. Note that the effects of stable stratification and buoyancy (with or without mean shear) could be studied in the same theoretical framework (Itsweire *et al.*, 1990).

Regarding the theoretical understanding, we hope that the non-linear non-isotropic trends predicted by the EDQNM (in the case of pure rotation) could be retrieved by a more straightforward analysis (deriving a dynamical system) starting from the same expansion in terms of the eigenmodes of the linear regime (inertial waves). Such an approach was successfully used by Waleffe (1989) for studying non-linear stability of the elliptical flows. Moreover, a new experimental approach of *Elliptical flows* but also hyperbolic or linear (pure shear) in progress (Moulin, Leuchter and Geoffroy, 1989) could benefit from the theoretical support by Waleffe and me.

Finally, the effects of an external compression on a *solenoidal* fluctuating velocity field are also revisited by means of RDT. Such a study is relevant for predicting the drop of the cross-correlation coefficient when the turbulent flow passes through a shock wave. Non-isotropic upstream conditions (sheared turbulence) are needed to complement the previous calculations by Lee *et al.* (1991). In the same framework, the interaction between periodic external compression and swirl could lead to comparisons between RDT, DNS and EDQNM, following the stability analysis by Mansour and Lundgren (1990).

2. Formalism

2.1. Fluctuating velocity field

Classic RDT formulations in Fourier space can be made simpler and more general if one considers the initial value problem for the fluctuating velocity and pressure fields and if one reduces the number of components by taking explicitly into account the incompressibility constraint. By decomposing the Fourier mode of the fluctuating velocity field into two solenoidal modes, any RDT solution can be generated by a simple matrix $g_{\alpha\beta}$ with only four coefficients (Cambon, 1982, Cambon *et al.*, 1985).

This approach is also very close to the linear stability analyses using a *time dependent wave vector* $\underline{k}(t)$ (and, therefore, not based upon the classic assumption of space and time separation, the perturbation phase being $\underline{k} \cdot \underline{x} - \sigma t$), proposed in the last years (Craik and Criminale, 1986, Baily, 1986, Waleffe, 1989). It can be pointed out that the strong analogies between stability analyses and RDT are masked if one looks only at statistical quantities. For example, linear solutions of the equation governing the spectral tensor of double correlations were studied at Lyon, following Craya (1958). Craya proposed to use a local frame to reduce the number of components of the spectral tensor of double velocity correlations, but

working with a covariance matrix (the spectral tensor) is more intricate and less general than working with the fluctuating field itself.

Townsend (1976) looked at the fluctuating field, but he did not use a local frame. Similarly, the use of the vorticity field, following Batchelor and Proudman (1954), presents interest only in the case of irrotational mean flows. For more detailed appreciation of RDT application, the reader is referred to the earlier reviews by Hunt (1978), Aupoix (1987) and Cambon (1989). I just would like to recall that a complete approach to homogeneous turbulent flows in the presence of a mean flow with uniform and arbitrary rates of strain and rotation (including a first evidence of the so-called "elliptical flows instability" for unbounded eddies) was carried out in my thesis where RDT and EDQNM were revisited. This general approach (including a numerical code) supports all the studies presented in this report. The formalism is given in what follows.

Let $\hat{u}_i(\underline{k},t)$ be the 3D Fourier transform of the fluctuating velocity field. It is convenient to introduce an orthonormal frame $(\underline{e}^1,\underline{e}^2,\underline{k}/k)$ attached to the wave vector $\underline{k}$, so that

$$\hat{u}_i(\underline{k},t) = \hat{\varphi}^1(\underline{k},t)e_i^1(\underline{k}) + \hat{\varphi}^2(\underline{k},t)e_i^2(\underline{k}) + \hat{\varphi}^3\frac{k_i}{k} \tag{1}$$

In this frame, the Fourier transform of the fluctuating vorticity field is also expressed as

$$\hat{\omega}_i(\underline{k},t) = -Ik\hat{\varphi}^2(\underline{k},t)e_i^1(\underline{k}) + Ik\hat{\varphi}^1(\underline{k},t)e_i^2(\underline{k}) \tag{2}$$

according to its derivation in spectral space

$$\hat{\underline{\omega}} = I\underline{k}\times\hat{u}_i(\underline{k},t) \tag{3}$$

where $k = \|\underline{k}\|$ and $I^2 = -1$.

The component $\hat{\varphi}^3$ along $\underline{k}$ corresponds to the *dilatation part* of the velocity field. It will be neglected in the following, except in subsections 3.3 and 3.4. The two solenoidal modes are orthogonal to each other and located in the plane normal to the wave-vector $\underline{k}$. As the definition of a system of spherical coordinates, the precise characterization of $\underline{e}^1$ and $\underline{e}^2$ requires to choose a preferential fixed axis $\underline{n}$, referred to as the *polar axis*. In accordance with Herring (1974), one has

$$\underline{e}^1 = \frac{\underline{k}\times\underline{n}}{\|\underline{k}\times\underline{n}\|}; \quad \underline{e}^2 = \frac{\underline{k}}{k}\times\underline{e}^1 \tag{4}$$

The first mode corresponds to the solenoidal part of the transverse planar flow (i.e. normal to $\underline{n}$), and the second one collects both the axial velocity (i.e. parallel to $\underline{n}$) and the residual (dilatation) part of the planar field. From equations (1), (2), and (4), it is clear that

$$\hat{\omega}_{\|} = -Ik_{\perp}\hat{\varphi}^1$$

$$\hat{u}_{\|} = -\frac{k_{\perp}}{k}\hat{\varphi}^2$$

(the notations $v_{\|} = v_i.n_i$ and $v_{\perp} = \sqrt{v^2 - v_{\|}^2}$ being systematically used). In accordance with the above equations and the terminology used by Reynolds, the first solenoidal mode $\hat{\varphi}^1 \underline{e}^1$ could be christened *axial vortical mode* and the second one $\hat{\varphi}^2 \underline{e}^2$, *axial jet mode*. Note that such a decomposition is current in geophysical turbulence (Riley (1981)) but is always considered from a very specific point of view (not as a general and convenient mathematical basis for any solenoidal velocity field!).

Regarding the homogeneous incompressible turbulence in the presence of uniform mean velocity gradients $\lambda_{ij} = \overline{U}_{i,j}$, the velocity field is governed by the following system of equations:

$$\begin{pmatrix} \dot{\hat{\varphi}}^1 \\ \dot{\hat{\varphi}}^2 \end{pmatrix} + \nu k^2 \begin{pmatrix} \hat{\varphi}^1 \\ \hat{\varphi}^2 \end{pmatrix} + \begin{pmatrix} e_i^1 \lambda_{ij} e_j^1 & e_i^1 (\lambda_{ij} - \lambda_{ji}) e_j^2 \\ 2 e_i^2 \lambda_{ij} e_j^1 & e_i^2 \lambda_{ij} e_j^2 \end{pmatrix} \begin{pmatrix} \hat{\varphi}^1 \\ \hat{\varphi}^2 \end{pmatrix} = \begin{pmatrix} R^1 \\ R^2 \end{pmatrix} \quad (5)$$

or

$$\dot{\hat{\varphi}}^{\alpha} + \nu k^2 \hat{\varphi}^{\alpha} + m_{\alpha\beta} \hat{\varphi}^{\beta} = R^{\alpha}$$

(Greek indices taking the value 1 or 2 only) in which R^{α} are non-linear terms. The superimposed dot represents a material derivative, so that

$$\dot{k}_i + \lambda_{ji} k_j = 0 \quad (6)$$

The solution of the latter equation is

$$k_i = F_{ji}^{-1}(t,0) K_j = 0$$

in which the role of the mean distortion gradient tensor

$$F_{ij}(t,0) = \frac{\partial x_i}{\partial X_j} \quad (7)$$

$$F_{ij}(0,0) = \delta_{ij}$$

is clearly displayed. Recall that the mean trajectories in physical and in spectral space are respectively

$$x_i = F_{ij} X_j \quad ; k_i = F_{ji}^{-1} K_j$$

so that $k_i x_i = K_i X_i$ (wave conservation law). Capital letters stand for material coordinates of the mean flow (also called Rogallo's space). In the case of RDT, the relation $l_i(t) = F_{ij}(t,0) l_j(0)$ allows calculation of the deviatoric tensor $\delta_{ij}/3 - l_i l_j / l^2$ proposed by Reynolds(1990) as a model for the deviatoric part of the structure tensor y_{ij}.

Solving equations (5) with $R^{\alpha} = 0$ is the simplest and the most general way for obtaining RDT. Non-linear terms can be reintroduced *in a statistical way* by a convenient two point closure. For the record, the formal solution of equation (5) is given as follows:

$$\hat{\varphi}^{\alpha}(\underline{k},t) = g_{\alpha\beta}(\underline{k},t,0) \hat{\varphi}^{\beta}[\underline{\tilde{F}}(t,0).\underline{k}, \quad 0] + \int_0^t g_{\alpha\beta}(\underline{k},t,t') R^{\beta}[\underline{\tilde{F}}(t,t').\underline{k}, \quad t'] dt' \quad (8)$$

where $\tilde{F}_{ij} = F_{ji}$. Linear as well as non-linear approaches start from equation (8). The matrix $g_{\alpha\beta}$ generates the basic linear solution (first term in the right hand side of (8)) and is also involved if an *explicit form of the non-linear terms* is given (second term in the right hand side).

2.1 Statistical approach

The spectral tensor of double correlation $\hat{U}_{ij}(\underline{K},t)$ is obtained by correlating $\hat{u}_i^*$ with $\hat{u}_j$. In the local frame $(\underline{e}^1,\underline{e}^2,\underline{k}/k)$, it has only four non-zero components in the case of incompressible turbulence. These four components $\Phi^{\alpha\beta}$ correspond to $\overline{\hat{\varphi}^{\alpha *}.\hat{\varphi}^{\beta}}$. Regarding the reduced spectral tensor at fixed $\underline{k}$, in the local frame $(\underline{e}^1,\underline{e}^2)$, the anisotropy is accurately characterized by using a set of variables (e,Z).

$$\begin{pmatrix} \Phi^{11} & \Phi^{12} \\ \Phi^{12*} & \Phi^{22} \end{pmatrix} = \begin{pmatrix} e & 0 \\ 0 & e \end{pmatrix} + \begin{pmatrix} -\Re eZ & \Im mZ \\ \Im mZ & +\Re eZ \end{pmatrix} \tag{9}$$

(Z is a complex term, having a real and an imaginary part). This decomposition of type trace-deviator exhibits the invariants of the spectral tensor (namely e and $\|Z\|$, with the *unique* realizability constraint $e > \|Z\|$). Moreover, a very simple expression of $\hat{U}_{ij}$ is found in the *fixed frame of reference*

$$\hat{U}_{ij}(\underline{k},t) = e(\underline{k},t).P_{ij}(\underline{k}) + \Re e[Z(\underline{k},t)N_i(\underline{k})N_j(\underline{k})] \tag{10}$$

Recall that $e = \frac{1}{2}\hat{U}_{ii}$ and $P_{ij} = \delta_{ij} - k_ik_j/k^2$ is the classic projector. One also has

$$Z = \frac{1}{2}\hat{U}_{ij}N_i^*N_j^*; \quad \underline{N} = \underline{e}^2 - I\underline{e}^1 \tag{11}$$

If the turbulence is isotropic, Z is null everywhere and e is only dependent on the modulus of $\underline{k}$. By reintroducing the averaged energy spectrum $E(k,t)$ (integral of e over spherical shells of radius k), it is now possible to distinguish two kinds of anisotropy

$$\hat{U}_{ij} = \frac{E}{4\pi k^2}P_{ij} + (e - \frac{E}{4\pi k^2})P_{ij} + \Re e(ZN_iN_j) \tag{12}$$

Regarding the three terms in the right hand side, the first one is the pure isotropic part, the second represents the anisotropy due to the angular dependence of the spectral distribution of energy, and the third reflects the polarization of this energy at fixed $\underline{k}$. Any one point correlation could be calculated in terms of these three contributions. So the Reynolds stress tensor is obtained by an integral of the spectral tensor over $\underline{k}$-space.

$$\overline{u_iu_j}(t) = \int\int\int \hat{U}_{ij}(\underline{k},t)d^3\underline{k}$$

From equation (12), a decomposition into three terms is easily derived,

$$\overline{u_iu_j} = \overline{q^2}(\frac{\delta_{ij}}{3} + b_{ij}^e + b_{ij}^z) \tag{13}$$

The deviatoric part b_{ij} of the Reynolds stress tensor is, therefore, split into two parts. b^e_{ij} reflects the *dimensionality* of the spectral tensor and b^z_{ij} reflects its *componentiality*. In accordance with equation (12) and with the spectral derivation of the structure tensor Y_{ij} used by Reynolds (1989), the following exact relation is found:

$$\overline{q^2} b^e_{ij} = -\frac{1}{2}(Y_{ij} - Y_{ll}\frac{\delta_{ij}}{3}) = -\frac{\overline{q^2}}{2} y_{ij} \tag{14}$$

Note that the structure tensor is also connected with the structure of the vorticity field. From equations (2) and (11) it is possible to derive a splitting equivalent to (14) for the vorticity correlations tensor $\overline{\omega_i \omega_j}$ *by only changing* e *into* $k^2 e$ *and* Z *into* $-k^2 Z$.

Finally, the Quasi-2D energy components are given by integration over a plane

$$\mathcal{E}^l_{ij} = \overline{u_i u_j} L^l_{ij} = \pi \int\int \hat{U}_{ij} \mid_{k_l=0} d^2\underline{k} \tag{15}$$

The two indices i and j, which refer to the components of the velocity fluctuation, are not summed, whereas l shows in what direction the integral length scale L^l_{ij} is calculated. As for the velocity and vorticity correlations tensor, a splitting in terms of e and Z can be found,*but the distribution in the wave plane* $k_l = 0$ *is only emphasized.*

From the equation which governs $\hat{U}_{ij}$ (usually referred to as Craya's equation), it is possible to derive an equation for the set (e, Z). The same result is more easily obtained from equation (5) and leads to

$$\dot{e} + 2\nu k^2 e + L_e = T_e$$

$$\dot{Z} + 2\nu k^2 Z + L_z = T_z \tag{16}$$

The detailed form of the linear terms L_e and L_z with respect to e, Z and Z^* (derived from $m_{\alpha\beta}$ in (5)) is not given for the sake of brevity. T_e and T_z represent spectral transfer terms (including also "slow" pressure effects) mediated by non-linear interactions.

3. Revisiting homogeneous shear flows

3.1 Behavior of the integral length scales

It is possible to show with the formalism presented in Section 2 that the products of the spanwise integral length scales by associated Reynolds stress components (see equation (15)) are conserved in the inviscid RDT limit for any planar mean flow, provided that the initial data are isotropic. These 2-D energy components

$$\mathcal{E}^3_{ij} = \overline{u_i u_j} L^3_{ij} = \text{ constant}$$

(where 3 corresponds to the spanwise direction) are derived from the spectral tensor of double correlations by integrating in the plane, $k_3 = 0$, in which no effect of

stretching by the mean flow is found. Recall that the incompressible planar mean flow is characterized by the following velocity gradient matrix (Craya, 1958):

$$\overline{U}_{i,j} = \lambda_{ij} = \begin{pmatrix} 0 & D+\Omega & 0 \\ D-\Omega & 0 & 0 \\ 0 & 0 & 0 \end{pmatrix} \tag{17}$$

In the case of a pure shear $D = \Omega = S/2$, a simple solution is also found for the streamwise quantities, which display the spectral distribution at $k_1 = 0$.

$$\mathcal{E}^1_{11}(t) = \overline{u_1 u_1}(t) L^1_{11}(t) = (1 + \frac{(St)^2}{2}) \frac{\overline{q}^2}{3}(0) L^1_{11}(0)$$

$$\mathcal{E}^1_{ii}(t) = \overline{u_i u_i}(t) L^1_{ii}(t) = \text{ constant}; \qquad i = 2,\ 3$$

Thus the increase in the component $\overline{u_1^2}$ with a quasi-linear law (for large St) corresponds to a decrease in L^3_{11} and an increase in L^1_{11} in the same proportion. The appearance of jet structures–or streaks–in the streamwise direction with a decreasing distance in the spanwise direction can be connected to these simple RDT solutions. Indeed, one can assume that L^1_{11} gives the length of the streaks (in the streamwise direction) and that L^3_{11} gives the distance across the streaks (in the spanwise direction). The DNS databases by Moon Lee (Lee, Kim and Moin, 1990) are in very good agreement with the RDT behavior of the streamwise quantities $\mathcal{E}^1_{ij}$ in the case of high shear rate.

Regarding the spanwise quantities at high shear rate $\mathcal{E}^3_{ij}$, a significant increase is found for $\overline{u_1 u_1} L^3_{11}$, whereas $\overline{u_3 u_3} L^3_{33}$ remains almost constant. Recall that both these terms are constant in RDT with isotropic initial data, where $\mathcal{E}^3_{11} = \frac{1}{2}\mathcal{E}^3_{33}$. The different behavior of $\mathcal{E}^3_{11}$ observed in DNS leads to a crossover of the two former quantities ($\mathcal{E}^3_{11} > \mathcal{E}^3_{33}$) about $St = 7$. Such a crossover is also observed in a low shear rate case, although a strong decrease in the $\mathcal{E}^3_{ij}$ prevails at the beginning of the evolution. The significant departure from isotropy (valid for very low shear rapidity) and RDT (valid for very high shear rapidity) presents a strong analogy with the non-linear non-isotropic behavior predicted for an intermediary range of Rossby numbers in the case of pure rotation. So a transport equation for the spanwise quasi-2D energy components is in progress. The closure model for non-isotropic non-linear terms in the transport equations for $\mathcal{E}^3_{ij}$ could be validated in pure shear and pure rotation. Note that the total transverse (with respect to the direction of the rotation axis, and thus spanwise) energy

$$\mathcal{E}^3_{\perp} = \pi \int\int \Phi^{11} \mid_{k_3=0} dk_1 dk_2 = \overline{u_1 u_1} L^3_{11} + \overline{u_2 u_2} L^3_{22}$$

displays exactly the contribution of the transverse mode of energy in the wave-plane normal to the mean rotation axis, which plays an essential role in the theoretical and experimental approach by Jacquin *et al.* (1990). Recall that the spectral energy is concentrated in $\Phi^{11} \mid_{k_\parallel=0}$ in the case of pure 2D turbulence.

3.2. Shear flow in a rotating frame

This case presents a particular interest in turbomachinery. It questions the current one-point closure models, which are almost exclusively sensitive to the Richardson number. Recall that the stability analysis in terms of the Richardson number ignores the complex redistribution effects of the pressure. Previous RDT calculations (for example Bertoglio, 1981) and DNS show that the Richardson number is not the uniquely relevant parameter, even for predicting the evolution of the turbulent kinetic energy. So C. Speziale proposed to revisit RDT, EDQNM, DNS, especially in order to compare different ratios $r = \Omega/S$ (i. e. rotation rate divided by shear rate) which give the *same* Richardson number $2r(1-2r)$.

A first investigation of the two coupled equations which govern the two incompressible modes for two different ratios r_1 and r_2 with $r_1 + r_2 = \frac{1}{2}$ clearly shows that the role of the"vortical" mode seems to be interchanged with the role of the"jet" mode (when changing r to $(\frac{1}{2} - r)$. Simpler equations are found by choosing the polar axis in the vertical direction, or $n_i = \delta_{i2}$, although the mean vorticity is in the spanwise direction. The vortical mode under consideration is, therefore, a *vertical* mode. Equation (5) leads to

$$\dot{\hat{\varphi}}^1 + (S - 2\Omega)\frac{k_3}{k}\hat{\varphi}^2 = 0 \tag{17.1}$$

$$(k\dot{\hat{\varphi}}^2) + 2\Omega k_3 \hat{\varphi}^1 = 0 \tag{17.2}$$

in the linear inviscid limit. The role of r is clearer by working with the dimensionless time St. A single second order equation is easily found

$$(k\ddot{\hat{\varphi}}^2) - 2\Omega(S - 2\Omega)(\frac{k_3}{k})^2(k\hat{\varphi}^2) = 0$$

Although the Richardson number seems to be the unique parameter in the latter equation, the individual role of the two solenoidal modes must be taken into account in the complete linear solution. These effects are particularly simple in the "marginal stability case" $Ri = 0$; for $r = 0$, the case of pure shear in an inertial frame is retrieved. The other "symmetric" case with $r = 1/2$ corresponds to a pure strain, the principal axes of which are being continuously rotated, when looking at the inertial frame, in which the total mean vorticity is null. As a consequence, the RDT solution for the fluctuating vorticity is an incredibly simple Cauchy solution

$$\omega_i(\underline{x}, t) = F_{ij}(t, 0)\omega_j(\underline{X}, 0)$$

in the case $r = 1/2$. Detailed solution of equations (17) also show that the increase in turbulent kinetic energy is stronger in the case of $r = 1/2$ than in the case of pure shear flow. Moreover, the structure of the vorticity correlations tensor is very different in the two cases. The increase in the turbulent vorticity (in $(St)^2$) is also stronger in the case $r = 1/2$. These results could explain why a DNS carried out by Rogallo seems to indicate opposite behavior with respect to RDT (a stronger increase in kinetic energy in the case $r = 0$ than in the case $r = 1/2$). Indeed, if the rapidity of the shear is not large enough, the increase in the turbulent vorticity, which strongly affects the dissipative scales, can significantly counterbalance the production of kinetic energy.

3.3. Stratified turbulence in the presence of shear

If we consider the framework of Boussinesq approximation and homogeneity, a complete analogy could be found with the former case. By taking into account the two previous incompressible modes of the fluctuating velocity field and by adding a pseudo-compressible mode connected to the fluctuating temperature θ (along the wave-vector) in eqn. (5),

$$\hat{\varphi^3} = \frac{\beta g}{N}\hat{\theta},$$

the RDT and EDQNM formalism are almost unchanged with respect to the flows in presence of system rotation (see Cambon, 1989). This approach suggests revisiting the databases by Holt (1990) in the same way.

Without shear, the straightforward study of linear and non-linear effects of the dispersive gravity waves very close to the inertial waves could lead to improve both the physical understanding and the modeling of stably stratified flows. Note that only vague and unconvincing considerations about the "collapse" were derived from the more recent DNS, or LES in this case. (see Metais and Lesieur, 1990).

If a mean vertical shear is also present, the unique difference with the case of shear in a rotating frame is that the Richardson number takes into account the ratio $r = N/S$ in a monotonic form, $Ri = r^2$. N is the Brumt-Waisala frequency, which plays the same role as 2Ω.

3.4. Towards compressible turbulent shear flows

The shear flow is one of the cases with constant mean velocity gradients, which is consistent with the homogeneity of a compressible fluctuating field. Recall that the skew part of the tensor $\lambda_{ij} + \lambda_{il}\lambda_{lj}$ must be zero in incompressible turbulence. Verifying such a condition is equivalent to following the Helmholtz equation for the mean vorticity. Moreover, the symmetric part must also vanish in the compressible case in order to eliminate the position-dependent term $\rho'(\dot{\lambda}_{ij} + \lambda_{il}\lambda_{lj})x_j$ in the equation governing the fluctuating velocity field u_i. ρ' is the density fluctuation. The databases of G. Blaisdell suggest considering a "true" dilatation term in the fluctuating velocity field and suggest looking at the associated new terms in the spectral tensor. In the local orthonormal frame $(e_i^1,\ e_i^2,\ e_i^3 = k_i/k)$, the general decomposition (1) into three orthogonal modes is applied (including the axial vortical mode, the axial jet mode, and the dilatation mode).

Regarding the spectral tensor (or the covariance matrix) *in the same frame*, we are concerned with six components ($\Phi^{ij} \quad i \leq j \leq 3$). The components $\Phi^{\alpha\beta}$ associated with the solenoidal part are collected into a solenoidal 3-D energy spectrum $e^s(\underline{k},\ t)$ and a deviator $Z^s(\underline{k},\ t)$, as previously (equation (10)). Three new components correspond to a dilatation 3-D energy spectrum, $e^d(\underline{k},\ t) = \frac{1}{2}\Phi^{33}$ and two cross-correlations $\Phi^{\alpha 3}$ between the dilatation mode and the solenoidal modes. As a first assumption, the contribution of these cross-correlations are neglected in the one point correlations. Damping effects of the acoustic waves could be invoked in accordance with the behavior of the integrals

$$f(ct) = \int_0^\infty h(k)\exp(\pm Ikct)dk$$

for large values of ct (c is the speed of sound). Accordingly, a generalized splitting of the Reynolds stress tensor is easily obtained:

$$\overline{u_i u_j} = q^{2s}\frac{\delta_{ij}}{3} + q^{2s}(b_{ij}^{es} + b_{ij}^{zs}) + Y_{ij}^{d}$$

where b_{ij}^{es} is exactly minus half the deviatoric part of the structure tensor introduced by Reynolds (y_{ij}), and Y_{ij}^{d} is exactly the structure tensor associated with the dilatation part of the energy spectrum.

$$Y_{ij}^{d} = \int\int\int 2e^{d}(\underline{k},t)\frac{k_i k_j}{k^2}d^3\underline{k}; \qquad e^{d} = \frac{1}{2}\hat{U}_{ln}\frac{k_l k_n}{k^2}$$

If one assumes that the solenoidal field evolves almost independently on the dilatation one, one can keep unchanged closed equations for the quantities with "s" and only add a new equation for Y_{ij}^{d}. DNS databases available at the CTR could be used to validate such a model.

4. Revisiting non-linear non-isotropic effects of pure rotation

The linear effects of the Coriolis force are easily characterized by looking at equations (5) and (16). The polar axis is now chosen to coincide with the system rotation axis ($n_i = \delta_{i3} = \Omega_i/\Omega$). Regarding the fluctuating field, linear combinations of the dependent variables in eqn. (5), $\hat{\varphi^1} \pm I\hat{\varphi^2}$, lead to a diagonal form of the matrix $m_{\alpha\beta}$, which exhibits the two eigenvalues $\pm 2I\Omega k_{\|}/k$. It is, therefore, very simple to work with the eigenmodes of the inertial waves. Recall that the eigenpulsation

$$\sigma(\underline{k},t) = 2\Omega\frac{k_{\|}}{k}$$

gives the dispersion relation. Regarding double correlations, e and Z correspond to quadratic products of the eigenmodes. In equation (16), $L_e = 0$ and $L_z = 2I\sigma$. The linear solution of equation (16) is, therefore,

$$e(\underline{k},t) = e(\underline{k},0)\exp(-2\nu k^2 t); \quad Z(\underline{k},t) = Z(\underline{k},0)\exp(4I\Omega t\frac{k_{\|}}{k})\exp(-2\nu k^2 t) \quad (18)$$

As a consequence, the quantities involving e, such as $\overline{q^2}$ and b_{ij}^{e}, are unaffected by a rapid rotation. This fact reflects that the Coriolis force produces no energy. The quantities involving Z in a 3D integral, such as b_{ij}^{z}, are damped in accordance with the behavior of the integral

$$f(\Omega t) = \int_{-1}^{1} h(\mu)\exp(4I\Omega t\mu)d\mu$$

for large values of Ωt. This fact reflects the *angular dispersivity* (influence of $\mu = k_{\|}/k$) of the inertial waves, and is called "phase-randomization" by Reynolds.

Nevertheless, the quantities which involve Z in the wave-plane $k_\parallel = 0$, such as $\mathcal{E}^3_{ij}$, are not affected by the linear Coriolis effects. These linear effects are now well known (see also Veeravalli, 1989).

Non-linear effects are reflected by T_e and T_z in the system of equations (16). The influence of the rotation on these terms is crucial for predicting the behavior of an initially isotropic turbulence. Indeed, the linear terms are null, at least in a preliminary phase. The generalized EDQNM model used by Cambon and Jacquin (1989) (for closing T_e and T_z) predicted very spectacular non-isotropic behavior of the integral length scales in agreement with results from experiment and DNS (Roy and Dang, 1985). Non-isotropic features in physical and spectral space began to be verified by 128^3 DNS (Teissedre and Dang, 1987). New DNS are in progress at the CTR in order to complement this information. The most important anisotropy criterion is chosen to be,

$$\mathcal{A} = \mathcal{E}^3_{33} - (\mathcal{E}^3_{11} + \mathcal{E}^3_{22}) = \overline{u^2_\parallel} L_\parallel - 2\overline{u^2_\perp} L_\perp \tag{19}$$

A dimensionless form could also be proposed by using $\overline{q^2} L_0$. Regarding the Reynolds stress tensor, the axisymmetric trend is quantified by

$$\mathcal{B} = \overline{u_3^2} - \frac{1}{2}(\overline{u_1^2} + \overline{u_2^2}) = (\overline{u_\parallel^2} - \overline{u_\perp^2}) = \frac{3}{2}\overline{q^2} b_{33} \tag{20}$$

The spectral derivation also leads us to separate the two contributions of the latter criterion, according to $\mathcal{B}/\overline{q^2} = \frac{3}{2}(b^e_{33} + b^z_{33})$.

Now, it is easy to explain why the anisotropic features occur only for an *intermediary* range of Rossby numbers. -If the Rossby number is too large, the specific effect of rotation is weak and the initially isotropic behavior prevails. -If the Rossby number is too small, the non-linear effects are assumed to be weak (in relative value, with respect to the linear ones), but the true feature is that the rotation tends to inhibit the level (in *absolute* value) of triple correlation. The phase scrambling of *cubic* products of fluctuating velocity components gives the simplest explanation of this phenomenon. So a regime of pure viscous RDT is obtained. Hence, an isotropic behavior is again retrieved. Previous DNS by Speziale, Mansour & Rogallo (1987) confirms these results at very low Rossby number.

The best indicator of the peculiar anisotropy, generated by non-linear interactions, is $\mathcal{A}$. This criterion, which is rigorously null in the isotropic case, is unaffected in any case by linear (RDT) Coriolis effects because it involves only the polarization part of the spectral energy Z in the transverse wave-plane ($\underline{k}$ normal to $\underline{\Omega}$). Considering Rossby number built on the axial integral length scale L^3_{33}, the new DNS by Mansour *et al.* 1990 predicts that the criterion is weak for initial Rossby numbers larger than the unity or smaller than 0.01. A maximum is found to be about 0.1. The upper limit of the intermediary range (about 1) is in good agreement with the experimental and EDQNM results (Cambon and Jacquin (1989), Jacquin *et al.* (1990)). The capture of the lower limit by DNS is also a surprisingly good result, regarding the risk of numerical inaccuracies (especially on the lengthscales) in the case of very strong rotation rates.

The DNS and the EDQNM (new computations carried out at the CTR) are also in agreement in predicting the rise of a *weak but significant axisymmetry of the Reynolds stress tensor, only due to the contribution of the structure tensor.* By using Reynolds' notations, it is found that

$$b_{33} = -\frac{1}{2}y_{33} > 0$$

This tendency corresponds to a relative concentration of the spectral energy in the transverse wave-plane. Unfortunately, it is weak, especially when looking at the classic invariants of b_{ij} (quadratic and cubic). The order of magnitude of the difference between the axial and a transverse component of the Reynolds stress tensor ($\mathcal{B}$ indicator) is no larger than 5 per cent of the trace (or $\frac{3}{2}b_{33} = 0.05$). Nevertheless, the different anisotropic trends remain consistent with the first phase of a transition towards two-dimensionality in accordance with our previous theoretical analyses. Regarding physical interpretation, the rise of a positive value for b^e_{33}, which reflects a preferential concentration of e in the wave-plane $k_\parallel = 0$, corresponds to a decrease in the axial variability $\partial/\partial x_\parallel \searrow$. Such a trend is often deduced from the Proudman-Taylor theorem, but one recalls that this theorem was proposed in the zero Rossby number limit. Although the exact RDT contradicts this theorem (and the dogma that a strong rotation makes two-dimensional any turbulent flow), weak but significant non-linear terms (and possibly boundary conditions) are able to reduce the axial variability, in agreement with the rise of columnar structures.

Moreover, the strong negative value of $\mathcal{A}$ indicates a polarization of the spectral energy in the more energetic wave-plane $k_\parallel = 0$. Accordingly, the axial vortical mode is found to dominate in this plane at least in the low wave-numbers range.

Both of these trends contribute to align the turbulent vortices with the system rotation axis, but they are not in agreement with the decrease in the axial velocity ($u_\parallel \searrow$). (See Cambon, 1990, for a more detailed analysis of the 2D tendencies in MHD, rotated, and stably stratified turbulence). During the evolution, the constant decrease of the Rossby number and the increasing action of the viscous effects tend to block these transient mechanisms. Accordingly, I think that only a very high Reynolds number and the presence of a forcing term (in the wave vectors range $k_\parallel = 0, \quad k < k_0$) would lead to complete transition towards 2D in the intermediary range of Rossby numbers.

5. Solenoidal turbulence undergoing external compression

5.1. Contribution to a study of boundary layer-shock wave interaction

A first approach of the effects of a strong one-dimensional compression on a non-isotropic turbulence was carried out by using a solenoidal homogeneous RDT. The upstream conditions are built by a preliminary application of a pure shear, so that an important cross-correlation coefficient (between u_1 and u_2) is created. The shock is then considered as a strong compression in the streamwise direction. The RDT solution shows a strong decrease of the absolute value of the cross-correlation coefficient and even a change of sign. If the "rapid" pressure-rate of strain correlations

are ignored or badly modeled (as in a current Reynolds stress model), this coefficient is conserved. Note that a new model, that includes the structure tensor of W. C. Reynolds, is in good agreement with RDT in this case. Regarding the role of the cross correlations in the balance of kinetic energy in a boundary layer, it is obvious that this mechanism must be correctly predicted. The idea of this RDT calculation was prompted by Mathieu (private communication), regarding experimental results obtained at ONERA.

5.2. Periodic compression with swirl

The validity of a solenoidal model in the presence of a strongly compressed mean flow requires moderate values of the "turbulent" Mach numbers. A previous analysis of Mansour justifies this framework of assumptions which is implicitly used in most of the turbulence models for reciprocating engines. Following a recent summer workshop at Lyon (Pepit workshop, July 1989), a particular emphasis is made in my laboratory about the interactions between external compression and rotation, so the stability analysis by Mansour and Lundgren (1990) is of great interest. The parameters are the ratio of the swirl rate to the period of the coaxial compression. An instability behavior is shown in narrow domains of angular dependence (in wave-space). First RDT calculations with a code based upon equations (5) (see the following section) and a DNS code (Mansour), in which the non-linear terms are omitted, seem to validate each other.

6. Towards a general one-point closure model

A very good agreement in the guidelines is found when one compares recent progress in the modeling of turbulent flows in the presence of rotation carried out in France (Jacquin *et al.*, Cambon *et al.*, 1990) with the works of the CTR, especially by W. C. Reynolds and S. Kassinos. The idea of introducing two contributions of the Reynolds stress tensor anisotropy, according to eqn. (13), leads to exactly the same amount of information that the use of the structure tensor together with the Reynolds stress tensor provides.

The validation in homogeneous turbulence of the most general model, recently proposed by Reynolds, could be made with the support of the numerical code "Thanatos", which could provide the spectra of the terms involved in the new single point closure model. This code takes into account any mean velocity gradient matrix, with possible time dependency and external compression, and solves the solenoidal RDT problem (time advancing eqn. (5) using a Runge-Kutta high order scheme). An EDQNM model using a parameterization of T_ϵ and T_z (eqn. (16)) in terms of angular harmonics is included but not yet completely validated.

Specific EDQNM models used for studying non-linear interactions of internal waves in sections 3.3 and 4 (pure rotation or stable stratification) are more complicated, although they are restricted to quasi axisymmetric turbulence. They do not use parameterization of angular dependence, and they are too expansive (in computational time) and too cumbersome to handle to be implemented in the general case.

Note that the specific expansion in terms of angular harmonics is used in eqn.(16) only for decomposing the general transfer terms T_e and T_z, in accordance with a 3D EDQNM formulation. It involves spherical coefficients (depending only on the modulus of the wave vector) of e and Z, which easily generates the spectra of both the structure tensor and the Reynolds stress tensor.

We hope that the use of two anisotropy tensors, namely $b^e_{ij} = -\frac{1}{2}y_{ij}$ and $b^z_{ij} = b_{ij} + \frac{1}{2}y_{ij}$, will improve the classic single point closure models, in which b_{ij} is used as the only anisotropy indicator. Regarding only RDT, the classic procedure leads to a connection between the rapid part of the pressure-rate of strain correlations and the production terms in the balance of the Reynolds stress tensor. It is questioned in the presence of system rotation, or more generally by the effect of any body forces generating waves (such as the buoyancy forces), and even in the case of pure straining processes applied to initial data influenced by rotation (as in section 5.1).

REFERENCES

AUPOIX B. 1987 Homogeneous turbulence. Two point closures and applications to one point closures. *AGARD-FDP-VKI.* Lecture series.

BAILY, B. J. 1986 *Phys. Rev. Lett.* **57**, 2160.

BERTOGLIO, J. P. 1982 Homogeneous turbulent field within a rotating frame. *AIAA 80-1353.*

CAMBON, C. 1982 Etude d'une turbulence homogene, soumise a des effets couples de rotation et de deformation. These de doctorat *es sciences.* Universite de Lyon.

CAMBON, C. 1989-a Spectral approach to axisymmetric turbulence in a stratified fluid. *Advances in turbulence 2.* Edited by H. H. Fernholtz and H. E. Fiedler. Springer Verlag.

CAMBON, C. 1989-b Linear spectral approach to turbulence subjected to mean velocity gradients and body forces: towards one and two point closures. PEPIT-ERCOFTAC summer workshop. Lyon (France).

CAMBON, C. 1990 Homogeneous MHD turbulence at weak magnetic Reynolds number. Approach to angular-dependent spectra. 6th Beer-Sheva international seminar on MHD flows and turbulence. Jerusalem.

CAMBON, C., TEISSEDRE, C. & JEANDEL, D. 1985 *J. Meca. Theor. Appl.* (French Journal) **4**, 629-657.

CAMBON, C. & JACQUIN, L. 1989 Spectral approach to non-isotropic turbulence subjected to rotation. *J. Fluid Mech.* **202**, 295-317.

CAMBON, C., JACQUIN, L. & LUBRANO, J. L. 1990 To be published.

CRAIK, A. D. D. & CRIMINALE, W. O. 1986 Proc. R. Soc. London; A **406**, 13.

CRAYA, A. 1958 Contribution a l'analyse de la turbulence associee a des vitesses moyennes. *P. S. T. Ministere de l'air* (France).

HERRING, J. R. 1974 Approach of axisymmetric turbulence to isotropy. *Phys. Fluids.* **17**, 859-872.

HOLT, S. E. 1990 The evolution and structure of homogeneous stably stratified sheared turbulence. Ph.D. Dissertation, Department of Civil Engineering, Stanford University.

HUNT, J. C. R. 1978 A review of the theory of rapidly distorted turbulent flows and its applications. *Fluid Dyn. Trans.* **9**, 121-152.

JACQUIN, L., LEUCHTER, O., CAMBON, C. & MATHIEU, J. 1990 Homogeneous turbulence in the presence of rotation. *J. Fluid Mech.* **220**, 1-52.

LEE, M. J., KIM, J. & MOIN, P. 1989 Turbulence structure at high shear rate. *J. Fluid Mech.*

LEE, S., LELE, S. K., & MOIN, P. 1990 Direct simulation and analysis of shock-turbulence interaction. *AIAA 91-0523.*

MANSOUR, N. N., CAMBON, C. & SPEZIALE, C. J. 1990 To be published.

MANSOUR, N. N. & LUNDGREN, S. L. 1990 Three-dimensional instability of rotating flows with oscillating axial strain. *Phys. Fluids A.* **2** (12), 2089–2091.

MOULIN, V., LEUCHTER, O. & GEOFFROY, P. 1989 Experimental study of homogeneous turbulence in the presence of transverse shear. *Turbulent shear flows 7.* Stanford University

RILEY, J. J., METCALFE, L. W. & WEISSMAN, M. A. 1981 Direct numerical simulations of homogeneous turbulence in density stratified fluids. Proc. AIP Conf. *Nonlinear properties of internal waves.* Bruce J. West, Ed., 79-112.

ORSZAG, S. A. 1970 Analytical theories of turbulence. *J. Fluid Mech.* **41** , 363-386.

REYNOLDS, W. C. 1989 Effects of rotation on homogeneous turbulence. *Proc. 10th Australasian Fluid Mech. Conf.* Melbourne, Dec. 11-15.

SPEZIALE, C. J., MANSOUR, N. N. & ROGALLO, R. S. 1987 Decay of turbulence in a rapidly rotating frame. *Report CTR-S87.* Center for Turbulence Research, Stanford University. 205-212.

TEISSEDRE, C. & DANG, K. 1987 Anisotropic behavior of rotating homogeneous turbulence by numerical simulation. *AIAA 87-1250.* AIAA Fluid and Plasma Dynamics Conf. Honolulu.

VEERAVALLI, S. V. 1989 CTR Annual Research Briefs. Center for Turbulence Research, Stanford University and NASA Ames Research Center.

WALEFFE, F. 1989 *Phys. Fluid. A* **2**, 76.

Large-eddy simulation of compressible turbulence

By Kyle Squires

1. Introduction and objectives

The increase in the range of length scales with increasing Reynolds number limits the direct simulation of turbulent flows to relatively simple geometries and low Reynolds numbers. However, since most flows of engineering interest occur at much higher Reynolds number than is currently within the capabilities of full simulation, prediction of these flow fields can only be obtained by solving some suitably-averaged set of governing equations. In the traditional Reynolds-averaged approach, the Navier-Stokes equations are averaged over time. This in turn yields correlations between various turbulence fluctuations. It is these terms, e.g. the Reynolds stresses, for which a turbulence model must be derived. Turbulence modeling of incompressible flows has received a great amount of attention in the literature. An area of research that has received comparatively less attention is the modeling of compressible turbulent flows.

In Reynolds-averaged modeling of compressible turbulence, one must account for correlations which arise in addition to those that occur after time-averaging the incompressible Navier-Stokes equations. For example, two new terms that require modeling are the pressure-dilatation and dilatation dissipation terms. Recently, Zeman (1990) and Zeman and Blaisdell (1990) have proposed models for these terms for use in second-order closure schemes. Zeman (1990) demonstrated the importance of modeling the dilatation dissipation in order to predict the reduced growth rates of compressible free shear layers. The model for the dilatation dissipation is predicated on the existence of turbulent eddy shocklets within the flow field. It is the dissipation due to eddy shocklets that in turn leads to a limiting turbulence Mach number. The model for the pressure-dilatation term proposed by Zeman and Blaisdell (1990) yielded good agreement with the time development of this quantity from the direct simulations of compressible, homogeneous turbulent shear flow by Blaisdell (1990).

Another approach to simulating compressible turbulence at high Reynolds numbers is through the use of Large-Eddy Simulation (LES). In LES the dependent variables are decomposed into a large-scale (resolved) component and a sub-grid scale component. It is the small-scale components of the velocity field which are presumably more homogeneous than the large scales and, therefore, more easily modeled. Thus, it seems plausible that simpler models, which should be more universal in character than those employed in second-order closure schemes, may be developed for LES of compressible turbulence. The objective of the present research, therefore, is to explore models for the Large-Eddy Simulation of compressible turbulent flows. Given the recent successes of Zeman in second order closure modeling of compressible turbulence, model development in the present work has been guided by principals employed in second-order closures.

2. Accomplishments

In the first phase of the research, a new sub-grid scale model was developed to account for resolved scale compressibility. Since a complete description of the model is given by Squires and Zeman (1990), only the essential features are summarized in section 2.1. In the next phase of the work, a code used by Lee, *et al.* (1990) was modified to include the sub-grid scale model. The model was then tested against a simple extension of the Smagorinsky (1963) model used for LES of incompressible turbulence. The models were used in simulations of both decaying and forced compressible turbulence. Results from these simulations are contained in sections 2.2 and 2.3.

2.1 Model development

Following Squires and Zeman (1990), filtering the compressible Navier-Stokes equations yields the following sub-grid scale quantities:

$$\tau_{ij} = (\overline{\rho U_i U_j} - \overline{\rho}\widetilde{U}_i\widetilde{U}_j) \approx \overline{\rho}\widetilde{u_i u_j} \tag{1}$$

$$q_j = c_v(\overline{\rho T U_j} - \overline{\rho}\widetilde{T}\widetilde{U}_j) \approx c_v\overline{\rho}\widetilde{tu_j} \tag{2}$$

$$\pi_j = \overline{PU_j} - \overline{P}\widetilde{U}_j \approx \overline{pu_j} \tag{3}$$

In equations (1)-(3), the variables U_i, P, and T are velocity, pressure, and temperature, respectively, and the decomposition of the dependent variables is $X = \widetilde{X} + x$ where $\widetilde{X} = \overline{\rho X}/\rho$ is the resolved scale quantity obtained by Favre filtering. The sub-grid scale stresses shown in equation (1) are analogous to those obtained by filtering the momentum equations for incompressible turbulence. Since the flow is compressible and the energy of the flow is explicitly computed, filtering the transport equation for total energy yields the additional sub-grid scale quantities shown in equations (2) and (3).

In the present work, the closures proposed for the sub-grid scale stress and heat flux are

$$\frac{\tau_{ij}}{\overline{\rho}} = \widetilde{u_i u_j} = -2\nu_T S^*_{ij} + \frac{1}{3}q^2\delta_{ij} \tag{4}$$

$$\frac{q_i}{c_v\overline{\rho}} = \widetilde{tu_i} = -\alpha_{ij}\frac{\partial T}{\partial x_j} \tag{5}$$

where

$$S^*_{ij} = \frac{1}{2}\left(\widetilde{U}_{i,j} + \widetilde{U}_{j,i} - \frac{2}{3}\nabla\cdot\widetilde{\mathbf{U}}\delta_{ij}\right) \tag{6}$$

is the trace-free strain rate tensor, $q^2 = \widetilde{u_j u_j}$ is twice the Favre-averaged kinetic energy of SGS turbulence, and ν_T and α_{ij} are, respectively, eddy viscosity and (tensor) eddy diffusivity due to SGS turbulence.

As is evident from equation (4), the proposed closure for the sub-grid scale stresses assumes that τ_{ij} is proportional to the resolved-scale strain rate where the constant of proportionality is the eddy viscosity. The essential difference between the model

for τ_{ij} in equation (4) and sub-grid scale models for incompressible turbulence is the explicit modeling of the trace of the stress tensor. The diagonal components of τ_{ij} for incompressible flows are simply absorbed into the pressure variable. The modeling of the sub-grid scale heat flux in the energy equation is another basic difference between LES of compressible and incompressible turbulence. The sub-grid scale heat flux as shown in equation (5) is assumed to be proportional to the resolved-scale temperature gradient.

It may be shown through use of inertial sub-range relations that for a grid of size Δx, the root-mean-square (rms) velocity of sub-grid scale turbulence is smaller by $O(\Delta x/L)^{1/3}$ than that of the energy-containing motions of scale L. Thus, for $L/\Delta x \approx 30$ (i.e., a simulation using 32^3 grid points), the rms Mach number of the sub-grid scales is $0.3M_t$ where M_t is the rms Mach number of the energy-containing motions. Therefore, even for values of M_t up to 1.0, the turbulence Mach number of the sub-grid scales is small and it is, therefore, justified to consider the sub-grid scales as being mostly incompressible. Under the assumption of incompressibility, the fluctuating part of the equation of state may be used to show that the correlation π_i given by equation (6) is negligible.

The functional forms of the eddy viscosity, ν_T, and the thermal eddy diffusivity, α_{ij}, were deduced using the transport equations for the sub-grid scale energy, q^2, and heat flux $\widetilde{tu_i}$. Following the methodology employed in second-order closure modeling, e.g. neglecting triple correlations, the transport equations for these quantities were solved, and the resulting expressions for q^2, α_{ij}, and ν_T are summarized below.

$$q^2 = 2\beta\Lambda^2 \left|S^*_{ij}\right|^2 + \beta\Lambda^2 \frac{\nabla\overline{P}\cdot\nabla\widetilde{T}}{\overline{\rho}\widetilde{T}Pr_t} - \frac{\sqrt{2\beta}}{3}\Lambda^2 \left|S^*_{ij}\right| \nabla\cdot\widetilde{\mathbf{U}}, \tag{7}$$

$$\alpha_{ij} = \frac{\nu_T}{Pr_t}\delta_{ij} - \frac{\nu_T}{3}\frac{\Lambda}{q}S^*_{ij}. \tag{8}$$

The eddy viscosity is then computed using

$$\nu_T = \beta\Lambda q \tag{9}$$

where β is an adjustable constant and Λ is a lengthscale related to the grid size, Δx. The constant β must be such that in the incompressible limit the sub-grid scale viscosity reduces to the well-known Smagorinsky eddy viscosity, $\nu_{T_s} = (C_s\Lambda)^2|S^*_{ij}|$. Using equation (9) and the expression given by (7) for q^2 in the limit $\nabla\cdot\widetilde{\mathbf{U}} \to 0$, the value of β is then $\beta = C_s^{4/3}$. An accepted value of C_s for LES of incompressible, homogeneous turbulence is 0.2. Therefore, a reasonable value of β for the present model is $\beta = 0.12$.

The remaining parameter for the model is the value of the turbulent Prandtl number, Pr_t. As discussed in Squires and Zeman (1990), filtering the pressure-work term in the energy equation gives rise to an additional sub-grid scale heat flux (i.e., other than that arising from the convective terms). Accounting for this additional flux in turn reduces Pr_t over that used for incompressible turbulence

by a factor of γ. Since an accepted value of the turbulent Prandtl number for incompressible turbulence is $Pr_t = 0.7$, the value of the turbulent Prandtl number used for the present work is 0.5.

It should also be remarked that a means of dissipation not directly represented in the current formulation of the model is that which occurs due to the presence of eddy shocklets in the flow field. As considered in Squires and Zeman (1990), dissipation by eddy shocklets is incorporated directly into the transport equations for the resolved scales through a virtual shocklet stress. Possible parameterizations of shocklet dissipation for LES have been tested using flow fields obtained from direct numerical simulations of forced, compressible turbulence. At the present time, however, the proposed parameterizations have not yielded good agreement with the DNS results. The incorporation of shocklet stresses for LES of compressible turbulence is further addressed in section 3.

2.2 LES of decaying, homogeneous turbulence

The proposed sub-grid scale model for LES of compressible turbulence as described in the previous section was tested using simulations of both decaying and forced compressible, homogeneous turbulence. Simulation results obtained using the proposed model were compared against a sub-grid scale model which neglects the effect of resolved scale velocity dilatation. This model is referred to as the 'Smagorinsky' model and is summarized below.

$$\nu_T = \sqrt{2\beta^3}\Lambda^2 \left|S^*_{ij}\right|, \tag{10}$$

$$\alpha_{ij} = \frac{\nu_T}{Pr_t}\delta_{ij} - \frac{\nu_T}{3}\frac{\Lambda}{q}S^*_{ij}, \tag{11}$$

and

$$q^2 = 2\beta\Lambda^2 \left|S^*_{ij}\right|^2. \tag{12}$$

The functional forms for the sub-grid scale stresses and heat flux for the Smagorinsky model are the same as those for the proposed model, i.e., equations (4) and (5). The value of the constant β and the turbulent Prandtl number, Pr_t, were the same as for the proposed model, i.e., $\beta = 0.12$ and $Pr_t = 0.5$.

The simulations of decaying, homogeneous turbulence have been previously described by Squires and Zeman (1990) and will, therefore, be only briefly summarized below. For these simulations, the initial temperature and density fields were uniform and the velocity field was initially solenoidal and constructed from an energy spectrum of the form

$$E(k) = Ak^4 \exp\left[-2(k/k_0)^2\right]. \tag{13}$$

Simulations using the proposed and Smagorinsky models were performed for initial turbulence Mach numbers of 0.61, 0.8, and 1.0. For each computation, 32^3 grid points were used. The development of the resolved-scale energy versus time (non-dimensionalized by the eddy turnover time in the initial field, τ_e) is shown in figure 1 for the simulations with $M_t(t_0) = 0.8$. As is clear from the figure, there is negligible

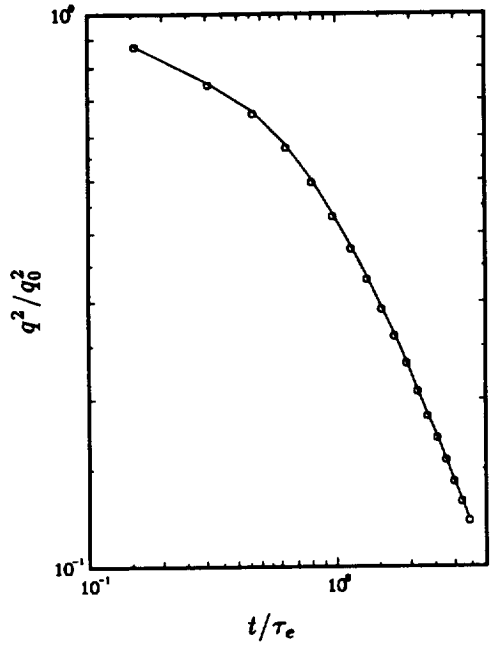

FIGURE 1. Time development of turbulence kinetic energy for an initial $M_t = 0.8$. ——— , Smagorinsky; o , proposed.

difference between the results obtained using either model. Radial spectra of the resolved scale velocity and dilatation fields for $M_t(t_0) = 0.8$ at $t/\tau_e = 1.3$ are shown in figures 2a and 2b. Consistent with the results in figure 1, the radial spectra of the resolved-scale velocity fields obtained using the two models are virtually identical (figure 2a). Figure 2b illustrates that there is greater energy content in the resolved-scale dilatation field from the simulations using the Smagorinsky model than from those computed using the proposed model. This difference can also be seen to become more significant at higher wavenumbers. The results for the $M_t = 0.8$ case are consistent with those obtained for the other Mach numbers, i.e. less energy content in the dilatation field from simulations using the proposed model while the solenoidal velocity field obtained using the two models are virtually identical. Thus, the proposed model provides additional dissipation in regions of resolved-scale dilatation as opposed to the Smagorinsky model. For the cases with $M_t(t_0) = 1.0$, it was found that simulations performed using the Smagorinsky model became physically unrealizable (negative energies) because of the inability to sufficiently dissipate fluctuations in regions of strong compression. The proposed model does provide the necessary dissipation and is, therefore, able to maintain the realizability of the flow (see Squires and Zeman 1990).

2.3 LES of forced, homogeneous turbulence

Simulations of compressible, homogeneous turbulence forced at the largest scales were also used to examine the performance of the sub-grid scale models. Another

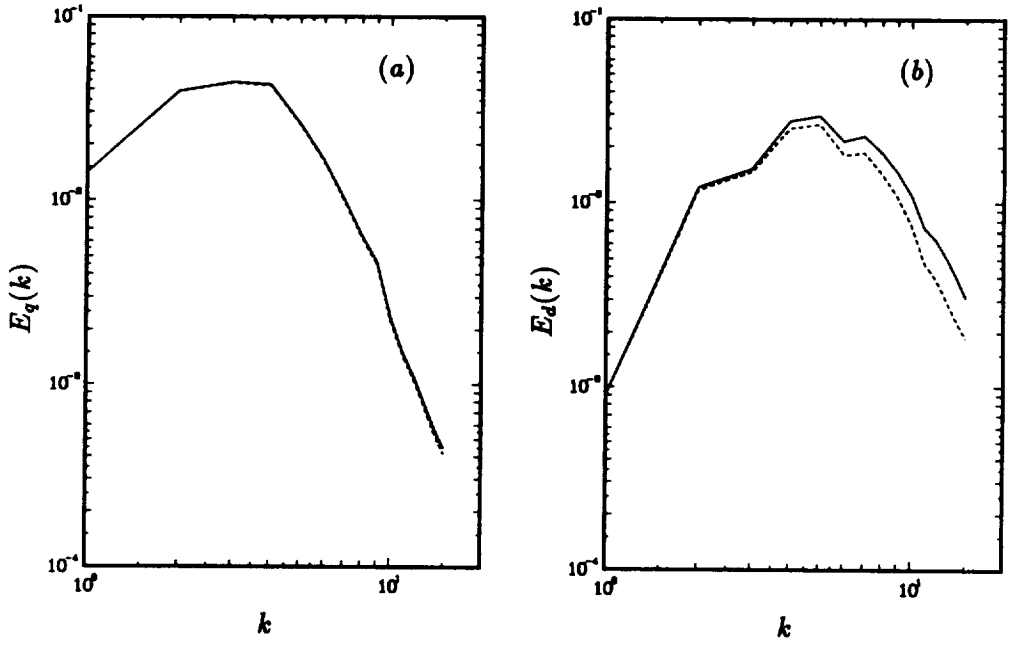

FIGURE 2. Radial spectra at $t/\tau_e = 1.3$ of (a) velocity, and (b) dilatation for an initial $M_t = 0.8$. ——— , Smagorinsky; ---- , proposed.

objective of forcing the flow is to facilitate the examination of various parameterizations of shocklet dissipation (see section 3 for further discussion). The method by which the flow was forced in the present work has been developed by Kida and Orszag (1990). In their formulation, the momentum and energy equations are modified by the addition of a body force, i.e.,

$$\frac{\partial \rho U_i}{\partial t} + \ldots = -\frac{\partial P}{\partial x_i} + \ldots + \rho F_i \tag{14}$$

$$\frac{\partial \rho E}{\partial t} + \ldots = -\frac{\partial P U_i}{\partial x_i} + \ldots + \rho U_i F_i. \tag{15}$$

In equation (15), the total energy per unit of mass is denoted as E and is the sum of the kinetic and internal energies of the flow. The force field, F_i, is chosen to act on the largest scales within the domain:

$$F_i(\mathbf{x}, t) = A_{ij}(t) \sin(x_j) + B_{ij} \cos(x_j). \tag{16}$$

The tensors A_{ij} and B_{ij} are Gaussian random variables with zero mean, and each element of these tensors is assumed to be statistically independent. The diagonal and off-diagonal components of A_{ij} and B_{ij} represent the compressive and rotational parts of the force, respectively. In the present work, the compressive components of the force are zero. As discussed in Kida and Orszag, there is no *a priori* criterion for partitioning the energy amongst the compressive and rotational components of the

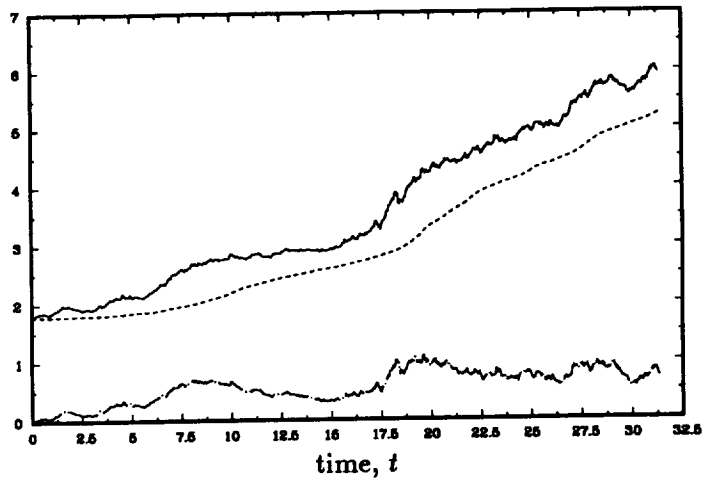

FIGURE 3. Time development of (———) total, (- - - -) internal, and (—·—) kinetic energies from direct numerical simulation of forced compressible turbulence.

force. In real flows, this partition will depend upon the actual means of excitation. For example, the compressive component of the force would be expected to be dominant in turbulence driven by shock waves while the rotational component will be more important for mixing layers.

The governing equations modified to include the external body force were first integrated directly, i.e., without any sub-grid scale model. The purpose of these simulations was to examine the basic characteristics of the flow for later comparison to the LES results. The direct simulations were computed using 64^3 grid points. For these simulations, the flow field was initially at rest with uniform density and temperature fields. From these initial conditions, the random force field continually excites the flow, and energy introduced at the largest scales is transferred to the smaller scales through non-linear interactions between the various modes. After a period of time following the imposition of the force field, the flow evolves to a quasi-stationary state. At 'steady state', the kinetic energy is balanced by viscous dissipation and, therefore, attains a statistically stationary value. Since the force field continually supplies energy to the flow, the total energy increases in time. Shown in figure 3 is the time development of the total, internal, and kinetic energies from the direct simulation. As can be observed from the figure, the kinetic energy attains a reasonably stationary value for times greater than about 20. Viscous dissipation is converted into thermal energy and causes the internal energy of the fluid to increase with time. The offset between the time traces of total and internal energy in figure 3 is precisely the kinetic energy of the flow. As is also clear from figure 3, a truly statistically stationary state cannot be attained.

Shown in figure 4 are the radial velocity spectra at $t = 28$. The spectra shown in figure 4 corresponds to the total, rotational, and compressive modes of the velocity. The rotational component of the velocity satisfies

$$\nabla \cdot \mathbf{U}_r = 0 \tag{17}$$

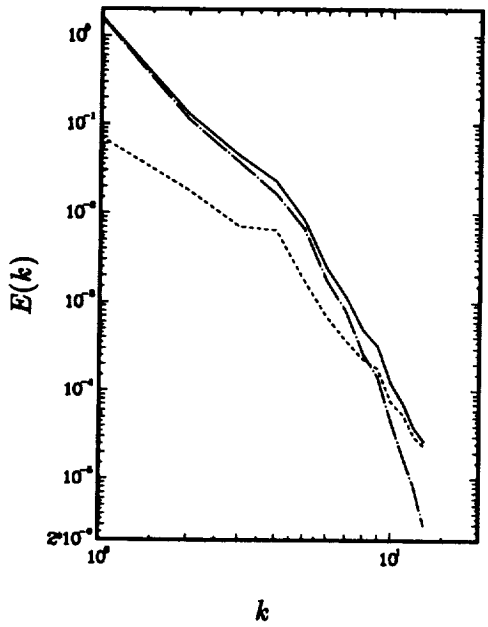

FIGURE 4. Radial velocity spectra from DNS of forced compressible turbulence. ——— , total; —·— , rotational; - - - - , compressive.

while the compressive component is defined by

$$\nabla \times \mathbf{U}_c = 0. \tag{18}$$

As can be seen from figure 4, the energy content of the rotational component of the velocity field is greater than that of the compressive mode at low wavenumbers. At higher wavenumbers, however, the opposite is true and the compressive velocity component possesses more energy than the rotational mode. This cross-over is due to the presence of shock waves in the flow field. The values of the turbulence Mach number, M_t, Taylor-microscale Reynolds number, Re_λ, and ratio of compressive to rotational mean-square energies at $t = 28$ are 0.74, 28, and 0.057, respectively.

The field from the direct simulation at $t = 23$ was filtered by volume averaging the DNS results on the 64^3 grid to a 32^3 grid for LES of forced turbulence. To provide a more rigorous test of the models, the large-eddy simulations of forced turbulence were also performed using zero molecular viscosity and thermal conductivity. Thus, all of the dissipation for these computations was provided by the sub-grid scale model. Shown in figure 5 is the radial velocity spectra from the simulations using the proposed model. The spectra shown in this figure correspond to 'steady-state' conditions. It can be observed from figure 5 that nearly all of the energy in the resolved-scale velocity field is possessed by the rotational velocity component. This is in contrast to the DNS results which showed the compressive modes to contain greater energy at the high wavenumbers due to shock waves in the flow field. Results

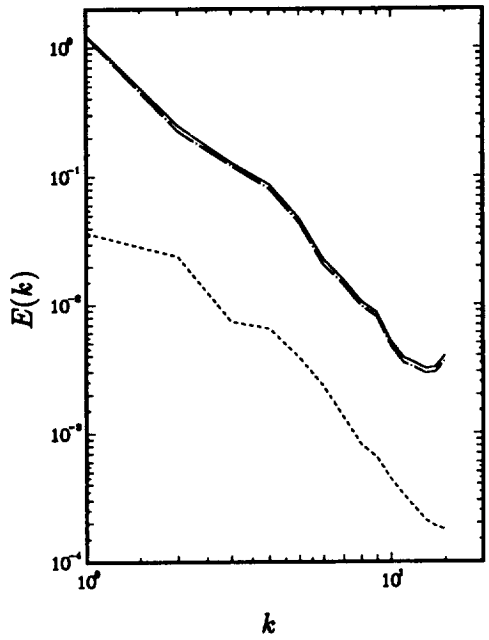

FIGURE 5. Radial velocity spectra from LES of forced compressible turbulence. ——— , total; —·— , rotational; - - - - , compressive.

from simulations of decaying turbulence showed that use of the Smagorinsky model did not sufficiently dissipate dilatational fluctuations, especially at higher M_t. When the Smagorinsky model was used for LES of forced turbulence, it was found that the flow field also became physically unrealizable, presumably due to the inability of the model to provide sufficient dissipation in regions of strong compression. Thus, while the proposed model does dissipate dilatational fluctuations, the results in figure 5 indicate that this dissipation is too large.

3. Summary and future work

A new sub-grid scale model for LES of compressible turbulence has been developed and tested using simulations of decaying and forced compressible, homogeneous turbulence. The proposed model accounts for resolved scale velocity dilatation and in the limit of $\nabla \cdot \widetilde{\mathbf{U}} \rightarrow 0$ reduces to the Smagorinsky model for the LES of incompressible turbulence. Preliminary results obtained using the present model have shown that there are negligible differences between the large-scale solenoidal velocity fields obtained using the proposed and Smagorinsky models. The proposed model, however, provides greater dissipation of dilatational velocity fluctuations than does the Smagorinsky model. At high turbulence Mach numbers, the inability of the Smagorinsky model to dissipate dilatational fluctuations in regions of strong compression causes the flow to become physically unrealizable. LES of forced compressible turbulence further illustrates that the proposed model dissipates more of

the dilatational energy than does the Smagorinsky model. For LES of forced turbulence using the Smagorinsky model, the flow was also found to become physically unrealizable. Comparison of the LES results obtained using the proposed model to the DNS data showed that the proposed model provides too much dissipation of the dilatational fluctuations.

As mentioned in section 2, another objective of incorporating a random body force into the simulations was to examine various parameterizations of dissipation due to turbulent eddy shocklets. Zeman (1990) successfully predicted the reduced growth rates of compressible free shear layers by correctly modeling dilatational dissipation. In Zeman's model, dilatational dissipation is predicated on the occurrence of turbulent eddy shocklets. Parameterization of shocklet dissipation similar to those Zeman applied in his second-order closure model have been investigated using the flow fields from the DNS of forced compressible turbulence. However, it was found that there existed no significant correlation of the modeled and exact values of dilatation dissipation. This is an area of the research which requires further effort. Further parameterizations of shocklet dissipation for use in sub-grid scale models for LES will be examined in the future.

Agreement between the proposed model and DNS results may also be improved by modifying the model constant. Therefore, an area of future work is to better estimate its value. Traditionally, flow fields obtained from DNS have been used to correlate exact and modeled turbulent stresses. In this manner, the appropriate model constants can be derived. Erlebacher, *et al.* (1990) have used this approach to evaluate the constant in a sub-grid scale model for LES of compressible turbulence. Using their database, the constant obtained in this manner was less than half that used in the present work. It should be expected that a lower value of the Smagorinsky constant would improve the LES results in that the compressive modes of the velocity field would be less damped relative to the rotational velocity components. Another new and more promising approach to 'tuning' the model to the flow has been developed recently by Germano, *et al.* (1990). These investigators have proposed a new sub-grid scale model for LES of incompressible turbulence in which the constant is determined interactively, i.e., as part of the computation. The formalism of their approach is general enough such that it may be applied to the compressible sub-grid scale model proposed in this work. Therefore, this interactive sub-grid scale modeling as described by Germano, *et al.* shall also be incorporated into the simulations. Another attractive feature of their model is that it is not strictly dissipative, i.e. backscatter from the small to large scales is permitted. In its present form, the proposed sub-grid scale model does not allow backscatter. It should certainly be expected that improvements in the model that take into account more of the effects of the underlying physical phenomenon will improve the results.

REFERENCES

BLAISDELL, G. A. 1990 Numerical simulations of compressible homogeneous turbulence. Ph.D. dissertation, Department of Mechanical Engineering, Stanford University, Stanford, California.

ERLEBACHER, G., HUSSAINI, M. Y., SPEZIALE, C. G., & ZANG, T. A. 1990 Toward the Large-Eddy Simulation of compressible turbulent flows. *ICASE report 90-76.*

GERMANO, M., PIOMELLI, U., MOIN, P., & CABOT, W. H. 1990 A dynamic subgrid-scale eddy viscosity model. *Proceedings of the Summer Program 1990.* Center for Turbulence Research.

KIDA, S., & ORSZAG, S. A. 1990 Energy and spectral dynamics in forced compressible turbulence. *Physics of Fluids.* in press.

LEE, S., LELE, S. K., & MOIN, P. 1990 Eddy shocklets in decaying compressible turbulence. *Physics of Fluids.* in press.

SMAGORINSKY, J. 1963 General circulation experiments with the primitive equations. *Monthly Weather Review.* **93,** 99.

SQUIRES, K. D., & ZEMAN, O. 1990 On the subgrid-scale modeling of compressible turbulence. *Proceedings of the Summer Program 1990.* Center for Turbulence Research.

ZEMAN, O. 1990 Dilatation dissipation: the concept and application in modeling compressible mixing layers. *Physics of Fluids.* **2,** 178-188.

ZEMAN, O., & BLAISDELL, G. A. 1990 New physics and models for compressible turbulence. to appear in *Advances in Turbulence.* Springer-Verlag.

Progress in understanding the renormalization group skewness and $\kappa - \varepsilon$ models

By L. M. Smith AND W. C. Reynolds

1. Motivation and objectives

The immediate goal of this work is to understand and validate the Yakhot-Orszag model for the velocity-derivative skewness and model equation for the rate of energy dissipation $\mathcal{E}$ (Yakhot and Orszag (YO), 1986). This report is a summary of a more detailed manuscript in preparation (Smith and Reynolds (SR), 1990a). Our purpose is to clarify some limitations of the theory by careful examination of key assumptions and approximations, and thereby to encourage its improvement. Our focus is as follows:

1. We reformulate their recursive solution for the velocity field of the removed scales as a perturbation analysis and show that it is unlikely to be quantitatively accurate at the perturbation levels involved.
2. We examine the effect of using the low wavenumber limit of the modified viscosity in the solution for the high wavenumber modes. This work suggest that their approach significantly overestimates the low wavenumber limit.
3. We introduce the concept of "displacement value" characterizing the contribution of the dissipative high wavenumber portion of the spectrum to various integrals in the theory.
4. We correct an identifiable algebraic error in the velocity derivative skewness, finding $\bar{S} = -0.59$ instead of their value of -0.488.
5. We correct several errors in the development of the transport equation for the rate of energy dissipation $\mathcal{E}$. The most important of these corrections gives zero as the coefficient of YO's term proportional to the rate of production of energy $P_\mathcal{K}$. There may exist a non-zero term responsible for the production of $\mathcal{E}$ at higher-order in the approximations involved. However, we show that its structure is different from the structure of the $\mathcal{E}$-production term reported by YO and in current turbulence models. Hence, the RG method has not yet placed the $\mathcal{E}$-transport model equation on solid ground.

In spite of these difficulties, it seems clear that YO have introduced an important approach worthy of further exploration. Although the method does not provide a derivation of the $\mathcal{E}$-transport model equation presently in use, the correct RG $\mathcal{E}$-transport equation may be useful and should be developed.

2. Accomplishments

2.1 The perturbation expansion for the high wavenumber modes

YO use RG techniques to develop a theory for the large scales in which the effects of the small scales are represented by modified transport coefficients. The effect of the very large scales on eddies in the inertial range is represented by a random force chosen to produce the correct form of the inertial range spectrum when opposed by the modified viscosity. The force is assumed Gaussian, white noise in time, homogeneous in time and space, and isotropic in space. YO assume that the statistics of the inertial range of homogeneous turbulence forced in this manner will be representative of the inertial range of turbulence sustained by inhomogeneities. They refer to this assumption as "the correspondence principle."

The dynamical equations for the large-scale field are derived by averaging over an infinitesimal band of the small scales to remove them from explicit consideration. This procedure yields infinitesimal modifications in the equations for the large scales. The removal process is iterated, and these corrections accumulate to give finite changes. YO retain only the modifications of the viscosity, arguing that other modifications are unimportant to the large-scale dynamics.

The iterative averaging is carried out in $(d+1)$-dimensional Fourier space in which the Fourier amplitudes are functions of the $(d+1)$-vector $\hat{\mathbf{k}} \equiv [\mathbf{k}, \omega]$, where $\mathbf{k}$ is the d-dimensional wavevector and ω is the frequency. At each stage, the averaging requires knowledge of the statistics of the scales being removed. YO generate these statistics by repeated substitution of the equation for $\hat{\mathbf{v}}^>$ into the equation for $\hat{\mathbf{v}}^<$, which is originally given in terms of $\hat{\mathbf{v}}^<$, $\hat{\mathbf{f}}^<$ and $\hat{\mathbf{v}}^>$. Since $\hat{\mathbf{v}}^>$ is in terms of $\hat{\mathbf{v}}^<$, $\hat{\mathbf{f}}^>$ and $\hat{\mathbf{v}}^>$, the statistics of $\hat{\mathbf{v}}^>$ are given by the assumed statistics of $\hat{\mathbf{f}}^>$.

One can show that the repeated substitution of $\hat{\mathbf{v}}^>$ is equivalent to a series expansion in which zeroth-order effects are linear and nonlinear effects are higher-order corrections,

$$\hat{\mathbf{v}}^> = \hat{\mathbf{v}}^{(0)} + \lambda \hat{\mathbf{v}}^{(1)} + O(\lambda^2) \tag{1}$$

$$\hat{v}_i^{(0)}[\hat{\mathbf{k}}] = \hat{f}_i^>[\hat{\mathbf{k}}] \tag{2}$$

$$\hat{v}_i^{(1)}[\hat{\mathbf{k}}] = \frac{i}{2} G_\nu[\hat{\mathbf{k}}] P_{imn}[\mathbf{k}] \int_*^{k_c} \frac{d\hat{\mathbf{q}}}{(2\pi)^{d+1}} \Big(\hat{v}_m^<[\hat{\mathbf{q}}] \hat{v}_n^<[\hat{\mathbf{k}} - \hat{\mathbf{q}}] + \hat{v}_m^<[\hat{\mathbf{q}}] \hat{f}_n^>[\hat{\mathbf{k}} - \hat{\mathbf{q}}]$$

$$+ \hat{v}_n^<[\hat{\mathbf{k}} - \hat{\mathbf{q}}] \hat{f}_m^>[\hat{\mathbf{q}}] + \hat{f}_m^>[\hat{\mathbf{q}}] \hat{f}_n^>[\hat{\mathbf{k}} - \hat{\mathbf{q}}] \Big) \tag{3}$$

where

$$G_\nu[\hat{\mathbf{k}}; k_c] \equiv (-i\omega + \nu_T[k, \omega; k_c] k^2)^{-1}. \tag{4}$$

Here k_c is the current cutoff wavenumber above which all scales have been previously removed, $\int_*$ indicates a $(d+1)$-dimensional integral, $P_{ijk}[\mathbf{k}]$ is a compound

projection operator, G_ν is called the "propagator", and $\lambda = 1$ is the ordering parameter. Square brackets [ ] will be used throughout to indicate functional dependence. The modified viscosity $\nu_T[k,\omega;k_c]$ is the term through which the high wavenumber modes affect the retained scales. YO assume that when $k_c = \Lambda_o$ is a Kolmogorov scale, all significant scales are retained and then $\nu_T[k,\omega;\Lambda_o] = \nu_o$ is the (constant) molecular viscosity. YO do not discuss the dependence of ν_T on k and ω, but it is implicit in their analysis.

Use of the above perturbation expansion can be expected to give quantitatively correct results only if the Reynolds number of the removed eddies, *based on the modified viscosity*, is small. We denote the Reynolds number of the removed eddies by $R_c \equiv v_c l_c/\nu_T$ where the velocity scale $v_c = D_o^{1/2} l_c/\nu_T^{1/2}$, time $t_c = l_c^2/\nu_T$, and length $l_c = 1/k_c$ are characteristic of the high wavenumber band to be eliminated and $D_o \propto \mathcal{E}$ is the amplitude of the two-point force correlation.

The requirement that R_c be small is not met very well because the removed scales are in the inertial range. One may estimate the actual value of R_c at each iteration of the fine-scale elimination (SR). One finds that $R_c = O(10)$ at each iteration of the removal process, which seems large for a perturbation parameter and suggests the possibility of quantitative inaccuracy.

2.2 The modified viscosity

The differential equation describing how the modified viscosity changes with cut-off wavenumber is developed by averaging over infinitesimal bands as described above in section 2.1. The modified viscosity at any low wavenumber Λ is calculated by integrating this equation from the first removal, where the viscosity was the fluid viscosity ν_o and the cutoff wavenumber was the Kolmogorov cut-off Λ_o.

The modified viscosity is in general a function of the retained wavenumber, the frequency and the cutoff wavenumber: $\nu_T = \nu_T[k,\omega;k_c]$. The modified viscosity is calculated to be independent of k and ω only in the "distant-interaction" limit $k << k_c$, $|i\omega| << \nu_T k_c^2$. It is important to realize that the distant interaction approximation includes only the effect of triad interactions between two modes in the removed shell and a retained mode at very small wavenumber. Hence, the modified equation will be most accurate at low wavenumber and least accurate near the new cutoff wavenumber, *where it will be used in the perturbation solution for the next band of removed wavenumbers.* Thus the YO procedure assumes

$$\nu_T[k_c,\omega;k_c] = \nu_T[0,0;k_c] \tag{5}$$

For the remainder of this section, we focus only on the k-dependence of ν_T and suppress the ω-dependence by writing $\nu_T[k;k_c]$.

Many studies suggest that a realistic eddy-viscosity model exhibits a plateau far from the cutoff ($k << k_c$) and increases to several times its plateau value very near the cutoff ($k \approx k_c$). This "cusp-up" behavior of the modified viscosity is predicted by EDQNM (ref) and the Test-Field model of Kraichnan (ref), and is consistent with direct numerical simulations (ref).

In order to study the effect of assumption (5), we instead use

$$\nu_T[k_c;k_c] = \zeta \nu_T[0;k_c] \tag{6}$$

where ζ is a constant. The differential equation for $\nu_T[0;k_c]$ is

$$\frac{d\nu_T[0;k_c]}{dk_c} = -\frac{\beta}{\nu_T^2[k_c;k_c]k_c^3} = -\frac{\beta}{\zeta^2\nu_T^2[0;k_c]k_c^3} \tag{7}$$

YO's approximate differential equation is

$$\frac{d\nu_T[0;k_c]}{dk_c} = -\frac{\beta}{\nu_T^2[0;k_c]k_c^3} \tag{8}$$

In the limit of small k_c, the solution to (8) overestimates the solution to the correct differential equation (7) by a factor $\zeta^{2/3}$.

We can estimate ζ by comparing YO's results and EDQNM (ref). We denote $\nu_T[0;k_c] = A_0\mathcal{E}^{1/3}k_c^{-4/3}$. EDQNM predicts $A_0 = 0.28$ for YO's value of the Kolmogorov constant $C_K = 1.6$, whereas YO predict $A_0 = 0.49$. These numbers suggest $\zeta = 2.3$.

The same assumption (5) is made in the differential equations to derive the skewness and the modified source term in the model $\mathcal{E}$-equation. Thus some quantitative error is expected in the YO skewness value and $\mathcal{E}$-model coefficients.

2.3 The concept of the "displacement value"

YO assume that the Fourier modes vanish when $k > \Lambda_o$, beyond which there is no significant physics. In their analysis, Λ_o is an ultraviolet cutoff of the inertial range. This is a reasonable assumption when dealing with the kinetic energy, since the Kolmogorov modes contain only negligible energy. However, turbulence quantities related to velocity derivatives, such as the dissipation, receive significant contribution from modes beyond the inertial range. Therefore, it seems essential in performing RG on such moments to allow for undetermined physics beyond the inertial range. We introduce the term " displacement value" to represent the cumulative effect of modes beyond the ultraviolet cutoff. The displacement value of the kinetic energy is taken to be zero.

Since interactions among wavenumbers above Λ_o are not modeled by the YO theory, only moments that are negligibly small above the ultraviolet cutoff Λ_o and, hence, have displacement value zero can be calculated using their method.

For moments of velocity derivatives, the displacement values are nonzero and dominant. Although the YO method does not provide values of individual velocity-derivative moments, YO use it to provide estimates for Reynolds-number independent combinations of derivative moments. They argue that such combinations can be evaluated from the statistics of RG-filtered turbulence acted on by the modified viscosity, which at large Reynolds numbers is independent of Reynolds number.

Two examples of Reynolds-number-independent combinations of derivative moments are the velocity-derivative skewness $\bar{S}$ and the "source" terms $\mathcal{Y}$ in the $\mathcal{E}$-transport equation. The RG models for $\bar{S}$ and $\mathcal{Y}$ are discussed in sections 2.4 and 2.5, respectively.

2.4 The RG skewness model

The velocity-derivative skewness is defined

$$\bar{S} \equiv \frac{\langle(\nabla_1 v_1)^3\rangle}{\langle(\nabla_1 v_1)^2\rangle^{3/2}} \equiv \frac{A}{B^{3/2}}. \tag{9}$$

Estimates of A and B are provided by a spectrum model of the form

$$E[k] = 0 \qquad \text{for} \qquad k < \Lambda_f$$

$$E[k] = C_K \mathcal{E}^{2/3} k^{-5/3} \exp[-\alpha(k\eta)^2] \qquad \text{for} \qquad \Lambda_f \leq k \leq \infty \tag{10}$$

where $\eta = (\nu_o^3/\mathcal{E})^{1/4}$, $\Lambda_o = .2/\eta$, Λ_f is the integral scale, and we take $C_K = 1.6$ for consistency with the YO theory. This form of the exponential tail has been predicted by various theoretical considerations and elsewhere (Smith and Reynolds, 1990b) we show that it is the preferred exponential form of the Kolmogorov spectrum.

Using the model spectrum (10), one can show (SR) that $A = O(R_T^{3/2})$ and $B = O(R_T)$ where $R_T \equiv \mathcal{K}^2/(\nu_o \mathcal{E})$ is the turbulent Reynolds number. Also, the displacement value accounts for 70% of B. The skewness for isotropic turbulence is found to be -0.694 in agreement with observations at moderate Reynolds numbers.

The RG differential equations for $A^>$ and $B^>$ are found from the Fourier transforms $\hat{A}$ and $\hat{B}$ by the averaging over infinitesimal bands of high-wavenumber modes as described in section 2.1. The distant-interaction approximation leads to (see section 2.2)

$$\frac{dA^>[k_c']}{k_c'} = \frac{a\mathcal{E}^2}{\nu_T^3[0,0;k_c'](k_c')^3} \tag{11}$$

$$\frac{dB^>[k_c']}{k_c'} = -\frac{b\mathcal{E}}{\nu_T[0,0;k_c']k_c'} \tag{12}$$

where a and b are constants. Notice that error is introduced in (11) and (12) by using $\nu_T[0,0;k_c']$ instead of $\nu_T[k_c',\omega;k_c']$.

Integration of (11) and (12) over $k_c \leq k \leq \Lambda_o$ gives $A^>[k_c]$ and $B^>[k_c]$. Taking $k_c = 0$ corresponding to elimination of the entire inertial range, one finds

$$A^>[0] = -0.0044\frac{\mathcal{E}^3}{\mathcal{K}^3}R_T^{3/2} + A_o \tag{13}$$

$$B^>[0] = 0.022\frac{\mathcal{E}^2}{\mathcal{K}^2}R_T + B_o \tag{14}$$

where A_o and B_o are the displacement values. One sees that the RG method yields the proper scaling of the individual moments A and B. However, their values cannot be determined because the displacement values A_o and B_o are unknown.

An estimate for the skewness is made from RG-filtered turbulence having scales $k < \Lambda$, acted on by the modified viscosity $\nu_T[0,0;\Lambda]$. One approximates $A^<[\Lambda]$

and $B^<[\Lambda]$ from the RG expressions for $A^>[k_c]$ and $B^>[k_c]$. To do this, the differential equations (11) and (12) are integrated over $0 \leq k_c' \leq \Lambda$, where $\Lambda/\Lambda_o \to 0$ corresponding to $R_T \to \infty$,

$$A^<[\Lambda] \approx a\mathcal{E}^2 \int_0^\Lambda \frac{dk_c'}{(k_c')^3 \nu_T^3[0,0;k_c']} \tag{15}$$

$$B^<[\Lambda] \approx b\mathcal{E} \int_0^\Lambda \frac{dk_c'}{k_c' \nu_T[0,0;k_c']}. \tag{16}$$

Then the RG skewness is formed as

$$\bar{S} = \frac{A^<[\Lambda]}{(B^<[\Lambda])^{3/2}} = -0.59 \tag{17}$$

where $A^<[\Lambda]$ and $B^<[\Lambda]$ are both $O(1)$ quantities. The RG prediction $\bar{S} = -0.59$ is in good agreement with experiments at moderate Reynolds numbers. YO made an algebraic error in their calculation of the constant a which defines $A^>$, which led them to find $\bar{S} = -0.488$ instead of the correct value -0.59 (SR).

2.5 The RG model $\mathcal{E}$-transport equation

The RG model $\mathcal{E}$-transport equation is derived by applying the iterative-averaging technique to the evolution equation for the instantaneous value of the dissipation rate ϕ in homogeneous flow,

$$\phi \equiv \nu_o(\nabla_j v_i)^2. \tag{18}$$

Then $\mathcal{E} =< \phi >$ under the assumption that the dissipative scales are locally homogeneous.

Differentiation in time of (18), followed by substitution from the Navier Stokes equations, gives

$$\frac{\partial \phi}{\partial t} = -v_j \nabla_j \phi + \chi_o \nabla_j \nabla_j \phi - \overbrace{2\nu_o^2 (\nabla_m \nabla_j v_i)^2}^{\mathcal{Y}_I[\mathbf{x},t]}$$

$$- \overbrace{2\frac{\nu_o}{\rho}(\nabla_j v_i)(\nabla_j \nabla_i p)}^{\mathcal{Y}_{II}[\mathbf{x},t]} - \overbrace{2\nu_o (\nabla_j v_i)(\nabla_j v_m)(\nabla_m v_i)}^{\mathcal{Y}_{III}[\mathbf{x},t]} \tag{19}$$

where $\chi_o = \nu_o$.

The RG calculation of the modified "source" terms $\mathcal{Y}_I =< \mathcal{Y}_I[\mathbf{x},t] >$, $\mathcal{Y}_{II} =< \mathcal{Y}_{II}[\mathbf{x},t] >$ and $\mathcal{Y}_{III} =< \mathcal{Y}_{III}[\mathbf{x},t] >$ follows the RG procedure to find velocity moments, outlined for the velocity-derivative skewness in section 2.4 above. Since the source term is observed to be independent of Reynolds number at high Reynolds number, the RG modified source term is calculated from the RG-filtered turbulence field acted on by the modified viscosity ν_T.

At this writing, our results for the RG modified source term differ from YO's results. We find a different decay rate for isotropic flow and a different form for the term responsible for the production of $\mathcal{E}$ in anisotropic flow. In the limit of high Reynolds number, we find

$$\frac{\partial \mathcal{E}}{\partial t} = -U_j \nabla_j \mathcal{E} + \nabla_j \chi_T \nabla_j \mathcal{E} - 5.65 \frac{\mathcal{E}^2}{\mathcal{K}} + \Pi^* \tag{20}$$

The decay rate for isotropic flow is 5.65, in poor agreement with observations and the $\mathcal{K} - \mathcal{E}$ models in current use. The term Π^* is responsible for production of $\mathcal{E}$ in anisotropic flow. The Fourier transform $\hat{\Pi}^*[\hat{\mathbf{k}}; k_c', k_c]$ has the form (SR)

$$\hat{\Pi}^* = \lambda^2 \frac{\mathcal{E}}{\nu_T^2} \frac{(k_c')^{d-y-4} - k_c^{d-y-4}}{4-y-d} \int_{*2}^{k_c'} \frac{d\hat{\mathbf{r}} d\hat{\mathbf{q}}}{(2\pi)^{2d+2}}$$

$$\times \left(O(r^2/k_c^2) + O(rq/k_c^2) + O(q^2/k_c^2) \right)_{jlbt} (k_j - r_j) \hat{v}_j^<[\hat{\mathbf{k}} - \hat{\mathbf{r}}] \hat{v}_b^<[\hat{\mathbf{q}}] \hat{v}_t^<[\hat{\mathbf{r}} - \hat{\mathbf{q}}]. \tag{21}$$

where $(\ )_{jlbt}$ is a function of the angles of $\mathbf{k}_c$, $\mathbf{r}$ and $\mathbf{q}$, and $\int_{*2}$ indicates two $(d+1)$-dimensional integrals. YO reported

$$\frac{\partial \mathcal{E}}{\partial t} = -U_j \nabla_j \mathcal{E} + \nabla_j \chi_T \nabla_j \mathcal{E} - 1.7 \frac{\mathcal{E}^2}{\mathcal{K}} + \Pi \tag{22}$$

where the decay rate 1.7 is in good agreement with observations and the $\mathcal{K} - \mathcal{E}$ models in current use. The Fourier transform $\hat{\Pi}[\hat{\mathbf{k}}; k_c', k_c]$ of the production term is given as (YO)

$$\hat{\Pi} = -i \frac{d-2}{d(d+2)} \frac{\tilde{B}_d \mathcal{E}}{\nu_T^2} \frac{(k_c')^{d-y-2} - k_c^{d-y-2}}{2-y-d}$$

$$\times \int_{*2}^{k_c'} \frac{d\hat{\mathbf{r}} d\hat{\mathbf{q}}}{(2\pi)^{2d+2}} (k_j - r_j) \hat{v}_i^<[\hat{\mathbf{k}} - \hat{\mathbf{r}}] \hat{v}_j^<[\hat{\mathbf{q}}] \hat{v}_i^<[\hat{\mathbf{r}} - \hat{\mathbf{q}}]. \tag{23}$$

where $\tilde{B}_d$ is a constant. We found that integrals of the form (23) exactly cancel, and that the power of the wavenumber in the integrand must be at least two (SR). We are in correspondence with YO over these differences.

3. Future Plans

We will continue our correspondence with Yakhot and Orszag until we agree on the correct form of the RG $\mathcal{E}$-transport model equation. This may involve calculations to higher-order in the distant-interaction limit in order to derive a term responsible for $\mathcal{E}$-production.

We may also consider an exponential roll-off to the inertial range spectrum, instead of an abrupt ultraviolet cutoff, by adjusting the statistics of the force. Then

displacement values could be calculated using RG and may have interesting consequences for the RG skewness and $\mathcal{K} - \mathcal{E}$ models.

A longer term project is the reformulation of the RG method to produce the cusp-up behavior of the modified viscosity (see section 2.2). The cusp-up behavior appears essential for a realistic eddy viscosity model (Kraichnan, 1976, Chollet and Lesieur, 1981, Domaradzki, Metcalfe, Rogallo and Riley, 1987). It has been shown (Zhou and Vahala, 1989) that the present RG modified viscosity (in the absence of the triple nonlinearity) cusps down instead of up: ν_T decreases instead of increases as k increases to the cutoff wavenumber k_c. One would like to correct this unphysical behavior.

Finally, we hope to derive the RG modified viscosity in the presence of a strong shear. This calculation will involve a forcing which is anisotropic at lowest order. We intend to find the appropriate form of the force correlation from the direct numerical simulation data for homogenous shear flow. One must also retain the sweeping and straining terms due to the mean shear in the equations of motion. These terms may be too cumbersome to allow for analytic RG, but present no difficulty for numerical implementation of an RG algorithm.

REFERENCES

CHOLLET, J. P. & LESIEUR, M. 1981 Parameterization of small scales of three-dimensional isotropic turbulence utilizing spectral closures.. *J. Atmos. Sci.* **38**, 2747.

DOMARADZKI, J. A., METCALFE, R. W., ROGALLO, R. S. & RILEY, J. J. 1987 Analysis of subgrid-scale eddy viscosity with use of direct numerical simulations.. *J. Atmos. Sci.* **38**, 2747. *Phys. Rev. Lett.* **58**, 547.

KRAICHNAN, R. H. 1976 Eddy viscosity in two and three dimensions.. *J. Atmos.Sci.* **33**, 1521.

SMITH, L. M. & REYNOLDS, W. C. 1990a A critical assessment of the Yakhot-Orszag renormalization group method for deriving turbulence statistics and models. To be submitted to Phys. Fluids A.

SMITH, L. M. & REYNOLDS, W. C. 1990b The dissipation range spectrum and the velocity-derivative skewness in turbulent flows. Submitted to Phys. Fluids A

YAKHOT, V. & ORSZAG, S. A. 1986 Renormalization group analysis of turbulence. *J. Sci. Comput.* **1**, 3.

ZHOU, Y., VAHALA, G., & HOSSAIN, M. 1989 renormalized eddy viscosity and Kolmogorov's constant in forced Navier-Stokes turbulence. *Phys. Rev. A.* **40**, 5865.

Recursive renormalization group theory based subgrid modeling

By Ye Zhou

The essential purpose of this research is to advance the knowledge and understanding of turbulence theory. Specific problems to be addressed will include studies of subgrid models to understand the effects of unresolved small scale dynamics on the large scale motion which, if successful, might substantially reduce the number of degrees of freedom that need to be computed in turbulence simulation.

1. Motivation and objectives

The study of turbulence is one of the most challenging and active research topic in classical physics. Since turbulence, by its usual definition, implies the existence of an extremely large number of degrees of freedom interacting nonlinearly, one is forced into a statistical description and so encounters the problem of obtaining a closed set of equations (Laudau and Lifshitz, 1982). A straightforward numerical approach to high Reynolds number fluid turbulence runs into hopeless storage/resolution problems for present-day and foreseeable future supercomputers. It is not likely that foreseeable advances in computers will allow the full simulation of turbulence flows at Reynolds numbers much larger than the $R = O(100 - 1000)$ already achieved.

The fundamental problem is that we must reduce the number of degrees of freedom to be considered, yet at the same time retain the correct physical behavior. If this can be accomplished, then the simplified model will correctly mimic (in a statistical sense) the real physical system.

As an example, traditionally one averages the Navier-Stokes equations over a range of small scales by applying an appropriate filter (Leonard, 1974; Rogallo and Moin, 1984; Zhou *et al.*, 1989a). The result is the Navier-Stokes equation for the large scale motion along with new terms representing the subgrid stresses. The subgrid stresses are now modeled using phenomenological arguments (Smagorinsky, 1963; Rogallo and Moin, 1984) and adjustable numerical factors (Deardorff, 1977). Recently, following the impressive success in critical phenomena (Wilson, 1975; Wilson and Kogut, 1974), renormalization group theory (RNG) has been applied to the subgrid modeling problem in fluid turbulence, especially since subgrid modeling is such a good candidate for the RNG approach (Rose and Sulem, 1978). The RNG subgrid calculations fall into two basic groups: (i) the ϵ-expansion (Forster *et al.*, 1977; Fournier and Frisch, 1983; Yakhot and Orszag, 1986; Zhou and Vahala, 1988), and (ii) the recursion (Rose, 1977; Zhou *et al.*, 1988, 1989b; Zhou and Vahala, 1990; Zhou, 1990) approach. We shall concentrate here only on the recursion RNG theories since we are particularly interested in the wavenumber dependence of the eddy viscosity, $\nu(k)$. In the ϵ-expansion RNG theories, the eddy viscosity is calculated only in the limit $k \to 0$. Now, unlike the ϵ-expansion procedure (i), both free decay (with given Kolmogorov energy spectrum) and forced turbulence (with spectral

forcing chosen to reproduce the Kolmogorov energy spectrum) can be handled, and there is no need to introduce a small parameter ϵ.

2. Previous work

Our purpose is to construct a systematic way to model the subgrid scale in Navier-Stokes turbulence. Originally, Rose (1977) applied recursive RNG to the subgrid modeling of the advection of a passive scalar. Later, we have extended Rose's technique and applied it to the cases of free decay (Zhou *et al.*, 1988) and forced (Zhou *et al.*, 1989b) Navier-Stokes turbulence. The resultant resolvable scale wavenumber dependent eddy viscosity in our model shows a cusplike behavior, in qualitative agreement with the test field model of Kraichnan (1976), the EDQNM closure calculation of Chollet and Lesieur (1981), the direct numerical simulation results of Domaradzki *et al.* (1987), and recent large eddy simulation of Lesieur and Rogallo (1989).

Another interesting feature of our recent work (Zhou *et al.*, 1989b; Zhou and Vahala, 1990) is that the time dependence of the subgrid modes is not ignored–in contrast to the treatments in the free decay of Navier-Stokes turbulence (Zhou *et al.*, 1988) and passive scalar convection (Rose, 1977). As a result, a nonlocal time (and space) behavior of the eddy damping is found, similar to that of Kraichnan (1976) in his test field model. Recently, a unified framework for subgrid scale closure is formulated, without the need to specify whether we are dealing with free decay or forced turbulence. The identification need only be made towards the end of the calculation when we must introduce the subgrid velocity autocorrelation function (Zhou and Vahala, 1990). This unified framework has been helpful in examining the effect of helicity on the subgrid scale closure (Zhou, 1990).

3. Current work

The novel feature of our model is an explicit triple nonlinearity in the renormalized equation of motion. On iteration to the fixed point, this term results in a cusplike contribution to the wavenumber dependent eddy viscosity which is required by elementary scaling arguments. However, a major difference between the recursive RNG eddy viscosity and that derived from the test field model (Kraichnan, 1976) and classical closure (Leslie and Qiarini, 1979) is the "strength" of the cusp behavior as $k \to k_c$, where k_c is the boundary between the resolvable and subgrid scales. Based on the energy transfer equation, we have shown that the triple nonlinearity will contribute a term equivalent to an eddy viscosity. This furnishes an explanation of why the renormalized eddy viscosity found by solving the recursive RNG equations exhibits only a mild cusp behavior as $k \to k_c$.

It is shown that the order of the statistical ensemble averaging procedure in recursive RNG technique can be interchanged. Regardless of the order of averaging process, the following results are obtained: First, the triple nonlinearity and a nonlocal time eddy damping functions are generated. Second, the only way to prevent the creation of triple nonlinearity is to assume that a spectral gap exists between the resolvable and subgrid scales.

These encouraging results, combined with the appealing structure of basic recursive RNG theory, has led to a considerable level of the activity in the area, both in the direction of more a sophisticated subgrid model and toward the extension of the recursive RNG approach to deal with different physical systems.

4. Future plan

The fact that the subgrid scale modes evolve at a faster time scale than that of the resolvable is the motivation behind the Markovian approximation in that the time dependent of the subgrid modes can be ignored (Rose, 1977; Zhou *et al.*, 1988). To account for this separation of scales, one may attempt a treatment by which the spatial and time coordinates are separated into two scales. A more elaborate study will be conducted, using the method of multiple scale analysis (Nayfeh, 1973) which has been useful in the derivation of transport theories for magnetohydrodynamic fluctuations in the solar wind (Zhou and Matthaeus, 1989; 1990a,b,c). The approach which combines the RNG with a scale parameter expansion method from perturbation theory can be considered as a further refinement from that of the Green's function technique (Zhou *et al.*, 1989b; Zhou and Vahala, 1990).

One aspect of the future research is the subgrid modeling of two dimensional (2-d) Navier-Stokes turbulence. While it is known that the eddy viscosity is negative in 2-d Navier-Stokes turbulence due to inverse cascades (Kraichnan, 1976), the eddy viscosity representing the effects of the unresolvable subgrid scale in the corresponding vorticity equation is positive owing to the direct enstrophy cascade. We plan to carry out a recursive RNG analysis of 2-d Navier-Stokes turbulence. The resultant resolvable scale wavenumber dependent vorticity eddy viscosity will be compared with the subgrid scale eddy viscosity computed from the results of high-resolution direct numerical simulations of homogeneous, isotropic 2-d Navier-Stokes turbulence. Our subgrid model of 2-d Navier-Stokes turbulence will be evaluated according to turbulence theory (Kraichnan and Montgomery, 1980) and compared with well-developed simulation results.

We also plan to extend our recursive RNG analysis to develop other forms of turbulence models (such as $K - \epsilon$ model), as well as attack other important physical systems, such as passive scalar transport equations. These efforts will make recursive RNG available for much broader practical applications. In particular, the direct numerical simulation of the renormalized Navier-Stokes equation (Zhou *et al.*, 1988, 1989b; Zhou and Vahala, 1990) may have major impact on the systematic turbulence modeling and large eddy simulation.

Furthermore, it is of great interest to use the recursive RNG for the modified Betchov model (Kraichnan and Panda, 1988) since both the direct-interaction approximation (Kraichnan, 1959) and constrained decimated scheme (CDC) of Kraichnan (1985) have been applied to the Betchov model (Betchov, 1966; Williams *et al.*, 1989). We hope that the modified Betchov model can be used as a test site for all available subgrid scale closure techniques because of the difficulties of applying CDS to 2- or 3-d Navier-Stokes turbulence. Of particular interest would be the comparison between RNG and CDS since, as Kraichnan (1985) has pointed out,

RNG removes high-tk modes by repetitive transformations while the CDS removes these modes in one step.

Strong collaboration with Professor W. C. Reynolds and Dr. L. M. Smith is anticipated in several RNG related topics.

REFERENCES

BETCHOV, R. 1966 in *Dynamics of fluid and plasma* ed., S.I. Pai. Academic.

CHOLLET, J. P., & LESIEUR, M. J. 1981 *J. Atmos. Sci.* **38**, 2747.

DEARDORFF,J. W. 1971 *J. Comp. Phys.* **7**, 120.

DOMARADZKI, J. A., METCALFE, R. W., ROGALLO, R. S., & RILEY, J. J. 1987 *Phys. Rev. Lett.* **58**, 547.

FOURNIER, J. P., & FRISCH, U. 1983 *Phys. Rev. A* **28**, 1000.

FORSTER, D., NELSON, D., & STEPHEN, M. 1977 *Phys. Rev. A* **16**, 732.

KRAICHNAN, R. H. 1959 *J. Fluid Mech.* **5**, 497.

KRAICHNAN, R. H. 1976 *J. Atmos. Sci.* **33**, 1521.

KRAICHNAN, R. H. 1985 in *Theoretical Approaches to Turbulence*, ed. by L. Dwoyer, M. Y. Hussaini, and R. G. Voigt. Springer.

KRAICHNAN, R. H., & MONTGOMERY, D. 1980 *Rep. Prog. Phys.* **43**, 547.

KRAICHNAN, R. H., & PANDA, R. 1988 *Phys. Fluids* **31**, 2395.

LAUDAU, L., & LIFSHITZ, E. 1982 *Fluid Mechanics.* Pergamon.

LEONARD, A. 1974 *Adv. Geophys. A* **18**, 237.

LESIEUR, M. & ROGALLO, R. 1989 *Phys. Fluids A* **1**, . *718.*

LESLIE, D. C., & QUARINI, G. L. 1979 *J. Fluid Mech.* **91**, 65.

NAYFEH, A. 1973 *Perturbation Methods.* Wiley.

ROGALLO, R. S., & MOIN, P. 1984 *Ann. Rev. Fluid Mech.* **16**, 99.

ROSE, H. A. 1977 *J. Fluid Mech.* **81**, 719.

ROSE, H. A., & SULEM, P. L. 1978 J. Phys. (Paris) **39**, 441.

SMAGORINSKY, J. 1963 *Mon. Weather Rev.* **91**, 99.

WILLIAMS, T., TRACY, E. R., & VAHALA, G. 1989 *Phys. Rev. A,* **40** 3272.

WILSON, K. G. 1975 *Rev. Mod. Phys.* **47**, 773.

WILSON, K. G., & KOGUT, J. 1974 *Phys. Rep.* **12C**, 75.

YAKHOT, V., & ORSZAG, S. A. 1986 *J. Sci. Comput.* **1**, 3.

ZHOU, Y. 1990 *Phys. Rev. A* **41**, 5683.

ZHOU,Y., & MATTHAEUS, W.H. 1989 *Geophys. Res. Lett.* **16**, 755.

ZHOU, Y. & MATTHAEUS, W. H. 1990a *J. Geophys. Res.* **95**, 10291.

ZHOU,Y., & MATTHAEUS, W. H. 1990b *J. Geophys. Res.* **95**, 14863.

ZHOU, Y., & MATTHAEUS, W. H. 1990c *J. Geophys. Res.* **95**, 14881.

ZHOU, Y., & VAHALA, G. 1988 *J. Plasma Phys.* **39,** 511.
ZHOU, Y., & VAHALA, G. 1990 *Phys. Lett. A* **147,** 43.
ZHOU, Y., VAHALA, G., & HOSSAIN, M. 1988 *Phys. Rev. A.* **37,** *2590.*
ZHOU, Y., HOSSAIN, M., & VAHALA, G. 1989a *Phys. Lett. A* **139,** 330.
ZHOU, Y., VAHALA, G., & HOSSAIN, M. 1989b *Phys. Rev. A* **40,** 5865.

Investigations of turbulent scalar fields using probability density function approach

By F. Gao

1. Motivation and objectives

1.1. Background

Scalar fields undergoing random advection have attracted much attention from researchers in both the theoretical and practical sectors (Chen *et al.* 1989, Pope 1990, Bilger 1989). Research interest spans from the study of the small scale structures of turbulent scalar fields to the modeling and simulations of turbulent reacting flows (Pope 1985, Lin & Pratt 1987).

The probability density function (PDF) method is an effective tool in the study of turbulent scalar fields, especially for those which involve chemical reactions. It has been argued that a one-point, joint PDF approach is the one to choose from among many simulation and closure methods for turbulent combustion and chemically reacting flows based on its practical feasibility in the foreseeable future for multiple reactants (Pope 1990).

Taking chemical species advected by an incompressible fluid as an example, the governing equations can be written as

$$\frac{\partial \vec{\phi}}{\partial t} + \vec{u} \cdot \nabla \vec{\phi} = D \nabla^2 \vec{\phi} + \vec{S}(\vec{\phi}), \tag{1}$$

where $\vec{\phi} = (\phi_1, \phi_2, ..., \phi_\sigma)$ are the mass fractions of the different chemical species and S_α is the reaction source term for species α. For simplicity, the Fickian diffusion coefficients have been assumed to be same for all species.

Defining the fine-grain density function

$$\rho(\vec{x}, t) = \delta(\vec{\phi}(\vec{x}, t) - \vec{\psi}),$$

the PDF equation corresponding to (1) can be derived (O'Brien 1980, Pope 1985)

$$\frac{\partial P(\vec{\psi})}{\partial t} + < \vec{u} \cdot \nabla \rho > = -\frac{\partial}{\partial \vec{\psi}} < D \rho \nabla^2 \vec{\phi} > - \frac{\partial}{\partial \vec{\psi}} [\vec{S}(\vec{\psi}) P(\vec{\psi})] \tag{2}$$

where $< \bullet >$ indicates ensemble average and $\frac{\partial}{\partial \vec{\psi}}$ is the gradient operator in the composition space.

Equation (2) shows that the reaction source term is expressed in a closed form, which distinguishes PDF approach from the traditional moment method. It should also be pointed out that if the joint PDF of the velocity and scalars is employed, the convective terms are also closed. Both of these properties are highly desirable.

However, the weakness of the PDF method is also obvious – it only provides the local information, thus the interaction between neighboring points has to be modeled, i.e. the term representing molecular diffusion has to be treated by *ad hoc* assumptions.

To deal with the interactions between different points in the flow field, multi-point PDF's are introduced (e.g. Jiang 1990). Unfortunately, the inclusion of more points does not resolve the diffusion closure problem and increases the dimension of the problem drastically. It is normally very difficult to solve a differential equation of many variables numerically. Thus the application of multi-point PDF is likely to be quite limited. Another problem with multi-point PDF is that it is not a suitable quantity to handle the small scale structures of the scalar field. Let ψ_1 and ψ_2 be the values of scalar $\phi(\vec{x})$ at points $\vec{x}_1$ and $\vec{x}_2$ respectively, the two-point PDF of ϕ has the property

$$\lim_{\vec{x}_2 \to \vec{x}_1} P_2(\psi_1, \psi_2; \vec{x}_1, \vec{x}_2, t) = P_1(\psi_1; \vec{x}_1, t)\delta(\psi_2 - \psi_1).$$

The numerical solutions of a multi-point PDF may encounter significant errors when applied to the points that are very close to each other.

The major advantage of the PDF method is that it avoids having to close both the convective and the highly nonlinear reaction terms. But the problems with modeling molecular diffusion have not been properly resolved. To model the diffusion term correctly, it is important for us to understand the small scale structures of the scalar fields, which are described by the statistical properties of the scalar gradient. This can be easily seen if we rewrite the diffusion term in (2) under homogeneous conditions as

$$< \rho \nabla^2 \phi >= \frac{\partial}{\partial \psi}[E\{(\nabla \phi)^2 | \psi\} P(\psi)],$$

where $E\{A|B\}$ is the expectation of A conditional on a given B.

1.2. Objectives

Instead of the multi-point PDF, we suggest introducing the joint PDF of a scalar and its gradient which represents the roles of both scalar and scalar diffusion. It is hoped that this study will lead to a proper closure model for the molecular diffusion term in the PDF equation.

Another direction in this research is to study the mapping closure method that has been recently proposed to deal with the PDF's in turbulent fields (Chen *et al.* 1989, Kraichnan 1990a). This method seems to have captured the physics correctly when applied to diffusion problems (Gao 1990). However, if the turbulent stretching is included, the amplitude mapping has to be supplemented by either adjusting the parameters representing turbulent stretching at each time step or by introducing the coordinate mapping. This technique is still under development and seems to be quite promising.

The final objective of this project is to understand some fundamental properties of the turbulent scalar fields and to develop practical numerical schemes that are capable of handling turbulent reacting flows.

2. Previous work

The following results concern the joint PDF of a scalar and its gradient and have been presented elsewhere (Gao & O'Brien 1990a). They are briefly outlined here in order to provide a clue for the future works in this direction.

Since scalar gradient is mainly affected by the small scale structures of the scalar field, we are, therefore, hopeful for two things. First, the isotropic conditions may be applied if the local isotropy condition is correct (Monin & Yaglom 1975). Under this condition, the joint PDF of ψ and $\vec{\xi} = (\xi_1, \xi_2, \xi_3)$, $\hat{P}(\psi, \vec{\xi})$, can be expressed by the joint PDF of ψ and ξ_1, $P(\psi, \xi)$ (Gao 1990a)

$$\hat{P}(\psi, \xi_1, \xi_2, \xi_3) = -[\frac{1}{2\pi\xi}\frac{\partial P(\psi, \xi)}{\partial \xi}]_{\xi=\sqrt{\xi_1^2+\xi_2^2+\xi_3^2}}.$$

Secondly, the universality of the scalar spectrum at small scales may be reflected in the PDF of the scalar gradient. It is argued that the PDF of ξ_1 conditional on a given ψ is a near Gaussian distribution (Gao & O'Brien 1990a). Hence, the conditional PDF $P(|\vec{\xi}|^2|\psi)$ is a χ^2-distribution with three degrees of freedom. Noticing that χ^2 is a special γ-distribution, our result is consistent with the *ad hoc* γ-distribution model for the scalar dissipation, which is used to investigate the intermittency effects of the scalar fields (Andrews & Shivamoggi 1990).

In the spectral space, the scalar is represented by the scalar spectrum $E_\phi(k)$ which is mostly distributed in the small k domain, while the scalar gradient is expressed by the dissipation spectrum $D_\phi(k)$ which is concentrated in the large k domain (see, e.g. Tennekes & Lumley 1973). Figure 1 shows such spectra schematically. When Péclet number is large, these two spectra are widely separated so that ψ and $\vec{\xi}$ are weakly correlated. This conclusion is in agreement with direct numerical simulation results (Rogers 1990).

To further investigate the joint PDF of a scalar and its gradient, the conditional PDF of ξ_1 is expanded according to the Gram-Charlier expansion,

$$P(\xi|\psi) = \frac{1}{\sqrt{2\pi}\sigma}e^{-\frac{\xi^2}{2\sigma^2}}\sum_{n=0}^{\infty}a_n(\psi)H_n(\frac{\xi}{\sqrt{2}\sigma}), \tag{3}$$

where H_n's are the Hermite functions and

$$\sigma^2(\psi) = E\{(\frac{\partial\phi}{\partial x})^2|\psi\},$$

$$a_n = \frac{1}{2^n n!}\int_{-\infty}^{\infty}P(\xi|\psi)H_n(\frac{\xi}{\sqrt{2}\sigma})d\xi.$$

The expansion coefficients can be evaluated as $a_0 = 1$ and $a_2 = 0$, and under isotropic conditions,

$$a_{2n+1} = 0.$$

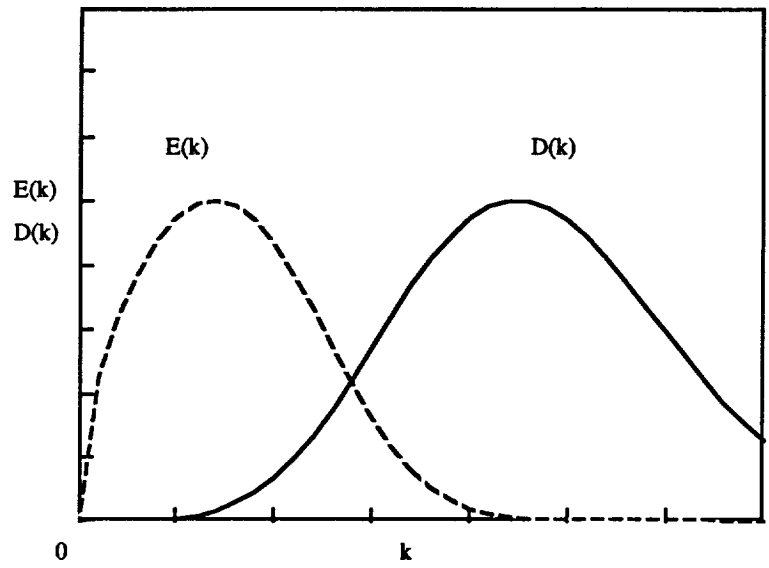

FIGURE 1. Sketch of the Spectra for Ψ, E(k), and ξ, D(k).

Direct numerical simulation (DNS) results are used to evaluate a_n and $\sigma(\psi)$. Primary results show that a_4 is of the same order of magnitude as a_1 and a_3, indicating that a_n is small for higher n, thus a Gaussian distribution is a good approximation for $P(\xi|\psi)$. DNS results also show that $\sigma(\psi)$ is almost a constant throughout most of the ψ domain and drops to zero rapidly as ψ approaches ψ_{max} and ψ_{min}, which is consistent with theoretical predictions.

The database available at the Center for Turbulence Research will be used to evaluate a_n and $\sigma(\psi)$ further under different flow conditions. The details will be outlined in Section 4.

3. Accomplishments

3.1. Mapping closure for PDF

In a different spirit, Chen *et al.* (1989) derive the governing equation for scalar PDF using a Liouville type of equation in the composition space. They then propose a closure method which maps the scalar field to a multivariate Gaussian reference field. This method is subsequently generalized to include the PDF's of various quantities such as that of velocity gradient, etc. (Kraichnan 1990a, 1990b).

Two types of mapping have been considered and both have given some encouraging results. The coordinate mapping has been used by Kraichnan to investigate the PDF of the velocity gradient in Burger's equation. Strong intermittency effects have been demonstrated (Kraichnan 1990a, 1990b). As for the amplitude mapping, the general mapping equation for a turbulent scalar field has been solved analytically (Gao 1990b). The amplitude mapping technique is subsequently generalized

to deal with the joint PDF of multispecies under Fickian diffusion (Gao & O'Brien 1990b).

3.2. Amplitude mapping

Suppose a one-to-one mapping is established between ψ and the reference field ψ_0, $\psi = X(\psi_0, t)$, the mapping equation can be written as (Chen *et al.* 1989)

$$\frac{\partial X}{\partial t} = S(X) + D < \xi_0^2 > (-\frac{\psi_0}{< \psi_0^2 >}\frac{\partial X}{\partial \psi_0} + \frac{\partial^2 X}{\partial \psi_0^2}), \tag{4}$$

where $\xi_0^2 = |\nabla \psi_0|^2$. It corresponds to the scalar evolution equation (1) for single scalar case.

When $S = 0$, the general solution of equation (4) can be written

$$X(\psi_0, t) = \frac{1}{\sqrt{2\pi}a}\int_{-\infty}^{\infty} X(u, 0)\exp[-\frac{(\phi e^{-\tau} - u)^2}{2a^2}]du, \tag{5}$$

where $\phi = \psi_0/\sqrt{< \psi_0^2 >}$, $\tau = D< \xi_0^2 >t/< \psi_0^2 >$ and

$$a^2 = 1 - e^{-2\tau}.$$

The probability density function can then be calculated according to the mapping relation

$$P(\psi, t) = P_0(\psi_0)(\frac{\partial X}{\partial \psi_0})^{-1},$$

where P_0 is a Gaussian distribution. Figure 2 demonstrates the evolution of an initially double-delta PDF

$$P(\psi, 0) = \frac{1}{2}[\delta(\psi - 1) + \delta(\psi + 1)].$$

Two properties of the scalar fields which have been difficult to recover using the traditional closure models (Pope 1985) now can be readily derived from (5). First, the boundedness of the scalar field is preserved as it can be easily seen that

$$[X(\psi_0, 0)]_{\min} \leq \psi = X(\psi_0, t) \leq [X(\psi_0, 0)]_{\max}.$$

Second, the relaxation to Gaussian of any scalar PDF under Fickian diffusion is captured since

$$X(\psi_0, t) \longrightarrow \alpha(t)\psi_0 \qquad \text{when} \qquad t \gg 1.$$

When n scalars are involved, it has been shown that mapping relations can be established between these scalars and n independent, multivariate Gaussian reference fields. The equations governing these mapping relations can be solved formally (Gao & O'Brien 1990b). This procedure is useful when time-splitting schemes are used to integrate the evolution of the scalar transport equations where the effects of convection, diffusion and chemical reaction can be treated independently.

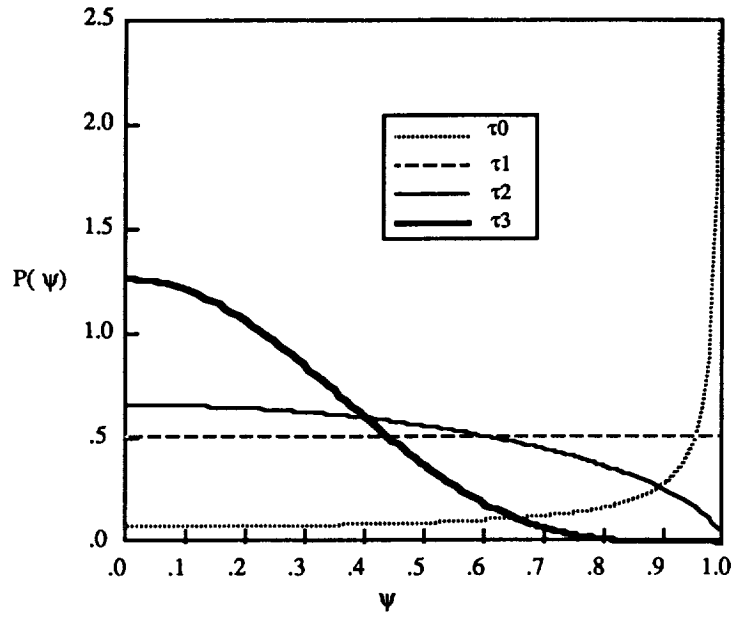

FIGURE 2. Evolution of an Initially Double-Delta PDF.

4. Future plans

The goal of this research is to develop a practical scheme to simulate turbulent reacting flows and combustion. According to Pope (1990), PDF method seems to be a prominent candidate among the available methods for this purpose. It has been identified that the major difficulty one would encounter in the PDF formulation is to close the diffusion term. The results presented above are aimed at addressing this problem. Since these results are mostly obtained from theoretical arguments, our first task will be to test them against experimental and/or numerical data. At the current stage, it is planned to use the extensive DNS data available at CTR for the following purposes.

1) To identify the role of the higher order terms in expansion (3), the coefficients a_n will be further evaluated under different flow conditions. It is hoped that two questions will be answered. First, is local isotropy a good approximation for the turbulent scalar fields? Second, are the higher order terms important?

2) To find out the statistical inter-dependency between a scalar and its gradient. An important quantity to calculate for this purpose is $\sigma^2 = E\{(\nabla\phi)^2|\phi\}$ if the higher order terms in the Gram-Charlier expansion are indeed negligible. Besides, proper modeling of the diffusion term also depends on our knowledge about this quantity.

3) To compare the scalar PDF's obtained from DNS with those derived from the mapping closure in order to determine the applicability of the mapping closure to the reacting flow problems. In this case, the amplitude mapping will be used with the parameter representing turbulent stretching effects being adjusted at each time step.

It is hoped that this research will lead to proper closure models for the PDF equations, which can be used to simulate practical problems in combustion and chemically reacting flows. This will be the first phase of this work.

The second phase of this research will be to explore the possibility of constructing a numerically efficient scheme for the reacting and combustion problems by using the closures obtained from the first phase. There are certain difficulties for this task, especially in the case of combustion where the heat release and temperature variation effects are strong and the diffusion and reaction are closely coupled. DNS results are expected to be used to investigate these problems.

Study on the joint PDF of a scalar and its gradient will also be pursued by using the amplitude and coordinate mappings with the hope that it will help us to better understand the structures of turbulent scalar fields as well as the interactions between the scalar and velocity fields.

REFERENCES

ANDREWS, L. C. & SHIVAMOGGI, B. K. 1990 The gamma distribution as a model for temperature dissipation in intermittent turbulence. *Phys. Fluid A.* **2**, 105.

BILGER, R. W. 1989 Turbulent diffusion flame. *Ann. Rev. Fluid Mech.* **21**, 101-135.

CHEN, H., CHEN, S. & KRAICHNAN, R. H. 1989 Probability distribution of a stochastically advected scalar field. *Phys. Rev. Lett.* **63**, 2657-2660.

CHEN, J.-Y., KOLLMANN, W. & DIBBLE, R. W. 1989 Pdf modeling of turbulent nonpremixed methane jet flames. *Combust. Sci. Tech.* **64**, 315.

GAO, F. 1990a Ph.D. thesis. State Univ. of New York at Stony Brook.

GAO, F. 1990b An analytical solution for the scalar probability density function in homogeneous turbulence. *CTR Manuscript 119,* Stanford University.

GAO, F. & O'BRIEN, E. E. 1990a On the joint probability density function of a scalar and its gradient in isotropic turbulence. Submitted to *J. Fluid Mech.*

GAO, F. & O'BRIEN, E. E. 1990b A mapping closure for multispecies Fickian diffusion. Submitted to Phys. Fluids A.

JIANG, T.-L. 1990 Ph.D. thesis. State Univ. of New York at Stony Brook.

KRAICHNAN, R. H. 1990a *Proc. 6th Beer-Sheva Seminar*, Jerusalem.

KRAICHNAN, R. H. 1990b Models of intermittency in hydrodynamic turbulence. *Phys. Rev. Lett.*. **65**, 575-578.

LIN, P. & PRATT, D. T. 1987 Numerical simulation of a plane turbulent mixing layer, with applications to isothermal, rapid reactions. *AIAA Paper 87-0224.*

MONIN, A. S. & YAGLOM, A. M. 1975 *Statistical Fluid Mechanics*, MIT Press.

O'BRIEN, E. E. 1980 in *Turbulent Reacting Flows*, Springer-Verlag.

POPE, S. B. 1981 Monte Carlo method for the PDF equations of turbulent reactive flow. *Combust. Sci. Tech.* **25**, 159-174.

POPE, S. B. 1985 PDF methods for turbulent reactive flows. *Prog. Energy Combust. Sci.* **11**, 119-192.

POPE, S. B. 1990 Computations of turbulent combustion: progress and challenges (Plenary Lecture). *23rd Symposium (International) on Combustion.*

ROGERS, M. M. 1990 Private communication.

TENNEKES, H. & LUMLEY, J. L. 1973 *A First Course in Turbulence*, MIT Press.

Center for Turbulence Research
Annual Research Briefs - 1990

Modeling turbulent boundary layers in adverse pressure gradients

By S. E. Belcher

1. Motivation and objectives

Many of the turbulent boundary layers encountered in practical flows develop in adverse pressure gradients; hence, the dynamics of the thickening and possible separation of the boundary layer has important implications for design practices.

What are the key physical processes that govern how a turbulent boundary layer responds to an adverse pressure gradient, and how should these processes be modeled? Despite the ubiquity of such flows in engineering and nature, these questions remain largely unanswered. The turbulence closure models presently used to describe these flows commonly use 'wall functions' that have *ad hoc* corrections for the effects of pressure gradients. There is, therefore, a practical and theoretical need to examine the effects of adverse pressure gradients on wall bounded turbulent flows in order to develop models based on sound physical principle.

The present study is focussed on the evolution of a turbulent boundary layer on a flat wall with an externally imposed pressure gradient. In practical flows, the pressure gradient may be associated with curvature of the wall, *e.g.* the boundary layer on an airfoil or the flow of the atmospheric boundary layer over a hill. Curvature is known to have a strong dynamical effect on turbulence (see, for example, the experiments of Gillis & Johnston, 1983) and so, in this initial theoretical investigation, it is preferable to consider the effect of only a pressure gradient. This simplification is appropriate and timely since there are recent and ongoing computational and experimental investigations of externally decelerated pressure gradient (Spalart & Watmuff, 1990). This flow is not separated, but recent laboratory studies by Simpson, Chew & Shivaprasad (1981), and Dengel & Fernholtz (1990) provide detailed measurements when separation is present.

We consider flows with 'gentle' or incipient separation, when the region of reversed mean flow, if it exists, is confined well within the boundary layer (figure 1*a*). This is an appropriate starting point for a theoretical study of separation and has practical value: in many engineering flows, 'large scale' separation, when the entire boundary layer breaks away from the wall (figure 1*b*)), is detrimental to performance; hence, in order to achieve the highest pressure drop along a device without stall, it is desirable to decelerate the flow such that the boundary layer is maintained as close to separation as possible. Furthermore, in atmospheric flows, the boundary layer is of the order of a kilometer deep, so that large scale separation occurs only due to the largest topographic features (*e.g.* the Rockies!), but gentle separation may occur over even gently undulating terrain.

The overall objectives are (i) to establish the significant scales of length, velocity, and shear stress in the different parts of the flow; (ii) to improve low order parameterizations of the effects of the deceleration on the turbulence; and (iii) to develop a

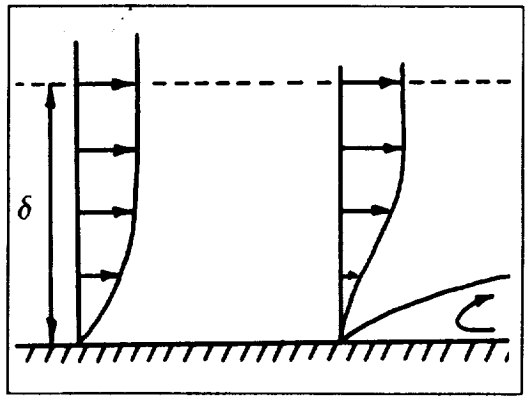

FIGURE 1*a*. Gentle separation.

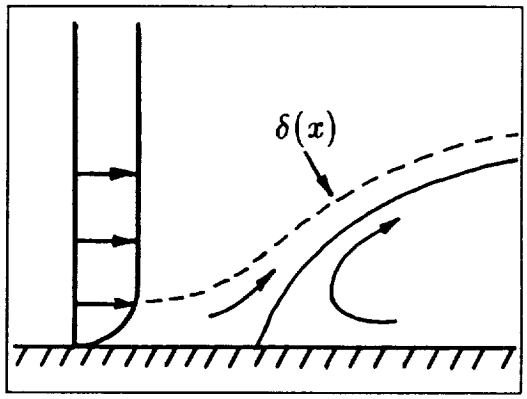

FIGURE 1*b*. Large scale separation.

low order closure model to describe the effects of the turbulence on the mean flow. This work has aspects in common with the study of Durbin (see elsewhere in this volume) and we aim to work together on some aspects of this work.

2. Present and future work

This investigation has only recently begun, so that no significant results can yet be reported. The methodology of the proposed work is now described in more detail.

As described above, the investigation proceeds in three parts. More details of these aspects are described below, and despite the separation of this discussion into three parts, it is anticipated that each strand of the research will be developed in parallel.

2.1 Determination of the significant scales

The initial part of this study is focussed on establishing the significant scales of length, velocity, and shear stress in the different regions of the flow using the method of matched asymptotic expansions. Two types of turbulent boundary layer need to

be considered. Far upstream, where the pressure gradient has no significant effect on the flow, the boundary layer has an equilibrium form and is described by the classical two layer form: a defect layer that extends through most of the boundary layer, where, at leading order, the mean velocity is equal to the free stream velocity; and close to the surface is a thin wall-layer, where, at leading order, the gradient of the Reynolds shear stress balances the viscous shear stress. The flow in such a boundary layer is characterized by the friction velocity, u_*, and the free stream velocity, u_e. Near the separation point, however, by definition, the surface shear stress is zero and the boundary layer has a quite different structure. Zero stress boundary layers have not been treated with asymptotic methods, and so the initial part of the investigation has focussed on their structure. Near the surface the appropriate velocity scale is $u_p = [\nu dp/dx]^{\frac{1}{3}}$, which leads to the well known square root profile for the mean velocity; the defect layer, which again constitutes the bulk of the boundary layer, is governed by nonlinear dynamics.

The key to understanding the structure of the decelerating flow is then to determine how the boundary layer evolves from the equilibrium form to the zero stress form (*i.e.* as value of the local ratio u_*/u_p changes in the streamwise direction). In particular, what is the streamwise length scale of the transition? An answer will provide a criterion, to be satisfied by the pressure gradient and the approach flow, for separation to occur and a length scale for the position of the separation point. Furthermore, the asymptotic structure of the flow provides a framework for examining the different processes controlling the dynamics of the turbulence in the flow.

There have been previous studies of the asymptotic structure of a separated boundary layer (Melnik, 1989; Neish & Smith, 1990; Sychev & Sychev, 1980), which have suggested rather complex structures for the flow. In these studies, much of the complexity of the resulting asymptotic structure arises from the use of a specific closure model (Melnik, 1989, and Neish & Smith, 1990, use the Cebeci-Smith algebraic eddy viscosity model) and not from any particular physical process associated with the development of the boundary layer. Furthermore, Sychev & Sychev (1980) have developed a twelve layer asymptotic description of a boundary layer with large scale separation; however, the assumption of a steady mean flow is less justified in this case, so the complex structure they discuss is of questionable practical value. We believe that the present approach of studying gently separated flows using asymptotic analysis without a specific closure model will produce interesting and important insights, whilst avoiding a highly complex structure that is unlikely to occur in the real flow.

2.2 Parameterization of the turbulence

It is proposed that the scalings derived for the different regions of the flow will be used to formulate a sequence of 'model flows' in order to examine the structure of the turbulence in the strongly perturbed boundary layer. It is anticipated that the turbulence will be analyzed using rapid distortion theory and by scaling existing model equations (*e.g.* the $k-\epsilon$ model equations). These studies will suggest which are the key terms in the transport equations for the Reynolds stresses.

2.3 A low order turbulence model for the flow

The results of the fundamental studies will be used to develop a low order closure model for the turbulent stresses to be used in practical engineering codes. This aspect of the study will draw on the recent work of Durbin (see elsewhere in this volume), who has developed a closure model for the near wall region of a boundary layer that does not use 'wall functions' (*i.e.* heuristic functions that damp the eddy viscosity to zero close to the wall).

In formulating the model, we intend to examine the properties of the model for the dissipation length scale recently suggested by Hunt, Stretch & Britter (1986), which has been tested against data obtained by direct numerical simulation of some simple boundary layer flows by Hunt, Spalart & Mansour (1989). This would obviate the need for a transport equation for the turbulence dissipation, thereby reducing the computational cost of the model. Furthermore, this approach would bypass the numerical difficulties that have been encountered with the ϵ-equation when separation is present (Newley, 1986).

REFERENCES

DENGEL, P. & FERNHOLTZ, H. H. 1990 An experimental investigation of an incompressible turbulent boundary layer in the vicinity of separation. *J. Fluid Mech.* **212**, 615-636.

GILLIS, J. C. & JOHNSTON, J. P. 1983 Turbulent boundary layer flow and structure on a convex wall and its redevelopment on a flat wall. *J. Fluid Mech.* **135**, 123-153.

HUNT, J. C. R., STRETCH, D. D. & BRITTER, R. E. 1988 Length scales in stably stratified flows and their use in turbulence models, *Proc. IMA Conference on stably stratified flow and dense gas dispersion*, Chester, April 9-10.

HUNT, J. C. R., SPALART, P. R. & MANSOUR, N. N. 1987 A general form for the dissipation length scale in turbulent shear flows, *Proc. 1987 CTR Summer Program*, CTR Report CTR-S87.

MELNIK, R. E. 1989 An asymptotic theory of turbulent separation. *Comp. and Fluids.* **17**, 165-184.

NEISH, A. & SMITH, F. T. 1990 On turbulent separation in the flow past a bluff body. *Manuscript.*

NEWLEY, T. M. J. 1986 Turbulent air flow over low hills. *PhD Thesis, University of Cambridge.*

SIMPSON, R. L., CHEW, Y.-T., & SHIVAPRASAD, B. G. 1981 The structure of a separating turbulent boundary layer. Part 1 mean flow and Reynolds stresses. *J. Fluid Mech.* **113**, 23-51.

SPALART, P. R. & WATMUFF, J. H. 1990 Experimental and numerical study of a turbulent boundary layer with pressure gradients. *Manuscript.*

SYCHEV, V. V. & SYCHEV, VIK. V. 1980 On turbulent separation. *Zh. Vyssh. Mat. Mekh. Fiz.* **20**, 1500.

N93-71433

Modeling hypersonic boundary-layer flows with second-moment closure

By P. G. Huang

This report presents an ongoing research effort designed to apply the best possible second-moment-closure model to simulate complex hypersonic flows. The baseline model under consideration is the Launder-Reece-Rodi Reynolds stress transport turbulence model. Two add-ons accounting for wall effects are tested, namely, the Launder-Shima low-Reynolds-number model and the compressible wall-function technique. Results are reported for flow over a flat plate, both adiabatic-wall and cooled-wall cases. It has been found that further improvements of the existing models are necessary to achieve accurate prediction in high Mach number flow range.

1. Motivation and objectives

It has been reported that Reynolds-stress models yield marked improvements in predicting a range of complex *incompressible* turbulent flows over models based on the conventional eddy-viscosity concept. This experience has encouraged the extension of the models to turbulent flows with strong shock/boundary-layer interaction. Dimitriadis and Leschziner (1990) have implemented an algebraic stress model with the Cell-Vortex scheme. Vandromme *et al.* (1983) and HaMinh *et al.* (1985) solved a complete Reynolds stress model employing the implicit/explicit MacCormack scheme.

While these Reynolds stress models offer a direct extraction of stress quantities without additional approximations, the models are numerically unstable. This is partly due to their highly non-linear and coupled nature and partly due to the lack of turbulent viscosity in the momentum equations as can be found in eddy-viscosity models. As a result, a numerical stabilizing strategy is often required to secure a solution. A major effect in this phase of the study has been focused on these numerical issues.

Calculations based on two variants of the Launder, Reece and Rodi Reynolds-stress model (1975) will be reported: one uses the wall function technique and the other is the low-Reynolds-number extension of Launder and Shima (1989). The former uses the law of the wall to bridge the region between the fully turbulent zone and the wall, while the latter allows a direct integration of all quantities to the wall. While the extension of the low Reynolds number model to compressible flow calculations is straightforward, the use of the wall-function technique requires special attention for the *compressible* law of the wall and the viscous heat generation inside the near-wall layer need to be taken into account.

Results reported in this study are limited only to flow over a flat plate. The Mach number ranges from 2 to 8 for insulated wall; the Mach number is fixed at 5 for

the cold-wall cases, and the wall temperature varies from 20 to 100 percent of the adiabatic wall temperature.

2. Turbulence models

2.1. Reynolds-stress equations

The turbulence model used here is the high-Reynolds-number Reynolds stress model of Launder, Reece and Rodi (1975). The transport equation for $\rho\overline{u_iu_j}$ is

$$\frac{D\rho\overline{u_iu_j}}{Dt} - D_{ij} = P_{ij} + \Phi_{ij} - \rho\epsilon_{ij} \tag{1}$$

The convective and the generation terms, $D\rho\overline{u_iu_j}/Dt$ and

$$P_{ij} = -\rho\left(\overline{u_iu_k}\frac{\partial U_j}{\partial x_k} + \overline{u_ju_k}\frac{\partial U_i}{\partial x_k}\right) \tag{2}$$

are exact and require no approximation. The diffusion term is represented by the generalized gradient diffusion hypothesis;

$$D_{ij} = \frac{\partial}{\partial x_k}\left[\left(c_k\rho\frac{k}{\epsilon}\overline{u_iu_j} + \mu\delta_{kl}\right)\frac{\partial\overline{u_iu_j}}{\partial x_l}\right] \tag{3}$$

The pressure-strain correlation Φ_{ij} is modeled according to Gibson and Launder (1978) to be composed of three processes, namely, Rotta, rapid, and wall-echo terms;

$$\Phi_{ij} = \Phi_{ij,1} + \Phi_{ij,2} + \Phi_{ij,w} \tag{4}$$

In equation (4)

$$\Phi_{ij,1} = -c_1\rho\epsilon a_{ij} \tag{5}$$

$$\Phi_{ij,2} = -c_2\left(P_{ij} - 2/3\delta_{ij}P_k\right) \tag{6}$$

where $P_k = 1/2P_{ii}$ and a_{ij} is the dimensionless anisotropic part of the Reynolds stress,

$$a_{ij} = \frac{\overline{u_iu_j}}{k} - 2/3\delta_{ij} \tag{7}$$

The wall-echo term arises from the reflection of pressure fluctuation from the rigid wall and contains contributions from turbulent and mean strains;

$$\Phi_{ij,w} = \Phi_{w1,ij} + \Phi_{w2,ij} \tag{8}$$

where

$$\Phi_{w1,ij} = c_{1w}\rho\frac{\epsilon}{k}(\overline{u_ku_m}n_kn_m\delta_{ij} - 3/2\overline{u_ku_i}n_kn_j - 3/2\overline{u_ku_j}n_kn_i)f \tag{9}$$

and

$$\Phi_{w2,ij} = c_{2w}\rho\frac{\epsilon}{k}(\Phi_{km,2}n_kn_m\delta_{ij} - 3/2\Phi_{ki,2}n_kn_j - 3/2\Phi_{kj,2}n_kn_i)f \tag{10}$$

The wall damping function, f, is taken as $0.4k^{3/2}/\epsilon y_n$, y_n being the distance normal to the wall. Finally, dissipation is assumed isotropic,

$$\epsilon_{ij} = 2/3\epsilon\delta_{ij} \tag{11}$$

The turbulence energy dissipation rate is governed by solving

$$\frac{D\rho\epsilon}{Dt} = \frac{\partial}{\partial x_k}\left[\left(c_\epsilon\rho\frac{k}{\epsilon}\overline{u_k u_l} + \mu\delta_{kl}\right)\frac{\partial\epsilon}{\partial x_l}\right] + c_{\epsilon 1}\frac{\epsilon}{k}P_k - c_{\epsilon 2}\frac{\rho\epsilon^2}{k} \tag{12}$$

The suggested constants are (Launder and Gibson, 1978):

c_1	c_2	c_{1w}	c_{2w}	c_k	c_ϵ	$c_{\epsilon 1}$	$c_{\epsilon 2}$
1.8	0.6	0.5	0.18	0.22	0.18	1.44	1.92

Launder and Shima (1989) have extended (1) to the viscous sub-layer. The basic ingredient is to introduce three dimensionless parameters to modify the model constants. The dimensionless parameters are the turbulent Reynolds number, $R_t = k^2/\nu\epsilon$, and the second and the third invariants of the stress tensor,

$$II = a_{ij}a_{ji} \tag{13}$$

and

$$III = a_{ik}a_{kj}a_{ji} \tag{14}$$

After systematic tuning, the following modifications to the constants are recommended;

$$c_1 = 1 + 2.58\,A\,II^{1/4}\left[1 - exp\left(-(0.0067R_t)^2\right)\right] \tag{15}$$

$$c_2 = 0.75A^{1/2} \tag{16}$$

$$c_{1w} = -2/3c_1 + 1.67 \tag{17}$$

$$c_{2w} = 2/3(c_2 - 1) + 0.5 \tag{18}$$

$$c_{\epsilon 1} = 1.45 + 2.5A(P_k/\epsilon - 1) + 0.3(1 - 0.3II)exp[-(0.002R_t)^2] \tag{19}$$

$$c_{\epsilon 2} = 1.9 \tag{20}$$

where $A = 1 - 9/8(II - III)$

Furthermore, in order to prevent the sink term of (12) going near to infinity as the wall is approached, the term is modified according to

$$\frac{\epsilon^2}{k} \longrightarrow \frac{\epsilon\,\tilde{\epsilon}}{k} = \frac{\epsilon}{k}\left[\epsilon - 2\nu\left(\frac{\partial k^{1/2}}{\partial y}\right)^2\right] \tag{21}$$

where $\tilde{\epsilon}$ vanishes at the wall.

It should be noted that in the high-Reynolds-number region, the constants provided by Launder and Shima do not revert to those recommended by Launder and Gibson.

2.2. Heat-flux equations

In addition to the stress equations, the heat flux equations are needed in compressible flow calculations. The following assumptions are made to obtain the heat-flux equations:

(1) Following the ASM local-equilibrium assumption, the transport terms are neglected.

(2) The fine scale dissipative motion is assumed to be isotropic, $\Phi_{\overline{u_iT'},w} = 0$.

(3) The wall influence on the pressure-temperature-gradient interaction is assumed insignificant.

The heat-flux equations yield:

$$P_{\overline{u_iT'}} + \Phi_{\overline{u_iT'}} = 0 \tag{22}$$

The generation $P_{\overline{u_iT'}}$ is exact and contains two parts, the stress-temperature-gradient and the heat-flux-strain interactions.

$$P_{\overline{u_iT'}} = P_{\overline{u_iT'},1} + P_{\overline{u_iT'},2} \tag{23}$$

where

$$P_{\overline{u_iT'},1} = -\overline{u_ku_i}\frac{\partial T}{\partial x_k} \tag{24}$$

$$P_{\overline{u_iT'},2} = -\overline{u_kT'}\frac{\partial U_i}{\partial x_k} \tag{25}$$

The pressure-temperature-gradient interaction is modeled to comprise two terms (Launder and Gibson, 1978):

$$\Phi_{\overline{u_iT'}} = \Phi_{\overline{u_iT'},1} + \Phi_{\overline{u_iT'},2} \tag{26}$$

where

$$\Phi_{\overline{u_iT'},1} = -c_{1T}\frac{\epsilon}{k}\overline{u_iT'} \tag{27}$$

$$\Phi_{\overline{u_iT'},2} = -c_{2T}P_{\overline{u_iT'},1} \tag{28}$$

The constants recommended are $c_{T1} = 3$ and $c_{T2} = 0.5$. These constants are used in Reynolds stress calculations employing wall functions.

In the present study, however, it was found that, with $c_{T1} = 3.19$ and $c_{T2} = 0$, the Launder-Shima model provides a better recovery factor for flow over an adiabatic flat plate. This set of constants is thus used for low-Reynolds-number calculations. It is noted that this set of constants is in accord with the one suggested by HaMinh *et al.* (1985).

2.3. Wall functions

The present wall functions follow closely the approach suggested by Bradshaw (1977) and independently by Viegas and Rubesin (1985). For compressible flows, the law of the wall can be expressed as

$$\frac{U_c}{u_\tau} = \frac{1}{\kappa}ln(\frac{u_\tau y}{\nu_w}) + C \tag{29}$$

where U_c is a pseudo-velocity representing the Van-Driest transformation and can be shown to have the following form:

$$\frac{U_c}{u_\tau} = \frac{1}{R}\left\{sin^{-1}\left[\frac{R(U/u_\tau + H)}{(C_1 + R^2H^2)^{1/2}}\right] - sin^{-1}\left[\frac{RH}{(C_1 + R^2H^2)^{1/2}}\right]\right\} \tag{30}$$

where

$$R = u_\tau\left(\frac{Pr_t}{2c_pT_w}\right)^{1/2} \tag{31}$$

$$H = \frac{q''_w}{\tau_w u_\tau} \tag{32}$$

The constant C and C_1 recommended by Bradshaw (1977) are:

$$C = 5.2 + 95M_t^2 + 30.7B_q + 226B_q^2 \tag{34}$$

$$C_1 = 1 \tag{33}$$

where

$$B_q = \frac{q''_w}{\rho_w c_p u_\tau T_w} \tag{35}$$

$$M_t = \frac{u_\tau}{c_w} \tag{36}$$

c_w and q''_w are the speed of sound and the rate of heat transfer at the wall. The turbulent Prandtl number, Pr_t, is fixed at 0.9 for all calculations.

The heat transfer from the wall to the first finite-volume cell (where $y^+ \approx 30$) is calculated according to:

$$q''_T = q''_w + U_m\tau_w \tag{37}$$

where U_m represents the velocity mid-way between the first grid point and the wall.

The production of Reynolds stresses is modified in the near-wall layer according to

$$-\rho\overline{uv}\frac{\partial U}{\partial y} \approx \frac{1}{y_{cv}}\int_0^{y_{cv}} \tau_w\frac{\partial U}{\partial y}dy \approx \frac{\tau_w U_{cv}}{y_{cv}} \tag{38}$$

where subscript cv indicates the position of control-volume face between the point adjacent to the wall and the one above it.

The average ϵ over the near-wall cell is approximated as:

$$\bar{\epsilon} \approx \frac{\rho c_\mu^{3/4} k^{3/2} U^+_{cv}}{y_{cv}} \tag{39}$$

Finally ϵ at the point adjacent to the wall, 2, is prescribed as;

$$\epsilon_2 = \frac{k_2^{3/2} c_\mu^{3/4}}{\kappa y_2} \tag{40}$$

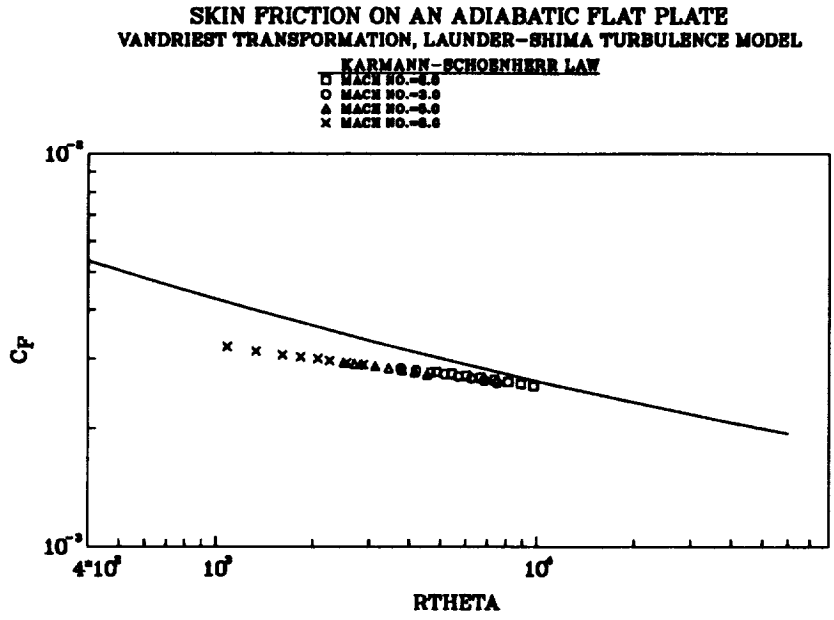

(a)

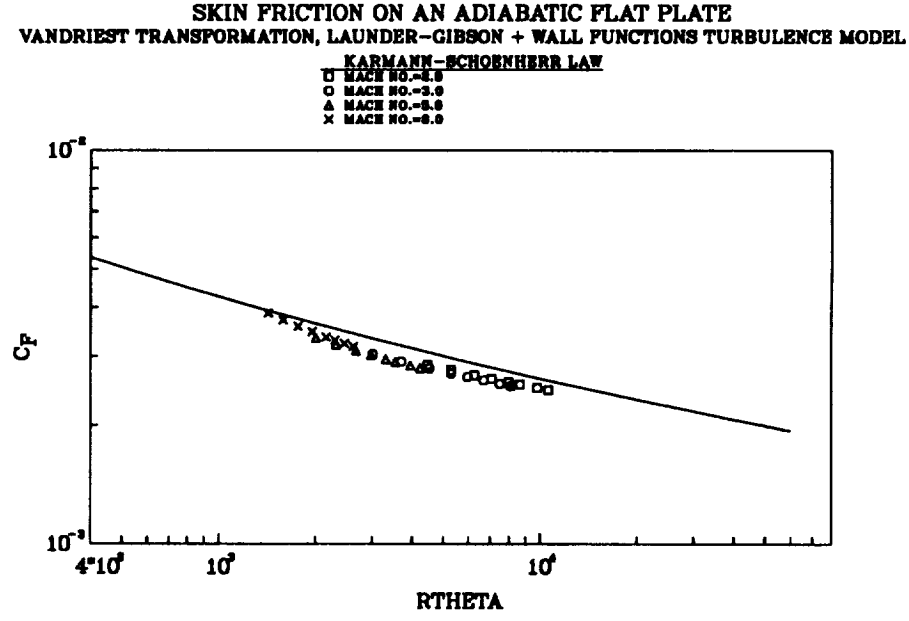

(b)

FIGURE 1. Generalization of adiabatic-wall skin friction, C_f vs. Re_θ, *(a)* L-S, *(b)* L-G.

3. Numerical method

Although the differential equations are expressed in Cartesian coordinates, the code implemented solves the complete 2-D Navier-Stokes' equations in non-orthogonal curvilinear mesh, plane and axisymmetric geometries. All dependent variables are stored at the center of the control-volume cell and a finite-volume principle is applied to impose conservation across the control-volume faces.

TVD schemes are used to discretize the convective terms (Huang, 1989) while the center differencing scheme is used for the diffusive terms. The numerical diffusion provided by the TVD schemes can, on the one hand, prevent unrealistic oscillation in regions where gradient of the dependent variable is high, and on the other hand, offer an "optimum" artificial diffusion to stabilize the calculation.

The numerical algorithm is implicit and is based on a symmetric Gauss-Seidel line-by-line relaxation method, which combines features derived from Gnoffo (1986) and MacCormack (1985). This method, coupled with implicit treatments of the boundary conditions, has been found to provide a rapid acceleration of solution, for it allows a large value of Courant number to be used in the calculation.

4. Accomplishments

Attention is confined in this section to computations of flow over a flat plate: insulated-wall and cooled-wall cases.† Comparisons are made with the Van Driest II theory, which has been found to provide good agreements with the available experimental data (Hopkins and Inouye, 1971).

Figures 1(a) and 1(b) show variations of the adiabatic-wall skin friction with Re_θ, obtained from the Launder-Shima model (L-S) and the Launder-Gibson-wall-function model (L-G), respectively. The Van Driest II theory is used to deduce the incompressible results from the compressible calculations. The solid line is the Kármán-Schoenherr formula, and the symbols represent results obtained from calculations. The results have shown that L-S returns an incorrect slope of the skin friction variation, reflecting a poor prediction of the skin friction at high Mach number, shown in Figure 2(a). In contrast, L-G results in a correct slope of the skin friction variation while the predicted values are slightly lower than the experimental correlation, as depicted in Figure 2(b).

The skin friction profiles on a non-adiabatic plate at Mach number equal to 5 are shown in Figure 3. Again, the Van Driest II formula is used to scale all predicted data to the incompressible one. For calculations based on T_w equal to adiabatic wall temperature, T_{aw}, both L-S and L-G return results similar to those shown in Figure 1.

As shown in Figure 3(a), L-S still displays the same incorrect slope of skin friction profile, resulting in a better skin friction prediction at low T_w. While Figure 4(a) shows that L-S provides a good prediction for $T_w/T_{aw} = 0.2$, it should be noted that the experimental data does not seem to support the Van Driest II theory for region where $T_w/T_{aw} < 0.3$. The failure of L-S can also be depicted in Figure 5(a)

† Some of these results are presented in a recent paper by Coakley *et al.* (1990)

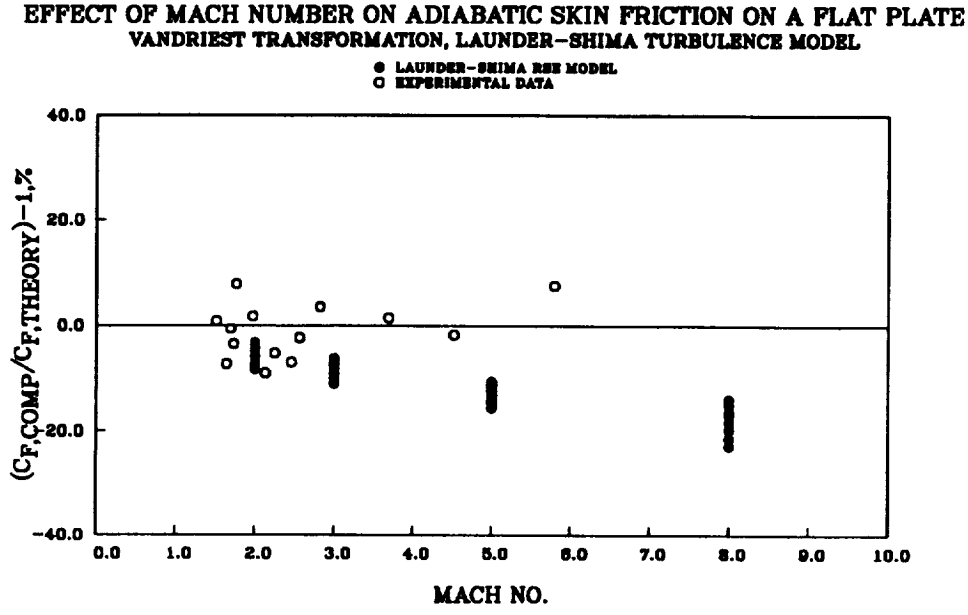

(a)

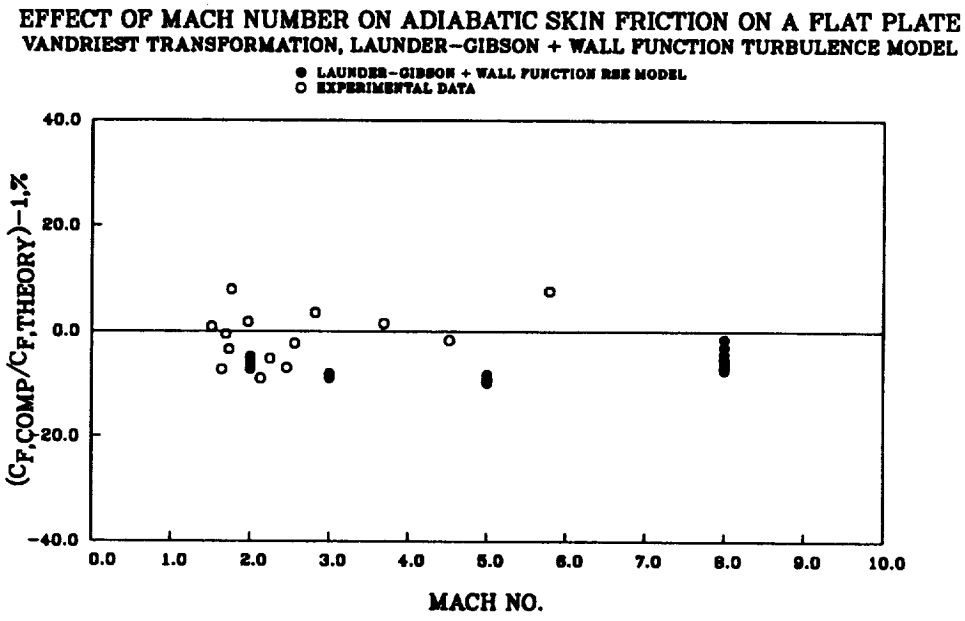

(b)

FIGURE 2. Effect of Mach number on adiabatic-wall skin friction, *(a)* L-S, *(b)* L-G.

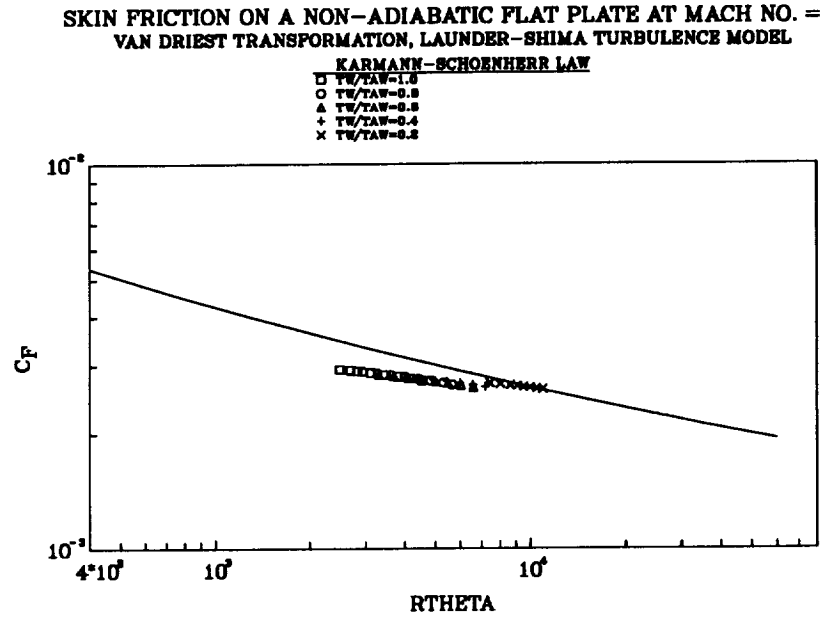

(a)

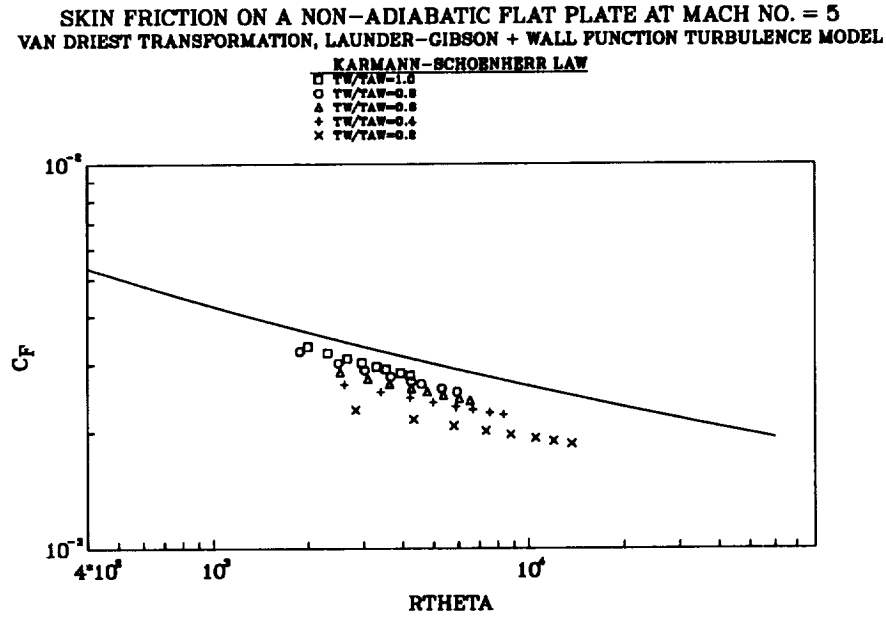

(b)

FIGURE 3. Generalization of non-adiabatic-wall skin friction, C_f vs. Re_θ, *(a)* L-S, *(b)* L-G.

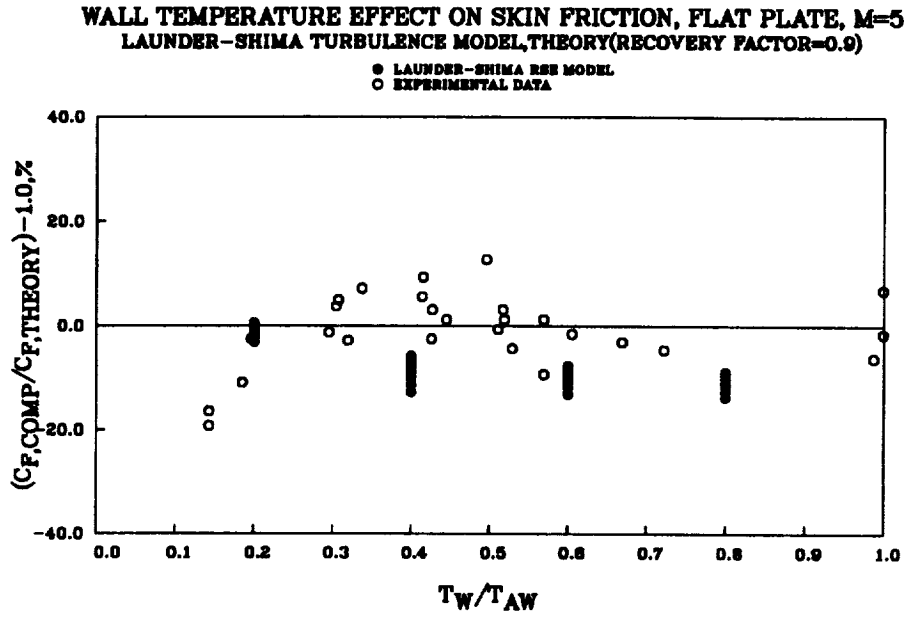

(a)

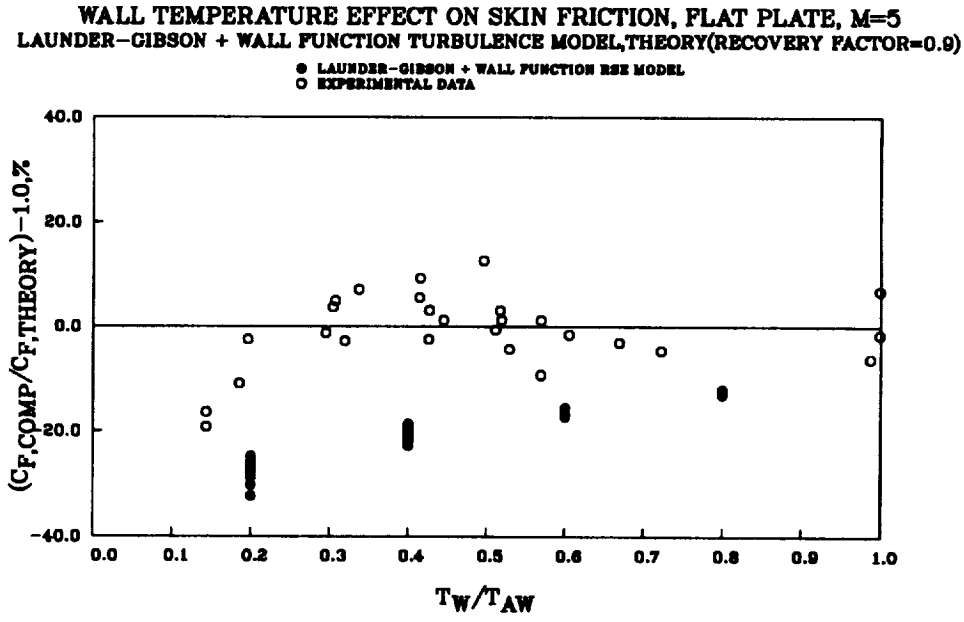

(b)

FIGURE 4. Wall temperature effect on skin friction at $M = 5$, *(a)* L-S, *(b)* L-G.

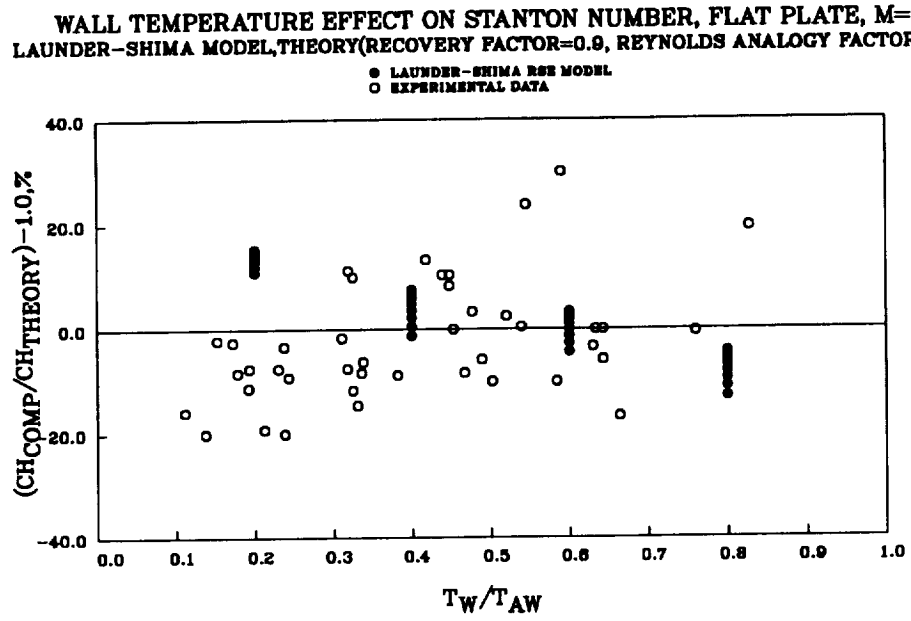

(a)

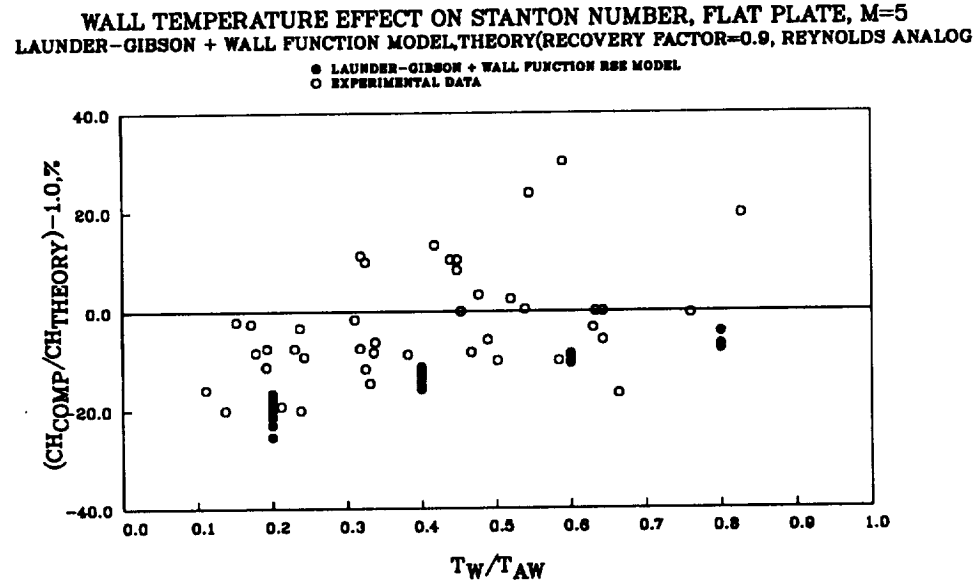

(b)

FIGURE 5. Wall temperature effect on Stanton number at $M = 5$, *(a)* L-S, *(b)* L-G.

where Stanton number are compared in a manner analogous to the skin friction shown in Figure 4(a). The theoretical Stanton number, $(C_h)_{the}$, is obtained by assuming a recovery factor of 0.9 and a Reynolds analog factor of 1.0. It can be found that Stanton number prediction does not agree well with the experimental data. The experimental data shows a positive slope across the theoretical line while the prediction displays a negative slope.

In contrast, L-G tends to under-predict the skin friction and the Stanton number at low wall temperature, showing a departure of the predicted values away from the theoretical ones as the wall temperature decreases. This observation has suggested that improvements of the wall functions for non-adiabatic flows are needed.

5. Future plans

(1) Improve the Launder-Shima model for high Mach number flow.

(2) Consider the FRAME model (HaMinh *et al.*, 1985), which has been found to offer excellent agreements in predicting the above-mentioned flow (Coakley *et al.*, 1990).

(3) Modify the wall functions to predict flow in non-adiabatic conditions.

(4) Extend the Reynolds Stress models to complex hypersonic flows.

REFERENCES

BRADSHAW, P. 1977 Compressible turbulent shear layers. *Ann. Rev. Fluid Mech.* **9**, 33-54.

COAKLEY, T. J., VIEGAS, J. R., HUANG, P. G. & RUBESIN, M. W. 1990 An assessment and application of turbulence models for hypersonic flows. 9th National Aero-Space Plane Technology Sym.. **106**, Orlando, Florida.

DIMITRIADIS, K. P.& LESCHZINER, M. A. 1990 Modeling shock/turbulent-boundary-layer interaction with a cell-vortex scheme and second-moment closure. 12th Int. Conf. on Num. Meths. in Fluid Dynamics, Oxford, England.

GIBSON, M. M.& LAUNDER, B. E. 1978 Ground effects on pressure fluctuation in the atmospheric boundary layer. *J. Fluid Mech.* **86**, 491-511.

GNOFFO, P. A. 1986 Application of program Laura to three dimensional AOTV flow fields. *AIAA-86-0565.* 24th Aerospace Sciences Meeting, Reno, NV.

HAMINH H., RUBESIN, M.W., VANDROMME, D. & VIEGAS, J. R. 1985 On the use of second order closure modeling for the prediction of turbulence boundary layer/shock wave interaction: physical and numerical aspects. Int. Sym. on Computational Fluid Dynamics, Tokyo, Japan.

HOPKINS, E.& INOUYE, M. 1971 An evaluation of theories for predicting turbulent skin friction and heat transfer on flat plates at supersonic and hypersonic Mach numbers. *AIAA J.* **9**, 6, 993-1003.

HUANG, P. G. 1989 A numerical method for prediction of compressible turbulent flows with closure models. *Annual Research Briefs - 1989.* Center for Turbulence Research, 185-193.

LAUNDER, B. E., REECE, G. J. & RODI, W. 1975 Progress in the development of a Reynolds-stress turbulence closure. *J. Fluid Mech.* **68**, 537-566.

LAUNDER, B. E. & SHIMA, N. 1989 Second-moment closure for the near-wall sublayer: development and application. *AIAA J.* **27**, 10, 1319-1325.

MACCORMACK, R. W. 1985 Current status of numerical solutions of the Navier-Stokes equations. *AIAA-85-0032.* 23rd Aerospace Sciences Meeting, Reno, NV

VANDROMME, D., HAMINH, H., VIEGAS, J. R., RUBESIN, M. W. & KOLLMANN, W. 1983 Second order closure for the calculation of compressible wall bounded flows with an implicit Navier-Stokes solver. 4th Sym. on Turbulent Shear Flows, Karlsruhe, Germany.

VIEGAS, J. R. & RUBESIN, M. W. 1985 On the use of wall-functions as boundary conditions for two-dimensional separated compressible flows. *AIAA-85-0180.* 23rd Aerospace Sciences Meeting, Reno, NV.

C-2

Direct simulation of turbulent combustion

By T. J. Poinsot[1]

1. Previous work and objectives

Understanding and modeling of turbulent combustion are key problems in the computation of numerous practical systems. Because of the lack of analytical theories in this field and of the difficulty of performing precise experiments, direct simulation appears to be one of the most attractive tools to use in addressing this problem.

The first part of the present work (September 1988-September 1989) was split into two parts:

1. Development and validation of a direct simulation method for turbulent combustion.

2. Applications of the method to premixed turbulent combustion problems and especially to computations of flame/vortex interactions.

Results obtained during phase 1 were related to the choice of the equations to consider for turbulent reacting flows and the development of a new method to impose boundary conditions for the compressible Navier-Stokes equations. These results are summarized for the reacting case in Poinsot and Lele (1989) and for the non-reacting case in Poinsot and Lele (1990). Some of them have been presented at the 1989 APS meeting (Poinsot, Colonius & Lele 1989).

Results related to phase 2 describe the effects of isolated vortex pairs interacting with premixed flame fronts. An analytical study of the expression of flame stretch and curvature in a turbulent flow was first done during the visit of Prof. Candel at Berkeley in 1989 (Candel and Poinsot 1990). The definition of flamelet regimes and the applicability of flamelet models for turbulent combustion were reconsidered in view of the direct simulation results. These simulations were first used to predict the occurrence of flame quenching by isolated vortex pairs and the type of regime for which flamelet regimes may be obtained. Some of these results have been presented at the Symposium on Combustion in Orleans (Poinsot, Veynante & Candel 1990) and a complete description of this work has been submitted to the Journal of Fluid Mechanics (Poinsot, Veynante & Candel 1991). This study has received some interest among experimentalists: an experimental study on flame vortex interaction has already been published by Roberts and Driscoll (1990). In this work, the spectral diagram derived in (Poinsot *et al.* 1990) is re-constructed using experimental results.

From September 1989 to September 1990, new problems have been studied using direct simulation but also experiments and theoretical models:

1 Ecole Centrale de Paris

1. The influence of curvature on premixed flame fronts

Curvature is a parameter which has been neglected in many models of turbulent combustion but appears to be more important than expected. Its effects were investigated using direct simulation and experimental data of Bunsen burner tips. This study was performed in collaboration with T. Echekki and Prof. G. Mungal (Stanford Univ.)

2. The construction of a model for the flame stretch based on direct simulation and multifractal analysis

The stretch rate of flamelets in premixed turbulent combustion is of utmost importance in combustion models because it represents the source term of the flame surface. It was computed here using (1) detailed numerical simulations of vortex/flame interactions and (2) a model for intermittent turbulence taking into account all possible turbulence scales acting on the flame front (Meneveau and Poinsot 1990).

3. The simulation of the interaction between a random flow field and a flame front

Although much may be learned from computations of isolated vortices interacting with flames, certain problems require the simulation of a more complete case where a complete turbulent flow interacts with a flame front.

The general objective was to improve our knowledge of turbulent combustion but also to use this information for turbulent combustion models. The transfer of direct simulation results towards models is also in progress. A submodel to evaluate the flame stretch has been derived from the present study (Section 3) and incorporated in the Coherent Flame model used in France for piston and aircraft engines.

2. The influence of curvature on premixed flame fronts.

2.1 Introduction

The flamelet concept is a simple and widely used concept in turbulent combustion modeling. It is based on the assumption that combustion occurs in thin layers (called flamelets) which are convected and distorted by the turbulent flowfield (Marble and Broadwell 1977, Bray 1980, Williams 1985, Peters 1986). To first order, this requires chemical times to be smaller than the turbulence times. Diagrams proposed by Borghi (1984) or Peters (1986) give a qualitative description of the response of a given flame to a given turbulent flow field. Knowing the turbulence integral scale and the turbulent kinetic energy, these diagrams indicate if the flow will feature flamelets. However, because of the complexity of the mechanisms involved (Poinsot, Veynante and Candel 1990), the exact limits of the flamelet domain are still an open subject.

Even when the flamelet assumption is valid, modeling premixed turbulent combustion remains a challenging problem. This is due to strong flamelet/flow field interactions. On one hand, density changes through the flame front (typically an order of magnitude) result in vorticity generation and flow acceleration. On the other hand, the flow alters the flame structure through different mechanisms: curvature, strain, and unsteady effects. In computations of turbulent combustion, the

flamelet assumption may be used in two different ways:

• If the flame is viewed as an infinitely thin interface between fresh and burned gases, its position may be tracked as a free boundary between the two phases (*flame front tracking*). This method does not solve for the internal structure of the flame but resolves all the flow turbulent motions. It may, therefore, be considered as a partial direct simulation method (Ghoniem *et al.* 1982, Ashurst 1987, Osher and Sethian 1987, Poinsot and Candel 1986). The concept of flame front tracking has also been used in fractal models of premixed turbulent combustion (Gouldin *et al.* 1989, Mantzaras *et al.* 1989).

• More global models (generally called *flamelet models*) are based on an average description of the turbulent reacting flow. The important quantity for modeling combustion is then the mean reaction rate (Bray 1980). Under the flamelet assumption, the mean reaction rate per unit volume is the product of the flame surface density (the mean flame surface per unit volume) and the mean local consumption rate per unit flame surface (Candel *et al.* 1988) or equivalently the product of the flamelet-crossing spatial frequency and the mean consumption rate per crossing (Bray and Libby 1986). In these models, the flow turbulence is not resolved. It is modeled, for example, through the turbulent kinetic energy and its dissipation rate. Similarly, the flame front topology is not resolved but modeled through the flame surface Σ.

Each of these two flamelet approaches makes use of a flame speed to characterize the local flame behavior. It is important to realize that these two flame speeds are fundamentally different.

• In flame front tracking models, the relevant flame speed is the normal flame front velocity with respect to the unburned gas. This is the only quantity required to describe the chemical process. We will call this speed *the displacement speed* S_d.

• In global flamelet models, the characteristic speed is a measure of the reaction rate per unit area of the flame front. We will refer to this quantity as *the consumption speed* S_c defined as:

$$S_c \equiv \frac{\int_{-\infty}^{+\infty} \dot{\omega}_R \, (\mathbf{n} \cdot d\mathbf{x})}{\rho_u Y_{R,u}}, \tag{1}$$

where $\dot{\omega}_R$ is the mass of reactant consumed per unit time per unit volume; ρ_u the density of the unburned gas; $\mathbf{x}$ the position vector of an infinitesimal amount of reactant; and $\mathbf{n}$ a unit vector normal to an isothermal surface at $\mathbf{x}$. Therefore, the integral in Eq. (1) is computed along the normal to the flame front. $Y_{R,u}$ is the mass fraction of the fuel in the fresh gases.

In the case of a one-dimensional, planar flame placed in a uniform flow of fresh gases, the displacement and consumption speeds reduce to the usual laminar flame speed S° ($S_d = S_c = S^\circ$).

When the flame front is curved or when the flow is non uniform, the displacement speed and the consumption speed may differ by orders of magnitude. In the case of a flame tip at unity Lewis number, the consumption speed S_c at the tip (on the symmetry axis) is of the order of the laminar flame speed S°, while the displacement speed S_d can be one order of magnitude larger than S° and S_c.

An important problem for all models based on the flamelet assumption is the correlation of the flame speeds of individual flamelets with the local flow properties. Which parameters should be used in a flamelet model to correlate the variations of the displacement and consumption speeds with the flow characteristics and the flame geometry is still an open question.

One possible answer to this question is the relation between flame stretch and the displacement flame speed S_d obtained by Clavin and Williams (1982). The flame stretch is defined by the fractional rate of change of a Lagrangian flame surface element Σ (Williams 1985):

$$\kappa = \frac{1}{\Sigma}\frac{d\Sigma}{dt}. \tag{2}$$

Assuming that the characteristic scales of the flame wrinkles are large compared to the flame thickness d and using asymptotic analysis, Clavin and Joulin (1983) show that the displacement speed is a linear function of a single parameter, the flame stretch κ .

$$\frac{S_d}{S^\circ} = 1 - \frac{\mathcal{L}}{S^\circ}\kappa, \tag{3}$$

where $\mathcal{L}$ is a characteristic length that depends on the thermal and diffusive properties of the combustible mixture. This relation has been used in studies of premixed turbulent flame propagation to express the displacement speed of the reaction front (Ashurst 1987).

The flame stretch κ may be written in terms of the kinematic and geometrical properties of the flame and of the flow field. It is the sum of two terms: a flame curvature term and a strain term (Matalon 1983, Candel and Poinsot 1990). When $\kappa > 0$, the flame front is positively stretched (in most cases, we will simply call it 'stretched'). The simplest example of a positively stretched flame is the planar stagnation point flame. When $\kappa < 0$, the flame front is negatively stretched (we will call it 'compressed'). A typical example of a compressed flame is a flame front curved towards the fresh gases.

The asymptotic relation (3) shows that, at least for small stretch values, stretch alone can be used to describe the flamelet behavior. The fact that curvature and strain play similar roles in flame stretch then suggests an important simplification: the flamelet behavior may be studied by considering only planar strained flames (these are simpler to study than curved flames). In other words, according to asymptotic analysis, a curved flame and a planar flame will feature the same dynamics if their total stretch is the same. Therefore, studying planar flames should be sufficient, and this explains why the basic emphasis of flamelet modeling of premixed turbulent combustion has been on planar strained flamelets where curvature is absent. In this context, the flame front is viewed as a collection of positively stretched laminar stagnation point flames (see Fig.1a). This geometry has been extensively investigated in analytical studies based on large activation energy asymptotic methods (Libby and Williams 1982, 1987, Libby, Linan & Williams 1983) as well as in computational works (Darabiha *et al.* 1986, Giovangigli and Smooke 1987) and experimental studies (Ishizuka and Law 1982).

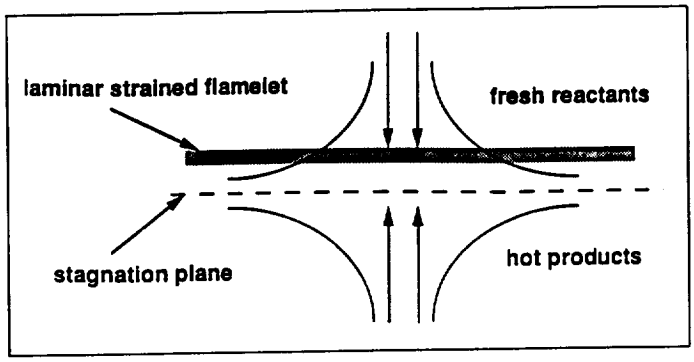

FIGURE 1A. The laminar stagnation point flame

Now, the first major difficulty in a description of turbulent flamelets based on planar stagnation point flames is that the asymptotic relation (3) (which is its first justification) has been established for low values of the flame stretch. Its extension to high stretch values (and strong curvature) has no rigorous basis. A second difficulty is that planar stagnation point flames are submitted to positive stretch and cannot really be expected to represent curved flamelets which are typically submitted to negative stretch. Since most turbulent flames involve high flame stretch and highly curved flame fronts, these questions have to be addressed to provide a satisfactory flamelet model. A simple examination of a turbulent flame (see Fig. 1.b) reveals that planar flamelets are not the only flamelets present along the flame front. Certain regions of the flame surface may be strongly curved towards the fresh gases and, therefore, negatively stretched (i.e. compressed). For example, a flame front embedded in a turbulent shear layer will be positively stretched at certain locations (typically in the braids) and strongly curved (and therefore negatively stretched or compressed) at locations where the flame is wrapped around the vortices. At this point it is worth mentioning that direct simulations of flames propagating in isotropic three-dimensional turbulence (Rutland 1989) show that flame fronts tend to align with the principal axis of strain and thereby suggest that in a statistical sense, the stagnation point flame picture is more probable than the curved flame. However, this does not mean that curved flames can be neglected. Although curved flamelets are not found in a turbulent flame brush as often as stagnation point flamelets, they might have a strong effect on the flame dynamics. Studying curved flames and more generally compressed flame fronts is clearly of interest.

Considering now strongly curved flames, we have first to wonder whether the dynamics of these flame fronts may be correlated with stretch only (in the same way that planar stagnation point flames are correlated with stretch). For example, the constant density analysis of Mikolaitis (1984) reveals significant effects of curvature on flame propagation. Mikolaitis claims that flame stretch alone is insufficient to explain the dynamical behavior of strongly curved flames (such as flame tips of Bunsen burners) and that curvature should also be included as an additional independent parameter in any model describing turbulent flamelets. Using similar

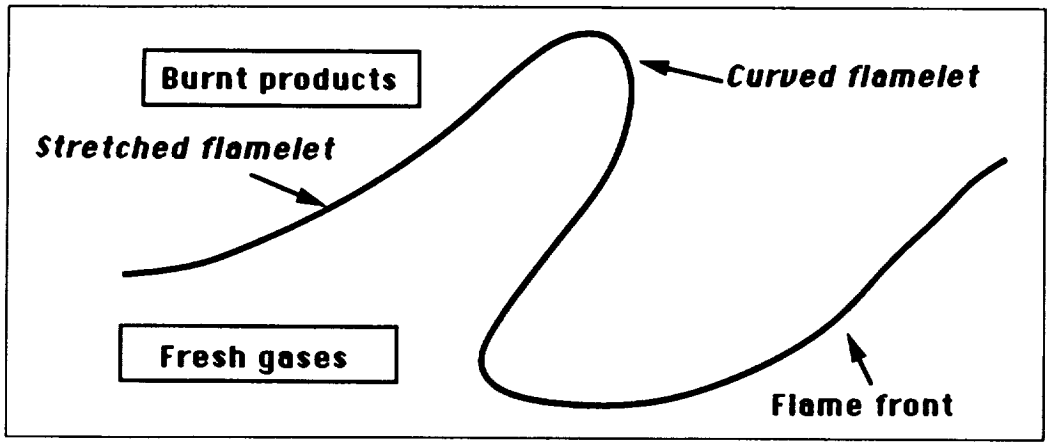

FIGURE 1B. A schematic of stretched and compressed flamelets in a turbulent flow.

ideas, the integral analysis of Chung and Law (1988) provides a relation for the displacement speed in terms of two parameters: the stretch κ and the curvature $\nabla_t \cdot \mathbf{n}$ (Law 1988):

$$\frac{S_d}{S^\circ} = 1 + \delta_T^\circ(\nabla_t \cdot \mathbf{n}) + (\frac{1}{Le} - 1)\,(\frac{\delta_T^\circ/S^\circ}{2T_{ad}/T_a})\,\kappa, \tag{4}$$

where δ_T° is the characteristic length of the preheat zone for the unstretched flame; T_{ad} the adiabatic flame temperature; T_a the activation temperature; $\mathbf{n}$ the unit vector normal to the flame pointing towards the burned gases; and Le the Lewis number. $\nabla_t \cdot \mathbf{n}$ is positive for a flame curved towards the unburned gases (convex flame) and may be written as $(\frac{1}{\mathcal{R}_1} + \frac{1}{\mathcal{R}_2})$ where $\mathcal{R}_1$ and $\mathcal{R}_2$ are the principal radii of curvature of the flame surface. $\nabla_t \cdot \mathbf{n}$ reduces to $\frac{1}{\mathcal{R}}$ in a two-dimensional geometry and to $\frac{2}{\mathcal{R}}$ in an axisymmetric geometry. According to Eq. (4), the displacement speed is a function of two geometrical parameters: flame stretch and flame curvature (and not only flame stretch). At unity Lewis number, Eq. (4) reduces to a form similar to the simple relation suggested by Markstein (1951) in his semi-phenomenological analysis. The relation suggests that the deviation of the displacement speed S_d from S° is proportional to the curvature parameter $\frac{1}{\mathcal{R}}$. We will refer to this relation as a Markstein type relation. The validity of Eqs. (3) and (4) may be checked later by comparing their predictions with numerical simulations and experimental results for unity Lewis number.

A convenient geometry to investigate the dependence of the characteristic flame speeds on strain and curvature is the flame tip of a Bunsen burner (Fig. 2). Flame tips are highly curved, steady flames. They may be viewed as a simple prototype of curved flamelets in a turbulent flow field. As indicated above, planar stagnation point flames are positively stretched ($\kappa > 0$) while flame tips are compressed ($\kappa < 0$). Since for most practical cases, the constant $\mathcal{L}$ in Eq. (3) is positive, Eq. (3)

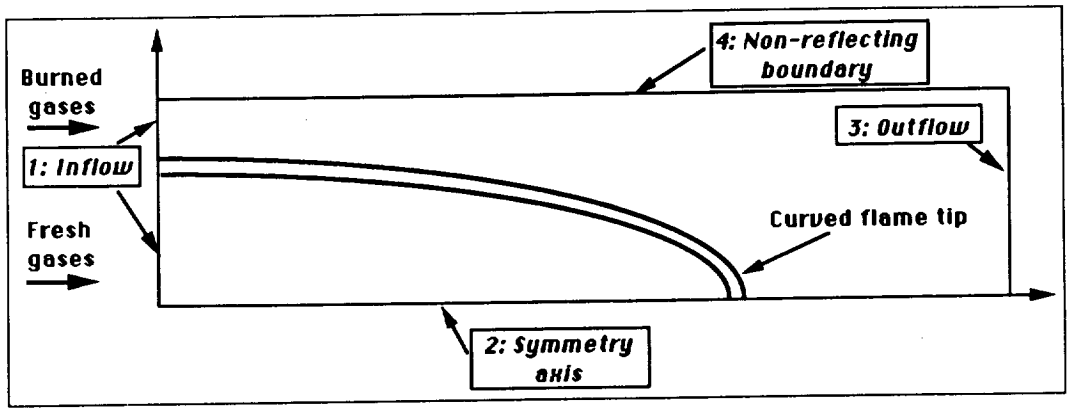

FIGURE 2. The flame tip as a prototype of curved flamelet.

shows that displacement speeds for a stagnation point flame will be lower than the unstretched flame speed while they will be higher for flame tips.

An advantage of the flame tip geometry is that both the displacement and consumption speeds can be unambiguously evaluated since the flow outside the flame region is almost uniform. In the case of a stagnation point flame, because the unburned gas flow is not uniform, the displacement speed cannot be measured directly. Moreover, the flame tip is less restrained by boundaries and is free to move in the flowfield to escape regions of intense strain, like flamelets in a turbulent flame brush. In terms of local flame structure, these properties suggest that the flame tip may be a good prototype of flamelets in premixed turbulent combustion.

The objective of the study of Poinsot, Echekki & Mungal (1990) was to investigate the physical mechanisms controlling flame tips and more generally strongly curved laminar flamelets embedded in a turbulent flowfield. This was done using a new one-dimensional analysis of curved flame propagation in a non-uniform flow along with numerical simulations and experimental data describing the two-dimensional flame tip. The discussion was restricted to gas mixtures of neutral diffusion (the Lewis number is equal to unity). Details of the analysis may be found in Poinsot, Echekki & Mungal (1990). We will only summarize the main results here.

2.2 Results

The quasi-one dimensional model giving a balance equation of fuel mass in a streamtube was first applied to the flame tip of the Bunsen burner. Results show that while the consumption speed is uniquely related to the processes occurring in the reaction zone, the displacement speed is strongly dependent on the hydrodynamic and diffusive processes occurring upstream of the reaction layer. Three mechanisms affecting the displacement speed were identified: a chemical mechanism associated with the modification of the reaction zone structure, a hydrodynamic mechanism due to lateral flow divergence and flame curvature, and a diffusive mechanism due to the diffusion of reactants and heat being non-aligned with the mean flow direction.

Direct simulations were then used to investigate the structure of the two-dimensional flame tip (with a Lewis number of unity):

(1) the reaction zone structure and, thereby, *the consumption speed* are not modified by curvature. Within the accuracy limits of the computation, any element of the flame front is characterized by the same distribution of the reaction rate along the normal to the front and, therefore, features the same local consumption speed (Figure 3). It is interesting to recall here that planar stagnation point flames also exhibit a large insensitivity to stretch when $Le = 1$ (Williams 1985). This is even more true in a turbulent flow where flamelets are able to move freely to escape from regions of high strain. Therefore, we may conclude that at unity Lewis number, the consumption speed of flamelets is affected neither by strain, nor by curvature. In other words, stretch (positive or negative) has no effect on the consumption speed. This is a considerable simplification for global flamelet models because (when the Lewis number is unity) the consumption speed may be assumed to be unaffected by turbulence and equal to the unstretched laminar flame speed $S°$.

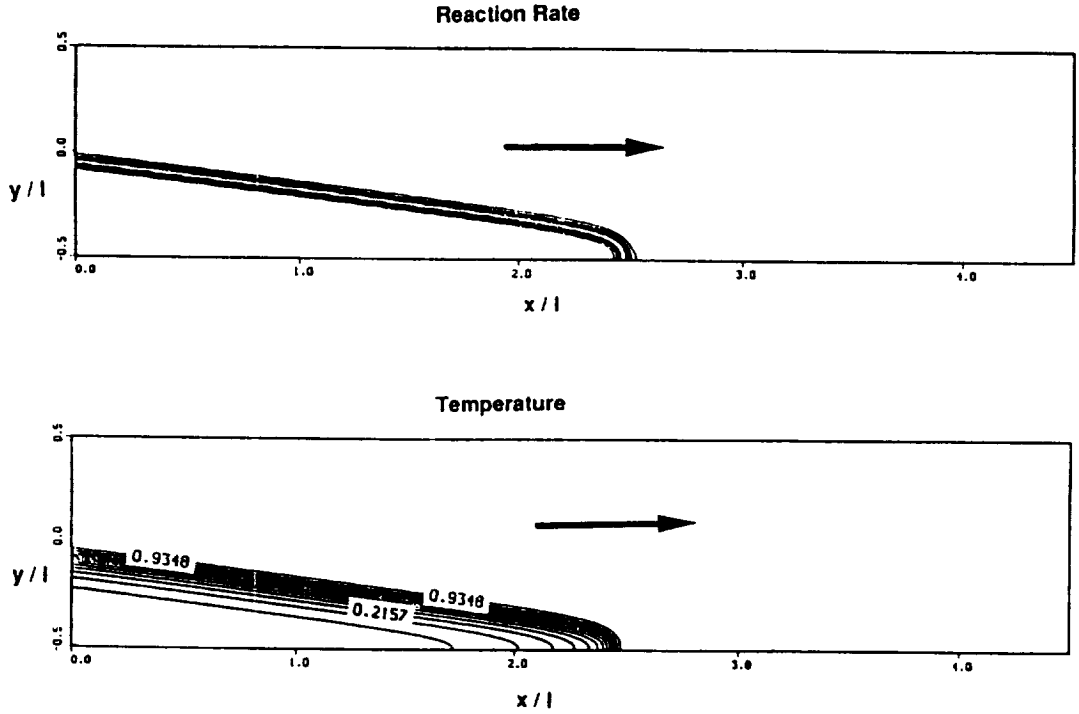

FIGURE 3. Computation of a flame tip of a Bunsen burner, Lewis = 1. Contours of reaction rate and of temperature.

(2) *the displacement speed* may be an order of magnitude higher than the unstretched flame speed $S°$. This effect is not due to any chemical mechanism because, as discussed above, the reaction zone structure at the tip is not affected by curvature (see Figure 3). The hydrodynamic mechanism was investigated by studying the divergence of the streamlines at the tip. It was found that this mechanism

accounts for approximately one half of the total increase of the displacement speed at the tip. The diffusive mechanism accounts for the other half. It was investigated by observing the divergence of the reactant pathlines relative to the mean flow streamlines and by comparing the flame structure at the tip with the structure of a one-dimensional planar flame. The calculations show that the reactant pathlines diverge faster than the streamlines of the mean flow resulting in a net 'leakage' of reactants across the boundaries of the central streamtube.

Correlations of the displacement speed with flame stretch show that a single parameter (the flame stretch) may be used to predict the displacement speed and that the linear relationship predicted by asymptotic analysis holds for a wide range of stretch values. In the case of constant transport properties ($\rho\mathcal{D}$ = constant), the simulations results agree with the prediction of asymptotic analysis. In the case of variable transport properties, the dependence of the displacement speed is also linear but the slope of the result has to be modified to account for the large variations of the transport coefficients with temperature. The classical Markstein relation as well as its extension proposed by Chung and Law (1988) are found to be valid only at low stretch.

In the context of turbulent combustion, a first result of the analysis is the existence of a minimum radius of curvature of a curved flame convex towards the fresh gases. When applied to the turbulent motion of a flame front in a non-uniform flowfield, the formulation also predicts that curvature will induce very different propagation speeds at different locations of the front. Flamelets which are strongly curved towards the fresh gases have very high displacement speeds and come back to more planar shapes rapidly. This effect attenuates the level of flame surface corrugations and may explain why the inner cut-off scales (the size of the smallest corrugation of the flame front in fractal theories) measured in experiments are very large (Shepherd, Cheng & Goix 1989). As a result, at a given instant, strongly curved flamelets are less likely to be found than positively stretched flamelets which correspond to a more 'stable' flame configuration. This point confirms previous results obtained by direct simulation of flame propagation in three-dimensional turbulence (Rutland 1989). Whether this justifies the use of the planar stagnation point flame as the only flamelet prototype in models for premixed turbulent combustion remains an open question. Although curved flamelets will have short lifetimes, they might have a strong effect on the flame dynamics and on the flame surface variations.

Finally, it is worth emphasizing that this work presents correlations between flame stretch and flame speeds valid only for unity Lewis number. It is well known that non-unity Lewis number leads to more complex situations like flame tip opening. In these cases, the consumption speed will depend strongly on curvature, but one may expect the hydrodynamic and diffusive mechanisms to still be the main parameters to determine the displacement speed.

3. A model for flamelet stretching and quenching rates

3.1 Introduction

The main simplification used in the studies of Poinsot, Veynante & Candel (1990)

was to neglect the effect of multiple vortices on the flame front and the structure of turbulence itself by considering the interaction of isolated vortices with a flame. The objective of the present work was to make some progress on these issues by combining the flame/vortex computations with the multifractal theory studied at CTR by C. Meneveau.

The starting point of this analysis is again the flamelet assumption (see Section 2.1) (Peters 1986, Williams 1985, Poinsot, Veynante & Candel 1990). This assumption was first extended to take partial quenching and non-laminar flamelet structures into account. In most flamelet models, one assumes that each flamelet behaves like a laminar flame. This is not a necessary assumption: the only important assumption in flamelet modeling is related to the topology of the flow and to the fact that fresh and burnt gases are separated by a relatively thin continuous region where chemical reactions take place. This region may have a laminar flame structure, but it may also be thickened by small scale turbulence without invalidating the flamelet assumption.

The flamelet assumption is not always satisfied. Knowing the turbulence integral scale and the turbulent kinetic energy, turbulent combustion diagrams indicate whether the flow will contain flamelets, pockets, or distributed reaction zones. This information is essential for building a model for turbulent combustion. A continuous flame front, without holes, will not be modeled in the same way than a flame which is broken into many small pockets and where combustion does not take place along a sheet but in a more distributed manner. Under the flamelet assumption, a central parameter for turbulent combustion modeling is flame stretch. Flame stretch is a measure of the variations of the flame surface A and is defined by (Candel and Poinsot 1990, Matalon 1983):

$$K = \frac{1}{A}\frac{dA}{dt}. \tag{5}$$

It is a local instantaneous characteristic of the flame front. Flame stretch controls the growth of the flame surface through two processes: (1) flame surface production and (2) flame quenching. Small to moderate flame stretch creates active flame surface, while high stretch might lead to flame quenching.

3.2 Flame surface production

When the flamelet assumption is valid, the modeling of turbulent combustion mainly reduces to the evaluation of the flame surface density Σ (defined as the flame surface per unit volume) (Darabiha *et al.* 1988, Marble and Broadwell 1977, Pope 1988) or the passage frequency of the flamelets (Bray and Libby 1986, Cant and Bray 1988, Cheng *et al.* 1988). For example, the formulation of the Coherent Flame model (Candel *et al.* 1988, Marble and Broadwell 1977) provides a conservation equation for Σ in a Lagrangian frame moving with the turbulent flame.

$$\frac{d\Sigma}{dt} = \bar{K}\Sigma - Q_c, \tag{6}$$

where $\bar{K}$ is the mean stretch rate averaged along the flame surface. The second term Q_c on the RHS of Eq. (6) corresponds to flame surface annihilation by mutual

interaction of flame fronts (for example, the merging of two flame fronts together). The average stretch $\bar{K}$ is of utmost importance in Eq. (6) because it imposes the source term for the flame surface and ,therefore, the mean turbulent reaction rate $\overline{\dot{w}}$ given by

$$\overline{\dot{w}} = w_L \Sigma. \tag{7}$$

where w_L is the mean consumption rate per unit surface along the flame front (if one assumes that the flamelet has a laminar structure, w_L will be the laminar consumption rate for the same chemical parameters and the same stretch).

3.3 Flame quenching and definition of the flamelet regime

The most important mechanism controlling the validity of the flamelet assumption is the occurrence of flame quenching by turbulence. When no quenching occurs in a premixed turbulent flame, the flame zone is 'active' everywhere and may be treated as an interface separating fresh unburnt reactants from hot burnt products. This regime is called the 'flamelet' regime.

It is necessary to discuss here the definition of a flamelet regime. Poinsot *et al.* (1990) propose:

Definition 1: *A premixed turbulent reacting flow is in a flamelet regime if, at any given time, any line connecting one point in the fresh gases to another point in the burnt products crosses (at least) one active flame front, i.e. there are no holes in the active flame surface.*

Definition 1 is very restrictive. First, it is reasonable to assume that a hole which persists only for a short time will not force the flow to a 'non-flamelet' regime. Second, even if the flame surface contains locally quenched surfaces, as long as these holes spread more slowly than the active flame surface, the regime will correspond to partial quenching and the flamelet approach will still provide a reasonable estimate of the reaction rate if quenching is accounted for. As we are interested in developing models for engineering applications, it is convenient to relax Definition 1 and to introduce a broader definition of the flamelet regime:

Definition 2: *A premixed turbulent reacting flow is in a flamelet regime if holes (generated by local quenching of the flame front) do not inhibit the growth of the active flame surface.*

Definition 2 allows us to consider regimes of partially quenched flames as flamelet regimes. What happens when holes in the flame front grow fast enough to interfere with the active flame surface is an open question. Fresh and hot gases will diffuse before they react, and our definition of flamelets will break down. In this case, it is possible that the flow will still be able to sustain combustion in a regime called distributed reaction zones. However, it might also be driven to total quenching. This point cannot be asserted at the present time. We will call this limit global (or total) quenching although it might, in fact, be only a transition to another regime of combustion (without flamelets).

Local flame quenching occurs when the flame front is submitted to external perturbations like heat losses or aerodynamic stretch which are sufficiently strong to

decrease the reaction rate to a negligible value or in some cases to completely suppress the combustion process.

Quenching in *laminar flames* has received considerable attention in the last years. Asymptotic studies of laminar stagnation point flames established by the counterflow of reactants and products reveal that a laminar flame can be quenched by stretch if the flow is non-adiabatic or if the Lewis number (defined as the ratio of the thermal diffusivity to the reactant diffusivity: $Le = \lambda/(\rho C_p \mathcal{D})$) is greater than unity. These results have been confirmed by numerical methods for simple or complex chemistry and by experiments.

The idea that quenching mechanisms evidenced in laminar flames may be responsible for partial or total quenching in premixed turbulent flames is an important ingredient of many models of turbulent combustion (Peters 1986, Darabiha *et al.* 1988). Experiments show that quenching can, indeed, occur in turbulent combustion (Abdel-Gayed and Bradley 1985, 1989). However, the prediction of quenching in *turbulent flames* is still an open question. The classical theoretical approach to predict quenching in turbulent flames is to assume that flamelets behave like laminar stagnation point flames (Bray 1980) and are quenched for similar critical values of stretch. This is a crude approximation. In laminar stagnation point flames, a constant steady stretch is imposed to a planar flame. In a turbulent reacting flow, flamelets are stretched by vortices. Therefore, the stretch they experience is changing with time because the vortices are convected by the mean flow and are dissipated by viscous effects. Flamelets are also free to move to escape from regions of high stretch (which is not the case for laminar stagnation point flames). Moreover, vortices curve the flame front, making the analogy between flamelets and planar stagnation point flames doubtful. These points suggest that information on quenching in laminar stagnation point flames are not relevant to predict quenching in turbulent flames. A central difficulty to improve on this classical approach is the estimation of the flame stretch K in a turbulent flow.

3.4 The Intermittent Turbulence Net Flame Stretch (ITNFS) model

From the previous discussion, it is clear that the mean value of the flame stretch $\overline{K}$ is an essential parameter in turbulent combustion. It controls flame quenching as well as flame surface creation. It is also clear that studies of laminar stagnation point flames cannot be used directly to study quenching or flame surface creation in a turbulent flow. Additional parameters like curvature, viscous dissipation, and thermodiffusive effects also have to be considered.

Different expressions may be found in the literature for the mean flame stretch $\overline{K}$. Bray (1980) and Cant and Bray (1987) propose

$$\overline{K} = \sqrt{\epsilon/\nu}, \tag{8}$$

where ϵ is the dissipation of turbulent kinetic energy and ν is the kinematic viscosity.

Candel *et al.* (1988) use

$$\overline{K} = \epsilon/k. \tag{9}$$

where k is the turbulent kinetic energy. We will give here a more precise estimate of the flame stretch by combining different approaches:

(1) Use of direct simulations of flame/vortex interactions to predict the effect of a given isolated structure on a laminar flame front. Using results on flame/vortex interaction allows us to take into account viscosity, curvature, and transient effects. The basis for these results is the work of Poinsot *et al.* (1990)

(2) Use detailed experimental data about intermittent turbulence to determine the distribution of stretch along the flame front (Meneveau and Sreenivasan 1987).

(3) Define a net stretch of the flame by subtracting the rate of destruction of existing flame surface by quenching from the rate of increase of surface due to hydrodynamic straining.

The idea behind the ITNFS model is to use a complex model to describe the interaction of one vortex with a flame front and to extend it to a complete turbulent flow by supposing that the total effect of all the turbulent fluctuations can be deduced from the behavior of each individual scale in the fresh gases. This is clearly an important approximation. First, the interaction of multiple scales with the flame front cannot, in the general case, be reduced to the sum of the interactions of each vortex with the flame. Non-linear effects are to be expected. Second, the flame is not affected only by the fluctuations present in the stream of fresh gases. Flame-generated turbulence can also play a role. Therefore, the present approach should be viewed only as a first step towards a more complete treatment of the turbulent reacting flow. However, it represents a substantial improvement on classical estimates of the flame stretch. The ITNFS model may be used in any flamelet model (Candel *et al.* 1988, Bray and Libby 1986).

9.5 Results

The details of the computation may be found in Meneveau and Poinsot (1990). The main results of this analysis are:

(1) the existence of an efficiency function which characterizes the effect of a vortex of given size and speed on a flame front. In particular, it is shown that small vortices have low efficiencies, i.e. that they do not create as much flame stretch as their own time scales would suggest,

(2) the fact that flame quenching of a flame front by a vortex proceeds on a time scale which is the flame time and not the vortex time. In other words, however strong a flame front is stretched, this stretch has to be maintained for a time which is at least l_F/S_0 before quenching occurs (l_F is the laminar flame thickness and S_0 is the flame speed),

(3) an expression for the actual flame stretch of a premixed front in a turbulent flow was derived. Figure 4 presents the variation of this parameter as a function of two quantities: the ratio of the RMS turbulent velocity to the laminar flame speed (u'/S_0) and the ratio of the integral scale to the flame thickness (l/l_F). The flame stretch is normalized by the characteristic strain at the Kolmogorov scale $\sqrt{\epsilon/\nu}$ which is a measure of the stretch of material surfaces (Yeung *et al.* 1990). It appears that only for very large turbulence scales ($l/l_F >> 1$) or very small turbulence intensities ($u'/S_0 << 1$) does the ratio $\overline{K}/\sqrt{\epsilon/\nu}$ reach a value of order

one (the limit of $\overline{K}/\sqrt{\epsilon/\nu}$ for material surfaces ($l/l_F >> 1$) is 0.28 as shown by Yeung *et al.* (1990)). Meneveau and Poinsot (1990) also show that the flame stretch is not simply related to the characteristic strain at the integral scale ϵ/k. These results contradict many of the approximations used in models (Bray and Libby 1986, Cant and Bray 1988, Candel *et al.* 1988) and provide a new basis for turbulent combustion models based on the flamelet concept.

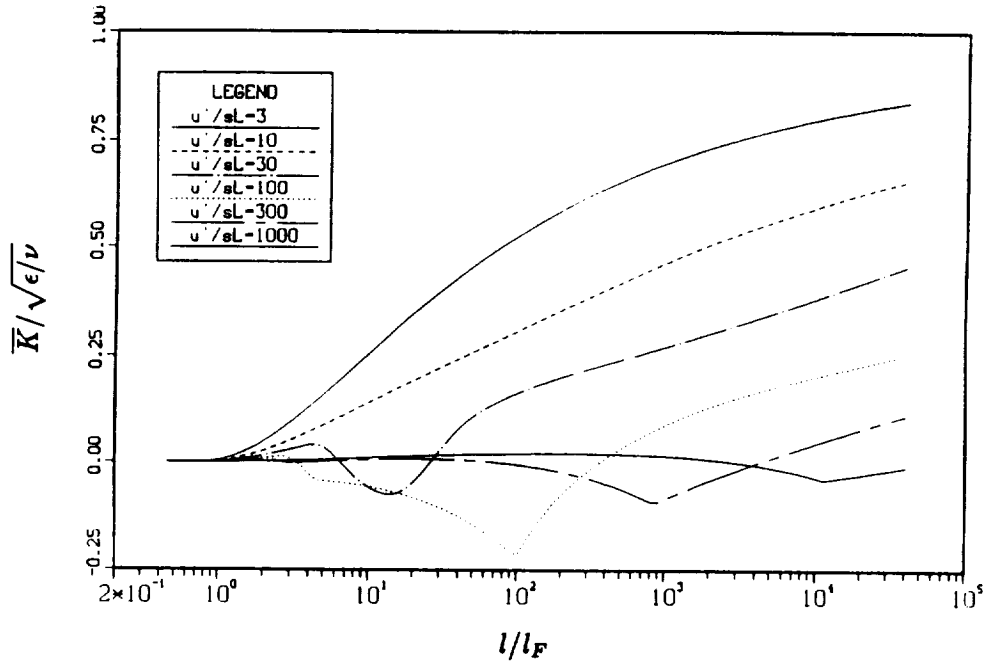

FIGURE 4. The total flame stretch in a turbulent flow.

(4) global quenching limits of premixed turbulent flames were obtained and compared to experimental and previous theoretical observations. Results show that, as assumed by Poinsot *et al.* (1990), quenching is quite difficult to generate in premixed flame fronts, and the flamelet domain is larger than expected from classical theories. Moreover, heat losses appear to have a large effect on the occurrence of quenching. These results agree with experimental studies.

4. The interaction of random flows with flame fronts

In the previous section, the interaction between a complete turbulent flow and a flame was studied using a theoretical description of the turbulent flow in the fresh gases (multifractal formulation). However, no simulation of such an interaction was actually performed. Starting in May 1990, such simulations were started in two dimensions and during the Summer Program in three dimensions. The main novelty in these studies is that we were able to compare two codes and evaluate their limits and common features:

(1) the first code was the one presented here: it uses a two-dimensional grid but solves for the compressible NS equations, with variable density, viscosity, and temperature.

(2) the second code was a three dimensional spectral code (Rutland 1989). This code solves for constant density flows and, therefore, ignores certain points which are clearly important for flames: dilatation, density and temperature changes, viscosity variations.

Similar runs were done using both codes. Results may be found in Haworth and Poinsot (1990) and Rutland and Trouve (1990). A general result was that many common conclusions were obtained. For example, the effect of the Lewis number on the structure of the reacting front appears to be exactly the same in 2 and 3 D cases. Higher Reynolds numbers, higher flow speed compared to the flame speed, and larger physical domains were obtained in two dimensions. However, many of the qualitative results were similar. An additional result provided by the two-dimensional code was the confirmation of the importance of vortex pairs (modons) in flame vortex interactions. Figure 5 shows a typical interaction between a premixed flame front and an initially isotropic turbulence.

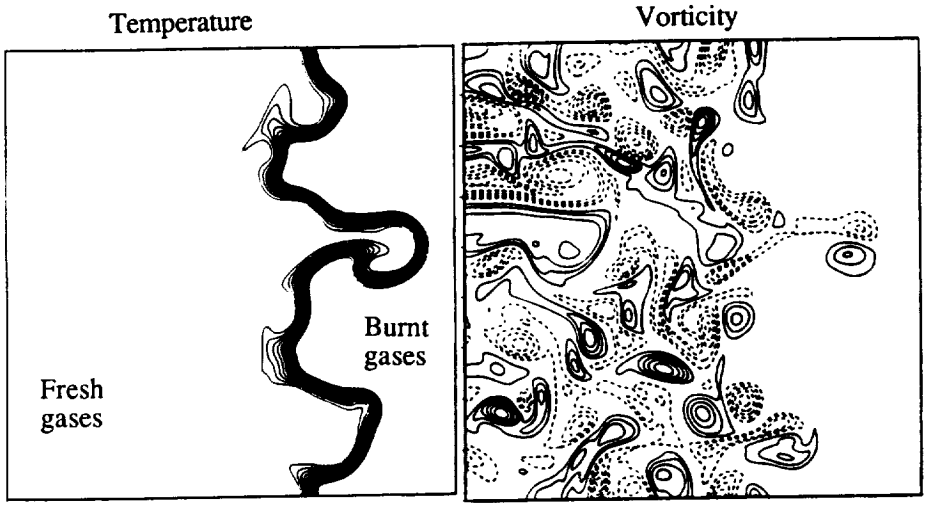

FIGURE 5. Temperature and vorticity contours in a two-dimensional direct simulation.

Vorticity and temperature contours are plotted. Pockets of fresh gases formed in the burnt gases (on the right side of the pictures) are created by vortex pairs originating in the cold gases and being convected at high speed through the flame front because of their self induced movement. The importance of vortex pairs in turbulent combustion was one of the main assumptions done in our two-dimensional studies of flame vortex interactions. That structures with self-induced velocities are quite important for turbulent combustion is clear. Which form these structures will

have in a three-dimensional flow (vortex rings, pair of vortex filaments) is still an open question. These studies are being pursued and will be published in 1991.

REFERENCES

ABDEL-GAYED, R. G. & BRADLEY, D. 1985 *Combus. and Flame.* **62**, 61-68.

ABDEL-GAYED, R. G. & BRADLEY, D. 1989 Combustion regimes and the straining of turbulent premixed flames. *Combus. and Flame.* **76**, 213-218.

ASHURST, W. T. 1987 Vortex simulation of unsteady wrinkled laminar flames. *Combus. Sci. and Tech.* **52**, 325.

ASHURST, W. T., PETERS N. & SMOOKE M.D. 1987 *Combus. Sci. and Tech.* **53**, 339-375.

BORGHI, R. 1984 *Recent Advances in Aeronautical Science.* C. Bruno, C. Caseci eds., Pergamon.

BRAY, K. N. C 1980 *Topics in Applied Physics.* P. A. Libby & F. A. Williams eds., Springer Verlag.

BRAY, K. N. C. & LIBBY, P. 1986 Passage times and flamelet crossing frequencies in premixed turbulent combustion. *Combus. Sci. and Tech.* **47**, 253.

CANDEL, S., MAISTRET, E., DARABIHA, N., POINSOT, T., VEYNANTE, D. & LACAS, F. 1988 *Marble Symposium.* Caltech, Pasadena.

CANDEL, S. M. & POINSOT, T. 1990 Flame stretch and the balance equation for the flame area. *Combus. Sci. and Tech.* **70**, 1-15.

CANT, R. & BRAY, K. 1988 Strained laminar flamelet calculations of premixed turbulent combustion in a closed vessel. *Twenty Second Symposium (International) on Combustion.* The Combustion Institute, p. 791.

CHENG, R., SHEPHERD, I. & TALBOT, L. 1988 Reaction rates in premixed turbulent flames and their relevance to the turbulent burning speed. *Twenty Second Symposium (International) on Combustion.* The Combustion Institute, p. 771.

CHUNG, S. H. & LAW, C. K. 1988 An integral analysis of the structure and propagation of stretched premixed flames. *Combus. and Flame.* **72**, 325.

CLAVIN, P. & WILLIAMS, F. 1982 Effects of molecular diffusion and of thermal expansion on the structure and dynamics of premixed flames in turbulent flows of large scale and low intensity. *J. Fluid Mech.* **116**, 251.

DARABIHA, N., CANDEL, S. & MARBLE, F. 1986 The effect of strain rate on a premixed laminar flame. *Combus. and Flame.* **64**, 203.

DARABIHA, N., GIOVANGIGLI, V., TROUVE, A., CANDEL, S. AND ESPOSITO, E. 1989 Coherent flame description of turbulent premixed flames. *French-USA Workshop on Turbulent Combustion.* R. Borghi & S. Murthy eds., Springer Verlag.

GHONIEM, A., CHORIN, A., & OPPENHEIM, A. 1982 Numerical modeling of turbulent combustion in a combustion channel. *Phil. Trans. Roy. Soc. London.* **A394**, 303.

GIOVANGIGLI, V. & SMOOKE, M. 1987 Extinction of strained premixed laminar flames with complex chemistry. *Combus. Sci. and Tech.* **53**, 23.

GOULDIN, F., BRAY, K. & CHEN, J.-Y. 1989 Chemical closure model for fractal flamelets. *Combus. and Flame.* **77**, 241.

HAWORTH, D. C. & POINSOT, T. 1990 The influence of Lewis number and non-homogeneous mixture on premixed turbulent flame structure. *CTR Summer Program 1990,* Center for Turbulence Research, Stanford University and NASA Ames Research Center.

ISHIZUKA, S. & LAW, C. K. 1982 An experimental study on extinction of stretched premixed flames. *Nineteenth Symposium (International) on Combustion.* The Combustion Institute, p. 327.

LIBBY, P., LINAN, A. & WILLIAMS, F. 1983 Strained premixed laminar flames with non-unity Lewis number. *Combus. Sci. and Tech.* **34**, 257-293.

LIBBY, P. & WILLIAMS, F. 1987 Premixed flames with general rates of strain. *Combus. Sci. and Tech.* **54**, 237.

MANTZARAS, J., FELTON, P. & BRACCO, F. 1989 Fractals and turbulent premixed engine flames. *Combus. and Flame.* **77**, 295.

MARBLE, F. E. & BROADWELL, J. 1977 The coherent flame model for turbulent chemical reactions. *Project SQUID.* Report TRW-9-PU.

MARKSTEIN, G. H. 1951 *J. Aero. Sci.* **18**, 199.

MATALON, M. 1983 On flame stretch. *Combus. Sci. and Tech.* **31**, 169.

MENEVEAU, C. & POINSOT, T. 1990 Stretching and quenching of flamelets in premixed turbulent combustion. *Combus. and Flame.* To appear.

MENEVEAU, C. & SREENIVASAN, K. R. 1987 The multifractal spectrum of the dissipation field in turbulent flows. *Nucl. Phys. B Proc. Suppl.* **2**, 49.

MIKOLAITIS, D. 1984 The interaction of flame curvature and stretch, Part 1: the concave premixed flame. *Combus. and Flame.* **57**, 25-31.

MIZOMOTO, M., ASAKA, Y., IKAI, S. & LAW, C. K. 1984 *Twentieth Symposium (International) on Combustion.* The Combustion Institute, p. 1933.

PETERS, N. 1986 Laminar flamelet concepts in turbulent combustion. *Twenty First Symposium (International) on Combustion.* The Combustion Institute, p. 1231.

POINSOT, T. & CANDEL, S. 1988 *Combus. Sci. Tech.* **61**, 121-153.

POINSOT, T., VEYNANTE, D. & CANDEL, S. 1990 Quenching processes and premixed turbulent combustion diagrams. Submitted to *J. Fluid Mech.*

POINSOT, T., VEYNANTE, D. & CANDEL, S. 1990 *Twenty Third Symposium (International) on Combustion.* The Combustion Institute.

POINSOT, T. , ECHEKKI, T. & MUNGAL, G. 1990 Studies of the laminar flame tip and implications for premixed turbulent combustion. *Combus. Sci. and Tech.* To appear.

POINSOT, T. & LELE, S. 1989 Boundary conditions for direct simulations of compressible viscous reacting flows. *CTR Manuscript 102.* Center for Turbulence Research, Stanford University and NASA Ames Research Center.

POINSOT, T., COLONIUS, T. & LELE, S. 1989 Boundary conditions for spatially-evolving compressible simulations. *42nd A. P. S. Meeting, Division of Fluid Mech.*

POINSOT, T. & LELE, S. 1990 Submitted to *J. of Comput. Phys.*

POPE, S. B. & CHENG, W. K. 1988 *Twenty Second Symposium (International) on Combustion.* The Combustion Institute.

ROBERTS, W. L. & DRISCOLL, J. F. 1990 A laminar vortex interacting with a premixed flame. *Eastern States Section of the Combustion Institute.*

RUTLAND, C. J. & FERZIGER, J. H. 1989 27th AIAA Aerospace Sciences Meeting. *AIAA Paper 89-0127.*

RUTLAND, C. J. 1989 Effects of strain, vorticity, and turbulence on premixed flames. Ph.D. Thesis, Stanford.

RUTLAND, C. J. & TROUVE, A. 1990 Premixed flame simulations for non-unity Lewis number. *CTR Summer Program 1990.* Center for Turbulence Research, Stanford University and NASA Ames Research Center.

SHEPHERD, I., CHENG, R. & GOIX, P. 1989 A tomographic study of premixed turbulent stagnation point flames. *Western States Section of the Combustion Institute,* Livermore CA.

VEYNANTE, D. & CANDEL, S. 1988 *Signal Processing.* **14**, 295-300.

VEYNANTE, D., LACAS, F. MAISTRET, E. & CANDEL, S. 1989 *7th Symp. on Turbulent Shear Flows.* Stanford.

WILLIAMS, F. A. 1985 *Combustion theory.* 2nd ed. Benjamin Cummings, Menlo Park.

YANG, V. & CULICK, F. E. C. 1986 *Combus. Sci. and Tech,* **45**, 1-25.

YEE, H. C. 1981 NASA Technical Memorandum 81265.

YEUNG, P., GIRIMAJI, S. & POPE, S. 1990 Straining and scalar dissipation on material surfaces in turbulence: implications for flamelets. *Combus. and Flame.* **79**, 340-365.

Simulation of flame-turbulence interactions in premixed combustion

By A. Trouvé

1. Motivation and objectives

Turbulent combustion is a challenging problem of fundamental interest with numerous practical applications. Direct Numerical Simulation is an attractive tool that provides detailed information on flame-flow interactions and, thereby, provides an ideal basis for testing and developing turbulent combustion models. This report describes the work being undertaken to investigate the laminar flamelet concepts as applied to premixed combustion. More specifically, the present work examines the influence of non-unity Lewis number with emphasis on the effects of hydrodynamic straining and flame front curvature.

The following subsections give a short introduction to the flamelet modeling approach.

1.1 Validity of the flamelet approach

Premixed turbulent combustion is a rather vague terminology that is used to designate very different situations. Dimensional analysis shows that, depending on the flame and turbulent flow characteristic scales, different modes of combustion are expected: flamelets, distributed reaction zones, and well-stirred reactors (Borghi 1984, Peters 1986, Williams 1985). These different modes of combustion correspond to different topologies of the reaction zone (front, pockets, or large volumes) and, consequently, different modeling approaches are required.

Following Poinsot, Veynante and Candel (1990), the flamelet regime corresponds to a situation where the flame front is chemically active everywhere and no quenching occurs. In other words, fresh reactants and burnt products cannot diffuse and mix without triggering reaction. Recent results from direct numerical simulations (Poinsot *et al.* 1990) show that classical arguments based on dimensional analysis underestimate the resistance of flame fronts to flow perturbations. Furthermore, these results suggest that most practical situations feature a flamelet mode of burning.

The definition of a flamelet regime based on the occurrence of quenching is valuable and rigorous, but it is also quite academic. From a practical viewpoint, current flamelet models make use of several assumptions that turn out to be less restrictive or more restrictive than those implied by this definition:

- The domain of application of flamelet models is usually extended to regimes of partially quenched flames. For example, the Coherent Flame Model (Candel *et al.* 1988, Darabiha *et al.* 1989) accounts explicitly for extinction phenomena due to excessive strain. This can only be legitimate if flame quenching is somewhat limited to local effects and does not alter significantly the global picture implied by the flamelet approach (Meneveau and Poinsot 1990).

• Flamelet models use laminar submodels to describe the local properties of the reactive elements. This approach relies on two additional assumptions: each flame element retains an identifiable structure; this structure may be modeled like a laminar reaction zone. When the flame thickness is smaller than all turbulent length scales, flow perturbations acting on the flame zone may be viewed as external perturbations, and the structure of flame elements remains essentially laminar. However, when turbulent eddies are small enough to penetrate into the reaction zone, intuitive ideas suggest that the structure of flame elements may be disrupted in a way that precludes any analogy with laminar theory.

If this holds true, the domain of application of flamelet models is limited by requiring the flame thickness to be smaller than the Kolmogorov length scale. This would be a practical rather than a theoretical limitation. Note that in principle, improved submodels may be developed within the flamelet framework to account for the non laminar behavior of the flamelet elements. Also, it is worth emphasizing that at this stage, little is known on the dynamics of the turbulent small scales and their interactions with the flame zone. Finally, from a practical viewpoint, it remains to be shown how sensitive the results are to the accuracy of the chemical submodel. Therefore, this problem is essentially open.

1.2 Modeling of the mean reaction rate

In the flamelet approach, the reaction occurs in relatively thin layers, and the flame may be considered as a propagating surface separating fresh reactants from burnt products. In the following, we show that the mean reaction rate may then be modeled as a flux term. Let us first introduce the quantities that characterize the flame behavior:

• The turbulent flame speed is a global quantity that measures the mean reaction rate over an arbitrary domain V. For the sake of clarity, we assume that the mean position of the flame is stationary in V (the volume V travels with the flame). In that case, the turbulent flame speed is defined as the total fuel consumption rate in V divided by the total mass inflow of fuel into V:

$$S_T \equiv \frac{\int_V \dot{\omega}_R \, dV}{\rho_u Y_{R,u} \Sigma_0}, \tag{1}$$

where $\dot{\omega}_R$ is the mass of fuel consumed per unit time and per unit volume; ρ_u and $Y_{R,u}$ are respectively the density and the fuel mass fraction in the unburnt gas; Σ_0 is the area of the inlet boundary of V.

• The consumption speed S_C is a local property of the flame front that characterizes the local inner structure of the reaction zone. Assuming that a normal to the flame front can be defined everywhere without ambiguity, the local flame speed is defined by integrating the reaction rate along this normal direction:

$$S_C \equiv \frac{\int_{-\infty}^{+\infty} \dot{\omega}_R \, dn}{\rho_u Y_{R,u}}, \tag{2}$$

where n designates the flame normal direction.

Clearly, the mean reaction rate is determined by the distribution of the local flame speed S_C along the flame surface:

$$S_T = \frac{\int_{\Sigma_T} S_C \, d\Sigma_T}{\Sigma_0}, \tag{3}$$

where $d\Sigma_T$ designates the area of a flame surface element and Σ_T is the total flame surface area within V.

Furthermore, let us define the area-weighted mean of S_C along the flame surface:

$$\langle S_C \rangle = \frac{\int_{\Sigma_T} S_C \, d\Sigma_T}{\Sigma_T}, \tag{4}$$

Combining the last two expressions, it is seen that the turbulent flame speed is essentially a flux term and as such can be expressed as the surface mean of the local fuel consumption speed times the total flame surface area:

$$S_T = \frac{\langle S_C \rangle \, \Sigma_T}{\Sigma_0}, \tag{5}$$

Eq. (5) may be conveniently re-written in terms of the mean reaction rate:

$$\overline{\dot{w}} = \frac{\int_V \dot{\omega}_R \, dV}{V} = \langle \int_{-\infty}^{+\infty} \dot{\omega}_R \, dn \rangle \, \frac{\Sigma_T}{V}, \tag{6}$$

In Eq. (6), the mean reaction rate is the product of the mean fuel consumption rate per unit flame area times the flame surface density (defined as the flame surface per unit volume). Therefore, the closure problem for $\overline{\dot{w}}$ requires modeling of two basic quantities: a speed and a surface. To provide these quantities, two basic ingredients of flamelet models are introduced: (1) a chemical submodel that describes the local properties of reactive elements embedded in the turbulent flow and gives the mean consumption rate per unit flame area; (2) a balance equation for the flame surface density that represents turbulence effects (hydrodynamic straining, convection, turbulent diffusion) and propagation effects (collisions of flame elements, wrinkling, dewrinkling).

1.3 Turbulence acting on the flame: the role of strain

The flamelet ingredients are coupled to a description of the turbulent flow field based on standard transport equations for the flow variables and the main species. A central problem is then to relate the flame properties $\langle S_C \rangle$ and Σ_T to the turbulent flow properties.

An idea shared by all flamelet models is that turbulent straining acting on the flame zone plays an essential role (see Poinsot 1990 for a more detailed discussion of this matter). Strain modifies both the flamelet's structure and the flame surface density. These effects are represented in the models by a single scalar, a mean strain rate ϵ, that influences both quantities $\langle S_C \rangle$ and Σ_T in the following way: (1) $\langle S_C \rangle$ in the flamelet submodel is determined from an analysis of a laminar stagnation point flame where the speed of the counter-flowing reactants and products is adjusted according to the strain rate ϵ; (2) the balance equation for the flame surface density accounts for the stirring process due to turbulent motions through a source term that depends linearly on ϵ.

1.4 Objectives

As discussed in the previous section, flamelet models recognize the importance of strain. However, one shortcoming in these models is the absence of curvature effects. Since curvature is a geometrical parameter that directly affects molecular diffusion processes, a simple way to highlight the nature and importance of this parameter is to study premixed flames featuring different molecular transport properties for different scalars (chemical species, temperature).

The objective of the study of Rutland and Trouvé (1990) is precisely to examine the effects of differential diffusion of heat and chemical species as represented by a single, non-unity Lewis number, Le. This study was performed in collaboration with Prof. Rutland while he was participating in the CTR 1990 Summer Program.

2. Accomplishments

The influence of Lewis number was examined using Direct Numerical Simulation of three dimensional, constant density, decaying isotropic turbulence with a single step, irreversible, finite rate (Arrhenius law) chemical reaction. A modified version of the Rogallo code (1981) was used. More detailed information on the simulations may be found in Rutland (1989) and Rutland and Trouvé (1990). A similar investigation was conducted by Haworth and Poinsot (1990) with a finite difference, two-dimensional, variable density code. Interestingly enough, similar results were obtained. We summarize them in the following sections.

2.1 Curvature effects

Curvature is defined in planes tangent to the flame surface, positive curvature being convex towards the reactants. The main result from simulations is the strong correlation between the local fuel consumption speed S_C and the local flame curvature. This result is presented in the form of joint pdf's in Figure 1. For $Le = 1$, the flame exhibits a large insensitivity to curvature (Poinsot, Echekki and Mungal 1990), and no correlation is observed. For $Le < 1$, the local flame speed is increased (decreased) in regions of positive (negative) curvature. The opposite effect occurs for $Le > 1$.

Also, the pdf's of flame curvature are nearly symmetric with near-zero mean value. Since the correlation of S_C with curvature is roughly linear (Figure 1), curvature effects tend to cancel out in the mean. In other words, the mean flamelet speed $\langle S_C \rangle$ does not exhibit any significant dependence on curvature.

Furthermore, because the distribution of the flame speed S_C along the flame surface tells us about the way the flame propagates in the unburnt gas, these results also indicate that when $Le < 1$ ($Le > 1$), more (less) flame surface Σ_T is produced by turbulent motions.

2.2 Strain effects

Strain effects may already be seen in Figure 1 by slicing the joint pdf's along a line corresponding to zero curvature. When the curvature is zero, only strain effects remain. It is then seen that, depending on the value of the Lewis number, the local flame speeds are shifted from unity: decreased for $Le > 1$ and increased for $Le < 1$.

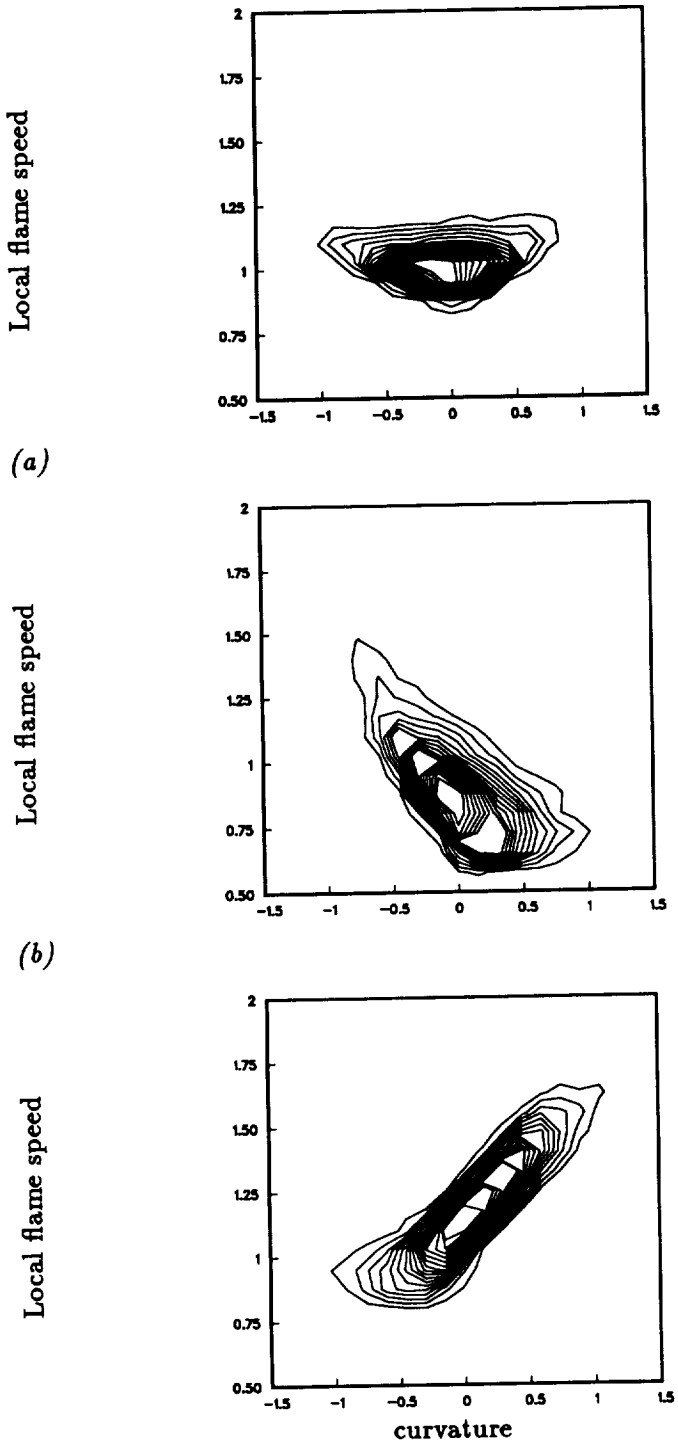

FIGURE 1. Joint pdf of the local flame speed S_C and local flame curvature. Flame speeds are normalized by the unperturbed laminar value. Curvature is normalized by the flame thickness; (a) $Le = 1.0$, (b) $Le = 1.2$, (c) $Le = 0.8$.

These trends are consistent with laminar flame theory (Libby *et al.* 1983), a result that is of primary importance for flamelet models, and with previous simulations (Ashurst *et al.* 1987). It is worth emphasizing that contrary to curvature effects, these trends do not cancel out when averaged along the flame surface, and the mean flamelet speed $\langle S_C \rangle$ is affected by strain.

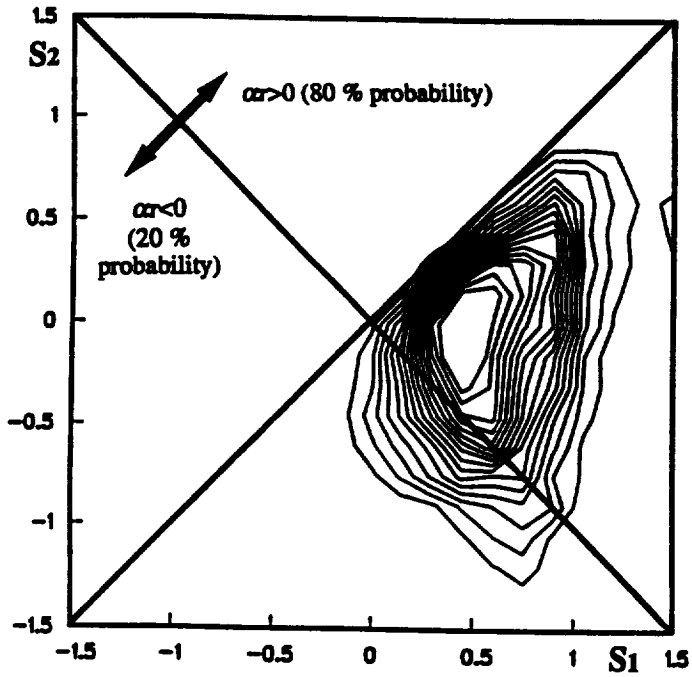

FIGURE 2. Joint Pdf of the principal strain rates in the flame tangent plane, $S_1 \geq S_2$. Strain rates are normalized by the laminar flame timescale. $Le = 0.8$.

An important quantity for the evolution of the flame surface density is the strain rate acting in the flame tangent plane (Candel and Poinsot 1990). Simulations show that independently of the Lewis number, there is an 80 % probability for positive values of this strain rate (Figure 2). This high value brings supports to the flamelet models picture where flame surface is produced by hydrodynamic straining.

A slightly different perspective is obtained when examining the alignment of the principal directions of the strain rate tensor with the flame normal. The strain rate tensor being symmetric, it may be characterized by its three principal directions and three eigenvalues:

$$\alpha \geq \beta \geq \gamma, \tag{7}$$

For incompressible flow, these eigenvalues sum to zero. α is positive and corresponds to the most extensive strain direction. γ is negative and corresponds to the most compressive strain direction. β is the intermediate strain rate and can take positive or negative values. Figure 3 shows that the flame normal tends to align with the most compressive principal direction. This again bears evidence of the effect of hydrodynamic straining on the flame dynamics.

However, contrary to the previous analysis of curvature, it was not possible to show any correlation between the local flame speed S_C and strain. This absence of correlation is believed to be associated with an excessive zooming effect resulting from Direct Numerical Simulation: the strain rate tensor as computed from simulation data is both localized in space (an arbitrary location is selected within the flame zone) and in time (quantities are instantaneous values). This would only be a minor problem if the straining field and the flame zone were always in dynamical equilibrium. However, referring to the idea of persistent straining, it is believed that to significantly modify the flame front structure, strain must act on a time scale that is commensurate with the flame characteristic time. Therefore, the local flame structure is likely to depend on the time history of strain, represented eventually by a time-averaged strain rate, rather than on instantaneous values. Also, among all the turbulent structures present in the vicinity of the flame and which contribute to the strain rate, only a certain class are dynamically active (an active structure would be a structure that satisfies some coherence conditions in space and time). In some sense, the signal to noise ratio is low in fully turbulent simulations.

This study of the effect of strain is now pursued in the context of a flame-vortex interaction problem (see Section 3.1), where some of the above difficulties are removed by considering only one well-characterized flow structure.

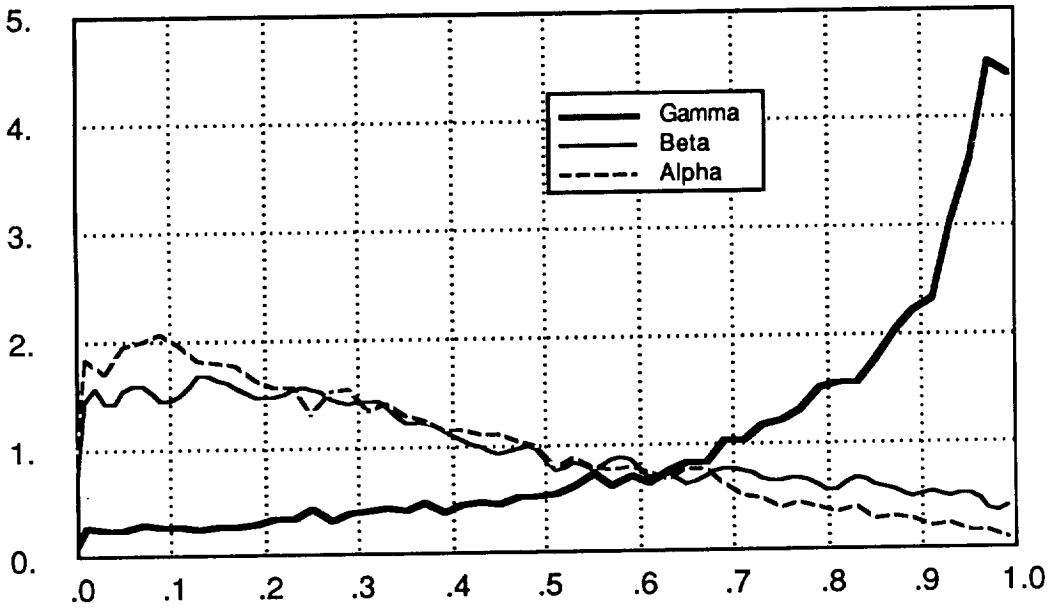

FIGURE 3. Pdf of the cosinus of the angle between the directions of principal strain at the flame and the flame normal. $Le = 0.8$.

2.3 Conclusions

Most notable in the results is the strong correlation between the local flame structure and the flame front curvature. Consistent with laminar flame theory, this

correlation is Lewis number dependent. It may appear at first sight that these findings invalidate some important assumptions used in current flamelet models. In these models, the prototype configuration for flamelet libraries is a strained stagnation point flame, and curvature effects are simply neglected. However, one should keep in mind that turbulent combustion models are developed for engineering applications, where computations are performed on coarse grids. In this context, the model predictions are only required to hold in an average sense (the laminar submodel used in the flamelet approach may be considered as a subgrid scale model). Therefore, fair comparisons between the models predictions and Direct Numerical Simulations should be performed at a global level. At this level, our results indicate that the mean flamelet speed $\langle S_C \rangle$ is affected by strain, not by curvature. In conclusion, while curvature determines the local characteristics of the reaction zone, global features are in good agreement with predictions based on the stagnation point flame picture.

Future work will require studying the effects of differential diffusion at higher Reynolds numbers (in our study the Reynolds number based on Taylor microscale was limited to values around 10). It is worth emphasizing that curvature effects are expected to be strong as long as molecular transport phenomena are important. It may be argued that turbulence wipes out at some point differences in the transport of heat and species (the turbulent Lewis number would then be unity). However, this argument is rather speculative, especially for chemical systems where diffusion processes play a dominant role for sustaining reaction. Therefore, this issue remains open.

3. Ongoing and future plans

3.1 Direct simulation of a single vortex interacting with a flame

It is the essence of flamelet models to reduce turbulent combustion mechanisms to elementary flame problems. It has been recognized for a long time in the combustion community that new insights into turbulent mechanisms could be gained by studying model laminar problems. For example, computations of laminar stagnation point flames provide insight into the effect of a plane strain acting on a flame element (Libby and Williams 1982, 1983). Similarly, situations where isolated vortices interact with laminar flames are considered as generic problems for turbulent combustion.

While at CTR, Dr. Poinsot performed direct simulations of a vortex-pair interacting at right angles with a laminar flame front and reached original conclusions with respect to quenching mechanisms (Poinsot *et al.* 1990, Meneveau and Poinsot 1990). The present study is a continuation of this work as applied to a different geometry: a single vortex structure interacts with a flame stabilized between coflowing fresh reactants and burnt products (Figure 4). This geometry simulates some of the features of practical dump combustors where premixed flames are anchored in shear flows and vortices develop and convect parallel to the reaction zone.

This problem is examined using a high-order, finite difference code for reacting compressible flows developed by Poinsot and Lele. The code features a single step,

irreversible, finite rate (Arrhenius law) chemical reaction with heat release. It is two-dimensional.

Only a few results are available at this time. For $Le = 1$, results indicate that the mean flame speed $\langle S_C \rangle$ is not altered by the vortex-induced perturbations. The total reaction rate is affected because of the production of flame surface resulting from vortex stretching. The increase in the flame surface density scales directly with the vortex lifetime (in the simulations, the vortex strength is continuously decaying because of viscous diffusion).

More results are presently obtained and will be expected in the near future, these include:

- the spatial variations of the fuel consumption speed S_C along the flame surface for various Lewis numbers,
- an analysis of the flame tip created by the vortex motion to characterize curvature effects,
- an analysis of strain effects by monitoring the time history of the strain field along the flame surface,
- the effects of vortices smaller than the flame thickness.

Another possible problem relevant to the control applications consists of simulating a train of vortices rather than a single vortex.

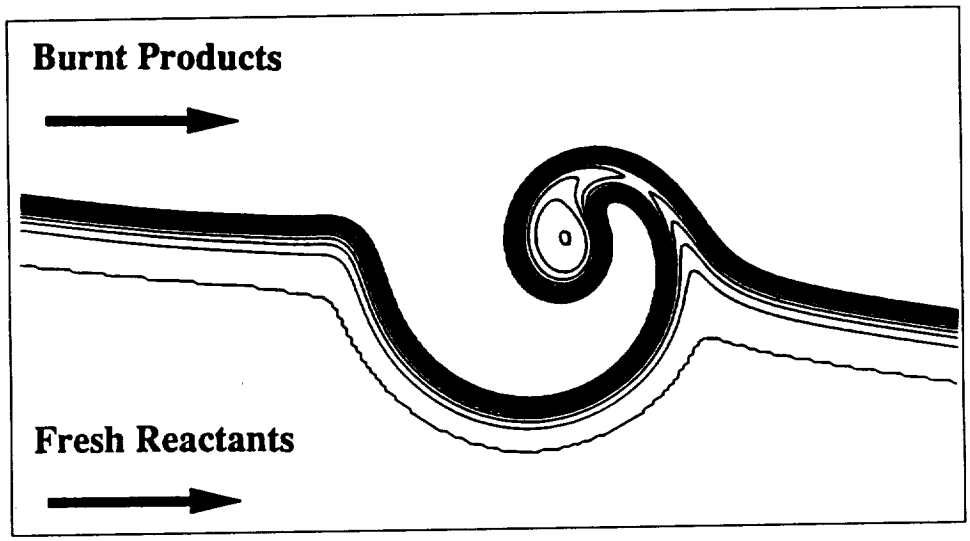

FIGURE 4. Flame-vortex interaction. Temperature contours.

3.2 Development of a three-dimensional code for turbulent combustion

Turbulent combustion problems where three-dimensional effects are important may be classified into two categories: (1) problems where vortex stretching plays a central role (for example: effects of stretched vortices on a flame sheet, effect of streamwise vorticity in reacting shear layers, mixing transition in reacting flows, etc); (2) problems where the flame develops in all space directions (for example:

ignition mechanisms in IC engines). To tackle these problems, it is planned to develop in the coming year a three-dimensional version of the Poinsot and Lele code.

REFERENCES

ASHURST, W. T. 1987 Vortex simulation of unsteady wrinkled laminar flames. *Combus. Sci. and Tech.* **52**, 325

ASHURST, W. T., PETERS, N. & SMOOKE, M. D. 1987 Numerical simulation of turbulent flame structure with non-unity Lewis number. *Combus. Sci. and Tech.* **53**, 339-375

BORGHI, R. 1984 *Recent Advances in Aeronautical Science.* C. Bruno, C. Caseci eds., Pergamon.

BRAY, K. N. C. 1980 *Topics in Applied Physics.* P. A. Libby & F. A. Williams eds., Springer Verlag.

CANDEL, S., MAISTRET, E., DARABIHA, N., POINSOT, T., VEYNANTE, D. & LACAS, F. 1988 *Marble Symposium.* Caltech, Pasadena.

CANDEL, S. M. & POINSOT, T. 1990 Flame stretch and the balance equation for the flame area. *Combus. Sci. and Tech.* **70**, 1-15.

CANT, R. & BRAY, K. 1988 Strained laminar flamelet calculations of premixed turbulent combustion in a closed vessel. *Twenty Second Symposium (International) on Combustion.* The Combustion Institute, p. 791.

CLAVIN, P. & WILLIAMS, F. 1982 Effects of molecular diffusion and of thermal expansion on the structure and dynamics of premixed flames in turbulent flows of large scale and low intensity. *J. Fluid Mech.* **116**, 251.

DARABIHA, N., GIOVANGIGLI, V., TROUVE, A., CANDEL, S. & ESPOSITO, E. 1989 Coherent flame description of turbulent premixed flames. *French-USA Workshop on Turbulent Combustion.* R. Borghi & S. Murthy eds., Springer Verlag.

HAWORTH, D. C. & POINSOT, T. 1990 The influence of Lewis number and non-homogeneous mixture on premixed turbulent flame structure. *CTR Summer Program 1990,* Center for Turbulence Research, Stanford University and NASA Ames Research Center.

LIBBY, P. & WILLIAMS, F. 1982 Structure of laminar flamelets in premixed turbulent flames. *Combus. and Flame.* **44**, 287-303.

LIBBY, P. & WILLIAMS, F. 1983 Strained premixed laminar flames under nonadiabatic conditions. *Combus. Sci. and Tech.* **31**, 1-42.

LIBBY, P., LINAN, A. & WILLIAMS, F. 1983 Strained premixed laminar flames with non-unity Lewis number. *Combus. Sci. and Tech.* **34**, 257-293.

LIBBY, P. & WILLIAMS, F. 1987 Premixed flames with general rates of strain. *Combus. Sci. and Tech.* **54**, 237.

MARBLE, F. E. & BROADWELL, J. 1977 The coherent flame model for turbulent chemical reactions. *Project SQUID.* Report TRW-9-PU.

MENEVEAU, C. & POINSOT, T. 1990 Stretching and quenching of flamelets in premixed turbulent combustion. *Combus. and Flame.* To appear.

PETERS, N. 1986 Laminar flamelet concepts in turbulent combustion. *Twenty First Symposium (International) on Combustion.* The Combustion Institute, p. 1231.

POINSOT, T. 1990 Direct simulation of turbulent combustion. *CTR Annual Research Briefs.* Center for Turbulence Research, Stanford University and NASA Ames Research Center.

POINSOT, T., VEYNANTE, D. & CANDEL, S. 1990 Quenching processes and premixed turbulent combustion diagrams. Submitted to *J. Fluid Mech.*

POINSOT, T., VEYNANTE, D. & CANDEL, S. 1990 *Twenty Third Symposium (International) on Combustion.* The Combustion Institute.

POINSOT, T. , ECHEKKI, T. & MUNGAL, G. 1990 Studies of the laminar flame tip and implications for premixed turbulent combustion. *Combus. Sci. and Tech.* To appear.

POINSOT, T. & LELE, S. 1989 Boundary conditions for direct simulations of compressible viscous reacting flows. *CTR Manuscript 102.* Center for Turbulence Research, Stanford University and NASA Ames Research Center.

POINSOT, T. & LELE, S. 1990 Submitted to *J. of Comput. Phys.*

ROGALLO, R. S. 1981 Numerical experiments in homogeneous turbulence. NASA Technical Memorandum 81315.

RUTLAND, C. J. & FERZIGER, J. H. 1989 27th AIAA Aerospace Sciences Meeting. *AIAA Paper 89-0127.*

RUTLAND, C. J. 1989 Effects of strain, vorticity, and turbulence on premixed flames. Ph.D. Thesis, Stanford.

RUTLAND, C. J. & TROUVE, A. 1990 Premixed flame simulations for non-unity Lewis number. *CTR Summer Program 1990.* Center for Turbulence Research, Stanford University and NASA Ames Research Center.

WILLIAMS, F. A. 1985 *Combustion theory.* 2nd ed. Benjamin Cummings, Menlo Park.

YEUNG, P., GIRIMAJI, S. & POPE, S. 1990 Straining and scalar dissipation on material surfaces in turbulence: implications for flamelets. *Combus. and Flame.* **79**, 340-365.

Center for Turbulence Research
Annual Research Briefs - 1990

A dynamical systems analysis of the kinematics of time-periodic vortex shedding past a circular cylinder

By J. M. Ottino[1]

Computer flow simulation aided by dynamical systems analysis is used to investigate the kinematics of time-periodic vortex shedding past a two-dimensional circular cylinder in the context of the following general questions: Is a dynamical systems viewpoint useful in the understanding of this and similar problems involving time-periodic shedding behind bluff bodies? Is it indeed possible, by adopting such a point of view, to complement previous analyses or to understand kinematical aspects of the vortex shedding process that somehow remained hidden in previous approaches? We argue that the answers to these questions are positive. What follows is the result of a collaborative work with K. Shariff from NASA-Ames.

We find that several kinematical aspects of the problem become clear when viewed in terms of dynamical systems concepts such as periodic points and their associated manifolds. The flow is shown to produce transversal heteroclinic and homoclinic intersections, and it is, therefore, mathematically chaotic; these findings easily translate into an understanding of the transport mechanisms operating in the flow. The analysis relies on the identification of two classes of periodic points: (i) parabolic periodic points associated with separating and attaching pathlines, which produce unstable and stable manifolds that are associated with zero time-averaged wall shear, and (ii) a period-one hyperbolic point located in the wake itself. Stretching and transport are largely dominated by manifolds belonging to period-one parabolic points attached to the cylinder and a period-one hyperbolic point in the wake. Computed manifolds agree well with experimentally obtained streaklines and give a good indication of the regions of maximum and minimum stretch. Passive tracers are deformed in such a way that they approximate the regions traced out by unstable manifolds, the fluid filaments that stretch the most originate from near the stable manifolds and are initially oriented normal to them..

1. Setting

The understanding of the flow behind a cylinder is important in fluid mechanics and transport processes from both theoretical and applied viewpoints. However, in spite of numerous studies, it is apparent that there are still a few basic points that deserve some clarification and that new approaches should probably be examined. One such possibility is the application of dynamical systems tools which have proved useful in the analysis of chaotic advection and mixing (for a review see Ottino 1990). Such a viewpoint does not seem to have been used in the context of wake flows.

1 Department of Chemical Engineering, University of Massachusetts at Amherst

Let us review a few of the most important experimental results. Consider a circular cylinder with diameter D placed in a stream of fluid moving with uniform speed U in the x-direction. For $R_e = \rho UD/\mu << 1$, the flow is symmetric with respect to both the x-axis and the y-axis; as the R_e increases, the flow loses y-symmetry, and two attached eddies form behind the cylinder which grow in size with increasing R_e until, at $R_e \approx 40$, the flow ceases to be steady and becomes time-periodic. Dye injection experiments show that when $R_e \approx 100$ eddies are shed periodically from the top and bottom part of the cylinder, all the vortices originating from the top rotate in one direction; all the vortices originating from the bottom rotate in the opposite direction while the whole pattern of vortices travels downstream but with a speed smaller than U. As R_e is increased above 200 or so, the flow develops three-dimensionality, time-periodicity is lost, and the flow ultimately produces a turbulent wake (see figures 40-48 in van Dyke, 1982).

Computations have been able to mimic several of these findings (a recent and fairly complete analysis is given by Eaton 1987). However, it is apparent that a few points remain imperfectly understood and that there is a need for further studies. For example, until rather recently, there seemed to be questions regarding the topology of the streamlines and the implications on transport in the time-periodic vortex shedding regime. In a recent work, Perry, Chong & Lim (1982) tried to get insight into the transport process by studying streamline patterns at various phases. They argued that once the vortex shedding process begins, instantaneous "alleyways" of fluid are formed which penetrate the cavity. Even though they acknowledged that the relationship between instantaneous streamlines and streaklines is far from trivial, they nevertheless put forward a picture of the folding of a sheet of dye in the Kármán vortex street in terms of a thought provoking "threading" diagram (figure 8 of their paper), which looks, to someone trained in dynamical systems, very much like a portrait of a manifold.

It was, in fact, this threading diagram that prompted us to pose the following question: Can we use dynamical systems tools to understand, reveal, or at least rationalize known or new aspects of the vortex shedding mechanism? We are of the opinion that the answer to this question is affirmative and that a dynamical systems approach provides a complementary viewpoint to previous analysis for the analysis of the shedding process. In order to apply these tools, we need first to numerically simulate the velocity field. Such simulations were carried at NASA-Ames by K. Shariff. The numerical method used was ARC2D (Pulliam 1985), and the Mach number was 0.1 in all cases. The computational analysis was restricted to $80 < Re_D < 180$, and the results show good agreement between the computational simulations and available experimental results such as vortex shedding frequencies as a function of the Reynolds number (Williamson 1989) and streakline experiments. The structure of the instantaneous streamlines agrees, in general, with previous observations: separation bubbles grow and decay, and the topology of the velocity field allows for the formation of open "alleyways" for transport of fluid. However, we find also that separation bubbles achieve a minimum size and do not disappear, that there are small secondary bubbles which periodically merge with the primary

bubbles, and that the instantaneous streamlines have at most one saddle point and sometimes they have none.

Once the velocity field is obtained, the analysis proceeds along the following points: (i) establishing the existence and location periodic points; (ii) determining the character of the periodic points; (iii) computing their associated manifolds and possible intersections. The analysis is conducted over a range of Reynolds numbers to study local and global bifurcations (changes in the character of periodic points and changes in intersections of manifolds, respectively; this program program of analysis is, in fact, very similar to that proposed for the analysis of other chaotic flows; see Table 7.1 in Ottino 1989). In our particular case, the key point resides in establishing the fact that there is a period-one hyperbolic point in the wake flow and that manifolds belonging to different periodic points produce transversal intersections.

2. Dynamical systems background

Consider a two-dimensional volume preserving time-periodic velocity field, i.e.

$$dx/dt = u(x,y,t), \tag{1a}$$

$$dy/dt = v(x,y,t), \tag{1b}$$

with $\partial u/\partial x + \partial v/\partial y = 0$ and $u(x,y,t) = u(x,y,t+T), v(x,y,t) = v(x,y,t+T)$. The fixed points (or critical points) of the system (1a, b) correspond to the condition $u = v = 0$, and as is well known, due to incompressibility, only saddles and centers are possible. In our case, however, we do not deal with the velocity field itself but rather with its associated "flow" or "motion", that is, the solution of (1a, b) for all possible initial conditions (x_0, y_0). The flow is typically written as

$$x(t) = \Phi t(x_0), \tag{2}$$

and indicates that the initial condition $x_0 = (x_0, y_0)$ is found at position $x = (x, y)$ at time t. However, since the velocity field (1a, b) is time-periodic, it is sometimes more convenient to deal with a map describing the state of the system at times $T, 2T, 3T, \ldots, nT$. This is usually written as

$$x_n = f(x_{n-1}), \tag{3a}$$

or, equivalently,

$$x_n = f^n(x_0). \tag{3b}$$

Flows and maps have fixed points and periodic points. Thus, P is a *fixed point of the flow* $x = \Phi_t(x_0)$ if

$$P = \Phi_t(P) \tag{4}$$

for all times t . On the other hand, P is designed as a *periodic point of period* τ if

$$P = \Phi_\tau(P) \quad \text{but} \quad \Phi_\tau(P) \neq P \quad \text{for} \quad t < \tau, \tag{5}$$

i.e. the material particle that happened to be at the position P at that time $t = 0$ will be located in exactly the same spatial position precisely after a time nT.

The definitions for mappings (3a, b) are similar. A point P is a *fixed point of the mapping* $f(\cdot)$ if

$$P = f^n(P) \quad \textit{for all} \quad n, \tag{6}$$

on the other hand, we say that P is a *periodic point of order* n of the map $f(\cdot)$ if

$$P = f^n(P) \quad \text{but} \quad f^m(P) \neq P \quad \text{for any} \quad m < n, \tag{7}$$

i.e. the particle initially located at P returns to its initial location after *exactly* n iterations [It is important to note that, in general, a fixed point of a flow and its corresponding mapping are in general not the same, and in general, the fixed point of a mapping corresponds to a periodic point of the flow.]

Fixed and periodic points of area-preserving maps and flows can be classified as hyperbolic, elliptic, or parabolic, according to the eigenvalues λ_1 and λ_2 of the flow in the neighborhood of the periodic point.

$$|\lambda_1| > 1 > |\lambda_2|, \quad \lambda_1\lambda_2 = 1, \qquad \text{hyperbolic}$$

$$|\lambda_k| = 1 \quad (k = 1,2) \quad \text{but} \lambda_k \neq 1, \qquad \text{elliptic}$$

$$\lambda_k = \pm 1 \quad (k = 1,2), \qquad \text{parabolic.}$$

The associated physical picture is as follows. A small circle surrounding an elliptic point returns to its original position and undergoes a net rotation; within periods, there is a periodic stretching and compression as well. On the other hand, a circle enclosing a hyperbolic point returns to its initial location stretched in one direction by an amount λ_1 and compressed in the other by $1/\lambda_1$; since the process is repetitive, this leads to outflow in one direction and inflow in the other. Finally, the parabolic case corresponds to simple shear.

In the case of hyperbolic points, the linearization captures the essential behavior of the full nonlinear system (Hartmann-Grobman theorem, see Guckenheimer & Holmes 1983, p. 13). Hyperbolic points have associated invariant sets called the stable $[W^s(P)]$ and unstable $[W^u(P)]$ manifolds defined as

$$W^s(P) = \{\text{all } x_0 \in R^2 \text{ s.t. } \Phi_t(x_0) \to P \text{ as } t \to \infty\} \tag{8a}$$

$$W^u(P) = \{\text{all } x_0 \in R^2 \text{ s.t. } \Phi_t(x_0) \to P \text{ as } t \to \infty\}, \tag{8b}$$

which are tangent to the eigendirections, ξ_1 and ξ_2, of the linearized problem in the neighborhood of P (the definitions for maps are entirely similar).

Manifolds admit a physical interpretation; for example, the unstable manifold corresponds to region of fluid traced by a blob of fluid injected at the periodic point

or to the streakline traced by a dye injected with an injection apparatus that moves as a whole with the periodic point (see figure 5.8.3 in Ottino 1989). It should be noted as well that in general, manifolds move in time. If observations, however, are made at the period of the hyperbolic point, the manifold remains motionless.

By definition, manifolds are invariant; particles x_0 belonging to $W^s(P)$ and $W^u(P)$ do so permanently and cannot escape from them. A point belonging simultaneously to both the stable and unstable manifolds of two different fixed (or periodic) points P and Q is called a *transverse heteroclinic point.* If $P = Q$, the point is called homoclinic. One intersection implies infinitely many and implies sensitivity to initial conditions. This is one of the fingerprints of chaos, and it is entirely equivalent to the formation of what is called a horseshoe map (Smale 1967, Moser 1973).

The definition of stable and unstable manifolds can be extended to parabolic points. In this case, however, as opposed to the case of hyperbolic points, the linearized flow fails to capture the essential aspects of the nonlinear system. In general, much less is known about this case in spite of its importance in transport processes near solid walls (see for example, Danielson & Ottino 1990, Camassa & Wiggins 1990).

The separation point point corresponds to a change of sign in the vorticity, $\partial u/\partial y = 0$, but it is evident that a linear expansion is unable to reveal this fact. A second order expansion about a point $x = x_0, y_0 = 0$ at a no-slip wall gives

$$u = A_{12}y + 2A_{112}(x - x_0)y + A_{122}y^2 \tag{9a}$$

$$v = -A_{112}y^2, \tag{9b}$$

where the coefficients

$$A_{12} = (\partial u/\partial y)_{x_0,y_0}, \tag{10a}$$

$$A_{112} = (1/2)(\partial^2 u/\partial x \partial y)_{x_0,y_0}, \tag{10b}$$

$$A_{122} = (1/2)(\partial^2 u/\partial y^2)_{x_0,y_0}, \tag{10c}$$

are, in general, functions of time which can obtained by forcing the expansion to satisfy the Navier-Stokes equations and suitable boundary conditions. The vorticity at the wall is given by

$$\omega|_{y=0} = [\partial v/\partial x - \partial u/\partial y]_{y=0} = -[2A_{112}(x - x_0) + A_{12}], \tag{11}$$

and the condition for $\omega = 0$ is met at

$$x_s - x_0 = -A_{12}/2A_{112}. \tag{12}$$

In general, the separation point x_s moves as a function of time. If $A_{112} < 0$, x_s corresponds to a point of separation and if $A_{112} > 0$, x_s corresponds to a point of attachment. The angle of separation is given by $\tan\Theta = 3\mu(\partial\omega/\partial x)/(\partial p/\partial x)$ where μ is the viscosity and p is the pressure (Oswatitsch 1958, Lighthill 1963). In

terms of the coefficients of the expansion (9), $\tan\Theta = -3A_{112}/A_{122}$. In this case, the manifold can be obtained by placing a blob at $x = x_s, y = 0$. These results for steady flow may be generalized to time-periodic flow, and this will be discussed elsewhere (Shariff, Pulliam & Ottino, 1990).

3. Periodic points and manifolds

The entire wall of the cylinder consists of parabolic points, and the points of special interest are those corresponding to a change of sign in time-averaged shear stress, i.e. separation and attachment points of the time-averaged flow. It can be shown that manifolds emanate from such points. There is as well a periodic point in the wake itself; this is a period-one hyperbolic point. It is important to stress that this point is completely unrelated to the critical points in the velocity field itself. An important difference is that periodic points do not disappear; on the other hand, critical points in the velocity field itself can appear or disappear as the topology of the streamlines changes in time.

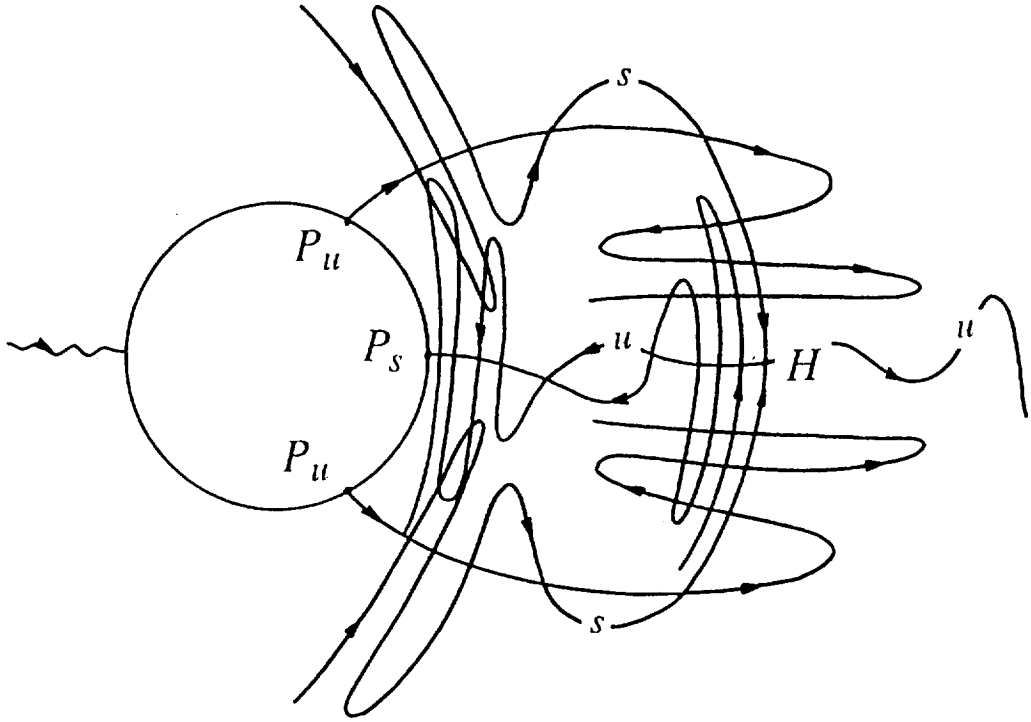

FIGURE 1. Qualitative picture of intersections between stable and unstable manifolds in the time-shedding regime.

Stable and unstable manifolds can produce heteroclinic and homoclinic intersections. In this particular flow, four types of transversal intersections are possible:

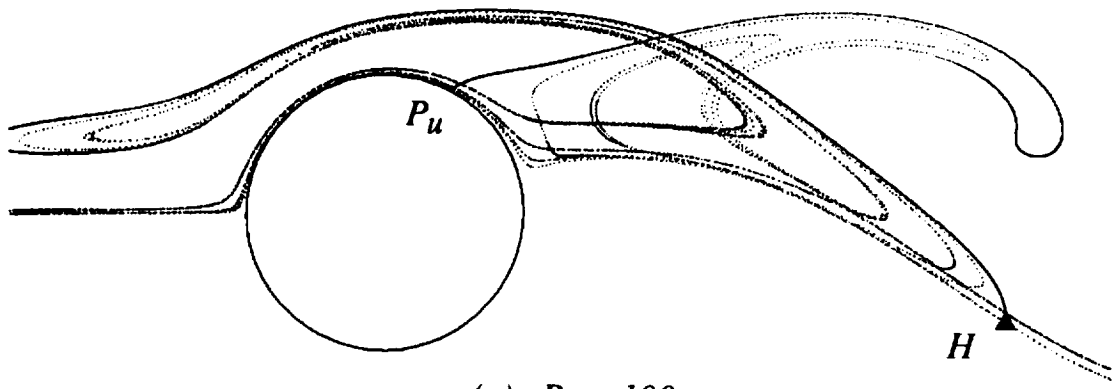

(a) Re= 100

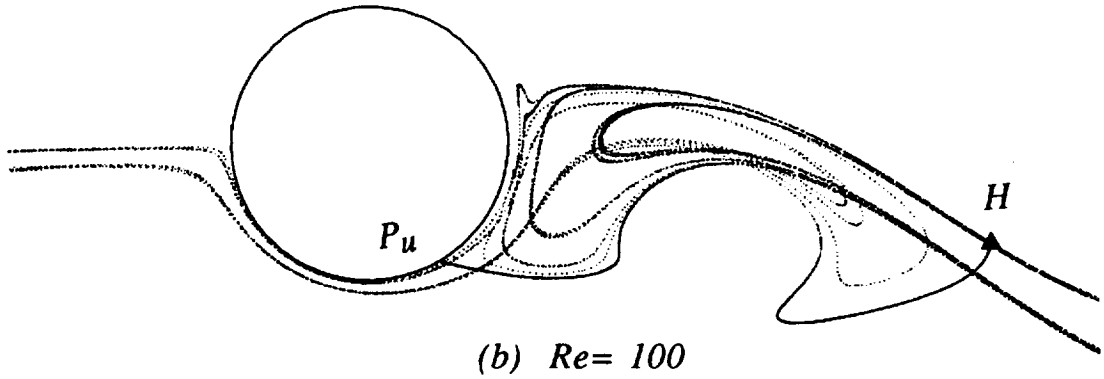

(b) Re= 100

FIGURE 2. Intersections between unstable manifolds associated with (parabolic) separation points attached to the cylinder (denoted P) and stable manifolds associated with a hyperbolic points (denoted H) at Re=100; (a) manifold structure corresponding to the upper wake, (b) manifold structure corresponding to the lower wake.

heteroclinic intersections are produced by intersections of stable manifolds of the period-one hyperbolic with unstable manifolds of the periodic points attached to the cylinder as well as by unstable manifolds of the hyperbolic point intersecting the stable manifolds attached to the surface of the cylinder, *homoclinic* intersections are produced by crossings of stable and unstable manifolds belonging to the hyperbolic point as well as those of parabolic points attached to the cylinder. The complete manifold picture of the system is, however, more complex since there are additional period-one hyperbolic points close to the surface of the cylinder as well as higher order periodic points; they, however, seem to contribute much less to the gross aspects of the transport in the flow.

The manifold structures of the periodic points described in the previous sections results in the qualitative picture shown in figure 1 (the picture has been deformed, without changing topology, to improve clarity). Such a picture is characteristic of chaotic systems and contains information regarding transport of material in the flow (Rom-Kedar, Leonard & Wiggins 1990). Figure 2 shows computed pictures corresponding to $R_e = 100$, whereas figure 3 shows the changes in structure at $R_e = 180$. For the sake of clarity, figures 2(a) and 3(a) show the manifold structure corresponding to the upper wake; figures 2(b) and 3(b) show the manifold structure corresponding to the lower wake.

The manifold structure of figures 2 and 3 provides a template for stretching and transport and provides a qualitative picture for the stretching and folding of a streakline in the wake. Previous work suggests that dye patterns are well represented by the unstable manifolds belonging to low order hyperbolic periodic points (Swanson & Ottino 1990, Shariff 1989). This expectation is confirmed in the present work, and unstable manifolds associated with low order periodic points provide an excellent template for the study of evolution of stretching in the flow; most of the stretching originates from regions in the neighborhood of the stable manifold, and the orientations corresponding to the maximum stretch are oriented normal to the manifold.

Another quantity of kinematical interest is the stretching history, $\nabla v : mm$, following a fluid element, which is related to the Lyapunov exponents (Khakhar & Ottino 1986). This quantity enters in the convection diffusion equation which governs the molecular diffusion of the dye comprising the streakline (Ottino 1989, p. 276). Regions with large values of $\nabla v : mm$ correspond to large stretching along m, which tends to minimize the spread of molecular diffusion normal to the streaklines but at the same time tends to make the streakline less visible since the thickness of the dye streak is significantly reduced. On the other hand, low or negative values of $\nabla v : mm$ blur the picture. Such a situation arises near the tip of folds since as the dye folds there is a change of sign of $D : mm$. A comparison of computational results and experiments shows that it is precisely in these regions where molecular diffusion effects become important. Another quantity of interest for which experiments are available is the computation of distribution of residence times of fluid elements behind the cylinder. A detailed presentation of all the above results is in preparation (Shariff, Pulliam & Ottino, 1990).

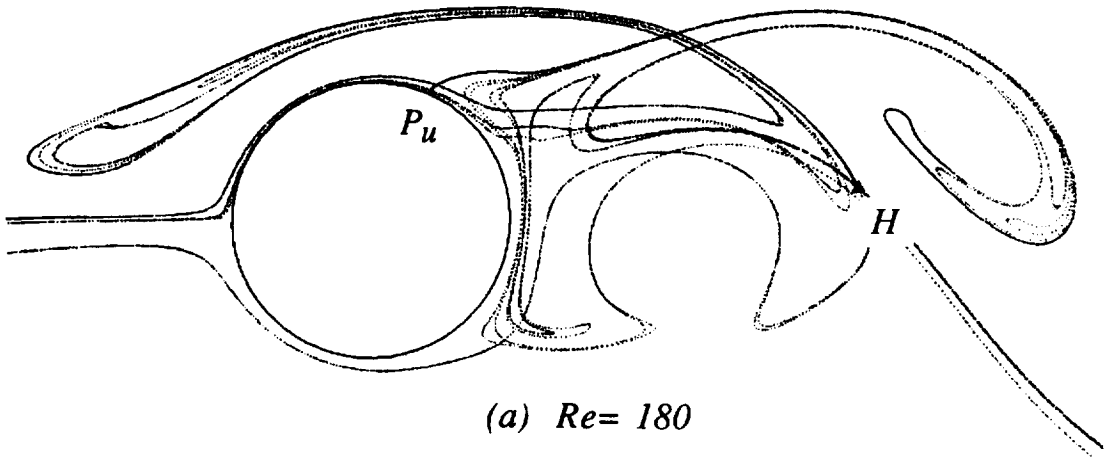

(a) Re= 180

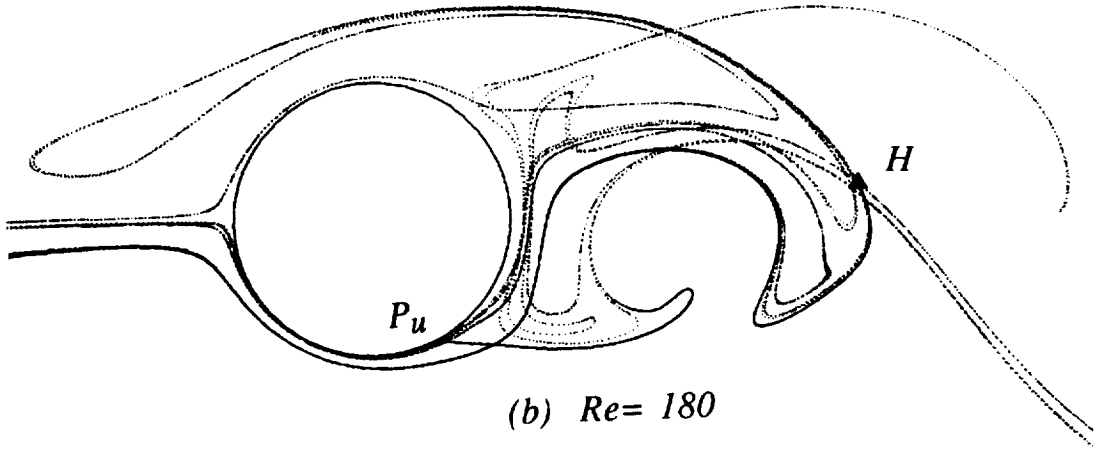

(b) Re= 180

FIGURE 3. Intersections between unstable manifolds associated with (parabolic) separation points attached to the cylinder (denoted P) and stable manifolds associated with a hyperbolic points (denoted H) at Re=180; (a) manifold structure corresponding to the upper wake, (b) manifold structure corresponding to the lower wake.

REFERENCES

CAMASSA, R. & WIGGINS, S. 1990 Chaotic advection in a Rayleigh-Bénard flow. *Phys. Rev. A,* to appear.

DANIELSON, T. J. & OTTINO, J. M. 1990 Structural stability in two-dimensional model flows: Eulerian and Lagrangian turbulence. *Phys. Fluids A.* **2,** 2024-2035.

EATON, B. E. 1987 Analysis of laminar vortex shedding behind a circular cylinder by computer-aided flow visualization. *J. Fluid Mech.* **180,** 117-145.

GUCKENHEIMER, J. & HOLMES, P. 1983 Nonlinear Oscillations, Dynamical Systems, and Bifurcations of Vector Fields, New York: Springer-Verlag (reprinted 1986).

KARNIADAKIS, G. E. & TRIANTAFYLOU, G. S. 1989 Frequency selection and asymptotic states in laminar wakes. *J. Fluid Mech.* **119,** 441-469.

KHAKHAR, D. V. & OTTINO, J. M. 1986 Fluid mixing (stretching) for time periodic sequences for weak flows. *Phys Fluids.* **29,** 3503-3505.

KHAKHAR, D. V., RISING, H. & OTTINO, J. M. 1986 An analysis of chaotic mixing in two model systems. *J. Fluid Mech.* **172,** 419-451.

LIGHTHILL, M. J., 1963 Introduction. Boundary layer theory. Ch. II, pp. 46-113 in *Laminar boundary layers,* L. Rosenhead, ed., London: Oxford University Press.

MOSER, J. 1973 Stable and random motion in dynamical systems Princeton: Princeton University Press.

OERTEL, H. 1990 Wakes behind blunt bodies. *Annu. Rev. Fluid Mech.* **22,** 539-564.

OSWATITSCH, K. 1958 Die Ablösungsbedingung von Grenzschichten. in *Symposium on Boundary Layer Research.* H. Görtler, ed., Berlin: Springer-Verlag, pp. 357-367.

OTTINO, J. M. 1989 *The kinematics of mixing: stretching, chaos, and transport.* Cambridge: Cambridge University Press.

OTTINO, J. M. 1990 Mixing, chaotic advection, and turbulence. *Ann. Revs Fluid Mech.* **22,** 207-254.

PERRY, A. E. & CHONG, M. S. 1987 A series expansion study of the Navier-Stokes equations with applications to three- dimensional separation patterns. *J. Fluid Mech.* **173,** 207-23.

PERRY, A. E., CHONG, M. S. & LIM, T. T. 1982 The vortex- shedding process behind two-dimensional bluff bodies. *J. Fluid Mech.* **116,** 77-90.

PULLIAM, T. 1985 Efficient solution methods of the Navier- Stokes equations. Lecture notes von Kármán institute for Fluid Dynamics, Lectures series-Numerical techniques for viscous computations in turbomachinery bladings, January 20-24, 1986, Brussels, Belgium.

ROM-KEDAR, V., LEONARD, A., & WIGGINS, S. 1990 An analytical study of transport, mixing and chaos in an unsteady vortical flow. *J. Fluid Mech.* **214**, 347-394.

SHARIFF, K. 1989 Dynamics of a class of vortex rings. Ph.D. thesis. Dept. Mech. Eng., Stanford University.

SHARIFF, K, PULLIAM, T. & OTTINO, J. M. 1990 In preparation for J. Fluid Mech.

SMALE, S. 1967 Differentiable dynamical systems. *Bull. Amer. Math. Soc.*. **73**, 747-817.

SWANSON, P. D. & OTTINO, J. M. 1990 A comparative computational and experimental study of chaotic mixing of viscous fluids. *J. Fluid Mech.* **213**, 227-249.

VAN DYKE, M. 1982 An album of fluid motion. Stanford: The Parabolic Press.

WILLIAMSON, C. H. K. 1989 Oblique and parallel modes of vortex shedding in the wake of a circular cylinder at low Reynolds numbers. *J. Fluid Mech.* **206**, 579-627.

Direct numerical simulation of turbulent plane Couette flow

By Moon Joo Lee[1]

Turbulent plane Couette flow was numerically simulated at a Reynolds number ($U_w h/\nu$) of 6000, where U_w is the relative wall speed and h is half the channel-height. Unlike in Poiseuille flow, where the mean shear rate changes its sign at the centerline, the sign of mean shear rate in plane Couette flow remains the same across the whole channel. This difference is expected to yield several differences between the two flows, especially in the core region. The most significant and dramatic difference observed in the present work was the existence of large-scale structures in the core region of the plane Couette flow. The large eddies are extremely long in the flow direction and fill the entire channel (i.e. their vertical extent is $2h$). The large-scale structures have the largest contribution from the wavenumber $(k_z h, k_z h) = (0, \pm 1.5)$, corresponding to a wavelength $\Lambda_z/h \simeq 4$. The secondary motion associated with the $k_z h = 0$ mode consists of the large-scale vortices. The large eddies contribute about 30% of turbulent kinetic energy.

1. Introduction

Plane Couette flow is a paradigm of shear flows because of its simple flow geometry and fundamental fluid-mechanical characteristics. A fully-developed plane Couette flow has a constant shear stress, $\tau = \mu\, dU/dy - \rho\,\overline{uv}$ (equal to its value at the walls, $\tau_w = \mu\, dU/dy|_w$), across the entire channel, $-1 \le y/h \le 1$, be it laminar or turbulent. This prominent property results directly from the zero mean pressure gradient in the flow as it is driven by shear generated at two plane, solid boundaries that are in rectilinear, parallel movement (at speed U_w) relative to each other.

Another characteristic of structural interest of the flow is that both the mean vorticity (or mean shear rate, $S = dU/dy$) and turbulent shear stress ($-\rho\,\overline{uv}$) are symmetric about the center plane ($y/h = 0$), yielding a finite production rate ($-\rho\, S\,\overline{uv}$) of turbulent kinetic energy even in the core region (say, 0.2–0.5 $\le y_\perp/h <$ 1, where $y_\perp$ is the distance normal to a nearest boundary). As a consequence, the profiles of turbulence intensities ($\overline{u^2}$, $\overline{v^2}$, $\overline{w^2}$) differ significantly among the three components (see El Telbany & Reynolds 1982), indicative of a high degree of anisotropy in the flow. We hypothesize that the structures of turbulence (both statistical and instantaneous) in the core region of plane Couette flow would be quite different from those of Poiseuille flow. This issue has not been addressed before. In the vicinity of the walls, say $y_\perp/h \le 0.1$–0.2, however, structures of turbulence in the two flows are expected to be similar, since the near-wall dynamics of a turbulent shear flow is primarily controlled by a mechanism universally represented by the

1 Permanent address: Pohang Institute of Science and Technology, Pohang, Korea

'law of the wall.' Identification and characterization of the possible new structures in turbulent plane Couette flow is one of the central questions addressed in this study. It is our goal to understand the mechanism by which the boundary shearing produces turbulence structures different from those generated in a pressure-driven flow.

Despite its apparent importance as a paradigm of shear flows, turbulent plane Couette flow has not been studied extensively. In most previous experiments (Reichardt 1956, 1959; Robertson 1959; Robertson & Johnson 1970; Leutheusser & Chu 1971; El Telbany & Reynolds 1980, 1981), the length of the shearing boundary realized by employing either a (flexible) moving belt or a fluid interface had to be made short ($L_B/h = 10$–80) since it is prone to deform at high speeds (or at high Reynolds numbers). Because of the difficulties arising from the moving boundaries, only the profiles of mean velocity, turbulent intensities and turbulent shear stress were obtained in most experiments, and measurements of higher-order statistics, if any, were limited to the streamwise direction (Robertson & Johnson 1970; Aydin & Leutheusser 1979, 1989). Direct numerical simulation approach taken in this work is ideally suited to study structures of turbulence in plane Couette flow without having such problems.

In this paper, we report the existence of the large-scale eddies in the core region of plane Couette flow. Some details of the kinematical characteristics of the large-scale structures are presented. Both the instantaneous and statistical structures of turbulence in the flow are compared with those in plane Poiseuille flow. Implications for turbulence modeling are also discussed.

2. Numerical methods

The three-dimensional, time-dependent Navier–Stokes equations were solved numerically for plane Couette flow at a Reynolds number ($\mathrm{Re} = U_w h/\nu$) of 6000; the Reynolds number $\mathrm{Re}_\tau = U_\tau h/\nu$ based on the wall-shear velocity $U_\tau = (\nu\, dU/dy|_w)^{1/2}$ is about 170. The particular choice of the Reynolds number was made in order to compare with the results of plane Poiseuille flow reported by Kim, Moin & Moser (1987, $\mathrm{Re}_\tau = 180$). The simulation reported in this paper was carried out by using a pseudo-spectral method with Fourier and Chebyshev polynomial expansions in the horizontal (x, z) and vertical (y) directions, respectively. The spectral expansion of the main computation reported here had $128 \times 129 \times 192$ (3 170 304) modes in (x, y, z). The computational domain has the streamwise and spanwise dimensions of $(B_x, B_z)/h = (4\pi, \frac{8}{3}\pi)$. No-slip and periodic boundary conditions were used at the walls and in the horizontal directions, respectively.

Time advancement was made through a low-storage, third-order Runge-Kutta method for the nonlinear terms and the second-order Crank–Nicolson scheme for the viscous terms. The initial field consisted of finite-amplitude random disturbances (about 10% of U_w) in all components of velocity with the linear mean profile, $U/U_w = \frac{1}{2}(y/h + 1)$. Subsequent development of the basic statistics such as the mean velocity profile, turbulent kinetic energy and turbulent shear stress was monitored in order to determine whether the flow reached a statistical steady-state. The

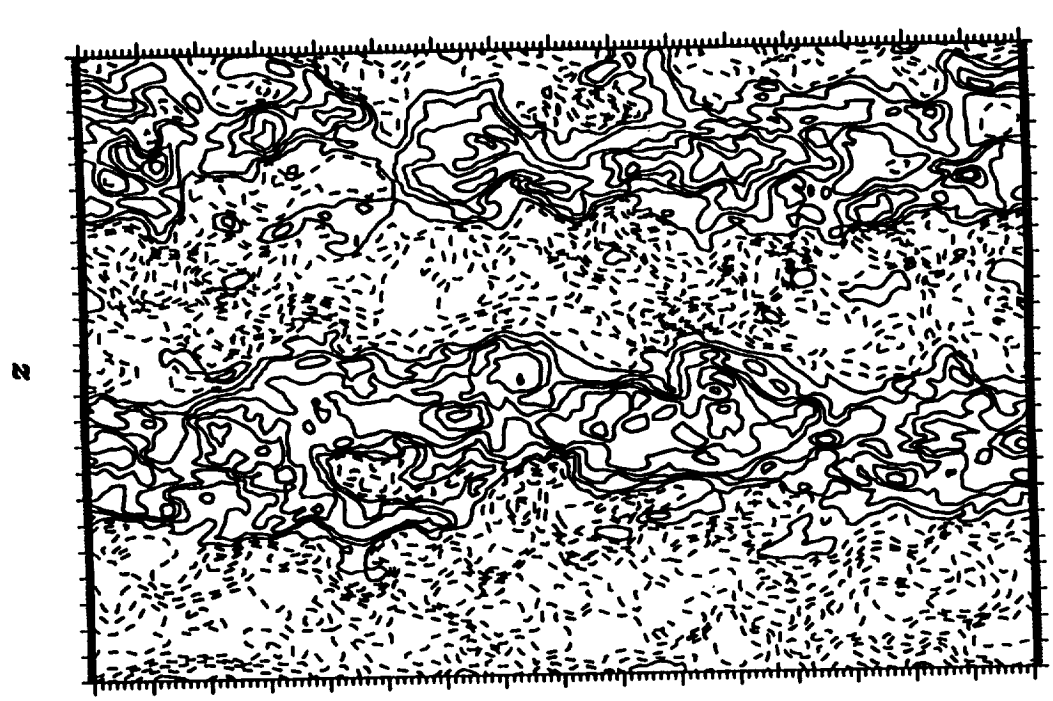

FIGURE 1. Contours of the instantaneous streamwise velocity (u) at the center plane ($y/h = 0$) of plane Couette flow: ——— , $u \geq 0$; - - - - , $u < 0$.

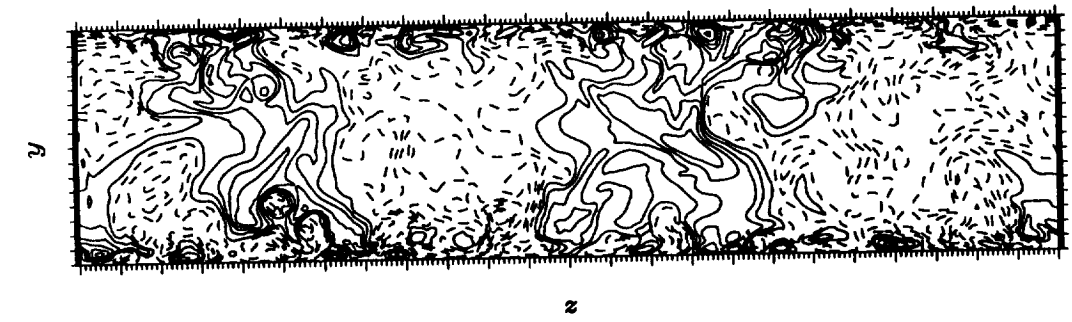

FIGURE 2. Contours of the instantaneous streamwise velocity (u) on a yz-plane (an end view) of plane Couette flow: ——— , $u \geq 0$; - - - - , $u < 0$.

computation was started with a coarse resolution ($32 \times 65 \times 48$ modes), and when the flow reached a statistical steady-state, the number of modes was successively increased. The final statistics were compiled after the flow reached the statistical steady-state with the final resolution ($128 \times 129 \times 192$ modes).

3. The large-scale structures

Contours of the instantaneous streamwise velocity (u) at the center plane ($y/h =$

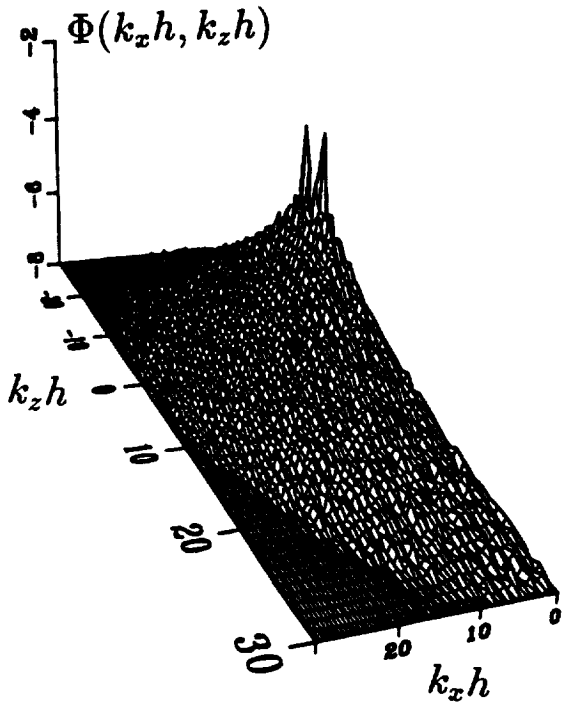

FIGURE 3. The two-dimensional energy spectrum $\Phi(k_x h, k_z h) = \overline{|\hat{u}|^2}$ at the center plane ($y/h = 0$) of plane Couette flow, showing that the energy density has two distinctive peaks at $(k_x, k_z)h = (0, \pm 1.5)$. The magnitude of the peaks is about seven times larger than the next largest contribution.

0) are shown in Figure 1. There are two pairs of high- and low-speed regions (denoted by solid and dashed lines in the figure) that are highly elongated in the flow direction and alternating in the spanwise direction. Note that the eddies are almost uniform in the flow direction (i.e. the eddies do not meander sideways much) and that the spanwise size of each region is about the channel-height ($2h$). In plane Poiseuille flow where the mean shear rate changes sign at the center plane, there are no such organized structures of turbulence in the core region. The spanwise (one-dimensional) energy spectrum, $\Theta_{uu}(k_z h)$, of the streamwise velocity (not shown here) has a distinctive peak at $k_z h = 1.5$, which corresponds to a wavelength $\Lambda_z/h \simeq 4$, consistent with the instantaneous contours shown in Figure 1.

To examine the vertical extent of the eddy structures, contours of instantaneous u are drawn on a yz-plane (an end view) in Figure 2. The figure shows that the eddies are as tall as the whole channel height, $2h$, and hence the aspect ratio of the large eddies is close to unity. In the wall region, however, the presence of eddies of much smaller lengthscales is evident. These small wall-region eddies are identical to those found in the wall region of a plane Poiseuille flow.

The two-dimensional energy spectrum, $\Phi(k_x h, k_z h) = \overline{|\hat{u}|^2}$, at $y/h = 0$ (Figure 3) shows that the energy density has two distinctive peaks at $(k_x, k_z)h = (0, \pm 1.5)$;

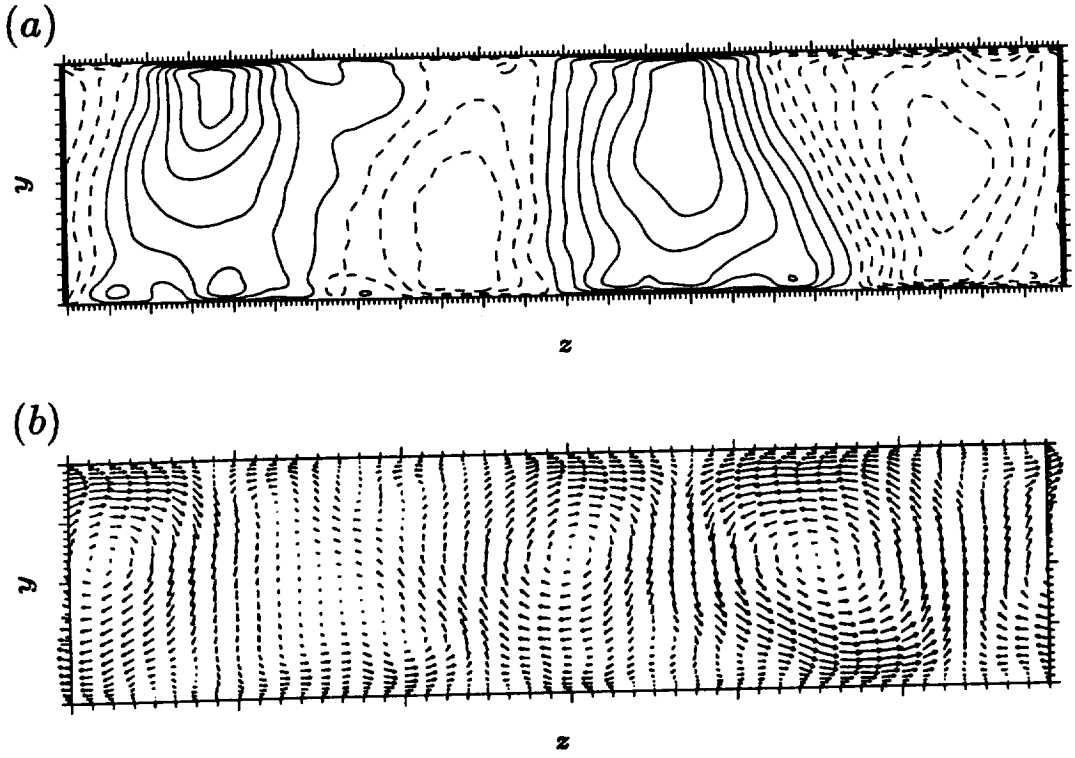

FIGURE 4. Velocity field of the $k_x = 0$ mode (or the large-eddy field) in plane Couette flow. (a) Contours of $\widetilde{u}$ in the yz-plane (perpendicular to the mean flow); (b) velocity vectors, $(\widetilde{v}, \widetilde{w})$, projected on the yz-plane. ——— , $\widetilde{u} \geq 0$; - - - - , $\widetilde{u} < 0$.

their magnitude is about seven times the next largest contribution. This dominant contribution of the $(k_x, k_z)h = (0, \pm 1.5)$ mode persists even close to the walls (the ratio is about three at $y_\perp/h = 0.001$), indicating that the large eddies have a significant effect across the whole channel.

To further investigate the characteristics associated with the large eddies, we decompose the flow field as $\mathbf{v} = \widetilde{\mathbf{v}} + \mathbf{v}'$, where $\widetilde{\mathbf{v}} = (\widetilde{u}, \widetilde{v}, \widetilde{w})$ is obtained by averaging over t and x, thus representing eddies independent of time and the streamwise direction (i.e., time-averaged $k_x = 0$ mode), and $\mathbf{v}'$ denotes the residual field. Contours of $\widetilde{u}$ in the yz-plane (perpendicular to the mean flow) are shown in Figure 4(a). The lengthscales associated with these large eddies are now more apparent; statistics associated with these eddies will be discussed in the next section. Note that the small-scale eddies that are quite strong in the instantaneous field (see Figure 2) are not present in the $k_x = 0$ mode. In Figure 4(b), the velocity vectors, $(\widetilde{v}, \widetilde{w})$, projected on the yz-plane show that the secondary flow consists of large-scale vortices that fill the entire channel. (For visual clarity, every fourth data points in the both directions were selected for the vector plot.) Notice that in the core region the streamwise velocity $(\widetilde{u})$ is distributed 180° out of phase with the vertical velocity

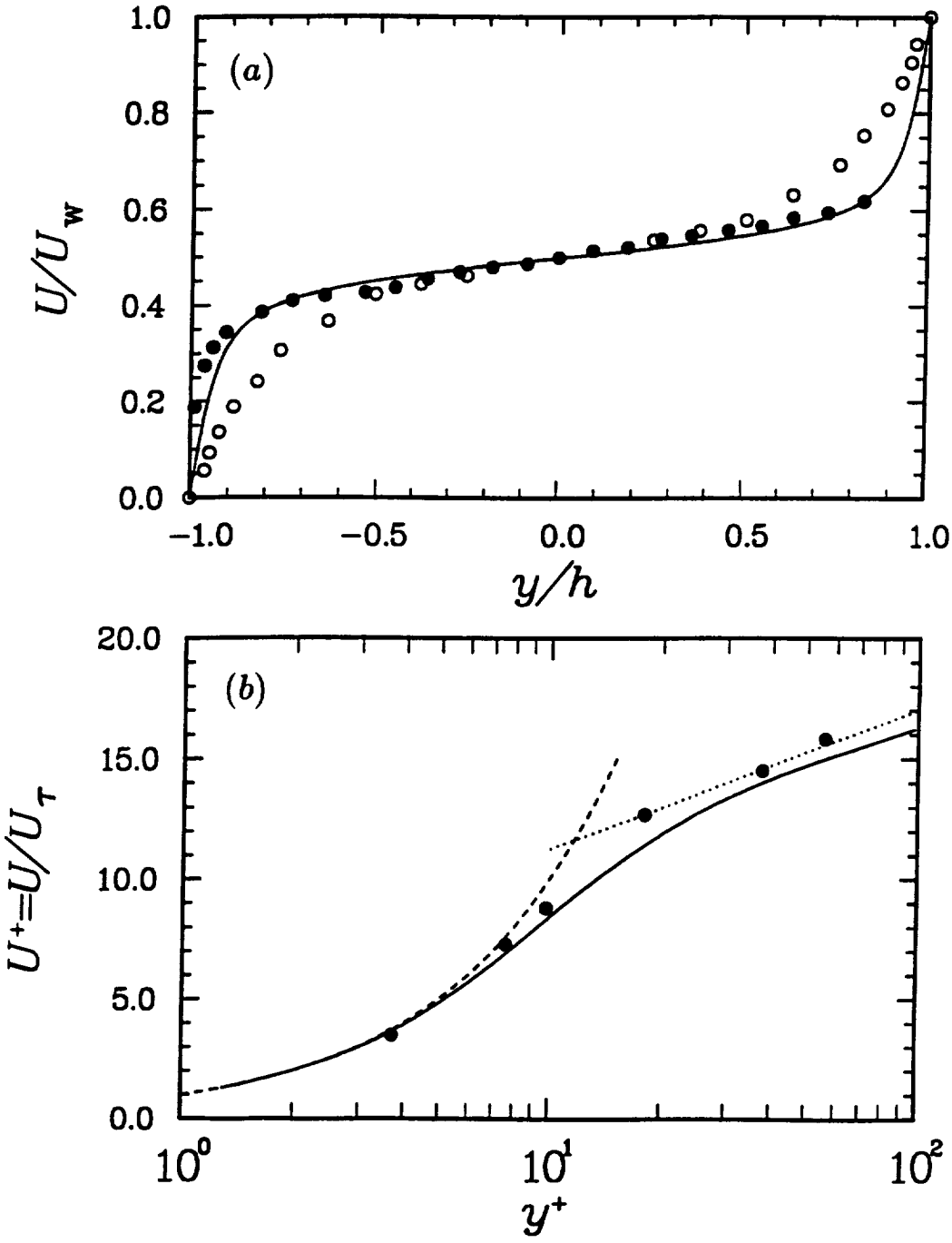

FIGURE 5. Mean velocity profile in plane Couette flow: (*a*) global profile, U/U_w *vs.* y/h; (*b*) near-wall profile, U^+ *vs.* y^+. ——— , present simulation; ○ , Reichardt (1959); • , El Telbany & Reynolds (1980); ---- , $U^+ = y^+$; ····· , $U^+ = (1/\kappa)\ln y^+ + B$ ($\kappa = 0.4$ and $B = 5.5$).

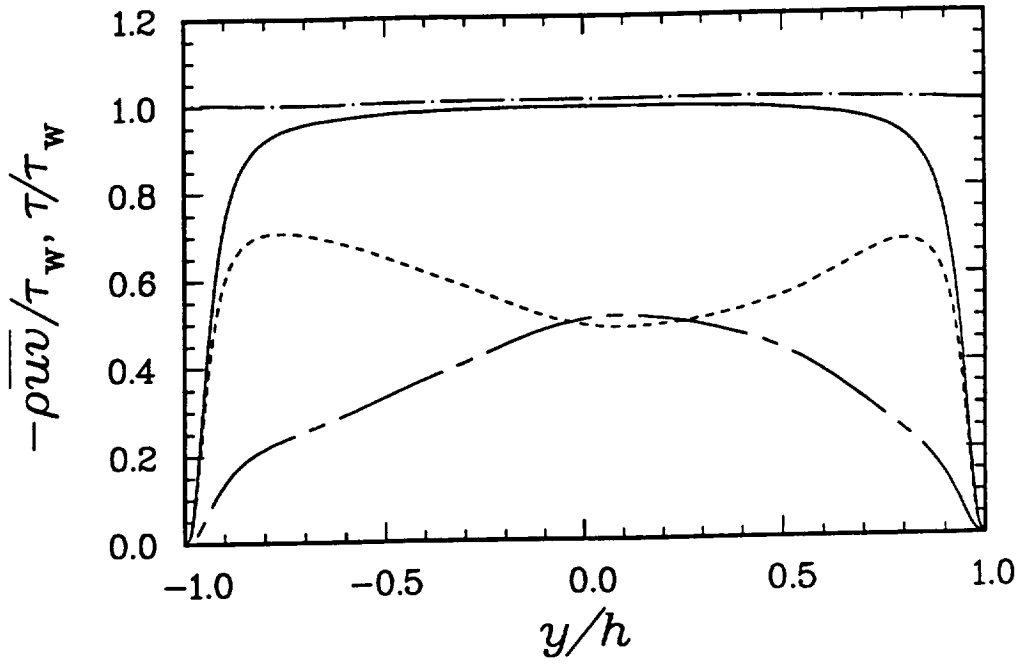

FIGURE 6. Profiles of shear stresses in plane Couette flow. —·— , total shear stress (τ/τ_w); ——— , Reynolds stress ($-\rho\overline{uv}$) of the full field; —·— , Reynolds stress of the $k_x = 0$ mode; ---- , Reynolds stress of the residual field.

($\widetilde{v}$), which leads to a significant contribution to shear stress from the secondary flow. Because of the large lengthscale of the secondary motion, the magnitude of its streamwise vorticity in the core region is only a few percent of the shear rate at the wall.

4. Statistics

In Figure 5(a), comparison of the mean velocity profile, U, is made between the computation and experiments conducted at different Reynolds numbers (Re = 2900, Reichardt 1959; Re $\simeq 2\times10^4$–4×10^4, El Telbany & Reynolds 1980). Note that the velocity profile at high Reynolds numbers changes rapidly within the narrow region close to the walls (say, $y_\perp/h \leq 0.1$), and that it has a seemingly constant slope in the core region ($|y/h| \leq 0.5$). The mean velocity gradient at the walls, $S_w = dU/dy|_w$, grows substantially with Reynolds number, whereas at the center plane the slope, $S_c = dU/dy|_{y/h=0}$, decreases with increasing Reynolds numbers. The value of S_c is about 5% of the wall value and it is about 30% of the value of a laminar flow with a linear velocity profile. Thus, the total shear stress in the turbulent case is about ten times higher compared with the laminar value. The near-wall profile, U^+ (made dimensionless by the wall-shear velocity, U_τ), *vs.* y^+ (the distance normal to the nearest wall scaled by the viscous length, $\ell_\nu = \nu/U_\tau$) is shown in Figure 5(b). The dashed and dotted lines denote the law of the wall: $U^+ = y^+$ and

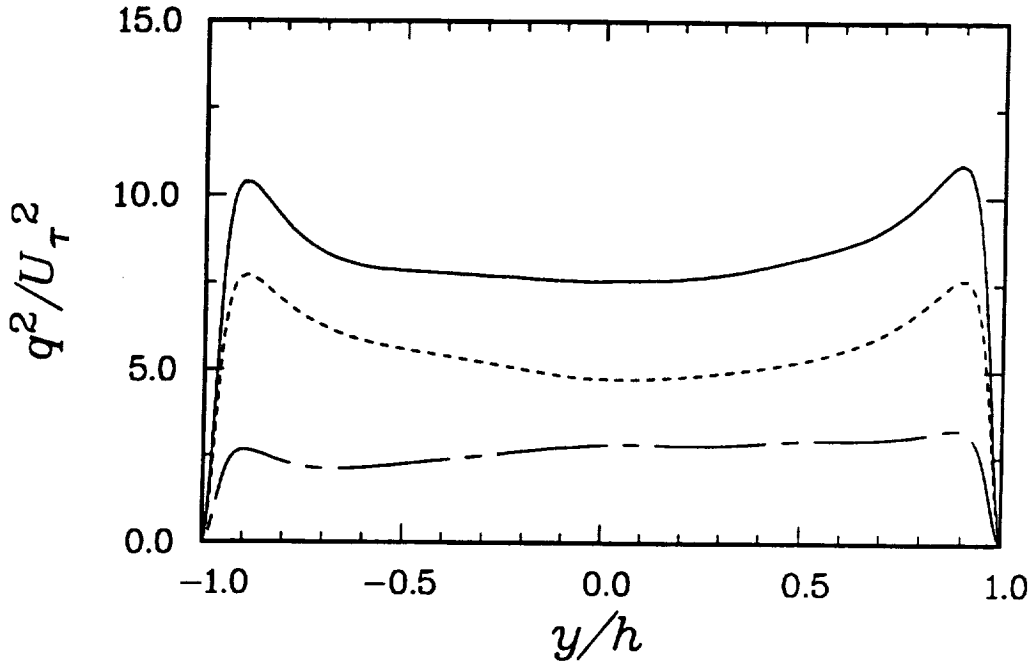

FIGURE 7. Profile of turbulent kinetic energy in plane Couette flow. ——— , q^2 of the full field; —·— , q^2 of the $k_z = 0$ mode; ---- , q^2 of the residual field.

$U^+ = (1/\kappa) \ln y^+ + B$ (where $\kappa = 0.4$ and $B = 5.5$), respectively, which fits the experimental data at a higher Reynolds number (El Telbany & Reynolds 1980).

Figure 6 shows the profiles of turbulent and total shear stresses across the channel. The shear stresses are symmetric about $y/h = 0$, and the uniformity of the total shear stress ($\tau/\tau_w = 1$) is apparent, indicating that the flow has indeed reached a statistical steady-state. Near the walls, the turbulent stress ($-\rho\overline{uv}/\tau_w$) increases rapidly with the distance from the wall. (Hence, the mean shear rate, $dU/dy = (\tau + \rho\overline{uv})/\mu$, decreases rapidly in the same vicinity of the walls.) In the core region, the total shear stress is completely dominated by the turbulent stress and the viscous stress is only a few percent.

It is of interest to examine how much the large-scale eddies contribute to energetics. In Figure 6, the contributions to the Reynolds stress from the large-scale eddies and residual field are drawn. The contribution from the large eddies increases with the distance from the wall and at the center line it is about the same as that from the residual field. Figure 7 compares the contributions to turbulent kinetic energy from the full, large-eddy and residual fields. Except in the vicinity of the wall (say $y_\perp/h \leq 0.1$), the contribution from the large eddies is about 30% over the whole channel, indicative of the importance of the large-scale eddies.

The profiles of turbulence intensities (u'^+, v'^+, w'^+) in Figure 8(a) show good agreement with the measurements (El Telbany & Reynolds 1981). Comparison with those in a plane Poiseuille flow (Figure 8b) at a comparable Reynolds number ($\mathrm{Re}_\tau =$

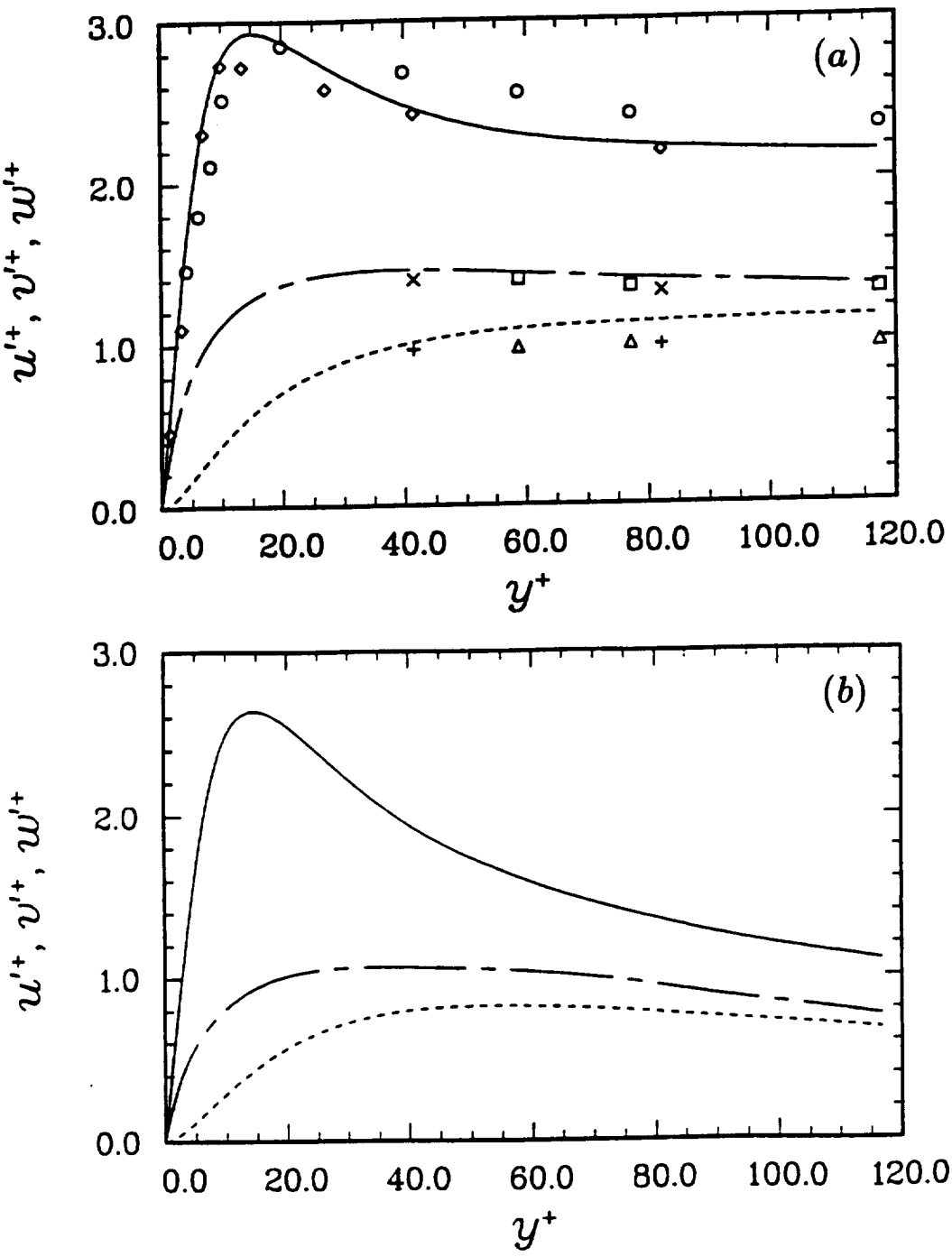

FIGURE 8. Near-wall profiles of turbulence intensities, (u'^+, v'^+, w'^+) *vs.* y^+: (*a*) plane Couette flow (present computation); (*b*) plane Poiseuille flow (from Kim *et al.* 1987). ——— , u'^+; - - - - , v'^+; — - — , w'^+. Symbols are the measured data from El Telbany & Reynolds (1981).

180, Kim *et al.* 1987) shows that the intensities in Couette flow are significantly higher at most locations in the channel, except in the vicinity of the wall ($y^+ \leq 30$) where the Couette values are only slightly higher. The marked difference in the core region is a direct consequence of the finite rate of production of turbulent kinetic energy in plane Couette flow. The figure also shows that the energy distribution among the three components in the core region is more anisotropic in Couette flow ($\overline{u^2} : \overline{v^2} : \overline{w^2} \simeq 0.61 : 0.17 : 0.22$) than in Poiseuille flow.

5. Summary and concluding remarks

Direct numerical simulation of turbulent plane Couette flow at Reynolds number of 6000 was carried out. Examination of the instantaneous and statistical structures revealed the existence of large-scale eddies in the flow. The large-scale structures have a extremely long lengthscale in the flow direction and they fill the entire channel. They appear as pairs of high- and low-speed regions alternating in the spanwise direction with an average lengthscale of $2h$ so that their aspect ratio is about unity. The (x, t)-averaged field shows the existence of secondary vortical motion that fills the entire channel.

It has been known that existing turbulence models based on two-dimensional flows have a difficulty in predicting structures of 'three-dimensional' flows such as curved channel flow and rotating channel flow. Despite the flow geometry of these flows is two-dimensional, large secondary flows develop and play a dominant role because of instabilities associated with centrifugal (curved channel) or Coriolis (rotating channel) force. Plane Couette flow does *not* have such instability, but similar large roll-cell-like structures exist in the core region as evidenced in the present work. Therefore, it would be of great interest to see how well the current turbulence models predict the behavior of turbulence in plane Couette flow.

We have also compiled a variety of turbulence statistics such as the probability density functions (and skewness and flatness) of velocity components, profiles of the terms in the transport equations of the Reynolds stresses, etc. Comparison with those in plane Poiseuille flow will be discussed in full later.

This work was performed in collaboration with John Kim of the NASA-Ames Research Center. I thank Parviz Moin and Javier Jimenez for the fruitful discussions. This work was supported in part by the National Science Foundation, for which I am grateful.

REFERENCES

AYDIN, M. & LEUTHEUSSER, H. J. 1979 Novel experimental facility for the study of plane Couette flow. *Rev. Sci. Instr.* **50**, 1362–1366.

AYDIN, E. M. & LEUTHEUSSER, H. J. 1987 Experimental investigation of turbulent plane-Couette flow. *Forum on Turbulent Flows–1987*, FED vol. 51, 1987 ASME Applied Mech., Bioeng. & Fluids Eng. Conf., Cincinnati, Ohio, June 14–17, 1987 (ed. W. W. Bower), pp. 51–54. Amer. Soc. Mech. Eng.: New York.

AYDIN, E. M. & LEUTHEUSSER, H. J. 1989 Plane-Couette flow between smooth and rough walls. *J. Fluid Mech.* (*sub judice*)

EL TELBANY, M. M. M. & REYNOLDS, A. J. 1980 Velocity distributions in plane turbulent channel flows. *J. Fluid Mech.* **100**, 1–29.

EL TELBANY, M. M. M. & REYNOLDS, A. J. 1981 Turbulence in plane channel flows. *J. Fluid Mech.* **111**, 283–318.

EL TELBANY, M. M. M. & REYNOLDS, A. J. 1982 The structure of turbulent plane Couette flow. *Trans. ASME, J. Fluids Eng.* **104**, 367–372.

KIM, J., MOIN, P. & MOSER, R. D. 1987 Turbulence statistics in fully developed channel flow at low Reynolds number. *J. Fluid Mech.* **177**, 133–166.

LEE, M. J. 1990 The large-scale structures in turbulent plane Couette flow. *Center for Turbulence Research Annual Research Briefs–1989*, pp. 231–245. Center for Turbulence Research: Stanford University and NASA-Ames Research Center.

LEUTHEUSSER, H. J. & CHU, V. H. 1971 Experiments on plane Couette flow. *Proc. ASCE, J. Hydr. Div.* **97** (HY9), 1269–1284.

REICHARDT, H. 1956 Über die Geschwindigkeitsverteilung in einer geradlinigen turbulenten Couetteströmung. *Zeit. angew. Math. Mech.* **36**, Sonderheft 26–29.

REICHARDT, H. 1959 Gesetzmäßigkeiten der geradlinigen turbulenten Couetteströmung. *Mitteil.* Nr. 22. Max-Planck-Inst. Strömungsforschung und Aerodynamischen Versuchsanstalt: Göttingen.

ROBERTSON, J. M. 1959 On turbulent plane-Couette flow. *Proc. Sixth Midwestern Conf. Fluid Mech.*, Univ. of Texas, Austin, Texas, Sept. 9–11, 1959, pp. 169–182.

ROBERTSON, J. M. & JOHNSON, H. F. 1970 Turbulence structure in plane Couette flow. *Proc. ASCE, J. Eng. Mech. Div.* **96** (EM6), 1171–1182.

Automated pattern eduction from turbulent flow diagnostics

By Derek Stretch

The development of an automated technique for the eduction of 3-D spatial patterns in vector or scalar diagnostics has been completed. The method is based on an iterative convolution between a trial pattern and the data field. It has been applied to the analysis of low Reynolds number turbulent channel flow and homogeneous shear flow. The results have yielded new information on the dominant flow structures in these flows, particularly with respect to the spatial relationships between various forms of organized motion. A particular application of the pattern eduction method, which we tentatively refer to as an "adaptive wavelet transformation", is proposed with the objective of investigating the way turbulence structure changes with scale. Preliminary results using data from homogeneous turbulent shear flow simulations are presented. At the low Reynolds numbers of the simulations, there is no evidence of scale similarity. The small scales appear to be associated with the edges of the larger scale vortical structures.

1. Objectives

A notable consequence of the recent application of powerful computers to the simulation of turbulent flows is the vast amount of data which has, and continues to be, generated. Reliable automated diagnostic tools are needed to assist in interrogating these data bases.

The pattern analysis technique developed in the present study is a simple and flexible diagnostic tool for the analysis of complex data fields. The procedure is an extension of that developed by Townsend (1979) and Mumford (1982) (see also Ferre and Giralt , 1989a,b). It is based on an iterative convolution between the data and a reference pattern. Details of our implementation are given elsewhere (Stretch, 1989 ; Stretch, Kim and Britter, 1990). Each iteration of the procedure yields an ensemble-averaged pattern which has an improved mean cross-correlation with the instantaneous patterns in the data. Major inputs required for each pattern analysis are the choice of flow diagnostic, the scale of the patterns, and the choice of pattern used to initialize the iterations.

In broad terms, the basic objective of the pattern eduction approach is to educe statistically significant spatial organization(s) of specified flow diagnostic(s). The terminology "statistically significant" is meant to imply that the patterns occur frequently, relative to other possible spatial organizations of the diagnostic in question.

Some of the issues which we wished to address using this diagnostic tool were as follows. Firstly, what are the structures educed by this method for turbulent channel flow, and how do they relate to results obtained previously using conditional sampling (stochastic estimation), orthogonal decomposition, and flow visualization?

How are the various turbulence structures which have been reported spatially related to one another? How "coherent" are the turbulence structures? That is, given a representation of a structure, such as an ensemble average, how much variation from this representation is typical for the actual instantaneous realizations? What is the dynamical relevance of the organized structures in terms of their contribution to the turbulence kinetic energy, average Reynolds stress, and dissipation? What can we say about the temporal evolution of the organized motions? What mechanism(s) is responsible for their origin, and what are characteristic time scales for their evolution? How do the characteristic turbulence structures change with scale? At high enough Reynolds number, conventional wisdom suggests a regime at large scales where the structures would reflect the large scale non-homogeneities of the flow, followed at smaller scales by an inertial range of self-similar (possibly isotropic) eddies and finally by a distinct dissipation range of structures. Of particular interest in this context is some knowledge of how the structures at different scales are spatially organized with respect to one another. This information may assist us in understanding how energy is transferred between scales in turbulence. Since the present methodology deals with eddies in their physical space representation rather than a spectral (Fourier) representation, the interpretation of inter-scale interactions and energy transfer may be simpler.

2. Outline of the pattern eduction method

Consider a turbulent flow which is sampled at time t by some chosen diagnostic field $\mathbf{D}(\mathbf{x}, t)$. The field $\mathbf{D}$ may be a scalar or vector valued function of the position vector $\mathbf{x}$. It need not represent a complete description of the flow, nor need it comprise the basic primitive dependant variables of velocity and pressure. For example, the field $\mathbf{D}$ may simply comprise one or more components of the velocity or vorticity vectors. Alternatively $\mathbf{D}$ may be a binary function reflecting a zonal or topological classification of the flow such as proposed by Hunt and Wray (1989), and Chong, Perry and Cantwell (1990).

Now we shall suppose that the field $\mathbf{D}$ comprises a set of discrete organized structures or eddies $\mathbf{E}_p(\mathbf{x} - \mathbf{x}_p)$, $p = 1, 2, \ldots m$, sprinkled in space and centered around reference positions $\mathbf{x}_p$. Note that by definition we expect $\mathbf{E}_p$ to have locality in space (compact spatial support) so that $\mathbf{E}_p(\mathbf{x} - \mathbf{x}_p) \to 0$ for $|\mathbf{x} - \mathbf{x}_p|/l \gg 1$ where l is a characteristic length scale of the eddy. While in general there could be a distinct independent eddy structure $\mathbf{E}_p$ at each position $\mathbf{x}_p$, we shall suppose for simplicity that each of the eddies may be described by a suitable transformation of a single basic eddy function $\mathbf{E}(\mathbf{x})$. In general, the possible transformations could include translation, rotation, and changes in the amplitude and length scales (dilation or contraction) of the eddy function $\mathbf{E}$. For the present purposes, we restrict ourselves to translation and amplitude transformations. We shall later address scale changes by a simple extension of the method. In order to locate the eddies embedded in a field of random noise, we require a pattern recognition method which is invariant with respect to changes in the position and amplitude of the patterns and is insensitive to the noise. As discussed elsewhere (e.g. Duda and Hart, 1973), a suitable matching criterion is cross-correlation (or convolution). If one had prior knowledge

of **E**, then simply carrying out a convolution between **D** and **E** should yield local maxima at the pattern locations $\mathbf{x}_p$. In the present context, however, we are primarily concerned with a situation where we do not have *a priori* information on the characteristic eddy or eddies. This issue is resolved by using an iterative application of convolution. At each iteration, the function **E** is updated by an ensemble average of the data centered around the local maxima at $\mathbf{x}_p$. The iterative convolution procedure must, however, be initialized, and several different approaches have been tested (see Stretch, 1989) with qualitatively consistent results obtained for all cases. For the results presented in this report, randomly selected samples from the data field **D** were used to initialize **E**. The random selection was performed using a pseudo random number generator to select a reference position from which a sample was extracted.

3. Application to low Reynolds number turbulent channel flow

The pattern eduction process has been applied to data from numerical simulations of low Reynolds number ($Re_\theta = 287$, $\delta^+ = 180$) turbulent channel flow (Kim, Moin and Moser, 1987). Preliminary results using various scalar diagnostics are reported in Stretch (1989). The outcome of an extensive series of analyses using a number of different diagnostics is summarized schematically in figure 1. More detailed quantitative results are given later.

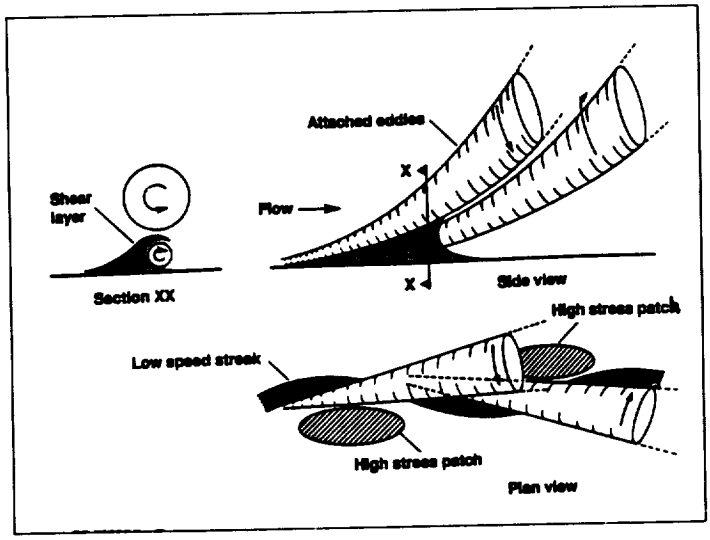

FIGURE 1. Sketch of the pattern educed for turbulent channel flow.

The ensemble-averaged structure educed from the data comprises attached eddies spanning most of the channel half-width. Attached eddies of this type have been proposed by Townsend (1976) and others. Note, however, that our results suggest that the primary pairing (if any) of eddies with opposite sense of rotation (streamwise vorticity) is in the vertical rather than the spanwise direction. In figure 1, we

have indicated how the present results unify a number of structural features which have been previously documented by many investigators. In particular, we find that near wall low (or high) speed streaks, shear layers, quasi-streamwise vortices, and "pockets" of high wall stress are spatially related as indicated in the sketch. These various structural elements are thus viewed as part of the same basic "coherent" structure. Unlike the usual conditional sampling methods, the pattern eduction approach does not rely on point-wise matching of velocity patterns or sampling criteria based on thresholding. It is the similarity in spatial structure as measured by the convolution (or cross-correlation) which is the basis of the pattern eduction. The method is thus well suited to clarifying the spatial relationship between various features of the flow.

The spatial distribution of the patterns in the data as determined by the positions of the local maxima in the convolution between the ensemble average pattern and the raw data is shown in figure 2. In this example, 70 patterns were located, which collectively represents 70% of the data volume. The normalized cross-correlation coefficients between the ensemble-average pattern and the data were computed at each of the positions indicated in figure 2. A histogram of these values is plotted in figure 3. The mean value of the cross-correlations was $\overline{R} = 0.4$.

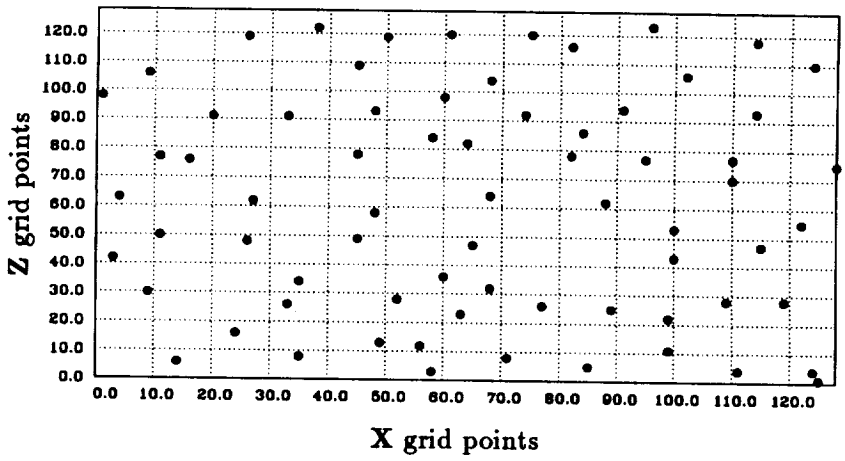

FIGURE 2. Spatial distribution of the detected patterns.

The cross-correlation coefficients provide a useful objective measure of the meaning of the word "coherent" in reference to the educed turbulence structure. We shall, therefore, further clarify what the observed cross-correlations imply by giving examples of the actual instantaneous patterns detected in the data. Figure 4 shows an series of zy plane views of the ensemble averaged pattern educed using the spanwise velocity component as the diagnostic. These results are qualitatively representative of those obtained using various flow diagnostics.

It can be seen that the basic elements of the ensemble averaged structure are attached eddies spanning the channel half-width, with two eddies (or vortices) with

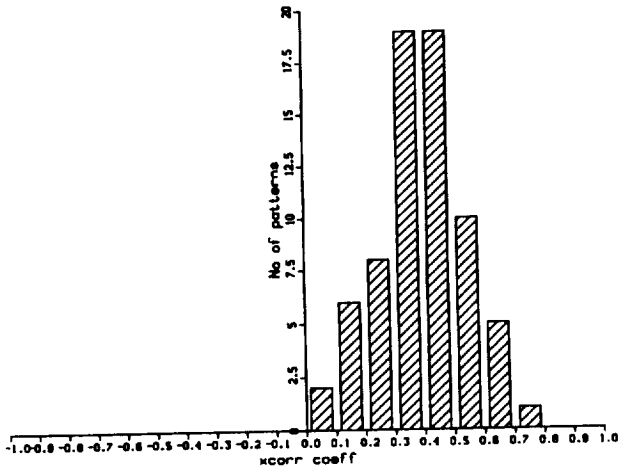

FIGURE 3. Histogram of cross-correlation coefficients.

opposite sense of rotation arranged one above the other as was depicted in figure 1. Also shown in figure 4 are two examples of "instantaneous" patterns as they were located in the data: these patterns produced local maxima in the convolution between the ensemble averaged pattern and the data. The magnitude of the cross correlation was 0.4 in the one case and 0.7 in the other. These examples were selected in order to represent a typical case as well as a special case where the correlation was unusually high. It is clear from these examples that a correlation coefficient of 0.7, while a rare occurrence, implies a strong similarity between the instantaneous patterns and the ensemble average. On the other hand, it appears that about half the located patterns (as defined by the detection of a local maxima in the convolution regardless of the magnitude of the maxima) which have cross-correlations less than 0.4, do not strongly resemble the ensemble average. It would be useful if objective measures such as these cross-correlations were more widely reported in discussions of conditionally sampled data. Clearly, they suggest that a good measure of caution is appropriate in using a single ensemble averaged result to characterize the flow structure, even at the low Reynolds number of the flow considered here.

Some further details of the educed patterns are shown in figures 5 and 6. The attached eddies have a characteristic spanwise velocity signature in the xy plane (fig 5), comprising elongated positive and negative (paired) regions extending from the wall to the outer part of the flow. Examples of this pattern are common in the instantaneous spanwise velocity field, as already noted in Stretch (1989). The characteristic inclination angle between the attached eddies and the wall can be deduced from figure 5: it increases from zero near the wall to about 40 degrees in the outer part of the flow.

The streamwise velocity fluctuations in an xz plane near the wall ($y^+ = 10$)

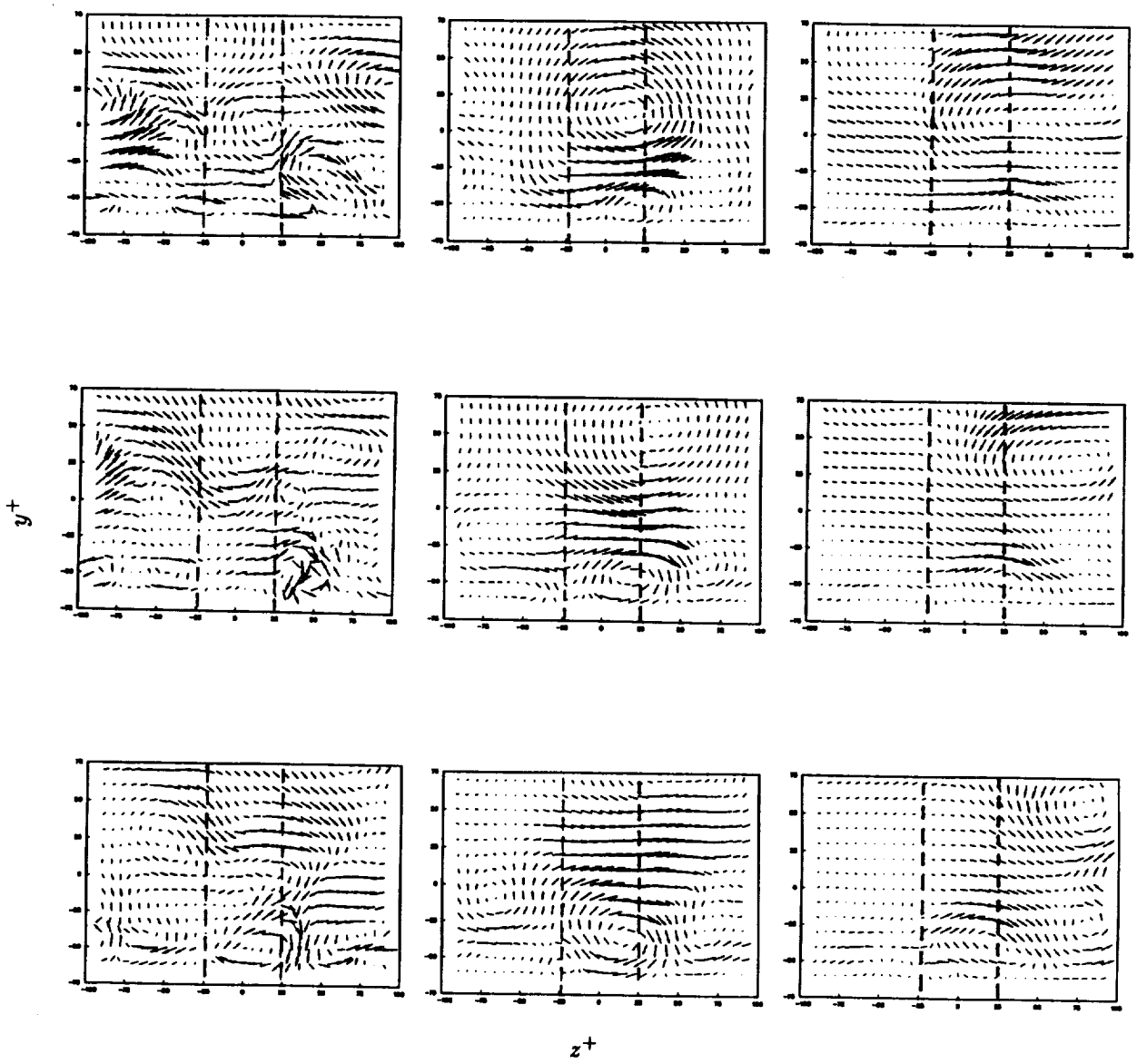

FIGURE 4. Example of the educed ensemble average pattern (center) shown as velocity vectors projected onto zy planes ($\Delta z^+ = 200$, $\Delta y^+ = 150$) at three streamwise locations ($\Delta x^+ = 36$). On the left is a sample of an instantaneous pattern with a cross-correlation of 0.4, and on the right a sample with a correlation of 0.7. Note that only the regions delineated by the dashed lines were used for the pattern matching.

are shown in figure 6(a) and in an xy plane in figure 6(b). Near the wall, as expected, the educed pattern in the streamwise velocity field comprises low and high speed "streaks" (fig 6a). There is a lateral asymmetry (spanwise kinking)

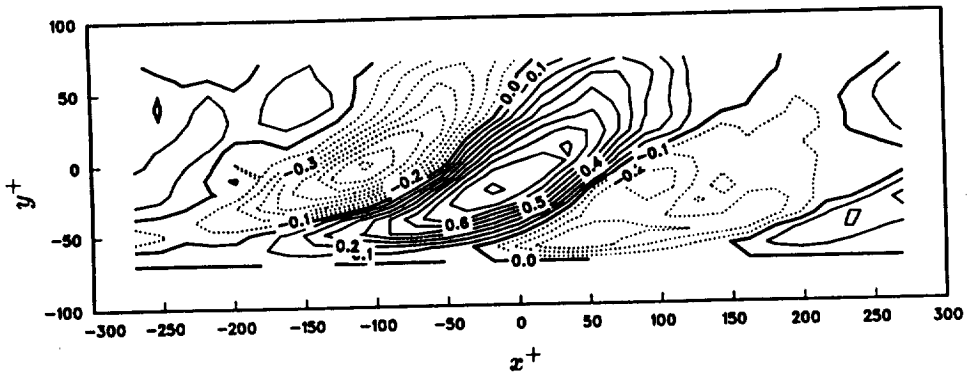

FIGURE 5. Spanwise velocity signature of the educed structure.

associated with the streaks, and this in turn is associated with a protruding shear layer structure (fig 6b) which is typical of those obtained from previous conditional sampling analyses. The attached eddies, which near the wall are quasi-streamwise vortices, have a characteristic stress signature at the wall comprising a small scale ($\triangle x^+ \simeq 150$, $\triangle z^+ \simeq 50$) region of high stress embedded within the more elongated high speed streaks (fig 6a). This result indicates that the surface stress can be a useful diagnostic for detecting the vortical structures nonintrusively by means of their stress "footprints" at the wall. This observation could form the basis for an active control strategy aimed at reducing the surface stress by modifying the vortical structures.

There is an interesting question concerning the contribution of the educed patterns to the flow kinematics. It is possible to use the pattern eduction procedure to decompose the flow into a deterministic contribution from the eddies **E** and a random "disorganized" background field. This can be achieved by performing a deconvolution of the data **D** with the educed eddy **E** and simply setting all contributions to zero except at the pattern locations $\mathbf{x}_p$. Subsequent convolution of this truncated field with the eddy function **E** will produce a new data field comprising only translation and amplitude transformations of the eddy function **E**. The turbulence statistics of this eddy field may then be computed and compared with that of the original data. Horizontally averaged second order statistics for a single educed eddy function **E** are shown in figure 7 and compared with the turbulence statistics for the full data field **D**. It is apparent from these results that a random superposition of the educed eddies can indeed produce a velocity field with at least second order statistics which reasonably approximate those of the original data.

The pattern analysis procedure has proven to be helpful in extracting kinematical information from the turbulent flow fields. Our ultimate objective, however, is to understand the detailed dynamics of the flow. Firstly, we would like to establish the dynamical relevance of the educed flow structures by assessing their contribution to turbulence production and dissipation processes. This has been done by computing ensemble averages, centered around the pattern locations, of the instantaneous Reynolds stress and dissipation fields. For example, second and fourth quadrant

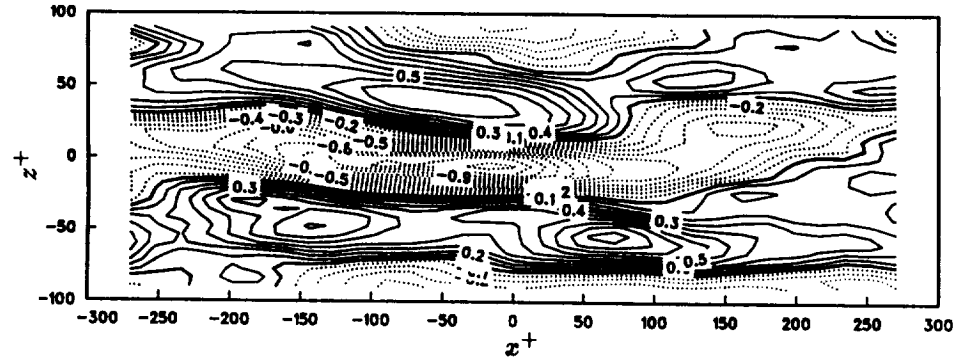

(a)

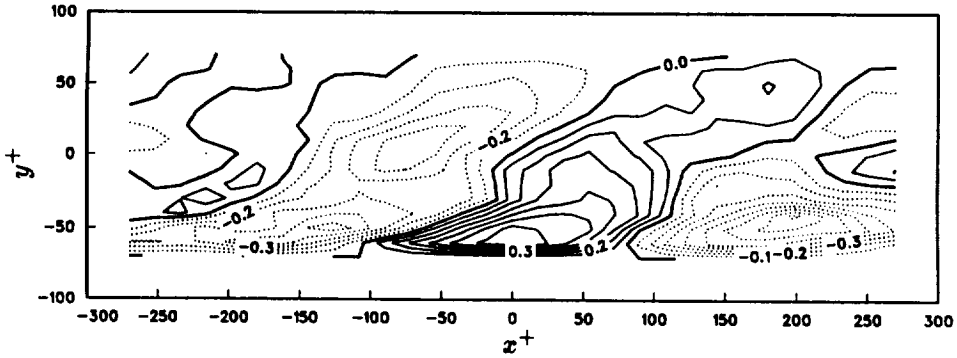

(b)

FIGURE 6. Streamwise velocity signature of the educed structure in (a) xz plane at $y^+ = 10$ and (b) xy plane.

Reynolds stress events, both with positive contributions to the average production of turbulent kinetic energy, are located around the sides of the attached eddies (refer fig 4). Most (in excess of 70%) of the turbulence production is associated with the located patterns, but note that the precise proportion depends on the particular pattern size used. For accurate assessment, it may be desirable to use a more constrained definition for the occurrence of the structures. For example, a threshold could be used for the cross-correlation coefficient.

A second important issue concerning the flow dynamics is the temporal evolution of the educed structures. It is illuminating to start by estimating some of the time scales involved. Focussing on the near-wall region, we shall consider three time scales for the evolution of the attached eddies: an advection time scale (T_a) characterizing the effect of the mean flow, a rotation time scale (T_r) characterizing the angular velocity of the fluid elements in a plane perpendicular to the axis of the eddy, and a viscous decay time scale (T_d) in a Lagrangian frame of reference moving with the eddies. Estimates of these time scales can be obtained from the ensemble average fields yielded by the pattern analysis. We estimate (Stretch *et al.*, 1990) that near the wall $T_a^+ \simeq 20$, $T_r^+ \simeq 60$, and $T_d^+ \simeq 200$. Since T_d is an order of

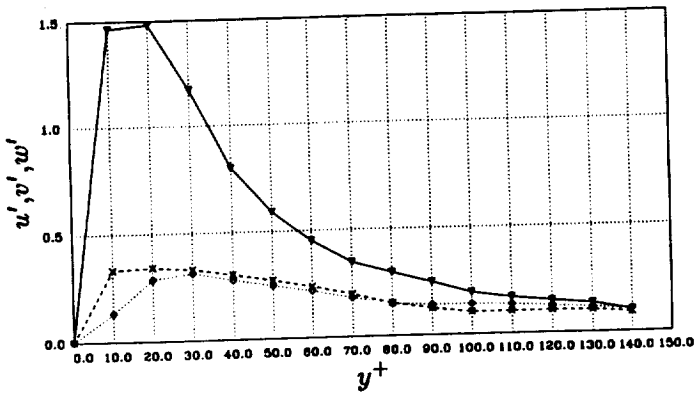

(a)

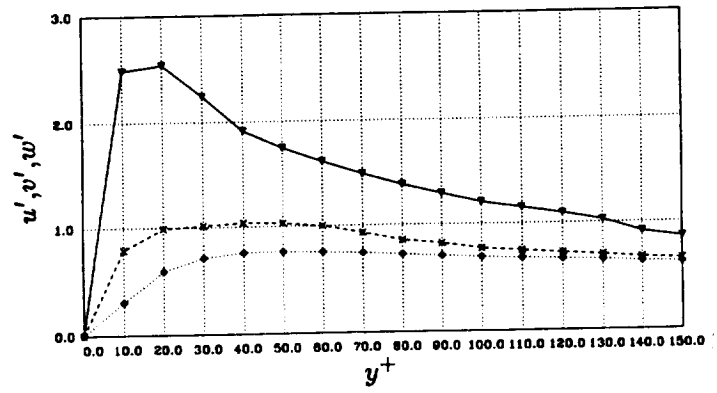

(b)

FIGURE 7. Horizontally averaged second order velocity statistics for the educed structure (a) compared with the statistics for the full flow field (b): ∇ , u'; $\diamond$, v'; $\times$, w'.

magnitude larger than T_a, the structures are essentially advected unchanged. The vorticity associated with the eddies, as characterized by T_r, is expected to give rise to a weak spiralling motion for the fluid elements. Note also that many cycles of rotation are not expected in general, an observation which is consistent with flow visualization experiments (Stretch and Britter, 1990).

The dynamical mechanism(s) responsible for the origin of the observed structures remains a key unresolved issue. Any proposed mechanism(s) must be capable of explaining the observed structures, but it should also be self-sustaining. Research on this issue is currently underway at the Center for Turbulence Research.

4. Application to homogeneous turbulent shear flow

The pattern eduction procedure has also been applied to data from direct numerical simulations of homogeneous turbulent shear flow (Rogers and Moin, 1987). Some results of the analysis where the pattern matching was done for the vertical

and spanwise velocity components are shown in figure 8. The zy plane view of the velocity vectors reveals a pair of vortices arranged one above the other, as for the channel flow results. The contours of the spanwise velocity in a xy plane at the center of the pattern show the characteristic inclined, paired features which are a signature of inclined roller eddies. Further investigation of the spatial configuration of the vortical structures has, however, indicated that in this case, there may not be a strong preference for pairing in a particular arrangement e.g. vertically as opposed to horizontally. The results in figure 8 are thus partly an artifact of the ensemble averaging process. In fact, single unpaired vortices may be the most common occurrence, although this remains unclear at this point.

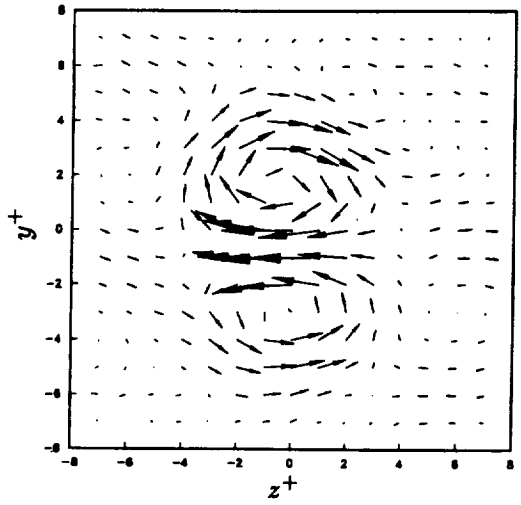

(a)

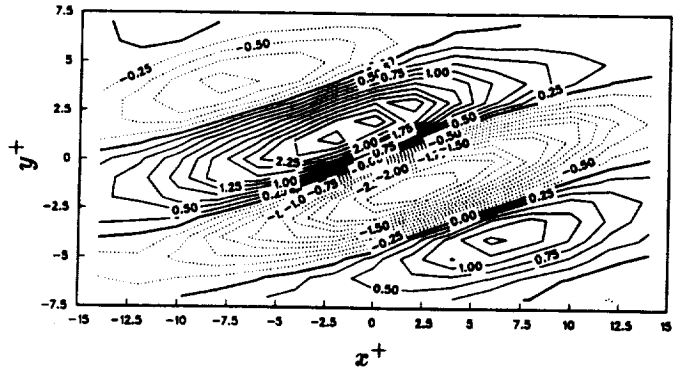

(b)

FIGURE 8. Pattern educed from homogeneous sheared turbulence: (a) velocity vectors projected onto the zy plane at $x = 0$, (b) Contours of the spanwise velocity component in a xy plane at $z = 0$.

5. Application as an adaptive wavelet transform

It is apparent that the pattern analysis procedure developed in this study has much in common with the so-called "wavelet transform" (see e.g. Meneveau, 1989 for a brief review). Each iteration of the pattern analysis can be viewed as a generalized form of wavelet transform at a particular scale, with the current ensemble averaged pattern as the wavelet. This is an attractive choice of wavelet since it represents actual eddies in the flow rather than being an arbitrarily chosen mathematical function. The iterations now have the interpretation of maximizing the locality of the wavelet energy by using the local maxima in the convolution as reference positions for updating the wavelet (using an ensemble average of the data around those positions).

In addition to information on the spatial distribution of the wavelet energy, wavelet transforms have been used to provide information on the way energy is distributed between different scales. This is achieved by successive dilation (or contraction) of the wavelet function between successive convolutions. A similar strategy could, of course, be adopted in the present context using an educed eddy pattern as the wavelet and doing repeated convolutions for different dilations or contractions of this pattern. However, there is no *a priori* reason to assume that the pattern educed at a given scale would also be obtained by applying the eduction procedure at different (say smaller) scales. Note that the scale of the pattern is naturally set by the specification of the size of the pattern domain and, hence, the spatial support of the function (which is set to zero beyond this domain for doing the convolution). In fact, it seems natural to allow the iterative pattern selection procedure to educe a structure at different scales. Then the issue of scale similarity can be explicitly tested, since we have allowed our wavelet to adapt to the scales being analyzed. From the above it is clear why the terminology "adaptive wavelet transform" is an appropriate description of this procedure.

Some preliminary results from application of this idea to the homogeneous turbulent shear flow data have been obtained and are shown in figure 9. These may be compared with the results presented in figure 8. It is apparent that at small scales, the educed pattern comprises a jet/shear-layer. The orientation of the jet is partly determined by the initial conditions for the pattern iterations, which in this case was a random selection from the data. The important feature of this result, however, is that if the velocity field is averaged in an extended region around the located patterns, we see that the small scale jets/shear-layers are simply a part of the larger scale vortices which were previously educed by the analysis. Therefore, in this case, there is no scale similarity which emerges from the analysis procedure, which is not surprising considering the low Reynolds number of the simulation. It would certainly be interesting to apply this method to much higher Reynolds number flows to see if a cascade of geometrically similar eddies does emerge from the analysis. Development and testing of the "adaptive wavelet transform" is still underway, including investigation of issues such as normalization procedures for the educed wavelets/eddies.

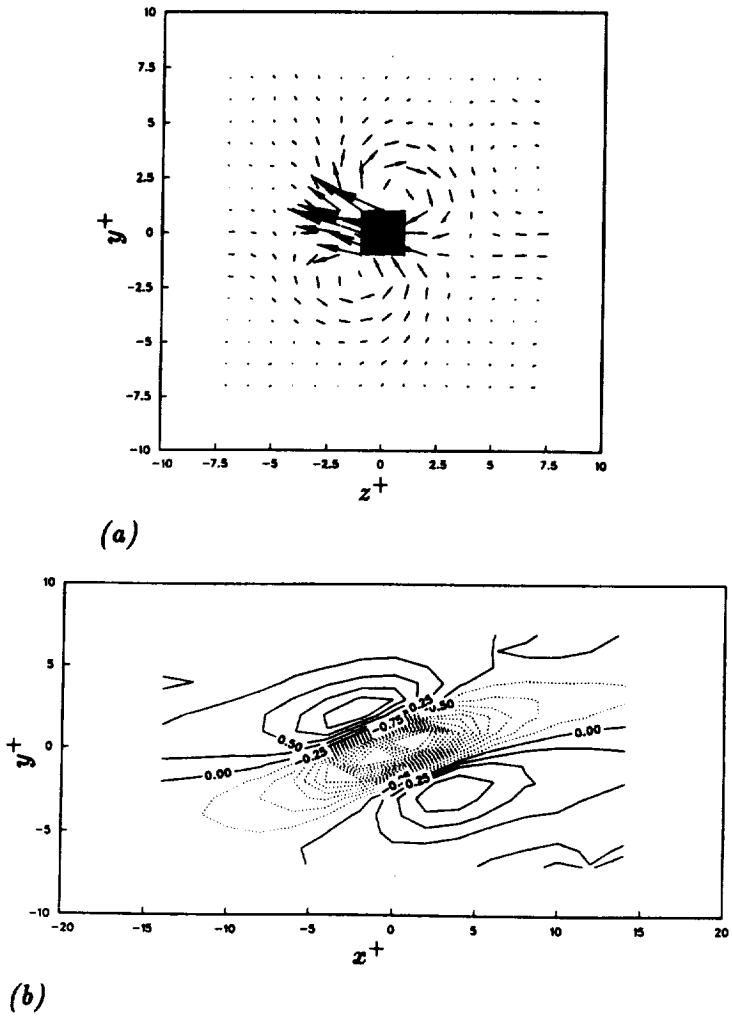

FIGURE 9. The eddy pattern educed from applying the "adaptive wavelet" method to homogeneous turbulent shear flow. The flow pattern shown was educed using the v and w velocity components on the scale of the shaded region : (a) velocity vectors projected onto the zy plane at $x = 0$, (b) Contours of the spanwise velocity component in an xy plane at $z = 0$.

6. Summary

The diagnostic tool which has been developed in this study is conceptually simple and yet provides a flexible means of interrogating complex data fields with the purpose of extracting spatial organization of relevant diagnostics. It is implemented using efficient spectral methods and is thus cheap computationally (all the analysis in this study was done interactively on a VAX). While we have not yet discovered any "new" structures using this approach, it has clarified the spatial relationship

between various features of the turbulence and thus presented a unified view of the turbulence structure. Furthermore, we have used the method to quantify the "coherency" of the structures as they occur in the flow by using a cross-correlation measure. We have proposed an extension of the method (or more particularly, in the way the method is used) which we refer to as an "adaptive wavelet transform" that can be used to examine issues of scale similarity, which is a widely used concept in turbulence. This approach has potential for studying (in physical rather than Fourier space) the way eddies or structures of different scales interact.

REFERENCES

FERRE, J. A. & GIRALT, F. 1989a Pattern-recognition analysis of the velocity field in plane turbulent wakes. *J. Fluid Mech.* **198**, 27-64.

FERRE, J. A. & GIRALT, F. 1989b Some topological features of the entrainment process in a heated turbulent wake. *J. Fluid Mech.* **198**, 65-78.

KIM, J., MOIN, P. & MOSER, R. 1987 Turbulence statistics in fully developed channel flow at low Reynolds number. *J. Fluid Mech.* **177**, 133-166.

MENEVEAU, C. 1989 Turbulence dynamics in the wavelet representation. *Annual Research Briefs - 1989. Center for Turbulence Research, Stanford, CA 94305-3030.*

MUMFORD, J. C. 1982 The structure of the large eddies in fully developed turbulent shear flows. Part 1. The plane jet. *J. Fluid Mech.* **118**, 241-268.

ROGERS, M. M. & MOIN, P. 1987 The structure of the vorticity field in homogeneous turbulent flows.. *J. Fluid Mech.* **176**, 33-66.

STRETCH, D. D. 1989 Patterns in Simulated Turbulent Channel Flow. *Annual Research Briefs - 1989. Center for Turbulence Research, Stanford, CA 94305-3030.*

STRETCH, D. D., KIM, J. & BRITTER, R. E. 1990 Patterns in Simulated Turbulent Channel Flow. *Unpublished manuscript to be submitted.*

STRETCH, D. D. & BRITTER, R. E. 1990 Surface stress patterns in wall- bounded turbulence. *Unpublished manuscript to be submitted.*

TOWNSEND, A. A. 1976 *The Structure of Turbulent Shear Flows.* C.U.P.

TOWNSEND, A. A. 1979 Flow patterns of large eddies in a wake and in a boundary layer. *J. Fluid Mech.* **95**, 515-537.

On the origin of the streak spacing in turbulent shear flows

By Fabian Waleffe

It is shown that the ideas of *selective amplification* and *direct resonance*, based on linear theory, can not provide an explanation for the well-defined streak spacing of about 100 wall units (referred to as 100^+ hereafter) in wall-bounded turbulent shear flows. In addition, for the direct resonance theory, the streaks are created by the non-linear self-interaction of the vertical velocity rather than of the *directly forced* vertical vorticity. In view of the failure of these approaches, it is then proposed that the selection mechanism must be inherently non-linear and correspond to a *self-sustaining* mechanism. The 100+ value should thus be considered as a critical Reynolds number for that mechanism. Indeed, in the case of Poiseuille flow, this 100+ criterion for transition to turbulence corresponds to the usually quoted value of 1000 based on the half-width and the centerline velocity. In Couette flow, it corresponds to a critical Reynolds number of about 400 based on the half width and half velocity difference.

1. Motivation and objectives

An intriguing feature of wall-bounded turbulent shear flows is the existence of bands of low- and high-speed fluid, elongated in the streamwise direction and with a very consistent spanwise spacing of about one hundred wall units, i.e. $100\nu/u_*$ where $u_* = (\nu dU/dy)^{1/2}$ is the friction velocity. In addition, those streaks appear to initiate a localized instability referred to as a "burst". That localized instability would be the mechanism by which momentum is exchanged between the wall and the outer fluid, thus sustaining the turbulent flow (Kline *et al.* 1967, Kim *et al.* 1971).

The goal of this project, performed in collaboration with John Kim, is to try to understand the mechanisms which lead to the creation and destruction of the streaks. We believe that those mechanisms are the key to understanding why and how a flow ceases to be laminar and maintains a turbulent state. Our approach was to first review and test some ideas which had been proposed in the literature for the origin of the streaks. If these theories were successful, our objective was then to extend them so as to explain the bursting and regeneration processes.

2. Work accomplished

2.1. RDT and selective amplification

A number of papers (e.g. Lee *et al.* 1990) show that the mechanism for streak generation is linear. The argument is that in the near wall-region the time scale for the mean $(d\bar{u}/dy)^{-1}$ is much shorter than the time scale for the non-linear effects,

measured by q^2/ϵ where q is a turbulent velocity scale and ϵ is the dissipation rate. The evolution is then dictated by linear equations, and streaks are created from the redistribution of the downstream momentum by vertical and spanwise motions. The mechanism is a simple advection and is most efficient when the fluctuating fields are elongated downstream. The question here is to determine whether the linear mechanism favors spanwise scales of about 100^+. The mathematical description of the mechanism is briefly stated in the next few paragraphs.

The governing equations for the fluctuating field, obtained by eliminating pressure and the continuity constraint, are:

$$(\frac{\partial}{\partial t} + \bar{u}\frac{\partial}{\partial x} - \frac{1}{R}\nabla^2)\nabla^2 v - \frac{d^2\bar{u}}{dy^2}\frac{\partial}{\partial x}v = NL_v \tag{1}$$

$$(\frac{\partial}{\partial t} + \bar{u}\frac{\partial}{\partial x} - \frac{1}{R}\nabla^2)\eta + \frac{d\bar{u}}{dy}\frac{\partial}{\partial z}v = NL_\eta \tag{2}$$

where v and η denote respectively the y-component of velocity and vorticity, and $\bar{u}$ is the mean velocity. The right-hand sides, NL_v, NL_η, represent non-linear terms. Flows in a channel will be considered in this paper (plane Poiseuille or plane Couette flow) with the boundary conditions $v = \partial v/\partial y = \eta = 0$ at the walls, located at $y = \pm 1$.

In the linear case, the equation for v is homogeneous and admits eigensolutions of the form:

$$v = \hat{v}(y)e^{i(\alpha x+\beta z-\omega t)} \tag{3}$$

where $\hat{v}(y)$ satisfies the *Orr-Sommerfeld* equation. In general, for a turbulent mean profile, all of these eigensolutions are decaying. The η-equation, on the other hand, is non-homogeneous for v fluctuations with a spanwise variation. When forced by an eigenmode of the v equation, the linear response of the vertical vorticity has the form:

$$\eta = \eta(y,t)e^{i(\alpha x+\beta z)} \tag{4}$$

with $\eta(y,t)$ given by:

$$\eta(y,t) = \beta\sum_n \lambda_n \frac{e^{-i\omega t} - e^{-i\mu_n t}}{\omega - \mu_n}\eta_n(y) \tag{5}$$

Where

$$\lambda_n = \frac{\int \bar{u}'\hat{v}\,\eta_n\,dy}{\int \eta_n\eta_n dy} \tag{6}$$

and $\eta_n(y)$, μ_n represent the eigenmodes and eigenvalues of the homogeneous η-equation. Note that the vertical vorticity response corresponds to streaks, as opposed to vortices.

When the OS eigenvalue ω is close to the Squire eigenvalue μ_n, the n-th coefficient will behave as $t\exp(-i\mu_n t)$. This corresponds to an algebraic growth followed by exponential decay as μ_n corresponds to a viscously decaying mode. For a significant

algebraic growth to occur, the real parts of ω and μ must be sufficiently close otherwise the modes will decorrelate, and the viscous damping must be small. Thus one expects and verifies numerically that the largest responses occur for downstream modes ($\alpha = 0$) for which the real parts of the eigenvalues vanish (downstream modes are not advected) and the decay rate is inversely proportional to the Reynolds number. In fact the, eigenvalue problems can be solved analytically in that case, and one finds (with $n > 0$)

- even modes:

$$\eta_{2n-1}(y) = \cos(2n-1)\frac{\pi}{2}y \qquad \mu_{2n-1} = -\frac{\beta^2 + (2n-1)^2\pi^2/4}{R}$$

$$v_{2n-1}(y) = (\cosh\beta\cos p_n y - \cos p_n \cosh\beta y) \qquad \omega_{2n-1} = -\frac{\beta^2 + p_n^2}{R}$$

- odd modes:

$$\eta_{2n}(y) = \sin n\pi y \qquad \mu_{2n} = -\frac{\beta^2 + n^2\pi^2}{R}$$

$$v_{2n}(y) = (\sinh\beta\sin q_n y - \sin q_n \sin h\beta y) \qquad \omega_{2n} = -\frac{\beta^2 + q_n^2}{R}$$

where p_n and q_n are the solutions of:

$$p_n \tan p_n = -\beta\tanh\beta$$
$$\beta\tan q_n = q_n\tanh\beta$$

and obey the ordering:

$$(2n-1)\pi/2 < p_n < n\pi < q_n < (2n+1)\pi/2$$

In the inviscid case, the streaks appear to grow indefinitely with time. However, the *exact* equation for the downstream velocity u is:

$$\frac{\partial}{\partial t}u + v\frac{\partial}{\partial y}u + w\frac{\partial}{\partial z}u = -\frac{\partial}{\partial x}P$$

where $\partial P/\partial x$ is a constant. This equation is linear, as v and w decouple, and expresses an advection of the momentum by the cross-stream flow. The term $v\partial u/\partial y$ creates the linear growth described above, creating $\partial u/\partial z$ which then limits the process through the term $w\partial u/\partial z$ which is considered "non-linear" in the preceding analysis. If ϵ is a measure of the amplitude of the cross stream flow (v, w), the "non-linear" saturation of the algebraic growth occurs on a time scale $O(\epsilon^{-1})$, the time scale for advection by the cross flow. It is faster than the usual ϵ^{-2}, characteristic of non-linear interactions.

The possibility of a scale selection by the linear mechanism was investigated numerically by introducing a downstream OS mode, normalized so that the maximum

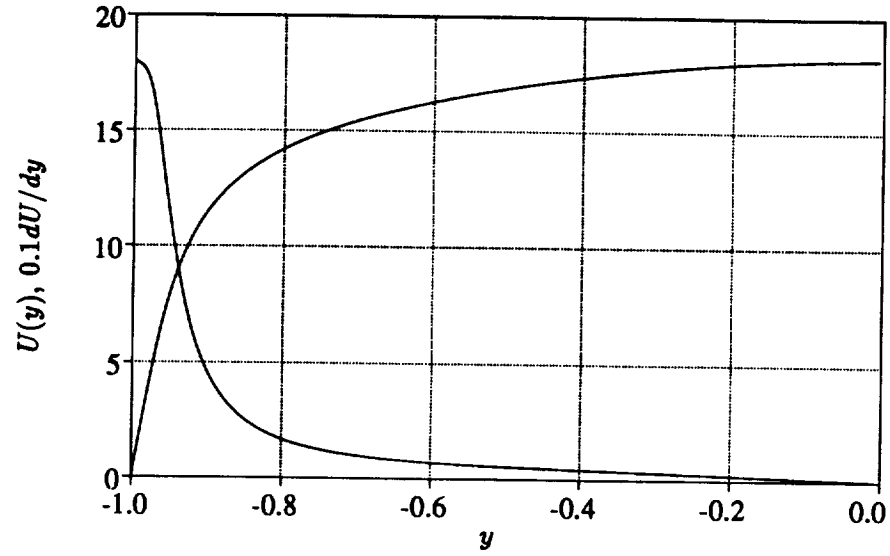

FIGURE 1. Mean profile and mean shear.

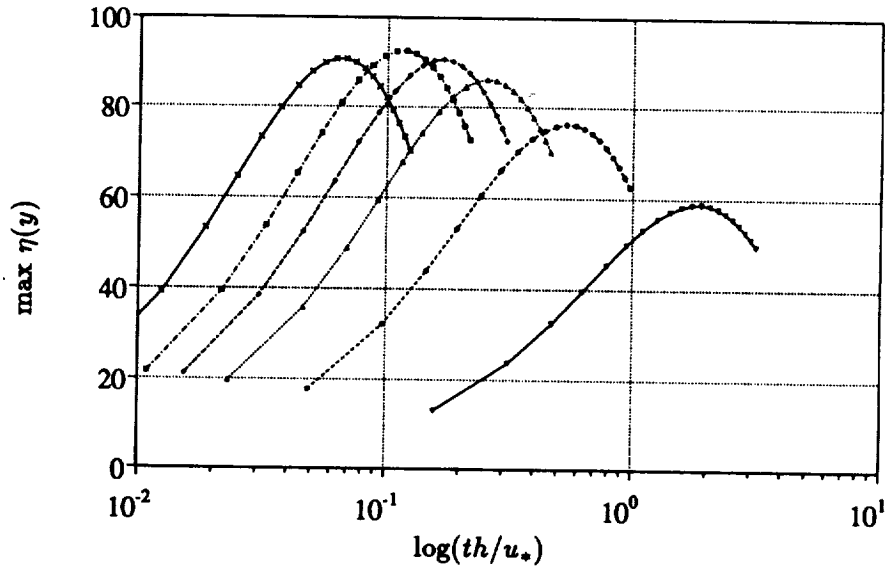

FIGURE 2. Maximum pointwise vertical vorticity response to a single downstream even OS mode. ∇ : $\lambda_z^+ = 188$; $\bullet$: $\lambda_z^+ = 94$; $\triangle$: $\lambda_z^+ = 63$; $\diamond$: $\lambda_z^+ = 47$; $\square$: $\lambda_z^+ = 38$; $\times$: $\lambda_z^+ = 27$.

vertical velocity is unity, onto a turbulent mean profile with $R_\tau = 180$. The mean velocity profile was chosen as a Reynolds-Tiederman profile, defined by :

$$\frac{d\bar{u}}{dy} = -\frac{Ry}{(1+\nu_t)}$$

$$\nu_t = \frac{1}{2}\{1 + [\frac{1}{3}KR(1-y^2)(1+2y^2)(1-\exp((1+y)R/A))]^2\}^{1/2} - \frac{1}{2}$$

where K and A were chosen respectively as 0.525 and 37. The mean profile and mean shear are shown in fig. 1.

The forced responses of the vertical vorticity are shown in fig. 2. It can be seen that there is a peak around $\lambda_z^+ = 35$, but it is too weak to represent a significant selection. The streamwise fluctuating velocity responses would be obtained by multiplying the vorticity by the wavelength, and the largest response would correspond to the largest wavelength. This does not match the experimental observations which show a scale selection both in the velocity and vorticity spectra. In any case, the "peak" does not correspond to the typical value for the streak spacing, which is between 80^+ and 100^+. We must conclude that the linear mechanism does not provide a scale selection.

2.2. Direct resonance theory

In the direct resonance scenario, streaks originate from a three-step process (Benney and Gustavsson 1981, Jang *et al.* 1986). The first step is linear and consists of the resonant forcing of the vertical vorticity by the velocity, exactly as in the previous section, but focuses on oblique disturbances for which the non-linear effects can be less trivial. The second step is the non-linear interaction of the vorticity with its mirror image across a vertical downstream plane. This would create downstream vortices which, finally, give rise to the streaks. That sequence of interaction is illustrated by the following diagram.

$$\begin{aligned} \epsilon v(\alpha, \pm\beta) &\longrightarrow \epsilon t\, \eta(\alpha, \pm\beta) \\ \eta\eta^* &\longrightarrow v(0, 2\beta) \\ v(0, 2\beta) &\longrightarrow \eta(0, 2\beta) \end{aligned}$$

A non-linear theory was developed in (Benney and Gustavsson 1981) and applied to turbulent boundary layers in (Jang *et al.* 1986). Using a turbulent boundary layer profile, Jang *et al.* found that an OS eigenvalue coincides with a "Squire" eigenvalue (a *direct resonance*) for the horizontal wavenumbers: $\alpha^+ = 0.0093$ and $\beta^+ = 0.035$. The common eigenvalue is equal to $\omega^+ = 0.090 - i\,0.037$. They showed that the interaction of that mode with its spanwise reflexion induces streamwise vortices with a spanwise wavelength around $\pi/\beta^+ \simeq 90^+$.

One problem with the direct resonance concept is that it must assume not only that the eigenvalues of the two linear homogeneous operators are close, but also that the damping rates are small. Otherwise, as discussed above, the algebraic growth will be quickly shut off by the exponential viscous decay. Another problem

comes from multiple resonances or near-resonances. There is no *a priori* criterion for which one should prevail.

Here, the direct resonance route to streaks is followed in the case of a turbulent channel flow obtained numerically (Kim *et al.* 1987). The Reynolds number is about 180, based on the half-width and the friction velocity. A near direct resonance is found for :

$$\alpha^+ \simeq 0.005 \quad \beta^+ \simeq 0.039$$

the eigenvalues being:

$$\omega_{14}^+ = 0.07871485 - i\,0.02168581$$
$$\mu_{15}^+ = 0.07871461 - i\,0.02168558$$

These values are different but quite close to the values reported above for the turbulent boundary layer. The non-linear interaction of the pair of modes $(\alpha, \pm\beta)$ leads to streaks with a spanwise spacing of about 80^+. The vertical vorticity responses are displayed in fig. 3. The initial conditions were such that the maximum v amplitude was 0.1 with no vertical vorticity. As indicated by the subscripts, this direct resonance occurs at the 14th OS mode and the 15th Squire mode, where the modes are ordered according to their decay rate. Although this looks encouraging, the picture is not as sharp when one analyzes other modes.

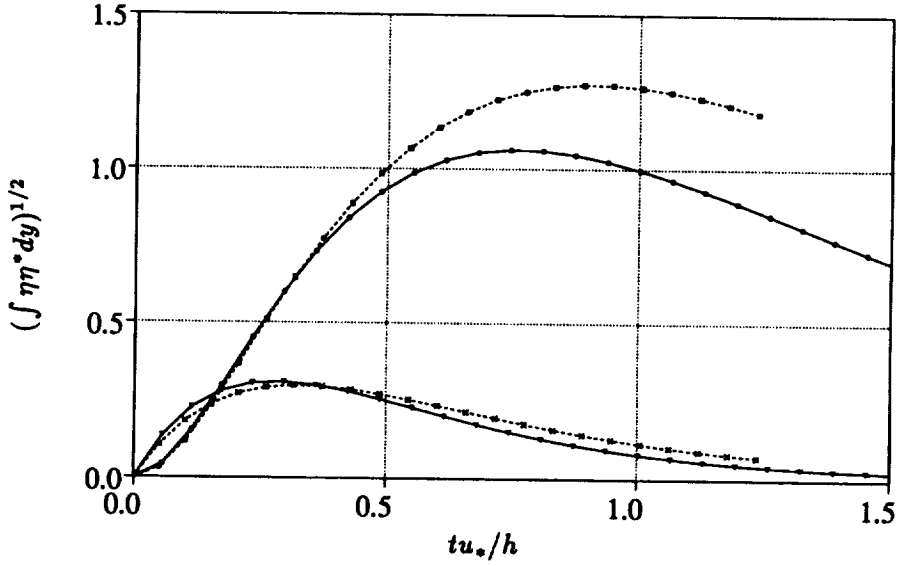

FIGURE 3. Linear (lower curves) and non-linear (upper curves) vertical vorticity response for direct resonance: ▽ : $(\alpha,\beta) = (0.9, 7.07)$ (forced by 14th OS mode); • : $(0, 14.14)$; × : $(0.8, 6)$ (forced by 13th OS mode); □ : $(0, 12)$.

For instance, the linear response obtained from the 13th OS mode for slightly different wavenumbers is very similar to the direct resonance mode, but the non-linear response is even larger (fig. 3.). Something seems very wrong once the

response to the 19th OS mode for $(\alpha,\beta) = (1.6,12)$ has been computed (fig.4.). In that case, the linear response is almost four times larger than the direct resonance one, but the non-linear response is much smaller. One would expect that if the linear response is four times larger than for the direct resonance modes, the non-linear response should be sixteen times larger than in the direct resonance case.

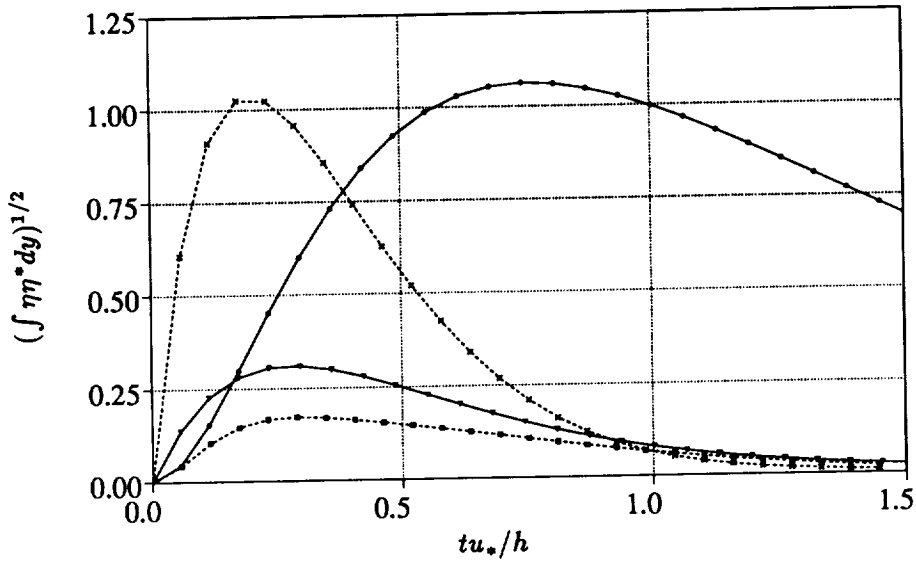

FIGURE 4. Linear and non-linear vertical vorticity response for direct resonance: ∇ : $(\alpha,\beta) = (0.9,7.07)$ (forced by 14th OS mode); $\bullet$: $(0,14.14)$; $\times$: $(1.6,12)$ (forced by 19th OS mode); $\square$: $(0,24)$.

To understand what went wrong, it is necessary to analyze the non-linear interactions. The computations and the theory are started with a pair of oblique rolls such as:

$$v = \cos\beta z\,(v_1(y,t)e^{i\alpha x} + v_1^*(y,t)e^{-i\alpha x})$$

The linear processes then introduce a pair of oblique streaks:

$$\eta = \sin\beta z\,(\eta_1(y,t)e^{i\alpha x} + \eta_1^*(y,t)e^{-i\alpha x})$$

The non-linear effect of primary interest is the generation of streamwise vortices $V(y,t)\cos 2\beta z$. The complete equation for $V(y,t)$ is obtained from (1) with the non-linear forcing provided by the pair of oblique rolls. After some manipulations (see e.g. Benney 1961, Lin and Benney 1962), one finds:

$$[\frac{\partial}{\partial t} - \frac{1}{R}(\frac{\partial^2}{\partial y^2} - 4\beta^2)](\frac{\partial^2}{\partial y^2} - 4\beta^2)\,V =$$

$$\beta(\frac{\partial^2}{\partial y^2} + 4\beta^2)(v_1 w_1^* + v_1^* w_1) + 4\beta^2 \frac{\partial}{\partial y}(v_1 v_1^* + w_1 w_1^*)$$

where w_1 is given in terms of v_1 and η_1 by

$$w_1 = k^{-2}(-\beta\frac{\partial v_1}{\partial y} + i\alpha\eta_1)$$

with $k^2 = \alpha^2 + \beta^2$, so that the right-hand side can be rewritten as the sum of three forcing terms $F_{vv} + F_{v\eta} + F_{\eta\eta}$, where:

$$F_{vv} = 4\frac{\alpha^2\beta^2}{k^2}\frac{\partial}{\partial y}(v_1 v_1^*) + 4\frac{\beta^4}{k^4}\frac{\partial}{\partial y}(\frac{\partial v_1}{\partial y}\frac{\partial v_1^*}{\partial y}) - \frac{\beta^2}{k^2}\frac{\partial^3}{\partial y^3}(v_1 v_1^*)$$

$$F_{v\eta} = \frac{i\alpha\beta}{k^2}[(\frac{\partial^2}{\partial y^2} + 4\beta^2)(\eta_1 v_1^* - \eta_1^* v_1) + \frac{4\beta^2}{k^2}\frac{\partial}{\partial y}(\eta_1^*\frac{\partial}{\partial y}v_1 - \eta_1\frac{\partial}{\partial y}v_1^*)]$$

$$F_{\eta\eta} = \frac{4\alpha^2\beta^2}{k^4}\frac{\partial}{\partial y}(\eta_1\eta_1^*)$$

In the direct resonance theory, the oblique streaks (η_1) are supposed to be much larger than the rolls so that only their non-linear interaction, i.e. the term $F_{\eta\eta}$, is considered. The three forcing terms are shown in fig. 5. for the direct resonance case at the time when $\eta(\alpha, \pm\beta)$ reaches its maximum amplitude (cf. fig.3).

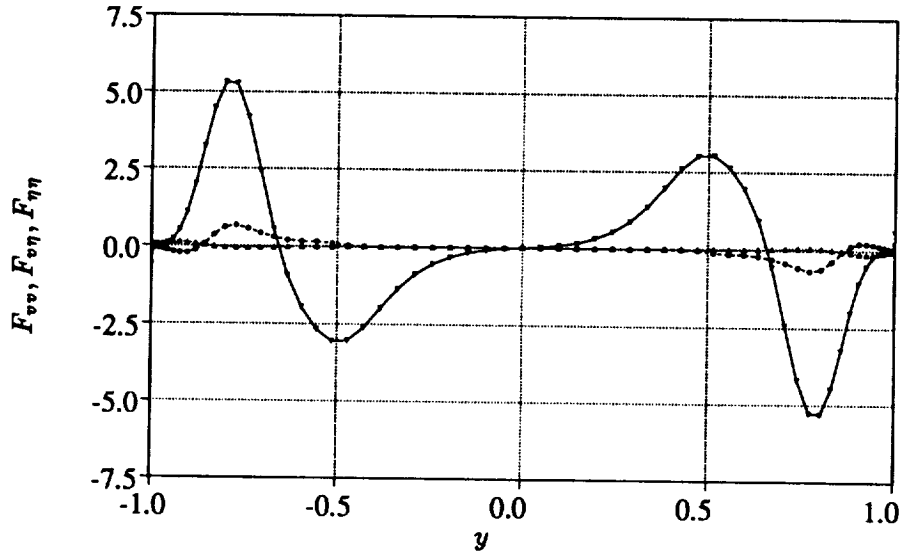

FIGURE 5. F_{vv}: ∇ , $F_{v\eta}$: $\bullet$ and $F_{\eta\eta}$: $\triangle$ at time when η is maximum. Computed for the direct resonance mode.

Figure 5 shows that the streamwise vorticity is the result of the non-linear interaction of the oblique rolls (v_1) and not of the "directly forced" oblique streaks (η_1). Thus the mechanism for the streamwise vorticity formation is the non-linear interaction of the vertical *velocity* of the oblique rolls, instead of the vertical *vorticity* as proposed in the direct resonance theory. We must conclude that the formation of streamwise vortices, and the streaks they induce, are not directly associated with "direct resonances".

2.3. Marginal flow

In view of the failure of the linear mechanism to provide a scale selection, we conclude that the selection must come from the original disturbance. In a turbulent flow the disturbance seems to arise from the breakdown of the streaks themselves (the bursting process). Thus the 100^+ selection must come from the complete *self-sustaining* mechanism. Our conjecture is that disturbances with a spacing smaller than about 100^+ can not be maintained. The 100^+ should then be considered as a *critical Reynolds number*. Experimental evidence for that proposal can be found in the work of Jimenez and Moin (1991). They show that for a channel flow at three different Reynolds numbers, $U_c h/\nu = 5000$, 3000, and 2000 (U_c is the centerline velocity, h is the half-height), the flow returns to a laminar state when the spanwise width of the periodic box is reduced below about 100^+.

We observe that for channel width of about 100^+, the channel is very narrow. The characteristic length for the scaling of the disturbance should then be taken as the half width as opposed to the half height. In more general terms, the characteristic length should be taken as the smallest of half the channel height and width. Doing so, it turns out that "turbulence" disappears if $u_*\lambda_z/\nu < 100$ which corresponds to $U_c\lambda_z/(2\nu) < 1000$ ($\lambda_z/2$ is the half-width), irrespectively of the value of $U_c h/\nu$. But 1000 is the usually quoted value for the critical Reynolds number in channel flow. If one had reduced the height h as opposed to the width λ_z, "turbulence" would have also disappeared when $U_c h/\nu < 1000$ or $u_* h/\nu < 100$.

In order to capture the self-sustaining process in its simplest form, the next step is to reduce both dimensions ($2h$ and λ_z) to their minimum value so as to eliminate all unnecessary scales. One should be reminded at this point that the streaks are expected to be an essential element of the whole mechanism. The streaks are created from the redistribution of downstream momentum. From the distribution of the mean shear in a channel flow, the simplest self-sustaining non-laminar flow should then consists of a pair of opposite streaks in the spanwise direction and in the direction perpendicular to the walls as well, i.e one pair of streaks in either half of the channel. In Couette flow, where the mean shear has only one sign, the simplest solution should correspond to only one pair of streaks in the middle of the channel. Thus the simplest marginal channel flow should have dimensions $u_* 2h/\nu \simeq 100$ and $u_*\lambda_z/\nu \simeq 100$, while the simplest marginal Couette flow should have $u_* 2h/\nu \simeq 50$ and $u_*\lambda_z/\nu \simeq 100$.

A number of simulations of both flows support the above reasoning. "Turbulent" Couette flow could not be maintained at Reynolds numbers of 324 and below (based on the half height and half velocity difference) but was maintained for over 2000 convective time units ($2h/2U_w$) at a Reynolds number $U_w h/\nu = 400$. Thus the non-laminar flow was maintained for over five viscous units (h^2/ν), a time scale over which the slowest decaying scales would decay by a factor $\exp(-2.5\pi^2)$ if they were not sustained. The computed flows show considerable similarity with the near wall-region of higher Reynolds number flows. The main mechanism appears to be the breakdown of the streaks due to a spanwise inflectional instability. That instability seems to roll up, creating vortices inclined downstream, probably because of the

effect of the mean vertical shear. This vortices then proceed to recreate the streaks. However, this latter part of the complete process is still somewhat too disordered to firmly establish the mechanisms at play. It is hoped that imposing symmetries will further constrain the mechanism and clarify the nature of the fundamental self-sustaining flow.

REFERENCES

BENNEY, D. J. 1961 A non-linear theory for oscillations in a parallel flow. *J. Fluid Mech.* **10**, 209-236.

BENNEY, D. J. & GUSTAVSSON, L. H. 1981 A New Mechanism for Linear and Nonlinear Hydrodynamic Stability. *Studies in Appl. Math.* **64**, 185-209.

JANG, P. S., BENNEY, D. J. & GRAN, R. L. 1986 On the origin of streamwise vortices in a turbulent boundary layer. *J. Fluid Mech.* **169**, 109-123.

JIMENEZ, J. & MOIN, P. 1990 The minimal flow unit in near wall turbulence. *CTR Manuscript 105.* Center for Turbulence Research, Stanford University and NASA Ames Research Center. To appear in *J. Fluid Mech.*

KIM, J., MOIN, P. & MOSER, R. D. 1987 Turbulence statistics in fully developed channel flow at low Reynolds number. *J. Fluid Mech.* **162**, 339-363.

KIM, H. T., KLINE, S. J. & REYNOLDS, W. C. 1971 The production of turbulence near a smooth wall in a turbulent boundary layer. *J. Fluid Mech.* **50**, 133-160.

KLINE, S. J., REYNOLDS, W. C., SCHRAUB, F. A. & RUNSTADLER, P. W. 1967 The structure of turbulent boundary layers. *J. Fluid Mech.* **30**, 741-773.

LEE, M. J., KIM, J. & MOIN, P. 1990 Structure of turbulence at high shear rate. *J.Fluid Mech.* **216**, 561-583.

LIN, C. C. & BENNEY, D. J. 1962 On the instability of shear flows. *Am. Math. Soc., Proc. Symp. Appl. Math.* **13**, 1.

WALEFFE, F. 1989 Organized motions underlying turbulent shear flows. *CTR Annual Research Briefs.* **89**, 107-115.

Fractal interfaces and product generation in the two dimensional mixing layer

By Javier Jiménez[1] AND Carlos Martel[2]

The dependence of product generation on Péclet and Reynolds numbers in a numerically simulated, reacting, two dimensional, temporally growing mixing layer is related theoretically to the fractal dimension of the passive scalar interfaces. This relation is verified using product generation measurements and dimensions derived from a standard box counting technique. A transition from a low initial dimension to a higher one of approximately 5/3 is identified and shown to be associated to the kinematic distortion on the flow field during the first pairing interaction. It is suggested that the structures responsible for this transition are non-deterministic, non-random, inhomogeneous fractals. Only the large scales are involved. No further transitions, either in the spectra of the vorticity field or in the mixing behavior, are found for Reynolds numbers up to 90 000.

Introduction

It has been realized for some time that smooth velocity fields can generate very complicated advective scalar distributions (Aref, 1984) and, in particular, that initially smooth interfaces can become very convoluted. In fact, even if such an interface remains technically rectifiable for any finite amount of time, its geometry becomes more and more complicated, and we shall give below simple examples in which it develops fractal properties over a wide range of length scales. When seen at those scales, its area increases substantially, and if the interface separates two fluids that are to be mixed by molecular diffusion, the stretching results in a enhancement of the mixing efficiency. A convenient measure of the complication of the interface and, indirectly, of its area increase is its fractal dimension (Mandelbrot, 1982).

We will show here that in the *two dimensional* mixing layer, a transition occurs at the location of the first pairing interaction, resulting in the development of a fractal range in the geometry of scalar interfaces with dimensions of the order of 5/3. We will also show that this fractal behavior can be related to the scaling properties of the total amount of product with Péclet number.

Assume a two dimensional situation in which the interface separating two immiscible fluids can be described by a line with a fractal dimension, F. Diffusion will "blur" the interface and generate a mixed region in the form of a strip centered around the original line whose width will, from dimensional considerations, be proportionally to $W = D^{1/2}$, where D is the molecular diffusivity. This is true both for flows in which strain is not important, in which case the width grows in time as

1 Center for Turbulence Research and Universidad Politécnica Madrid

2 Universidad Politécnica Madrid

$W = (Dt)^{1/2}$, and for those dominated by interface straining, in which the mixed region attains a steady width $W = (D/\gamma)^{1/2}$ where γ is the strain.

Directly from the definition of the fractal dimension (Mandelbrot, 1982), if a fractal line is covered with elements of diameter, W, the number of elements needed for the covering is proportional to $N \sim W^{-F}$, and the line length seen at that scale is $L(W) \approx NW \sim W^{1-F}$. In the same way, the area of the strip formed by all the covering elements which, in the case of the diffusive interface is proportional to the area occupied by the mixed fluid, is $S \approx N W^2 \sim W^{2-F}$. Note that since for non intersecting fractal lines in a plane, $1 < F \leq 2$, the length of a fractal interface will always diverge as we sample it at increasingly smaller scales, but the strip area will vanish in the limit (except for the surface filling case, $F = 2$). If we now go back to the problem of mixing and repeat the same mixing experiment with all dimensions constant but with different diffusivities, the area of the mixed strip and, therefore, the amount of mixed fluid will be proportional to

$$S \sim D^{1-F/2} \sim Pe^{F/2-1}, \tag{1}$$

where $Pe = UL/D$ is the Péclet number. This equation contains the "practical" implication of the fractal dimension of the fluid interface, and we will use it in the next section to estimate F from product generation data. An equivalent formulation exists for three dimensional situations in which the exponent in equation (1) is replaced by $(F-3)/2$.

Note that if we compare two flows with interfaces having different fractal dimensions, nothing in equation (1) guarantees that for a given Pe, the amount of mixing will increase with fractal dimension. However, if the diffusivity is reduced, the amount of mixing will decrease more slowly for the flow with higher F, and for some sufficiently high Pe, the more highly fractal flow will always generate more mixing. The assumption in this argument is that the immiscible interface itself is independent of Pe, either because the velocity field is kept constant among different experiments, as in those cases in which Pe is increased by varying only the Schmidt number, Sc, or because the changes in the velocity field are small and irrelevant to the global geometry of the interface. This latter seems to be the case in the two dimensional flows described here but probably does not apply to the mixing transition observed in three dimensional layers (Konrad, 1977, Breidenthal, 1981), in which the flow itself becomes considerably more complex as Re increase (Moser and Rogers, 1990). In those cases, it is still possible to use the arguments given above to explain the variation of the mixing efficiency with Sc, but the discussion of the Reynolds number dependence must include considerations of the flow dynamics.

In this paper, we describe some numerical experiments on the generation of product by a simple chemical reaction in a two dimensional, incompressible, temporally growing, mixing layer. The amount of product is controlled by diffusion, and it will be taken as representative of the amount of mixing and used as such in equation (1). The initial conditions are held constant as the Reynolds and Péclet numbers are changed both together and independently, and the variation in product generation is used to deduce the fractal dimension of a theoretical interface separating

two immiscible species. These fractal dimensions are then compared with those obtained by a purely geometrical analysis of the interface. The numerical code and the experimental procedure are discussed briefly in the next section, and the results are then presented and discussed.

Experimental arrangements

The numerical code is a full Navier-Stokes simulator, developed at the Universidad Politécnica in Madrid using the vorticity-stream function formulation in conservative form, and includes the transport equation for a passive scalar. It uses a Fourier spectral representation in the streamwise (x) direction and a fourth order (Padé) finite difference scheme in the transverse (y) coordinate. The grid is mapped to infinity, and the nonlinear terms are computed using a fully de-aliased collocation scheme. Typical grids use 512 Fourier modes (341 after de-aliasing) and 400 transverse points (1024×800 for $Re = 1600$). The code solves the initial value problem, starting with a initial velocity distribution, $u(y) = \tanh(y)$. This profile is perturbed initially with a small sinusoidal transverse deformation of amplitude, $\Delta y \approx 0.1$ and wavelength, $\alpha = 0.4$, which is close to the most amplified one for the initial Kelvin Helmholtz instability. In most of the runs, the computational box contains four initial wavelengths, resulting in the formation of four primary eddies that later interact through pairing. To insure this, small subharmonic and sub-subharmonic components are added to the initial perturbation.

A dimensionless viscosity is defined in terms of a Reynolds number based on the half velocity difference across the layer and on half the initial vorticity thickness, $\delta_\omega = 2$. The initial distribution of the passive scalar is taken as $s = 0.5(1 + \tanh(y/L_s))$, and its evolution is controlled by a Schmidt number, Sc, related to Re and the Péclet numbers by $Pe = Sc\,Re$. In most cases, $Sc = 1$, but some tests were done with Schmidt numbers in the range 0.25 to 4. The evolution of the scalar is used to model the behavior of a fast binary chemical reaction, $A + B \rightarrow P$, between species A and B, each of which is initially assumed to be distributed uniformly in one stream. Later they diffuse through the mixing layer and react immediately. The parameter, L_s, determines the width of the initial mixed region and should ideally be as small as possible to approximate a sharp interface. Numerical limitations prevent this, and all our experiments have been done with $L_s = 0.3$. For the most unfavorable case of high Péclet number, the memory of this initial thickness seems to be lost by the flow before $t = 20$, approximately the time necessary for the formation of the primary Kelvin-Helmhotz eddies.

In the Burke-Schumann limit assumed here, given the local concentration of the scalar, s, the concentration of product, P, can be shown to be proportional to

$$P = 2s \quad \text{if} \quad s < 1/2, \qquad P = 2(1 - s) \quad \text{otherwise.}$$

With this normalization, the maximum product concentration is always locally equal to one, and the center of the product distribution follows the $s = 0.5$ isoline. The product thickness,

$$\delta_p = \int_0^{L_x} P\,dx/L_x, \tag{2}$$

is a good measure of the area occupied by the reaction product, and we will take it as a measure of the mixed fluid area to be used in computing the fractal dimension through the arguments leading to equation (1). L_x is the length of the computational box.

The temporal evolution of flow

Some typical time histories of the vorticity and momentum thickness are shown in figure 1. There are several bumps in the vorticity thickness evolution which mark the initial roll-up into vortex cores and two consecutive pairings. It is a property of temporal simulations that the time at which each pairing occurs can be controlled by varying the amplitudes of the initial subharmonic perturbations. These were chosen so as to reproduce as closely as possible the experimental observations in an unforced half jet (Jiménez, 1983). The evolution of the vorticity thickness is too irregular to be described by a linear growth rate, but a least square fit to the lines in figure 1a has a slope of 0.22, which is in reasonable agreement with the experimental growth rates for tripped shear layers. The evolution of the momentum thickness also shows bumps, although shallower, and its mean growth rate, 0.14 ± 0.02, is also approximately consistent with experiments. Later we will discuss briefly simulations in which the first and second pairings were purposely inhibited. In those cases, the vorticity thickness grows at the beginning as in the natural case but eventually levels off and oscillates about a fixed value.

Figure 2 shows the temporal evolution of the product thickness, which is much more linear and much less affected by the pairing. Its rate of growth is very dependent on Pe, decreasing with decreasing diffusivity. In fact, Pe, as opposed to Re, seems to be the controlling parameter in product generation. All the solid lines in figure 2 represent simulations with $Sc = 1$, while the dashed lines correspond to simulations at different Schmidt numbers. Those lines always correspond to the Péclet number to which they are closest, and the effect of Re seems to be slight. In particular, $Pe = 1600$ was run both at $Sc = 1$, and at $Re = 400$, $Sc = 4$. Also $Pe = 800$ and $Pe = 200$ were both run at $Re = 200$ and $Re = 800$. In all these cases, even if the Reynolds numbers were quite different and even if the vorticity fields shows appreciably more visual complication at the higher ones (see figure 3), the product thickness scales almost exclusively with Pe, with variations below 3% which, at the end of the run, even tend to be of the opposite sign to those at the earlier moments. This suggests that most of the interface is generated by the action of the large vortical structures which are relatively independent of Reynolds number instead of by the small scales, whose energy in this two dimensional flow is relatively small.

Note that these Re and Pe are actually quite high since they are referred to the initial state of the layer. In fact, when they are reduced to local quantities at the last stage in the simulation, $Re_\omega = \Delta U\, \delta_\omega / \nu$ is of the order of 90 000 for $Re = 1600$ (the fitted value, $\delta_\omega = 0.22t$, has been used for this reduction.)

Figure 4 contains enstrophy spectra for the highest Reynolds number simulation at different times. They are one dimensional (x) spectra and have been averaged

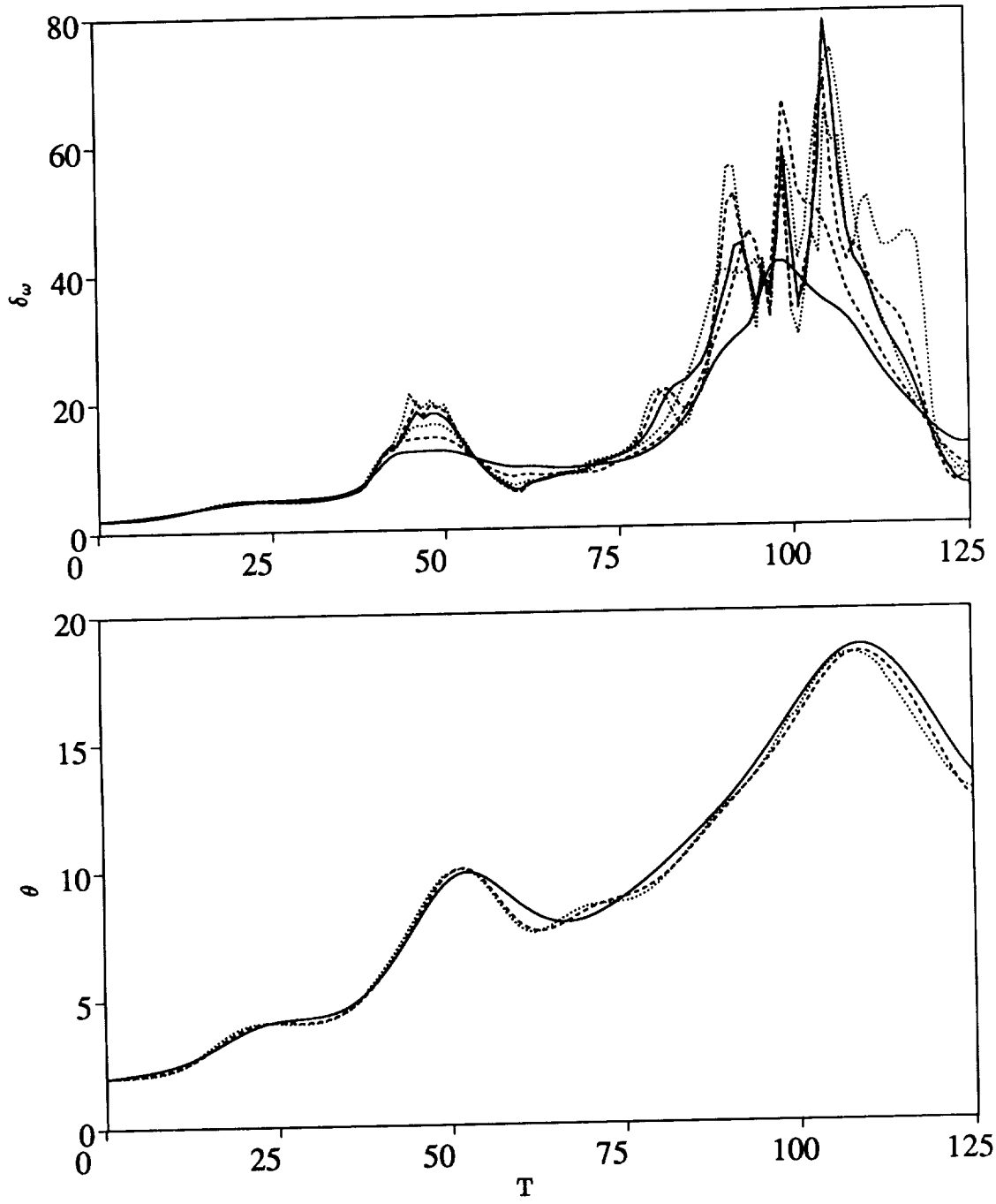

FIGURE 1. Time evolution of vorticity (top) and momentum thickness (bottom). For δ_ω, Re = 50, 100, 200, 400, 800, 1600, in order of increasing thickness during the first pairing. For the momentum thickness, Re = 100, 400, 1600.

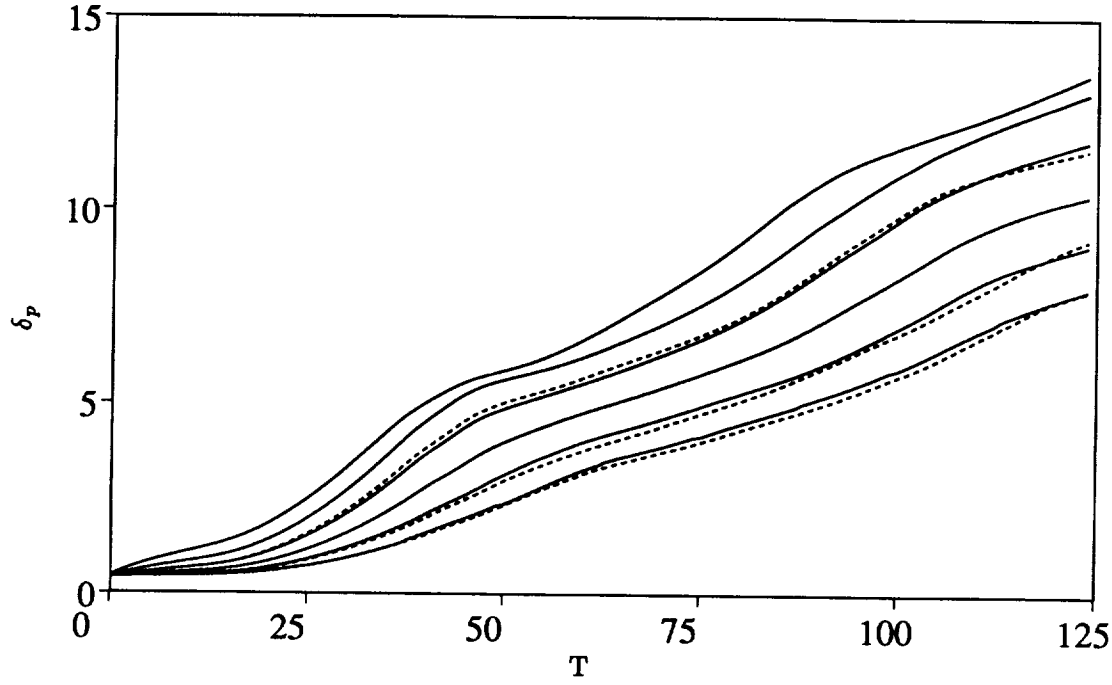

FIGURE 2. Time evolution of product thickness. Solid lines: $Re = Pe = 50$, 100, 200, 400, 800, 1600, in order of decreasing thickness. Dashed lines, also in order of decreasing thickness: $Re = 800$, $Pe = 200$; $Re = 200$, $Pe = 800$, and $Re = 400$, $Pe = 1600$. Note that histories with $Sc \neq 1$ cluster near equivalent Pe, independent of Re.

in each case over approximately the central 60% of the vorticity thickness. No normalization is introduced, and each spectrum should integrate to the averaged value of ω^2. A steep viscous range is always present, extending up to the maximum numerical wavenumber, ($\kappa = 10^2$). Approximately after the first pairing, ($t = 50$) an "inertial" range appears with an exponent slightly shallower than κ^{-2}, corresponding to an energy spectrum behavior, $E(\kappa) \sim \kappa^{-4}$, in good agreement with the results of Lesieur *et al.* (1988). It is interesting to note that the break between the two ranges is always close to $\kappa \approx 8 - 10$, corresponding to lengths of O(1), which are comparable to the smallest scales introduced by the initial conditions. Also, after the initial roll-up, the inertial range of the spectra moves uniformly to weaker energies, and there is never a tendency for a turbulent cascade to generate small scales in the same sense as in three dimensional flows. Correspondingly, the maximum vorticity stays bounded below its maximum initial value, $\omega = 1$, which is, of course, a consequence of the two dimensionality and incompressibility assumptions, and which contrasts sharply with the behavior of three dimensional flows, in which transition occurs through the generation of strong concentrated vortices through stretching, and through the appearance of scales much smaller that the pre-transition ones. As a consequence, this two dimensional flow suffers no "mixing

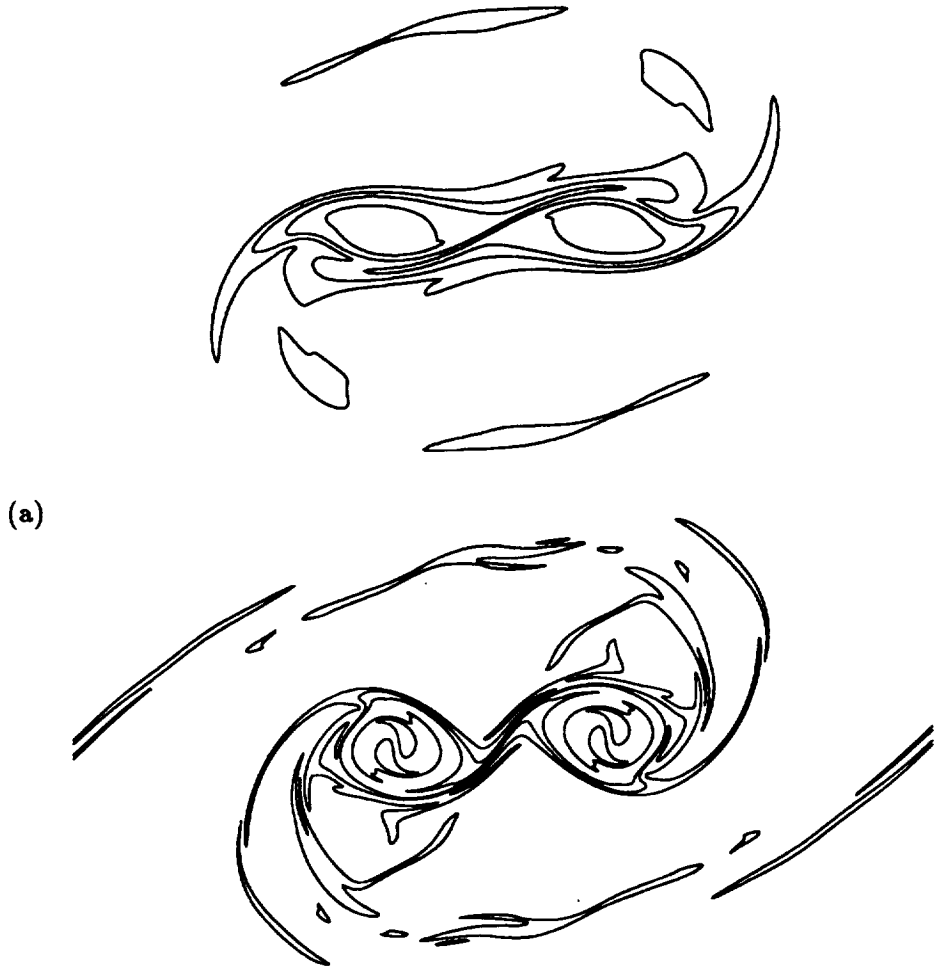

(a)

(b)

FIGURE 3. Vorticity maps for the flow at identical evolution stages, $t = 125$, after second pairing. (a) $Re = 400$, $Re_\omega = 2.2 \times 10^4$, (b): $Re = 1600$, $Re_\omega = 8.8 \times 10^4$. Isolines: $\omega = 0.1, 0.9\,(0.2)$.

transition" in the same sense as the three dimensional mixing layer.

In fact, figure 2 shows that the generation of product decreases uniformly with increasing Reynolds and Péclet numbers. A plot of δ_p against Pe is given in figure 5, where each line represents an instant in time for different Péclet numbers, and time increases upwards. Especially at the later times, a self similar range develops in which the product dependence with Pe can be well approximated by a power law. The slopes of these lines are the exponents discussed in equation (1) and can be related directly to the dimension of the fractal interfaces. At the last stages of the evolution of the layer where the self similarity holds over a wide range of scales, this dimension has a direct geometric meaning, while at the initial stages it should

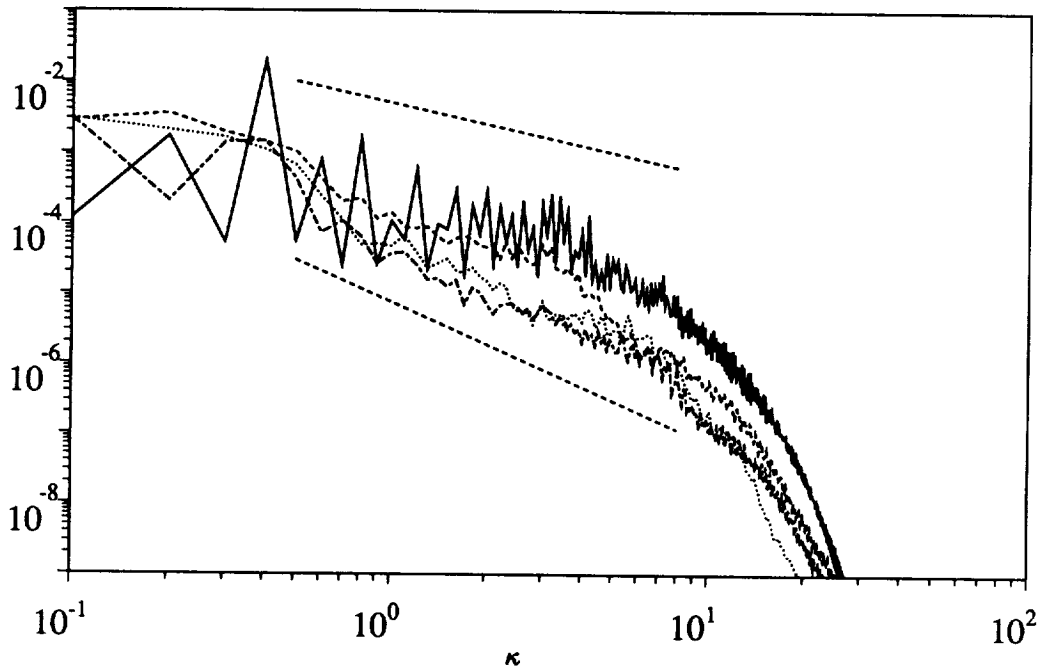

FIGURE 4. Enstrophy (ω^2) spectra *vs.* wavenumber, κ. Solid line: $t = 25$, chain-dashed: 75, dotted: 100, dashed: 125. Lower straight line: κ^{-2}. Upper: κ^{-1}.

be understood more as an averaged value over the range of scales sampled by the thickness of the diffusion layers. The time evolution of F computed in this way is given by the open circles in figure 6. It is clear that a transition occurs near $t = 50$, which corresponds to immediately after the first pairing interaction. The second pairing near $t = 100$ also induces a slight increase in F, but a much weaker one, and the dimension seems to asymptote to a value close to 5/3. Before $t = 20$, the time of initial roll-up, the measurement of F is prevented by the effect of the finite thickness of the initial condition for s, but the dimension has to approach that of a smooth line ($F = 1$) for short times. The two other sets of open symbols in figure 6 refer to two different sets of runs in one of which the second pairing was inhibited, while in the other both pairings were prevented. It is clear that the effect of the second pairing is small but that the absence of the first pairing prevents completely the appearance of the fractal transition. The closed symbols in this figure correspond to fractal dimensions computed directly from the interface geometry and will be discussed below.

The geometry of the product distribution

Before we are ready to identify the quantity, F, obtained in the last section with the fractal dimension of the immiscible interface, we need to prove that it coincides with the dimension derived from standard geometric methods, and we have to clarify over which range of length scales the implied power law is valid. As explained in

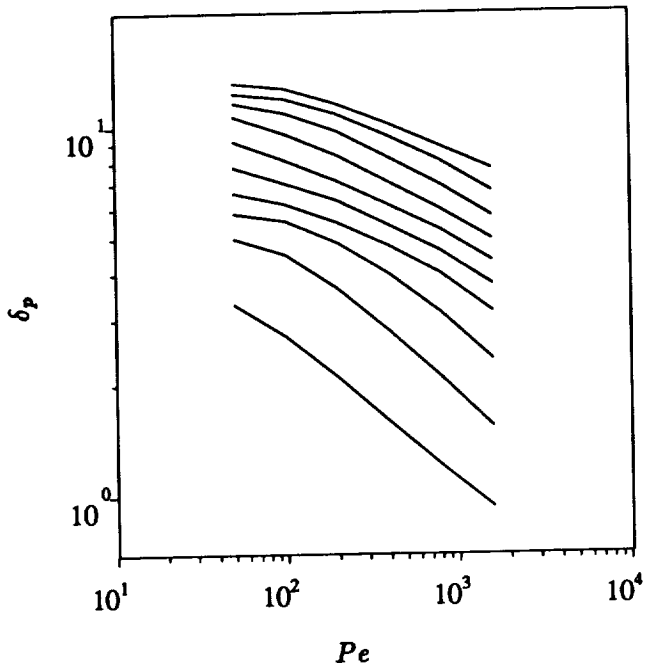

FIGURE 5. Variation of product thickness with Péclet number for different times. $t = 30$, 120, (10), increasing upwards. Data as in figure 2, $Sc = 1$.

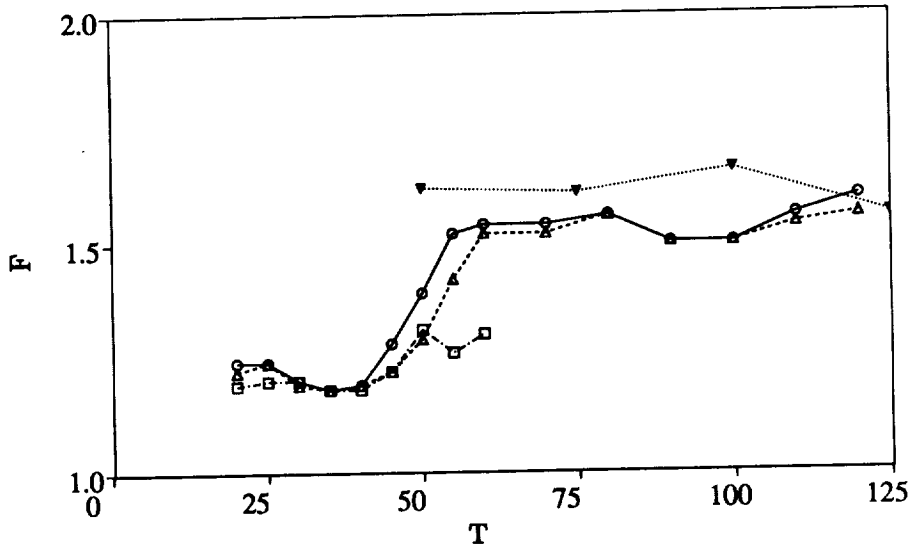

FIGURE 6. Fractal dimension of the interface, computed from figure 5, and from other similar data sets. ○: Natural layer, two pairings; △: Second pairing inhibited; □: All pairings inhibited. Closed triangles: Fractal dimensions obtained from direct box counting.

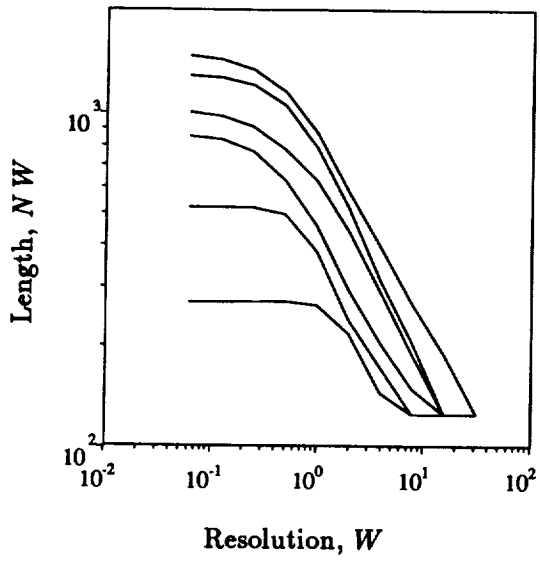

FIGURE 7. Length-resolution fractal diagrams for the $s = 0.5$ isoline for the $Re = Pe = 1600$ simulation. Times: 25, 37.5, 50, 75, 100, 125, moving upwards.

the introduction, the simplest way of measuring the fractal dimension of a line is to count the number, $N(W)$, of elements of uniform size, W, that are needed to cover it. Directly from the definition, the dimension is then given by the exponent in the relation

$$N \sim W^{-F}. \tag{3}$$

The easiest way to do this is to cover the line with a square grid of a small pitch and to plot how the number of grid cells crossed by the line changes as the pitch of the grid is successively doubled. The result for the $s = 0.5$ isoline of the convected scalar for the simulation at $Re = Pe = 1600$ is given in figure 7. That isoline corresponds to the location of an infinitely thin diffusion flame for a reaction with unit stoichiometric ratio. It is seen that initially the fractal range, if it exists at all, is very short but that eventually a substantial self similar range develops, spanning scales almost over two orders of magnitude. The corresponding fractal dimensions are represented in figure 6 by closed symbols and agree reasonably well with those obtained from the product generation. Note that the quantity plotted in figure 7 is the product, $N W$, proportional to the line length, and that the horizontal segments on the upper left hand part of the plot correspond to a range of scales for which the interface can be considered to be smooth and to have a well defined length. The horizontal segments at the bottom of the graph mark the opposite limit in which the whole mixing layer appears as a "thick" line, (2×1 cells across).

The extent of the fractal range

It is interesting to estimate the range of scales that can be considered fractal and

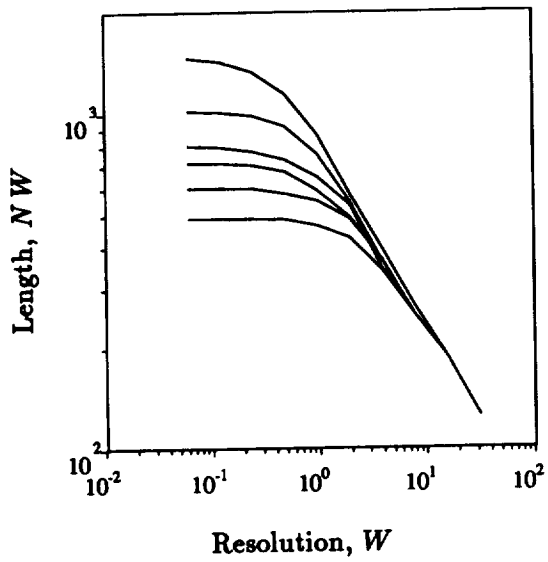

FIGURE 8. Length-resolution fractal diagrams for the $s = 0.5$ isoline for $t = 125$. $Pe = Re = 50, 100, 200, 400, 800, 1600$, moving upwards.

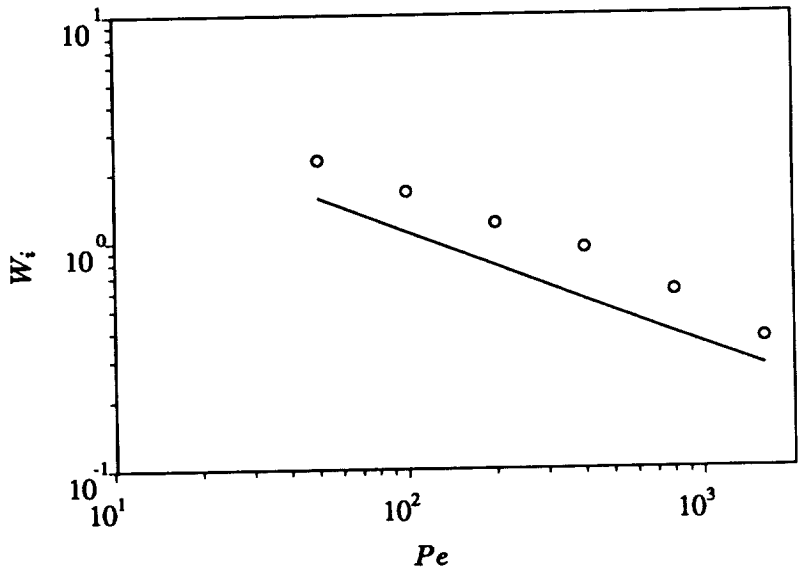

FIGURE 9. Inner cut-off scale for the fractal range, as function of Pe number. $t = 125$. Straight line is estimation of minimum diffusion scale, see text.

to compare it with the extent of the self similar power law ranges observed in figure 7. It is clear that even in the absence of diffusion, there are minimum and maximum length scales beyond which the fractal assumption fails. The solutions of the two dimensional Navier Stokes equations are smooth (for finite Reynolds number and smooth initial conditions), and any smooth material line of finite length is deformed into lines of finite length. Since we have shown above that fractal lines are not rectifiable, an interface cannot become strictly fractal in a finite time, and there will always be a minimum scale below which the interface is smooth. It is possible, however, for this inner scale to be a decreasing function of time and for the interface to become a true self similar fractal in the asymptotic limit of infinite time.

Consider the simple model of a initially straight interface being rolled into a tight spiral around a potential vortex with an inner core of radius, ρ, and total circulation, Γ. This is, in fact, a good model for the initial phase of interface creation in the mixing layer, and it can be shown to lead to a fractal dimension of 4/3 (Jiménez & Martel, 1990). The source of the infinite length of this spiral is the infinite number of turns that eventually appear as the interface is wound around the inner core, and the inner scale of the fractal range can be identified as the distance between consecutive turns just outside the rotational core. It can easily be shown by direct calculation that this distance decreases asymptotically for large times as

$$W_i = \frac{\Delta r}{\rho} = \frac{t_\Gamma}{2t}, \qquad t_\Gamma = \frac{(2\pi\rho)^2}{\Gamma}, \tag{4}$$

The time scale, t_Γ, is the vortex turnover time measured at the edge of the inner core. In actual shear layers, this process is interrupted by the pairing and by viscous diffusion, but it probably explains the mild fractal properties of the interface in the early layer, which are apparent in figure 6 as the $F \approx 1.3$ plateau of the product generation dimension before the first pairing.

In fact, if we approximate the initial conditions as a layer of uniform vorticity and assume that it rearranges itself into uniform vortex cores without appreciable entrainment of irrotational fluid, we can estimate the radii of the initial cores as $\rho = (\delta_{\omega 0}\lambda_0/\pi)^{1/2}$, and their circulation as $\Gamma = \Delta U\,\lambda_0$, where $\delta_{\omega 0}$ is the initial vorticity thickness and λ_0 is the wavelength of the initial instability. The minimum length scale can then be written as $W_i = 2\pi\delta_{\omega 0}^2/\Delta U\,t$ which, in the units of our simulation, is just $W_i = 4\pi/t$. For the two curves in figure 6 which belong to this initial phase and taking into account that the initial roll-up occurs at $t \approx 20$, the result is $W_i = 2.5$ at $t = 25$ ($t - t_0 \approx 5$), and $W_i = 0.7$ at $t = 37.5$. These values are in reasonable agreement with the location of the upper "corners" which mark in both curves the transition between the fractal behavior at large scales and the small scale smooth limit. This agreement suggests that the creation of interface in this initial phase is not limited by diffusion at the Péclet numbers of the simulation.

That this is not always the case can be seen in figure 8, which displays the behavior of the fractal diagram at $t = 125$ for different Péclet numbers. It is clear that the fractal range grows with increasing Pe. Let us define the location of the small scale cut-off as the point where the straight line defining the fractal range in the log-log

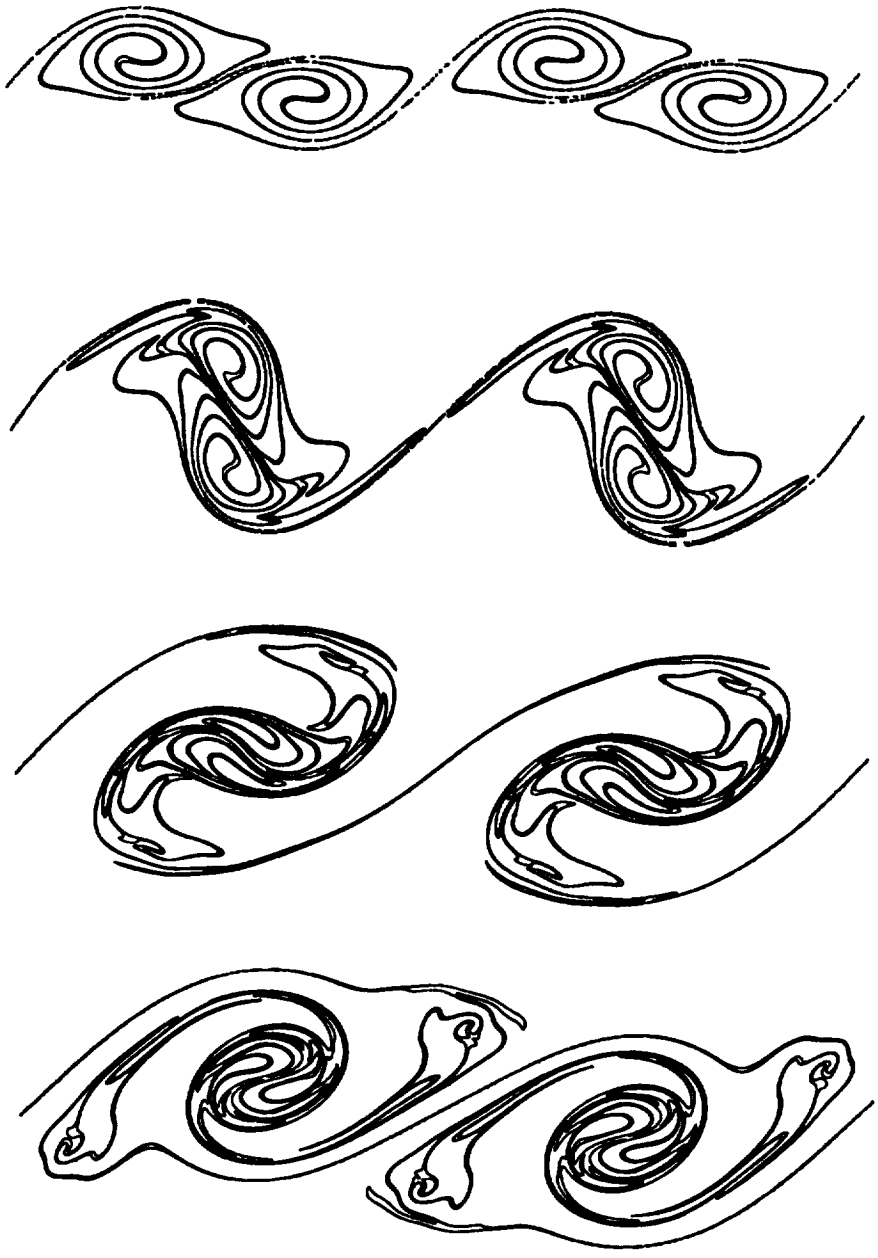

FIGURE 10. Product concentration maps during the first pairing. Time, top to bottom: $t = 37.5, 50, 62.5, 75$. $Re = Pe = 1600$. Isoline: $P = 0.8$ (equivalent to $s = 0.4, 0.6$). Note how initial spirals are deformed and stretched by pairing, especially in outer parts.

plot intersects the horizontal line marking the asymptotic value of the line length for small scales. The variation with Pe of the length scale corresponding to this point is given in figure 9, and scales quite closely with $Pe^{-1/2}$, suggesting that it is diffusion limited. In fact, it is of the same order of magnitude as the Batchelor scale for the mixing at that particular time, which can be estimated by noting that a diffusive interface in a strain $v = -\gamma y$ reaches an equilibrium thickness $\delta_\gamma = (2\pi/Pe\,\gamma)^{1/2}$. The maximum strain in a shear layer, modeled as a row of compact vortices, is of the order of $\gamma = \pi\,\Delta u/2\lambda$, where λ is the distance between consecutive vortices, and the equilibrium thickness becomes for the simulation corresponding to figure 9 $\delta_\gamma = (4\lambda/Pe\,\Delta U)^{-1/2} \approx 11\,Pe^{-1/2}$. This is the line drawn in figure 9 and agrees with the measured data not only in slope but also in order of magnitude.

These last estimates prove that, contrary to the situation during the early stages of roll-up, the generation of interface at these later stages and at this particular Péclet number is limited by molecular diffusion, and that simulations at higher Péclet numbers will reveal still more interface at the smaller scales.

The source of these small scales can be seen in figure 10, which shows the evolution of the interface through the first pairing. After roll-up, the interface forms tight spirals similar to those described previously, but during the pairing, these spirals are stretched, in part into elongated ellipses near the centers, but especially into long filamentary stacks in their outer parts, whose fractal character derives from the close proximity of successive leaves. Since area is conserved during the deformation, the distance between two leaves originating from the deformation of spiral turns of radius, R, and initially separated by a distance, W_R, becomes of the order of $W_L = W_R R/L$, where L is the length of the strip into which the initial circle is deformed. If we take this length to be of the order of the distance between eddies after pairing and the initial radius to be of the order of the vorticity thickness before pairing, the reduction in the minimum length scales imposed by the kinematics during pairing is roughly one decade. In our simulations, that will make it $W_i \approx 0.05$ after pairing, well below the resolution imposed by the diffusion scale which, as computed above, is $\delta_\gamma \approx 0.4$ for our $Pe = 1600$ case. It can be shown (Jiménez & Martel, 1990) that the appearance of these stacks leads to a fractal dimension of 5/3, and they are in all probability responsible for the fractal behavior of the interface in the late evolution of the layer.

Discussion

We have measured the change in time of the fractal dimension of an ideal interface in a two dimensional mixing layer, and we have related it to the scaling properties of product generation with Péclet number. We have also shown that this scaling holds independently of the Reynolds number, even for fairly high values of this latter quantity. Since the effect of Re is mainly on the small scales, this suggests that mixing, in this two dimensional case, is controlled predominantly by the large coherent eddies. This is confirmed by inspection of the flow fields at high Re and Pe. The structure of the product is dominated by large folds and structures, with few small scales in the sense of fine random corrugations. This is also confirmed by

the relatively low values of the fractal dimension encountered. Several investigators have studied and measured the fractal dimensions of interfaces in *three dimensional* turbulence (Sreenivasan and Meneveau, 1988), arriving at $F \sim 7/3$, and have justified this value using models based on random homogeneous fractals. The same arguments when applied to two dimensional turbulence (Meneveau, private communication) result in $F = 2$. This is inconsistent with our observations.

The assumptions of randomness and homogeneity are not necessary for a fractal model. We have noted above that both the spirals generated by the deformation of initially plane interfaces by point vortices and the "stacks" resulting from the stretching those spirals by a plane strain are fractals. In fact, the stacks are both common in the two dimensional mixing interface and have a fractal dimension of $5/3$, close to that observed in the layer after the first pairing. It is, therefore, tempting to conclude that they are the structures responsible for the fractal behavior of the interface in the two dimensional mixing layer and that the fractal transition observed at the pairing is caused by the straining of spirals formed by the original mixing eddies. A consequence of this interpretation is that, by inhibiting pairing altogether, we should be able to observe a transition to a lower fractal dimension of $4/3$, and it can be argued that this is indeed the dimension implied by the product behavior in the case in figure 6 for which both pairings were inhibited. This case is, however, not representative of natural mixing layers and was not studied in great detail.

Note that this picture is very different from that of the wrinkled interface of a homogeneous fractal. The fractional dimension comes in this case from the accumulation of turns near the center of the spirals and from the accumulation of sheets in the central part of the stacks. Note also that this picture is very similar to that arising from the *tendril-whorl* mapping studied in (Khakar *et al.*, 1986).

Conclusions

In summary, we have shown that the scalar interfaces in a two dimensional plane mixing layer acquire fractal properties, we have measured their fractal dimensions, and we have related them to the Péclet number dependence of product generation in a fast binary, diffusion controlled, chemical reaction. We have also shown that those dimensions and the generation of product are fairly independent of Reynolds number (for $\Delta U \delta_\omega / \nu \leq 90\,000$), although they are strongly dependent on molecular diffusivity, suggesting that the mixing is mostly due to "chaotic advection" from the large scale eddies. This is probably different from the behavior of the three dimensional mixing layer, in which a substantial part of the mixing seems to be associated to longitudinal vorticity and small scales.

The fractal dimension undergoes a transition from low values, in the range $F \approx 1 - 1.3$ to $F \approx 5/3$, which coincides in time with the first pairing and which is inhibited when this pairing is inhibited. The effect of the second pairing is not as marked. We have presented a model for these dimensions in terms of non-random, non-homogeneous, fractal structures. The transition is then explained as the generation during pairing of strained spirals ("stacks"). Finally, up to the Re

and Pe quoted above, we found no further transition either in the mixing efficiency or in the structure of the vorticity field.

It is especially significant that a simple geometric quantity, that can easily be measured by geometric means on flow fields at some high but finite Reynolds or Péclet numbers can be related to a scaling behavior valid for arbitrarily high Pe. The question of the behavior of diffusion limited chemical reactions in the limit of vanishing diffusivity is an important unsolved problem for real *three dimensional* mixing layers. It is not known, for example, whether any reaction will occur in the limit $Pe \to \infty$, and experimental evidence is scarce and difficult to come by. If a relation similar to the one discovered here could be proved in that case, all that would be needed would be a measurement of the fractal dimension of the interface at some Péclet number high enough for a clear separation to exist between the Batchelor and outer scales of the flow. Some preliminary experiments with existing numerical flow fields show that the available Reynolds numbers do not satisfy this condition. The arguments in section 5, on the other hand, suggest that the usual estimates for the turbulent scales can be used to estimate the extent of the fractal range, if one exists, in which case the smallest fractal scale should decrease faster with Pe in the three dimensional case (where $W \sim Pe^{-3/4}$) than in the two dimensional one ($W \sim Pe^{-1/2}$). If this is so, a computation of a mixing flow with the appropriate Pe might be just within the capability of the next generation of computers, and that numerical experiment might provide a simple answer to the question of asymptotic product behavior in three dimensional layers.

The part of this work that was carried out in the University of Madrid was supported by United Technologies Corporation of Hartford, Conn.

REFERENCES

AREF, H. 1984 Stirring by chaotic advection. *J. Fluid Mech.* **143**, 1-21.

BREIDENTHAL, R. 1981 Structure in turbulent mixing layers and wakes, using a chemical reaction. *J. Fluid Mech.* **109**, 1-24.

JIMÉNEZ, J. 1983 A spanwise structure in the plane mixing layer. *J. Fluid Mech.*. **132**, 319-336.

JIMÉNEZ, J. & MARTEL, C. 1990 Fractal properties of interfaces in two dimensional shear layers, *Proc. IUTAM Symp. Stirring and Mixing.* La Jolla, 20-24 August, 1990.

KHAKHAR, D. V., RISING, H. & OTTINO, J. M. 1986 An analysis of chaotic mixing in two chaotic flows. *J. Fluid Mech.* **172**, 419-451.

KONRAD, J. H. 1977 An experimental investigation of mixing in two dimensional turbulent shear flows with applications to diffusion limited chemical reactions, *Ph.D. Thesis.* Caltech.

LESIEUR, M., STAQUET, C., LE ROY, P. & COMTE, P. 1988 The mixing layer and its coherence examined from the point of view of two dimensional turbulence. *J. Fluid Mech.* **192**, 511-534.

C-3

MANDELBROT, B. B. 1982 *The fractal geometry of nature.* W. H.Freeman.

MOSER,R. D. & ROGERS,M. M. 1990 Mixing transition and the cascade to small scales in a plane mixing layer, *Proc. IUTAM Symp. Stirring and Mixing.* La Jolla, 20-24 August, 1990.

SREENIVASAN, K. R. & MENEVEAU, C. 1986 The fractal facets of turbulence. *J. Fluid Mech.* **173**, 357-386.

Studies of supersonic mixing

By N. T. Clemens AND M. G. Mungal

This report describes studies of supersonic mixing which have been accomplished over the last year with CTR support. During this period, a Nd:Yag laser, optical components, and data acquisition computer were obtained. This allowed detailed visualizations of the flow structure to be performed at a rapid rate, representing a significant improvement over our previous attempts. Aspects of the flow structure are described below. In addition, preliminary findings on a possible mixing enhancement strategy are also shown using the flow visualization technique.

1. The visualization technique

The technique developed in this work uses planar laser Mie scattering from fine alcohol droplets seeded into the flow. Figure 1 shows a schematic of the supersonic wind tunnel. The high-speed side (side 1) is capable of a maximum Mach number of 2.5, while the low-speed side (side 2) is capable of a maximum Mach number of 1.0. Optical access is provided from all sides. The test section pressure is about 10-12 psia, with both stagnation temperatures about 300K.

Two visualization approaches were developed. In the first, alcohol (ethanol) is injected far upstream into side 2. The alcohol vaporizes and uniformly mixes with the low-speed fluid. Upon mixing with the cold high-speed fluid in the mixing layer, condensation of fine alcohol droplets occur and mark the mixing region. This technique is called the "product formation" technique in analogy to chemically reacting systems.

An alternate technique is to seed the alcohol far upstream into side 1. Here, droplets are formed in the supersonic nozzle and uniformly mark the high-speed fluid. The concentration of droplets owing to dilution with the low-speed fluid then decreases across the mixing layer region. This technique is called the "passive scalar" technique in analogy to mixing studies using passive scalars.

Several studies were made to determine the droplet diameters and number densities of the alcohol "fog". Clemens & Mungal (1991a) describe these measurements in some detail and conclude that the diameters were less than 0.2 micron, but are more likely closer to 0.05 micron. Number densities were about $10^{12}/\text{cm}^3$. Using the conservative estimate of diameter, we are able to easily meet the criterion of Samimy & Lele (1990) for proper flow visualizations, in the sense that the particles accurately track the flow. Three additional issues related to visualizations concern: (1) droplet evaporation in the passive scalar case, (2) finite rate formation effects in the product formation case, and (3) droplet coagulation in both cases. It is concluded in Clemens and Mungal (1991a) that while these effects are at play, they are relatively small and do not significantly bias the visualizations to be presented next. Using the current laser and digital camera approach, Fig. 2, we are able to acquire

images to video at about 10 Hz and to computer memory at 3 Hz. Computer storage eliminates film processing which greatly shortens processing time, while digital data allows ease of image processing.

2. Results

Figures 3-6 show visualizations of a low compressibility case using both techniques. Figure 3 shows a schlieren image extending from the splitter tip to 45 cm downstream (0 to 3000 initial momentum thicknesses downstream). Observe that the Brown-Roshko rollers appear past the $x = 15$ cm station. The flow conditions are: $M1 = 1.6$, $M2 = 0.9$, $U1 = 430$ m/s, $U2 = 275$ m/s resulting in a convective Mach number of $Mc = 0.28$ (Papamoschou & Roshko, 1988). To remove the spatial integration of the schlieren, Fig. 4 shows a portion of the flow extending from 15 to 28 cm downstream. Both techniques clearly reveal the Brown-Roshko structure. Plan views of the central 5 cm of the test section are shown in Fig. 5. (The full span of the test section is 10 cm). The product formation technique reveals the two-dimensionality of the Brown-Roshko rollers. The passive scalar approach is best at revealing regions where high-speed fluid is in close proximity to low-speed fluid, namely the braid regions. Careful examination reveals the instantaneous streamwise structure seen in incompressible flows. Finally, Fig. 6 shows end views of the flow in which the core and the braid are captured. The images are consistent with the side and plan views.

Figures 7-10 show analogous photos for a compressible case, $Mc = 0.62$. The flow conditions are: $M1 = 2.0$, $M2 = 0.4$, $U1 = 480$ m/s, and $U2 = 130$ m/s. The most obvious difference is the lack of two-dimensional organization as compressibility increases, and an apparent increase in three-dimensionality. Figure 10 shows that for the compressible case the layer generally appears to be of similar thickness as opposed to the thick core and thin braid seen earlier. The changes to structure are also not a Reynolds number effect as we are able to match Reynolds numbers at different convective Mach numbers and still demonstrate the changes seen here. These results are also generally consistent with the work of Sandham & Reynolds (1989) who predict an increase in three dimensionality with increasing compressibility. Additional photos at $Mc = 0.79$ can be found in Clemens & Mungal (1990), with little changes seen when compared to the $Mc = 0.62$ case.

A final use of the technique is in its application to a possible mixing enhancement. Several studies (e.g. Shau & Dolling, 1989) have attempted to enhance mixing by interaction of a spanwise shock with the two-dimensional mixing layer. While there is a local enhancement, the layer quickly recovers to its slow growth mode. Here we present an alternate technique, the Side Wall Shock Vortex Generator (SWSVG), described in Fig. 11. We have found that placement of a disturbance in the supersonic nozzle, normal to the span as shown, generates an oblique shock wave which upon interacting with the splitter tip generates a streamwise vortex. Figure 12 shows time averaged end views of the flow with (a) no disturbance, (b) one disturbance, and (c) two sidewall disturbances respectively. While the thickness of the layer appears unchanged, the overall mixing volume has increased by about

60%. Clemens & Mungal (1991b) also show that it is possible to change the location of the vortex by movement of the SWSVG within the supersonic nozzle.

3. Conclusions

This work has demonstrated through planar visualizations that low compressibility, high Reynolds number mixing layers continue to show the Brown-Roshko structure seen in incompressible layers. Compressible layers are also seen to be more three-dimensional. These changes are a result of compressibility, and are not a Reynolds number effect.

In addition, it is suggested that shock waves which interact with the splitter plate in a direction normal to the span are better candidates for mixing enhancements than interactions which occur in the spanwise direction.

REFERENCES

CLEMENS, N. T. & MUNGAL, M. G. 1990 Two- and three-dimensional effects in the supersonic mixing layer. *AIAA-90-1978.*

CLEMENS, N. T. & MUNGAL, M. G. 1991a A planar Mie scattering technique for visualizing supersonic mixing flows. To appear, *Expts. Fluids* (1991).

CLEMENS, N. T. & MUNGAL, M. G. 1991b Side-wall shock vortex generator for supersonic mixing enhancement. To appear in *J. Prop. Power* (1991)

PAPAMOSCHOU, D. & ROSHKO, A. 1988 The compressible turbulent shear layer: an experimental study. *J. Fluid Mech.* **197**, 453-477.

SAMIMY, M. & LELE, S. K. 1990 Motion of particles with inertia in a compressible shear layer. Submitted to *Phys. Fluids A*, (1990)

SANDHAM, N. D. & REYNOLDS, W. C. 1989 Growth of oblique waves in the mixing layer at high Mach number. *Turbulent Shear Flows 7,* Stanford University, Paper #9-5.

SHAU, Y. R. & DOLLING, D. S. 1989 Experimental study of spreading rate enhancement of high Mach number turbulent shear layers. *AIAA-89-2458.*

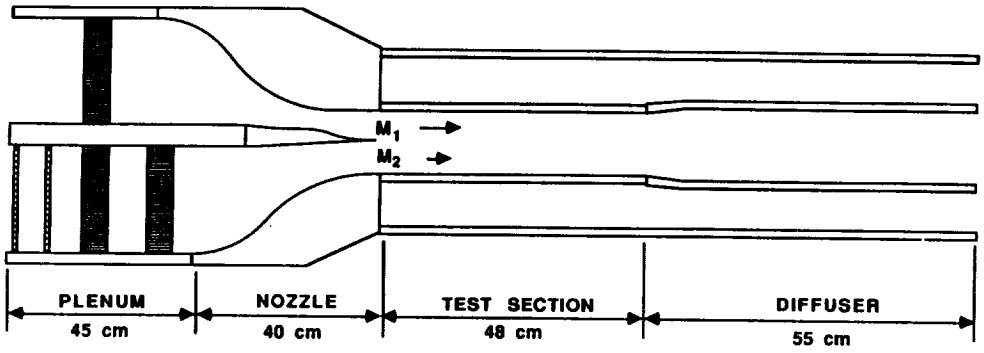

FIGURE 1. Supersonic wind tunnel schematic

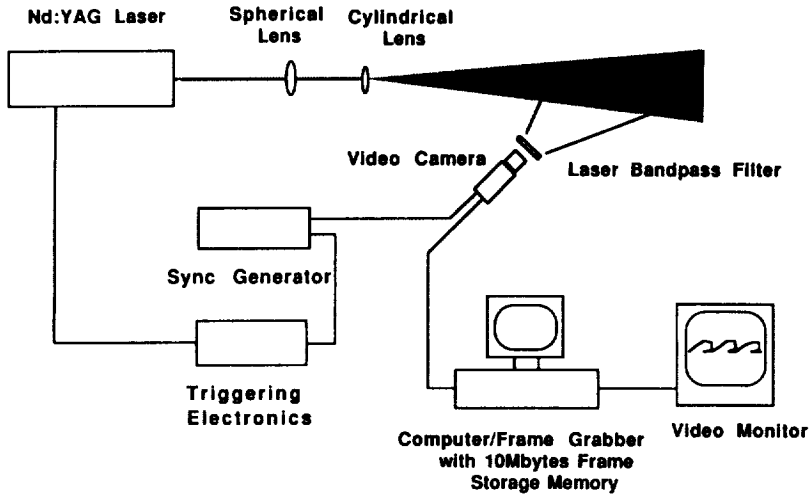

FIGURE 2. Schematic of the imaging setup.

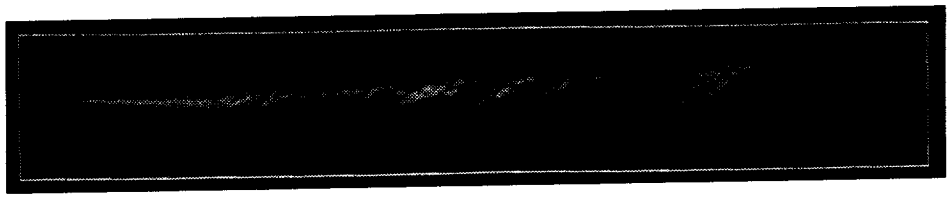

FIGURE 3. Composite schlieren for $Mc = 0.28$, $x = 0 - 45$ cm. Flow is from left to right.

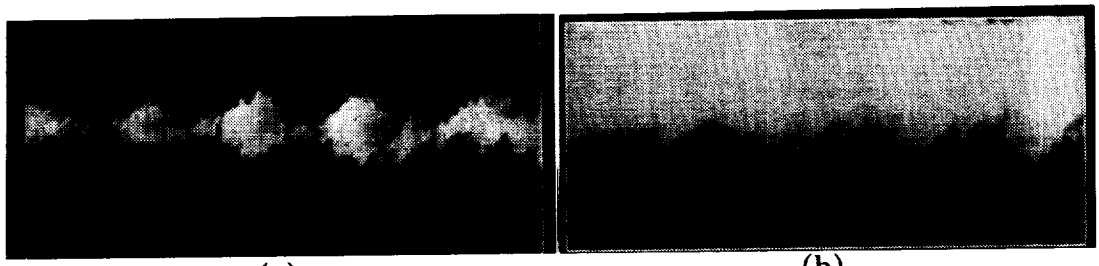

(a) (b)

FIGURE 4. Side view Mie scattering for $Mc = 0.28$, $x = 15 - 28$ cm: (a) product formation method, (b) passive scalar method. Flow is from left to right.

(a) (b)

FIGURE 5. Plan view Mie scattering for $Mc = 0.28$, $x = 15 - 30$ cm: (a) product formation method, (b) passive scalar method. Flow is from left to right.

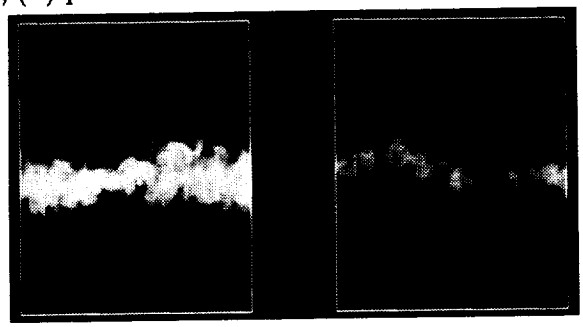

FIGURE 6. Product formation end view Mie scattering images for $Mc = 0.28$, $x = 18$ cm. Image on left shows cut through vortex core, image on right shows cut through braid.

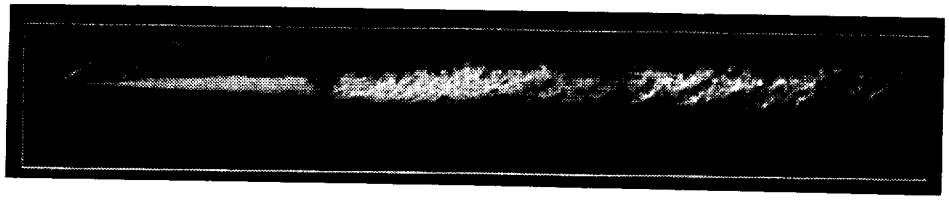

FIGURE 7. Composite schlieren for $Mc = 0.62$, $x = 0 - 45$ cm. Flow is from left to right.

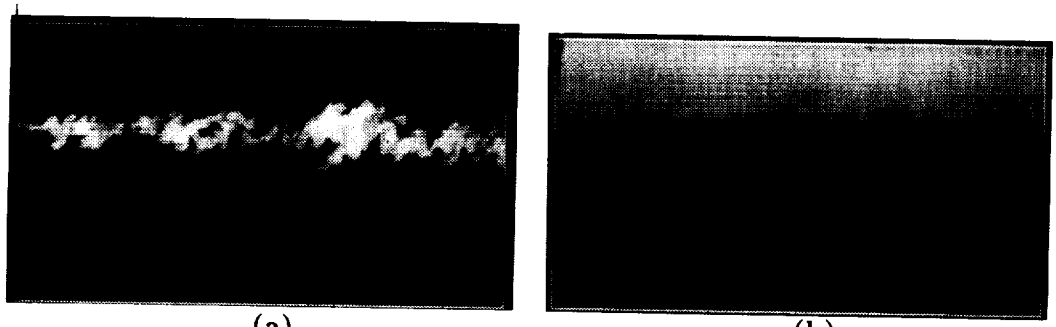

(a) (b)

FIGURE 8. Side view Mie scattering for $Mc = 0.62$, $x = 15 - 28$ cm: (a) product formation method, (b) passive scalar method. Flow is from left to right.

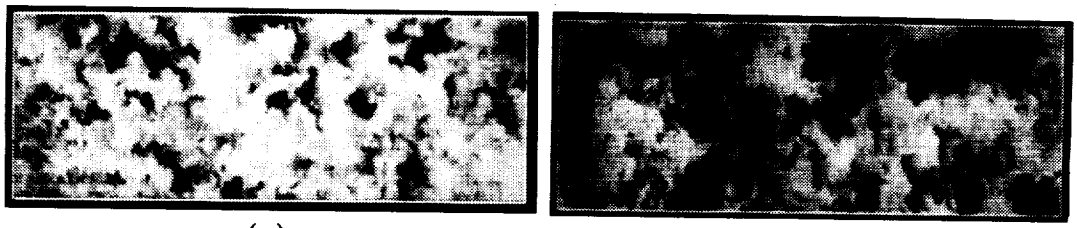

(a) (b)

FIGURE 9. Plan view Mie scattering for $Mc = 0.62$, $x = 15 - 30$ cm: (a) product formation method, (b) passive scalar method. Flow is from left to right.

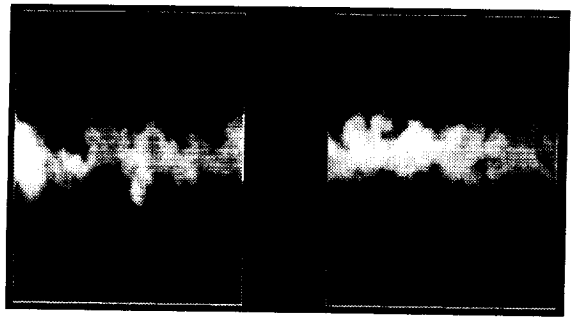

FIGURE 10. Product formation end view Mie scattering images for $Mc = 0.62$, $x = 22$ cm.

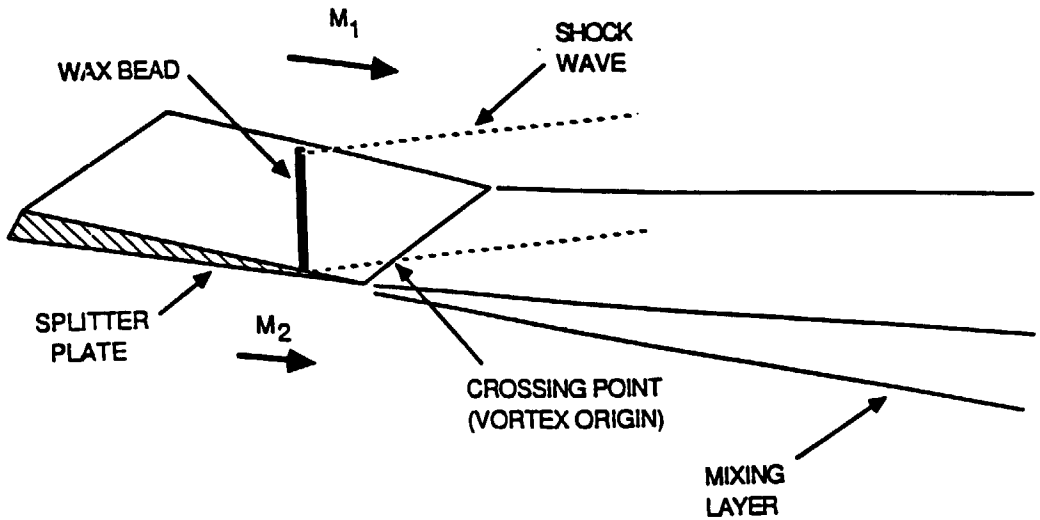

FIGURE 11. Perspective view of the supersonic mixing layer and the SWSVG.

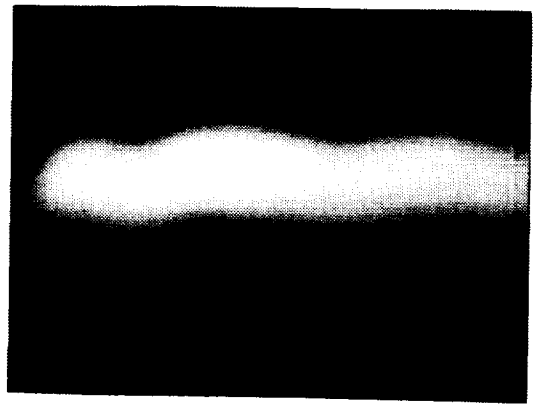

(a)

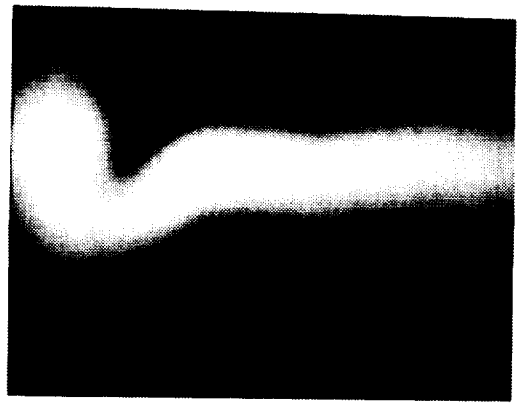

(b)

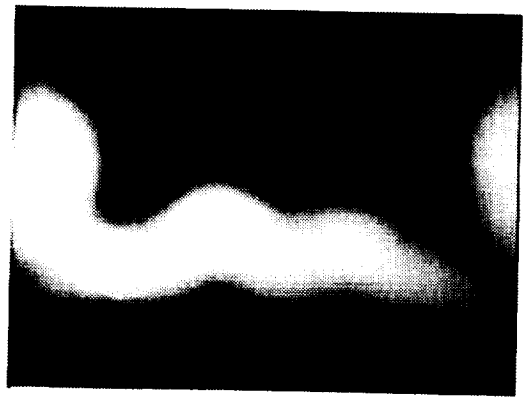

(c)

FIGURE 12. Experimental result: End views of mixed fluid using laser light-sheet visualization for $M_1 = 2$, $M_2 = 0.4$, $M_c = 0.6$. (a) No wax bead. (b) Vortex generator wax bead on left side-wall at the splitter tip produces vortex on the left side. (c) Beads on both sides produce two counterrotating vortices.

Center for Turbulence Research
Annual Research Briefs - 1990

An experimental study of curved mixing layers: flow visualization using volume rendering

By P. S. Karasso AND M. G. Mungal

1. Motivation and objectives

The existence and importance of large-scale spanwise vortical structures for 2-D straight mixing layers has been well documented in the last decade (Brown & Roshko, 1974; Dimotakis & Brown, 1976; Mungal *et al.*, 1985; Konrad 1976; Winant & Browand, 1974). Computer models and simulations have sought to reproduce these vortical structures associated with the Kelvin-Helmholtz (K-H) instability mode which is due to the shear per se (Sandham & Reynolds, 1989). Secondary streamwise vortical structures for the same flows were also seen experimentally (Konrad, 1976; Breidenthal, 1981; Bernal & Roshko, 1986; Lasheras & Choi, 1988); Huang & Ho, 1989) and have recently been given importance in computational efforts. Jimenez *et al.* (1985) first performed a reconstruction of the plane mixing layer for Reynolds numbers of about 2,000 and 7,500 (based on the velocity difference and the visual thickness). They found that a system of streamwise vortices exists on top of the spanwise vortices. The streamwise vortical structures were very well defined for the $R_e \sim 2,000$ case but less so for the $R_e \sim 7,500$ case.

Curved mixing layers can be characterized as stable (the high-speed stream is placed on the outside of the longitudinal bend), leading to a suppression of the Taylor-Görtler (T-G) instability, and unstable (high-speed stream on the inside of the bend), leading to an enhancement of the T-G instability (Figure 1). The T-G instability is associated with the centripetal acceleration that the curvature imparts (Wang, 1984; Taylor, 1923). Thus, curvature superimposed on 2-D shear layer flows provides a way for studying the importance of streamwise vorticity, its competition with spanwise vorticity, and changes to entrainment and mixing. Furthermore, the outcome of the competition of a relatively enhanced or suppressed T-G instability with the K-H instability offers the possibility of achieving passive mixing enhancement.

Konrad (1976) and Koochesfahani & Dimotakis (1986), performed measurements of the probability density function (pdf) of the mixture fraction in a plane mixing layer and found it to be invariant with lateral distance across the layer for a Reynolds number not greater than 23,000. This result is consistent with the characterization of the K-H instability as the dominant one in the plane mixing layer. In the case of curved mixing layers, similar pdf measurements are our long term goal, with differences in the shape of these pdf's reflecting differences in the entrainment and mixing of this flow field. The Reynolds number dependence of the structure of the mixing layers will also be explored. As a first step in understanding the competition between the K-H and the T-G instabilities and the resulting changes to the structure of the flow, we attempt here to provide highly resolved visualizations of the flow

structure for the stable and the unstable configurations. The straight layer is also visualized for comparison with earlier works.

2. Accomplishments

2.1. Experimental facility and conditions

The experimental facility consists of a blow-down water tunnel which is described in Karasso *et al* (1989). A passive scalar, sodium fluorescein, is diluted uniformly in the low-speed fluid. An Argon-ion laser is used to generate a laser sheet at the $y-z$ plane, normal to the flow direction (Figure 2). Two positions are examined, at $x = 4.8$ cm and $x = 9.5$ cm downstream from the splitter plate, yielding Reynolds numbers of about 6,500 and 12,000 respectively, based on the velocity difference and the visual thickness. These Reynolds numbers correspond to the pre-transition and to the transition field of the straight layer. Laser induced fluorescence movies are acquired using a motion picture camera operated at 400 frames/sec with an exposure time of 1/1000 sec. The experiments are performed for both the stable and the unstable configuration as well as for the straight shear layer configuration.

Photos showing planar cuts, taken with 3200 ASA photographic film, were presented in Karasso *et al* (1989). The photos showed that the mixing layer grows about 50% more for the unstable than for the stable case. Hence, the unstable case can be immediately characterized by growth enhancement. Detailed changes to the pdf of the mixture fracture are not known at present, so it is unclear if the growth changes correspond to mixing changes.

Single, unrelated instantaneous cuts such as the ones shown in Karasso *et al* (1989), although useful, have an inherent difficulty in presenting the time evolution of the flow and more importantly in simultaneously displaying the streamwise vortical structures of the flow field. To circumvent this difficulty, we use the technique of volume rendering, which is described next.

2.2. Volume rendering results

The essential idea of volume rendering (Van Cruyningen *et al*, 1991; Drebin *et al*, 1988) consists of stacking sequential frames to produce a three-dimensional data-object. Here, $y-z$ views of the layer (the high framing rate movies), once digitized, are stacked sequentially as a function of time t on a Pixar image computer. This three-dimensional data volume is used to extract surfaces that retain the resolution of the digitized frames. Viewing the rendered surfaces is made possible by shading with a white light source, the position of which is preselected. Rotating the rendered surfaces with respect to the light source provides different views corresponding to the rotation of a 3-D object in $y-z-t$ space. The results for all cases appear in Figures 3 and 4, where the temporally growing layers are shown from an angle that best displays the streamwise and the spanwise vortical structures. The coordinate system $y-z-t$ is shown at the top left corner of each of the figures. About 60 frames compose each view, corresponding to a real time interval of 0.15 sec, which is converted to length by assuming the average velocity of the two streams of the shear layer.

The renderings show that the two instability modes occur together in a non-destructive way. In the pre-transition field, Figure 3 ($R_e \sim 6,500$), the T-G instability induces streamwise vortices (lines that run from top to bottom on each photograph) which are well defined for all three cases. The width (z) of the field of view shown in the renderings is about 13 cm. The spacing of the streamwise vortical structures is seen to be $\lambda \sim 0.9$ cm for all cases. The K-H instability is also evident at this station. The T-G vortices are seen to ride both on the cores and the braids of the K-H vortices, consistent with the model presented by Bernal & Roshko (1986). The passage frequency of the K-H rolls corresponds to a streamwise length δ of about 1 cm; a ratio of $\lambda/\delta \sim 0.9$ then characterizes all cases at this station. Notice how the present results, for the straight case, show well defined streamwise vortical structures compared to the case of $R_e \sim 7,500$ of Jimenez *et al.* (1985). This difference, we believe, is due to the fact that the present rendering calculations are done by retaining the pixel resolution of the frames that are originally used for stacking, resulting in fewer overall approximations.

In the transition region, Figure 4 ($R_e \sim 12,000$), small scales begin to develop as seen in the irregularities of the rendered surfaces. In the stable case, the K-H instability appears to dominate the T-G instability, while in the unstable case the T-G rolls remain very well defined. The spacing λ for the stable and the unstable cases is seen to be about 1 cm, showing a small increase from the previous station. The straight case shows results that are intermediate to the stable and unstable case. The streamwise to spanwise structure spacing ratio is now $\lambda/\delta \sim 0.5$ due to a decrease in the passage frequency of the K-H rolls.

Although no quantitative measurements for the mixture fraction can be extracted from the present photos, it is clear that the large-scale structures that are seen to persist must be associated with entrainment patterns in shear layer flows and are of ultimate importance in gaining an understanding of the physics of the flow, the resulting mixing, and in modeling. The volume rendering technique presented here seems to be a convenient way to simultaneously demonstrate the occurrence of both K-H and T-G instabilities.

2.3. Summary

In this work, the curved mixing layer is used to provide a means to study the competition of the T-G and the K-H instabilities in a systematic way. At pre-transition Reynolds numbers, both instabilities are evident as seen in the volume renderings. Transition Reynolds numbers are marked by the addition of smaller scales. For the stable and the straight case, the K-H instability appears dominant, while for the unstable case the T-G instability is enhanced.

3. Future plans

The philosophy underlying future work is to generate highly resolved data that characterize the dynamics of mixing in shear layers by varying different parameters of the flow such as: (i) The Reynolds number: The facility allows a change of velocity magnitudes and location of measuring stations. Thus, pre-transition, transition and fully-developed regimes are easily obtainable. (ii) The different cases

of stable, unstable and straight mixing layers. (iii) The effect of initial momentum thickness (boundary layer tripping) on mixing growth and characteristics. (iv) The effect of resolution on measurements by using passive scalar and chemical reaction techniques.

The experiment will thus be focused to:

1) Improve the quality of the volume renderings. The use of a more powerful laser such as a pulsed 20-Watt Copper-vapor laser will allow shorter exposure times while filming, thus giving sharper pictures and renderings. Also the possible use of a Spin Physics Camera recording system instead of the 16mm film will allow the renderings to be more time-efficient and with better signal to noise ratio.

2) Measure the concentration field pdf. For this purpose, a very low noise camera must be used (a 2-D Amperex imaging array with a light sheet from a 1.5 Watt Nd:Yag laser, available at the High Temperature Gasdynamics Laboratory- HTGL). For statistical convergence, many frames must be acquired, corresponding to at least 100 structures for each location and case. Although acquisition can be effected with a 386 IBM compatible, the data storage and processing will probably require the use of a workstation, also available at HTGL.

REFERENCES

BERNAL, L. P. & ROSHKO, A. 1986 *J. Fluid Mech.* **170** 499.

BREIDENTHAL, R. E. 1981 *J. Fluid Mech.* **109** 1.

BROWN, G. L. & ROSHKO, A. 1974 *J. Fluid Mech.* **64** 775.

DIMOTAKIS, P. E. & BROWN, G. L. 1976 *J. Fluid Mech.* **78 (3)** 535.

DREBIN R. A., CARPENTER L. & HANRAHAN, P. 1988 *Computer Graphics* **22 (4)** 65.

HUANG, L. S. & HO, C. M. 1989 *J. Fluid Mech.* **210** 475.

JIMENEZ, J., COGOLLOS, M. & BERNAL, L. P. 1985 *J. Fluid Mech.* **152** 125.

KARASSO, P. S. & MUNGAL, M. G. 1989 *Annual Research Briefs-Center for Turbulence Research.* 27.

KONRAD, J. H. 1976 *Ph.D. Thesis.* Caltech.

KOOCHESFAHANI, M. M. & DIMOTAKIS, P. E. 1986 *J. Fluid Mech.* **170** 83.

LASHERAS, J. C. & CHOI, H. 1988 *J. Fluid Mech.* **189** 53.

MUNGAL, M. G., HERMANSON, J. C. & DIMOTAKIS P. E. 1985 *AIAA J.* **23** 1418.

SANDHAM, N. D. & REYNOLDS, W. C. 1989 *Turbulent Shear Flows 6.* Berlin.

TAYLOR G. I. 1923 *Phil. Trans.* **A 223** 289.

VAN CRUYNINGEN, I., LOZANO, A., MUNGAL, M. G. & HANSON, R. K. 1991 *AIAA J.* to appear.

WANG, C. 1984 *Ph.D. Thesis.* Caltech.

WINANT, C. D. & BROWAND, F. K. 1974 *J. Fluid Mech.* **63** 237.

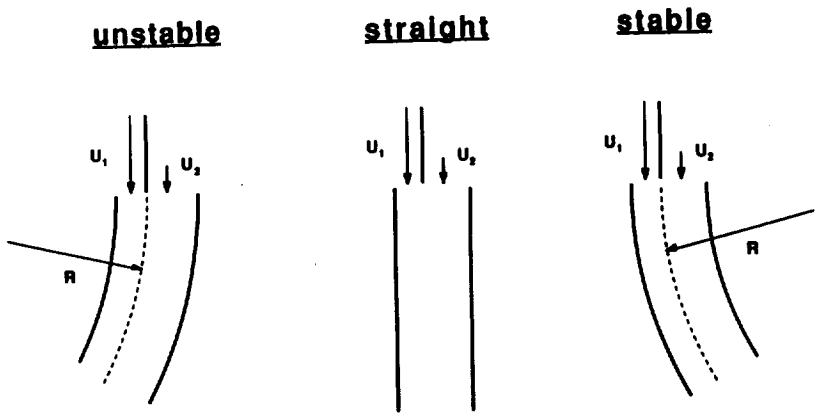

FIGURE 1. Definition of stable and unstable curved shear layers.

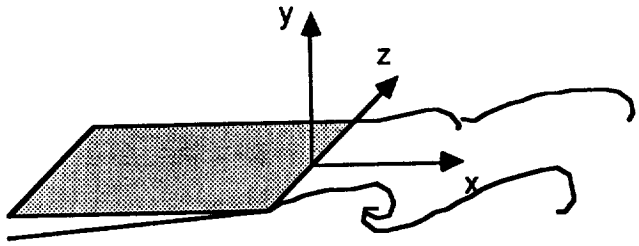

FIGURE 2. The $x - y - z$ coordinate system.

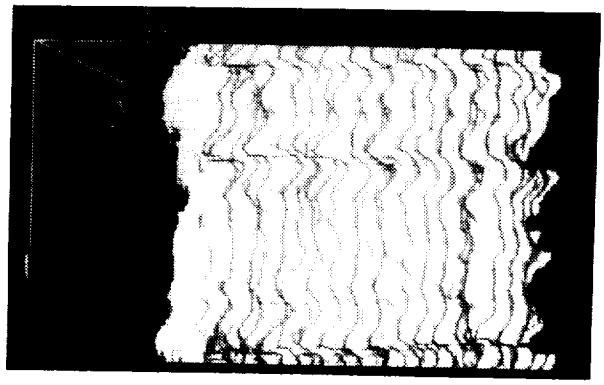

(a: unstable)

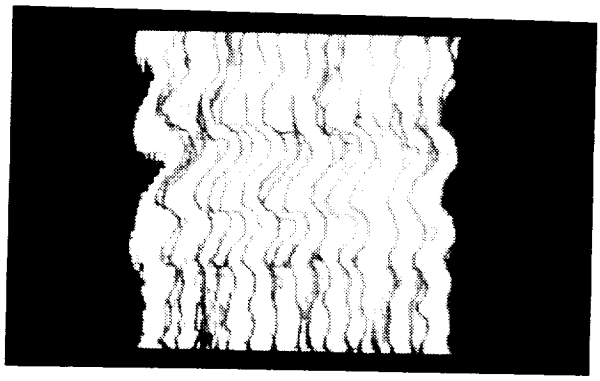

(b: straight)

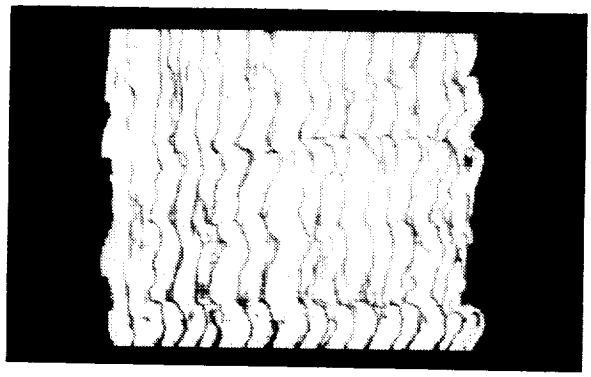

(c: stable)

FIGURE 3. Volume rendering of mixing layers at pre-transition, viewed from low-speed side ($R_e \sim 6,500$).

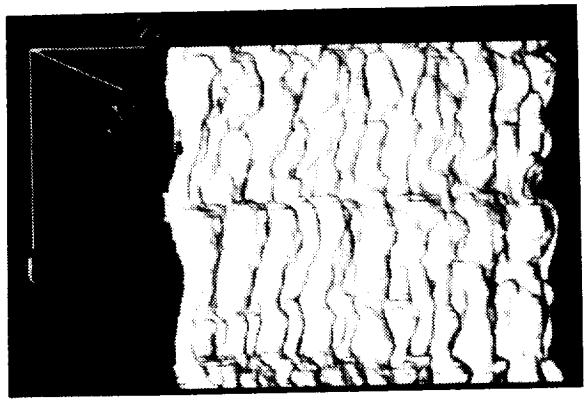

(a: unstable)

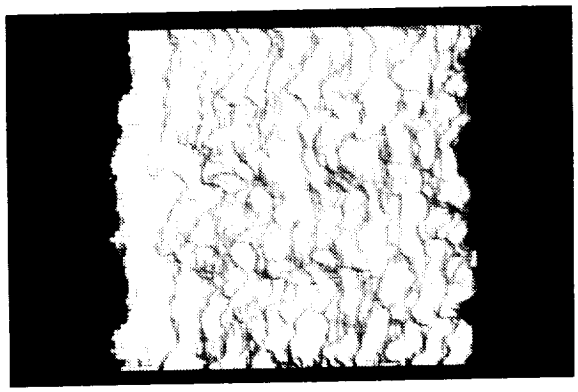

(b: straight)

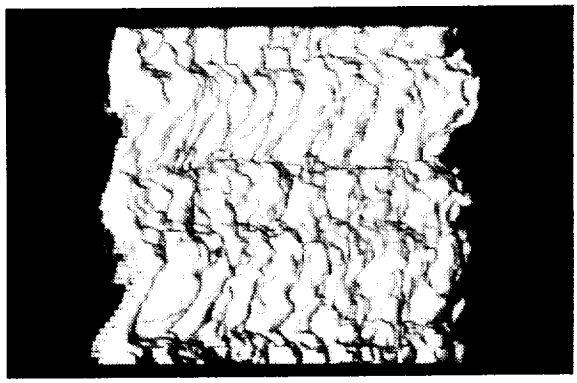

(c: stable)

FIGURE 4. Volume rendering of mixing layers at transition, viewed from low-speed side ($R_e \sim 12,000$).

Center for Turbulence Research
Annual Research Briefs - 1990

An experimental study of the effects of rapid rotation on turbulence

By Srinivas V. Veeravalli

The effects of rotation on grid turbulence were studied in a low speed tunnel. Results are presented for both axisymmetric and non-axisymmetric flows. As observed by previous workers, the cascade process was seen to be effectively blocked by rotation leading to reduced dissipation. In the non-axisymmetric case, rotation caused the flow to tend rapidly towards axisymmetry; however, for the length studied, the flow tended to move away from isotropy. Based on the results, some recommendations are made on the design of a larger facility for studying similar flows.

1. Motivation and objectives

Experiments (Traugott, 1958, Wigeland & Nagib, 1978, and Jacquin *et al.*, 1988, 1990), large eddy simulations (Bardina *et al.*, 1985), and direct numerical simulations (Bardina *et al.*, 1985 and Speziale *et al.*, 1987) all show that rapid rotation (i.e. the rotation time scale $(1/\Omega)$ << the turbulence time scale) has a striking effect on homogeneous nearly isotropic turbulence. The cascade process is effectively inhibited by rotation, thus dissipation is greatly reduced. Some attempts have been made to incorporate this effect in turbulence models (Bardina *et al.*, 1985 and Speziale *et al.*, 1987); however, none of the present models fully account for the subtle effects of rotation. Numerical simulations further showed the somewhat surprising result that anisotropic homogeneous turbulence subjected to rotation tended towards an isotropic state; however, the residual anisotropy was not necessarily zero. Reynolds (1989) performed a detailed analysis using Rapid Distortion Theory (RDT) and showed that a reduction in the anisotropy is indeed expected, and if the anisotropy is produced by irrotational strain, then the anisotropy tensor b_{ij} is asymptotically driven to half its initial value.

Our objective was to extend the work of the experiments mentioned above to lower turbulent Rossby numbers ($R_{o\lambda} \equiv (\frac{1}{3}q^2)^{\frac{1}{2}}/(\lambda\Omega)$, where λ is the Taylor microscale and q^2 is twice the turbulent kinetic energy), and to study the effects of rotation on non-axisymmetric turbulence.

2. Previous work

Experimental studies of rotating turbulence can be broadly classified into two groups: *a*) rotating tank experiments and *b*) wind tunnel experiments.

The work of Ibbetson & Tritton (1975) and Hopfinger *et al.* (1982) belong to category *a*. Ibbetson & Tritton dropped a grid into a rotating tank and found that the turbulence behind the grid decayed much faster in the presence of rotation. Hopfinger *et al.* (1982) used a shaking grid to generate turbulence and found that

away from the grid the flow exhibited a strong tendency towards 2-dimensionality and essentially consisted of columnar vortices aligned with the axis of rotation.

Traugott (1958), Wigeland & Nagib (1978), and Jacquin *et al.* (1988, 1990), on the other hand, imposed solid body rotation on grid turbulence in a wind tunnel, thus these experiments approximate homogeneous turbulence better. The smallest value of $R_{o\lambda}$ achieved in the Wigeland & Nagib (1978) experiment was approximately 0.4 while Jacquin *et al.* (1988, 1990) obtained a value of 0.6. These experiments showed that the mildly anisotropic grid turbulence tended towards isotropy and that the kinetic energy decay was greatly reduced due to an inhibition of the cascade process. Jacquin *et al.* (1990) conducted a detailed study of length scales and showed that the length scales along the axis of rotation grew at a much faster rate compared to the non-rotating case and showed departures from the behavior expected in isotropic flow (the direct numerical simulation results of Bardina *et al.*, 1985 show a similar behavior for the length scales). However, no two-point measurements were made and all the length scales were obtained from the time series, invoking Taylor's hypothesis.

Large eddy simulations and direct numerical simulations (Bardina *et al.*, 1985 and Speziale *et al.*, 1987) also showed the dramatic suppression of the spectral transfer term observed in experiments. In particular, Speziale *et al.* (1987) found that the development of the energy spectrum $E(\underline{\kappa}, t)$ agreed extremely well with

$$E(\underline{\kappa}, t) = E(\underline{\kappa}, t_o)\, exp[-2\nu\kappa^2(t - t_o)] \tag{1}$$

which is what is expected for purely viscous decay with the spectral transfer term equal to zero. (ν is the kinematic viscosity, $\underline{\kappa}$ the wave number vector, and the development is for $t > t_o$.) Speziale *et al.* (1987) also showed that homogeneous (unbounded) turbulence does not undergo Taylor-Proudman reorganization.

3. Apparatus and instrumentation

The experiments described here were carried out in a facility similar in design to those used by Wigeland & Nagib (1978) and Jacquin *et al.*(1990). The output of standard blower tunnel consisting of a wide angle diffuser, a plenum chamber with 4 screens, and a honeycomb, followed by a contraction (8:1) section, is fed into a rotating section which is 15.24cm in diameter. The rotating section (figure 1) houses the swirl generator at the entrance and the turbulence generating grid near the exit. It consists of a cylinder mounted between slender bearings and driven by a pair of friction wheels, which are in turn driven by a 1 h.p. motor. The swirl generator consists of a layer of low density foam (8 pores per cm, 0.64cm thick) followed by a honeycomb (cell size 3.7mm and 4.0cm long) and a screen (of 0.07cm mesh size and a porosity of approximately 0.6) placed approximately 40 cell diameters downstream of the honeycomb. Circumferential velocity is imparted to the fluid mainly by the honeycomb; however, the axial velocity resulting from the use of a honeycomb alone is non-uniform because of higher blockage at the periphery due to the higher angles of flow incidence there. The use of the foam alleviates this problem since part of the swirl is imparted by the foam. Any residual inhomogeneities in the axial velocity

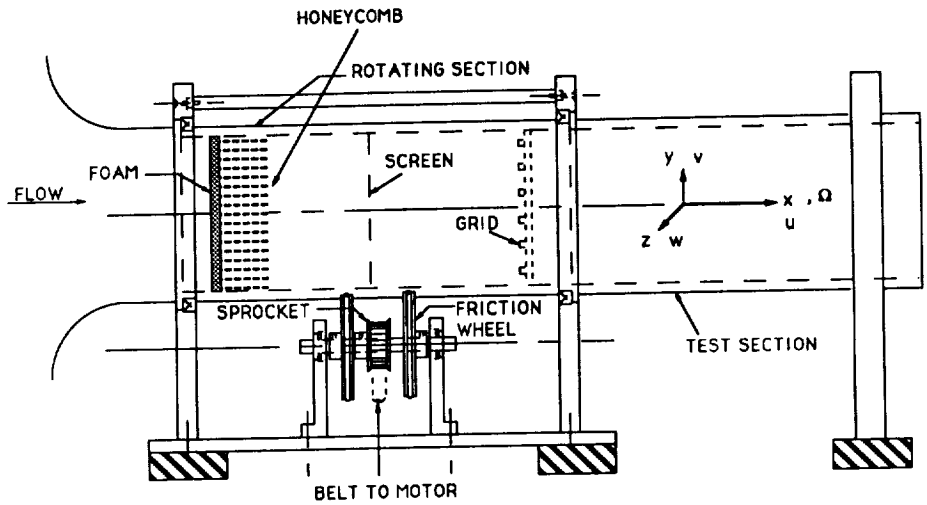

FIGURE 1. Schematic Diagram of the rotating section.

distribution are smoothed out by the screen. As shown in section 4, the resulting velocity distribution shows that the fluid is indeed in solid-body rotation away from the walls and is convected downstream with a uniform axial velocity. Measurements were made in a stationary test section approximately 1.4m long. The test section is mounted on a separate table and a small air gap ($\approx 0.5mm$) was maintained between the rotating section and the test section so that no vibrations were transmitted from the rotating section to the test section. For all the measurements described below, the turbulence generating grid consisted of a bi-planar array of square bars, with a mesh size (M) of 1cm and solidity (ratio of closed area to the total area) of 0.37.

Measurements were made with Dantec 55P51 cross-wire probes (5 μm in diameter and approximately 1mm long) operated by Microscale HWM-100 anemometers. The hot-wire signals were low-pass filtered before being digitized by a Data Translation DT2828 data acquisition board.

4. Accomplishments

Figure 1 shows the coordinate frame used in the ensuing discussions. For off-axis measurements, y denotes the radial direction and z denotes the azimuthal direction.

Figure 2 shows profiles of the mean velocity and velocity variances obtained at $x/M = 20$ and $x/M = 100$ with the cylinder spinning at approximately 1200 r.p.m. As can be seen, the swirl generator is quite successful in producing the required velocity field. Away from the wall, the axial velocity is uniform, while the azimuthal velocity varies linearly with radius. The slight spin-up that is observed at $x/M = 100$ is due to the growth of the boundary layers. At $x/M = 20$, the region where the fluctuation field is homogeneous has a diameter of approximately 10M and this drops to approximately 5M at the larger downstream distance. We

note that the variance values reported off-axis are obtained from mean values (over angle) of phase-locked averages. This procedure was necessary since small variations in the mean axial velocity with angle gave rise to fairly large spurious fluctuations since the turbulence intensity was small.

4.1 Axisymmetric turbulence

The decay of the turbulent kinetic energy, and its components, with downstream distance is shown in figure 3 for $\Omega = 0$ rad/s and $\Omega \approx 126$ rad/s. The measurements were made along the centerline. Let us first look at the behavior for x/M less than 100. We see that although the variances are nearly equal initially, for the two cases, the decay rate is much slower in the presence of rotation as was observed by Wigeland & Nagib (1978) and Jacquin *et al.* (1990). The kinetic energy decay exponent drops from 1.34 in the non-rotating case to 0.91 for Ω of 126 rad/s. As noted by previous researchers, in the presence of rotation, the spectral modes get de-coupled, thus spectral transfer is inhibited, leading to a reduced dissipation rate. A study of spectra further reveals this process. Figure 4 compares u and v spectra at $x/M = 20$ and $x/M = 60$. Initially ($x/M = 20$), the spectra for the rotating and non-rotating cases are nearly identical; however, at $x/M = 60$, the low frequency (wavenumber) energy content is higher in the presence of rotation, while the high frequency (wavenumber) energy content is lower. This is what one would expect when spectral transfer is inhibited — the low wavenumber motions would be preserved, while the high wavenumber motions would decay more rapidly since the energy lost due to viscous effects is not replaced by spectral transfer. A more detailed study of spectra and length scales will be made when two-point correlations are measured. For the present, we note that the evolution of the length scales is similar to that observed by Jacquin *et al.* (1990). Various turbulence parameters corresponding to the axisymmetric flow are presented in Table 1.

(x/M)	$k\ (m^2/s^2)$	$\epsilon\ (m^2/s^3)$	$l(cm)$	$\lambda\ (cm)$	Re_λ
20	0.191	11.8	0.71	0.16	35.9
60	0.045	0.95	1.0	0.28	30.1

TABLE 1a: Turbulence parameters for $M = 1cm$, $\Omega = 0$ and $U \approx 9.2\ m/s$.

(x/M)	$k\ (m^2/s^2)$	$\epsilon\ (m^2/s^3)$	$l(cm)$	$\lambda\ (cm)$	Re_λ	Ro_λ
20	0.202	8.13	1.12	0.20	45.6	1.46
60	0.081	1.13	2.04	0.34	49	0.54

TABLE 1b: Turbulence parameters for $M = 1cm$, $\Omega = 126\ rad/s$ and $U \approx 9.5\ m/s$.

Let us now examine the behavior for x/M greater than 100, in figure 3. We see that $\overline{u^2}$ becomes nearly constant, while $\overline{v^2}$ actually increases with increasing downstream distance. To examine this phenomenon in greater detail, centerline measurements were made without the grid at different rotation rates. Figure 5

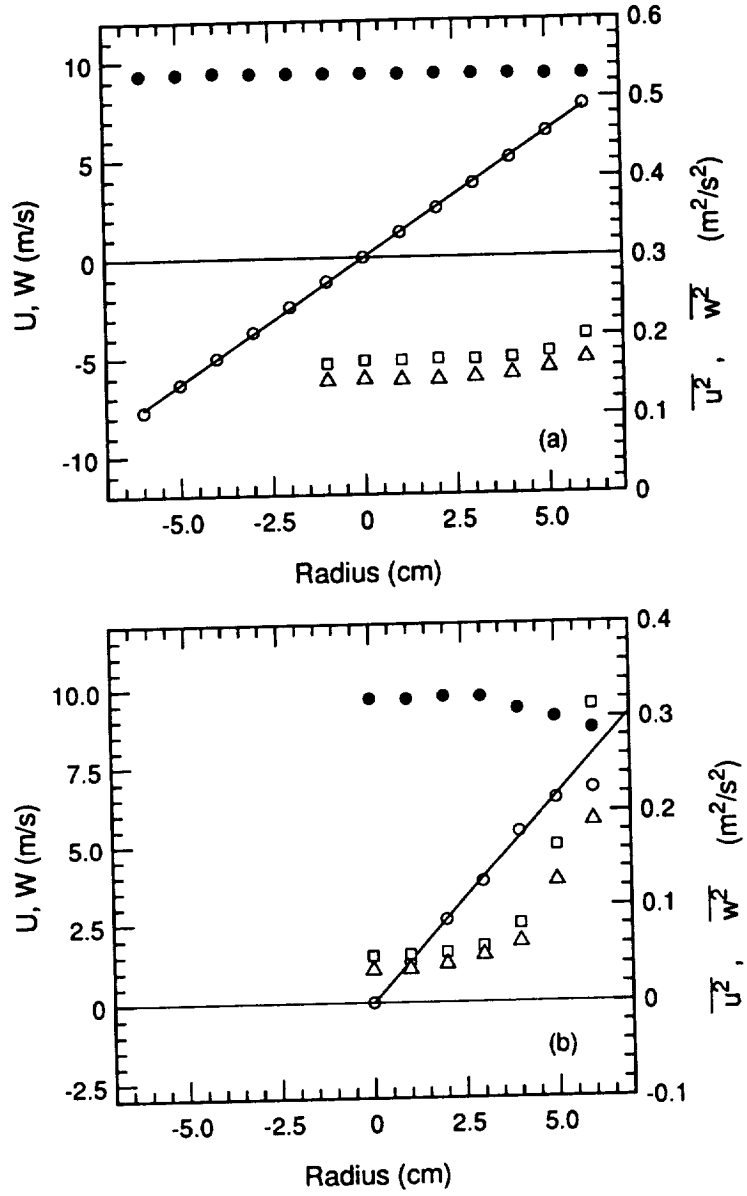

FIGURE 2. Mean velocity and variance profiles at; a) $x/M = 20$ and b) $x/M = 100$. The symbols are: • U; ○ W; □ $\overline{u^2}$ and △ $\overline{w^2}$. The straight line fit to the azimuthal velocity data in a) has a slope corresponding to 126 rad/s and in b) the slope is 130.6 rad/s.

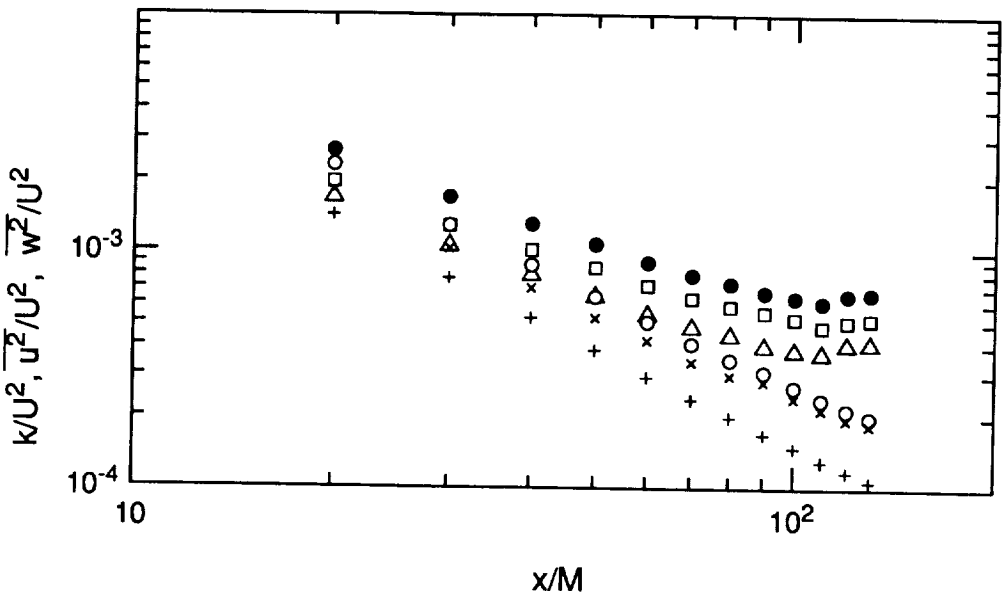

FIGURE 3. Decay of normalized variances and kinetic energy with and without rotation. The symbols are: 1) $\Omega = 126 rad/s$, • k/U^2; □ $\overline{u^2}/U^2$; △ $\overline{w^2}/U^2$ and 2) $\Omega = 0$, ○ k/U^2; × $\overline{u^2}/U^2$; + $\overline{w^2}/U^2$

shows the evolution of the turbulent kinetic energy for various rotation rates. We see that k increases dramatically beyond a certain x in each of the three cases with rotation. The mean velocity profiles indicate that there is no turbulence production in the region near the center, thus the data is contaminated by boundary effects — originating either from the side wall or from the exit. To examine if end effects were propagating upstream, the end condition (for Ω = 126 rad/s) was modified in two ways: a) the test section was lengthened by 20% and b) an obstruction (grid) was placed at the exit. In either case, the results were identical to those shown in figure 5. Thus, the contamination of the centerline data is due to disturbances originating from the cylinder wall. It can be shown that the contribution of irrotational fluctuations originating from the edge of the boundary layer is at least three orders of magnitude smaller than the observed levels, thus the increase in centerline intensity is due to the propagation of the boundary layer fluctuations in the form of inertial waves. The speed of propagation of these waves is proportional to the size of the disturbance and to the rotation rate (Greenspan, 1968). The size of the disturbance is approximately constant between the three rotation rates — the boundary layer thickness (δ_{99}) varies by approximately 30% for the three rotation rates. Thus, assuming that the growth of the boundary layer is linear, it can be shown that the downstream location at which the waves originating from the boundary reach the center should vary approximately as $\Omega^{-\frac{1}{2}}$. This is consistent with the behavior seen in figure 5.

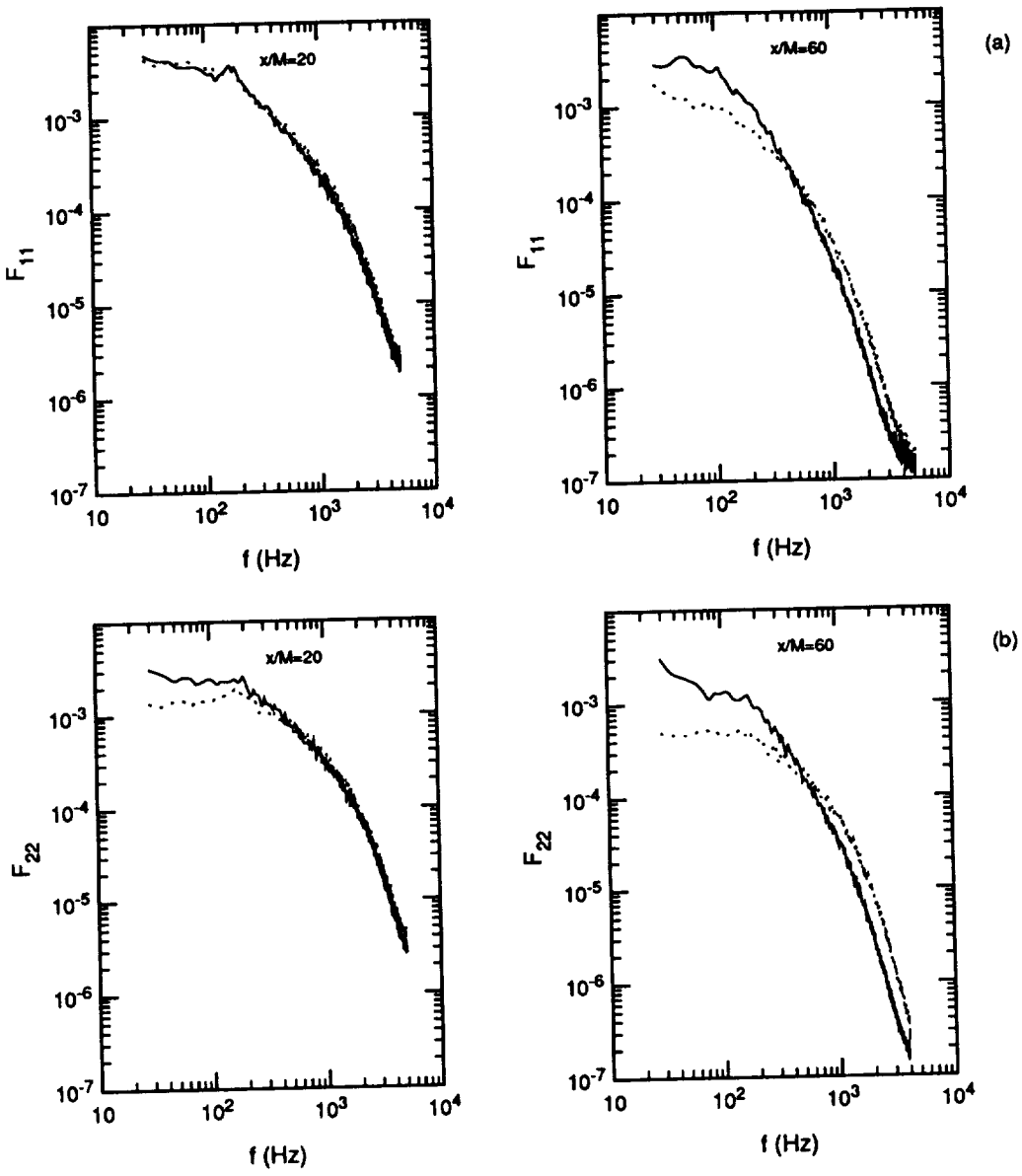

FIGURE 4. Comparison of a) u-spectra (F_{11}) and b) v-spectra (F_{22}) with and without rotation. ——, $\Omega = 126 rad/s$; and ····· , $\Omega = 0 rad/s$. The vertical scale is arbitrary.

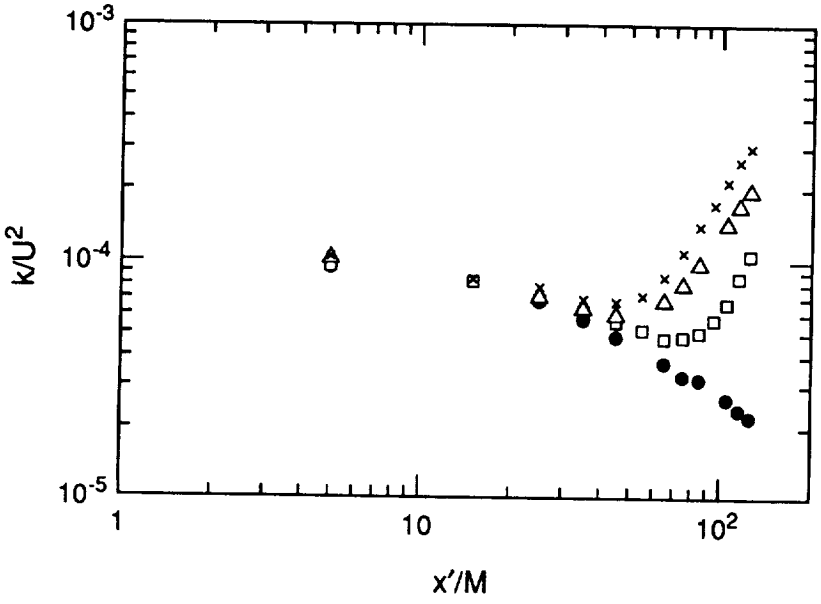

FIGURE 5. Behavior of the background fluctuations for different rotation rates. • $\Omega = 0$; □ $\Omega = 53 rad/s$; △ $\Omega = 93 rad/s$; and × $\Omega = 126 rad/s$. (x' denotes the distance from the start of the test section.)

4.2 Non-axisymmetric turbulence

A number of different mono-planar grids with rectangular bars of various aspect ratios were tested in an effort to generate non-axisymmetric homogeneous turbulence, without much success. We finally decided to use a bi-planar grid to generate homogeneous nearly isotropic turbulence and modify it with an array of vanes, placed within the rotating section, to introduce the non-axisymmetry. A schematic view of this arrangement is shown in figure 6. (Note that y now denotes the direction perpendicular to the vanes and z is parallel to the vanes.) Various chord sizes, (c), and vane spacings, (d), were tried, and it was found that a spacing of 1.5cm and a chord size of 1.27cm yielded the best results with the 1cm mesh grid. Even with this optimal configuration, the resulting non-axisymmetry was not large — $\overline{w^2}$ was at most 30% larger than $\overline{v^2}$.

Figure 7 shows the variation of the principal Reynolds stresses in the y and z directions at $x/M = 25$ and $x/M = 105$ for the case without rotation. We see that the flow is reasonably homogeneous in the core region. The smaller x/M corresponded to a distance of 10 vane spacings from the vane array, thus, in those measurements, the uniformity is better in the z direction than in the y direction.

The evolution of the normalized variances $\overline{u^2}/U^2$, $\overline{v^2}/U^2$ and $\overline{w^2}/U^2$, is shown in figure 8 with and without rotation. The background turbulence levels shown in figure 5 were subtracted in each case. This caused the a drop in variance of

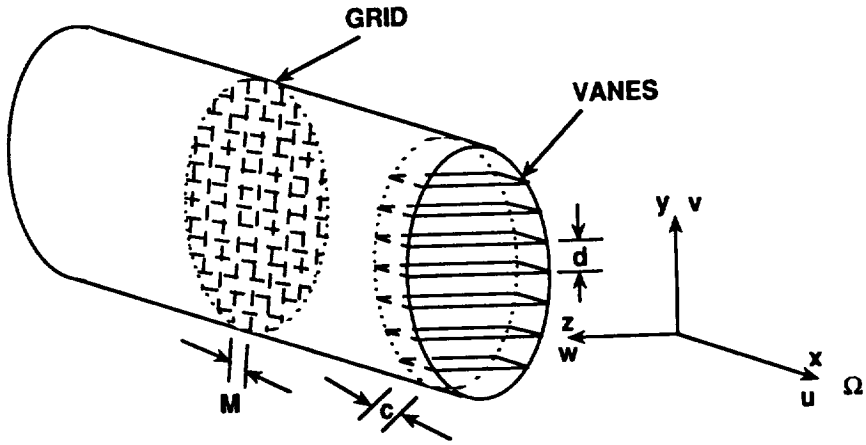

FIGURE 6. Schematic view of the non-axisymmetric-turbulence generator.

approximately 20% in the worst case (largest x/M), but the qualitative features of the curves remained unchanged. The various turbulence parameters corresponding to these flows are given in table 2. Just as in the axisymmetric case, the decay is much slower in the presence of rotation. We also note that while $\overline{v^2}$ and $\overline{w^2}$ remain distinct in the non-rotating case, they are nearly equal in the rotating case.

(x/M)	$k\ (m^2/s^2)$	$\epsilon\ (m^2/s^3)$	$l(cm)$	$\lambda\ (cm)$	Re_λ
20	0.178	11.49	0.66	0.17	39.6
60	0.037	0.80	0.9	0.30	32.4
100	0.019	0.26	1.04	0.38	30.0

TABLE 2a: Turbulence parameters for $M = 1cm$, $\Omega = 0$ and $U \approx 9.2\ m/s$.

(x/M)	$k\ (m^2/s^2)$	$\epsilon\ (m^2/s^3)$	$l(cm)$	$\lambda\ (cm)$	Re_λ	Ro_λ
20	0.17	7.96	0.87	0.19	42.5	1.92
60	0.056	0.9	1.49	0.26	45.3	.64
100	0.037	0.37	1.91	0.32	47.7	0.41

TABLE 2b: Turbulence parameters for $M = 1cm$, $\Omega = 93\ rad/s$ and $U \approx 9.3\ m/s$.

In both the flows, all six Reynolds stresses were measured. In the absence of rotation, this was achieved by choosing four orientations of the vanes such that the instantaneous cross stream velocity measured was $(w - v)/\sqrt{2}$, w, $(w + v)/\sqrt{2}$

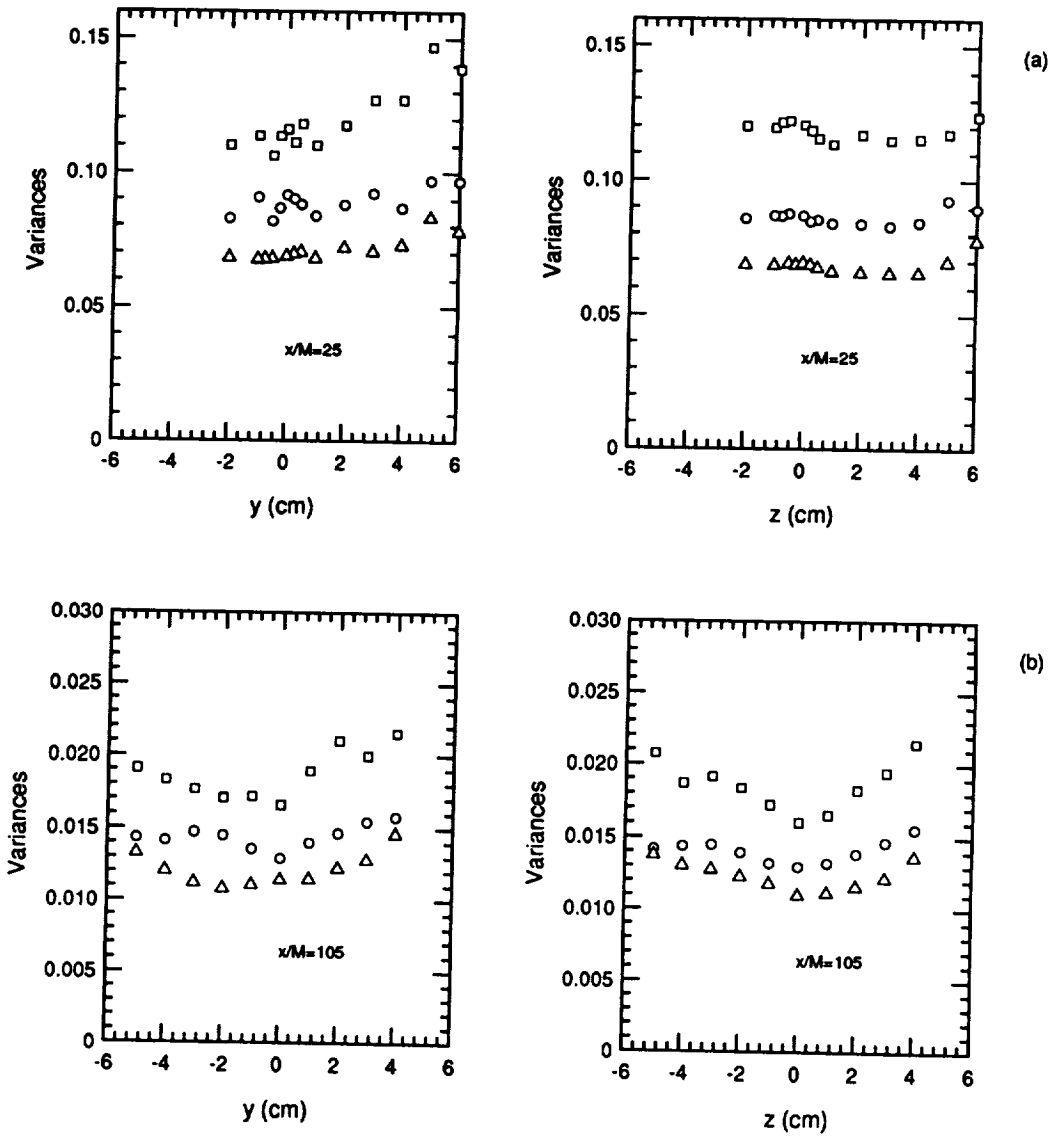

FIGURE 7. Variation of the velocity variances in the transverse plane (non-axisymmetric turbulence). a) $x/M = 25$ and b) $x/M = 105$. The symbols are: □ $\overline{u^2}$; △ $\overline{v^2}$; and ○ $\overline{w^2}$.

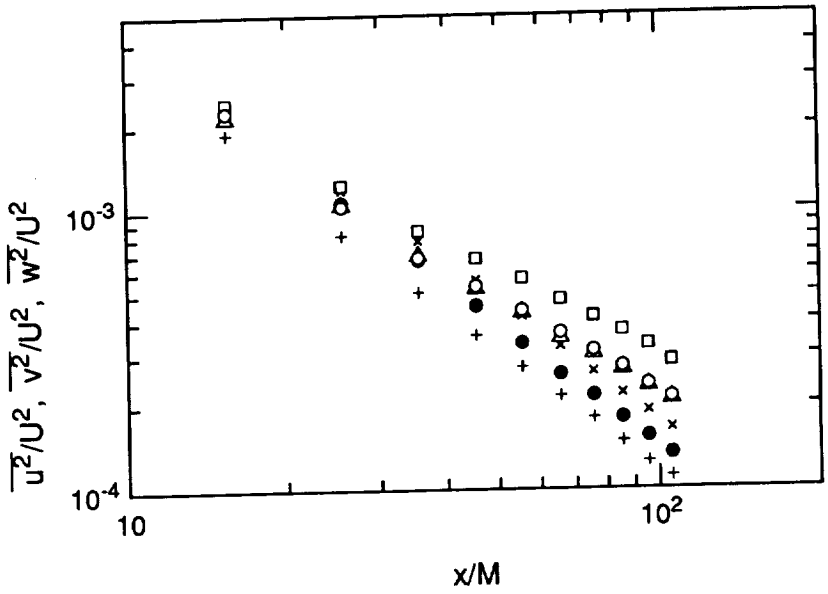

FIGURE 8. Evolution of the velocity variances (non-axisymmetric turbulence).The symbols are:1) $\Omega = 93 rad/s$, □ $\overline{u^2}/U^2$; △ $\overline{v^2}/U^2$; ○ $\overline{w^2}/U^2$ and 2) $\Omega = 0$, × $\overline{u^2}/U^2$; + $\overline{v^2}/U^2$; • $\overline{w^2}/U^2$

and v respectively. In the rotating case, the stresses in the transverse plane were obtained by fitting sine functions to phase-locked averages. This procedure is shown in figure 9. (Here, z lags the trigger by 33°, thus $\overline{w^2}$ is obtained when θ is 33° and $\overline{v^2}$ corresponds to θ of 123°.) For comparison, a similar distribution obtained from the axisymmetric case is also shown. The data in figure 9a are clearly well represented by the best-fit sine curve with a period of 180°, while the data in figure 9b do not exhibit any such trend. The larger scatter in figure 9b is due to the fact that a smaller number of samples was used in computing these averages.

The evolution of $\overline{w^2}/\overline{v^2}$, the ratio of the principal stresses in the transverse plane, σ_1^2/σ_2^2, and $2\overline{u^2}/(\overline{v^2}+\overline{w^2})$ are shown in figure 10. Figure 10a shows the non-rotating case. Here σ_1^2/σ_2^2 increases to approximately 1.3 initially, then decays to approximately 1.2 and then remains nearly constant. Further, σ_1^2/σ_2^2 is almost identical to $\overline{w^2}/\overline{v^2}$ throughout, indicating that the principal directions remain approximately fixed. The ratio $2\overline{u^2}/(\overline{v^2}+\overline{w^2})$ also increases initially and then remains nearly constant. The overall behavior is consistent with that observed in grid-turbulence, wherein the tendency towards isotropy is slight for the small anisotropies encountered (Comte-Bellot & Corrsin, 1966).

The evolution is quite different in the presence of rotation as shown in figure 10b. Here, $\overline{w^2}$ and $\overline{v^2}$ are nearly equal throughout. However, the principal stresses are not equal and their ratio increases initially to approximately 1.2 before decaying to a value close to 1 at the end of the test section. Barring the last data point, the value of $2\overline{u^2}/(\overline{v^2}+\overline{w^2})$ seems to increase steadily with downstream distance.

The behavior described above is summarized in figure 11, where the evolution

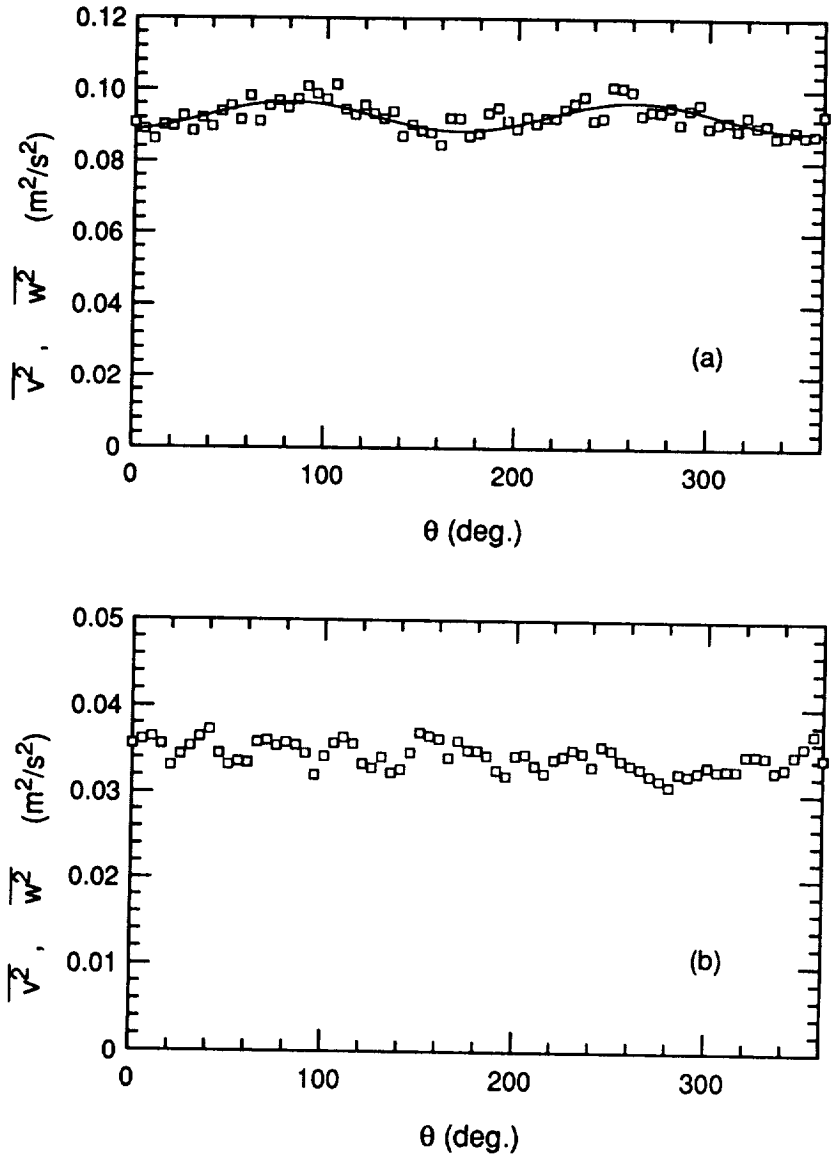

FIGURE 9. Typical plots of the variation of the transverse velocity component with angle. a) Non-axisymmetric turbulence, $\Omega = 93 rad/s$ and b)axisymmetric turbulence, $\Omega = 126 rad/s$. The solid line in figure a) is a best fit sinusoid.

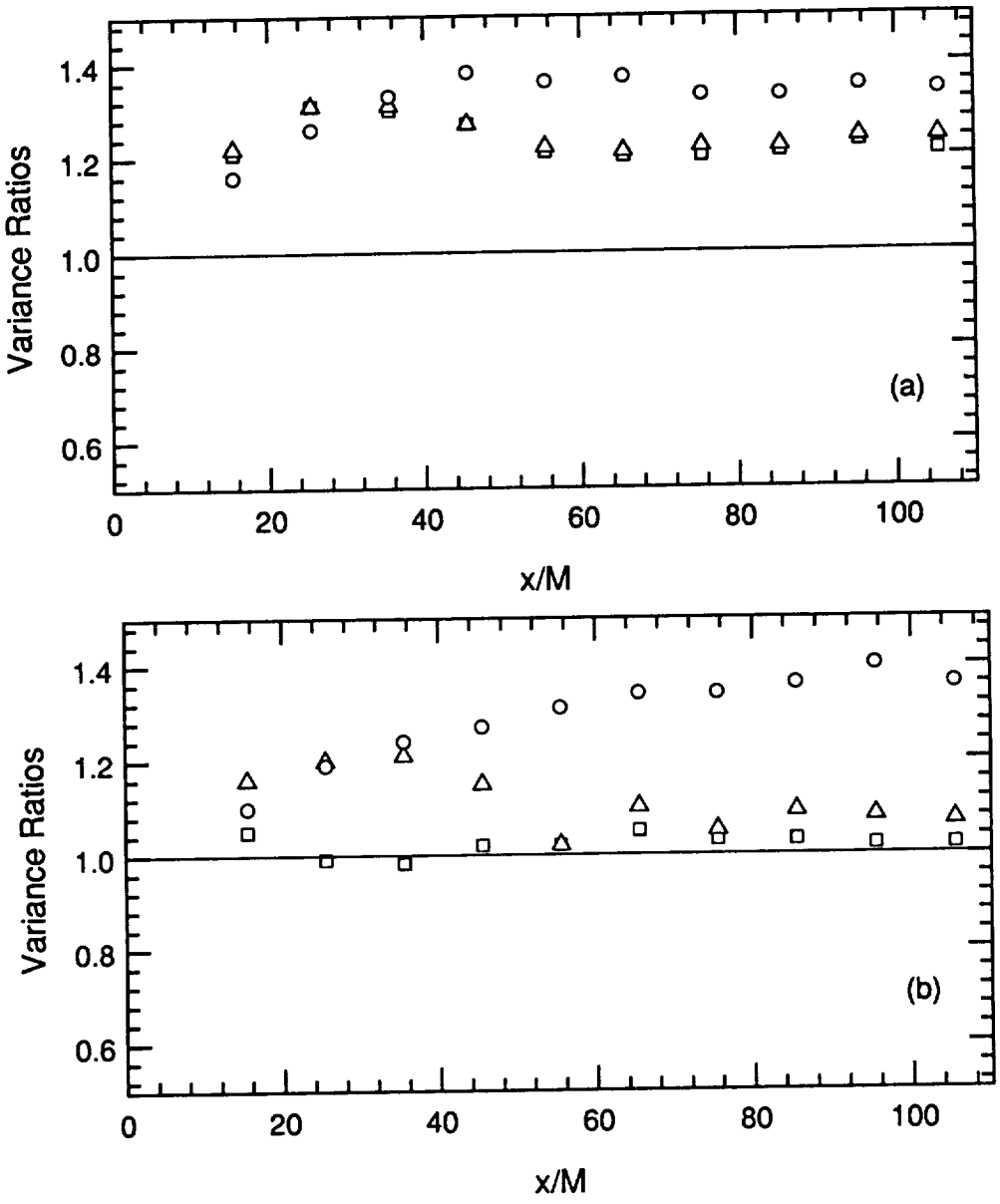

FIGURE 10. Evolution of the variance ratios (non-axisymmetric turbulence). a) $\Omega = 0$ and b) $\Omega = 93 rad/s$. The symbols are : o $2\overline{u^2}/(\overline{v^2 + w^2})$; □ $\overline{w^2}/\overline{v^2}$; and △ σ_1^2/σ_2^2.

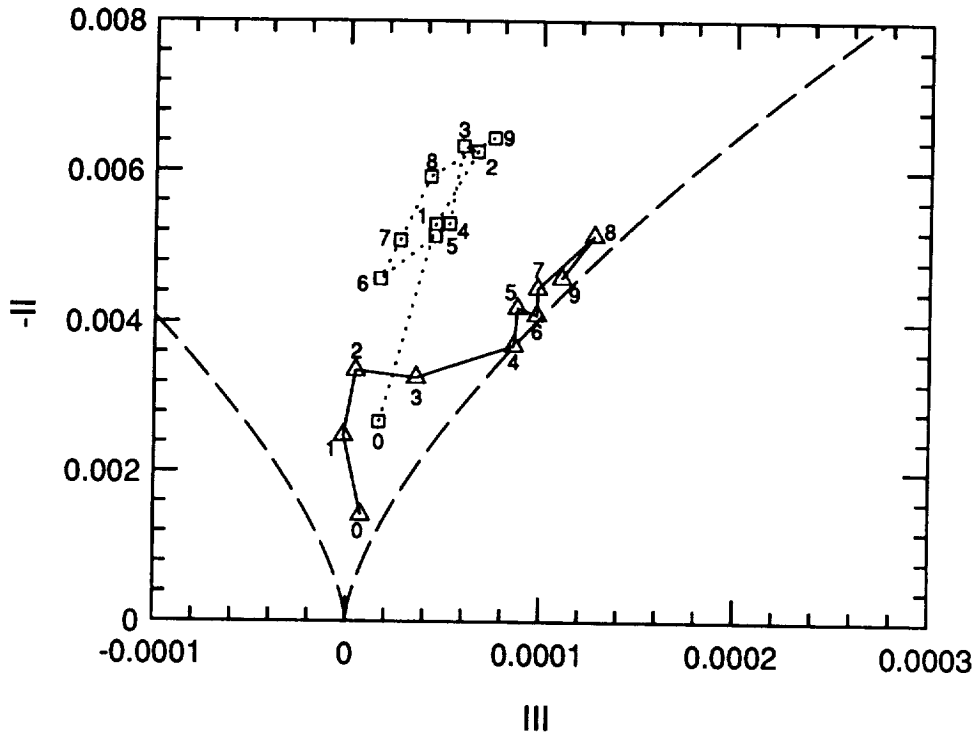

FIGURE 11. Evolution of non-axisymmetric turbulence on the II, III plane. □ $\Omega = 0$ and △ $\Omega = 93 rad/s$. The numbers alongside the symbols indicate the downstream position starting with $x/M = 10$ and ending at $x/M = 100$. (Note, the numbers start at 0 and end at 9.)

is studied on the II, III map. (II and III refer to the second and third invariants of the anisotropy tensor $b_{ij} \equiv (\overline{u_i u_j} - \overline{u_i u_i}\delta_{ij}/3)/\overline{u_i u_i}$, respectively.) We note that the values of II and III are very small and obtained from small differences of the variances, thus the error bars are very large. Indeed, the data points changed by as much 25% between different runs and for slightly different (the changes in the variances were less than 1%) hot-wire calibrations. However, the topological features of the curves remained unchanged, and we are confident that the qualitative behavior has been captured quite accurately. We see that in the absence of rotation there is initial region of development wherein the curve rapidly moves away from the isotropic point, after which the data points cluster around $(5\text{x}10^{-5}, -5.5\text{x}10^{-3})$. With rotation, however, after the initial departure from the isotropic point, the curve swings sharply towards the axisymmetry line and, except for the last data point, seems to climb up along it.

The equations governing the evolution of the Reynolds stresses in a co-ordinate system rotating with the swirl generator (assuming homogeneity) are:

$$U\frac{\partial\overline{u^2}}{\partial x} = \frac{2}{\rho}\overline{p\frac{\partial u}{\partial x}} + 2\nu\overline{\frac{\partial u}{\partial x_j}\frac{\partial u}{\partial x_j}}, \tag{2}$$

$$U\frac{\partial\overline{v^2}}{\partial x} = \frac{2}{\rho}\overline{p\frac{\partial v}{\partial y}} + 4\Omega\overline{vw} + 2\nu\overline{\frac{\partial v}{\partial x_j}\frac{\partial v}{\partial x_j}}, \tag{3}$$

$$U\frac{\partial\overline{w^2}}{\partial x} = \frac{2}{\rho}\overline{p\frac{\partial w}{\partial z}} - 4\Omega\overline{vw} + 2\nu\overline{\frac{\partial w}{\partial x_j}\frac{\partial w}{\partial x_j}}, \tag{4}$$

and

$$U\frac{\partial\overline{vw}}{\partial x} = \frac{1}{\rho}\overline{p\left(\frac{\partial v}{\partial z} + \frac{\partial w}{\partial y}\right)} + 2\Omega(\overline{w^2} - \overline{v^2}) + 2\nu\overline{\frac{\partial v}{\partial x_j}\frac{\partial w}{\partial x_j}}. \tag{5}$$

If we look only at the terms containing Ω, then we see that initially $\overline{vw}$ increases (since $\overline{w^2}$ is larger than $\overline{v^2}$), and this causes $\overline{v^2}$ to increase and $\overline{w^2}$ to decrease, thereby causing them to equalize as the data shows. We can go one step further and evaluate the principal stresses (in the transverse plane) as:

$$\sigma_1^2 = \frac{\overline{w^2} + \overline{v^2}}{2} + \left(\left(\frac{\overline{w^2} - \overline{v^2}}{2}\right)^2 + \overline{vw}^2\right)^{\frac{1}{2}}, \tag{6}$$

and

$$\sigma_2^2 = \frac{\overline{w^2} + \overline{v^2}}{2} - \left(\left(\frac{\overline{w^2} - \overline{v^2}}{2}\right)^2 + \overline{vw}^2\right)^{\frac{1}{2}}, \tag{7}$$

We can then write the evolution equations for σ_1^2 and σ_2^2 by differentiating both sides of equations (6) and (7) by x and substituting for the terms on the r.h.s. from equations (3), (4), and (5) (these are presented in the Appendix). It can then be shown that in the evolution equations for σ_1^2 and σ_2^2, the terms containing Ω cancel out exactly! Thus, we see that the terms proportional to Ω in equations (3), (4), and (5) are responsible only for the rotation of the principal directions, while the principal stresses are equalized by the pressure-strain terms which are subtly but significantly modified by rotation.

5. Future plans

We now have a fairly good understanding of the capabilities of the preliminary rig. The next step would be to study the development of both axisymmetric and non-axisymmetric turbulence over a range of Reynolds numbers and Rossby numbers by varying the mesh size and rotation rate. Two-point measurements would also be made to compare $R_{33}(r,0,0)$ and $R_{33}(0,r,0)$ so as to address the tendency towards two-dimensionality at intermediate Rossby numbers seen in the single point measurements of Jacquin *et al.*(1990).

5.1 Recommendations for rig II

Under rapid rotation, grid-generated turbulence decays approximately as

$$k = A\,U^2\left(\frac{x}{M}\right)^{-1}, \tag{8}$$

thus the dissipation term evolves as

$$\epsilon = \frac{A\,U^3}{M}\left(\frac{x}{M}\right)^{-2}. \tag{9}$$

Thus Re_λ and Ro_λ are given by

$$Re_\lambda = \sqrt{\frac{20A}{3\nu}}\,(U\,M)^{\frac{1}{2}}, \tag{10}$$

and

$$Ro_\lambda = \sqrt{\frac{A}{15\nu}}\,\frac{U^{\frac{3}{2}}\,M^{\frac{1}{2}}}{\Omega\,x}. \tag{11}$$

As noted in section 4.2, the maximum uncontaminated length of the test section is proportional to $\Omega^{\frac{1}{2}}$. More specifically, one can write

$$x_{max} \approx \sqrt{\frac{R\,U}{C\,b\,\Omega}}, \tag{12}$$

where R is the radius of the duct, b is the rate of growth of the boundary layer ($\partial\delta/\partial x$, assumed to be constant with x and ω), and C is a constant. Thus*,

$$(Ro_\lambda)_{min} = \frac{1}{2}\sqrt{\frac{A\,C\,b}{15\nu}}\,(U\,M)^{\frac{1}{2}}. \tag{13}$$

Hence, if we want to lower the Ro_λ for a fixed Re_λ (i.e. fixed UM), we have to reduce b. One option would be to spin the test section also — the data indicate that at the highest rotation rate examined, the boundary layer is twice as thick as in the non-rotating case. However, the gains from this method are more than offset by the complexity in making measurements. With hot-wires, the probes would have to be mounted on a sting extending the length of the test section, and this would definitely contaminate the measurements. With LDV systems, one would either need an optically-perfect transparent test section or a system with a focal length in excess of 1m (an LDV system with a 10-20m focal length is described in Reinath,

* Note that we have used the constraint $(\Omega R)/U \leq 1$, since, if this is violated, the vortex exiting the test-section could break down (Dellenback *et al.*,1988), thus generating a disturbance with a sufficiently large scale and, therefore, sufficiently large propagation velocity as to cause disturbances upstream of the exit. This is confirmed by the data of Jacquin *et al.*, (1990) for very large Ω.

1989, but it is expensive and shows more scatter than hot-wire measurements). The other option is to reduce the growth of the boundary layers through suction. Since the peripheral pressure is increased by rotation, one could expect a moderate reduction in boundary layer growth by simply making the test-section walls porous and perhaps adding a pressure drop device like a honeycomb at the end of the test-section to increase the bulk gauge pressure inside the test-section. However, to permit better control, the test section would have to be enclosed in another chamber connected to a fan which would provide the suction. Although increasing the diameter would not yield much benefit in terms of Rossby number, the facility would lend itself more readily to two-point measurements and would also permit us to examine higher *Re* flows, albeit at the price of higher Rossby numbers.

Additionally, although we have been reasonably successful in generating non-axisymmetric homogeneous turbulence, the departures from axisymmetry are not large. One could conceivably achieve larger departures by using two sets of vanes in tandem (experiments on drag reduction with LEBU's indicate that the optimal configuration is one with two plates in tandem, separated by approximately 7 chord widths, Savill, 1989). Thus, the rotating section should be long enough to permit such an arrangement.

Acknowledgements

I wish to thank Prof. Bradshaw for his helpful comments and suggestions through all the stages of this work, and in particular, for suggesting the use of a 'one-dimensional honeycomb' to generate non-axisymmetric homogeneous turbulence.

Appendix

The principal stresses are given by

$$\sigma_{1,2}^2 = \frac{\overline{w^2}+\overline{v^2}}{2} \pm \left(\left(\frac{\overline{w^2}-\overline{v^2}}{2}\right)^2 + \overline{vw}^2\right)^{\frac{1}{2}}. \tag{A1}$$

Thus,

$$\begin{aligned} U\frac{\partial \sigma_{1,2}^2}{\partial x} &= \frac{U}{2}\frac{\partial}{\partial x}\left(\overline{v^2}+\overline{w^2}\right) \pm \frac{U\left[\frac{1}{4}\left(\overline{w^2}-\overline{v^2}\right)\left(\frac{\partial \overline{w^2}}{\partial x}-\frac{\partial \overline{v^2}}{\partial x}\right)+\overline{vw}\,\frac{\partial \overline{vw}}{\partial x}\right]}{\left(\left(\frac{\overline{w^2}-\overline{v^2}}{2}\right)^2+\overline{vw}^2\right)^{\frac{1}{2}}} \\ &\approx \frac{1}{\rho}\overline{p\left(\frac{\partial v}{\partial y}+\frac{\partial w}{\partial z}\right)} + \nu\overline{\left(\frac{\partial v}{\partial x_j}\frac{\partial v}{\partial x_j}+\frac{\partial w}{\partial x_j}\frac{\partial w}{\partial x_j}\right)} \\ &\quad \pm \frac{\left(\overline{w^2}-\overline{v^2}\right)\left[\frac{1}{2\rho}\left(\overline{p\frac{\partial w}{\partial z}}-\overline{p\frac{\partial v}{\partial y}}\right)\right]+\frac{\overline{vw}}{\rho}\overline{p\left(\frac{\partial v}{\partial z}+\frac{\partial w}{\partial y}\right)}}{\left(\left(\frac{\overline{w^2}-\overline{v^2}}{2}\right)^2+\overline{vw}^2\right)^{\frac{1}{2}}}. \end{aligned} \tag{A2}$$

REFERENCES

BARDINA, J., FERZIGER, J. H. & ROGALLO, R. S. 1985 Effect of rotation on isotropic turbulence: computation and modeling. *J. Fluid Mech.* **154**, 321-336.

COMTE-BELLOT, G. & CORRSIN, S. 1966 The use of a contraction to improve the isotropy of grid generated turbulence. *J. Fluid Mech.* **25**, 657-682.

DELLENBACK, P. A., METZGER, D. E. & NEITZEL, G. P. 1988 Measurements in turbulent swirling flow through an abrupt axisymmetric expansion. *AIAA Journal.* **26**, No.6, 669-681.

GREENSPAN, H. P. 1968 *The theory of rotating fluids.* Cambridge University Press.

HOPFINGER, E. J., BROWAND, F. K. & GAGNE, Y. 1982 Turbulence and waves in a rotating tank. *J. Fluid Mech.* **125**, 505-534.

IBBETSON, A. & TRITTON, D. 1975 Experiments on turbulence in a rotating fluid. *J. Fluid Mech.* **68**, 639-672.

JACQUIN, L., LEUCHTER, O. & GEFFROY, P. 1988 Experimental study of homogeneous turbulence in the presence of rotation. *Turbulent Shear Flows 6*,ed. by L.T.S. Bradbury *et al.*, 46-57.

JACQUIN, L., LEUCHTER, O., CAMBON, C. & MATHIEU, J. 1990 Homogeneous turbulence in the presence of rotation. *J. Fluid Mech.* In press.

PHILLIPS, O. M. 1963 Energy transfer in rotating fluids by reflection of inertial waves. *Phys. Fluids.* **6**, 513-520.

REINATH, M. S. 1989 A long-range laser velocimeter for the national full-scale aerodynamics complex: new developments and experimental application. *NASA TM 101081.*

REYNOLDS, W. C. 1989 Effects of rotation on homogeneous turbulence. *Proc.* $10^{\underline{th}}$ *Australian Fluid Mech. Conf., University of Melbourne, Dec. 11- 15.*

SAVILL, A. M. 1989 The effect of an adverse pressure gradient on the drag reduction performance of manipulators. *Int. J. Heat and Fluid Flow.* **10**, No. 2, 118-124.

SPEZIALE, C. G., MANSOUR, N. N. & ROGALLO, R. S. 1987 Decay of turbulence in a rapidly rotating frame. *In Studying Turbulence Using Numerical Simulation Databases.* Proc. 1987 Summer Program, Center for Turbulence Research, Stanford U., Report CTR-S87,*205-212.*

TRAUGOTT, S. C. 1958 Influence of solid-body rotation on screen-produced turbulence. *NACA Tech. Note 4135.*

WIGELAND, R. A. & NAGIB, H. M. 1978 Grid-generated Turbulence with and without rotation about the streamwise direction. *IIT Fluids and Heat Transfer Rep.* **R78-1**, Illinois Inst. of Tech., Chicago, Illinois.

Phase-averaged measurements of perturbations introduced into boundary layers

By J. H. Watmuff

1. Motivation and objectives

Large-scale structures in turbulent and transitional wall-bounded flows make a significant contribution to the Reynolds stress and turbulent energy. The objective of this study is to examine the behavior of these structures. Small perturbations are introduced into a laminar and a turbulent boundary layer to trigger the formation of large-scale features. Both flows use the same inlet unit Reynolds number, and they experience the same pressure gradient history, i.e. a favorable (FPG) followed by an adverse pressure gradient (APG). The perturbation consists of a small short duration flow repetitively introduced through a hole in the wall located at the C_p minimum. Hot-wire data are averaged on the basis of the phase of the disturbance, and automation of the experiment has been used to obtain measurements on large spatially dense grids. In the turbulent boundary, the perturbation evolves into a vortex loop which retains its identity for a considerable streamwise distance. In the laminar layer, the perturbation decays to a very small magnitude before growing rapidly and triggering the transition process in the APG. The "time-like" animations of the phase-averaged data are used to gain insight into the naturally occurring physical mechanisms in each flow.

2. Background

2.1 Design of the DNS validation boundary layer experiment

The pressure gradient was specially designed to create an APG turbulent boundary layer with a high enough R_e to sustain turbulence and allow accurate experimental measurements, but low enough for Direct Numerical Simulations (DNS) using a newly developed "fringe" method by Spalart. The design incorporates a region of FPG just downstream of the trip (experiment) or inflow boundary (DNS) to let the flow develop without unduly increasing the local R_e. The pressure-gradient parameter β then rises from about about -0.3 to about +2 within the region accessible to the simulation. The APG flow is far from "equilibrium" and, therefore, represents a significant challenge for DNS. The streamwise extent of the measurements exceeds the current capabilities of direct simulations, and the results are also serving as a useful data base for Reynolds-averaged boundary layer prediction methods. The properties of the unperturbed layer have been documented by Watmuff (1989).

2.2 Automation of the experiment

In the DNS validation experiment, closely spaced profiles were required in the FPG to examine the asymptotic approach to self-similarity and in APG where there

is rapid growth with streamwise distance. A sophisticated high-speed computer-controlled 3D probe positioning system was integrated into the wind tunnel. A considerable investment in both hardware and software enabled all experimental functions (including crossed-wire calibration) to be totally automated under computer control. During the course of the DNS validation experiment, the operation of the facility was refined to the point where experiments could be performed continuously (24 hours a day) over several weeks without manual supervision.

2.3 Phase-averaging technique

An illustrative way of obtaining information about the large-scale motions of turbulent flows is to take averages on the basis of phase. For example, Reynolds and Hussain (1972) used a phase-averaging technique to look at the large-scale motions in a turbulent boundary layer which was excited by vibrating ribbons. Kovaznay, Fujita and Lee (1974) repeatedly produced a turbulent puff from a loud speaker and conditionally sampled the data on the basis of phase. More recently, Cantwell and Coles (1984) and Perry and Watmuff (1981) pioneered flying the hot-wire technique for examining the large-scale features in turbulent wakes. The primary motivation for flying the wires is to avoid hot-wire directional ambiguity in regions of large turbulence intensity or reversed flow. Another advantage of flying the wires is that the data can be obtained on spatially dense grids, allowing large-scale features to be examined in detail. This latter capability can also be exploited using the automated facility, i.e. the phase-averaging technique can applied to an extremely large number of grid points by performing the measurements on a point-by-point basis.

3. A vortex loop introduced into the APG turbulent layer

3.1 Experimental technique

Phase-averaged (64 phase-interval) velocity and Reynolds stress measurements have been made in the DNS validation boundary layer based on the phase of a small disturbance repetitively introduced into the flow. The disturbance consists of a short duration flow from a 0.6mm diameter hole located on the centerline of the test plate at the C_p minimum. The flow was initiated by a rubber diaphragm driven by a small electromagnetic shaker. By examining data taken at single points while tuning the duration, magnitude, and frequency (repetition rate) of the flow from the hole, it was discovered that even with a relatively small perturbation, phase-averaged data could be extracted 0.45m downstream, although the washout was quite severe and some smoothing was required. The magnitude and duration (3.5 msec) of the disturbance were fixed such that the flow from the hole penetrated only to about 8mm into the boundary layer ($\delta \approx$ 12mm). A frequency of 40Hz ensured that the streamwise distance between the regions influenced by the disturbance was large enough (approximately 0.15m) to prevent mutual interaction during the downstream motion.

Measurements have been obtained at over 5000 grid points on the centerline plane and five cross-stream planes. The data were reduced on-line and consist of phase-averaged velocities, Reynolds stresses at constant phase and temporal mean

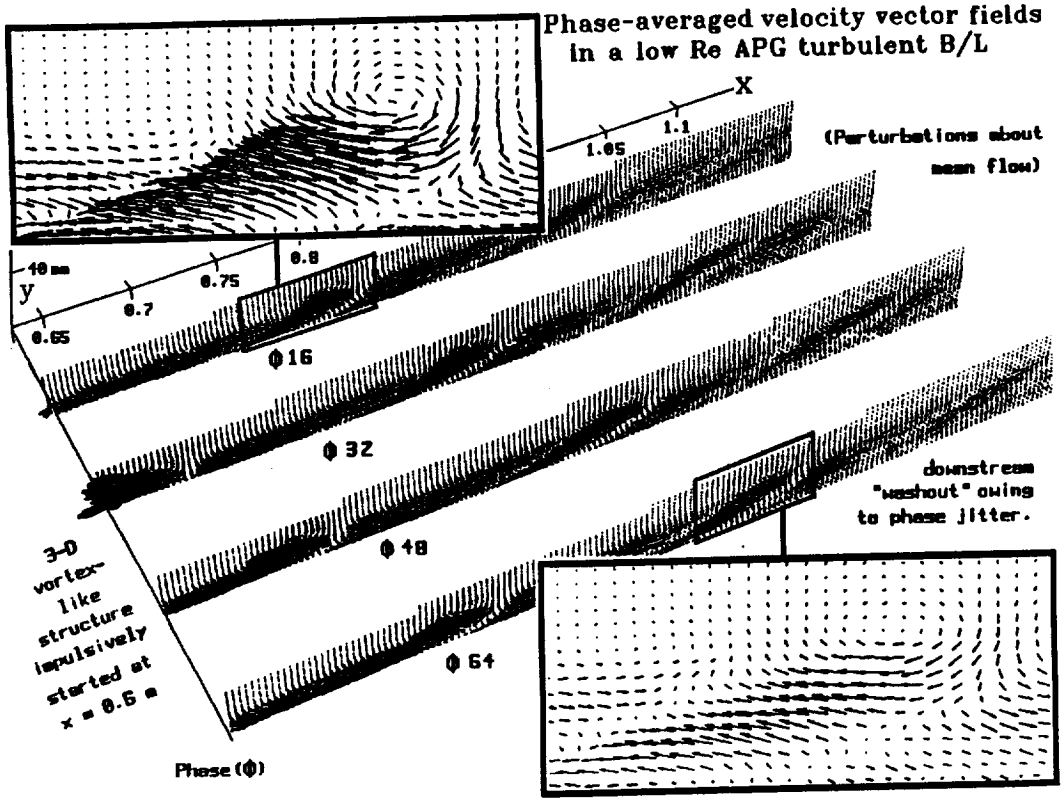

FIGURE 1. Phase-averaged perturbation velocity vector fields in centerline plane of adverse pressure gradient turbulent boundary layer.

velocity, and Reynolds stresses which were all calculated from the same raw hot-wire voltages. Over 1.5×10^5 samples were used for the averages (2400 per phase interval) at each grid point over a sampling period of 60 seconds. About 300 hours of experimental run-time of the automated system were required.

3.2 Interpretation of flow patterns

The velocity vectors in the vicinity of the hole have a "mushroom" shape, characteristic of a vortex-ring. About 50mm downstream of the hole, the strength of the phase-averaged streamwise velocity perturbations is quite small, i.e. about 3% of the local temporal mean velocity. The flow pattern is barely discernible in the streamwise plane when viewed in a frame of reference moving with the perturbations because of the mean shear. However, vortex-like flow patterns appear in the *perturbation* velocity vector fields for the centerline plane as shown in figure 1. The four (out of a total of sixty-four) vector fields are plotted using phase as the third coordinate. The perturbation flow pattern occupies the full height of the layer. Details can be seen in the two small regions which have been plotted using a larger scale. A thin region trails behind the vortex-like pattern where the gradients of the

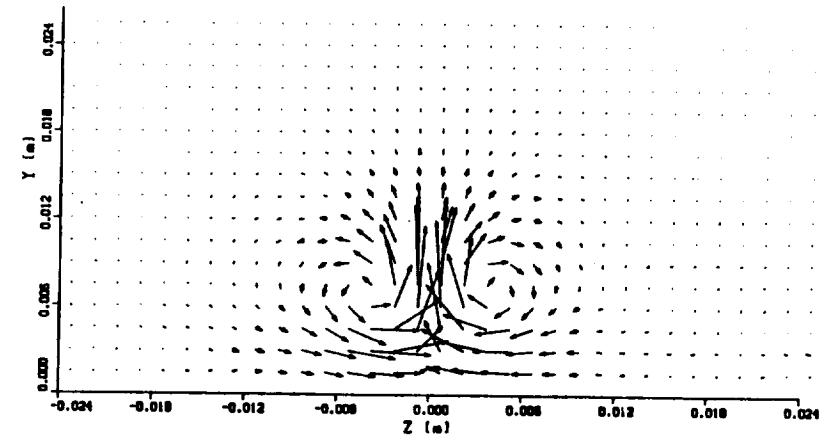

(a)

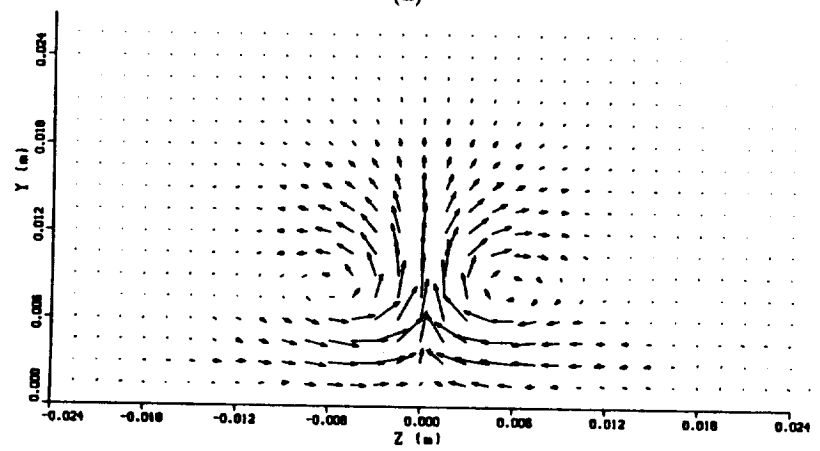

(b)

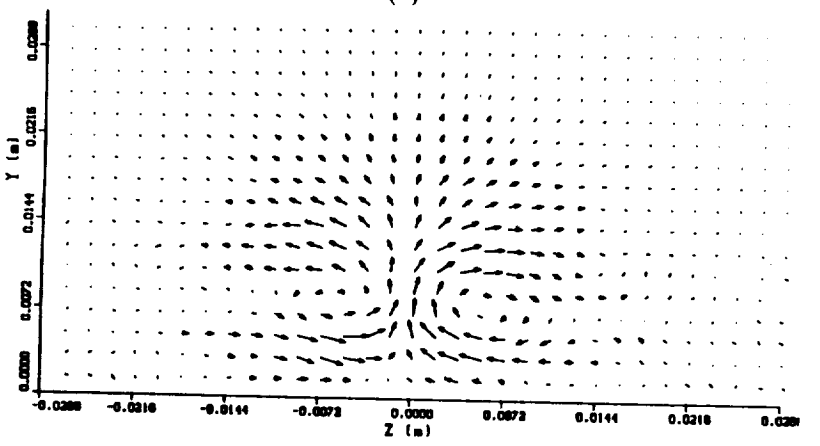

(c)

FIGURE 2. Phase-averaged vectors in spanwise yz-planes located at (a) X=0.651m, (b) X=0.702m, (c) X=0.804m.

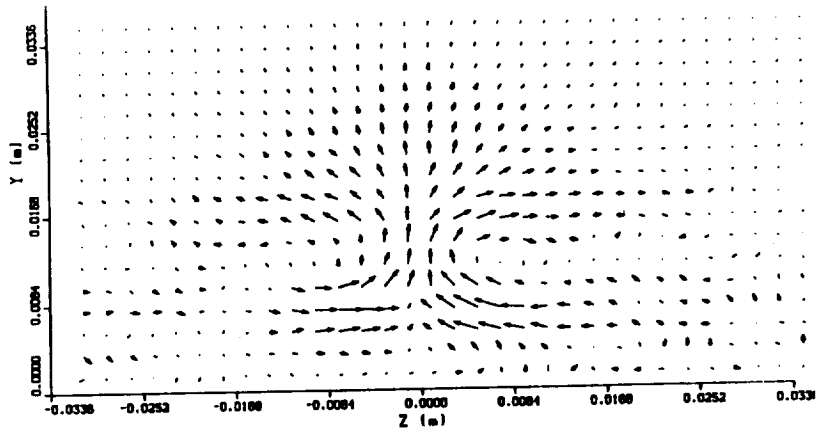

(d)

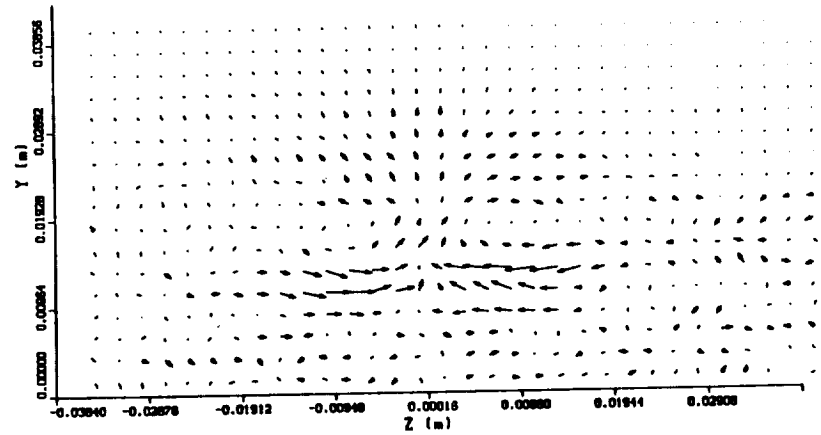

(e)

FIGURE 2. (continued) Phase-averaged vectors in spanwise yz-planes located at (d) X=0.906m (e) X=1.008m.

velocity perturbations are very large. This region is inclined at about 30° to the wall. By about 0.45m downstream of the hole, the strength of the velocity vectors decays to less than 1/2% of the mean velocity owing to phase jitter. However, the same characteristic flow pattern is still discernible in the perturbation vectors, i.e. the loop retains its identity for at least 30δ in the streamwise direction.

The mean shear does not obliterate the pattern in the spanwise planes, and two counter rotating vortex-like motions can be seen in figures 2(a)-(e). Animation of the spanwise vector fields shows that the patterns move apart and towards the wall as the pattern in the streamwise plane passes through. Three-dimensional data have been created by applying Taylor's Hypothesis to each of the spanwise planes. Contours of perturbation vorticity magnitude corresponding to the second spanwise plane are shown in figure 3. The contours provide convincing evidence that the perturbation has evolved into a vortex-loop.

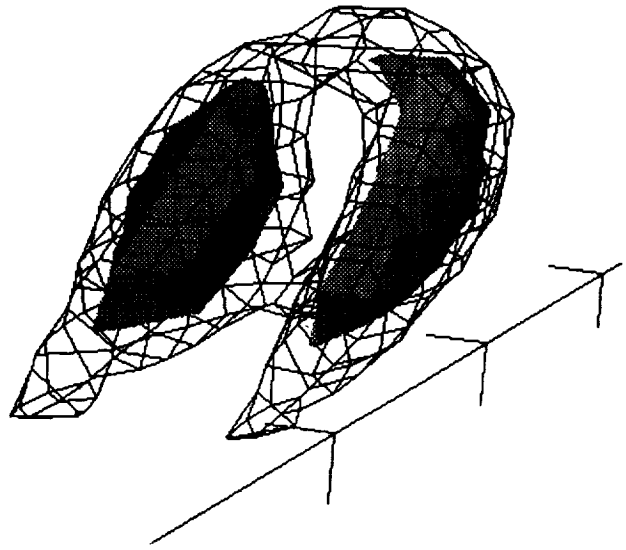

FIGURE 3. Contour surfaces of vorticity magnitude obtained by applying Taylor's Hypothesis to spanwise plane at X=0.702m in turbulent boundary layer.

3.3 Other results

Spanwise Preston tube C_f measurements are within $\pm 1.5\%$ whether the impulsive disturbance is on or whether it has been turned off, even very close to the hole. The centerline mean velocity and Reynolds stress profiles are the same (within the experimental uncertainty) except in the vicinity of the hole. Further, the presence of the disturbance does not alter the power spectral density in the region downstream of the hole. A spectrum analyzer set for a 5Hz span centered around the disturbance frequency showed the same spectra even when 256 rms averages were used. These observations suggest that the phase-averaged vortex-loop could be representative of the behavior of naturally occurring vortex-loops in APG turbulent boundary layers.

3.4 Discussion

The observations could act as a guide for the formulation of physical models of boundary layer turbulence. For example, the model of wall turbulence proposed by Perry and Chong (1982) is physical in the sense that distributions of Λ-vortices are used to explain the mean flow, Reynolds shear stress, and turbulence intensities observed in experiments. Turbulence spectra having all the correct properties were derived from the velocity signatures of the potential-flow vortices. Various scenarios were considered in the formulation of the model such as pairing of the Λ-vortices. Another possibility considered by Perry and Chong is one in which the eddy continuously draws vorticity from the viscous sublayer as it moves downstream.

The phase-averaged vortex-loop study tends to support the latter scenario. The sublayer vorticity in the APG decreases by a factor of 2 in the region covered by the phase-averaged measurements. If vortex-loops do continuously draw up sublayer

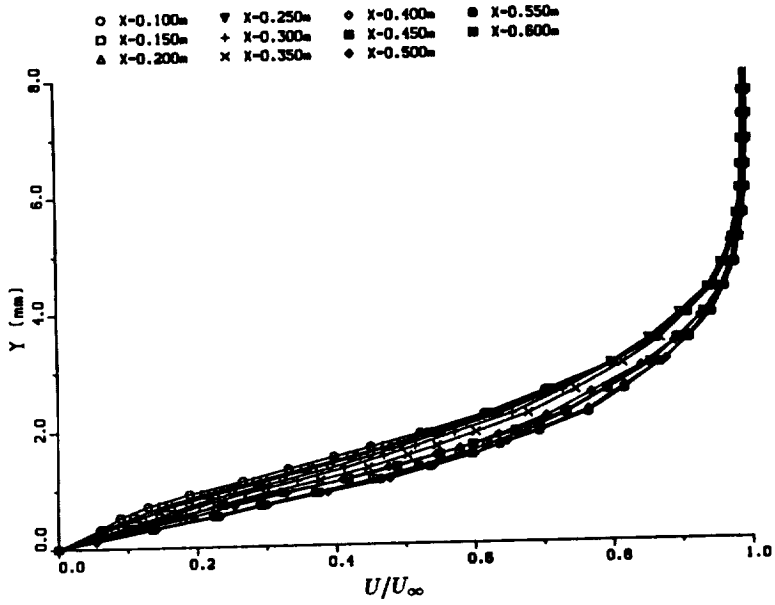

FIGURE 4. Development of laminar velocity profiles in FPG.

vorticity, then the axial vorticity distribution along the loop is likely to increase with wall distance in the APG since the vorticity at greater distances from the wall would have originated from further upstream. The two counter-rotating vortex-like motions in the most downstream spanwise plane are stronger when they are far from the wall, and this is consistent with the above conjecture. Of course, vortex-stretching and other dynamical phenomena would modify the axial vorticity distribution. Nevertheless, increasing axial vorticity of vortex loops with increasing wall distance provides a plausible physical explanation for the bulging of peak values of turbulence intensities away from the wall that are observed in APG layers.

4. Boundary layer transition in an adverse pressure gradient

4.1 Introduction

Emmons (1951) proposed that transition from laminar to turbulent flow occurs through the generation, growth, and amalgamation of turbulent spots. It has been suggested (e.g. Schubauer and Klebanoff 1956) that spots are dynamically similar to turbulent layers, but simpler, so that their study could provide insight into the physical processes occurring within turbulent boundary layers. This suggestion has motivated many investigations into the nature of turbulent spots.

Previous studies have been performed in nominally zero pressure gradients and have used rather large disturbances (e.g. an electric spark as well as flow from a hole in the wall) to force spot formation to occur close to the source of the disturbance. Often, natural spot formation was not observed when the disturbance

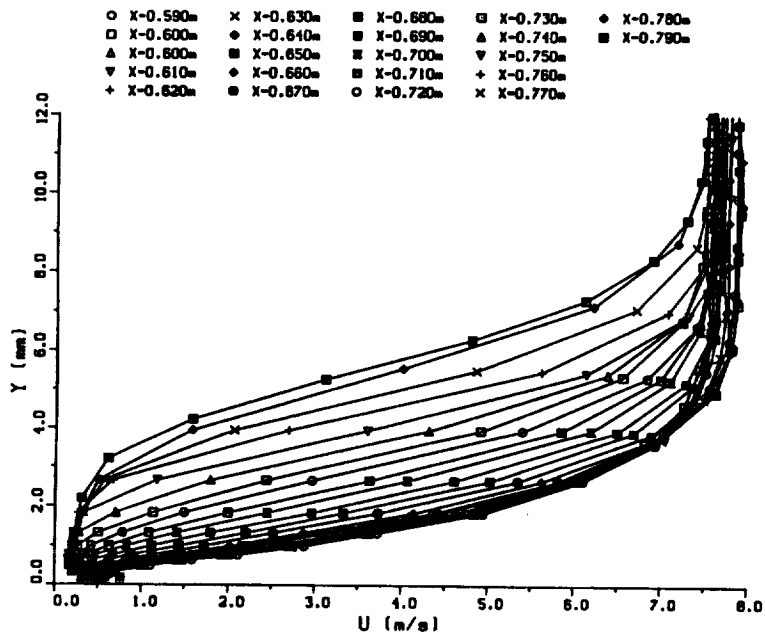

FIGURE 5. Development of laminar velocity profiles in APG.

was removed, even very far downstream, e.g. in the study of Cantwell, Coles and Dimotakis (1978), the unforced layer remained laminar along the entire test section length. Perry, Lim and Teh (1981) observed that too strong a disturbance changes the initial character of a spot, but that it "would look much the same as any other spot" after sufficient development. However, the observations of Perry *et al.* were made for a single location of the disturbance, and measurements were not made, so it is uncertain whether the downstream character of a spot is truly independent of the nature of its formation. Further, it is uncertain whether spots generated in laminar layers which are far from instability are representative of spots that form as part of the natural transition process.

4.2 Experimental technique

Removal of the trip wire while maintaining the same wing-like pressure distribution and inlet unit Reynolds number as in the DNS validation experiment leads to a laminar boundary layer which undergoes natural transition about 0.2m downstream of the C_p minimum. Perry *et al.* reported that attempts to produce identical spots using periodic disturbances failed and suggested that phase-averaged hot-wire measurements would simply result in a "big-eddying-type" of description because of the phase jitter and associated washout. However, examination of hot-wire signals in the vicinity of natural transition in the APG revealed that extremely complex signals could be generated in a very repetitive manner by initiating a short duration flow from the hole located at the C_p minimum (where $\delta \approx 6$mm, $U_\infty \approx 7.5$

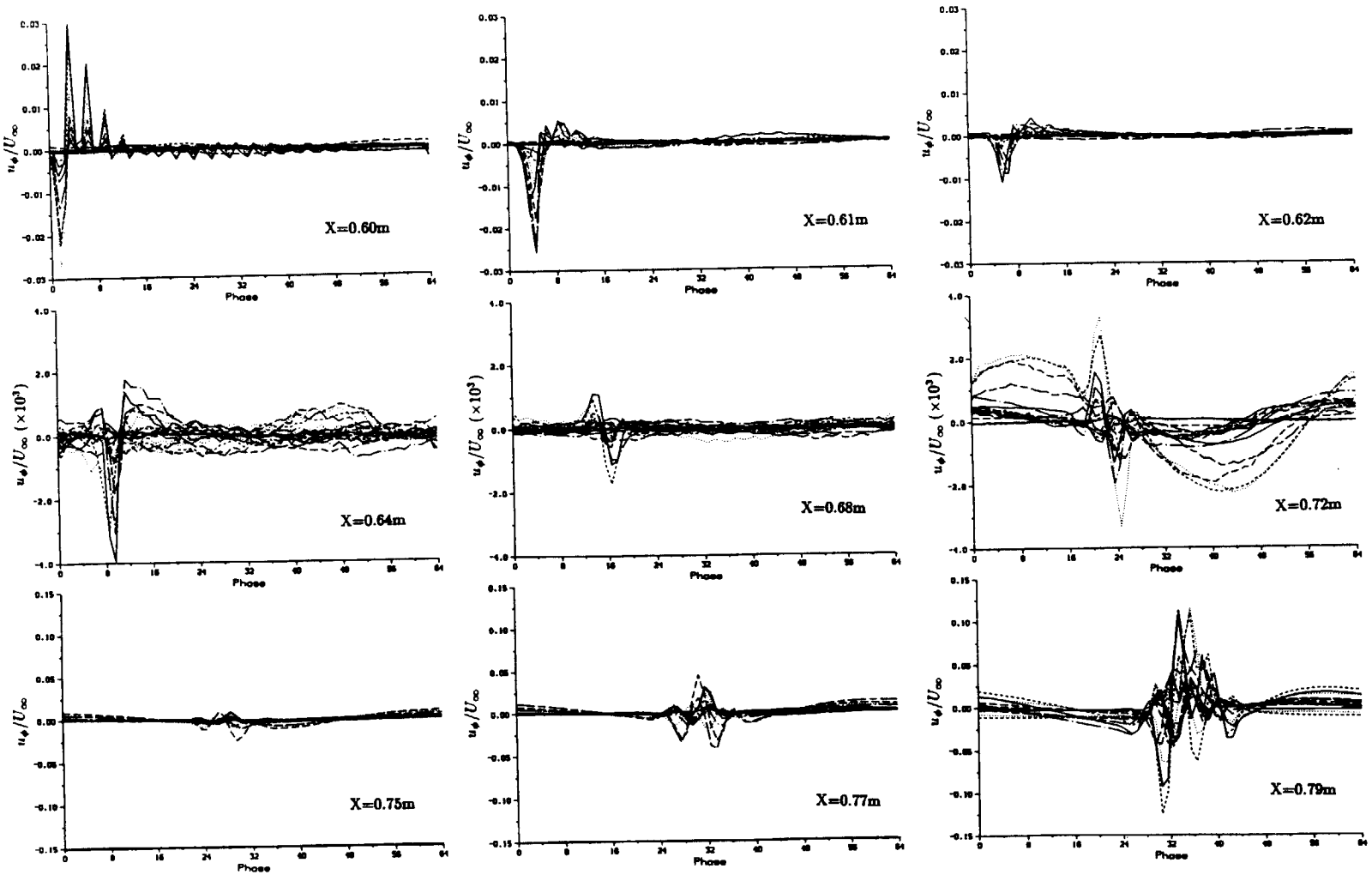

FIGURE 6. Evolution of phase-averaged streamwise velocity perturbations in adverse pressure gradient laminar layer.

m/s). The laminar layer develops severe inflection points in the APG leading to the formation of a strong shear layer close to the wall. As shown below, the repetitive signals are the result of rapid growth of waves developing on the shear layer which ultimately lead to the formation of a spot-like flow containing vortex-loops.

Signals with a wide variety of characteristics can be produced at a fixed position by adjusting the magnitude and duration of the flow. For example, when the magnitude of the impulsive-like flow is small and its duration is 3 msec, the rapid growth of the instability occurs only 25mm upstream of the point of natural transition. Under these conditions, the injected fluid is barely detectable in the laminar layer and then only very close to the wall. Further downstream, the hot-wire signals appeared to be fully turbulent and oscilloscope traces seemed to be uncorrelated with the disturbance. However, cursory measurements indicated that phase-averaged data could be extracted far downstream of the transition region.

The extremely repetitive formation process meant that phase-averaged crossed-wire measurements could be used to examine detailed motions. The disturbance frequency must be low enough to allow the downstream flow to recover between the passage of successive instabilities. However, too low a frequency is undesirable because the phase resolution would be insufficient. Lower frequencies also means a longer time for a given number of cycles, increasing the total experimental run-time. A maximum generating frequency was determined by examining hot-wire signals at a number of points close to the wall downstream of the transition region. The signals at points closest to the wall required the longest time to recover from the transients. High generation frequencies (e.g. 20Hz) did not allow the transients to decay sufficiently, and this altered the character of the signals (i.e. the structure of the flow). A frequency of 8Hz was finally selected for performing a detailed study. The signals observed for this disturbance frequency were the same as those produced by using much lower frequencies (e.g. 1Hz) while allowing very nearly the same degree of recovery from transients. Phase-averaged (64 interval) crossed-wire (UV-orientation) measurements of velocity and Reynolds stress as well as temporal mean velocity and Reynolds stress have been measured on a number of planes. The centerline streamwise plane normal to the wall (250 X by 17 Y positions= 4250 grid points) was measured only with the UV-orientation of the crossed-wire. The data on spanwise planes contain U, V, and W data requiring that the measurements be performed twice (once for UV- and again for UW-orientations of the crossed-wire). The spanwise planes consist of a uniform 10mm $\times$ 10mm horizontal grid at a fixed Y=10mm containing 126 points in X and 41 points in Z (5166 grid points) and eight spanwise planes normal to the wall, each consisting of 41 points in Z and 17 points in Y. These measurements at 26,554 grid points required about 25 days of continuous operation (including hot-wire calibrations etc.) of the automated facility. The averages at each point were derived from 25,600 samples taken at 1024Hz corresponding to the passage of 200 disturbances. Temporal mean velocity and Reynolds stress measurements have also been obtained without the disturbance (i.e natural transition) to examine the effect of introducing the disturbance. The same streamwise and horizontal grids were used while only five of the spanwise

planes normal to the wall were needed for the comparison. These 2D slices through the measurement volume originate just upstream of the region of rapid growth of the instabilities.

Normal hot-wires can be positioned very close to the wall, and this makes them superior to crossed-wires for measuring the thin laminar velocity profiles ($\delta = 6 \rightarrow$ 10 mm). Also, the effects of high shear are almost negligible, and they are less susceptible to error in regions of high turbulence intensity. Phase-averaged normal hot-wire data have been measured on 42 spanwise planes at 10mm intervals along the test-section from just upstream of the disturbance to about 0.2m downstream of the transition region.

4.3 Development of laminar layer in the favorable pressure gradient

The incoming profiles have inflection points close to the wall, presumably caused by the APG near the exit of the contraction. These inflection points disappear with streamwise distance and a self-similar profile shape is observed over about 15δ towards the end of this region. The FPG also has another beneficial effect of increasing the spanwise uniformity of the layer. Measurements with a Pitot tube resting on the wall were used to study the spanwise uniformity of the layer. The measurements were uniform to within $\pm 3\%$ over a spanwise distance of about 35δ. It is interesting to note that an inflection point develops in the laminar layer about 10mm upstream of the C_p minimum. The observations suggest that a Falkner and Skan similarity solution would adequately describe the layer in this region if an equivalent X and β (wedge angle) can be found. This would form a suitable starting point for an analytical or numerical study of the instability.

4.4 Development of laminar layer in the adverse pressure gradient

The closely spaced velocity profiles in figure 5 show the growth of strong inflection points leading to the formation of a shear layer. Development of the perturbation velocity with streamwise distance is shown in figure 6. Directly above the hole, the disturbance penetrates only 1mm into the layer (δ=6mm), and it has a maximum amplitude of -3% of U_∞. Small magnitude high frequency positive oscillations are also observed in time, but these are probably the result of transient mechanical vibrations in the shaker-diaphragm-tube system used to inject the disturbance. These positive oscillations decay rapidly with streamwise distance and disappear by 20mm downstream of the hole. The size of the perturbation continues to decay with streamwise distance reaching a minimum value 80mm downstream of the hole. At this streamwise location, the disturbance has the appearance of a short duration isolated sine-wave with a magnitude 0.15% U_∞. By about 150mm downstream of the hole, the disturbance starts to undergo rapid growth and complex phase relations begin to emerge between the signals obtained at different distances from the wall.

4.5 Transition region

The evidence suggests that the laminar layer eventually separates and that the transition mechanism is a shear-layer instability. The contours of spanwise vorticity

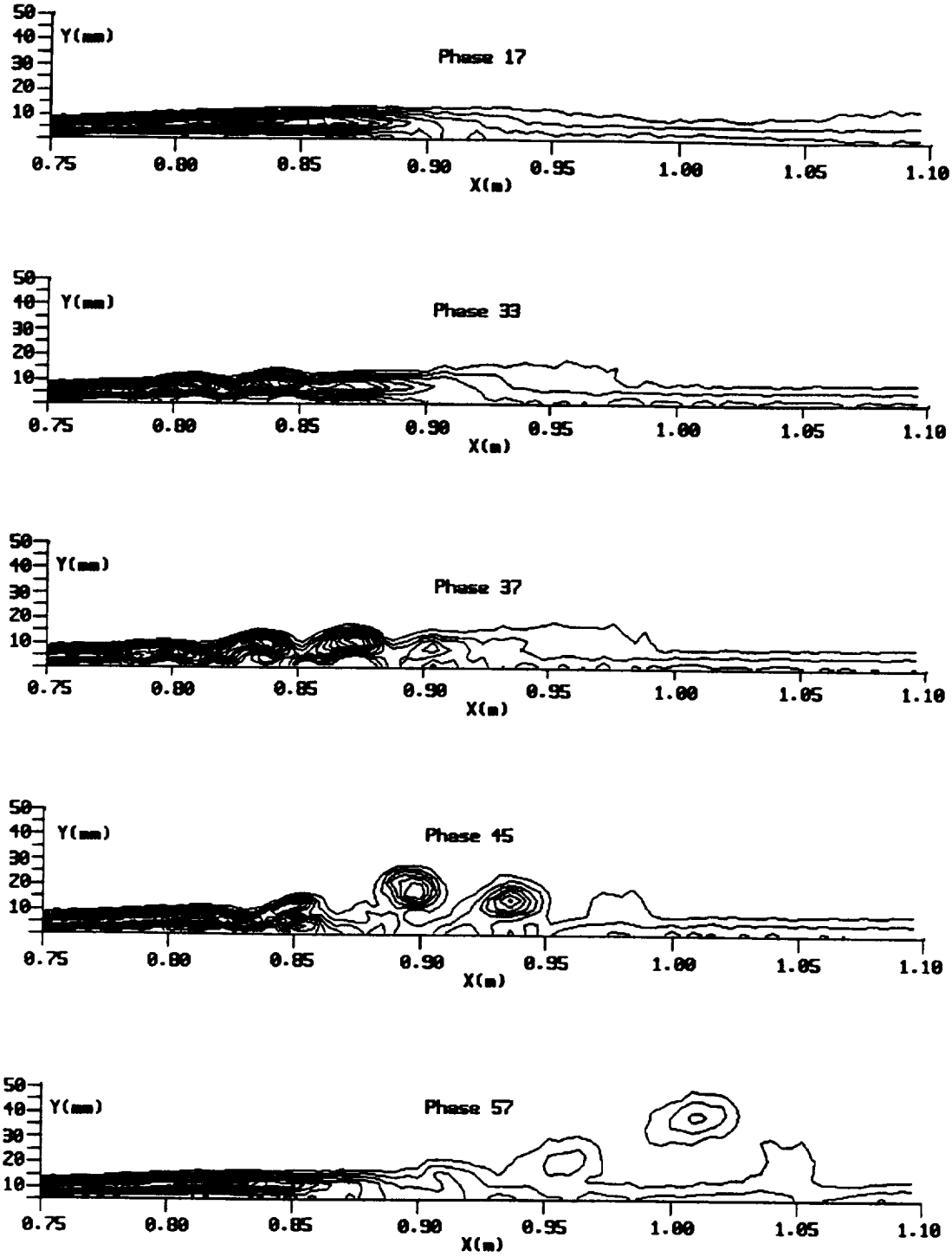

FIGURE 7. Selected phases showing roll-ups reminiscent of a free shear layer and their subsequent interaction with the wall.

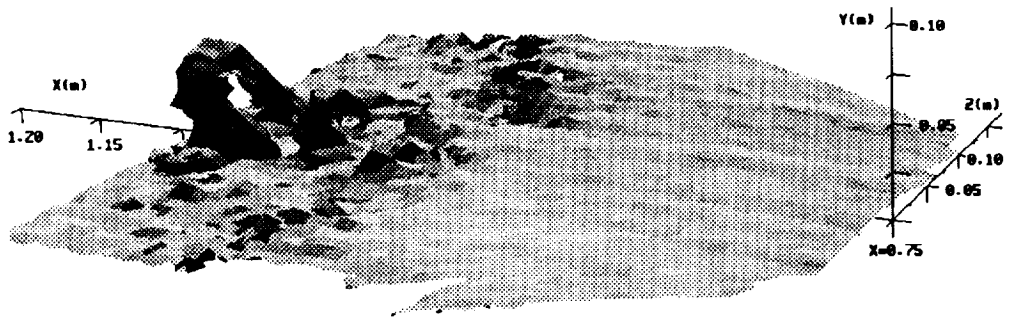

FIGURE 8. Contour surface of vorticity magnitude showing the vortex loops just downstream of the transition region.

in figure 7 show the formation of roll-ups which are reminiscent of a free shear layer. Four distinct spanwise vortex-like motions emerge, but subsequent interaction with the wall eventually leads to rapid growth of the second vortex. Smaller-scale vortex-like motions are also observed to propagate through the spanwise planes normal to the wall. In the horizontal plane, the region of large phase-averaged velocity perturbations has a wedge shape which is reminiscent of a turbulent spot. (It should be noted that the surrounding flow is turbulent, so using the term "turbulent spot" does not strictly conform to prior usage of the term.) The evolution of the "spot-like" flow pattern is slightly asymmetrical, and the large vortex-like motions become slightly displaced to one side of the centerline.

This region has recently been mapped out on a 3D (45×17×41) point grid in XYZ with greater spatial resolution. The 31,365 grid points were measured twice using both orientations of the crossed-wire probe to obtain U, V, and W data (as well as the Reynolds stresses at constant phase). Animation sequences of surfaces of constant vorticity magnitude show the formation of 3D waves which ultimately evolve into the large-scale vortex loops as shown in figure 8. At this stage, it is not clear whether smaller vortex-loops form as well. Visualization of the data is extremely difficult because the 3D contour surfaces are not transparent. Volume rendering techniques (transparency) are being explored as a means of examining the data. The spanwise propagation of the phase-averaged pattern is extraordinarily rapid, i.e. the spot-like flow expands to the ±0.2m width of the measurement grid (or greater) after streamwise development of about one only spot-length ($\approx$ 0.15m). Details of the organized motion gradually become "lost", and the phase-averaged contribution of the Reynolds stress falls to a relatively small fraction of the temporal mean value.

4.6 Downstream turbulent boundary layer

By about 0.5m downstream of the transition, the mean flow begins to develop

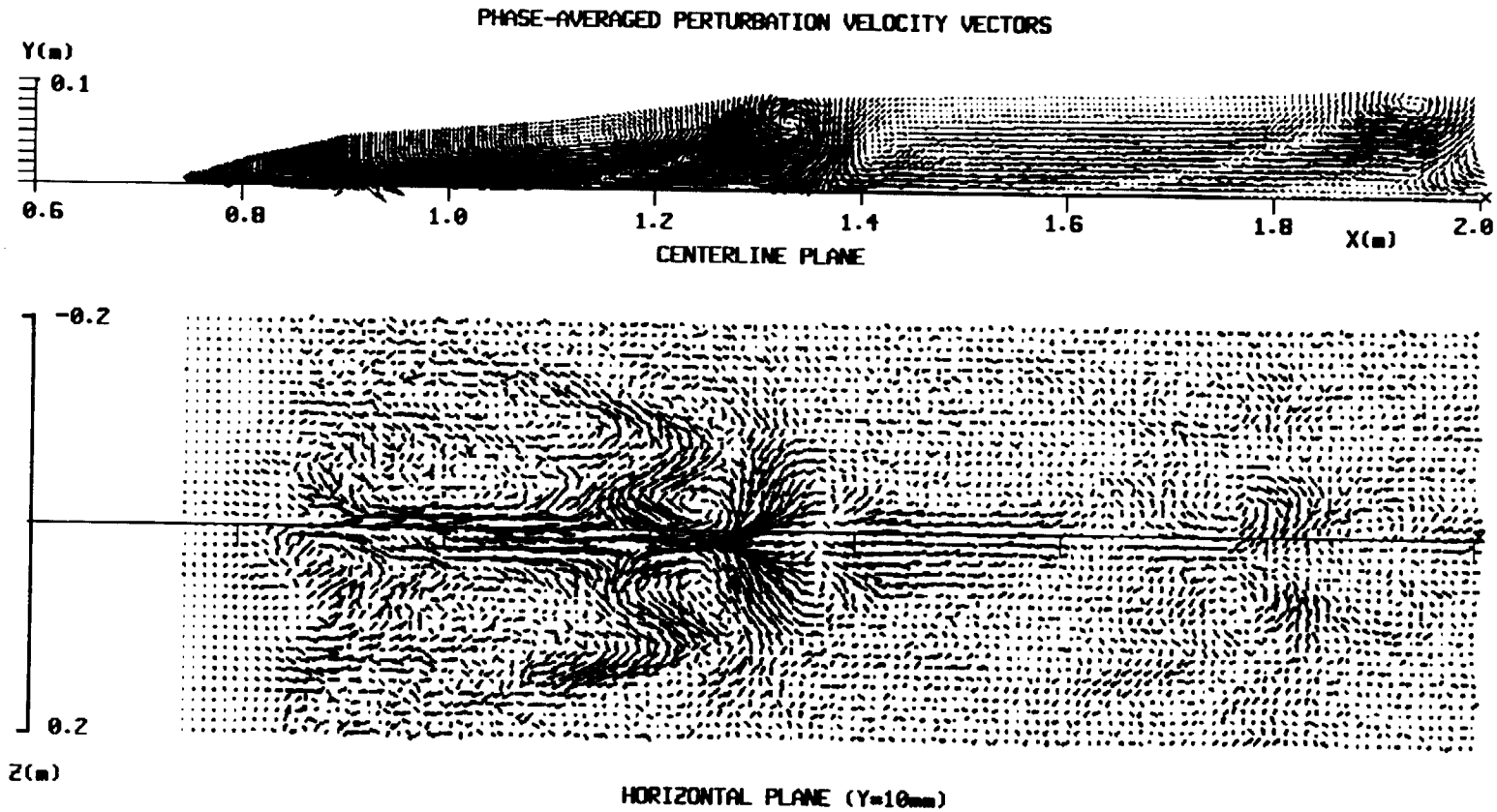

FIGURE 9. The large-scale vortex-loop that forms in the transition region retains its identity downstream in the turbulent boundary layer all the way to the end of the test-section.

many of the characteristics of a turbulent boundary layer. The individual vortex-like motions observed in the centerline plane appear to decay and merge into a single large eddy. Phase-averaged velocity vectors in the spanwise planes indicate that this large eddy has the form of a vortex-loop, similar in appearance but larger than the loop observed in the turbulent boundary layer study. Remarkably, the vortex loop remains visible in the velocity vector fields all the way to the end of the measurement grid (1.25m downstream of the point of transition) despite the interaction with the surrounding turbulent boundary layer, as shown in figure 9. In the horizontal plane, the two legs of the vortex loop have the appearance of two vortices of opposite sign which define the front edge of the spot-like flow. The edges of the spot-like structure can be observed where there are gradients of the phase-averaged velocities. This is probably the result of phase jitter, i.e. smearing of vorticity in the phase-averaging process.

5. Plans for future work on turbulent spots

The pressure distribution used for the transition study is rather arbitrary in the sense that it was designed to establish the DNS validation turbulent boundary layer. The laminar profiles in the APG are far from self-similar, and the APG is severe enough to cause separation. An APG distribution will be designed to produce closely self-similar laminar profiles. The advantage of self-similar profiles is that classical 2D linear stability theory can be used. The Reynolds number and the strength of the APG will be tuned by trial-and-error to see if a more conventional "spot-like" flow can be established. An important constraint is that the formation of spots occurs repetitively. Without this feature, the phase-averaging technique cannot be used. The automated facility will be used to obtain measurements on large 3D grids to examine the internal structure of the spot in detail.

The work was performed in the Fluid Mechanics Laboratory (FML) at NASA Ames Research Center. The project was partially supported by the FML.

REFERENCES

CANTWELL, B. J. & COLES, D. 1983 An experimental study of entrainment and transport in the turbulent near wake of a circular cylinder. *J. Fluid Mech.* **136**, 321-374.

CANTWELL, B. J., COLES, D. & DIMOTAKIS, P. 1978 Structure and entrainment in the plane of symmetry of a turbulent spot. *J. Fluid Mech.* **87**, 641-672.

EMMONS, H. W. 1951 The laminar-turbulent transition in a boundary layer. *J. Aero. Sci.* **18**, 490.

KOVAZNAY, L. S. G., FUJITA, H. & LEE, R. L. 1974 Unsteady turbulent puffs. *Advances in Geophysics.* **B18**, 229.

PERRY, A. E. & CHONG, M. C. 1982 On the mechanism of wall turbulence. *J. Fluid Mech.* **119**, 173-218.

PERRY, A. E., LIM, T. T. & TEH, E. W. 1981 A visual study of turbulent spots. *J. Fluid Mech.* **104**, 285.

PERRY, A. E. & WATMUFF, J. H. 1981 Phase-averaged large-scale structures in three-dimensional turbulent wakes. *J. Fluid Mech.* **103**, 33-51.

REYNOLDS, W. C. & HUSSAIN, A. K. M. F. 1972 The mechanics of a an organized wave in turbulent shear flow. Part 3. Theoretical models and comparison with experiments. *J. Fluid Mech.* **54**, 263.

SCHUBAUER, G. B. & KLEBANOFF, P. S. 1956 Contributions on the mechanics of boundary layer transition. *N.A.C.A. Rep. 909.*

WATMUFF, J. H. 1989 An experimental investigation of a low Reynolds number turbulent boundary layer subject to an adverse pressure gradient. *CTR Annual Research Briefs.* Center for Turbulence Research, Stanford University. 37-49.

Effect of initial conditions on secondary vortex structure in mixing layers

By J. H. Bell

1. Motivation and objectives

This report covers the final months of an experimental research project aimed at obtaining quantitative data on the behavior of the secondary vortex structure in a turbulent mixing layer at moderate Reynolds numbers ($Re_\delta = 2.9 \times 10^4$). This project was terminated before all the contemplated measurements could be made, and data were obtained only on the spatially stationary part of the secondary structure. Nonetheless, these data reveal some interesting facets of mixing layer behavior, which are discussed in the following report.

It is now widely appreciated that the turbulent mixing layer can support a wide array of vortex structures. Indeed, it is known that mixing layer growth is dominated by the development and interaction of large-scale spanwise vortices (Ho & Huerre 1984). In addition, a second mixing layer structure, consisting of rows of "rib" vortices winding in between adjacent spanwise vortices, has also been revealed (Bernal & Roshko 1986, Lasheras & Choi 1988). The role which this secondary structure plays in mixing layer development is not yet clear. It was first reported in conjunction with "mixing transition" (Konrad 1977), and it has been speculated that there is a connection between the secondary structure and the sudden appearance of small scale fluctuations in the layer, which enhance mixing (Ho 1990). In addition, recent direct Navier-Stokes simulations (Moser & Rogers 1990) have shown that the spanwise structures can be strongly distorted by the rib vortices riding between them. Finally, experiments conducted by Nygaard & Glezer (1991) have shown that both the primary spanwise structures and the secondary vortices are simultaneously controllable to a high degree. These studies may eventually lead to a time when mixing layer behavior can be predicted and precisely controlled to suit the needs of a particular application.

Past investigations of the secondary structure in turbulent mixing layers have focussed almost exclusively on mixing layers originating from laminar initial conditions, i.e. the boundary layers on the splitter plate are laminar. To some extent, this is due to the inability of simulations to reach Reynolds numbers appropriate to turbulent initial conditions. Another reason, however, is that the secondary structure occurring within a mixing layer starting from laminar initial conditions is strikingly obvious and remarkably stable (Bernal & Roshko 1986). When the secondary structure is spatially stationary in this manner, its gross features can be easily resolved with relatively simple single-point, time-averaged velocity measurements. When such measurements are made on a cross-sectional grid through the mixing layer, the secondary structure takes on the appearance of a row of counter-rotating streamwise vortices, embedded within the layer. But this is not observed in mixing

layers where the splitter plate boundary layers are turbulent. No secondary vortex structure can be discerned with single-point, time-averaged measurements, indicating that the structure is either "jittering" in some way or that it is not present in the flow. The primary, spanwise structure, on the other hand, is believed to behave in the same manner regardless of initial conditions. This change in the behavior of the secondary structure is especially interesting in light of the slightly increased far-field spreading rate of mixing layers with laminar initial conditions versus those with turbulent initial conditions in the same facility (Browand & Latigo 1979, Bell & Mehta 1990a).

In order to gain a real understanding of the behavior of the secondary vortex structure, it is necessary to use measurement techniques which can detect this structure even when it is "jittering". In the absence of such techniques, however, a simpler approach might be to impose a spatially stationary secondary structure on a mixing layer originating from turbulent initial boundary layers. The structure which occurs naturally in mixing layers with laminar initial conditions is known to be triggered by small spanwise perturbations in the upstream boundary layers (Bell & Mehta 1989b). If spanwise perturbations could be used to fix the structure in an initially turbulent mixing layer, it would be possible to observe the behavior of the secondary structure in this flow with relatively simple techniques. The following sections describe the results, originally intended as a preliminary study, of an experiment on a mixing layer with different types of strong spanwise perturbations imposed at the origin.

2. Accomplishments

Data have been obtained on the development of a two stream mixing layer with four different sets of initial conditions. In all four cases, the velocity ratio was set to $\lambda = 0.25$, and the maximum Reynolds number achieved was $Re_\delta = 2.9 \times 10^4$. A rotatable crossed hot-wire probe was used to make single-point, time-averaged measurements in the mixing layers. The results for three cases were previously described in Bell (1989); the results for one case are new. This case also includes some runs at different velocities, as described later.

2.1 Experimental apparatus and techniques

All work was performed in the *Mixing Layer Wind Tunnel* located in the Fluid Mechanics Laboratory at the NASA Ames Research Center (Figure 1). The wind tunnel consists of two separate legs which are driven individually by centrifugal blowers connected to variable speed motors. The two streams are allowed to merge at the sharp edge of the tapered splitter plate. The facility is more fully described in Bell (1989) and further details of the mixing layer wind tunnel design and calibration are given by Bell & Mehta (1989a).

Measurements were made using a single rotatable cross-wire probe held on a 3-D traverse and linked to a fully automated data acquisition and reduction system controlled by a MicroVax II computer. Individual statistics for the baseline and vortex-generator cases were averaged over 5,000 samples obtained at a rate of 400

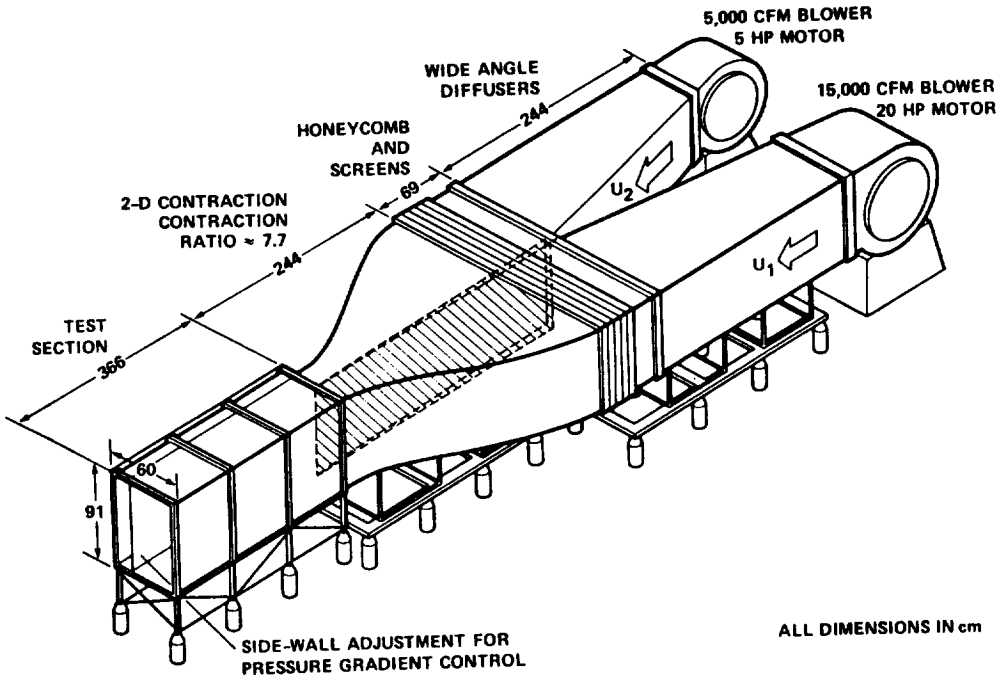

FIGURE 1. Mixing layer wind tunnel.

Hz. Upgraded equipment made available for the corrugated splitter plate case allowed 5,000 samples to be taken at a rate of 2.5 KHz.

Four cases are described in this report, each with differing initial conditions. These are sketched in figure 2, which shows the modifications made to the splitter plate in each case. In the *laminar* case, the splitter plate boundary layers were left undisturbed and remained in a laminar state. In the other three cases, round wire trips were installed on the splitter plate so as to produce fully-developed turbulent boundary layers at the splitter plate trailing edge. In the *tripped* case, no additional perturbations were imposed on the turbulent splitter plate boundary layers. In the remaining two cases, however, regular spanwise perturbations to the flow were also imposed. In the *vortex generator* case, a row of small vortex generators was installed on the high-speed side of the splitter plate. In the *corrugated* case, a cross-stream corrugation was added to the splitter plate trailing edge. The first three cases have been further described in Bell (1989) and Bell & Mehta (1990b). They are included here for comparison to the corrugated case, which is new. In all cases, the free-stream velocities were set at 15 m/s on one side and 9 m/s on the other, thus giving a mixing layer with velocity ratio, $U_2/U_1 = 0.6$, and $\lambda = 0.25$. The details of both the laminar and turbulent boundary layer properties near the splitter plate trailing edges are given below in table 1.

Table 1. Initial Boundary Layer Properties

Condition	U_e (m/s)	δ_{99} (mm)	θ (mm)	Re_θ	H	$C_f \times 10^3$
High-Speed Side, Laminar	15.0	4.0	0.53	525	2.52	0.7
Low-Speed Side, Laminar	9.0	4.4	0.61	362	2.24	0.9
High-Speed Side, Tripped	15.0	7.6	0.82	804	1.49	5.3
Low-Speed Side, Tripped	9.0	8.5	0.94	567	1.50	4.9

In the vortex generator case, streamwise vortices were injected into the mixing layer by a row of half-delta wing vortex generators, arranged as shown in figure 2. The vortex generator spacing was chosen to be comparable to the Kelvin-Helmholtz wavelength, and the semi-span was chosen to be approximately equal to the local boundary layer thickness.

In the corrugation case, a 2.5 cm plastic extension was attached to the end of the splitter plate. The extension was corrugated in the cross-stream direction, giving the splitter plate a three-dimensional trailing edge. The corrugation wavelength was 3.8 cm, and the amplitude increased from zero to 1.3 cm over a 2.5 cm distance. Since each full cycle of the corrugation would produce a pair of opposite-signed regions of cross-stream vorticity, the wavelength was chosen to be roughly twice the Kelvin-Helmholtz wavelength; the amplitude was chosen to be close to the local boundary layer thickness.

Data were obtained in the XY- and XZ-planes with a cross-wire probe at eight streamwise stations for each case. In the cases with turbulent initial boundary layers, the last station is $3050\theta_1$ downstream of the trailing edge. At each station, data were obtained in a cross-sectional plane which typically extended over 20 points in the cross-stream direction, and 60 points in the spanwise direction. The spanwise extent of each cross-sectional plane ranged from three to ten mixing layer thicknesses, depending on the streamwise location. The global properties presented below were *spanwise-averaged* for all cases. The measurements of U, W and $\overline{u'w'}$ were corrected for mean streamwise velocity gradient ($\partial U/\partial Y$) effects as described in Bell & Mehta (1989b). The streamwise component of mean vorticity ($\omega_x = \partial W/\partial Y - \partial V/\partial Z$) was computed using the central difference method. The overall circulation was defined as the surface integral of the streamwise vorticity over the cross-flow plane with vorticity levels less than 10% of the maximum value being set to zero in order to provide immunity from "noise".

2.2 Results and Discussion

The differing initial conditions result in considerable differences in the growth rates and turbulence levels, not only in the near-field but extending to the far downstream as well. Figure 3 shows the mixing layer thickness, δ, determined by fitting the mean velocity profile to an error function profile shape, for all four cases. All four cases attain linear growth in the far-field, but with striking differences in both near- and far-field growth rates. In the near-field, the perturbed cases grow

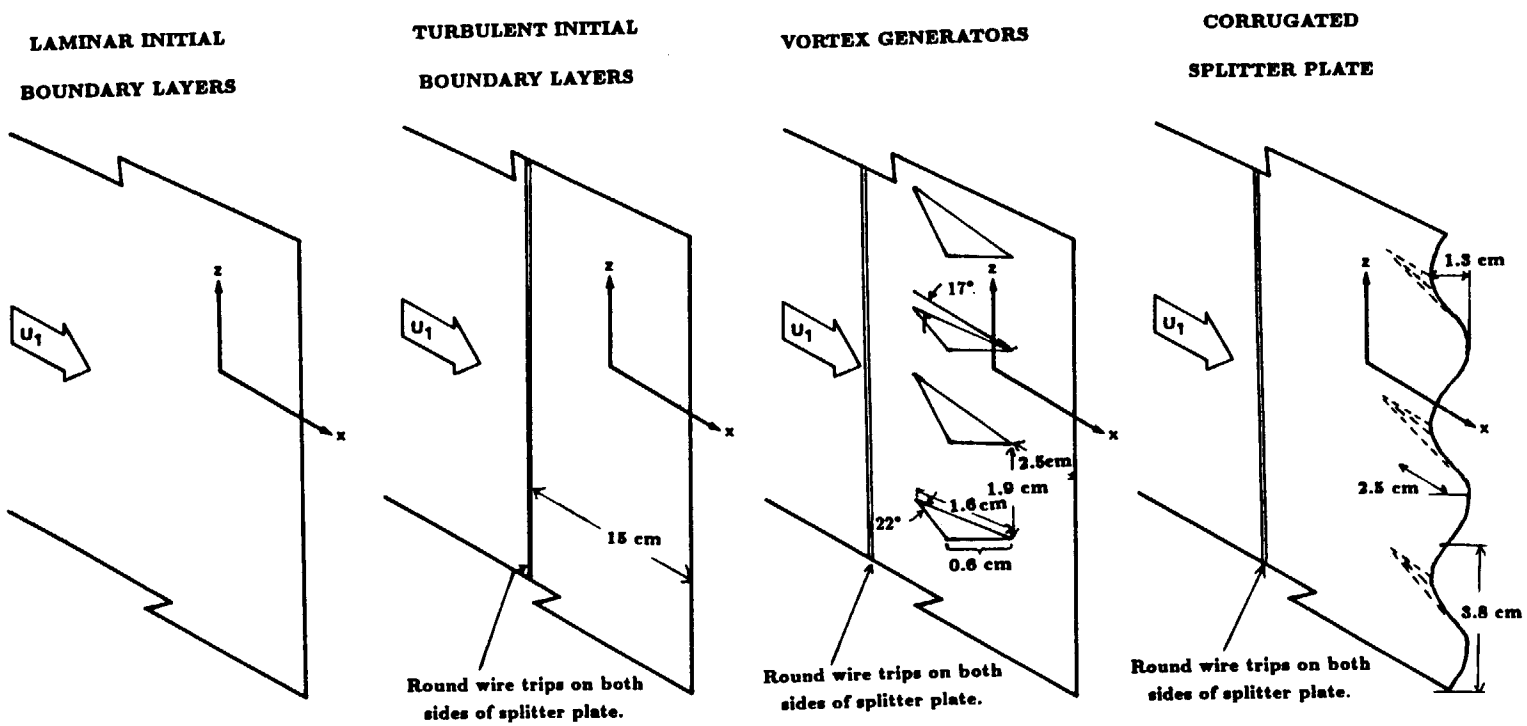

FIGURE 2. Sketches of the splitter plate trailing edge configurations for the four cases. Views are of the high-speed side of the splitter plate.

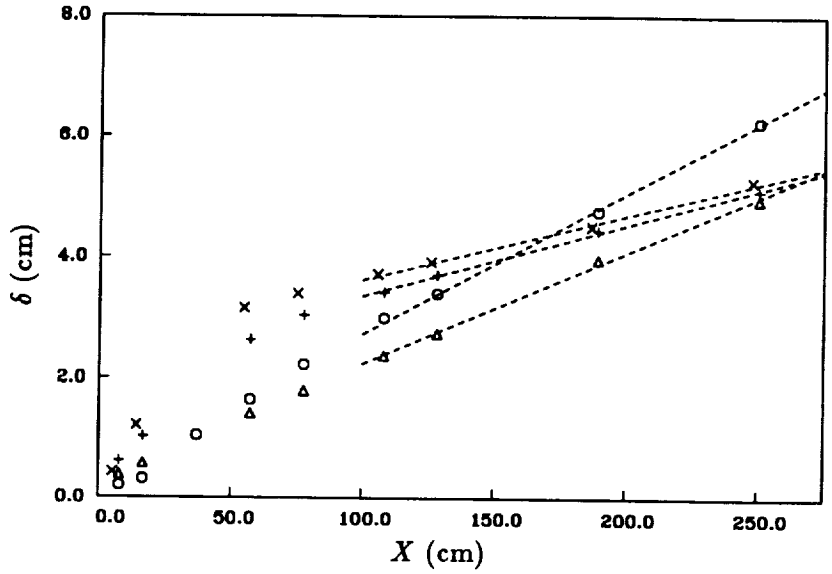

FIGURE 3. Mixing layer thickness, δ, vs. streamwise distance, X. The dashed lines are best fits to the far field data, and the far field growth rates are listed below: ○ laminar case $d\delta/dx = 0.023$, △ tripped case $d\delta/dx = 0.019$, + vortex generator case $d\delta/dx = 0.012$, × corrugated case $d\delta/dx = 0.011$.

much more rapidly than the unperturbed cases, but their far-field growth rates are much reduced. The tripped case growth rate in the linear region is $d\delta/dx = 0.023$, which is close to the value typically observed for mixing layers with $\lambda = .25$ (Rodi 1975). However, the far-field growth rate for the laminar case is 28% higher than that for the tripped case, and that for the vortex generator and corrugated splitter plate cases are 33% and 39% lower, respectively. Despite the difference in the perturbations, the vortex generator and corrugated cases both grow at nearly the same rate.

Since the mixing layer growth rates are so drastically affected by the perturbations at the origin, the Reynolds stresses levels might be expected to show a comparable effect. This is indeed the case, as shown in figure 4, which plots the streamwise development of the peak turbulent kinetic energy, $\overline{q^2}_{max}$. Both the laminar and tripped cases asymptote to about the same constant level beyond $X \sim 125$ cm. By the same streamwise location, the perturbed cases have achieved a significantly lower constant level (Which is nearly identical for the two cases.). In the near-field, the laminar case displays the classically observed "overshoot" in turbulence intensity, before dropping down to the asymptotic level. This overshoot is most likely due to the coherent passage of spanwise vortex structures. The overshoot seen in the perturbed cases is due to the generation of very high turbulence levels as the mixing layer is strained by the strong streamwise vortices induced by the perturbations. In the laminar case, the overshoot is made up of very strong fluctuations at the Kelvin-Helmholtz frequency, while in the perturbed cases it is much more broadband. The

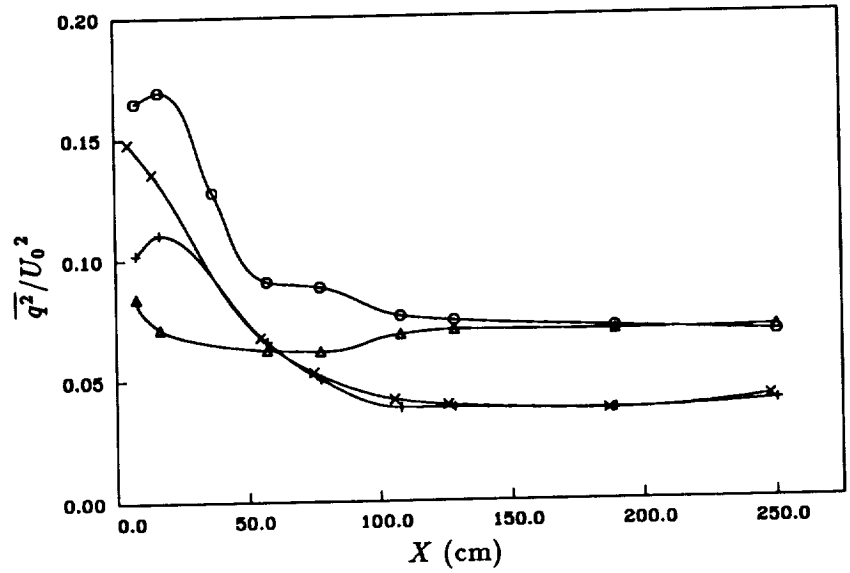

FIGURE 4. Peak level of $\overline{q^2}/U_0{}^2$, or twice the turbulent kinetic energy vs. streamwise distance,, X, for the four cases. ○ laminar case, △ tripped case, + vortex generator case, × corrugated case.

very slight overshoot in the turbulent case is due to the high turbulence levels generated in the wake behind the splitter plate.

In a self-similar mixing layer, it is possible to relate the peak level of primary shear stress, $(\overline{u'v'})_{max}$, to the mixing layer growth rate, $d\delta/dx$, and the velocity ratio parameter λ. The relation that evolves from the analysis given by Townsend (1976), is:

$$-\frac{\overline{u'v'}_{max}}{U_0^2} = 0.141\frac{d\delta}{dx}\frac{1}{\lambda}$$

This relationship is used to calculate $(\overline{u'v'})_{max}$ for each case. The results are compared with the measured values of $(\overline{u'v'})_{max}$, below in table 2.

Table 2. Measured and Calculated $(\overline{u'v'})_{max}$

$(\overline{u'v'})_{max}$	Laminar	Tripped	Vortex Generators	Corrugated Splitter Plate
Measured	0.011	0.011	0.0061	0.0065
Calculated	0.013	0.010	0.0067	0.0060

With the exception of the laminar case, the measured and calculated values of $\overline{u'v'}_{max}$ agree to within approximately 10%. The poor agreement in the laminar case suggests that this flow has possibly not reached a fully self-similar state, in spite of other indications that it has. The perturbed cases, on the other hand, behave in a manner consistent with the assumption of self-similarity, despite their abnormally low growth rates. The question which then arises is how far downstream this lowered

growth rate persists. In the present facility, measurements downstream of $X = 250.3$ cm, or $3050\theta_1$, are beginning to show the effects of sidewall interference. In order to effectively extend measurements farther downstream, data were taken for the corrugated case at different operating conditions.

First, the flow velocity on both sides was doubled, effectively doubling Re_x. This change had the effect of increasing the growth rate to $d\delta/dx = 0.013$, and increasing $\overline{u'v'}_{max}$ proportionately, to 0.0071. Second, the high speed side velocity was increased to 30 m/s, while the low speed side velocity remained at 9 m/s, giving $\lambda = 0.54$. This had the effect of increasing the velocity difference relative to the convection velocity. Thus, it was expected that the same physical distance downstream would correspond to a greater number of pairings of the spanwise structures, i.e., the mixing layer would be dynamically "older". In this case, $d\delta/dx$ was increased to 0.034, while the measured $\overline{u'v'}_{max}$ was 0.0069. If the mixing layer were self-similar, $\overline{u'v'}_{max} = .0088$ would be expected. However, it is clear that the growth rate and turbulence levels in this case are still much lower than would be expected from previous studies of turbulent mixing layers.

Contour plots of various mixing layer properties show a considerable difference in the near-field evolution of the four cases. Figure 5 shows contours of mean streamwise velocity at $X = 17$ cm. This station is fairly close to the splitter plate, and the distortion of the U^* distribution in to the presence of strong streamwise and cross-stream vorticity can be clearly observed in all but the tripped cases. The distortion is quite severe in the vortex generator and corrugated cases, especially so in the later because of the bending of the mixing layer by the strong cross-stream vorticity in this case. Turbulence distributions in the mixing layer are similarly affected, as seen in figure 6, which shows contour plots of $\overline{q^2}/{U_0}^2$ at the same location. The streamwise vortices produce isolated regions of high turbulence. In the laminar case, these tend to be lost in the background of the high fluctuation levels produced by the organized passage of the spanwise vortices. In the vortex generator and corrugated cases, especially high turbulence is found between the streamwise vortices, where the vortex-induced thinning of the mixing layer has increased the mean shear dramatically.

The mean streamwise vorticity contours show the most marked difference between the four cases. In the laminar case (figure 7a), an irregular row of $8-10$ streamwise vortices of varying strengths can be observed. In contrast, the tripped case (figure 7b) has a much lower level of vorticity in an irregular pattern, not at all suggestive of concentrated streamwise vortices. In the vortex generator and corrugated cases, a single row of 7 round, well-defined counter-rotating vortices are clearly observed. The variation in vortex strengths is much smaller than in the laminar case. The spacing between the vortices in the perturbed cases is approximately 2 cm, the same as the wavelength of the original spanwise disturbance. The mean streamwise vorticity is strongest at the first measurement station ($X = 8$ cm), and its effects on the other flow quantities are greatest at this location.

The behavior of the streamwise vorticity, in the three cases for which this quantity is significant, is presented in figure 8. The peak vorticity and circulation data

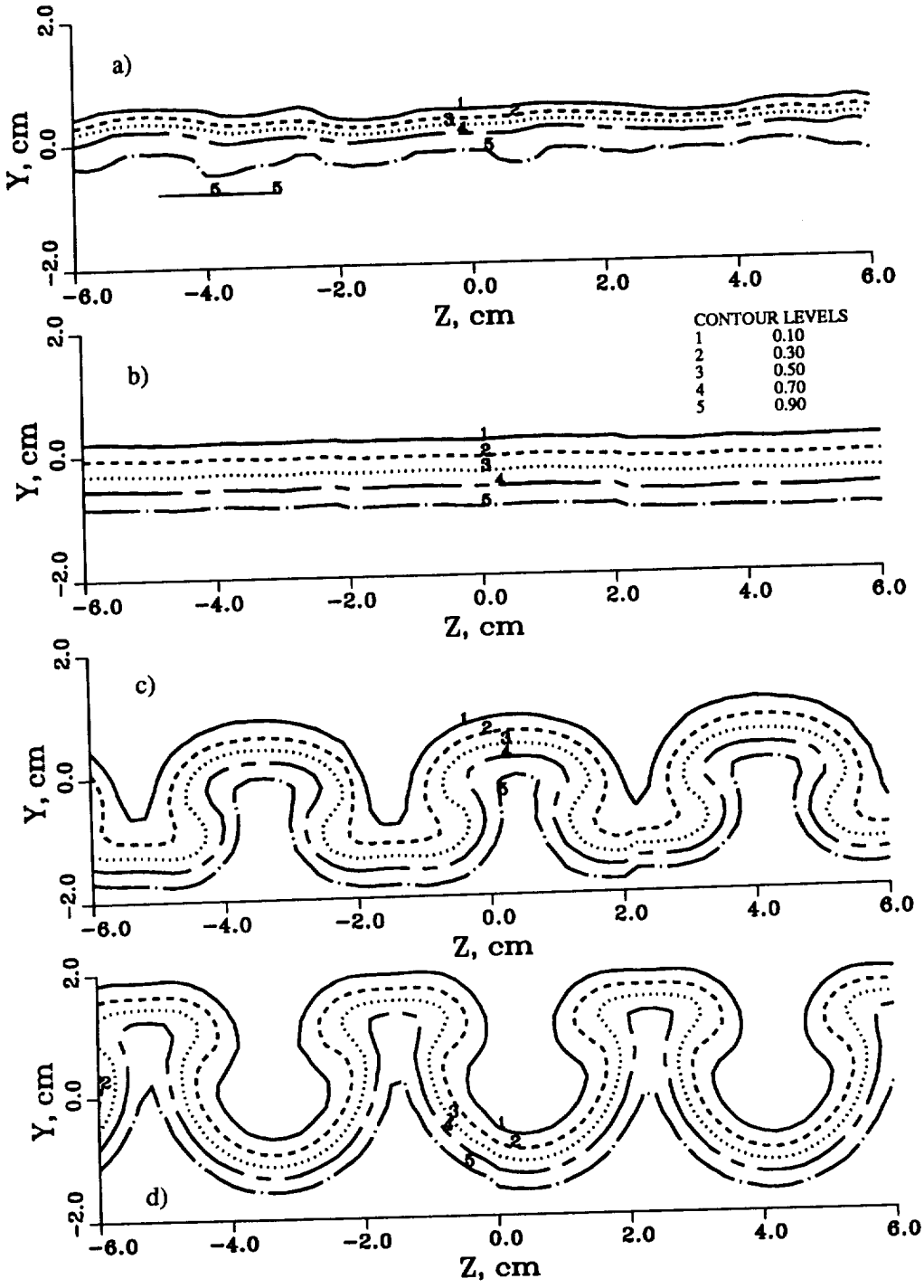

FIGURE 5. Contours of mean streamwise velocity U/U_0 at $X = 17$ cm. a) laminar case, b) tripped case, c) vortex generator case, d) corrugated case.

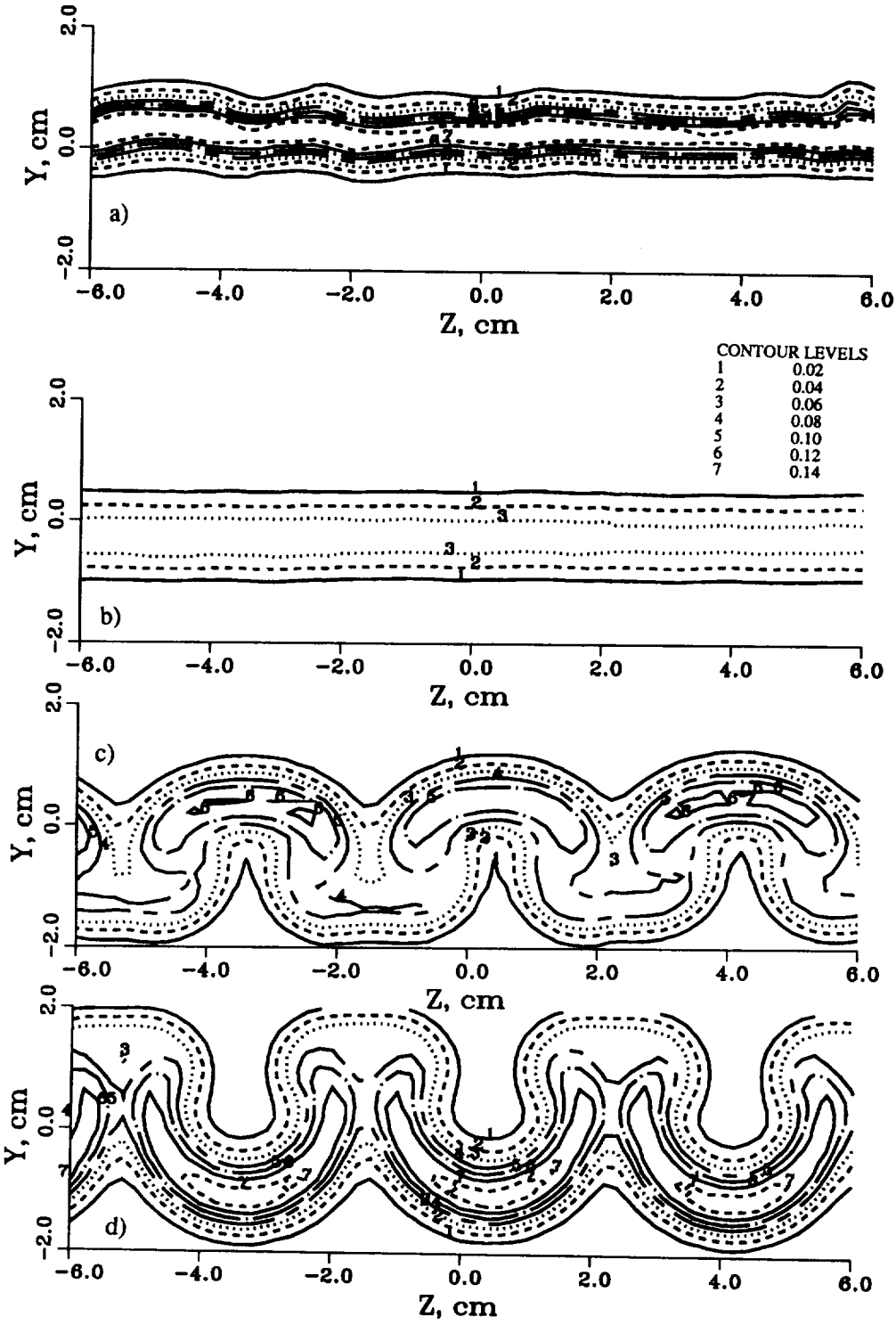

FIGURE 6. Contours of turbulent kinetic energy $\overline{q^2}/{U_0}^2$ at $X = 17$ cm. a) laminar case, b) tripped case, c) vortex generator case, d) corrugated case.

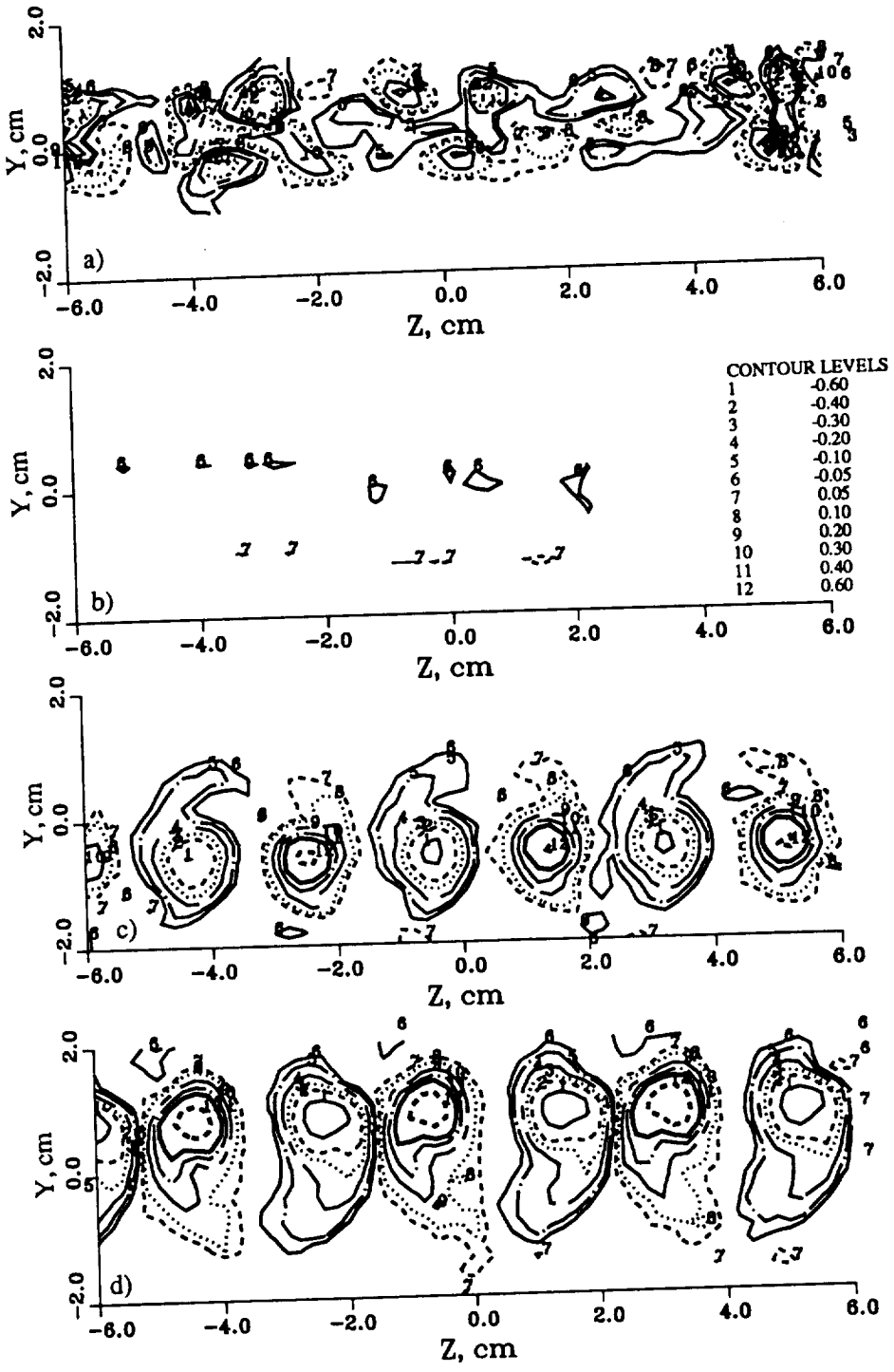

FIGURE 7. Contours of mean streamwise vorticity Ω_z/U_0 (cm^{-1}) at $X = 17$ cm. a) laminar case, b) tripped case, c) vortex generator case, d) corrugated case.

presented in figure 8 are left unnormalized. This is done because the most appropriate normalizing parameters — the initial strength and circulation of the spanwise structures — can only be estimated in the present study. Mean spanwise vorticity, $\Omega_z = (\frac{\partial V}{\partial x} - \frac{\partial U}{\partial y})$ was estimated by assuming that the $\frac{\partial V}{\partial y}$ term is negligible. Spanwise vortex circulation was estimated using an initial streamwise wavelength determined by the convection velocity and the measured natural frequency of the mixing layer. For the three cases, the estimated values of spanwise vorticity at the first measurement station are as follows. Laminar case: $\Omega_{z_{max}} = 1400\ s^{-1}$ and $\Gamma_z = 0.11\ m^2/s$, vortex generator case: $\Omega_{z_{max}} = 1100\ s^{-1}$ and $\Gamma_z = 0.11\ m^2/s$, corrugated case: $\Omega_{z_{max}} = 920\ s^{-1}$ and $\Gamma_z = 0.11\ m^2/s$. In the latter two cases, the estimates are made more uncertain by the highly distorted state of the mixing layer and the lack of a clearly observable natural frequency.

The streamwise development of the peak mean vorticity for the three cases is presented on a log-log scale in figure 8a. The peak vorticity values tend to fall along a straight line on this scale, indicating a power-law decay rate. The vortex generator case has the highest initial mean vorticity level, but also the fastest decay rate; dropping as roughly $1/X^{1.8}$. The vorticity decay rate for the laminar case is approximately $1/X^{1.5}$, and for the corrugated case, roughly $1/X^{1.6}$. As noted previously, these values reflect only the decay of the spatially stationary part of the secondary structure. It is possible that the structure is actually maintaining its strength, but "jittering" with increasing amplitude as it moves downstream.

The secondary vortex structure contains both streamwise and cross-stream vorticity. It is possible to estimate the latter by neglecting the $\frac{\partial W}{\partial x}$ term; thus $\Omega_y \cong \frac{\partial U}{\partial z}$. The ratio of streamwise to cross-stream vorticity at a given station gives some indication of the orientation of the secondary structure. This ratio, plotted in figure 8b, is initially very different for the three cases. In the laminar case, the developing secondary structure only gradually begins to kink the mixing layer, resulting in a very high Ω_x/Ω_y ratio initially. In the corrugated case, the high level of cross-stream vorticity imposed by the corrugations produces a much lower Ω_x/Ω_y ratio. Further downstream, Ω_x/Ω_y collapses to approximately the same value for all three cases, suggesting that the secondary structure is behaving in a similar fashion in all three flows, despite differences at the origin.

Plots of the vortex circulation (Figure 8c), however, show very different behavior for the three cases. The laminar case vortex circulation shows a very slow decrease, with a small intermediate peak at $X \sim 60$ cm — this was associated with the change in scale of the streamwise vortex structure (described below). However, the vortex generator case shows a relatively fast linear decay and by $X \sim 125$ cm, the level is comparable to that of the naturally occurring vortices. In the corrugated case, the circulation at the first two stations is quite high; it then drops to a level close to that of the vortex generator case. This result is surprising, since the peak vorticity of the corrugated case at the first station is lower than that for the vortex generator case. Evidently, the corrugations produce relatively diffuse, large-scale streamwise vortices which the mixing layer cannot support, and these decay rapidly.

The mean spacing of the streamwise vortices can be easily found by counting the

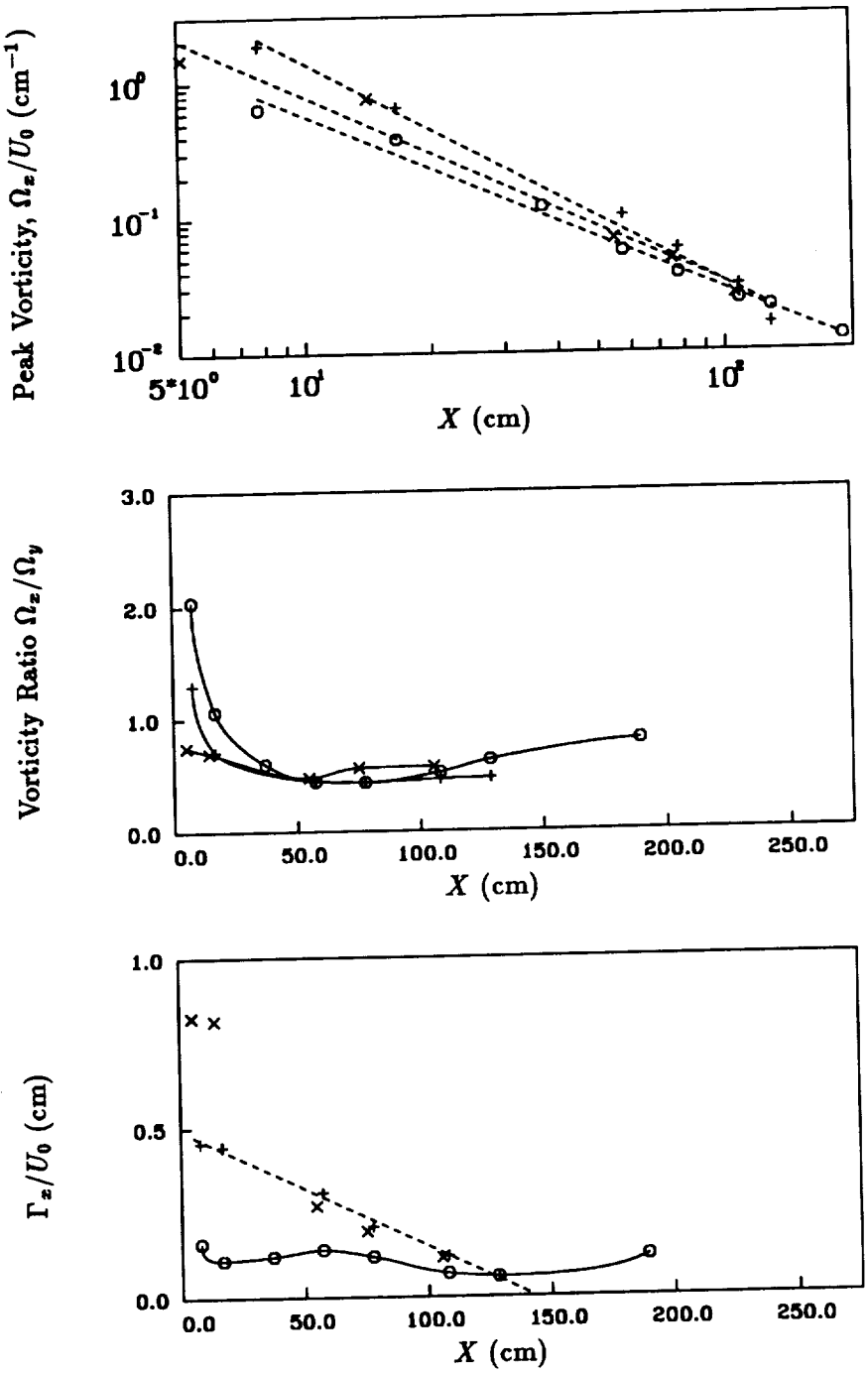

FIGURE 8a-c. Mean streamwise vorticity (Ω_z/U_0 cm^{-1}) properties for laminar and perturbed cases. ○ laminar case, + vortex generator case, × corrugated case. a) Peak streamwise vorticity vs X, log-log scale, b) Ratio of streamwise to cross-stream vorticity, Ω_z/Ω_y, c) Streamwise vortex circulation vs X.

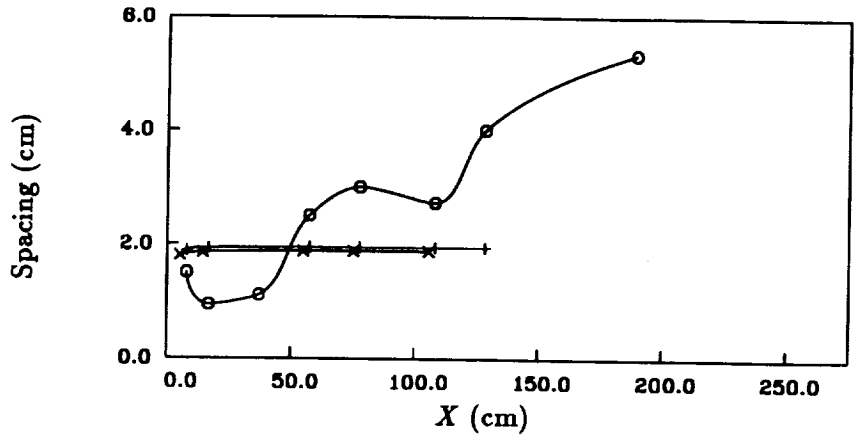

FIGURE 8d. Mean streamwise vortex spacing vs X, for laminar and perturbed cases. ○ laminar case, + vortex generator case, × corrugated case.

number of vortices present at each station. The vortex spacing in the laminar case increases in a step-wise fashion, scaling approximately as the mixing layer vorticity thickness (Fig. 8d). On the other hand, the spacing for the vortex generator and corrugated cases is *constant* within the measurement domain. This may simply be due to the fact that the injected vortices are of equal strength and spacing, unlike the naturally occurring structures, and so there is no tendency for self-induced motion. Another possibility, related to the pairing of the *spanwise* structures, is discussed below.

3. Conclusions

The imposition of strong spanwise perturbations at the origin of a mixing layer produces a well-defined secondary vortex structure. The effects of this structure are striking. The initial ($X \leq 60$ cm) growth rate is increased significantly, most likely due to the extra entrainment provided by the streamwise structures. However, the growth rate further downstream ($X \geq 100$ cm) is reduced drastically over the unperturbed cases with either laminar or turbulent splitter plate boundary layers. These effects are essentially independent of the means used to impose the spanwise perturbations (either vortex generators or a corrugated end to the splitter plate). The region of reduced growth and turbulence levels extends very far downstream — at least 3000 times θ_1, the momentum thickness of the high-speed side splitter plate boundary layer. In addition, experiments in the corrugated case indicate that the region may extend more than twice this far downstream. In the region of reduced growth, the mixing layer gives every indication of having reached a self-similar state.

A possible explanation for this change can be made by postulating that the strong initial secondary vortex structure affects the pairing of the spanwise vortices. Most of the growth of a mixing layer occurs due to entrainment during the pairing process of the nominally two-dimensional spanwise vortical structures (Sandham *et al.* 1988). If the spanwise structures were altered so as to reduce the pairing rate,

entrainment by the mixing layer, and thus its growth rate, would be decreased. The naturally occurring streamwise vorticity in the laminar case first appears in the regions of maximum extensional strain, in the braid region. The two structures become interlaced in such a way that, in flow-visualization studies, it appears that the only effect of the secondary structure on the spanwise vortices is to produce a regular, gentle undulation in the latter (Lasheras *et al.* 1986). Therefore, the entrainment due to the spanwise structures proceeds undisturbed; total growth may in fact be enhanced by the additional entrainment in the braids due to the secondary structure. However, the injected vorticity in the vortex generator and corrugated cases imposes its own pattern on the spanwise structures, as indicated by the gross distortions in the mean velocity contours. It is possible that this changes the pairing process, reducing the pairing rate. In the near-field, entrainment by the secondary structure more than makes up for this deficit. However, entrainment due to the rib vortices decreases much faster than the spanwise structure recovers, so the overall entrainment rate is reduced, and hence the growth rate of the mixing layer drops. This hypothesis is also consistent with differences noted in the behavior of the streamwise vortices in the three cases. Previous investigations have suggested that the scale change in the streamwise vortices occurs during the pairing of the spanwise rollers (Jimenez *et al.* 1985, Bell & Mehta 1989b). A scale change is not observed in the vortex generator or corrugated cases, but the behavior of the vorticity ratio, Ω_z/Ω_y, suggests that the secondary structure achieves the same state in all three cases. The most reasonable explanation, then, is that the lack of a scale change in the vortex generator and corrugated cases indicates that the pairing of the spanwise rollers has been suppressed.

Acknowledgments

I wish to thank Dr. Rabi Mehta, of the Joint Institute for Aeronautics and Acoustics, Stanford University for his considerable assistance during this project. The facilities used for this study were provided by the Fluid Dynamics Research Branch, NASA Ames Research Center.

REFERENCES

BELL, J. H. 1989 An Experimental Study of Secondary Vortex Structure in Mixing Layers. *CTR Annual Research Briefs - 1989*. Center for Turbulence Research, Stanford University, 59-79.

BELL, J. H. & MEHTA, R. D. 1989a Design and Calibration of the Mixing Layer Wind Tunnel. *JIAA Report TR-89*. Dept. of Aero/Astro, Stanford University.

BELL, J. H. & MEHTA, R. D. 1989b Three-Dimensional Structure of Plane Mixing Layers. *JIAA Report TR-90*. Dept. of Aero/Astro, Stanford University.

BELL, J. H. & MEHTA, R. D. 1990a Development of a Two-Stream Mixing Layer From Tripped and Untripped Boundary Layers. *AIAA Paper 90-0505*.

BELL, J. H. & MEHTA, R. D. 1990b Effects of Streamwise Vorticity Injection on Turbulent Mixing Layer Development. *AIAA Paper 90-1459.*

BERNAL, L. P. & ROSHKO, A. 1986 Streamwise Vortex Structure in Plane Mixing Layers. *J. Fluid Mech.* **170**, 499-525.

BROWAND, F. K. & LATIGO, B. O. 1979 Growth of the Two-Dimensional Mixing Layer from a Turbulent and Nonturbulent Boundary Layer. *Phy. Fluids.* **22**, 1011-1019.

HO, C.-M. & HUERRE, P. M. 1984 Perturbed Free Shear Layers. *Ann. Rev. Fluid Mech.* **16**, 365-424.

HUANG, L.-S. & HO, C.-M. 1990 Small-Scale Transition in a Plane Mixing Layer. *J. Fluid Mech.* **210**, 475-500.

JIMENEZ, J., COGOLLOS, M., & BERNAL, L. P. 1985 A Perspective View of the Plane Mixing Layer. *J. Fluid Mech.* **152**, 125-143.

KONRAD, J. H. 1977 An Experimental Investigation of Mixing in Two-Dimensional Turbulent Shear Flows with Applications to Diffusion-Limited Chemical Reactions. *Ph.D. Thesis.* California Institute of Technology

LASHERAS, J. C., CHO, J. S. & MAXWORTHY, T. 1986 On the Origin and Evolution of Streamwise Vortical Structures in a Plane, Free Shear Layer. *J. Fluid Mech.* **172**, 231-258.

LASHERAS, J. C. & CHOI, H. 1988 Stability of a Plane Turbulent Shear Layer to Axial Perturbations. *J. Fluid Mech.* **189**, 53-86.

MOSER, R. D., & ROGERS, M. M. 1990 Spanwise Scale Change in a Time-Developing Mixing Layer. *Bulletin of the American Physical Society.* **35**, 10, 2294.

NYGAARD, K., & GLEZER, A. 1991 Spanwise-Nonuniform Excitation of a Plane Shear Layer. *AIAA Paper 91-0625.*

ROGERS, M. M., & MOSER, R. D. 1989 The Development of Three-Dimensional Temporally-evolving Mixing Layers. *Proceedings of the 7th Symposium on Turbulent Shear Flows, Aug. 21-23, Stanford University.* **1**, 9.3.1-9.3.6.

RODI, W. 1975 In: *Studies in Convection* (ed. B. E. Launder), *vol.* 1, *pp.* 79-165, Academic Press, London.

SANDHAM, N. D., MUNGAL, M. G., BROADWELL, J. E., & REYNOLDS, W. C. 1988 Scalar Entrainment in Mixing Layers. *Proceedings of the 1988 Summer Program, Center for Turbulence Research.* **CTR-S88**, 69-76.

TOWNSEND, A. A. 1976 *Structure of Turbulent Shear Flow* (2nd Edition). *Cambridge University Press, Cambridge.*

Center for Turbulence Research
Annual Research Briefs - 1990

Characterization of length and velocity scales of free stream turbulence and investigation of their effects on surface heat transfer

By S. Yavuzkurt[1]

The main objective of this research is the characterization of the length and velocity scales of free stream turbulence and investigation of their effects on the length and velocity scales within the boundary layer and on surface heat transfer. An experimental and theoretical research has been carried out in order to achieve these goals. In the experimental arena, a new real-time hot wire technique is being developed using triple and quad wire probes. Both probes have been calibrated and qualified in a fully-developed turbulent channel flow. Reynolds stresses are calculated from the real-time data and compared with the previous data obtained with other means. Quadrant plots of fluctuating velocity components compare well with the numerical data.

These probes will later be used to measure vertical and transverse length scales for all the Reynolds stresses and velocity-temperature correlations, both in the free stream and within the boundary layer.

The surface heat transfer rates will also be measured. The relationship between the character of the free stream turbulence and the surface heat transfer will be explored. An existing wind tunnel capable of generating high levels of free stream turbulence with different length and velocity scales and with heat transfer measurement capability will be used for this purpose.

In the theoretical front, computational data generated from the full solutions of the Navier-Stokes equations for the case of fully-developed two-dimensional turbulent channel flow is being used to study the effect of large centerline structures on the events near the wall. This research is expected to lead into the determination of the relevant length and velocity scales that play a role in the processes near the wall. It will help in understanding of the free stream turbulence effects and will contribute in planning the experimental research.

1. Motivation and objectives

1.1. Introduction

Free stream turbulence is the turbulence in the approach stream. It is experienced in many applications. For example, nozzle guide vanes and the rotor blades in a gas turbine are exposed to the high levels of free stream turbulence.

The free stream turbulence has an important influence on the surface heat transfer. Under high levels of turbulence (10-20%), there is an appreciable increase in the heat transfer rate regardless of the character of the boundary layer.

1 Permanent Address: Pennsylvania State University, on sabbatical at CTR

Some representative results in this area can be found in the studies by Kestin (1966), Kearney *et al.* (1970), Brown and Burton (1978), Bradshaw and Simonich (1978), and Blair (1983). A detailed review of this literature is given by Moffat and Maciejewski (1984). They conclude that the free stream turbulence levels up to 10% cause a proportional increase in heat transfer for constant velocity and accelerating turbulent boundary layers. It is indicated that large effects on the average values may result if the turbulence affects the location of the transition and if the heat transfer data are compared at constant x-Reynolds numbers.

One of the important observations from the literature in this area is that under the same levels of turbulence, different researchers found different enhancement of heat transfer rates. This leads to the speculation that not only the velocity scale but also the length scale of the turbulence is important. In fact, Moffat and Maciejewski (1984) relate to this fact and suggest that the effect of the length scale should be investigated.

Most of the studies that were discussed used, one way or another, grid generated turbulence in their experiments where the length and velocity scales are usually small. More recently, the flow fields of jets and wall jets have been used in order to simulate high free stream turbulence encountered in turbomachinery. Moffat and Maciejewski (1985) used a circular wall jet in order to obtain free stream turbulence intensities up to 48%. They measured Stanton numbers which are as much as 350% above the standard zero free stream turbulence correlations. Ames and Moffat (1990) have investigated the effects of free stream turbulence created by 2.5 inch diameter jet injection into a main flow in a plenum chamber followed by a wind tunnel test section on the heat transfer to a flat plate boundary layer. This study used autocorrelations to measure the length scales. In another recent study, MacMullin *et al.* (1989) investigated the effects of free stream turbulence from a circular wall jet on a flat plate boundary layer heat and momentum transfer with turbulence intensities 7-18%. They also observed increased Stanton numbers and skin friction coefficient with increasing turbulence intensities. They used autocorrelations for the determination of length scales. The influence of length scale on the Stanton numbers was not conclusive.

The present belief of the author is that the length scales in the vertical direction to the wall and in the transverse direction to the flow are more important in determining the scales within the boundary layer which affect the heat transfer. The measurement of these scales using autocorrelations will not give correct answers as indicated by Bradshaw (1971) in flows with high levels of turbulence. These length scales should be measured using space correlations.

There has been also several investigations on the effects of free stream turbulence on the stagnation region heat transfer and hydrodynamics. Some examples are: Sutera *et al.* (1963), Sutera (1965), Britter *et al.* (1979), Sadeh and Bauer (1981), and Vanfossen and Simoneau (1984). Since the boundary layer is thin in the stagnation region and the flow is accelerating, the effects of free stream turbulence can be seen more clearly. General observation obtained from these studies is that not only the level of the free stream turbulence and its length scale are important in

understanding and predicting the heat transfer, but also its distortion as the flow approaches a stagnation point.

A detailed discussion on the free stream turbulence distortion for flows approaching stagnation and its effects on heat transfer can be found in Yavuzkurt and Tafti (1987) and Tafti (1989).

One can observe from these references that the free stream turbulence (especially at large scales and high intensities) is not isotropic. Therefore, in characterizing this phenomenon , the measurement of all velocity scales, i.e. Reynolds stresses and their corresponding length scales, is necessary. It is also important to measure these scales within the boundary layer in order to be able to determine the effects of the free stream scales on the boundary layer scales, which in turn determine the surface heat transfer rate. Interactions of temperature and velocity fluctuations also play an important role in the turbulent heat transfer. Therefore, measurement of velocity and temperature correlations and corresponding length scales is also necessary. For example, interactions of temperature fluctuations with the transverse fluctuating velocity component w' is believed to be an important mechanism; whereas, most of the data in the literature is concentrated upon the measurement of the streamwise component of the fluctuating velocity.

1.2. Objectives

The main objective of this research is to address two important but unresolved problems: The first is the measurement of vertical and transverse length scales via space correlations for all Reynolds stress components and velocity-temperature correlations, both in the free stream and within the boundary layer using the existing triple and quad-wire probes; the second is to relate the character of the free stream turbulence to the character of the turbulence within the boundary layer in order to determine the effect on surface heat transfer.

1.3. Theoretical speculations

There does not exist a complete theory about how the free stream turbulence affects the heat transfer and hydrodynamics within a boundary layer. However, there exists some educated guesses and speculations. Most work consists of experimental observations and some semi-empirical explanations of these observations. A few of these will be mentioned. Kestin (1966) tries to explain the phenomena using an oscillating free stream velocity and speculates that the effect of the free stream turbulence is similar to the secondary steady flow generated by oscillations. However, he acknowledges that the effect produced this way is an order of magnitude smaller than the effect created by the free stream turbulence. Another observation by Sutera *et al.* (1963) indicates that at the stagnation point, the axis of the vortices becomes stretched and certain wavelengths get amplified to affect the boundary layer. This study in general deals with the vorticity amplification near a stagnation point. However, it fails to explain how the free stream turbulence affects the boundary layer and the heat transfer at the stagnation point. Another common opinion is that the free stream turbulence changes the point of transition and thereby increases the heat transfer at a certain location. Again, this idea is

not enough to explain all of the observed behavior, since the free stream turbulence also enhances the heat transfer in a full turbulent boundary layer. In order to address this problem, Moffat and Maciejewski (1985) argued that the turbulence should be treated as a separate property of the flow, measured by a set of attributes such as its intensity components, scale components, spectra, etc. The hypothesis is that whenever the free stream turbulence can disrupt the innermost region of the boundary layer, it will affect the heat transfer. Therefore, small and large scale turbulence may act by quite different means to affect surface heat transfer: small scale turbulence by diffusion and large scale by pressure and shear interactions in the near-wall region. There exists other investigations; however, there is almost no quantitative relationship between the enhancement of heat transfer and the character of the free stream turbulence. The ones which exist are not general enough. In fact, it is still not known what properties of free stream turbulence are the ones which are responsible for the observed behavior. Obviously, one is the velocity scale, but which one is unknown since several velocity scales exist (transverse, vertical, and axial).

In this study, all of the velocity and length scales will be investigated. Space correlations will be used for these measurements. As explained by Bradshaw (1971), as the Reynolds stress and intensity of turbulence increases, deviations from Taylor hypothesis will increase. Therefore, autocorrelations will not give correct length scales in flows with high turbulence intensity, which is exactly the case studied here.

In the author's opinion, interaction between the free stream turbulence and the boundary layer scales and thereby surface heat transfer should be related to the time scales of the free stream turbulence and the time scales of the structures within the boundary layer. Further, the length scales of the velocity fluctuations which interact with the temperature fluctuations could be different. It is most probable that conditional sampling will be needed in order to get the dominant length scales and relationship between them. There is also evidence (although not published yet) which leads this author to think that there might be two different events that are responsible for the action of high free stream turbulence. One is the large unsteady coherent structures like unsteady wake, the other is smaller scale but high frequency turbulent fluctuations. Therefore, two different length and velocity scales might be needed to characterize the free stream turbulence. During the experimental study, conditional sampling will be used to see if this speculation is correct.

2. Accomplishments

2.1. Experimental

The triple wire probe is used with a constant temperature anemometry system to obtain quadrant plots of fluctuating velocities in a fully developed turbulent channel flow at different Reynolds numbers. The data is reduced both digitally and also in an analog fashion using the "three dimensional turbulent flow analyzer" module developed earlier by the author. (Yavuzkurt *et al.* (1978,1980)). Plots of v' vs. u' and v' vs. w' are shown in figure 1. The fluctuating velocities are normalized with

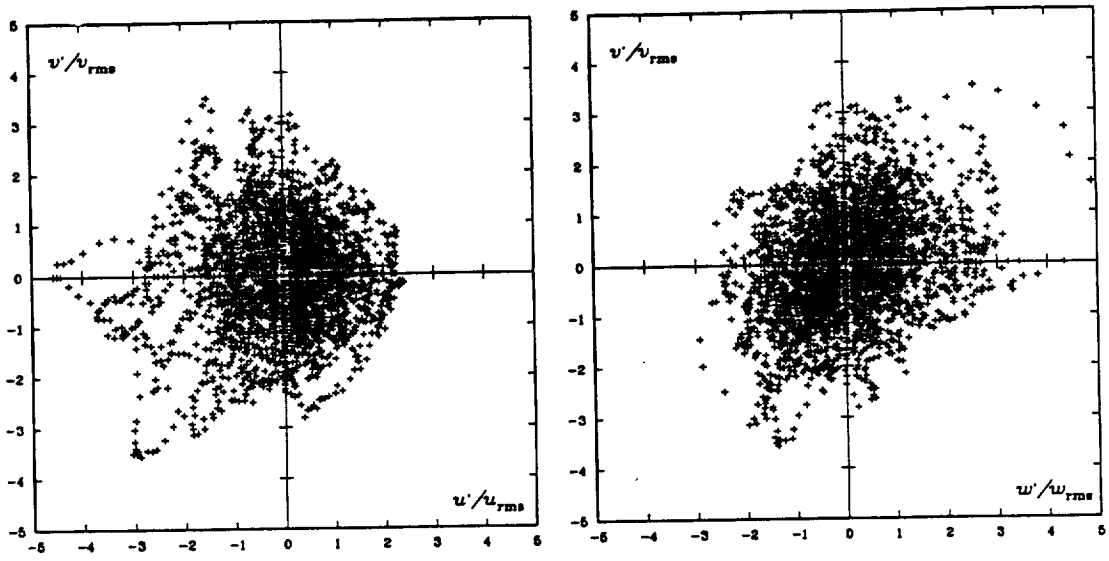

FIGURE 1. Quadrant plots of normalized fluctuating velocity components in the centerline of a fully developed channel flow (left: v' vs u', right: v' vs w'). Reynolds number based on channel half width and centerline velocity is 3300. Obtained using triple wire probe.

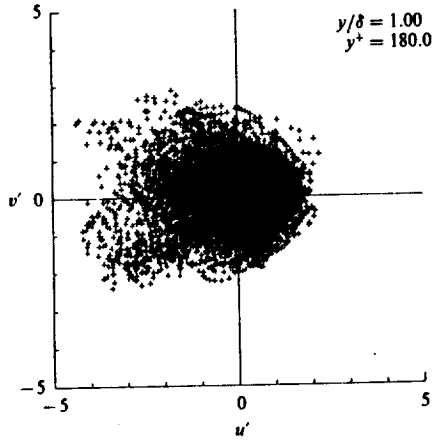

FIGURE 2. Quadrant plots of normalized fluctuating velocity components in the centerline of a fully developed channel flow. Reynolds number is 3300. Obtained from the numerical data of Kim *et al.* (1987).

their own rms values. They compare very well with the numerical results obtained by Kim *et al.* (1987), which are shown in the figure 2. The data was taken at the channel centerline at a Reynolds number based on the centerline velocity and channel half width of 3,300.

The data shown in figure 1 consists of 8,000 data points which were obtained at 5,000 hz. Therefore, the figure shows only about 1.6 seconds of real time data. The data loops which can be seen in the areas away from the figure center are the trajectory of large scales structures in the velocity space. They appear much more clearly in low Reynolds number flows such as this. The triple wire probe and the three-dimensional flow analyzer are also used to obtain the quadrant plots of u', v', and w' on an oscilloscope in real time at Reynolds numbers of 20,000 and 6,000 at different locations. The data is collected at different frequencies by using a low pass filter at 20, 200, 2,000, and 20,000 Hz. The output of the oscilloscope is recorded on a video tape along with the sound generated by the different fluctuating velocity components. The results show that most of the energy of u' is at low frequencies, whereas v' has higher frequency components. This is evident from the pictures and the sound generated by u' and v' under different cut-off frequencies. These measurements showed the capabilities of the triple wire probe and the measurement technique.

The quad wire which is much smaller than the triple wire probe is described in Frota (1982). This probe is shown in figure 3. It has a fourth wire for the measurements of the temperature. This allows the probe to be used in non-isothermal flows and also makes it possible to obtain the velocity-temperature fluctuations in real time. The probe measurement volume is much smaller than the triple wire due to its special construction (3mm vs 1mm). Its diameter being 2mm, it can get much closer to the wall. All the wires has a common prong at the center. The common grounding problems created by this have been solved by a new electronic circuitry. This probe and its circuitry which has not been used earlier is being checked thoroughly. The early results are encouraging. The quad wire has been successfully calibrated and checked in a fully developed channel flow. The shear stress profile obtained using this probe is shown in figure 4 at two different velocities. The comparison between the shear stress profiles obtained with this probe and the ones obtained from the channel pressure drop is excellent.

The quadrant plots of normalized velocity fluctuations u' and v' obtained with the quad wire probe are shown in figure 4 at a Reynolds number of 5,000 at the channel centerline and at a location $y/h = 0.57$ where h is the half channel width. They again compare very well with the previous results. These qualifications show that the quad wire probe with its electronic circuitry can be used for achieving the goals of this research.

2.2. Computational

The data of Kim *et al.* (1987) which is obtained from the full solutions of the Navier-Stokes equations for a fully developed turbulent channel flow is used to correlate the vertical component of the fluctuating velocity v' at the centerline with the temperature fluctuations t' at different planes parallel to the wall-specifically at

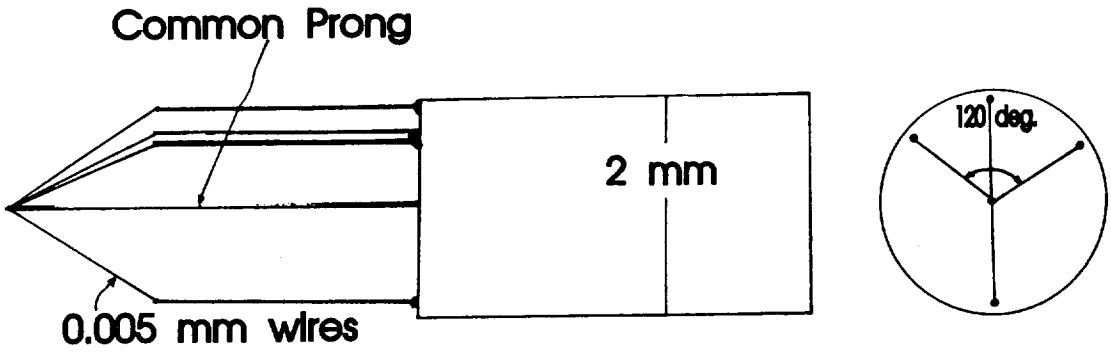

FIGURE 3. Quad wire probe.

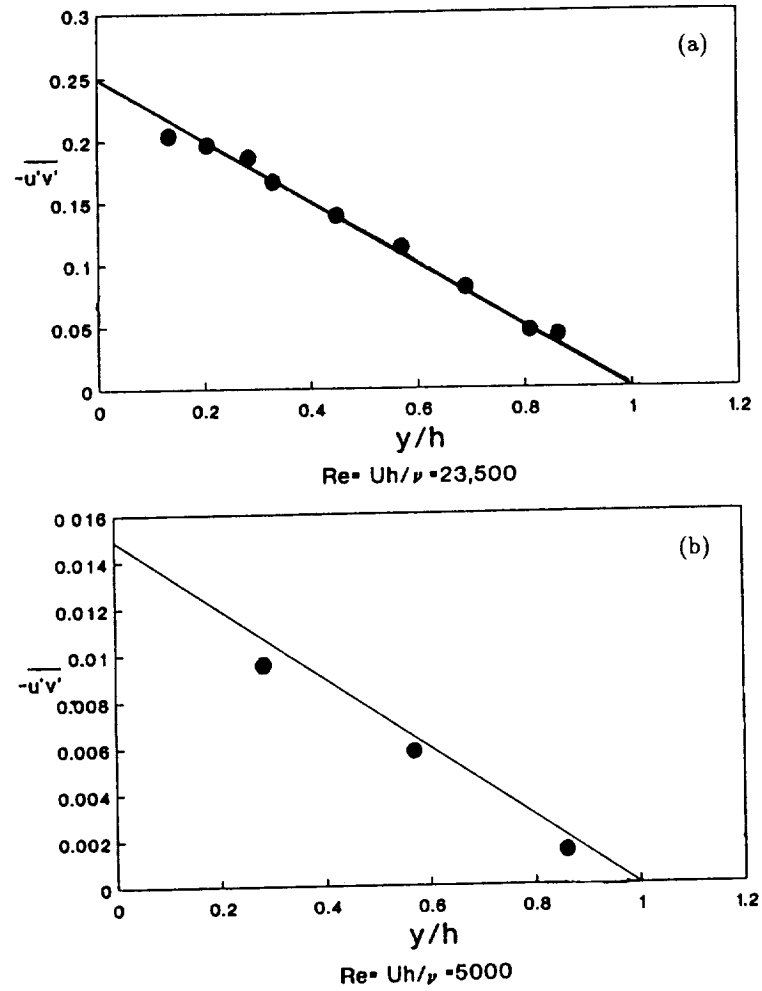

FIGURE 4. Shear stress profiles obtained with the quad wire probe (•) and the channel pressure drop (——) in a fully developed channel flow, a: Re = 23,500, b: Re = 5,000.

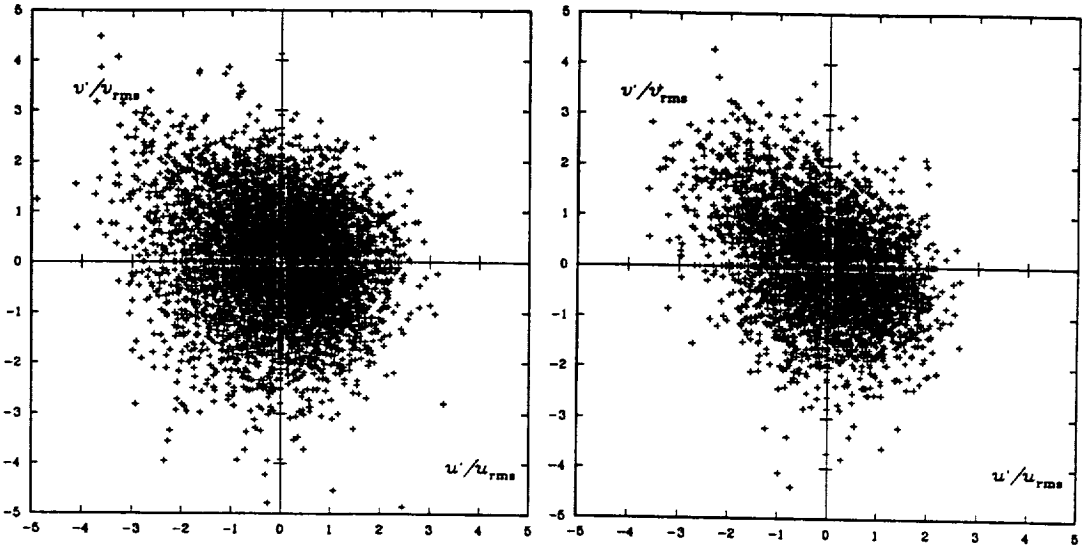

FIGURE 5. Quadrant plots of the velocity fluctuations u' and v' at the centerline (left) and at $y/h = 0.57$ (right) at a Reynolds number of 5,000 in a fully developed channel flow. Obtained with the quad wire probe.

locations $y+ = 180$ (centerline), 100, 60, 10- for different x and z separations. When the full set of wavelengths are used, no correlation is obtained between the centerline and $y+ = 10$ position as will be expected. However, when the filtered data is used, the value of the correlation coefficient is higher and results are more promising. Promising results are also obtained when negative v' is used for the correlations. The calculations using filtered data and different quantities for correlations are continuing. More computational data is needed for long time averaging and for more meaningful results.

3. Future plans

Future plans include using two quad wire probes in the high free stream turbulence rig to obtain the space correlations of the Reynolds stresses and velocity-temperature correlations leading to determination of the effective length and velocity scales of the free stream turbulence which affect the heat transfer as discussed in section 1.3. The computational research will continue in order to determine the proper velocity and length scales which exchange information between the centerline and the wall in a fully developed channel flow using the data of Kim *et al.* (1987). This will help in determining what type of a conditional sampling should be used in the experiments. It is hoped that the final output of this research will be better empirical correlations for the heat transfer with high levels of turbulence. It will also facilitate understanding of how the large scale structures far from a wall interact with the small scales near it.

Acknowledgements

The author would like to express his sincere thanks to Drs. R. J. Moffat, P. Moin,

and J. Kim for their very productive and friendly discussions with him during this research.

REFERENCES

BLAIR, M. F. 1983 Influence of free stream turbulence on turbulent boundary layer heat transfer-part I and II. *ASME J. of Heat Transfer.* **Feb.**

BRADSHAW, P. 1971 *An Introduction to Turbulence and Its Measurement.* Pergamon Press. 30-31

BRADSHAW, P., & SIMONICH, P. 1978 Effect of free stream turbulence on heat transfer through a turbulent boundary layer. *ASME J. of Heat Transfer.* **100-4,**

BRITTER, R. E., HUNT, J. C. R., & MUFFORD 1979 The distortion of turbulence by a circular cylinder. *J. Fluid Mech.* **92,** 269-301.

BROWN, A., & BURTON, R. C. 1978 The effects of free stream turbulence intensity and velocity distribution on heat transfer to curved surfaces. *J. of Engr. for Power.* **100,** 159-168.

FROTA, M. N. 1982 *Analysis of the uncertainties in velocity measurements and technique for turbulence measurements in complex heated flows with multiple hot wires.* Phd. Dissertation, Stanford University, Dept. of Mechanical Engr.

KEARNEY, D. W., KAYS, W. M., & MOFFAT, R. J. 1970 The effect of free stream turbulence on heat transfer to a strongly accelerated turbulent boundary layer. *Proc. of 1970 Heat Transfer and Fluid Mechanics Institute*, edited by T. Sarpkaya.

KESTIN, J. 1966 The effect of free stream turbulence on heat transfer rates. *Advances in Heat Transfer.*

KIM, J., MOIN, P., & MOSER, R. 1987 Turbulence statistics in fully developed channel flow at low Reynolds number. *J. Fluid Mech.* **177,** 133-166.

MACMULLIN, R., ELROD, W., & RIVIR, R. 1989 Free stream turbulence from a circular wall jet on a flat plate heat transfer and boundary layer flow. *Trans. ASME J. of Turbomachinery.* **iii,** 78-86.

MOFFAT, R. J., & MACIEJEWSKI, P. K. 1984 Effects of very high turbulence on convective heat transfer. *Proc. of HOST Conference*, NASA Conference Publication 2339, NASA Lerc, 381-388.

MOFFAT, R. J., & MACIEJEWSKI, P. K. 1985 Heat transfer with very high free stream turbulence. *Proc. of HOST Conference*, NASA Conference Publication 2405, NASA Lerc,203-215.

SADEH, W. Z., & BRAUER, H. J. 1981 Coherent substructure of turbulence near the stagnation zone of a bluff body. *J. of Wind Engr. and Industrial Aerodynamics.* **8,** 73-91.

SUTERA, S. P., MEADER, P. F., & KESTIN, J. 1963 On the sensitivity of heat transfer in the stagnation point boundary layer to free stream vorticity. *J. Fluid Mech.* **16**, 497-520.

SUTERA, S. P., 1965 Vorticity amplification in stagnation point flow and its effect on heat transfer. *J. Fluid Mech.* **21**, 513-534.

VANFOSSEN, G. J., & SIMONEAU, R. J. 1985 Preliminary results of a study of the relationship between free stream turbulence and stagnation region heat transfer. *ASME paper no. 85-GT-84*

TAFTI, D., 1989 *Prediction of Heat Transfer Characteristics for Discrete Hole Film Cooling on Flat Plate and Turbine Blades.* Ph.D. Dissertation, Penn. State Univ., Dept. of. Mechanical Engr.

YAVUZKURT, S., MOFFAT, R. J., & CRAWFORD, M. E. 1978 Real time hot wire measurements in three dimensional flow. *Proc. of 5th Biennial Symp. on Turbulence*, Rolla, Missouri.

YAVUZKURT, S., MOFFAT, R. J., & KAYS, W. M. 1980 Full coverage film cooling: Part 1-three dimensional measurements of turbulence structure. *J. Fluid Mech.* **101**, 129-159.

YAVUZKURT, S., & TAFTI, D. 1987 *Turbulence Modeling for Flat Plate and Turbine Airfoil with Discrete Film Cooling.* Contractors Report RFQ:PC693359, Textron Lycoming Corp., Stratford, Conn.

Center for Turbulence Research
Annual Research Briefs - 1990

Dual spectra and mixed energy cascade of turbulence in the wavelet representation

By C. Meneveau[1]

The wavelet-transformed Navier-Stokes equations are used to define quantities such as the transfer of kinetic energy and the flux of kinetic energy through scale r at position $\vec{x}$. Direct numerical simulations of turbulent shear flow reveal that although their mean spatial values agree with their traditional counterparts in Fourier space, their spatial variability at every scale is very large, exhibiting non-Gaussian statistics. The local flux of energy involving scales smaller than some r also exhibits large spatial intermittency, and it is negative quite often, indicative of local inverse cascades.

1. Introduction

Much has been learned about the physics of turbulence by transforming the velocity and the Navier-Stokes equations to Fourier space. The velocity field $\vec{u}(\vec{x},t)$ is then represented as a linear combination of plane waves, characterizing the motion at different scales. For isotropic turbulence, the energetics of turbulence is described (Monin & Yaglom 1971) by the three-dimensional energy spectrum $E(k,t)$ obeying

$$\frac{\partial E(k,t)}{\partial t} = T(k,t) - 2\nu k^2 E(k,t), \tag{1}$$

where $T(k,t)$ is the net transfer of energy to wavenumbers of magnitude k. $T(k,t)$ is formally defined in terms of triple products of velocity and, thus, embodies the closure problem resulting from the nonlinearity of the equations. For the statistically stationary case, the total spectral flux of energy through wavenumber k to all smaller scales is given by

$$\pi(k) = \int_{k'=k}^{\infty} T(k')dk' = -\int_{0}^{k} T(k')dk'. \tag{2}$$

Usually the energy transfer is thought to occur by creation of small scales through stretching and folding of vortical elements, which is modeled by simplified processes such as the successive break-down of 'eddies' (see e.g. Meneveau & Sreenivasan 1990). One then argues that through scales of motion of size k^{-1}, there is a net flux of kinetic energy to smaller scales, which is equal to $\pi(k)$. In the 'inertial range' (Monin & Yaglom 1971), one expects this flux to be equal to the average rate of dissipation of kinetic energy $< \epsilon >$.

1 Department of Mechanical Engineering, Johns Hopkins University, Baltimore MD

Of course, it has been known for a long time that the local rate of dissipation is distributed very intermittently in space and time. This can be modeled within the framework of breakdown of eddies but with the assumption that the flux of energy to smaller scales exhibits spatial fluctuations at every scale (see e. g. Frisch *et al.* 1978, Meneveau & Sreenivasan 1990) . Thus, we need to define a flux of kinetic energy which, as opposed to Eq. 2, should also depend on position (see, for instance, the discussion in Kraichnan (1974)). In general terms then, it is clear that from Fourier spectra, any information related to position in physical space is completely hidden, which is a disadvantage when dealing with spatially localized flow structures or intermittency. On the other hand, with the purely spatial representation, the information about different scales of motion is hidden. This information is often a useful ingredient for modeling and physical insight. This difficulty calls for a representation that decomposes the flow-field into contributions of different scales *as well as* different locations. In other words, we want to use basis functions that behave more like localized pulses than extended waves. If one wishes them to be self-similar, one is led to rather special basis functions called wavelets.

Using the wavelet representation of the velocity field, we introduce quantities that are analogous to the Fourier spectra of energy $E(k,t)$, transfer $T(k,t)$, and energy flux $\pi(k,t)$, but which depend on location as well as scale. These quantities can be used in several ways, e.g. to correlate specific local events with possible structures or topological features of the flow field. Here we will restrict our attention to statistical descriptions of the spatial distribution of these quantities via their probability densities and second-order moments. Measurements are performed in two 3-D fields obtained from direct numerical simulations of isotropic and homogeneous shear flows. Here we present only results on transfer of energy to some scale of motion, and on the flux of energy to scales smaller than some cutoff r for the shear flow simulation. More extensive results and a more detailed description of this study can be found in Meneveau (1990).

2. Orthonormal wavelets

Wavelets (Grossmann & Morlet, 1984) are pulse-like functions of zero mean whose dilations are convolved with the signal, providing simultaneous resolution in scale and position. In the field of turbulence for instance, continuous wavelet analysis has been used for the study of coherent structures (Farge & Rabreau, 1987) and of two-dimensional data from a turbulent jet (Everson *et al.* 1990). Recently, several orthonormal wavelet basis functions have been constructed by using a logarithmic spacing of scales and increasingly coarser spatial discretization at larger scales (Meyer 1986, Daubechies 1988, Mallat 1989); the absence of redundancy of information makes this form of wavelets particularly useful in higher dimensions. In one dimension, orthonormal wavelets are of the form

$$\psi^{(m)}(x - 2^m hi) = 2^{-\frac{m}{2}} \psi(\frac{x - 2^m hi}{2^m h}), \tag{3}$$

where m indicates the octave band of the scale parameter, h is the mesh-spacing of the basic lattice (smallest scales), and the index i refers to location in units of

$2^m h$. Notice that the basis functions corresponding to the larger scales are spaced more coarsely, according to a dyadic arrangement on a binary tree structure. Some particular functions $\psi(x)$ exhibit the property that $\{\psi^{(m)}(x - 2^m hi)\}$ forms an orthonormal base for all (i, m), as for instance the Lemarie-Meyer-Battle (LMB) wavelet shown in Fig. 1. It has exponential decay in x space and ω^{-4} decay in Fourier space. For more details on this, on discrete transforms, and on fast algorithms, see Mallat (1989), Daubechies (1988) and Meneveau (1990).

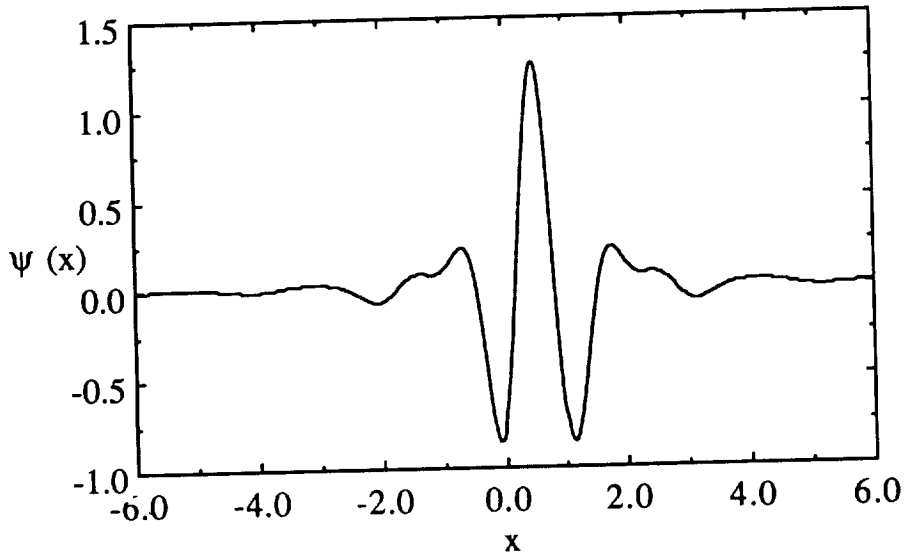

FIGURE 1. Example of an orthonormal wavelet basis function $\psi(x)$ (Lemarie-Meyer-Battle wavelet).

In an extension of this formalism to three dimensions (Meneveau 1990), the velocity field (at some instant t) is written as

$$u_i(\vec{x}) = \sum_m \sum_{q=1}^{7} \sum_{\vec{i}} w^{(m,q)}[\vec{i}]\ \Psi^{(m,q)}(\vec{x} - 2^m h\vec{i}), \tag{4}$$

where m denotes again the scale, $\vec{i} = (i_1, i_2, i_3)$ is the three-dimensional position index on a cubic lattice of mesh-size $2^m h$, and q gives additional internal degrees of freedom (this is needed because $\Psi^{(m,q)}$ is decomposable into functions such as Fig. 1 in each Cartesian direction). Because of orthonormality, the discrete wavelet coefficients can be computed as

$$w_i^{(m,q)}[\vec{i}] = \int u_i(\vec{x})\ \Psi^{(m,q)}(\vec{x} - 2^m h\vec{i})\ d^3\vec{x}. \tag{5}$$

3. Energetics of turbulence in wavelet space

We now start with the Navier-Stokes equations in physical space written for the fluctuating velocity and pressure, and we take its inner product with the wavelet basis function $\Psi^{(m,q)}(\vec{x} - 2^m h\vec{i})$. This yields an evolution equation for the wavelet coefficients $w_i^{(m,q)}[\vec{i}]$. Multiplication by $w_i^{(m,q)}[\vec{i}]$ and contraction over the three directions i and the index q yields an evolution equation for the local kinetic energy density,

$$\frac{\partial}{\partial t} e^{(m)}[\vec{i}] = t^{(m)}[\vec{i}] - v^{(m)}[\vec{i}], \tag{6}$$

where

$$t^{(m)}[\vec{i}] = -\sum_{i=1}^{3}\sum_{q=1}^{7} w_i^{(m,q)}[\vec{i}] \int (u_j \frac{\partial u_i}{\partial x_j} + \frac{1}{\rho}\frac{\partial p}{\partial x_i})\ \Psi^{(m,q)}(\vec{x} - 2^m h\vec{i})\ d^3\vec{x}. \tag{7}$$

is the net energy transfer through scale $2^m h$ at location $2^m h\vec{i}$. $e^{(m)}[\vec{i}]$ is the kinetic energy and $v^{(m)}[\vec{i}]$ is the contribution of the viscous terms, including molecular diffusion of energy and dissipation at that scale and location. Equation 6 is the (discrete) analogue of Eq. 1, written for the energy of orthonormal pulses rather than waves. In analogy to Eq. 2, the flux of kinetic energy through a spatial region of characteristic size $2^m h$ and location $2^m h\vec{i}$ can be computed by adding the transfer-density (local transfer divided by the total number of grid-points at each scale) over all scales larger than $2^m h$ at that particular location:

$$\pi^{(m)}[\vec{i}] \ = \ -\sum_{n=m}^{M} \ 2^{3(M-n)}\ t^{(n)}[\vec{j}]. \tag{8}$$

Here M is the scale index of the largest scale considered, and $\vec{j}$ (given by the integer part of $2^{m-n}\vec{i}$) is the position index of the larger scales (n). Several studies (Siggia 1978, Zimin 1981 and Nakano 1988) have used 'wavepackets' (essentially wavelets) for obtaining approximations to the Navier-Stokes equations and have then deduced energy cascade models. Here we perform actual measurements of these quantities relevant to the energetics of turbulence, without approximations.

To proceed, we compute the spectral transfer density at wavenumber $k_m = 2\pi/(2^m h)$ by dividing the total transfer in the band m,

$$\sum_{\vec{i}} t^{(m)}[\vec{i}] = 2^{3(M-m)} < t^{(m)}[\vec{i}] > \tag{9}$$

by $\Delta k_m = k_m ln(2)$ and by the total number of points 2^{3M}. We obtain

$$T_w(k_m) = 2^{-3m} k_m^{-1} [ln(2)]^{-1} < t^{(m)}[\vec{i}] >, \tag{10}$$

where the average extends over all points $[\vec{i}]$. $T_w(k_m)$ is equivalent to the Fourier transfer spectrum $T(k)$ but is not necessarily identical at every k because of the

width of the wavelet in Fourier space. Also, the wavenumber resolution is poorer in the orthonormal wavelet case because of the discretization of scales in octaves. The additional information is available as spatial resolution which increases with decreasing scale. In addition to the spectral content, one can inquire about the spatial variability of $t^{(m)}[\vec{i}]$, which is given in terms of its standard deviation (in units of $T(k_m)$) according to

$$\sigma_t(k_m) = 2^{-3m} k_m^{-1} [ln(2)]^{-1} \; (< t^{(m)}[\vec{i}]^2 > - < t^{(m)}[\vec{i}] >^2)^{\frac{1}{2}}, \qquad (11)$$

where the average again extends over all points $[\vec{i}]$. A plot of $T_w(k_m)$ and $T_w(k_m) \pm \sigma_t(k_m)$ as a function of k_m will be called the *dual spectrum* of transfer, dual because it gives information both about the contribution of various scales *and* about the spatial variability associated with it. Similar definitions of dual spectra can be introduced for the kinetic energy and the flux of energy (Meneveau 1990). Furthermore, in Meneveau (1990), it is shown that the local kinetic energies form a (non-conservative) multifractal measure.

4. Analysis of turbulent fields

Next we turn to the analysis of three-dimensional turbulent fields. We consider direct numerical simulation of homogeneous sheared turbulence on a 128^3 grid, described in detail in Rogers *et al.* (1986) and Rogers & Moin (1986). We consider the field C128U12, which is at $t = 12$ in units of the imposed shear, when the Taylor microscale-scale Reynolds number is about 110. The field is not isotropic as elongated vortical structures are visible (isotropic turbulence of lower Reynolds number was also considered (Meneveau 1990). We compute the 3-D wavelet transform of the three velocity components, using the LMB wavelet basis. To compute the local transfer $t^{(m)}[\vec{i}]$, we need to compute the wavelet transform of the nonlinear terms of the Navier-Stokes equation (the pressure is computed from the known fluctuating velocity field using the Poisson equation), and then we apply Eq. 8.

Figure 2 shows the dual transfer spectrum $T(k_m)$ and $T(k_m) \pm \sigma_t^{(m)}$ computed from the homogeneous shear-flow, in Kolmogorov units.

The mean transfer (circles) is negative for low-wavenumbers and positive at high wavenumbers, showing that on the average energy is being transferred from large to small scales. The solid line indicates the corresponding radial Fourier transfer spectrum (obtained from the usual Fourier analysis), in reasonable agreement with the mean wavelet transfer. However, the standard deviation $\sigma_t^{(m)}$ is seen to be very large, implying that locally the transfer of energy is often quite far from its spectral mean value. This is borne out even clearer in the probability-density functions of $t^{(m)}[\vec{i}]$ of Fig. 3, which is for three scales $m = 1, 2, 3$. Large deviations away from the mean are visible, both on the positive and negative side. Also, we note the long tails of the distributions, which are of the exponential type. The same calculations for the isotropic flow yield similar results (Meneveau 1990).

The quantity $t^{(m)}[\vec{i}]$ represents the local transfer through a certain scale without discriminating between the other two scales involved in the nonlinear interactions. In order to define a position-dependent flux of kinetic energy to all scales smaller

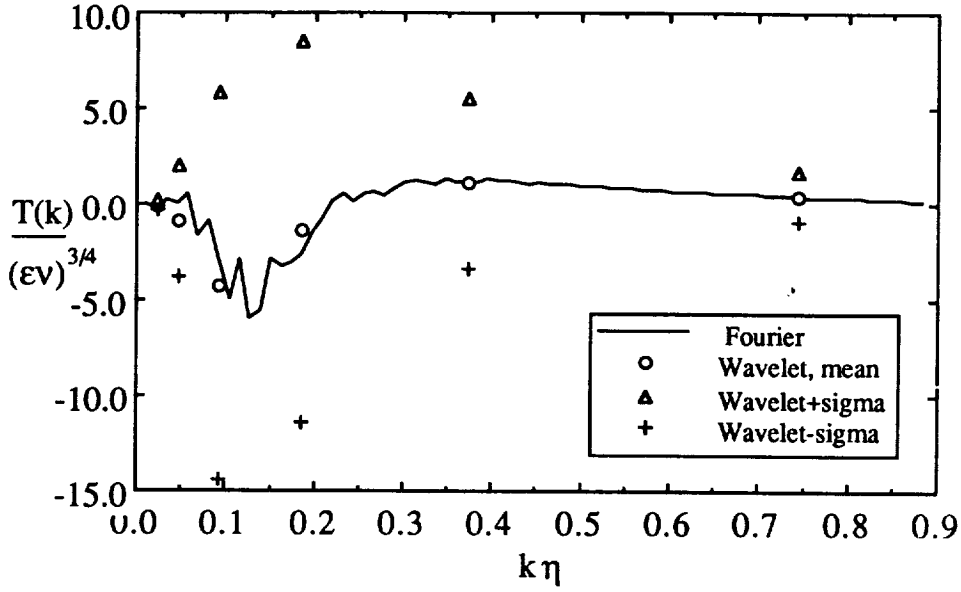

FIGURE 2. Dual spectrum of transfer of kinetic energy for homogeneous shear simulation, in Kolmogorov units. The solid line is the usual Fourier transfer, the circles are the mean wavelet spectrum, and the triangles and crosses are the wavelet mean, plus and minus one standard deviation computed from the spatial fluctuations at every scale.

than some cutoff-band m which does not include sweeping by the larger scales, one needs to decompose the non-linear terms in more detail. In Meneveau (1990) we show that

$$t^{(m,n)}[\vec{i}] = \sum_{i=1}^{3}\sum_{q=1}^{7} w_i^{(m,q)}[\vec{i}] \int \{\frac{\partial}{\partial x_j}[u_i u_j - u_i^{>n} u_j^{>n}] + \rho^{-1}\frac{\partial}{\partial x_i} p^{<n}\} \Psi^{(m,q)}(\vec{x} - 2^m h\vec{i})\, d^3\vec{x}, \quad (12)$$

represents the transfer of energy between scales m and all scales smaller than n, a quantity that is analogous to the Fourier transfer spectrum $T(k \mid k_n)$ (Kraichnan 1976), defined as the total contribution to $T(k)$ from triads of wavenumbers $(k, q, k-q)$ having $k < k_n$ and at least one of the other two legs larger than k_n. In Eq. 12, the superscripts $> n$ ($< n$) refer to low-pass (high-pass) filtered fields obtained from Eq. 4 by performing the sum over all $m \geq n$ ($m < n$).

A quantity of great practical importance (Rogallo & Moin 1984) is the effective sink of kinetic energy due to scales of motion smaller than some cutoff. In the Fourier representation, this sink of energy is given (Kraichnan 1976) as a flux

$$\pi_{sg}(k) = -\int_{k'=0}^{k} T(k' \mid k)\, dk'. \quad (13)$$

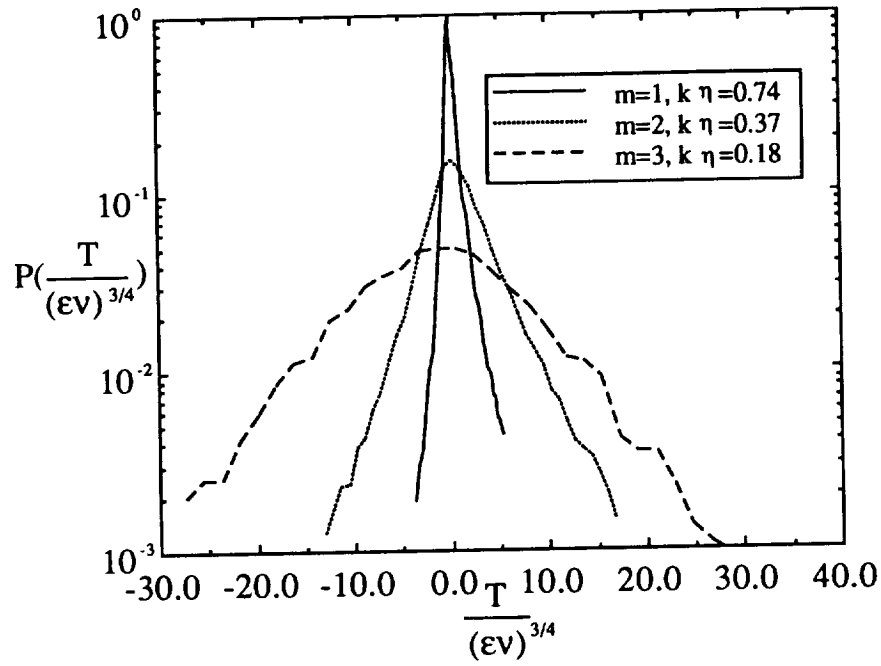

FIGURE 3. Probability density distribution of transfer of kinetic energy at scale $m = 1, 2, 3$, in Kolmogorov units.

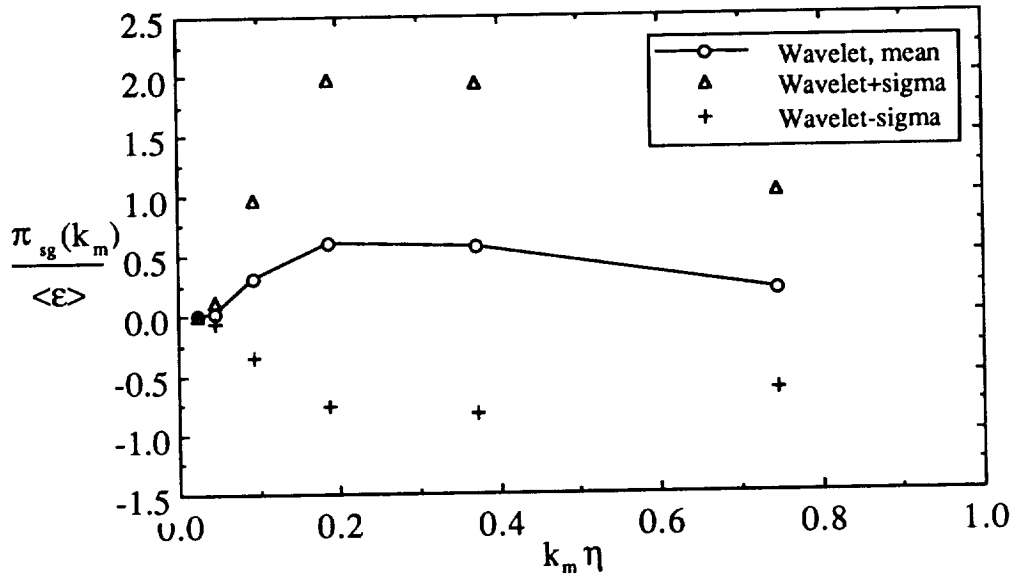

FIGURE 4. Dual spectrum of the flux of kinetic energy from interactions with all smaller scales of motion (flux to or from the subgrid scales), for the homogeneous shear flow simulation. Symbols as in Fig. 2.

The analogous definition in the wavelet representation is the local flux of energy to smaller scales,

$$\pi_{sg}^{(m)}[\vec{i}] = - \sum_{k=m}^{M} 2^{3(M-k} \, t^{(k,m)}[2^{m-k}\vec{i}]. \tag{14}$$

This quantity is measured in the homogeneous shear flow simulation, its dual spectrum is computed, and we obtain the probability density of this subgrid flux at every scale. The results are shown in Figs. 4 and 5.

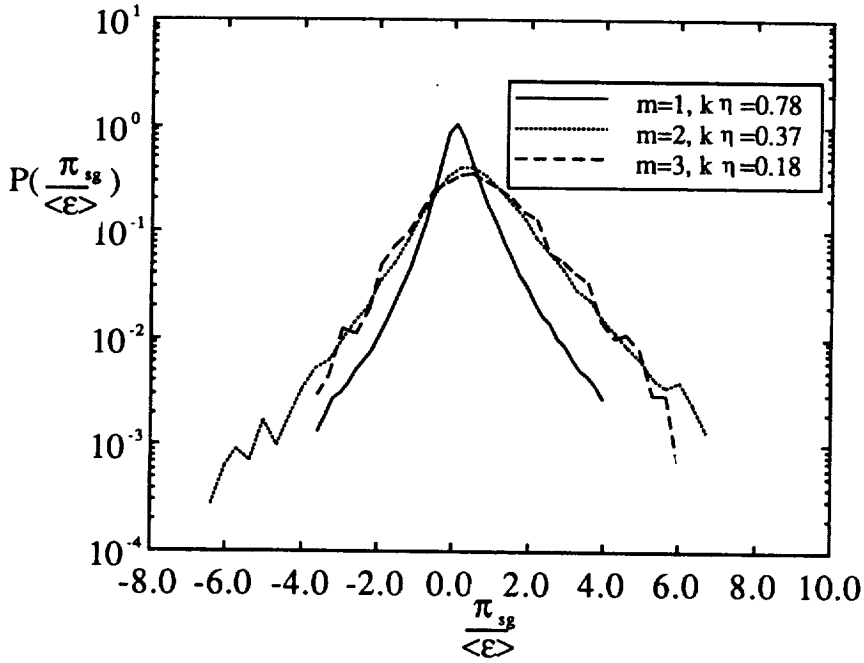

FIGURE 5. Probability density function of spatial fluctuations of local subgrid flux of kinetic energy for the homogeneous shear simulation, for scales corresponding to $m = 1$, $m = 2$, and $m = 3$.

We make the following observations: The mean subgrid flux is always positive, indicating that on the average, energy flows from large to small scales. There are strong spatial fluctuations, and the statistics of π_{sg} are far from Gaussian, exhibiting very clearly, again, long and exponential tails. These long tails mean that the flux is very intermittent in space at every scale of motion. The fluctuations of the subgrid flux are such that it can be negative very often (local backscatter). In such locations, energy actually flows from the small to the large scales of motion, i.e. there are local inverse cascades. The phenomenon of local backscatter has also been observed recently during analysis of channel flow and compressible turbulence (Piomelli *et al.*, 1990), with very similar results concerning the fraction of points at which backscatter is observed. The tails of the distributions are nearly symmetric to both sides; thus, the average being positive comes from a delicate balance between

large positive and not-so-large negative excursions of localized events. The analysis of isotropic decaying turbulence yields similar results (Meneveau 1990).

We have shown elsewhere (Meneveau 1990) that these results are relatively robust with respect to the precise wavelet used. One of those wavelets was essentially a sharp Fourier band-pass filter in octaves (Fourierlet), suggesting that statistical results obtained by such approaches (e.g. the study of Domaradzki & Rogallo 1990) give results that are comparable to the ones using wavelet analysis.

5. Concluding remarks

We conclude with some general observations regarding the usefulness of orthonormal wavelets and will then proceed to recapitulate the results regarding spatial distribution of turbulence energetics.

The traditional discrete Fourier transform maps a 3-D function sampled on N^3 points onto $N^3/2$ complex Fourier coefficients (conserving the amount of information N^3). From this, useful and compact statistical information can be extracted as power-spectra of the field, either the radial spectrum or separate spectra in the different Cartesian directions. The usefulness of this approach stems from a variety of reasons including: (a) the existence of the Fast Fourier Transform, which allows efficient calculation of the transform (this also has permitted the manufacture of appropriate hardware such as digital spectral analyzers); (b) the straight-forward interpretation of the power-spectral density as related to the squared amplitude of waves in which the field is being decomposed; (c) the fact that the discrete Fourier transform is used not only as a tool of analysis but also to solve partial differential equations. Other basis functions such as Tchebychev polynomials are often employed to deal with particular boundary conditions; for the purpose of the present discussion, however, we consider them of the same family as the Fourier modes due to their global nature.

Orthonormal wavelet functions have the property that they also conserve information, that is, a discretely sampled field on N^3 points will yield only N^3 coefficients. However, these will be organized in a fashion that allows distinction between scale and location. This property is best illustrated in one dimension: here we have a total of N gridpoints and, thus, N coefficients: $N/2$ of them give information at $N/2$ different locations about the smallest scale, $N/4$ on the spatial distribution at the next largest scale, etc. The last coefficient is related to the global mean of the field. This dyadic arrangement not only makes sense physically (the larger scales are sampled more coarsely than the smaller ones), but it also allows for the implementation of a fast algorithm, analogous to the Fast Fourier Transform.

One of the objectives of the present work was to propose a variety of tools to analyze turbulence using the orthonormal wavelet decomposition instead of the Fourier transform. In order for the analysis to be practical, we had to achieve significant reductions in the amount of data. In the case of the 3-D Fourier transform where we start with N^3 values, the spectra essentially reduce to a single-valued function consisting of $O(N)$ points. This is easy to visualize and to interpret physically. Here we obtain more than the spectrum, using the additional spatial information that

is now available. In this work, the focus is still statistical, but the idea is to postpone spatial averaging as long as possible. In comparison with the discrete Fourier analysis, we have then that the orthonormal wavelet approach has the following properties: (a) there is an efficient fast wavelet algorithm allowing the computation of all the coefficients with at most $O(NlogN)$ operations (for some wavelets, the operation count can be as low as $O(N)$!); (b) The interpretation of the square of the coefficients as the energy of localized pulses is straight-forward and very intuitive; (c) statistical properties (or more detailed spatial characterizations) of these coefficients in addition to the power-spectrum can be obtained and are easy to visualize and interpret. So far then, there is no practical difference between Fourier and wavelet analysis, but the latter allows more meaningful analysis of spatial properties at every scale, which is of great importance in the case of turbulence. The other important point raised in connection with the usefulness of the discrete Fourier transform, namely that it can play a key role in actually solving the equations, can not be made so far with the wavelet basis functions (there are several preliminary efforts in that direction, but it is too early to emphatically conclude as to their usefulness in this context). Therefore, for the time being, we only concentrated on properties (a), (b), and (c) listed above, which we feel are worth exploring in the hope of characterizing turbulent flow-fields in a systematic fashion.

The idea of studying turbulence using a space and scale dependence is not new: It was the motivation for band-pass filtering turbulent signals, an approach that was employed to study intermittency (see e.g. Kennedy and Corrsin 1961). Such studies were decisive in showing that turbulent activity becomes more and more intermittent at smaller and smaller scales, as quantified by appropriate statistical measures such as flatness factors. However, such methods of analysis are rather arbitrary in terms of the shape of filters, their bandwidth, etc. Here we attempted to circumvent this arbitrariness by invoking the more rigorous foundations of orthonormal wavelet analysis, which has the prospect of becoming a more standardized tool.

The relative simplicity of the *analysis* of turbulence with wavelets stems from the fact that they are generated from a single function, known *a priori*, and this, therefore, does not depend on the specific flow. This is in contrast to the method of 'proper orthogonal decomposition' (Lumley 1967), which constructs basis functions that maximize the energy contained in the smallest number of modes. Here we do not attempt any such optimization, and so the number of wavelets needed is generally high. However, such an approach is necessary to study local properties of instantaneous realizations of turbulent flows because, for example, in the case of homogeneous flows, the proper orthogonal decomposition yields the usual non-local Fourier modes.

We introduced the dual spectral representation, which measures the contributions of each scale as well as its spatial variability. This could then be used to quantify the intermittency of the local transfer of kinetic energy in wavelet space. This quantity was then measured in direct numerical simulations of turbulence, and strong spatial fluctuations were observed, their mean spectral value being quite unrepresentative of local values. This is consistent with the findings of Piomelli *et al.* (1990).

By appropriately decomposing the non-linear terms of the Navier-Stokes equation, we could subtract the transfer (and flux) due to the interactions with the large scales from the total values. This then allowed the definition of a dual spectrum of $\pi_{sg}(r, \vec{x})$, the flux of energy involving the scales smaller than r, at location $\vec{x}$. Again, this quantity exhibited intermittent spatial behavior with exponential tails in its probability density distributions, while its spatial mean values were consistent with the usual spectral behavior. The importance of exponential tails in turbulence is confirmed by these observations. Quite importantly, large negative values of $\pi_{sg}(r, \vec{x})$ were observed, implying local inverse energy flux from small to large scales of motion. Although these results have been obtained for a low-Reynolds number flow where no fully developed inertial range exists, it seems unlikely that the local backscatter would disappear completely at higher Reynolds numbers. In fact, the analysis of channel flow by Piomelli *et al.* (1990) suggests a modest increase of backscatter with Reynolds number. Much of the phenomenological cascade models of intermittency work under the assumption of local (in x- and k-space) energy transfer from large to small scales, where, from dimensional arguments, the locally averaged rate of dissipation (always positive) is the quantity representative of the local inertial-range flux of energy. Such a picture must be revised in order to allow for negative fluxes to occur.

In Meneveau 1990, we have proposed a simple extension to the traditional cascade models of energy, which allows for backscatter (negative energy flux) in an intermittent fashion. The model suggests (but does not prove) that the detailed spatial statistics of the backscatter are intimately linked to the intermittency of the cascade. In this mixed cascade model, if there was no intermittency (as in the original Kolmogorov cascade picture), there also would not be negative flux. Only the strong spatial fluctuations produced by intermittency allow some small scales to be very active, so that if they pair (passing a part of their flux of energy to the larger scale), the resulting negative flux may locally overwhelm the positive one. We have shown that such mixed cascade models exhibit the same qualitative features as the real local flux: increasing intermittency at decreasing scale, exponential-like tails of the probability density for both positive and negative values. However, measurements of $\pi^{(m)}(\vec{x})$ need to be made at higher Reynolds numbers before we can make more quantitative comparisons with such mixed cascade models.

In summary, the general picture of turbulence that is confirmed by this analysis is that there is strong spatial intermittency in all non-linear quantities, their mean spectral behavior resulting from a delicate balance given by the difference of large positive and negative excursions in space. The wavelet analysis is a way of quantifying these observations in a standardized fashion by using 'flow-independent eddies' to decompose the velocity field. The present study shows that orthonormal wavelet analysis can be performed just as easily as Fourier analysis, and we believe the physical interpretation of the wavelet coefficients is more natural to the phenomenon of turbulence than the coefficients of globally extended functions such as Fourier modes. As remarked by Stewart (1989), one is decomposing the motion into 'solitons', a concept more appropriate for non-linear phenomena.

Acknowledgements

It is my pleasure to express my gratitude to Prof. P. Moin for his numerous suggestions and for many stimulating conversations on this topic. I am indebted to Dr. M. Rogers for his help and for making available his simulations of homogeneous shear flow, as well as to Dr. R. Rogallo for providing me with his simulation of decaying isotropic turbulence and for very interesting discussions. I have also greatly benefitted from comments and conversations with Prof. A. Grossmann, Prof. W. C. Reynolds, Prof. J. Ferziger, Prof. M. Farge, Dr. J. van der Vegt, Dr. S. Veeravalli, and Mr. M. Krishnan.

REFERENCES

DAUBECHIES, I. 1988 *Comm.Pure Appl. Math* **XLI**, 909.

DOMARADZKI, J. A. & ROGALLO, R. 1990 *Phys. Fluids A* **s**, 413.

EVERSON, R., SIROVICH, L. & SREENIVASAN, K. R. 1990 *Phys. Lett. A* **145**, 314.

FARGE, M. & RABREAU, G. 1988 *C. R. Acad. Sci. Paris* **II 307**, 1479.

FRISCH, U., SULEM, P. L. & NELKIN, M. 1978 *J. Fluid Mech.* **87**, 719.

GROSSMANN, A. & MORLET, J. 1984 *SIAM J. Math. Anal.* **15** 723.

KENNEDY, D. A. & CORRSIN, S. 1961 *J. Fluid Mech.* **10**, 366.

KRAICHNAN, R. H. 1974 *J. Fluid Mech.* **62**, 305.

KRAICHNAN, R. H. 1976 *J. Atmos. Sci.* **33** 1521.

LUMLEY, J. L. 1970 *Stochastic Tools in Turbulence.* Academic Press, New York.

MALLAT, S. J. 1989 *IEEE Patt. Anal. and Mach. Int.* **11** 674.

MENEVEAU, C. 1990 Analysis of Turbulence in the Orthonormal Wavelet Representation. CTR Manuscript No. 120, Center for Turbulence Research, Stanford University

MENEVEAU, C. & SREENIVASAN, K. R. 1990 *J. Fluid Mech.* To appear.

MEYER, Y. 1986 in *Seminaire Bourbaki* page 662.

MONIN, A. & YAGLOM, A. 1971 *Statistical Fluid Mechanics.* MIT Press, Cambridge MA.

NAKANO, T. 1988 *Phys. Fluids* **31**, 1420.

PIOMELLI, U., CABOT, W. H., MOIN, P. & LEE, S. 1990 in *Proceedings of the Summer Program 1990*, Center for Turbulence Research, Stanford University.

ROGALLO, R. & MOIN, P. 1984 *Ann. Rev. Fluid Mech.* **16**, 99.

ROGERS, M., MOIN, P. & REYNOLDS, W. C. 1986 *Technical Report TF25*, Stanford University.

ROGERS, M. & MOIN, P. 1986 *J. Fluid Mech.* **176**, 33.

STEWART, I. 1989 *Nature* **338**, 18.

SIGGIA, E. D. 1977 *Phys. Rev. A* **15**, 1730.
ZIMIN, V. D. 1981 *Izvestiya, Atm. Oceanic Phys.* **17**, 941.

Stationary turbulent closure via the Hopf functional equation

By H. H. Shen

1. Motivation and objectives

"It is commonly accepted that turbulent flow is necessarily statistical in nature. Hopf formulated an equation governing the probability function for such flows (Hopf 1952), but so far no genuinely physical explicit solutions have been obtained ..." (Foias, Manley, Temam 1987). Thus, despite the fact that the Hopf approach has been characterized by some as "the most compact formulation of the general turbulence problem" (Monin, Yaglom 1965) and even "the only exact formulation in the entire field of turbulence" (Stanisic 1985), its actual usefulness in predicting statistics has until now been extremely limited by the lack of explicit solutions. By applying the Navier-Stokes equation to the moment-generating functional for the velocity, the Hopf approach transforms a nonlinear differential equation describing a single flow realization to a linear functional-differential equation governing an ensemble of flows. However, in the absence of a general method for solving such equations, results have until now been mostly of a formal nature (Rosen 1971, Alankus 1989).

It is our purpose here to exhibit explicit solutions of the stationary Hopf equation and begin to explore their computational possibilities. The motivation is to circumvent the infinite hierarchy of coupled equations for the velocity moments and obtain an exact closure of the steady-state 3D Navier-Stokes equations, without modeling assumptions or truncation. In section 2, we review the Hopf formulation of the Navier-Stokes equation. In section 3.1, we display and discuss a stationary homogeneous solution for 2D flow. In section 3.2, we show how depletion of nonlinearity may arise for 3D forced homogeneous flow. Section 3.3 considers the general 3D forced case while section 3.4 derives a method for closing the 3D unforced equations with arbitrary boundary conditions. We conclude with future plans.

2. Review: Hopf Equation

Recall (Hopf 1952) the definition of the Hopf functional

$$\Phi\left[\mathbf{f}(\mathbf{x})\right] \equiv \left\langle \exp\left(i \int_{-\infty}^{\infty} d\mathbf{x}\, \mathbf{f}(\mathbf{x}) \cdot \mathbf{u}(\mathbf{x}) \right) \right\rangle \qquad (A1)$$

Its input is an arbitrary nonrandom time-independent "conjugate", "dummy", or "test" function $\mathbf{f}(\mathbf{x})$; the values of $\mathbf{f}$ at *all* $\mathbf{x}$ are required. The output is a number independent of $\mathbf{x}$, namely, the ensemble average (over the velocity field $\mathbf{u}(\mathbf{x})$ at *all* points, with probability density functional $P[\mathbf{u}(\mathbf{x})]$) of the quantity within the brackets.

If one defines the functional derivative

$$\frac{\delta\Phi[\mathbf{f}(\mathbf{x})]}{\delta f_j(\mathbf{x}')} \equiv \lim_{\epsilon\to 0}\left\{\frac{\Phi\left[\mathbf{f}(\mathbf{x})+\hat{j}\epsilon\delta(\mathbf{x}-\mathbf{x}')\right]-\Phi[\mathbf{f}(\mathbf{x})]}{\epsilon}\right\} \tag{A2}$$

(which depends upon $\mathbf{x}'$ but not $\mathbf{x}$; $\hat{j}$ is a unit vector), then one may readily verify that

$$\left[\frac{\delta\Phi[\mathbf{f}(\mathbf{x})]}{\delta f_j(\mathbf{x}')}\right]_{\mathbf{f}=0} = \langle (i)u_j(\mathbf{x}')\rangle, \left[\frac{\delta^2\Phi[\mathbf{f}(\mathbf{x})]}{\delta f_j(\mathbf{x})\delta f_k(\mathbf{x}')}\right]_{\mathbf{f}=0} = \langle (i)^2 u_j(\mathbf{x})u_k(\mathbf{x}')\rangle \tag{A3}$$

etc. This arises from identities such as

$$\lim_{\epsilon\to 0}\left\{\frac{\exp\left[i\epsilon\int d\mathbf{x}\, u_j(\mathbf{x})\delta(\mathbf{x}-\mathbf{x}')\right]-1}{\epsilon}\right\} = (i)u_j(\mathbf{x}') \tag{A3'}$$

In other words, Φ is the characteristic functional or moment-generating functional for the velocity field $\mathbf{u}(\mathbf{x})$, containing all equal-time statistical information about $\mathbf{u}(\mathbf{x})$. Intermittency is included in this description insofar as it can be captured in the higher moments of velocity.

If one defines the inverse functional Fourier transform

$$\tilde{\Phi}[\mathbf{v}(\mathbf{x})] \equiv \int e^{-i\int d\mathbf{x}\,\mathbf{f}\cdot\mathbf{v}}\Phi[\mathbf{f}(\mathbf{x})]\prod_{\mathbf{x}} d\mathbf{f}(\mathbf{x}) \tag{A4}$$

where the outer integral is over all values of $\mathbf{f}$ evaluated at all points in space $\mathbf{x}$, then one may verify that $\tilde{\Phi}[\mathbf{v}(\mathbf{x})]$ is just the probability density functional $P[\mathbf{v}(\mathbf{x})]$ for the velocity field $\mathbf{v}(\mathbf{x})$. This result is expected because, for discrete $\mathbf{x}$, the functional derivative and functional Fourier transform reduce to the conventional partial derivative and multivariable Fourier transform, respectively. Furthermore, as desired, the result does not depend on $\mathbf{v}$ being independent at different points $\mathbf{x}$, i.e., it does not require P to factor into a product of probability distributions for $\mathbf{v}$ at each $\mathbf{x}$.

The time evolution of Φ is given by

$$\partial_t\left\langle e^{i\int d\mathbf{x}\,\mathbf{f}\cdot\mathbf{u}}\right\rangle = \left\langle i\int d\mathbf{x}\,\mathbf{f}\cdot\partial_t\mathbf{u}\, e^{i\int d\mathbf{x}\,\mathbf{f}\cdot\mathbf{u}}\right\rangle \tag{A5}$$

where $\partial_t\mathbf{u}$ is given by the Navier-Stokes equation. Now $\mathbf{f}$ may be decomposed (Monin, Yaglom 1965) into 2 components, namely, a gradient term ∇g and a remainder $\bar{\mathbf{f}}$. These 2 components will be orthogonal functions in the sense that $\int d\mathbf{x}\,\bar{\mathbf{f}}\cdot\nabla g = 0$ if $\bar{\mathbf{f}}$ is chosen to be solenoidal and have vanishing normal component at the boundary (as one may verify by integrating by parts.) But these are just the conditions satisfied by $\mathbf{u}$. Hence, $\int d\mathbf{x}\,\mathbf{u}\cdot\nabla g = 0$ and $\mathbf{f}$ may be replaced by $\bar{\mathbf{f}}$ in all

of the above equations. The advantage of this replacement is that it eliminates the pressure contribution to equation (A5). Also, because $\bar{\mathbf{f}}$ is solenoidal, the number of independent scalar fields which comprise it has been reduced from 3 to 2.

The equation of motion then becomes

$$\partial_t \left\langle e^{i\int d\mathbf{x}\,\bar{\mathbf{f}}\cdot\mathbf{u}} \right\rangle = \left\langle i\int d\mathbf{x}\,\bar{\mathbf{f}}\cdot\partial_t\mathbf{u}\, e^{i\int d\mathbf{x}\,\bar{\mathbf{f}}\cdot\mathbf{u}} \right\rangle \tag{A6}$$

$$= \left\langle i\int d\mathbf{x}\,\bar{\mathbf{f}}\cdot(-\mathbf{u}\cdot\nabla\mathbf{u}+\nu\nabla^2\mathbf{u})\, e^{i\int d\mathbf{x}\,\bar{\mathbf{f}}\cdot\mathbf{u}} \right\rangle \tag{A6'}$$

which, using equation (A3), becomes the Hopf equation:

$$\frac{\partial\Phi}{\partial t} = \int d\mathbf{x}\bar{f}_j \left(i\frac{\partial}{\partial x_k}\frac{\delta^2}{\delta\bar{f}_k\,\delta\bar{f}_j} + \nu\nabla^2\frac{\delta}{\delta\bar{f}_j}\right)\Phi \tag{A7}$$

where repeated indices are summed over and the $\bar{f}$'s are understood as having the argument $\mathbf{x}$ unless otherwise noted.

3. Accomplishments

3.1. Steady-State Solutions

To find steady-state solutions, let us rewrite this equation as

$$\frac{\partial\Phi}{\partial t} = \int d\mathbf{x}\,\bar{f}_j\frac{\partial}{\partial x_k}\left[\left(i\frac{\delta}{\delta\bar{f}_k}+\nu\frac{\partial}{\partial x_k}\right)\frac{\delta\Phi}{\delta\bar{f}_j}\right] \tag{B1}$$

Note that the expression inside the parenthesis is essentially the kernel for a "wave" equation in which $\bar{f}_k$ and x_k play the role of position and time, respectively. Hence, we will have stationarity if, for example,

$$\frac{\delta\Phi}{\delta\bar{f}_j} = G_j\left(\frac{i}{\nu}\mathbf{x} - \int d\mathbf{x}'\,\bar{\mathbf{f}}(\mathbf{x}')\right) \tag{B2}$$

where G_j is an arbitrary function and the integral is over all space.

The first term inside the parentheses is acted upon by the viscous term of the Navier-Stokes equation while the second term inside the parentheses is acted upon by the convective term. The steady-state balance between the two terms corresponds (in the parlance of a harmonic-oscillator formulation (Shen 1990) of the Navier-Stokes equations) to a state in which creation and annihilation processes balance, i.e., an oscillator at its apogee or perigee. (This condition of balance distinguishes our solution from the Lewis and Kraichnan (1962) solution of the Hopf equation for the time-dependent but *linearized* Navier-Stokes equation.) This particular solution appears to be physically-implausible since it suggests a balance in the absence of explicit external forcing and/or implicit energy input through boundary conditions (Shen 1987). However, it (and its generalization (B5)) serve as useful paradigms for more realistic solutions, to be discussed in later sections.

More generally,

$$\frac{\delta\Phi}{\delta\bar{f}_j} = G_j\left(\frac{i}{\nu}H(\mathbf{x}) - \int d\mathbf{x}'\,\bar{\mathbf{f}}(\mathbf{x}')\cdot\nabla H(\mathbf{x}')\right) \tag{B3}$$

satisfies the steady-state Hopf equation. However, by the construction of $\bar{\mathbf{f}}$, the second term inside the parentheses vanishes unless one restricts oneself to flows in which the pressure gradient may be neglected in the equations of motion (which would be the "opposite" of inviscid Beltrami flows in the sense that the gradient of kinetic energy would not be balanced by the pressure gradient but by the viscous and Coriolis forces). An example would be 2D flow (Vishik, Fursikov 1988), in which the equation of motion (as derived from the vorticity equation) for the joint velocity-vorticity characteristic functional

$$\Phi[\mathbf{f}(\mathbf{x}),\mathbf{g}(\mathbf{x})] \equiv \left\langle \exp\left(i\int_{-\infty}^{\infty} d\mathbf{x}\,\mathbf{f}(\mathbf{x})\cdot\mathbf{u}(\mathbf{x}) + \mathbf{g}(\mathbf{x})\cdot\boldsymbol{\omega}(\mathbf{x})\right)\right\rangle \tag{B4}$$

has neither pressure gradient nor vortex-stretching terms. Its steady-state first functional derivative would then be given by

$$\frac{\delta\Phi}{\delta g_j} = G_j\left(\frac{i}{\nu}H(\mathbf{x}) - \int d\mathbf{x}'\,\mathbf{f}(\mathbf{x}')\cdot\nabla H(\mathbf{x}')\right) \tag{B5}$$

(B3) would also constitute a steady-state solution of the Hopf equation for the *one*-dimensional fluid (Burger's equation).

One could in principle perform a functional integration upon (B3) or (B5) to obtain Φ. However, for computational purposes it is easier to work directly with the first functional derivative of Φ, as we will see. Note that joint functional (B4) is overcomplete in the sense that the $\mathbf{f}$ and $\mathbf{g}$ in (B4) are not independent, because $\mathbf{u}$ and $\boldsymbol{\omega}$ are not independent. If they were independent, one could immediately integrate (B5) to obtain

$$\Phi = \int_{-\infty}^{\infty} d\mathbf{x}\,\mathbf{g}(\mathbf{x})\cdot\mathbf{G}\left(\frac{i}{\nu}H(\mathbf{x}) - \int d\mathbf{x}'\,\mathbf{f}(\mathbf{x}')\cdot\nabla H(\mathbf{x}')\right) \tag{B6}$$

whose velocity moments would all vanish, contrary to reality. Alternatively, working in $\mathbf{k}$ space, one may verify that functional derivatives with respect to $\tilde{\mathbf{g}}(\mathbf{k})$ are equivalent to those with respect to $i\mathbf{k}\times\tilde{\mathbf{f}}(\mathbf{k})$.

For the particular choice

$$\begin{aligned} H(\mathbf{x}) &= e^{i\mathbf{k}\cdot\mathbf{x}} \\ G_j(x) &= a_j \ln x \end{aligned} \tag{B7}$$

the statistics generated by Φ turn out to be homogeneous in space. To see this, consider

$$\frac{\delta\Phi}{\delta g_j} = \sum_m \left(\frac{a_{mj}}{\nu k_{mj}}\right)\ln\left(\frac{e^{i\mathbf{k}_m\cdot\mathbf{x}}}{\nu} - \int d\mathbf{x}'\,\mathbf{f}(\mathbf{x}')\cdot\mathbf{k}_m e^{i\mathbf{k}_m\cdot\mathbf{x}'}\right) \tag{B8}$$

Then, taking one more functional derivative, we obtain

$$\frac{\delta^2\Phi[\mathbf{f}(\mathbf{x})]}{\delta g_j(\mathbf{x})\delta f_k(\mathbf{x}')} = \sum_m \left(\frac{a_{mj}}{\nu k_{mj}}\right) \frac{-k_{mk}e^{i\mathbf{k}_m\cdot\mathbf{x}'}}{z_m(\mathbf{x})} \tag{B9}$$

where

$$z_m(\mathbf{x}) \equiv \left(\frac{e^{i\mathbf{k}_m\cdot\mathbf{x}}}{\nu} - \int d\mathbf{x}'\,\mathbf{f}(\mathbf{x}')\cdot\mathbf{k}_m e^{i\mathbf{k}_m\cdot\mathbf{x}'}\right) \tag{B10}$$

Hence, setting $\mathbf{f} = 0$ and using equation (A3) yields

$$\langle\omega_j(\mathbf{x})u_j(\mathbf{x}')\rangle = \sum_m a_{mj}\, e^{i\mathbf{k}_m\cdot(\mathbf{x}-\mathbf{x}')} \tag{B11}$$

which exhibits homogeneity.

In order to construct velocity moments which are real, note that the complex conjugate of (B8) is *not* a solution of (A7) but rather of the complex conjugate of (A7). However,

$$\frac{\delta\Phi}{\delta g_j} = \sum_m \left(\frac{a_{mj}}{\nu k_{mj}}\right) \ln\left(\frac{-e^{-i\mathbf{k}_m\cdot\mathbf{x}}}{\nu} - \int d\mathbf{x}'\mathbf{f}(\mathbf{x}')\cdot\mathbf{k}_m e^{-i\mathbf{k}_m\cdot\mathbf{x}'}\right) \tag{B12}$$

is a solution of (A7). Linearity allows us to choose any linear combination of (B8) and (B12) as our solution; we choose the difference between the two expressions, since this has the additional property that its integral with respect to the Fourier component of $\mathbf{f}$ converges. This difference solution has the structure function

$$\langle\omega_j(\mathbf{x})u_j(\mathbf{x}')\rangle = 2\sum_m a_{mj}\cos[\mathbf{k}_m\cdot(\mathbf{x}-\mathbf{x}')] \tag{B13}$$

which is real as desired.

We may in general add another term

$$J \equiv i\int d\mathbf{x}'\,(C\mathbf{x}'+\mathbf{D})\cdot\mathbf{g}(\mathbf{x}') \tag{B14}$$

to Φ, since the Hopf equation is linear in Φ and quadratic in spatial and functional derivatives. C is a constant matrix and $\mathbf{D}$ is a constant vector, to be determined. Then the mean vorticity becomes

$$\langle\omega_j(\mathbf{x})\rangle = i(\ln\nu)\sum_m\left(\frac{a_{mj}}{\nu k_{mj}}\right) + \sum_m\left(\frac{a_{mj}}{\nu k_{mj}}\right)\mathbf{k}_m\cdot\mathbf{x} + C\mathbf{x} + \mathbf{D} \tag{B15}$$

Reality dictates that the first sum vanish while incompressibility and the prevailing mean vorticity and vorticity gradient determine $\mathbf{D}$ and C, respectively. One may

also match the homogeneous intensity $\langle \omega^2 \rangle$ of the vorticity fluctuations by adding a term

$$J' \equiv E \left| \int d\mathbf{x}' \, \mathbf{g}(\mathbf{x}') \right|^2 \tag{B16}$$

to Φ, where E is a constant.

Again, it is not clear at this time how statistical stationarity is physically possible in the absence of forcing or boundary conditions, except possibly as an approximation for decaying turbulence at high Reynolds number and small length scales (which are effectively forced by the large scales). Consistent with this viewpoint is the fact that, although $\langle \omega_j \rangle$ and $\langle \omega_j u_m \rangle$ as derived above are in general nonzero, taking the curl of the latter and Fourier transforming yields an energy spectrum $\sim \delta^2(\mathbf{k})$, indicating that the energy (and, hence, the forcing) resides in the large scales. In order to achieve mathematical *and* physical stationarity, we modify our approach as follows.

3.2. Depletion of Nonlinearity

Let us consider the 3D case (i.e., restore vortex-stretching to the equations) and add explicit external forcing $\mathbf{F}(\mathbf{x})$. If we consider the joint velocity-vorticity-force characteristic functional

$$\Phi[\mathbf{f}(\mathbf{x}), \mathbf{g}(\mathbf{x}), \mathbf{h}(\mathbf{x})] \equiv \left\langle \exp\left(i \int_{-\infty}^{\infty} d\mathbf{x} \, \mathbf{f}(\mathbf{x}) \cdot \mathbf{u}(\mathbf{x}) + \mathbf{g}(\mathbf{x}) \cdot \boldsymbol{\omega}(\mathbf{x}) + \mathbf{h}(\mathbf{x}) \cdot \mathbf{F}(\mathbf{x}) \right) \right\rangle \tag{C1}$$

then the conditions that viscosity and forcing balance (implying that stretching and advection balance, in order to achieve stationarity) take the respective forms

$$\nabla \times \nu \nabla^2 \frac{\delta \Phi}{\delta \mathbf{f}(\mathbf{x})} = -\nabla \times \frac{\delta \Phi}{\delta \mathbf{h}(\mathbf{x})} \tag{C2}$$

$$\nabla \times \left(\frac{\delta}{\delta \mathbf{f}(\mathbf{x})} \times \frac{\delta \Phi}{\delta \mathbf{g}(\mathbf{x})} \right) = 0 \tag{C3}$$

This is a special case of general stationarity, with the "Eulerization" constraint that $\nabla \times (\mathbf{u} \times \boldsymbol{\omega})$ vanishes everywhere. Technically, this constraint is only *weakly* or statistically imposed, i.e., only its ensemble average with any moment of velocity is required to vanish (Constantin, Foias 1988). This constraint is motivated by a suggestion by Moffatt (1985) and by recent experimental, numerical, and analytical work by Kraichnan and Panda, Herring and Kerr, Shtilman and Polifke and others (Tsinober 1990 and references therein) indicating that decaying turbulent flows tend to spend a significant portion of their time in the vicinity of fixed points of the Euler equation, in which $\mathbf{u} \times \boldsymbol{\omega} = \nabla(P + \frac{1}{2}u^2)$. This amounts to a depletion of nonlinearity, since the total nonlinear term is the solenoidal part of $\mathbf{u} \times \boldsymbol{\omega}$. This is directly relevant to issues of turbulent drag reduction and coherent structures, since both can arise from reduced enstrophy production.

Taking the functional derivative with respect to $\mathbf{f}(\mathbf{x}')$ of equations (C2) and (C3) (for $\mathbf{x}' \neq \mathbf{x}$) yields

$$\nabla \times \nu \nabla^2 \frac{\delta^2 \Phi}{\delta \mathbf{f}(\mathbf{x}) \delta \mathbf{f}(\mathbf{x}')} = -\nabla \times \frac{\delta^2 \Phi}{\delta \mathbf{h}(\mathbf{x}) \delta \mathbf{f}(\mathbf{x}')} \tag{C4}$$

$$\nabla \times \left(\frac{\delta}{\delta \mathbf{f}(\mathbf{x})} \times \frac{\delta^2 \Phi}{\delta \mathbf{g}(\mathbf{x}) \delta \mathbf{f}(\mathbf{x}')} \right) = 0 \tag{C5}$$

Substituting the ansatz

$$\frac{\delta \Phi}{\delta f_j(\mathbf{x}')} = G_j \left[\int_{-\infty}^{\infty} d\mathbf{x}\, \mathbf{B}(\mathbf{x}) \cdot \mathbf{f}(\mathbf{x}) + \mathbf{p}(\mathbf{x}) \cdot \mathbf{g}(\mathbf{x}) + \mathbf{q}(\mathbf{x}) \cdot \mathbf{h}(\mathbf{x}), \mathbf{x}' \right] \tag{C6}$$

(where G_j is an arbitrary functional) we obtain

$$\begin{aligned} \mathbf{q}(\mathbf{x}) &= -\nu \nabla^2 \mathbf{B}(\mathbf{x}) + \nabla C(\mathbf{x}) \\ \mathbf{B}(\mathbf{x}) \times \mathbf{p}(\mathbf{x}) &= \nabla A(\mathbf{x}) \end{aligned} \tag{C7}$$

where C(x) and A(x) are arbitrary. This yields

$$\begin{aligned} \frac{\delta \Phi}{\delta f_j(\mathbf{x}')} = G_j [\int_{-\infty}^{\infty} d\mathbf{x}\, \mathbf{B}(\mathbf{x}) \cdot \mathbf{f}(\mathbf{x}) + [\alpha \mathbf{B}(\mathbf{x}) - \frac{\mathbf{B}(\mathbf{x})}{|\mathbf{B}(\mathbf{x})|^2} \times \nabla A(\mathbf{x})] \cdot \mathbf{g}(\mathbf{x}) \\ + [-\nu \nabla^2 \mathbf{B}(\mathbf{x}) + \nabla C(\mathbf{x})] \cdot \mathbf{h}(\mathbf{x}), \mathbf{x}'] \end{aligned} \tag{C8}$$

where α is a scalar field to be determined and $\mathbf{B}(\mathbf{x})$ is chosen to be orthogonal to $\nabla A(\mathbf{x})$.

One may verify that

$$\alpha(\mathbf{x}) = \frac{\langle u_j \boldsymbol{\omega}(\mathbf{x}) \cdot \mathbf{u}(\mathbf{x}) \rangle}{\langle u_j \mathbf{u}(\mathbf{x}) \cdot \mathbf{u}(\mathbf{x}) \rangle} \tag{C9}$$

For flow localized in a narrow range of wavenumbers about k, α may be viewed as the ratio of helicity and energy currents in k-space, since (as a crude estimate (Townsend 1976)) $[\partial_t k]/k \sim -[\partial_t \tilde{u}(k)]/\tilde{u}(k)$ by incompressibility $\sim k\tilde{u}(k)$ so that $\partial_t (1/k) \sim \tilde{u}(k)$. Negative α, for example, would be consistent with opposite energy and helicity cascades (Levich 1987). One expects α to be proportional to the inverse of the integral length scale.

Similarly, one may verify that

$$\frac{\nabla_n C}{\nabla^2 B_n} = \frac{\langle u_j (F_n - \nu \nabla^2 u_n) \rangle}{\langle u_j \nabla^2 u_n \rangle} \tag{C10}$$

In order to insure homogeneity of velocity statistics, we choose a solution of the form (C6) with

$$\begin{aligned} \mathbf{B}(\mathbf{x}) &\sim \mathbf{b}_m e^{i\mathbf{k}_m \cdot \mathbf{x}} \\ G_j[z, \mathbf{x}'] &= \sum_m \left(\frac{a_{mj}}{b_{mj}} \right) \ln \left(e^{i\mathbf{k}_m \cdot \mathbf{x}'} - z \right) \end{aligned} \tag{C11}$$

With this choice, homogeneity of vorticity and force statistics requires that

$$\alpha = \text{constant} \equiv \alpha_m$$

$$A(\mathbf{x}) \sim A_m e^{i2\mathbf{k}_m \cdot \mathbf{x}}$$

$$C(\mathbf{x}) \sim C_m e^{i\mathbf{k}_m \cdot \mathbf{x}} \tag{C12}$$

Hence, substituting into (C8), the argument in the above expression

$$z = \int d\mathbf{x}\, e^{i\mathbf{k}_m \cdot \mathbf{x}} \{\mathbf{b}_m \cdot \mathbf{f}(\mathbf{x}) + \left[\alpha_m \mathbf{b}_m - 2i\mathbf{b}_m \times \frac{\mathbf{k}_m A_m}{|\mathbf{b}_m|^2}\right] \cdot \mathbf{g}(\mathbf{x})$$

$$+ [\nu k_m^2 \mathbf{b}_m + i\mathbf{k}_m C_m] \cdot \mathbf{h}(\mathbf{x})\} \tag{C13}$$

where $\mathbf{b}_m$ is chosen to be orthogonal to $\mathbf{k}_m$.

Given $\delta\Phi/\delta f_j(\mathbf{x}')$ satisfying (C4,5), the functional Φ obtained (in principle) by functional integration satisfies (C2,3), as may be seen by commuting a functional integration over $f_j(\mathbf{x}')$ back in through the other operators acting on $\delta\Phi/\delta f_j(\mathbf{x}')$ in (C4,5) and setting the arbitrary constants of the functional integration (functions independent of $f_j(\mathbf{x}')$) equal to zero. Hence, (C6, 11, 13) constitutes an implicit solution of the Hopf equation *and* gives explicit statistics.

This leads to mean velocity

$$\langle u_j(\mathbf{x}) \rangle = \sum_m \left(\frac{a_{mj}}{b_{mj}}\right) (i\mathbf{k}_m \cdot \mathbf{x}) \tag{C14}$$

One might consider adding a term of the form (B14) (with $\mathbf{g}$ replaced by $\mathbf{f}$) to Φ. However, although the Hopf equation *is* invariant under this operation, the additional contributions to the mean velocity and strain rate are unphysical since they contain no energy (as may be verified by functional-differentiating (B14) twice with respect to f.) Hence we choose to disregard this spurious "inhomogeneous Galilean" invariance. Applying incompressibility and the requirement of zero-mean-shear imposes seven further constraints upon the $5N$ remaining coefficients in $\mathbf{a}_m$ and $\mathbf{b}_m$, where N is the number of wavevectors in our expansion (C11).

The velocity-force correlation function takes the form

$$\langle u_j(\mathbf{x}) F_j(\mathbf{x}') \rangle = \sum_m a_{mj} \left[\nu k_m^2 + i \frac{k_{mj}}{b_{mj}} C_m\right] e^{i\mathbf{k}_m \cdot (\mathbf{x} - \mathbf{x}')} \tag{C15}$$

One may compare this with the mean transfer into vector component E_j of the energy

$$\epsilon_{jnp} \langle u_j(\mathbf{x}) u_n(\mathbf{x}') \omega_p(\mathbf{x}') \rangle = \sum_m \frac{a_{mj}}{b_{mj}} [2k_{mj} A_m]\, e^{i2\mathbf{k}_m \cdot (\mathbf{x} - \mathbf{x}')} \tag{C16}$$

(no sum over j). The associated autocorrelation function

$$\langle u_j(\mathbf{x})u_j(\mathbf{x}')\rangle = \sum_m a_{mj}\, e^{i\mathbf{k}_m\cdot(\mathbf{x}-\mathbf{x}')} \qquad (C17)$$

tells us that $a_{mj} = \langle|\tilde{u}_j(\mathbf{k}_m)|^2\rangle$. From this, we see that the role of the factor of 2 in the exponential on the right- hand-side of the nonlinear-transfer term (C16) is to generate the cascade; energy initially localized in k-space around $\mathbf{k}_m$ will give rise to a transfer of energy to $2\mathbf{k}_m$, which in turn results in transfer to $4\mathbf{k}_m$ and so on. Of course, because the sum of the nonlinear terms vanishes for this class of flows, there is no *net* cascade. In fact, from (D4) and (C16), we see that transfer due to Coriolis forces cancels the transfer due to the gradient of the kinetic energy, implying that velocity and pressure gradient are uncorrelated for these flows. This suggests that the *statistical* fixed point of the forced Navier-Stokes equation which corresponds to the deterministic fixed point of the Euler equation may in fact be stable since there is no pressure-driven tendency to isotropize the angle between $\tilde{\mathbf{u}}(\mathbf{k}) \times \tilde{\boldsymbol{\omega}}(\mathbf{k})$ and $\mathbf{k}$. The fixed point is statistical because (*i*) the statistics are stationary whereas the flow field in any individual realization may not be, (*ii*) the correlation functions obtained do not factor as a deterministic correlation function would, and (*iii*) the "Eulerization" constraint is only imposed weakly.

Three-point correlations may also be derived, e.g.,

$$\langle u_j(\mathbf{x})u_n(\mathbf{x}')u_p(\mathbf{x}'')\rangle = \sum_m \frac{a_{mj}}{b_{mj}} b_{mn}b_{mp}\, e^{i\mathbf{k}_m\cdot(\mathbf{x}+\mathbf{x}''-2\mathbf{x}')} \qquad (C18)$$

Symmetry then implies that

$$a_{mj} = b_{mj}^2 \qquad (C19)$$

Writing $(\mathbf{x}+\mathbf{x}''-2\mathbf{x}')$ as $(\mathbf{x}-\mathbf{x}')+(\mathbf{x}''-\mathbf{x}')+(\mathbf{x}'-\mathbf{x}')$ and using homogeneity to translate the origin by $\mathbf{x}'$ yields a manifestly-symmetric form for (C18). Equivalently, a necessary condition for (C18) to be symmetric is that $\mathbf{x}' = 0$; however, for a homogeneous system, this condition can always be satisfied by translation. (For a more rigorous treatment including sufficiency, see Appendix.) C_m is constrained to vanish, as may be seen by computing the correlation of any product of velocities with both sides of the stationary Navier-Stokes equation and substituting (C15)-(C17). However, force- force statistics are still undetermined; the external force may have an arbitrary component which is uncorrelated with $\mathbf{u}$ as well as a component satisfying (C15), e.g., white noise (Sargent *et.al.* 1974).

3.3. Homogeneous Steady Solution with Forcing

Let us extend this solution to the case of *general* balance in which (C2,3) are not individually valid but their *sum* is. Then (C7) becomes

$$\mathbf{q}(\mathbf{x},\mathbf{x}') = -\nu\nabla^2\mathbf{B}(\mathbf{x}) + \nabla C(\mathbf{x}) - \mathbf{H}(\mathbf{x})\frac{G_j''(z,\mathbf{x}')}{G_j'(z,\mathbf{x}')}$$

$$\mathbf{B}(\mathbf{x}) \times \mathbf{p}(\mathbf{x}) = \nabla A(\mathbf{x}) + \mathbf{H}(\mathbf{x}) \qquad (D1)$$

where $\mathbf{H}(\mathbf{x})$ is not a gradient and the primes on G_j denote derivative with respect to z. Without loss of generality, the potential component of $\mathbf{H}(\mathbf{x})$ may be absorbed into the definitions of C and A. Then homogeneity implies that

$$\mathbf{H}(\mathbf{x}) \sim \mathbf{H}_m e^{i2\mathbf{k}_m \cdot \mathbf{x}} \tag{D2}$$

where $\mathbf{H}_m$ is orthogonal to $\mathbf{k}_m$. Since by incompressibility $\mathbf{b}_m$ is orthogonal to $\mathbf{k}_m$ and, hence, to $\mathbf{H}_m$(by (D1)), we obtain that the three vectors $\mathbf{b}_m$, $\mathbf{k}_m$ and $\mathbf{H}_m$ form an orthogonal triad. The self-consistency requirement $\nabla \times \mathbf{u} = \boldsymbol{\omega}$ then implies that

$$i\mathbf{k}_m \times \mathbf{b}_m = \alpha_m \mathbf{b}_m - \mathbf{b}_m \times \frac{(2i\mathbf{k}_m A_m + \mathbf{H}_m)}{|\mathbf{b}_m|^2} \tag{D3}$$

This can be satisfied if

$$|\mathbf{b}_m|^2 = 2A_m \tag{D4}$$

$$\alpha_m \mathbf{b}_m = -\mathbf{H}_m \times \frac{\mathbf{b}_m}{|\mathbf{b}_m|^2} \tag{D5}$$

$$\mathbf{H}_m \cdot \mathbf{b}_m = 0 \tag{D6}$$

(D4) fixes the normalization of $\mathbf{b}_m$. (D5,6) are satisfied for nonzero α_m if $\alpha_m \mathbf{b}_m$ is chosen to be the vector Fourier coefficient at "wavevector" $i\mathbf{H}_m/\alpha_m$ ($\mathbf{H}_m$ chosen such that $\mathbf{H}_m/\alpha_m$ is imaginary) of any hypothetical incompressible Arnold-Beltrami-Childress flow $\mathbf{v}(\mathbf{r})$ with $\nabla \times \mathbf{v}(\mathbf{r}) = 2A_m \mathbf{v}(\mathbf{r})$.

$\mathbf{H}$ plays the role of a rotational stirring force; the number of nonzero coefficients $\mathbf{H}_m/\alpha_m$ is a measure of the nonlinearity of the flow, i.e., deviation of the flow from the case of fully-depressed nonlinearity in which $\mathbf{u}(\mathbf{x}) \times \boldsymbol{\omega}(\mathbf{x}) = \nabla A(\mathbf{x})$. If all of the $\mathbf{H}_m$ vanish, we recover the balance discussed in the previous section, in which A_m is given by (D4) and $\alpha_m = 0$.

The nonlinear transfer (C16) now becomes

$$\epsilon_{jnp}\langle u_j(\mathbf{x}) u_n(\mathbf{x}') \omega_p(\mathbf{x}')\rangle = \sum_m \frac{a_{mj}}{b_{mj}} [2k_{mj} A_m - iH_{mj}] \, e^{i2\mathbf{k}_m \cdot (\mathbf{x}-\mathbf{x}')} \tag{D7}$$

$\mathbf{k}_m$ is constrained to be orthogonal to $\mathbf{H}_m$ and $\mathbf{b}_m$. (C6, 11, 13) with the right hand side of (D3) replacing the corresponding expression in (C13) then constitutes a homogeneous, stationary, incompressible, and self-consistent closed solution of the Hopf equation (if there exists a force $\mathbf{F}(\mathbf{x})$ which gives rise to homogeneous stationary flow.)

In the absence of homogeneity (but with forcing), equation (D3) is replaced by the condition (C8) with the modification that $\mathbf{H}$ is added onto ∇A, where

$$\mathbf{B} \text{ satisfies the boundary conditions on } \mathbf{u} \tag{D8}$$

$$\nabla \cdot \mathbf{B} = 0 \tag{D9}$$

A and $\mathbf{H}$ are fixed by self-consistency. For example, setting $\alpha = 0$ yields

$$\nabla A + \mathbf{H} = \mathbf{B} \times (\nabla \times \mathbf{B}) \tag{D10}$$

satisfied by

$$\mathbf{H} = \mathbf{B} \cdot \nabla \mathbf{B} \tag{D11}$$

$$A = |\mathbf{B}|^2/2 \tag{D12}$$

Dropping the $\mathbf{x}'$ dependence on the right hand side of the modified (C8) also yields a possible expression for, not $\delta\Phi/\delta f_j(\mathbf{x}')$ but Φ itself (except for the case of homogeneous statistics). Again, the resulting statistics are (by construction) consistent with the boundary conditions as well as with stationarity, incompressibility and self- consistency.

3.4. Inhomogeneous Steady Solution with Boundary Conditions

For the unforced inhomogeneous case, the above may be simplified by returning to the velocity-vorticity characteristic functional (B4) where

$$\frac{\delta\Phi}{\delta g_j} = G_j \left(\frac{i}{\nu} H(\mathbf{x}) - \int d\mathbf{x}' \, \mathbf{f}(\mathbf{x}') \cdot [\nabla H(\mathbf{x}') + \mathbf{M}(\mathbf{x}')] \right) \tag{E1}$$

$\nabla H + \mathbf{M}$ is chosen to be solenoidal and satisfy boundary conditions on $\mathbf{u}$. Noting that

$$\nu \nabla^2 \boldsymbol{\omega} = -\nu \nabla \times \nabla \times \boldsymbol{\omega} \tag{E2}$$

the condition for stationarity becomes

$$\nabla \times \left(i \frac{\delta}{\delta \mathbf{f}} + \nu \nabla \right) \times \frac{\delta\Phi}{\delta \mathbf{g}} = 0 \tag{E3}$$

(compare with (C3)) implying

$$\nabla \times [\mathbf{M}(\mathbf{x}) \times \mathbf{G}'(z(\mathbf{x}))] = 0 \tag{E4}$$

where the prime denotes derivative of $\mathbf{G}$ with respect to its argument $\mathbf{z}(\mathbf{x})$ (given in parentheses in (E1)), not to be confused with the "del" (∇) which as usual denotes derivative with respect to $\mathbf{x}$. Stationarity may then be achieved by choosing $\mathbf{G}'$ to be parallel to $\mathbf{M}$, or more generally, for

$$\mathbf{G}' \cdot \nabla \mathbf{M} - \mathbf{M} \cdot \nabla \mathbf{G}' + \mathbf{M} \nabla \cdot \mathbf{G}' - \mathbf{G}' \nabla \cdot \mathbf{M} = 0 \tag{E5}$$

The longitudinal counterpart of (E3) determines the steady-state pressure.

The requirement that the mean vorticity be the curl of a mean velocity can be satisfied only if

$$\nabla \cdot \mathbf{G} = 0 \text{ at } \mathbf{f} = 0 \tag{E6}$$

Noting

$$\nabla \cdot \mathbf{G} = \mathbf{G}' \cdot \nabla H \tag{E7}$$

yields

$$\mathbf{G}' = \mathbf{b} \times \nabla H \tag{E8}$$

for some vector field **b**. The spatial dependence of **b** may be determined by noting that solenoidality of vorticity requires

$$\nabla \cdot \frac{\partial^n \mathbf{G}(\mathbf{f}=0)}{\partial H^n} = 0 \tag{E9}$$

Linearity of the Hopf equation allows us to generalize (E1) to

$$\frac{\delta \Phi}{\delta g_j} = \sum_q a_q G_{qj} \left(\frac{i}{\nu} H_q(\mathbf{x}) - \int d\mathbf{x}' \, \mathbf{f}(\mathbf{x}') \cdot [\nabla H_q(\mathbf{x}') + \mathbf{M_q}(\mathbf{x}')] \right) \tag{E10}$$

In general, we may write

$$G_{qj}(z_q(\mathbf{x}); \mathbf{f}=0) = \sum_p A_{qj}(p) \, e^{\frac{ip}{\nu} H_q(\mathbf{x})} \tag{E11}$$

Then (E9) implies

$$0 = (ip)^n \mathbf{A_q}(p) \cdot \nabla H_q(\mathbf{x}) \tag{E12}$$

which requires that $\nabla H_q(\mathbf{x})$ lies in a plane for all $\mathbf{x}$ and that the $\mathbf{A_q}(p)$ be normal to that plane for all p.

The additivity of probabilities implied by the linearity of the Hopf equation suggests that (E10) may be interpreted as a decomposition of the flow into statistically-orthogonal (mutually-exclusive) states. The vorticity associated with each state is arbitrarily-aligned but uniaxial (i.e., different from state to state but everywhere-parallel or antiparallel within any given state). Of course, the sum over states yields a mean vorticity whose direction may vary in space, as is generally desired. The sum over states also implies that the correlation functions in general do not factor (unless there is only one H_q and each G_{qj} happens to be exponential in H_q). In other words, we have a true statistical solution rather than a deterministic solution; the vorticity associated with each state (and the mean vorticity) need not satisfy the curl of the Navier-Stokes equation. (For example, a set of H_q and $\mathbf{M}_q$ can be found that would correspond to a representation of the flow as an ensemble of vortex filaments of varying core diameters; the a_q would then be given by the Bose distribution (Shen 1991).) This allows us to identify those coherent structures which characterize the *ensemble*, rather than particular realizations (Hussain 1986).

Explicitly, (E10) becomes

$$\frac{\delta \Phi}{\delta g_j(\mathbf{x})} = \sum_{q,p} a_q A_{qj}(p) \exp \left(\frac{ip}{\nu} H_q(\mathbf{x}) + \int d\mathbf{x}' \, p\mathbf{f}(\mathbf{x}') \cdot [\nabla H_q(\mathbf{x}') + \mathbf{M_q}(\mathbf{x}')] \right) \tag{E13}$$

implying

$$\langle \omega_j(\mathbf{x}) \rangle = \sum_{q,p} a_q A_{qj}(p) \exp \left(\frac{ip}{\nu} H_q(\mathbf{x}) \right) \tag{E14}$$

$$\langle \omega_j(\mathbf{x}) u_n(\mathbf{x}') \rangle = \sum_{q,p} a_q ip A_{qj}(p) \exp\left(\frac{ip}{\nu} H_q(\mathbf{x})\right) [\nabla_n H_q(\mathbf{x}') + M_{qn}(\mathbf{x}')] \qquad (E15)$$

$$\langle \omega_j(\mathbf{x}) \omega_{j'}(\mathbf{x}') \rangle = \sum_{q,p} a_q ip A_{qj}(p) \exp\left(\frac{ip}{\nu} H_q(\mathbf{x})\right) [\nabla \times M_q]_{j'}(\mathbf{x}') \qquad (E16)$$

etc.

Velocity autocorrelation functions may be obtained by applying Biot-Savart to the velocity-vorticity correlation functions. Alternatively, we see that from $\langle \mathbf{u}(\mathbf{x})\mathbf{u}(\mathbf{x}') \rangle$, one may take the curl to find (E15) and, hence, $\langle \mathbf{u}(\mathbf{x}) \cdot \mathbf{u}(\mathbf{x}') \times \boldsymbol{\omega}(\mathbf{x}') \rangle$, thereby effecting a closure for unforced 3D Navier-Stokes flow with arbitrary boundary conditions.

Positivity of the energy spectrum implies that the Fourier transform of (E16) with respect to $\mathbf{x}$ and $\mathbf{x}'$ must be nonnegative. This imposes a restriction on the coefficients a_q appearing in (E13).

Symmetry under interchange of $\mathbf{x}$, j and $\mathbf{x}', j'$ implies

$$\mathbf{G}'_{\mathbf{q}}(\mathbf{x}) = \sum_p ip \mathbf{A}_{\mathbf{q}}(p) \exp\left(\frac{ip}{\nu} H_q(\mathbf{x})\right) = \nabla \times \mathbf{M}_{\mathbf{q}}(\mathbf{x}) \qquad (E17)$$

If we denote

$$\mathbf{B}_{\mathbf{q}}(\mathbf{x}) = \nabla H_q(\mathbf{x}) + \mathbf{M}_{\mathbf{q}}(\mathbf{x}) \qquad (E18)$$

we find that

$$\nabla \times \mathbf{B}_{\mathbf{q}}(\mathbf{x}) = \mathbf{G}'_{\mathbf{q}}(\mathbf{x}) \qquad (E19)$$

where the basis functions $\mathbf{B}_{\mathbf{q}}(\mathbf{x})$ are solenoidal (which fixes ∇H_q, given $\mathbf{M}_{\mathbf{q}}$) and satisfy the same boundary conditions as $\mathbf{u}$. Note that $\hat{\zeta}_q \cdot \mathbf{M}_q(\mathbf{x}) = \hat{\zeta}_q \cdot \mathbf{B}_q(\mathbf{x})$, where the unit vector $\hat{\zeta}_q$ is defined to be along $\mathbf{A}_q$, with mutually-perpendicular vectors $\hat{\xi}_q$ and $\hat{\eta}_q$.

Hence, given $\mathbf{B}_q$, we can obtain $\mathbf{G}'_q$ by invoking symmetry; the problem now becomes to find the coefficients a_q (by using stationarity) so that we may write down expressions for the two-point moments, given one-point moments. The stationarity conditions may be written as

$$\nabla_\perp \cdot \mathbf{M}_{\mathbf{q}}(\mathbf{x}) = -\nabla_\perp \ln |\mathbf{G}'_q| \cdot \mathbf{M}_{\mathbf{q}}(\mathbf{x}) \qquad (E20)$$

$$\hat{\zeta}_q \cdot \nabla[\hat{\eta}_q \cdot \mathbf{M}_q(\mathbf{x})] = \hat{\zeta}_q \cdot \nabla[\hat{\xi}_q \cdot \mathbf{M}_q(\mathbf{x})] = 0 \qquad (E21)$$

where $\nabla_\perp \equiv (\hat{\xi}_q \cdot \nabla, \hat{\eta}_q \cdot \nabla, 0)$. We can use (E12) and the fact (from (E17)) that $\nabla \times \mathbf{M}_q(\mathbf{x})$ only has a ζ_q- component to deduce that $\hat{\zeta}_q \cdot \mathbf{B}_q$ only depends upon ζ_q while $\hat{\xi}_q \cdot \mathbf{B}_q$ and $\hat{\eta}_q \cdot \mathbf{B}_q$ do not depend upon ζ_q.

Changing variables to

$$\mathbf{M}_q(\mathbf{x}) = \mathbf{M}^0_q(\mathbf{x}) / |\mathbf{G}'_q(\mathbf{x})| \qquad (E22)$$

equation (E20) becomes

$$\nabla_\perp \cdot \mathbf{M}_\mathbf{q}^0(\mathbf{x}) = 0 \tag{E23}$$

This implies that we may write

$$\hat{\xi}_q \cdot \mathbf{M}_q^0(\mathbf{x}) \equiv \hat{\eta}_q \cdot \nabla \Phi_q, \; \hat{\eta}_q \cdot \mathbf{M}_q^0(\mathbf{x}) \equiv -\hat{\xi}_q \cdot \nabla \Phi_q \tag{E24}$$

for some $\Phi_q(\xi_q, \eta_q)$. Substituting (E23, 24) into (E17) then yields

$$\nabla^2 \Phi_q - \nabla \ln |\mathbf{G}'_q| \cdot \nabla \Phi_q + |\mathbf{G}'_q|^2 = 0 \tag{E25}$$

Solving for Φ_q and using (E22, 24) then yields $\mathbf{M_q}(\mathbf{x})$.

From (E18), we obtain ∇H_q; multiplying by $\mathbf{G}'_q$ and integrating yields $\mathbf{G}_q$. Given one-point moments, we may expand them in terms of $\mathbf{G}_q$ to obtain the coefficients a_q, which finally may be substituted into (E15) to give us the two-point moments.

One stumbling block with this approach is that although the basis functions $\mathbf{B}_q$ with which we start may be orthogonal, the resulting $\mathbf{G}_q$ in which we expand the one-point moments may not in general be orthogonal. Hence, we must approach the problem from the other end: given the one-point moment $\langle \omega_j(\mathbf{x}) \rangle$ (and its expansion coefficients a_q in terms of orthogonal functions $\mathbf{G}_q$), find the basis functions $\mathbf{B}_q$ and $\mathbf{G}'_q$ so that we may write down two-point moments such as $\langle \omega_j(\mathbf{x}) u_n(\mathbf{x}') \rangle$. To do this, note that (E22, 24) may be written as

$$(B_{qi} - \nabla_i H_q) \nabla_i (\hat{\zeta}_q \cdot \mathbf{G}_q) = (\nabla \Phi_q \times \hat{\zeta}_q)_i \nabla_i H_q \tag{E26}$$

(no sum over i). This may be solved to obtain

$$\nabla_i H_q = B_{qi} \left[1 + \frac{(\nabla \Phi_q \times \hat{\zeta}_q)_i}{\nabla_i (\hat{\zeta}_q \cdot \mathbf{G}_q)} \right]^{-1} \tag{E27}$$

while (E19) becomes

$$\hat{\zeta}_q \cdot \{ \nabla \times \mathbf{B}_q \} = \frac{\nabla_i (\hat{\zeta}_q \cdot \mathbf{G}_q)}{\nabla_i H_q} \tag{E28}$$

(i = ξ_q, η_q, no sum implied). Together with the solenoidality condition

$$\nabla \cdot \mathbf{B}_q(\mathbf{x}) = 0 \tag{E29}$$

we have three equations for the three unknown fields $(\hat{\xi}_q \cdot \mathbf{B}_q), (\hat{\eta}_q \cdot \mathbf{B}_q)$, and Φ_q. Note that $(\hat{\zeta}_q \cdot \mathbf{B}_q)$ is an arbitrary function of ζ_q (it does not appear in either the stationarity or symmetry conditions) and is constrained only by the boundary conditions on $(\hat{\zeta}_q \cdot \mathbf{u}(\mathbf{x}))$. Separation of variables then yields

$$\nabla_\perp \cdot \mathbf{B}_q(\mathbf{x}) = \text{constant} \tag{E30}$$

The uniaxial decomposition reduces to an ordinary Fourier transform if H_q is linear in $\mathbf{x}$ (i.e., $\mathbf{q} \cdot \mathbf{x}$); more generally, the $(ip/\nu)H_q$'s may be chosen to be the logarithms of a set of complete orthogonal functions suitable for decomposition of the mean vorticity.

4. Future Plans

We have reduced the stationary turbulence closure problem, given general boundary conditions (and presumably inhomogeneous statistics) to the problem of solving three coupled first-order nonlinear differential equations. This offers us an exact method for computing two- and higher-point moments, given one-point moments. Many examples remain to be worked out and tested against results from simulation studies.

We have also found closed solutions to the problem of homogeneous forced stationary turbulence. As an example, we have derived a solution exhibiting depletion of nonlinearity, not inconsistent with recent findings. These solutions, however, are less-readily-compared with experiments due to the difficulty of computing force-force statistics from force-velocity statistics. One would have to solve the coupled equations (Kraichnan 1975) for the velocity-force response function and the velocity-velocity correlation function, which may be nontrivial even given the latter.

We have also derived other, more-specialized solutions to the stationary Hopf equation (e.g., in the presence of mean uniform shear, as well as operator or matrix solutions) whose physical significance, if any, remains to be clarified. Further intriguing longer-range questions include: (*i*) nonuniqueness (Constantin, Foias 1988) of solutions, their selection mechanism and stability, (*ii*) the feasibility of inverse-functional Fourier transforming Φ to obtain the steady-state velocity probability density function (pdf) (which one certainly hopes will turn out to be positive), (*iii*) the possibility of incorporating initial conditions and time dependence (to find two-time correlations), and (*iv*) the actual prediction (rather than assumption) of one-point statistics from the boundary conditions.

Appendix

Explicit symmetrization of the correlation functions for the homogeneous forced case may be obtained by generalizing (C6) to

$$\frac{\delta\Phi}{\delta f_m(\mathbf{x})} \equiv G_m[z,\mathbf{x}] + \int_{-\infty}^{\infty} d\mathbf{x}'\, f_j(\mathbf{x}') g^{(1)}_{jm}(\mathbf{x},\mathbf{x}') + \int_{-\infty}^{\infty} d\mathbf{x}'d\mathbf{x}''\, f_j(\mathbf{x}') f_n(\mathbf{x}'') g^{(2)}_{jnm}(\mathbf{x},\mathbf{x}',\mathbf{x}'') + \cdots \tag{F1}$$

We then impose

$$g^{(1)}_{jm}(\mathbf{x},\mathbf{x}') = \frac{1}{2}\left[\frac{\delta G_j(\mathbf{x}')}{\delta f_m(\mathbf{x})} - \frac{\delta G_m(\mathbf{x})}{\delta f_j(\mathbf{x}')}\right]_{\mathbf{f}=\mathbf{g}=\mathbf{h}=\mathbf{0}} \tag{F2}$$

$$g^{(2)}_{jnm}(\mathbf{x},\mathbf{x}',\mathbf{x}'') = \frac{1}{3}\left[\frac{\delta^2 G_j(\mathbf{x}')}{\delta f_m(\mathbf{x})\delta f_n(\mathbf{x}'')} - 2\frac{\delta^2 G_m(\mathbf{x})}{\delta f_j(\mathbf{x}')\delta f_n(\mathbf{x}'')} + \frac{\delta^2 G_n(\mathbf{x}'')}{\delta f_m(\mathbf{x})\delta f_j(\mathbf{x}')}\right]_{\mathbf{f}=\mathbf{g}=\mathbf{h}=\mathbf{0}} \tag{F2'}$$

etc. Correlation functions then become manifestly symmetric, e.g.,

$$\langle u_j(\mathbf{x})u_n(\mathbf{x}')u_p(\mathbf{x}'')\rangle = \sum_m b_{mj}b_{mn}b_{mp}\cdot$$

$$\{e^{i\mathbf{k}_m\cdot(\mathbf{x}+\mathbf{x}''-2\mathbf{x}')} + e^{i\mathbf{k}_m\cdot(\mathbf{x}+\mathbf{x}'-2\mathbf{x}'')} + e^{i\mathbf{k}_m\cdot(\mathbf{x}'+\mathbf{x}''-2\mathbf{x})}\} \qquad (F3)$$

More generally, Φ is invariant under transformations upon G of the form

$$\left[\frac{\delta G_m(\mathbf{x})}{\delta f_j(\mathbf{x}')}\right] \to \left[\frac{\delta G_m(\mathbf{x})}{\delta f_j(\mathbf{x}')} + \frac{\delta F_m^{(1)}(\mathbf{x})}{\delta f_j(\mathbf{x}')} - \frac{1}{2}\left\{\frac{\delta F_m^{(1)}(\mathbf{x})}{\delta f_j(\mathbf{x}')}\right\}\right] \qquad (F4)$$

$$\left[\frac{\delta^2 G_m(\mathbf{x})}{\delta f_j(\mathbf{x}')\delta f_n(\mathbf{x}'')}\right] \to$$

$$\left[\frac{\delta^2 G_m(\mathbf{x})}{\delta f_j(\mathbf{x}')\delta f_n(\mathbf{x}'')} + \frac{\delta^2 F_m^{(2)}(\mathbf{x})}{\delta f_j(\mathbf{x}')\delta f_n(\mathbf{x}'')} - \frac{1}{3}\left\{\frac{\delta^2 F_m^{(2)}(\mathbf{x})}{\delta f_j(\mathbf{x}')\delta f_n(\mathbf{x}'')}\right\}\right] \qquad (F4')$$

etc. where the braces denote summation over all permutations of the position arguments (carrying the vector subscripts along with the corresponding arguments) and the $F_m^{(i)}(\mathbf{x})$ are arbitrary functionals of $\mathbf{f}(\mathbf{x})$. Using (C11, 13) and the orthogonality of $\mathbf{b}_m$ and $\mathbf{k}_m$, we find that a sufficient condition for stationarity (C4, 5) is

$$\nabla^2 g^{(k)}_{jm\ldots}(\mathbf{x},\mathbf{x}') = 0 \qquad (F5)$$

which constrains the $\mathbf{b}_m$'s appearing in the correlation functions. A similar procedure is followed for the general balance forced homogeneous case of §3.3. Applying symmetrization to the unforced inhomogeneous case allows us to collapse the sum over p in (E11, 14-16) to a single exponential term.

Acknowledgements

The author is indebted to Alan Wray and Robert Rogallo for countless illuminating and critical discussions. He is also grateful to Robert Kraichnan for his support and criticism and Dongho Chae for bringing the Vishik reference to his attention.

REFERENCES

ALANKUS, T. 1989 An exact representation of the space-time characteristic functional of turbulent Navier-Stokes flows with prescribed random initial states and driving forces. *J. Statis. Phys.* **54**, 859.

CONSTANTIN, P.& FOIAS, C. 1988 *Navier-Stokes Equation.* U. Chicago Press, p.84

FOIAS, C.& MANLEY, O.& TEMAM, R. 1987 Self-similar invariant families of turbulent flows. *Phys. Fluids.* **30**, 2008.

HOPF, E. 1952 Statistical hydromechanics and functional calculus. *J. Rat. Mech. Anal.* **1**, 87.

HUSSAIN, A. K. M. F. 1986 Coherent structures and turbulence. *J. Fluid Mech.* **173**, 303.

KRAICHNAN, R. H. 1975 Remarks on turbulence theory. *Adv. in Math* . **16**, 305.

LEVICH, E. 1987 Certain problems in the theory of developed hydrodynamical turbulence. *Phys. Rep.* **151**, 149.

LEWIS, R. M.& KRAICHNAN, R. H. 1962 A space-time functional formalism for turbulence. *Comm. Pure and Appl. Math.* **15**, 397.

MOFFATT, H. K. 1985 Magnetostatic equilibria and analogous Euler flows of arbitrary complex topology. *J. Fluid Mech.* **159**, 359.

MONIN, A. S.& YAGLOM, A. M. 1965 *Statistical Fluid Mechanics* Vol.2, M.I.T. Press; §28.1 and references therein.

ROSEN, G. 1971 Functional calculus theory for incompressible fluid turbulence. *J. Math. Phys.* **12**, 812.

SARGENT, M., SCULLY, M.& LAMB, W. 1974 *Laser Physics* Addison- Wesley, p.323.

SHEN, H. H. 1987 Viscous Lagrangian invariance and equipartition. *Devel. in Mech.* **14**, 510.

SHEN, H. H. 1990 Boson Hamiltonians and Stochasticity for the Vorticity Equation. *Can. J. Phys.* In press.

SHEN, H. H. 1991 Nonconservative dynamics of vortical structures: a statistical-mechanical perspective. *Physica D.* In press.

STANISIC, M. M. 1985 *The Mathematical Theory of Turbulence*, Springer- Verlag, Chap. 12.

TOWNSEND, A. A. 1976 *Structure of Turbulent Shear Flow*, Cambridge U. Press §3.10.

TSINOBER, A. 1990 On one property of Lamb vector in isotropic turbulent flow. *Phys. Fluids.* **A2**, 484 and references therein.

VISHIK, M. J.& FURSIKOV, A. V. 1988 *Mathematical Problems of Statistical Hydromechanics*, Kluwer Acad. Publ. §9.6.

The interaction of superfluid vortex filaments with a normal fluid channel flow

By D. C. Samuels

Vortex filaments in superfluids such as helium II may provide new insights into very high Reynolds number flows. We simulate the behavior of a superfluid vortex ring interacting with a normal fluid shear flow, specifically channel flow. The vortex ring evolves into a stable horseshoe configuration which propagates without further change of form. In this simulation, we demonstrate a boundary layer behavior in a superfluid through the coupling of the superfluid and the normal fluid.

1. Motivation and objectives

Superfluids such as helium II provide a true vortex filament system which can be explored both experimentally and numerically. Vorticity in helium II is confined to filaments with a measured radius of approximately one Å. These superfluid vortices may be treated as one-dimensional singularities to a good approximation for all length scales greater than $\sim 10^2 \mathring{A}$. The circulation about each vortex filament is quantized in units of h/m where h is Planck's constant and m is the mass of the helium atom. Due to energy considerations, only a single quantum of circulation is present around each vortex; therefore, we have the circulation $\Gamma = h/m$ for all helium II vortices. For a detailed discussion of vortices in helium II, see Glaberson and Donnelly (1986).

The motion of a vortex filament in the rest frame of the superfluid is determined from the Biot-Savart law,

$$\vec{v}(\vec{r}) = \frac{\Gamma}{4\pi} \int \frac{(\vec{s} - \vec{r}) \otimes d\vec{s}}{|\vec{s} - \vec{r}|^3} \tag{1}$$

where the integral is taken over all of the vortex filaments in the fluid. Since evaluation of the Biot-Savart integral is very expensive in computer time, the local induction approximation (LIA) is commonly employed (Arms & Hama 1965). In this approximation, the velocity at any point on the vortex filament is given by

$$\vec{v}(\vec{r}) \simeq \frac{\Gamma}{4\pi} \ln(\frac{R_{eff}}{a_0})(\vec{s}' \otimes \vec{s}'') \tag{2}$$

where $'$ denotes differentiation by arclength, a_0 is the core radius, and R_{eff} is an arbitrary length scale. In this project, we choose $R_{eff} = 8R$, where R is the local radius of curvature of the filament. This choice gives the correct velocity for vortex rings (Glaberson & Donnelly 1986). The LIA is only valid if the Biot-Savart integral is dominated by the local region $\vec{s} \simeq \vec{r}$. A practical rule of thumb is that the LIA is not applicable if 'non-local' sections of the vortex filament approach within a

 INTENTIONALLY BLANK

distance of one R. Note that the logarithmic term in Eq. 2 prevents us from non-dimensionalizing the equation of motion unless the logarithmic term is considered constant. In this project, we have allowed the logarithmic term to vary and have, therefore, not non-dimensionalized the equations.

A major difficulty in applying the results of superfluid turbulence experiments to high Reynolds number flows is that helium II is not a pure superfluid but instead behaves as a combination of two fluids, a superfluid and a normal fluid (Wilkes & Betts 1987). The normal fluid is a classical Navier-Stokes fluid with a very small but non-zero viscosity ($\sim 20\mu P$). The quantum excitations which form the normal fluid are scattered by the superfluid vortices, allowing momentum and energy transfer between the two fluids. This coupling, known as mutual friction (Vinen 1957), is represented as a force per unit length on the vortex filament.

$$\vec{F}_{drag} = \gamma_0(\vec{v}_n - \vec{v}_L) \tag{3}$$

where γ_0 is a temperature dependant parameter, $\vec{v}_n$ is the velocity of the normal fluid, and $\vec{v}_L$ is the velocity of the vortex filament. Including this drag force, the filament velocity is given by

$$\vec{v}_L = \vec{v}_s + \vec{v}_I + \alpha\vec{s}' \otimes (\vec{v}_n - \vec{v}_s - \vec{v}_I) \tag{4}$$

where α is another temperature dependant parameter, $\vec{v}_s$ is the imposed superfluid flow, and $\vec{v}_I$ is the self-induced vortex velocity given by either the Biot-Savart law or the LIA.

In our simulation, superfluid vortex filaments are represented by a series of linked straight vortex segments connected at nodes. The velocity at each node is calculated by Eq. 4 using the LIA and the positions of the nodes are integrated forward in time by an adaptive Runge-Kutta-Fehlberg method.

Experiments in superfluid turbulence (Tough 1982) reveal a wealth of turbulent behavior with four possibly distinct turbulent states characterized by geometrical factors and the relative velocity $(\vec{v}_n - \vec{v}_s)$. Through simulation studies, Schwarz (1988) has developed a theory of homogeneous, isotropic superfluid turbulence. This theory has had mixed success in explaining some of the behavior observed in superfluid turbulence experiments.

A feature which has been neglected in superfluid simulations is the interaction of the vortex filaments with a shear flow (or boundary layer) in the normal flow. In simulations of classical vortex filaments, Aref and Flinchem (1984) have found that an initially linear vortex filament placed in the spanwise direction of an imposed external shear flow is unstable (in the LIA) to small perturbations, developing oscillations which the authors liken to turbulent spots. In a similar study, Leonard (1980) has demonstrated an instability of an array of interacting vortex filaments initially arranged to represent a shear layer. Though these studies involve different couplings of the vortex filament and a shear flow than is present in superfluids, they do suggest that such couplings are dynamically interesting.

2. Accomplishments

The first phase of this project has been to upgrade the simulation code of the author so that the full effects of mutual friction may be accurately included. The most important adaptation was to implement a remeshing algorithm to allow the computational grid to adjust to the shrinking and growing of the vortex filaments. These subroutines compare the length, ℓ, of each vortex element to the local radius of curvature, R, of the vortex filaments. Nodes are added or subtracted from the filament meshing to keep the ratio ℓ/R within set limits. This allows the behavior of the vortex filament to be followed as the length scales evolve over many orders of magnitude. When nodes are added to the filament meshing, I have found that the new nodes must be interpolated using splines of at least third order so that the second derivative (corresponding to curvature) is modeled continuously along the filament. If lower degree interpolation is used, artificial curvature fluctuations are introduced which affect the vortex dynamics. It is possible that fourth order interpolation may be necessary to avoid artificial discontinuities in the torsion of the filament. This question is currently being examined.

The physical situation under study at the present time is channel flow of superfluids. We assume that the normal fluid is in laminar channel flow

$$v_n = \frac{3}{2} v_{avg} (1 - (\frac{z}{a})^2) \tag{5}$$

where a is the half-width of the channel, and that the superfluid has a constant velocity v_s. In the simulations discussed in this report, the superfluid velocity is chosen so that the net superfluid and normal fluid flow through the channel are equal, $v_s = v_{avg}$. The vortex behavior that we have observed should not depend qualitatively on the magnitude of v_s. The flow is in the positive y direction, the x axis is spanwise to the flow, and the z axis is normal to the channel boundaries. We initialize the simulation with a small vortex half-ring attached to the lower wall. The ring lies in the x-z plane and is oriented against the flow. The initial radius of the ring is $10^{-1}a$. We find that the final shape of the vortex filament is independent of the initial size of the vortex ring, provided that the initial radius is larger than a small value dependant upon v_s. Since rings are unlikely to be generated with small radii (Schwarz 1990), this limitation is unimportant here. The vortex ring evolves into a horseshoe shape (Figures 1 and 2) with a length longer than the channel height (Figure 3). This horseshoe vortex propagates against the direction of the external flow with little or no change in shape or size. The coupling between the superfluid vortex and the normal fluid boundary layer causes a boundary layer behavior to appear in the superfluid. The existence of these long vortex filaments may play a crucial role in the initiation of superfluid turbulence.

3. Future work

The immediate future phase of this project is to examine the dynamics of the horseshoe vortex filament. Of particular interest is the process which transports energy from the boundary, where mutual friction is causing growth, to the tip of

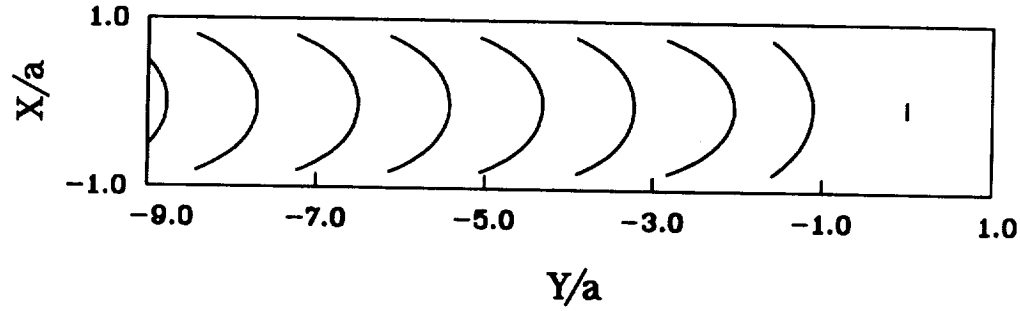

FIGURE 1. Instantaneous configurations of the vortex filament in the $X - Y$ plane as the filament evolves. The time evolution is from right to left.

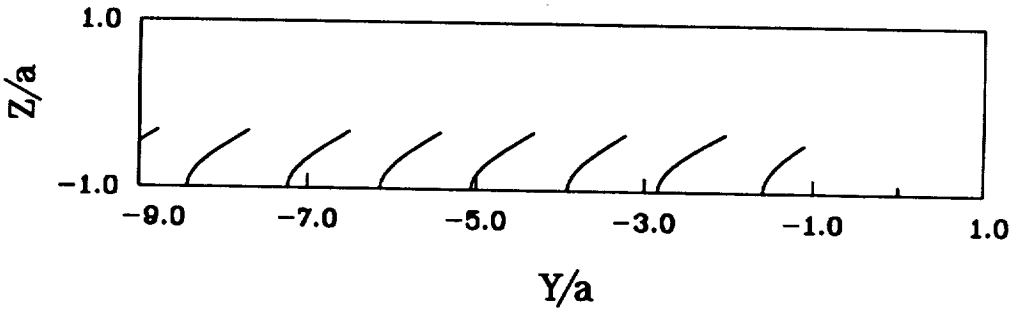

FIGURE 2. Instantaneous configurations in the $Y - Z$ plane.

the vortex, where mutual friction causes the vortex filament to shrink. How is this energy balance maintained to form a vortex with constant length and shape? And very importantly, does this balance break down at higher external flow rates, causing unlimited growth of the vortex filament?

A problem which must be addressed is the possibly non-negligible interaction of a vortex filament of this shape with the solid boundary, represented by an image vortex. In this situation, the local induction approximation may not be sufficient, and full Biot-Savart calculations may be necessary.

In the less immediate future, interactions of these horseshoe vortices will be studied, including merger of vortices and the possible formation of regular arrays of these vortices as is seen in classical fluids (Herbert 1988). It will be necessary to use full Biot-Savart calculations in these simulations.

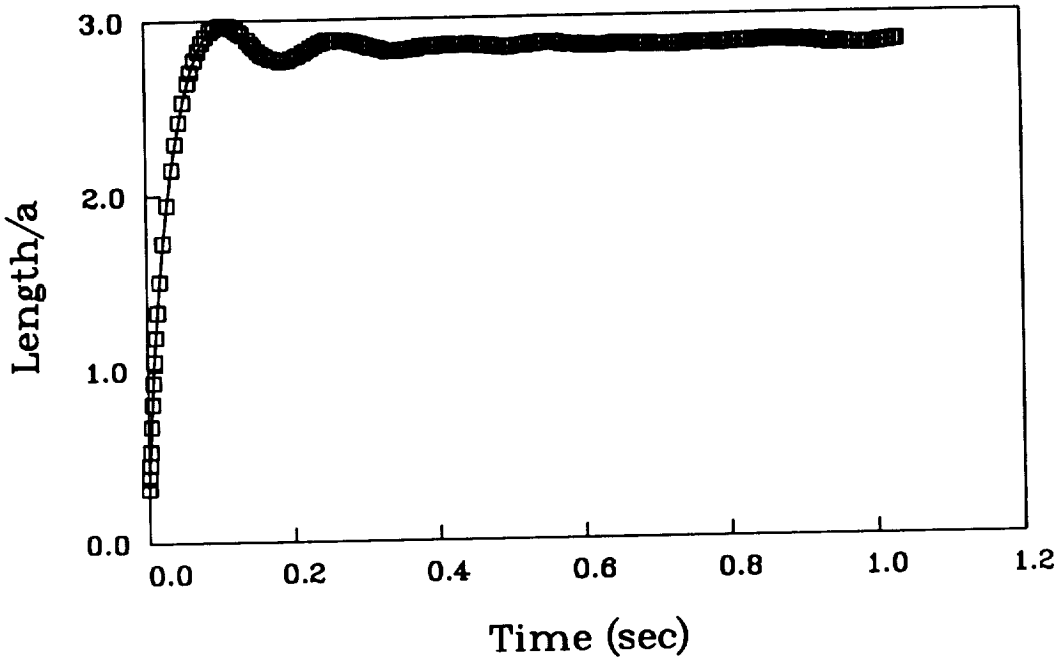

FIGURE 3. Total length of the vortex filament. These results were taken from a simulation with $a = 10^{-2}$ cm and $v_{avg} = 5.0$ cm/sec.

REFERENCES

AREF, H., & FLINCHEM, E. P. 1984 Dynamics of a Vortex Filament in a Shear Flow. *J. Fluid Mech.* **148**, 477-497.

ARMS, R. J., & HAMA, F. R. 1965 Localized-Induction Concept on a Curved Vortex and Motion of an Elliptic Vortex Ring. *Phys. of Fluids.* **8**, 553-559.

GLABERSON, W. I., & DONNELLY, R. J. 1986 Structure, Distributions and Dynamics of Vortices in Helium II. *Prog. in Low Temp. Phy.* **9**, 1-142.

HERBERT, T. 1988 Secondary Instability of Boundary Layers. *Ann. Rev. Fluid Mech.* **20**, 487-526.

SCHWARZ, K. W. 1988 Three-Dimensional Vortex Dynamics in Superfluid He^4 : Homogeneous Superfluid Turbulence. *Phys. Rev. B.* **38**, 2398-2417.

SCHWARZ, K. W. 1990 Phase Slip and Turbulence in Superfluid He^4 : A Vortex Mill That Works. *Phys. Rev. Lett.* **64**, 1130-1133.

TOUGH, J. T. 1982 Superfluid Turbulence. *Prog. in Low Temp. Phys.* **8**, 133-219.

VINEN, W. F. 1957 Mutual Friction in a Heat Current in Liquid Helium II: III. Theory of the Mutual Friction. *Proc. Roy. Soc.* **A242**, 493-515.

WILKS, J. & BETTS, D. S. 1987 *An Introduction to Liquid Helium.* Oxford Science Publications

Center for Turbulence Research
Annual Research Briefs - 1990

Simulations of curved turbulent boundary layers: a progress report

By P. Orlandi[1]

1. Introduction

The objective of this work is to develop a space-time accurate numerical method for the solution of incompressible Navier-Stokes equations in generalized coordinates. The resulting code is to be used for direct and large-eddy simulation of turbulence in complex geometries. In a previous paper (Orlandi 1989), the system of Navier-Stokes equations in general curvilinear coordinates was solved by a second-order accurate finite-difference scheme. Satisfactory results were obtained for several flows in two and three dimensions. The system of Navier-Stokes for the fluxes are given in Orlandi (1989). The main deficiency of the numerical scheme was the large CPU time required for the solution of the Poisson equation for the "pressure" field. The point SOR relaxation, in conjunction with a multigrid scheme, was used for the Poisson equation. In some cases, particularly with very fine grids, it was impossible to obtain a divergent-free flow.

The "pressure" solver has been improved by introducing a Fourier transform in the direction with Cartesian coordinates, and a line zebra iterative scheme has been used for the relaxation scheme. The line sweeps are used for the direction of stretched coordinates. The zebra scheme allows a very efficient vectorization of the "pressure" solver and reduces the required CPU time. This improvement resulted in a higher convergence rate and the divergence-free condition was always obtained. The Fourier transform leads to a series of 2-D Helmholtz equations with the reduced wave number $\mathbf{k}$ as the parameter. At high $\mathbf{k}$, as expected, the convergence rate of the relaxation scheme is very high because the negative eigenvalues of the matrix have large magnitudes. Slower convergence was obtained for the zero-wave number, however. In all cases, tested a very small reduction factor was found for the first cycle $O(10^{-2})$, and in the subsequent cycles the reduction factor was approximately 0.3. The maximum residual of 10^{-6} is reached at $\mathbf{k} = 0$ by few **W** multigrid cycles with two iteration sweeps at each line zebra relaxation. At high $\mathbf{k}$, the convergence was obtained by a single multigrid cycle. This efficient "pressure" solver has been incorporated into the direct simulation of flows over riblets by Choi (1990). As a consequence, he could employ a much finer grid than the grid previously used by Orlandi (1989). A very fine grid is required to represent the physics of drag reduction by the riblets. The entire numerical method and the associated computer program have reached a level of robustness that permits its use as a tool to obtain reliable flow fields.

1 Dipartimento di Meccanica ed Aeronautica Universita' di Roma "La Sapienza"

In practical applications, one often encounters turbulent flows along curved boundaries with inflow and outflow conditions. In these cases, the conventional Reynolds averaged turbulence models have not been very satisfactory, as found in the 1980-81 Stanford conference on complex turbulent flows (Kline *et al.* 1981). A full numerical simulation, e.g. for a flow around a turbine blade or an airfoil, requires an enormous amount of computer resources, mainly because these flows develop along the streamwise direction for hundreds of boundary layer thicknesses. Considering that usually in the direct simulation it is necessary to have at least ten grid points per boundary layer thickness, at least 10^3 grid points are required in the streamwise direction. A grid of 128×128 is necessary along the vertical and spanwise directions to describe the interaction of large and small structures at moderately low Reynolds numbers. With such large grid requirements, it appears to be difficult to do a direct simulation of the flow considered by Barlow and Johnston (1988), consisting of a boundary layer growing on a flat plate subjected to a relatively strong curvature followed by a recovery section. The direct simulation of this flow requires inflow conditions for the instantaneous turbulent velocity field similar to those currently tested for other flows in the CTR.

The use of a large eddy simulation, with an affordable grid of say $64 \times 64 \times 64$, could give satisfactory results in simulating the Barlow & Johnston flow at a $Re_\theta = 1300$. On the other hand, it is unlikely that two-dimensional Reynolds averaged computations of such flows can give good predictions if the dominant role of the three dimensional structures is not incorporated somehow in the turbulence model.

Enroute to large-eddy simulation of curved turbulent flows, we investigated whether the aforementioned numerical scheme can predict the well-known features of flows in presence of curved boundaries. In presence of concave walls, centrifugal instabilities cause the generation of Gortler vortices which enhance transition to turbulence. For this case, a well-documented experiment of Swearingen & Blackwelder (1987) exists together with the numerical simulation of Liu & Domaradzki (1990). In the numerical simulation of Liu & Domaradzki, it was assumed that the boundary layer is parallel; this assumption allows the application of periodic boundary conditions in the streamwise direction. This is not a realistic assumption, and in the past it was criticized by Hall (1983), who showed that the assumption could give erroneous results. Liu & Domaradzki computed a time developing flow rather than a spatially evolving flow. They were able to reproduce qualitatively the results of Swearingen & Blackwelder, but the transition to turbulence in the numerical simulation occurred later than in the experiment. A reason for the disagreement could reside on the assumption of parallel flow.

In the present paper, a preliminary attempt is made to compute the spatially evolving flow of Swearingen & Blackwelder. To reduce the streamwise distance, the inflow was at a distance $x = 60cm$ from the leading edge, as done by Liu & Domaradzki. See the sketch of the geometry in Fig.1. In the experiments of Swearingen & Blackwelder, Gortler vortices were not present at $x = 60cm$, but they were present at $x = 90cm$. At this position, the displacement thickness δ^* in between the vortices reaches the maximum value, and the δ^* outside the vortices

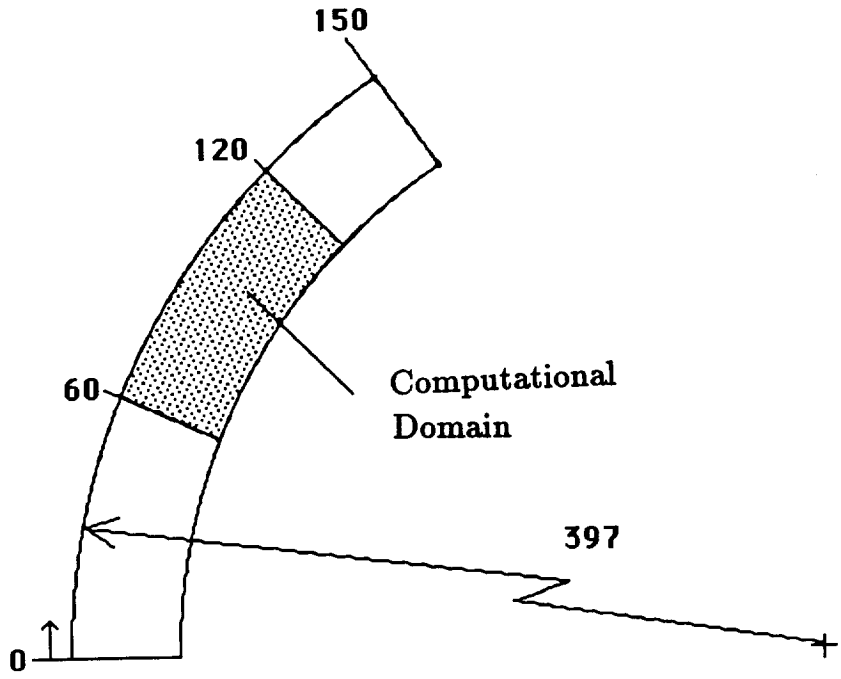

FIGURE 1. Sketch of the geometry.

reaches the minimum. We do not intend to compute the transition to turbulence, thus the outflow condition has been located at $x = 110cm$.

The parameters of the present simulation are those of the experiment. The initial Gortler number is $Go = (U_0\theta/\nu)\sqrt{\theta/R} = 5.6$, the radius of curvature of the wall is $R = 320cm$, the kinematic viscosity $\nu = 0.15cm^2/sec$, and the free-stream velocity $U_0 = 500cm/sec$; from these values it follows that the initial momentum thickness θ is $0.095cm$. For the sake of simplicity, at the inflow the Polhausen rather than the Blasius profile was used. In this case, $\theta/\delta = 37/315$. The initial boundary layer thickness is $\delta = 0.81cm$ and $Re = U_0\delta/\nu = 2685$. At $Go = 5.6$, the theoretical neutral stability limit corresponds to the non-dimensional wave number $k\theta = 2\pi\theta/\lambda = 0.24$; the spanwise dimension of the domain is then $\lambda = 3.0175\delta$. The "free-stream" was located at $y/\delta = 5$. The computational domain has been discretized by 65×79 points in the streamwise and normal directions, respectively. In the spanwise direction, two grids were used, the first with 33 and the second one with 65 points. The coarse grid, used particularly in the streamwise direction, is not sufficient for obtaining very accurate results. However, in this preliminary study, we intend to examine whether and in what degree the numerical method captures the growth of the Gortler vortices. These vortices modify the distribution of the streamwise velocity in (y, z)-planes, generating low-speed regions separated from high speed regions. These vortices enhance the transition to turbulence, and

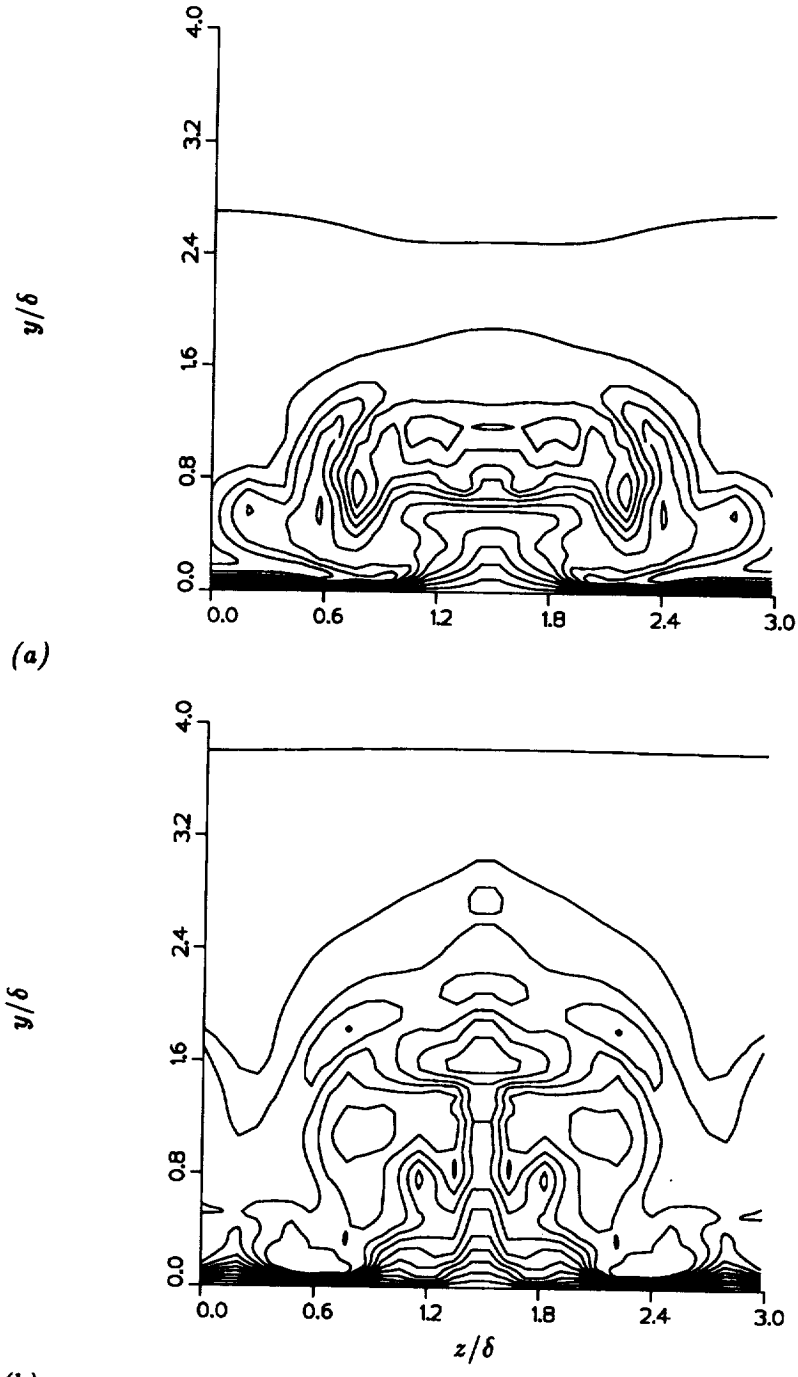

FIGURE 2. Contours of streamwise velocity in (y, z)-planes, grid $65 \times 79 \times 33$: a) $x/\delta = 98.25$; b) $x/\delta = 121.5$.

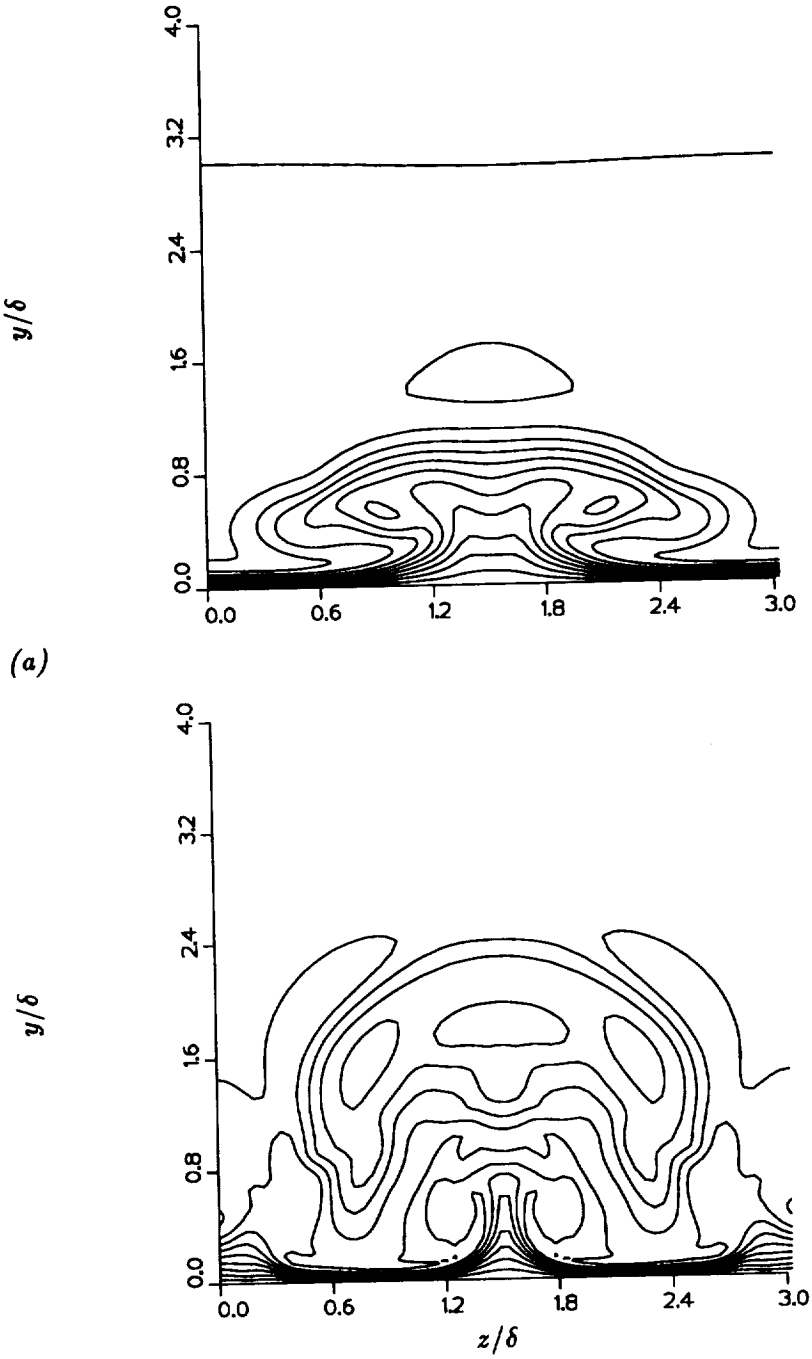

FIGURE 3. Contours of streamwise velocity in (y, z)-planes, grid $65 \times 79 \times 65$: a) $x/\delta = 98.25$; b) $x/\delta = 121.5$.

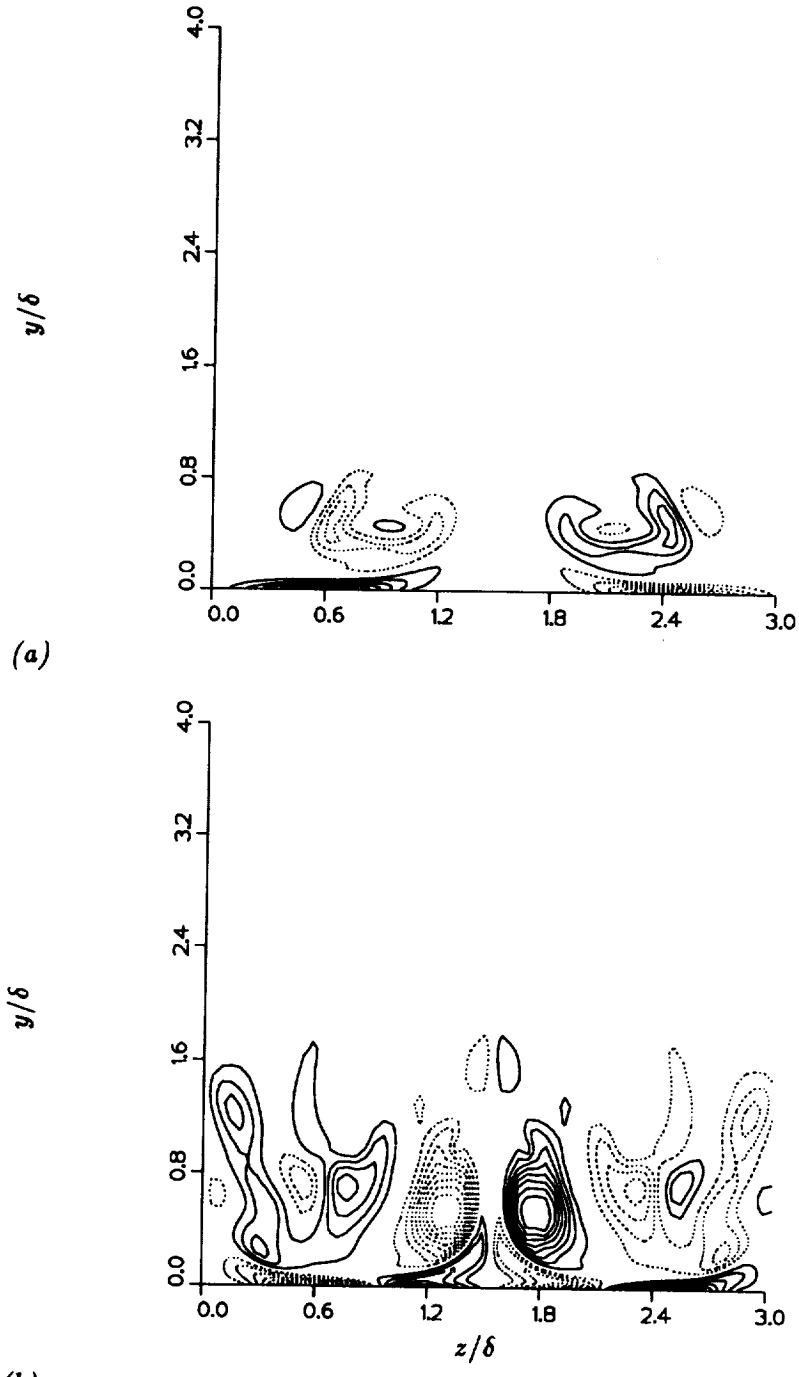

FIGURE 4. Contours of streamwise vorticity in (y, z)-planes, grid $65 \times 79 \times 65$: a) $x/\delta = 98.25$; b) $x/\delta = 121.5$.

as pointed out by Swearingen & Blackwelder, inflectional spanwise profiles of the streamwise velocity are much more effective.

Liu & Domaradzki used the following initial velocity distribution

$$u(x,y,z) = u_0(y) + \epsilon u_1(y) cos(2\pi z/\lambda)$$

$$v(x,y,z) = \epsilon v_1(y) cos(2\pi z/\lambda)$$

$$w(x,y,z) = \epsilon w_1(y) sin(2\pi z/\lambda)$$

where $u_0(y)$ is the laminar Blasius profile and $u_1(y), v_1(y)$ and $w_1(y)$ are the component of the eigenmode obtained by the linear stability theory. We used a much simpler relation for the perturbations

$$w(x,y,z) = \epsilon sin(2\pi z/\lambda) sin(2\pi y/\delta), \quad y/\delta < 1.$$

and $w = 0$ elsewhere. In order to have a faster growth in time, $\epsilon = 0.05$ was used. The perturbation $u(y,z)$ was set to 0 and $v(y,z)$ was obtained from continuity. At the outflow, convective boundary conditions were imposed.

2. Results

In this section, we present some qualitative results which will demonstrate the formation and growth of the Gortler vortices. Quantitative comparisons with the experiment of Swearingen & Blackwelder will be made only after checks of grid independence has been completed. At present, the results strongly depend on the grid.

We wish to point out that the number of grid points used in the present finite difference simulation (up to $65 \times 79 \times 65$) is much smaller than that used in the numerical simulation of Liu & Domaradzki. Considering that they were using a spectral method, the present grid is too coarse to lead to reliable results. The present scheme, however, has the advantage that it can be extended to different boundary shapes. Fig. 2 shows contour plots of streamwise velocity in the (y,z)-planes at the streamwise locations $x/\delta = 98.25$ and $x/\delta = 121.5$ obtained using a $65 \times 79 \times 33$ grid. The larger growth of the boundary layer between the vortices is apparent. The numerical solution also shows that the spanwise extent of the Gortler vortices grows with the downstream direction.

Fig.3 shows that the solution improves with doubling the number of grid points in the spanwise direction; a more defined structure is observed in the low-speed region. The numerical diffusion in the spanwise direction, although reduced in respect to the previous grid, is still quite large. The effect of the numerical diffusion is observed also in the contour plot of streamwise vorticity (Fig. 4), where two very strong vortices appear at the center, with some scattered vorticity on the side. The numerical simulation predicts that the boundary layer in the low-speed region grows by a factor of 1.8 at $x/\delta = 98.25$ and 3.4 at $x/\delta = 121.5$. The experiments reports

factors of 2.0 and 2.6, respectively. A further grid refinement has been performed by using 128 points along the streamwise direction; the results improve, but still the high-speed regions are contaminated by the low-speed regions. The reason of this is the very coarse mesh used in the streamwise direction.

We have presented in this paper the work in progress to simulate turbulent boundary layers along concave walls. The numerical scheme requires 10 secs of CPU for the grid $65 \times 79 \times 65$ for a full-third order Runge-Kutta step, which is slightly larger than the typical times required by a spectral method. However, with finite-difference schemes, larger time steps can be taken as compared to spectral methods. The complete grid convergence test has not been finished. When this check is done, quantitative comparison with the experiments will be presented.

Acknowledgements

I am grateful to H. Choi, P. Moin, and J. Kim for many fruitful discussions.

REFERENCES

BARLOW, R. S. & JOHNSTON, J. P. 1988 Structure of turbulent boundary layer on a concave surface. *J. Fluid Mech.* **191**, 137-176.

CHOI, H. Private communication.

HALL, P. 1983 The linear development of Gortler vortices in growing boundary layers. *J.Fluid Mech.* **130**, 41-58.

KLINE, S. J., CANTWELL, B. J. & LILLEY, G. M.(EDS) 1981 The 1980-81 AFOSR-HTTM Stanford Conference on Complex Turbulent Flows: A Comparison of Computation and Experiment Volumes I, II and III. Stanford University.

LIU, P & DOMARADZKI, J. 1990 Direct numerical simulation of transition to turbulence in Gortler flow. *AIAA paper 90-0114*. 28th Aerospace Science Meeting, Reno.

ORLANDI, P. 1989 A numerical method for direct simulation of turbulence in complex geometries. *CTR Annual Research Briefs*. 215-228.

SWEARINGEN, J. D. & BLACKWELDER, R. F. 1987 The growth and breakdown of streamwise vortices in the presence of a wall. *J. Fluid Mech.* **182**, 255-290.

Methods for direct simulation of transition in hypersonic boundary layers

By J. J. W. van der Vegt AND J. H. Ferziger

An implicit numerical algorithm for the time accurate solution of the compressible Navier-Stokes equations is described. Results for steady flow past a finite flat plate are presented, together with preliminary results for the temporal simulation of second mode instability in a flat plate boundary layer at Mach 4.5.

1. Motivation and objective

The proposed new generation of supersonic and hypersonic vehicles pose tremendous challenges to prediction methods for high speed flows. Transition to turbulence is crucial to the design of these vehicles but is far from completely understood. Direct simulations can complement experiments by offering opportunities to study cases which are very difficult or impossible to realize experimentally. This report discusses numerical methods for direct simulation of transition in boundary layers. We have developed and improved a time-accurate numerical method for flows with both strong shocks and boundary layers; for more details see van der Vegt (1991). Efficient ways to obtain steady state solutions, needed as initial conditions, have been implemented. Calculations of the temporal stability of the second mode in a flat plate boundary layer have been started; the main objective is to study the effects of wall temperature on stability.

2. Accomplishments

The main activities in 1990 have been the further development of a time accurate method for the Navier-Stokes equations; a start has been made on transition calculations on a flat plate. The requirements of time accuracy and rapid convergence to a steady state are partially conflicting because one can improve convergence by adding dissipation while one tries to minimize dissipation in time-accurate calculations. Whenever there is conflict between these requirements, time accuracy is favored. Strong shocks and boundary layers present different problems. It was decided to develop a fully implicit method because the equations are stiff, resulting in an impractical time step limitation for explicit methods.

An implicit method is, however, more complicated than an explicit method. There are a number of implicit methods available for the compressible Navier-Stokes equations. One of the most widely used methods is that of Beam and Warming (1978), which is not well suited for our problem. For time-accurate solutions, the approximate factorization adds an additional error and the viscous cross-coupling terms cannot be factorized. In addition, the use of central differences requires artificial viscosity to obtain stable solutions when there are shocks. The Beam-Warming

method obtains steady state solutions efficiently but is not well suited to time-accurate calculations.

An alternative is to choose one of the modern upwind methods developed for the Euler equations such as flux splitting according to Steger and Warming or van Leer, approximate Riemann solvers, and TVD methods; for a review see Vinokur (1989). These methods all incorporate some properties of the Euler equations and accurately compute shocks without explicit artificial dissipation. We chose Steger-Warming splitting in which the components related to the positive and negative eigenvalues of the operator are treated differently. The method accounts for information travel along the (inviscid) characteristics. At high Reynolds number, this is nearly correct in most of the flow. Flux splitting for the non-linear terms has an additional beneficial effect; it yields a diagonally dominant matrix well suited to iterative solution. In the viscous region, however, flux splitting can produce unwanted numerical dissipation, as was demonstrated by MacCormack and Candler (1989). The correction to the Steger-Warming splitting proposed by MacCormack was adopted and modified for the boundary layer, whereas the Steger-Warming splitting, described in Steger and Warming (1981), is used in a shock. The diagonal dominance of the matrix allows iterative solution and all the viscous components to be treated implicitly. It also gives more freedom in the choice of boundary conditions.

Numerical Method

A finite-volume method is used because an integral formulation is conservative and better suited to flows with shocks. The present algorithm solves the two-dimensional compressible Navier-Stokes equations in conservation form in an arbitrary coordinate system. These can be written:

$$\frac{\partial}{\partial t}\hat{\mathbf{U}} + \frac{\partial}{\partial \xi}(\hat{\mathbf{E}} - \hat{\mathbf{V}}_{vis_\xi}) + \frac{\partial}{\partial \eta}(\hat{\mathbf{G}} - \hat{\mathbf{V}}_{vis_\eta}) = \mathbf{0} \tag{1}$$

with:

$$\hat{\mathbf{U}} = \frac{\mathbf{U}}{J}; \quad \hat{\mathbf{E}} = \frac{\xi_x}{J}\mathbf{E} + \frac{\xi_z}{J}\mathbf{G}; \quad ,\hat{\mathbf{G}} = \frac{\eta_x}{J}\mathbf{E} + \frac{\eta_z}{J}\mathbf{G}$$

$$\hat{\mathbf{V}}_{vis_\xi} = \frac{\xi_x}{J}\mathbf{V} + \frac{\xi_z}{J}\mathbf{I}; \quad \hat{\mathbf{V}}_{vis_\eta} = \frac{\eta_x}{J}\mathbf{V} + \frac{\eta_z}{J}\mathbf{I}$$

and:

$$\mathbf{U} = \begin{pmatrix} \rho \\ \rho u \\ \rho w \\ e \end{pmatrix}; \quad \mathbf{E} = \begin{pmatrix} \rho u \\ \rho u^2 + p \\ \rho uw \\ (e+p)u \end{pmatrix}; \quad \mathbf{G} = \begin{pmatrix} \rho w \\ \rho uw \\ \rho w^2 + p \\ (e+p)w \end{pmatrix}$$

$$\mathbf{V} = \frac{1}{Re}\begin{pmatrix} 0 \\ \tau_{xx} \\ \tau_{xz} \\ u\tau_{xx} + w\tau_{xz} - \frac{q_x}{(\gamma-1)M^2 Pr} \end{pmatrix}; \; \mathbf{I} = \frac{1}{Re}\begin{pmatrix} 0 \\ \tau_{xz} \\ \tau_{zz} \\ u\tau_{xz} + w\tau_{zz} - \frac{q_z}{(\gamma-1)M^2 Pr} \end{pmatrix}$$

$$\tau_{xx} = (2\mu + \lambda)\frac{\partial u}{\partial x} + \lambda\frac{\partial w}{\partial z}; \quad \tau_{xz} = \mu(\frac{\partial u}{\partial z} + \frac{\partial w}{\partial x}); \quad \tau_{zz} = (2\mu + \lambda)\frac{\partial w}{\partial z} + \lambda\frac{\partial u}{\partial x}$$

$$q_x = -\kappa\frac{\partial T}{\partial x}; \quad q_z = -\kappa\frac{\partial T}{\partial z}$$

The equation of state is: $p = \frac{\rho c_v T}{\gamma M^2}$

Here ρ represents the density, u and w the velocity components in a Cartesian coordinate system, p the pressure, T temperature, and e the total energy. The variables x and y represent Cartesian coordinates, whereas ξ and η represent curvilinear coordinates. The coefficients M and Pr are the Mach and Prandtl numbers, while μ, λ, and κ are the two viscosities and thermal conductivity. The shear stress and heat flux components in $\mathbf{V}$ and $\mathbf{I}$ are functions of ξ and η. All variables are non-dimensionalized using free-stream variables and a characteristic length. Use of a general coordinate system adds flexibility but greatly increases the complexity of the code.

The numerical scheme will now be summarized. The first step is the choice of a time integration method. The time integration is formulated as a Padé relation, cf. Beam and Warming (1978):

$$\Delta\hat{\mathbf{U}}^n = \frac{\alpha\Delta t}{1+\beta}\frac{\partial}{\partial t}\Delta\hat{\mathbf{U}}^n + \frac{\Delta t}{1+\beta}\frac{\partial}{\partial t}\hat{\mathbf{U}}^n + \frac{\beta}{1+\beta}\hat{\mathbf{U}}^{n-1} + O[(\alpha - \tfrac{1}{2} - \beta)\Delta t^2 + \Delta t^3]$$

with: $\Delta\hat{\mathbf{U}}^n = \hat{\mathbf{U}}^{n+1} - \hat{\mathbf{U}}^n$

The coefficients α and β allow different time integration schemes to be obtained. For instance, $\alpha = 1$, $\beta = 0$ give the implicit Euler method, $\alpha = .5$, $\beta = 0$ give the trapezoid rule, and $\alpha = 1$, $\beta = 0.5$ give a three point backward scheme. The superscript n refers to time $t = t_n$.

Introducing the compressible Navier-Stokes equations (1) into this relation yields:

$$\begin{aligned}\Delta\hat{\mathbf{U}}^n = &\frac{\alpha\Delta t}{1+\beta}\{-\frac{\partial}{\partial\xi}(\Delta\hat{\mathbf{E}}^n - \Delta\hat{\mathbf{V}}^n_{vis_\xi}) - \frac{\partial}{\partial\eta}(\Delta\hat{\mathbf{G}}^n - \Delta\hat{\mathbf{V}}^n_{vis_\eta})\}+ \\ &\frac{\Delta t}{1+\beta}\{-\frac{\partial}{\partial\xi}(\hat{\mathbf{E}}^n - \hat{\mathbf{V}}^n_{vis_\xi}) - \frac{\partial}{\partial\eta}(\hat{\mathbf{G}}^n - \hat{\mathbf{V}}^n_{vis_\eta})\} + \frac{\beta}{1+\beta}\Delta\hat{\mathbf{U}}^{n-1}\end{aligned} \tag{2}$$

which is first or second order accurate in time, depending on the choice of α and β.

Applying Gauss' theorem and integrating equation (2) over a small volume gives the finite-volume formulation for the compressible Navier-Stokes equations:

$$\begin{aligned}\Delta\overline{\mathbf{U}}_{i,j} = &\frac{\alpha\Delta t}{1+\beta}\{-\Delta\overline{\mathbf{G}}^n_{i,j-\frac{1}{2}} + \Delta\overline{\mathbf{E}}^n_{i+\frac{1}{2},j} + \Delta\overline{\mathbf{G}}^n_{i,j+\frac{1}{2}} - \Delta\overline{\mathbf{E}}^n_{i-\frac{1}{2},j}\}+ \\ &\frac{\Delta t}{1+\beta}\{-\overline{\mathbf{G}}^n_{i,j-\frac{1}{2}} + \overline{\mathbf{E}}^n_{i+\frac{1}{2},j} + \overline{\mathbf{G}}^n_{i,j+\frac{1}{2}} - \overline{\mathbf{E}}^n_{i-\frac{1}{2},j}\} + \frac{\beta}{1+\beta}\Delta\overline{\mathbf{U}}^{n-1}\end{aligned} \tag{3}$$

where a barred quantity with index i, j is an average of the unbarred quantity over the cell with index i, j and indices $i \pm \frac{1}{2}$ and $j \pm \frac{1}{2}$ refer to values at the cell faces.

Flux Vector Splitting

Flux vector splitting is powerful for computing flows with strong shocks. Upwind methods are, however, dissipative. Dissipation is necessary in shocks but not in smooth flows such as boundary layers. MacCormack and Candler (1989) presented a way to improve the accuracy of flux vector splitting significantly in regions outside shocks. This method, in modified form, is discussed in this section.

The Steger-Warming splitting is based on the homogeneity property of the Euler equations:

$$\hat{\mathbf{E}}^n(\mathbf{U}) = \left(\frac{\partial \hat{\mathbf{E}}^n}{\partial \mathbf{U}}\right) \mathbf{U}^n = S^{-1}C^{-1}\Lambda C S \mathbf{U}$$

with : $S = \frac{\partial \mathbf{U}}{\partial \mathbf{V}}$, where $\mathbf{V} = (\rho, u, v, p)^T$, C is related to the metrics, density and speed of sound a, and $\Lambda = (u, u, u+a, u-a)^T$, the eigenvalue matrix.

In the Steger-Warming approach, the flux vector is split in vectors $\hat{\mathbf{E}}^{\pm}$ by separating the matrix Λ in matrices with positive and negative eigenvalues. As demonstrated by MacCormack and Candler (1989), this gives a dissipative approximation to the flux at the cell surface when using a finite-volume method. They demonstrated that for the incompressible flat plate boundary layer, it is much better to approximate the Jacobian matrix $\frac{\partial \hat{\mathbf{E}}^n}{\partial \mathbf{U}}$ at the surface $i + \frac{1}{2}$ by alternately using its value at i and $i+1$ for the components related to the momentum equations. This method was tested in great detail, but like the explicit predictor-corrector MacCormack scheme, it has the disadvantage that the error is oscillatory and depends on the time step, so the computation never reaches completely a steady state. Also, the location at which the metrics of the coordinate transformation are computed is not clear in their paper. In their finite-volume formulation of the Steger-Warming splitting, they use the metrics at the cell center, while the metrics at the cell faces should be used. This requires four times as many computations of the metrics, but it pays off in terms of accuracy.

The modified MacCormack splitting can now be defined in terms of:

$$D = \mathrm{diag}(\alpha_1, \alpha_2, \alpha_3, \alpha_4)$$

$$\tilde{S}_{i+\frac{1}{2}} = DS_i + (I - D)S_{i+1}$$

Similar expressions define $\tilde{C}_{i+\frac{1}{2}}$ and $\tilde{\Lambda}_{i+\frac{1}{2}}$. Here I represents the identity matrix and D a diagonal matrix. The modified flux is defined as:

$$\hat{\mathbf{E}}^+_{i+\frac{1}{2}} = \tilde{S}^{-1}_{i+\frac{1}{2}} \tilde{C}^{-1}_{i+\frac{1}{2}} \tilde{\Lambda}_{i+\frac{1}{2}} \tilde{C}_{i+\frac{1}{2}} \tilde{S}_{i+\frac{1}{2}} \mathbf{U}_i$$

with an equivalent relation for $\hat{\mathbf{E}}^-_{i+\frac{1}{2}}$, with $\mathbf{U}_i$ replaced by $\mathbf{U}_{i+1}$.

The main difference between the splitting presented in MacCormack and Candler (1989) and the one used in this paper is that the computation of the inverse matrices

$\tilde{S}^{-1}_{i+\frac{1}{2}}$ and $\tilde{C}^{-1}_{i+\frac{1}{2}}$ is exact and removes the oscillations of the MacCormack scheme but requires about 30% more work per time step than the Steger-Warming splitting. Another advantage of the new scheme is that it unifies several types of flux splitting, which is helpful when changing schemes. The Steger-Warming splitting is obtained using $D = \mathrm{diag}(1,1,1,1)$ for the positive flux vector and $D = \mathrm{diag}(0,0,0,0)$ for the negative flux vector. The MacCormack splitting is obtained by using at odd time intervals $D = \mathrm{diag}(1,1,1,1)$ and $D = \mathrm{diag}(0,1,1,0)$ and at even time intervals $D = \mathrm{diag}(1,0,0,1)$ and $D = \mathrm{diag}(0,0,0,0)$ for the positive and negative flux vectors respectively. More details can be found in Van der Vegt (1991).

Linearization

The flux vectors defined in the previous section are all non-linear functions of $\mathbf{U}$, so in order to solve the set of non-linear equations (3) implicitly, they have to be linearized around their value at time $t = t_n$. This is a delicate procedure if time accuracy is to be maintained. If only a steady state solution is needed, one can use the Steger-Warming splitting for the implicit part, but this adds a significant error when time accuracy is important. Due to the averaging process, the flux vector at surface $i + \frac{1}{2}$ is a function of both $\mathbf{U}_i$ and $\mathbf{U}_{i+1}$:

$$\Delta\hat{\mathbf{E}}^{\pm}(\mathbf{U}_i, \mathbf{U}_{i+1}) \cong \frac{\partial\hat{\mathbf{E}}^{\pm}}{\partial\mathbf{U}_i}\Delta\mathbf{U}_i + \frac{\partial\hat{\mathbf{E}}^{\pm}}{\partial\mathbf{U}_{i+1}}\Delta\mathbf{U}_{i+1}$$

with similar linearization for the vector $\Delta\mathbf{G}^n$. Analogously we have to linearize the viscous terms:

$$\Delta\hat{\mathbf{V}}^n_{vis_\xi}(\mathbf{U}) \cong \frac{\partial\hat{\mathbf{V}}^n_{vis_\xi}}{\partial\mathbf{U}}\Delta\mathbf{U}^n + \frac{\partial\hat{\mathbf{V}}^n_{vis_\xi}}{\partial\mathbf{U}_\xi}\Delta\mathbf{U}^n_\xi + \frac{\partial\hat{\mathbf{V}}^n_{vis_\xi}}{\partial\mathbf{U}_\eta}\Delta\mathbf{U}^n_\eta$$

A similar linearization is used for $\Delta\hat{\mathbf{V}}^n_{vis_\eta}$. The suffices + and − on the Jacobian matrices of the inviscid flux vectors refer to the components corresponding to positive and negative eigenvalues. In order to maintain time accuracy, none of the components in the matrices obtained by linearization should be neglected; this is not possible with approximate factorization. However, this greatly increases the difficulty of solving the linear system of equations, as discussed in the next section. Careful linearization is important because it greatly extends the stability limit of the scheme. If, for instance, the homogeneity property is used to linearize the inviscid flux vectors $\mathbf{E}$ and $\mathbf{G}$ then, in many cases, the time step can not be much larger than the time step for an explicit scheme.

Iterative Solution of Matrix Equation

After discretization, a system of linear algebraic equations is obtained:

$$\hat{A}^n_{ij}\Delta\mathbf{U}^n_{i,j} + \hat{B}^n_{ij}\Delta\mathbf{U}^n_{i,j+1} + \hat{C}^n_{ij}\Delta\mathbf{U}^n_{i,j-1} + \hat{D}^n_{ij}\Delta\mathbf{U}^n_{i+1,j} + \hat{E}^n_{ij}\Delta\mathbf{U}^n_{i-1,j} +$$

$$\hat{F}^n_{ij}\Delta\mathbf{U}^n_{i+1,j+1} + \hat{G}^n_{ij}\Delta\mathbf{U}^n_{i-1,j+1} + \hat{H}^n_{ij}\Delta\mathbf{U}^n_{i+1,j-1} + \hat{I}^n_{ij}\Delta\mathbf{U}^n_{i-1,j-1} = \hat{\mathbf{R}}^n_{ij}$$

Here $\hat{A}^n_{ij}, \cdots, \hat{I}^n_{ij}$ represent the Jacobian matrices obtained by linearizing the flux vectors and $\mathbf{R}^n_{ij}$ is the right-hand side. For the compressible Navier-Stokes equations in two dimensions, they are 4×4 matrices.

Solution of this system is a time consuming part of the algorithm, taking about 30% of the total time. The use of flux splitting for the non-linear terms makes the matrices diagonally dominant and allows use of iterative methods. Gauss-Seidel line relaxation in the streamwise direction reduces the block nona-diagonal matrix to a block tri-diagonal matrix. The block tri-diagonal matrix is solved by direct inversion. If a steady flow is being computed, it is not necessary to iterate the Gauss-Seidel line relaxation to convergence at each time step, but for time-accurate solutions, convergence to accuracy smaller than the truncation error is required. Direct inversion may become then prohibitively expensive. An alternative must be found. Dexun *et al.* (1989) suggested that using LU decomposition of abridged matrices, consisting of the main diagonals of the block tri-diagonal matrices, as a preconditioner and solving the block tri-diagonal matrices iteratively gives a significant improvement. It is convergent for moderate time steps, fully vectorizable, and gives a significant reduction in computing time. The full iterative scheme so obtained converges very rapidly. Dexun *et al.* (1989) only used two iterations for a steady state problem. Machine accuracy is obtained in two to four Gauss-Seidel sweeps. The inner iteration, used to invert the block tri-diagonal matrices within each Gauss-Seidel sweep, converges in about ten to fifteen iterations for the first sweep and one to four iterations for the following inner iterations. Residual correction and under- or over-relaxation were tried out and did not improve the convergence rate. If a steady state solution is required, solving the block tridiagonal matrices with a direct method allows a significantly larger time step.

Boundary Conditions

Outflow boundary conditions within the boundary layer present problems. The main trouble is in the subsonic region close to the wall. Setting the pressure in this region to the free-stream pressure does not work because it creates instabilities whenever the pressure becomes smaller than the free-stream pressure. The outflow boundary conditions adopted are zeroth order extrapolation, which performed well and had no noticeable upstream influence. For some applications, this condition is not suitable because it is reflective. The boundary conditions at the solid surface also require special attention. For an adiabatic wall, the conditions were zero velocity and heat flux at the wall, determination of the pressure from the equation of state, and use of the continuity and energy equations to close the system. For an isothermal wall, the temperature was fixed and only the continuity equation was used to close the system. The conditions are implemented using a half cell at the solid wall, as discussed in Vinokur (1989), and works very well. Conditions such as zero normal pressure gradient and/or zero density gradient are not valid at the wall in a viscous fluid and should not be used. In regions with nearly inviscid flow, characteristic boundary conditions are used which minimize reflections, for more detail see Giles (1988).

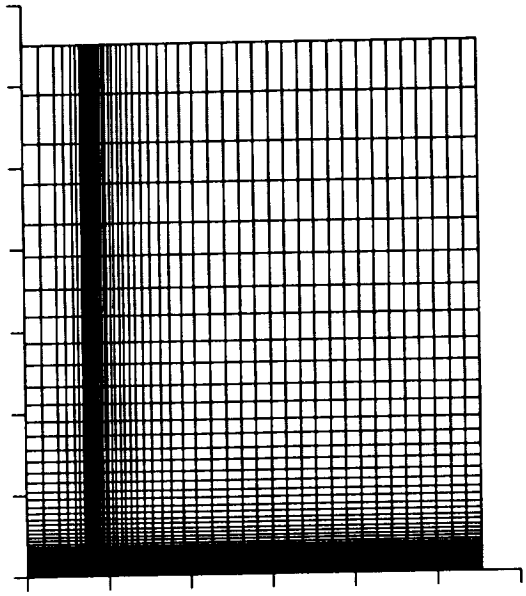

FIGURE 1. Grid for calculation of flow field above flat plate.

Boundary Layer on a Finite Flat Plate

Careful testing has been performed to investigate the accuracy of the numerical scheme. The first test case was the flow about an adiabatic flat plate at zero angle of incidence. Results were compared with the analytically derived results of Crocco (1941); see also Schlichting (1979). The Mach number was 2 and Prandtl number, 1. The viscosity law $\mu = T$ was used in order to enable comparison with the results of Crocco. All quantities are non-dimensionalized with their free-stream values and plate length. In order to test the ability of the model to compute shocks, the case of a finite plate in a uniform flow was considered and the results at the trailing edge were compared with Crocco. This removed the problem of choosing an inflow profile. Because the x- and y-derivatives are equally important at the nose of the plate, it is necessary to use small square grid cells in this region, see Fig. 1, while strong grid stretching is required in the boundary layer region further downstream. If the grid is stretched too much in one direction at the nose, the computations diverge. In Fig. 2 and 3, the Steger-Warming and MacCormack splittings on a 100×100 grid are compared with the results of Crocco. It is clear that the MacCormack splitting gives much better results; the Steger-Warming splitting is much too dissipative in the boundary layer. It must be remarked, however, that the Steger-Warming splitting does not perform as badly as claimed by MacCormack *et al.* (1989) for the Blasius boundary layer. The small deviations from the Crocco results must be attributed to the effects of the shock.

The second test case was the same flat plate but with an isothermal wall and Prandtl number .7. The general features of the flow field are presented in Fig. 4, which shows the density field at steady state. There is a large density jump at the

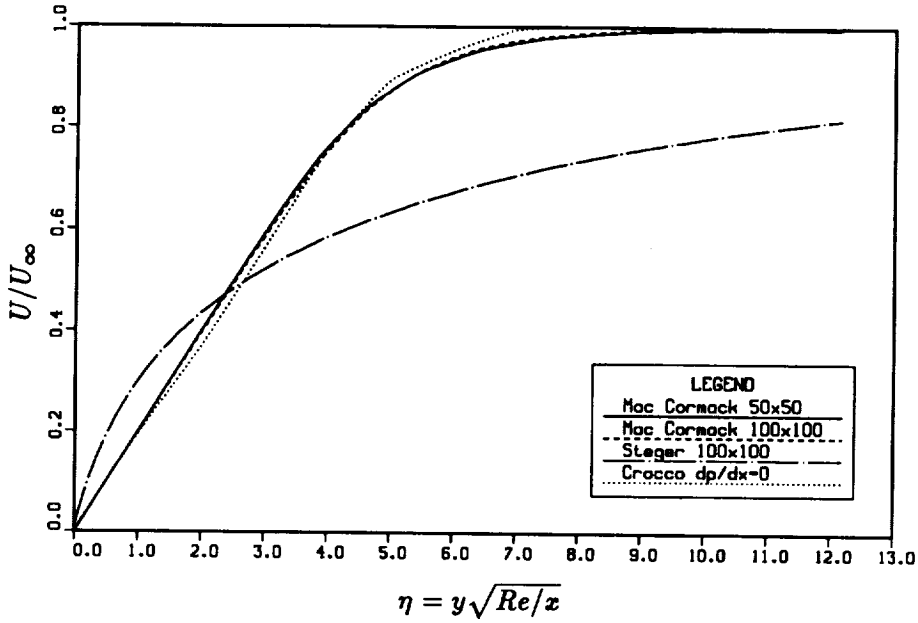

FIGURE 2. Velocity profile in flat plate boundary layer with adiabatic wall. Mach = 2, Pr=1, Re=530000.

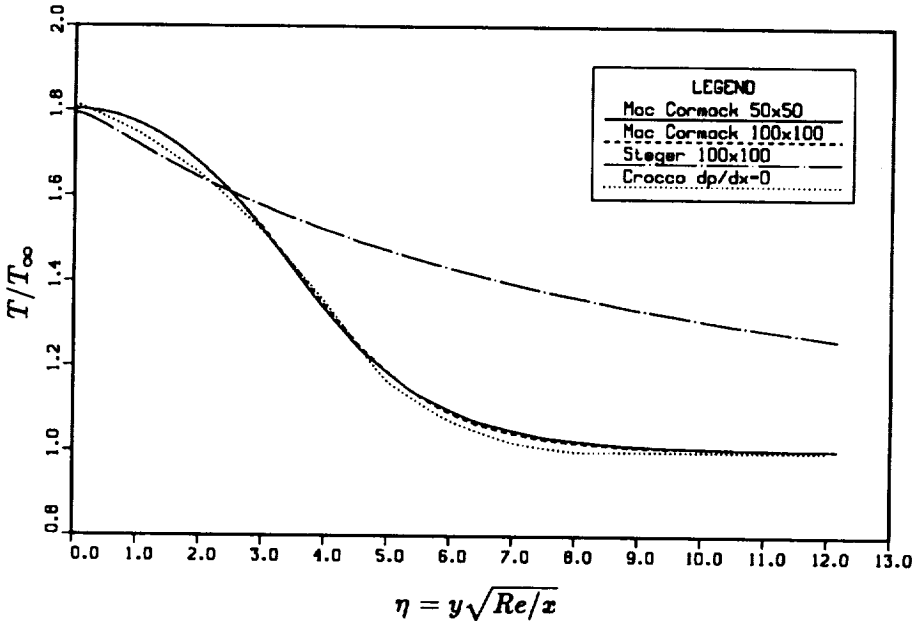

FIGURE 3. Temperature profile in flat plate boundary layer with adiabatic wall. Mach = 2, Pr=1, Re=530000.

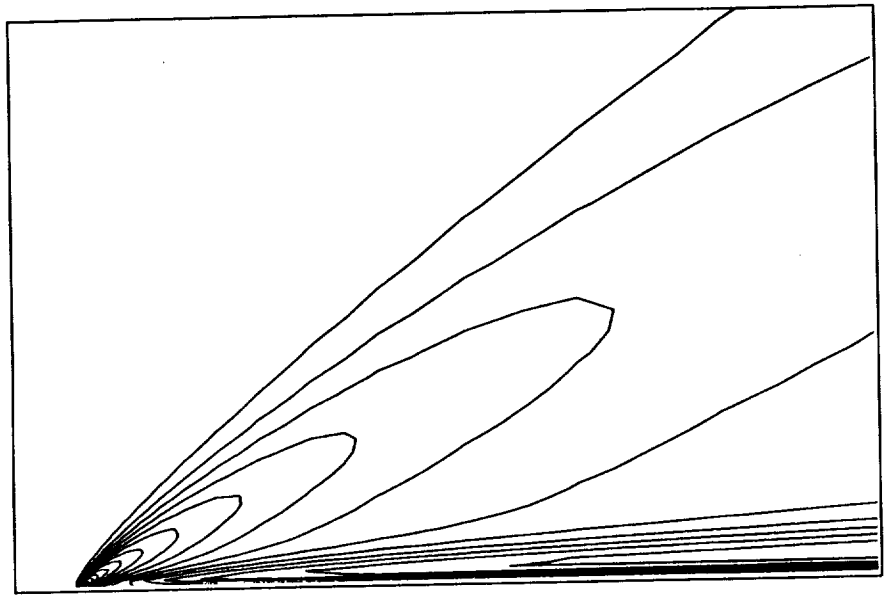

FIGURE 4. Density contours at nose of isothermal flat plate. Mach = 2, Pr=.7, Re=530000.

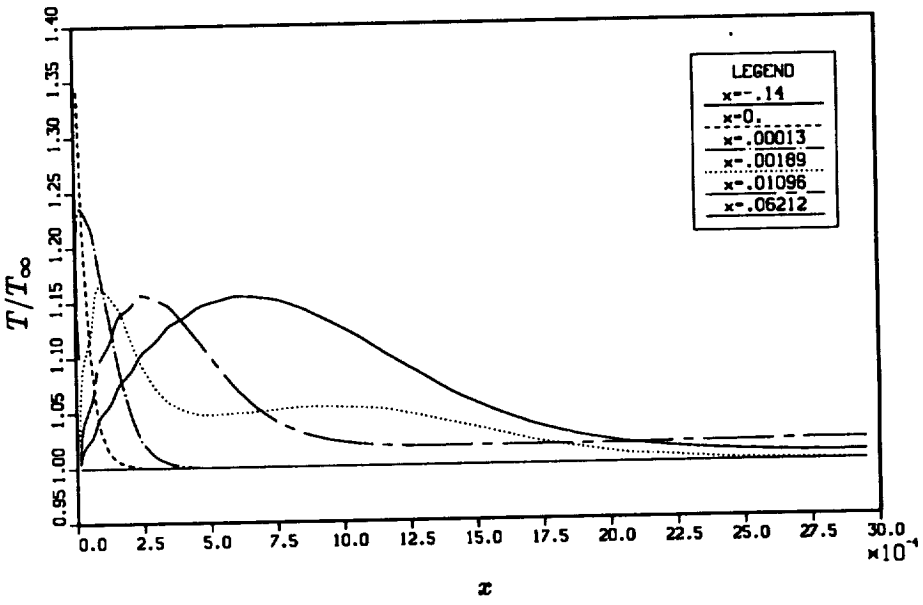

FIGURE 5. Temperature profile at nose of isothermal flat plate. Mach = 2, Pr=.7, Re=530000.

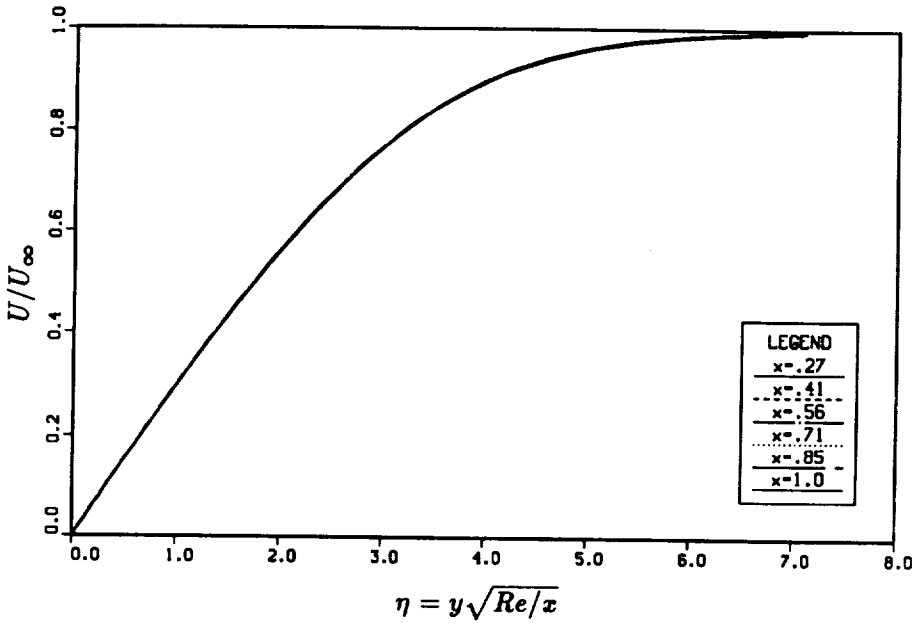

FIGURE 6. Velocity profile at different stations in flat plate boundary layer with isothermal wall. Mach = 2, Pr=.7, Re=530000.

nose of the plate, followed by expansion around the outer edge of the boundary layer; a weak shock originates from the nose of the plate. After the nose region, the flow relaxes to a boundary layer. Fig. 5 shows how fast the temperature profile relaxes from the nose to the boundary layer profile. The rapid change puts severe demands on the numerical scheme. In order to test the outflow boundary conditions and to see how well the similarity laws are satisfied, the velocity and temperature profiles at several downstream locations are plotted in Fig. 6 and 7. The plots show that the similarity law is very well satisfied, even at x=1, the last grid point on the plate, so there are no noticeable effects of outflow boundary conditions, even in the subsonic region. The results also compare well with those obtained by Hantzsche *et al.*; see also Schlichting (1979). Good agreement with the similarity profile was also obtained for the adiabatic flat plate at Mach=2.

The third test case is the flat plate with adiabatic wall, Mach number 5 and Prandtl number 1. This is a much more severe case due to the rapid changes at the nose of the plate. Fig. 8 and 9 show the velocity and temperature profiles at various downstream locations plotted against the similarity parameter η. The temperature rise is now as large as a factor of six in the boundary layer and much higher at the nose. The boundary layer is much thicker than in the Mach 2 cases due to heating. Another problem is the definition of the initial field. The computations for $M = 2$ were started from a uniform flow field, but at higher Mach numbers, the converged Mach 2 result was used as initial field.

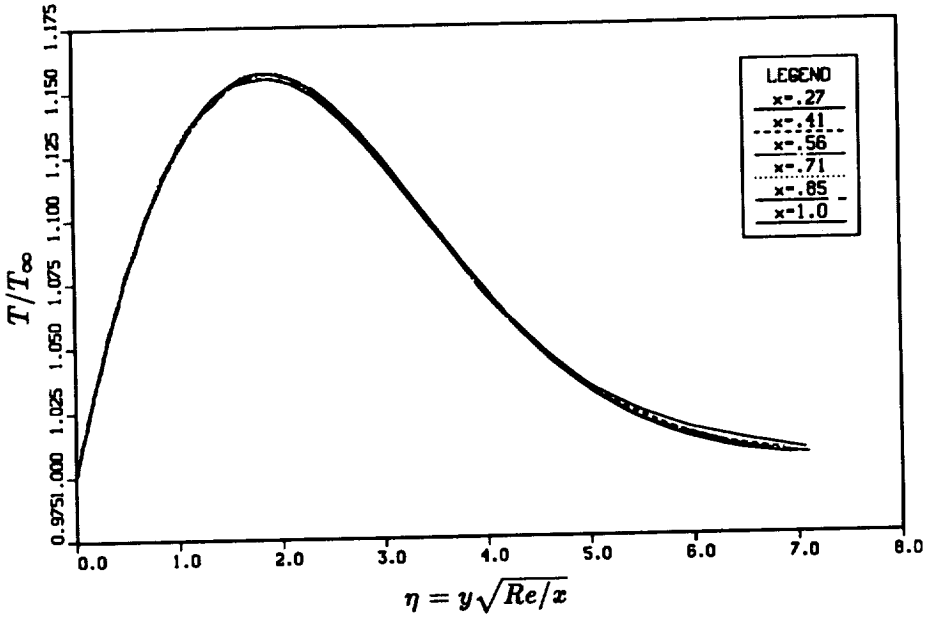

FIGURE 7. Temperature profile at different stations in flat plate boundary layer with isothermal wall. Mach = 2, Pr=.7, Re=530000.

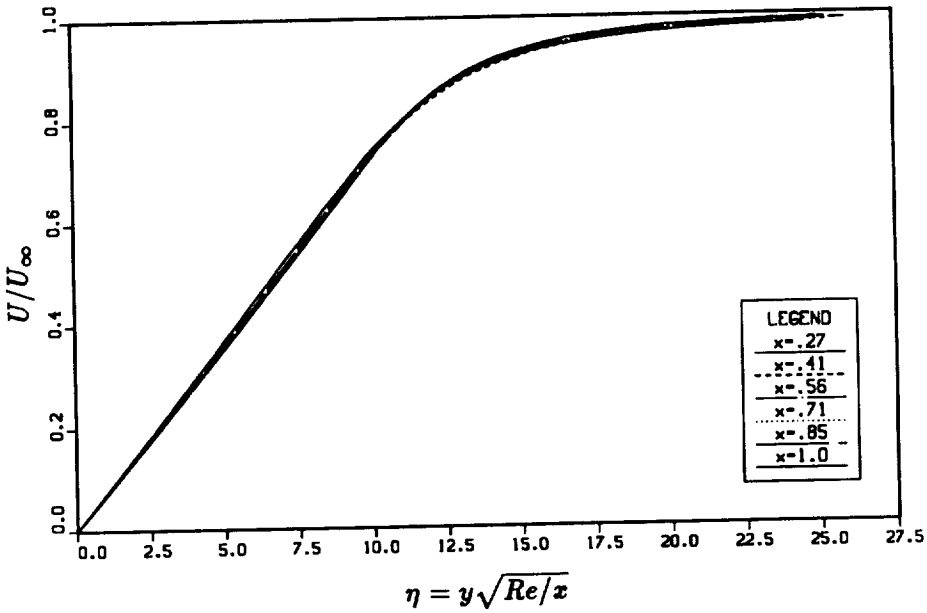

FIGURE 8. Velocity profile at different stations in flat plate boundary layer with adiabatic wall. Mach = 5, Pr=1, Re=530000.

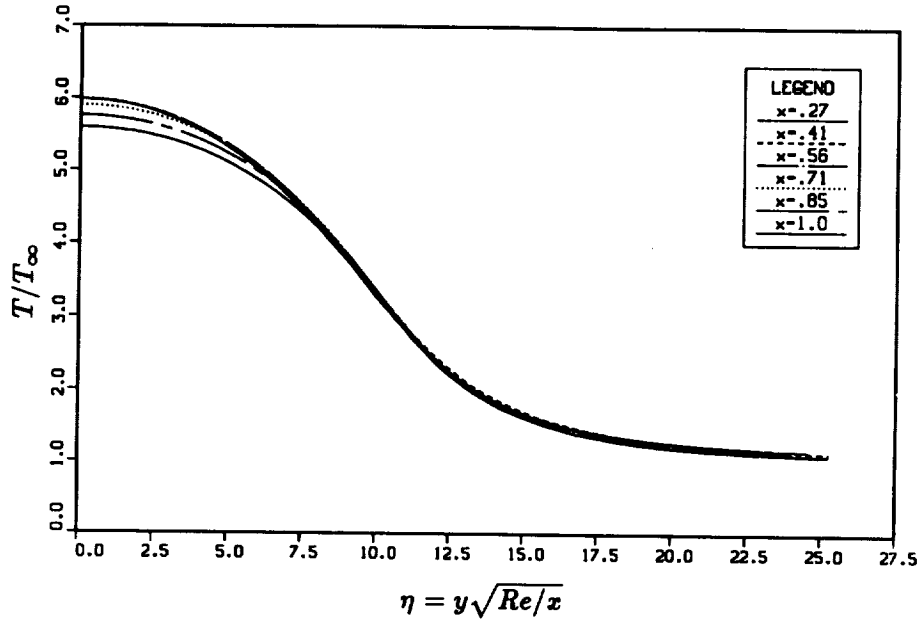

FIGURE 9. Temperature profile at different stations in flat plate boundary layer with adiabatic wall. Mach = 5, Pr=1, Re=530000.

Second Mode Instability in a Flat Plate Boundary Layer at Mach 4.5

Calculations are currently being done on the transition in a flat plate boundary boundary layer with an adiabatic wall at a Mach number 4.5. This case has been studied by Erlebacher and Hussaini (1990), (E&H), with a spectral code and is a severe test case of a finite-volume code because a spectral code is better suited to this problem. The stability calculations investigate the temporal stability of the second mode in the flat plate boundary layer. The existence of multiple unstable modes at high Mach numbers is a feature not found in low Mach number flows. For a review of compressible stability theory see Mack (1984). The appearance of multiple unstable modes starts at a Mach number of approximately 2.2. The purpose of the direct simulations is to study the effect of wall boundary conditions on flow stability. It turns out that the first mode is stabilized by wall cooling, which was discovered by Lees and Lin (1946), but the second mode is destabilized by wall cooling; for a detailed discussion see Mack (1984). Another motivation for studying the second mode is that two-dimensional waves are the most unstable second modes. The simulations are temporal, so the boundary layer is assumed to be parallel and periodic along the flat plate. The initial perturbations are of the form:

$$u'(x,y,t) = \hat{u}(y)e^{i(\alpha x - \omega_r t)+\omega_i t}$$

so ω_r is the frequency and ω_i is the growth rate. In order to prevent the boundary layer from growing, source terms are added to the right-hand side of the Navier-Stokes equations to cancel the terms which would create a non-zero vertical velocity

in the laminar flow. With this modification, the mean flow remains the constant mean flow used in the stability calculations, which generate the initial disturbances for the direct simulation. These disturbances are now added to the mean flow profile.

Linear stability calculations were made using the Cosal code of Malik (1982) for the case done by E&H. Identical results were obtained for the first mode, but for the second mode the results were slightly different. We used the parameters $M_\infty = 4.5$, $Re_{\delta^*} = 8000$, $\alpha = 2.25$, $Pr = .7$, and Sutherlands viscosity law. All parameters are non-dimensionalized using the displacement thickness δ^* and free stream values. The growth rate obtained from Cosal was: $\omega = 2.04706 + .02283i$, whereas E&H obtained $2.04674 + .02149i$, using a spectral code. Their Reynolds number was reported incorrectly as $Re_{\delta^*} = 10000$ instead of $Re_{\delta^*} = 8000$. It was decided to test the convergence of the eigenvalue computation with Cosal and use this result in the direct simulation. Table 1 shows the results of the growth rate for various numbers of grid points:

npoint	ω_r	ω_i
250	2.047045514267	.02294520289382
500	2.047060523908	.02285383626108
750	2.047063145850	.02283708143864
1000	2.047064045772	.02283124312681
1250	2.047064484897	.02282849820898
1500	2.047064741600	.02282702318168

Table 1. Convergence History of Eigenvalue Calculation for Flat Plate, $M_\infty = 4.5$, $Pr = .7$, $Re_{\delta^*} = 8000$.

This table shows that a large number of grid points is needed. This can be partly attributed to inefficiencies in the Cosal code, which is currently being improved, and to the steep gradients in the eigenfunctions; see Figures [10]-[13].

Using these as initial profiles pointed out several problems in direct simulations of transition. The two main problems are the boundary conditions far from the flat plate and providing enough resolution at the right places. At the top surface, non-reflecting characteristic boundary conditions based on inviscid flow are imposed. If reflecting boundary conditions are being used, as in E&H, the reflections influence the transition after some time. The problem with the non-reflecting boundary conditions is that they enforce zero mean vertical velocity, which is unphysical. The zero vertical velocity makes the top wall a characteristic surface for the mean flow and does not allow imposition of boundary conditions. Most theories for non-reflecting boundary conditions assume small disturbances around some mean value, but this becomes a singular case in our situation. The alternative, linearizing about the eigenfunctions, does not work either because this creates local inflow and outflow which change in time. These boundary conditions allow information to travel from infinity into the boundary layer, which is unphysical. It was finally decided to impose outflow everywhere on the top surface because this reflects most closely the

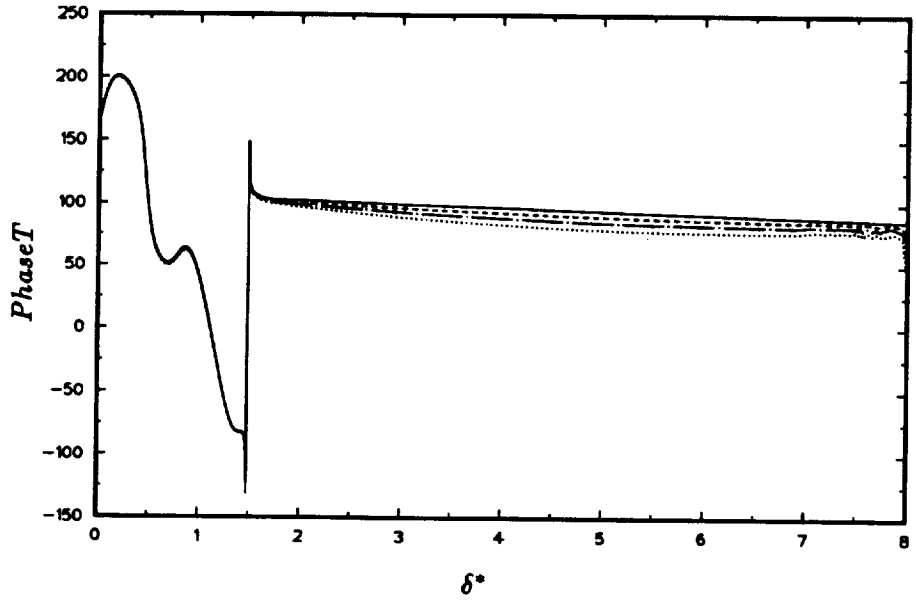

FIGURE 10. Phase of Temperature Disturbances in Flat Plate Boundary Layer. $M_\infty = 4.5$, $Pr = .7$, $Re_{\delta^*} = 8000$.

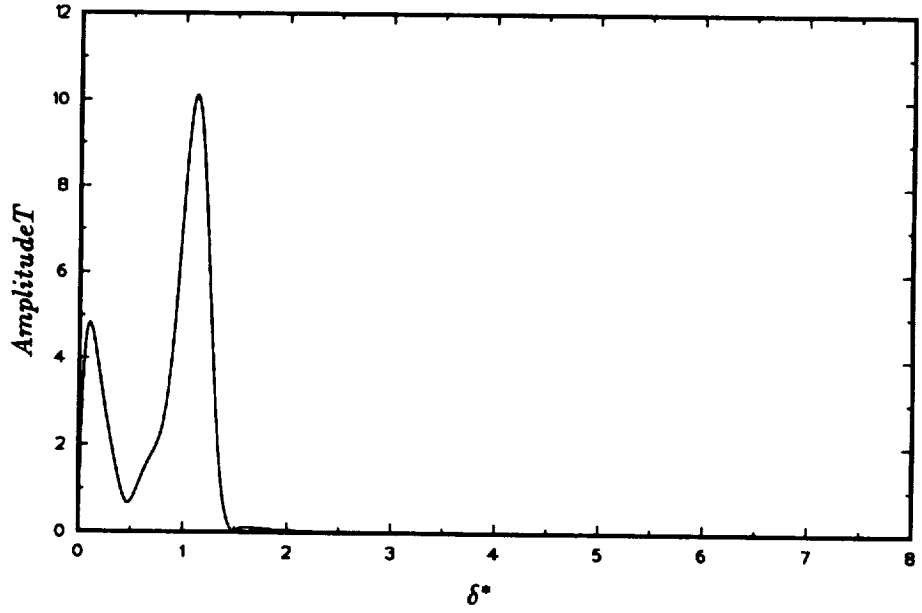

FIGURE 11. Amplitude of Temperature Disturbances in Flat Plate Boundary Layer. $M_\infty = 4.5$, $Pr = .7$, $Re_{\delta^*} = 8000$.

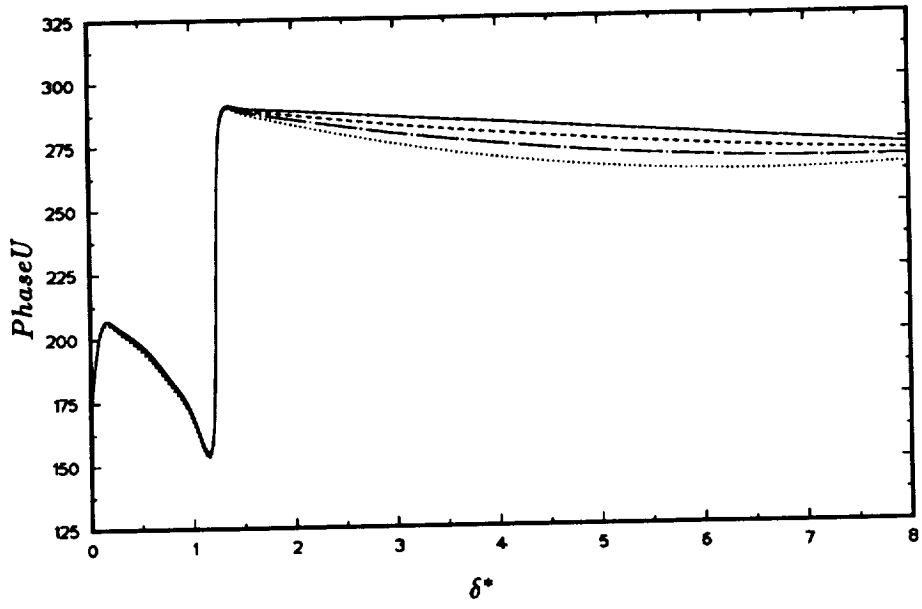

FIGURE 12. Phase of Velocity Disturbances in Flat Plate Boundary Layer. $M_\infty = 4.5$, $Pr = .7$, $Re_{\delta^*} = 8000$.

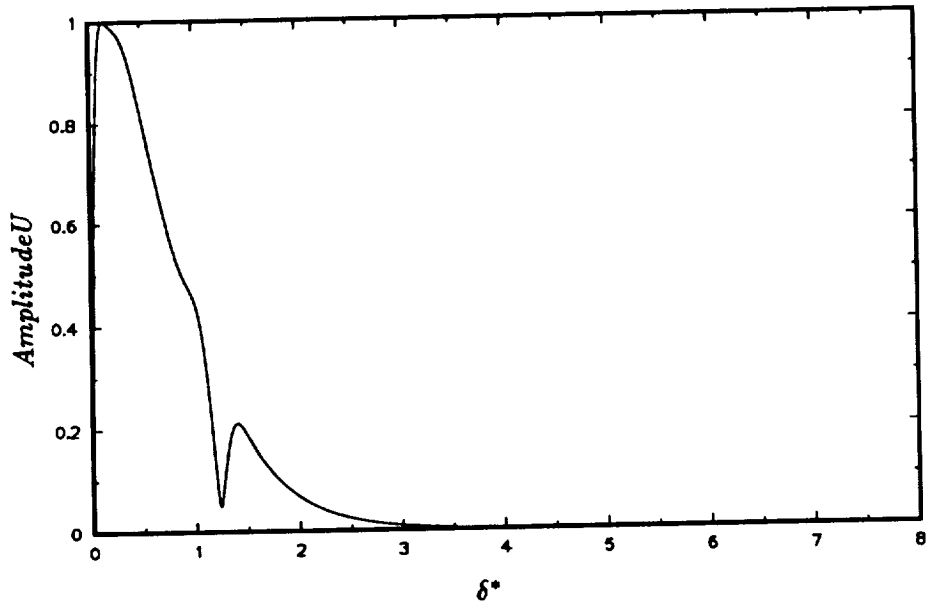

FIGURE 13. Amplitude of Velocity Disturbances in Flat Plate Boundary Layer. $M_\infty = 4.5$, $Pr = .7$, $Re_{\delta^*} = 8000$.

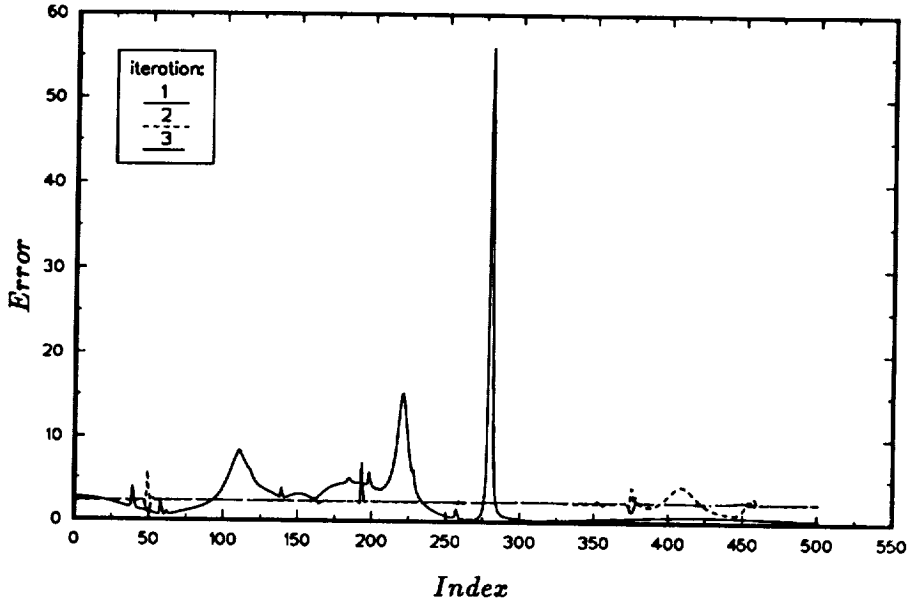

FIGURE 14. Local Error in Flat Plate Calculations at Different Grid Points. $M_\infty = 4.5$, $Pr = .7$, $Re_{\delta^*} = 8000$.

physical processes. This removed oscillations between the critical layer and the top wall, although some small oscillations are still visible in the temperature phase angle at the top wall, Fig. [10].

Figures [10] to [13] show the amplitudes and phases of the disturbances of temperature and velocity at several time steps. The initial disturbances are the eigenfunctions obtained from the linear stability code, with amplitude 2% of the free steam velocity. The number of grid points for this calculation was 128x500, with grid stretching outside the boundary layer. The results do not show strong numerical oscillations. The phase angle shows that the flow field is changing, although not clearly visible, the amplitudes also grow.

Unfortunately, problems remain. One is that it takes a long time for the disturbances to start growing. This can be attributed to small numerical errors in the eigenfunctions obtained from the linear stability code; they slightly differ from the eigenfunctions of the most unstable mode. Lack of resolution in some parts of the flow field also contributes to a slower growth through numerical diffusion. In order to improve the accuracy, it was decided to implement an adaptive grid method. For a general review of these methods, see Thompson (1985). The adaptive grid scheme tries to generate a grid which has a uniform error in computational space; the control parameters are the gradient and radius of curvature. Figure [14] shows that three iterations greatly reduce the error and make it more uniform. The original grid did not have enough points, especially in the temperature critical layer, which becomes clear comparing the original grid and the modified one in Figure [15]. For transition calculations, this region is dominant because the temperature

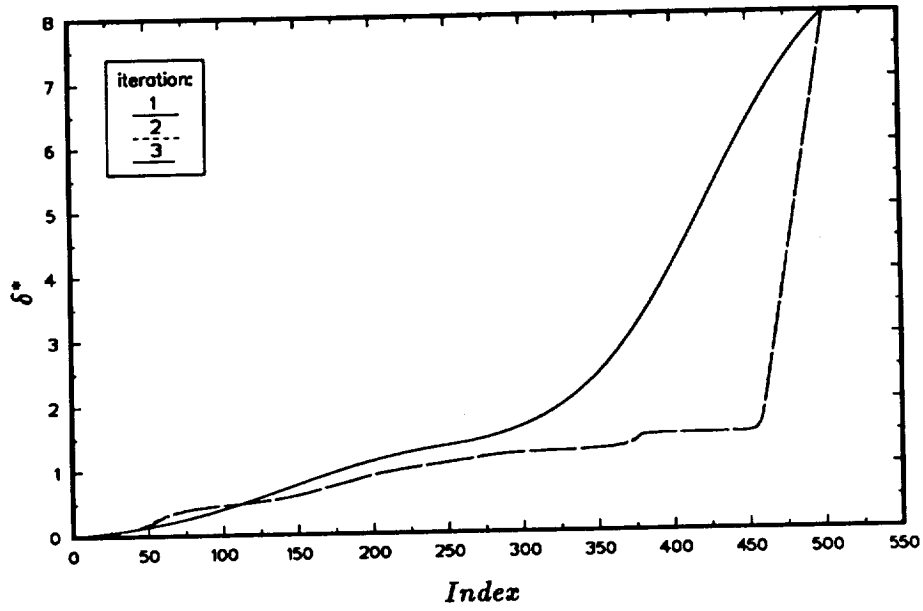

FIGURE 15. Grid for Flat Plate Calculations. $M_\infty = 4.5$, $Pr = .7$, $Re_{\delta^*} = 8000$.

fluctuations are the largest in the flow field. The simulations are currently being repeated using the adaptive grid scheme. Improvements in the linear stability code are also being pursued.

3. Work to be done

- Continue simulations of temporal stability of second mode for a flat plate with different temperature boundary conditions.
- Improvement of non-reflecting boundary conditions to be able to study spatial stability on a flat plate and a wedge.
- Continue activities to transform code to solve three-dimensional flows.
- Study of stability of a shock layer perturbed by sound waves.

Acknowledgement

Thanks are due to Dr. G. Erlebacher for providing the linear stability code.

REFERENCES

BEAM, R. M. & WARMING, R. F. 1978 An Implicit Factored Scheme for the Compressible Navier-Stokes Equations. *AIAA Journal.* **16**, No 4, 393-402.

CROCCO, L. 1941 Sullo Strato Limite Laminare Nei Gas Lungo Una Lamina Piana, Rendiconti di Matematica delle sue Applicazioni, University Rome, 139-152.

DEXUN, F. & YANWEN, M. 1989 On Efficiency and Accuracy of Numerical Methods for Solving Aerodynamic Equations, Symposium Tokyo.

ERLEBACHER, G. & HUSSAINI, M. Y. 1990 Numerical Experiments in Supersonic Boundary-Layer Stability. *Physics of Fluids.* **A2**, 94-104.

GILES, M. 1988 Non-Reflecting Boundary Conditions for the Euler Equations. *Report MIT CFDL-TR-88-1.*

HANTZSCHE, W. & WENDT, H. 1940 Zum Kompressibilitätseinfluss bei der Laminaren Grenzschicht der Ebenen Platte. *Jahrbuch Deutsche Luftfahrtforschung.* **I**, 517-521.

LEES, L. & LIN, C. C. 1946 Investigation of the Stability of the Laminar Boundary-Layer in a Compressible Fluid. *NACA Technical Note 1115.*

MACCORMACK, R. W. & CANDLER, G. V. 1989 The Solution of the Navier-Stokes Equations using Gauss-Seidel Line Relaxation. *Computers and Fluids.* **17**, 135-150.

MACK, L. M. 1984 Special Course on Stability and Transition of Laminar Flow. *AGARD Report 709.*

MALIK, M. R. 1982 Finite-Difference Solution of the Compressible Stability Eigenvalue Problem. *Nasa Contracter Report NAS1-16572.*

SCHLICHTING, H. 1979 Boundary Layer Theory, Mc Graw-Hill.

STEGER, J. L. & WARMING, R. F. 1981 Flux-Vector Splitting of the Inviscid Gasdynamic Equations with Application to Finite- Difference Methods. *Journal of Computational Physics.* **40**, 263-293.

THOMPSON, J. T., WARSI, Z. U. A. & MASTIN, C. W. Numerical Grid Generation 1985 North-Holland.

VAN DER VEGT, J. J. W. 1991 Assessment of Flux Vector Splitting for Viscous Compressible Flows. *AIAA Paper 91-0243.* 29th Aerospace Sciences Meeting and Exhibit, Reno, Nevada.

VINOKUR, M. 1989 An Analysis of Finite-Difference and Finite-Volume Formulations of Conservation Laws. *Journal of Computational Physics.* **81**, 1-52.

Effect of heat release on the stability of compressible reacting mixing layer

By D. S. Shin AND J. H. Ferziger

1. Motivation and objectives

Reacting free shear layers are of fundamental importance in many industrial systems including gas turbine combustors and rockets. Efficient propulsion systems are essential for air breathing supersonic ramjets in the high Mach number range. A limiting factor in these engines is the time for fuel and oxidizer to mix in the combustion chamber; for fast mixing, the flow must be vigorously turbulent which requires the laminar flow to be unstable. Understanding the stability characteristics of compressible reacting free shear layers is, therefore, very important and may allow one to control the flow. Low speed shear layers are highly unstable but, as chemical reaction (Shin & Ferziger 1990) and compressibility effects (Brown & Roshko 1974; Papamoschou & Roshko 1988) tend to stabilize them, it is important to investigate the stability of high speed reacting mixing layers. The latter consists of two fluid streams containing fuel and oxidizer respectively, and the conclusions are expected to apply, with quantitative modifications, to other shear flows, e.g., jets. Since low speed reacting cases have been studied earlier (Shin & Ferziger 1990), we concentrate on the effects of Mach number and heat release.

We are primarily interested in solving the stability problem over a large range of Mach number and heat release. In order to understand the effect of the heat release on the stability of this flow, one must first study the characteristics of the non-reacting flow. Inviscid theory is a reliable guide for understanding stability of compressible shear flows at moderate and large Reynolds numbers and is the basis for this work.

2. Accomplishments

2.1 Laminar flow profiles

Since in our previous report (Shin & Ferziger 1990) we have shown the importance of using correct laminar profiles rather than assumed analytical ones, we began by computing such profiles. To generate mean profiles, we solved the (parabolic) compressible boundary-layer equations. Uniform pressure across the shear layer and unity Lewis and Prandtl numbers are assumed for simplicity. Prandtl number 0.7 does not produce large quantitative differences. We considered only the case in which the ratio of the speed of the slow stream to that of the fast stream is 0.5 to reduce the parameter range. The static temperature is initially uniform, and the mass fractions of free streams are specified. The inlet profiles are taken from self-similar solutions of the equations without heat release; their effect diminishes downstream.

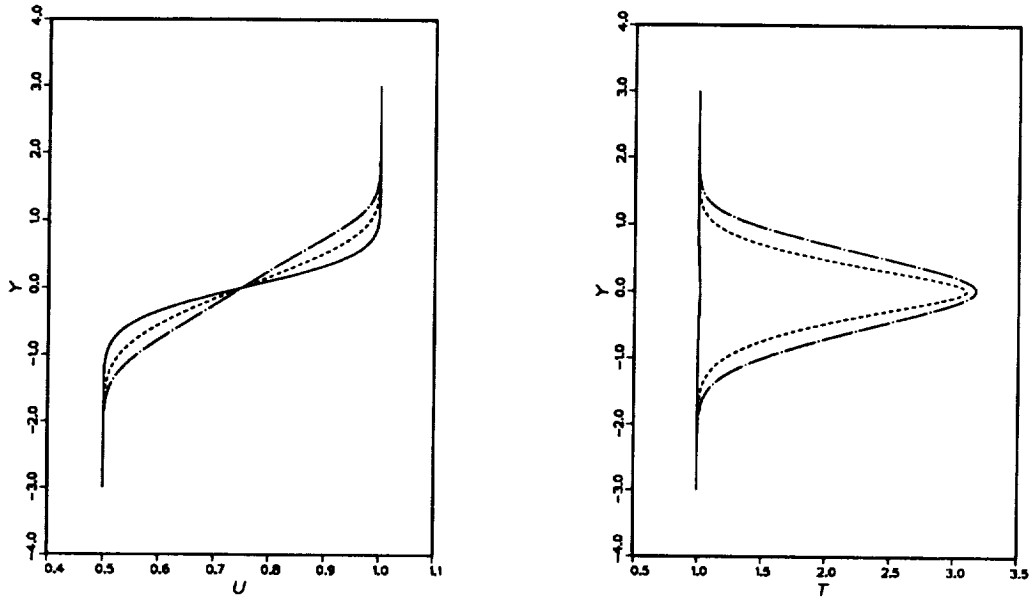

FIGURE 1. Effect of heat release and variable transport properties of the spatially developing layer at M_c=0.25 on the (a) velocity (b) temperature profiles. ——— , T_{ad}=1; - - - - , T_{ad}=7 (constant property); —·— , T_{ad}=7 (variable property).

Variable transport properties and chemical reaction, which were shown to be important in low-speed flow, are included. For the transport properties, power laws in temperature and pressure are assumed:

$$\mu \propto P^0 T^{0.7}\,; \quad \kappa \propto P^0 T^{0.7}\,; \quad D \propto P^1 T^{1.7} \tag{1}$$

where μ is the viscosity, κ, the thermal diffusivity, and D, the mass diffusivity. Chemistry is treated by a single step irreversible scheme involving fuel and oxidizer reacting to yield product.

To satisfy the boundary-layer approximation, we used an initial Reynolds number of 1000 based on the initial vorticity thickness and cold viscosity. To include the coupling among the chemical reaction, heat release, and the velocity field, the conservation equations for the mass, energy, and species equations are solved simultaneously with the equation of state. As the compressible boundary-layer equations are parabolic, an implicit method (Crank-Nicolson) is used. Figure 1 compares the streamwise velocity and temperature profiles of spatial layers with the same inlet profiles and shows the effects of heat release and variable properties for a case with upper-stream Mach number M_1=1 and convective Mach number M_c=0.25. The non-dimensional adiabatic flame temperature T_{ad} is 7 for the reacting cases. These profiles are compared at a streamwise distance x normalized by the initial vorticity thickness of 57 downstream of the ignition point. The significant difference between the constant and variable property solutions indicates that property variations need

to be included whenever there are large temperature variations. Note that these flows have significantly different Reynolds numbers.

2.2 Inviscid linear stability equation

We assume that the laminar flow is parallel and subjected to small disturbances in the form of travelling waves. Each dimensionless quantity can be expressed as

$$F(x,y,z,t) = \overline{F}(y) + \hat{F}(y)e^{i(\alpha x+\beta z-\omega t)} \tag{2}$$

where $\overline{F}(y)$ is the laminar flow quantity, $\hat{F}(y)$ is eigenfunction depending only on the y coordinate, α, β are wavenumbers in the streamwise and spanwise directions respectively, and ω is the frequency. The relation between the wavenumbers and the angle of disturbance is

$$\tan\theta = \beta/\alpha. \tag{3}$$

For the temporal stability analysis, α is real and ω is complex, while for the spatial analysis, ω is real and α is complex. The corresponding amplification rates are ω_i and $-\alpha_i$. The perturbation equations are derived by linearizing the full compressible equations. Substituting (2) into these equations and neglecting the products of disturbances yields the disturbance equation for the pressure.

$$\hat{p}'' - \left\{\frac{2\alpha U'}{(\alpha U-\omega)} + \frac{R}{T}(\alpha U-\omega)^2[RXN1]\right\}\hat{p}' - q\hat{p} = 0$$

$$q = (\alpha^2+\beta^2) - \gamma {M_1}^2(\alpha U-\omega)^2\left\{\frac{1}{T} + \frac{R}{T}[RXN2]\right\} \tag{4}$$

where U, R and T are the laminar velocity, density and temperature respectively, and a prime denotes differentiation with respect to y. γ is the specific heat ratio and M_1 is the Mach number of the upper stream. $[RXN1]$ and $[RXN2]$ are terms which represent the effect of chemical reaction and associated heat release on the instability. The boundary conditions are obtained by considering the asymptotic form of the solutions of Equation (4). As $y \to \pm\infty$, U' and $[RXN1]$ become negligible and the solutions must behave like:

$$\hat{p}(y \to -\infty) = C_1 \exp(\sqrt{q}y)$$

$$\hat{p}(y \to \infty) = C_2 \exp(-\sqrt{q}y) \tag{5}$$

where C_1, C_2 are arbitrary constants, chosen as unity. An iterative method based on the shooting and Newton-Raphson methods are used to solve Equation (4). First, a guess of the eigenvalue is made. For a spatial analysis, ω is specified and α is guessed, whereas for temporal analysis, α is specified and ω guessed. Given the eigenvalue, we compute $\hat{p}$ for large y from Equation (5). Then we integrate Equation (4) from both free streams toward the centerline of the mixing layer, at y=0. At the centerline, the values of $\hat{p}$ and $\hat{p}'$ computed by integrating from the upper-stream, $\hat{p}_+(0)$ and $\hat{p}'_+(0)$, are compared with the values computed by integrating from the

lower-stream, $\hat{p}_-(0)$ and $\hat{p}'_-(0)$. If they match, the process has converged; if not, a new eigenvalue is chosen, and iteration continues until the eigenvalue converges to the specified tolerance. The integrations were carried out using subroutine ODE, and the update of the eigenvalue is based on the Newton-Raphson method. An error control of 10^{-6} was used for the integration, and iteration continued until the eigenvalue changed less than 10^{-7}. This method is applicable to both the temporal and spatial problems.

2.3 Multiple modes of instability

For compressible mixing layers, an inviscid neutral solution has a critical layer at a generalized inflection point where $(U'/T)'=0$. This is the necessary condition for neutral instability and is a generalization of the condition for low Mach number reacting flow (Shin & Ferziger 1990). We find that non-reacting incompressible flow has a single inflection point, whereas reacting or highly compressible flows have three.

We calculated the growth rates of the unstable modes. Figure 2 gives the maximum with respect to wavenumber of the amplification rate of two-dimensional modes as a function of the convective Mach number for $T_{ad}=1$ and 4 in the temporal layer. First consider the unheated flow ($T_{ad}=1$). As has been demonstrated by Groppengiesser (1970) and others (Blumen *et al.* 1975; Sandham & Reynolds 1989), the growth rate of the center mode decreases dramatically as the Mach number increases. In the highly supersonic regime, the growth rate is miniscule compared to its incompressible value. At supersonic speeds, a second set of modes, which we shall call the outer modes, become unstable. The growth rates of these modes are relatively insensitive to Mach number and are much larger than the growth rate of the center mode. They increase slightly in the very high Mach number regime. However, the growth rates are small compared to the growth rate of the center mode at low speeds. The outer modes should be the predominant instabilities at supersonic Mach numbers.

Next, consider the reacting flow ($T_{ad}=4$). As shown by Shin & Ferziger (1990) and others (Mahalingam *et al.* 1989), the low density created by reaction in the center of the shear layer reduces the growth rate of the center mode. Figure 2 shows that the growth rate of this mode is further reduced as the Mach number increases and is always smaller than the corresponding cold flow mode growth rate. As shown by Shin & Ferziger (1990), when T_{ad} is large enough, a set of outer modes arises in the reacting flow at low Mach numbers. For the case shown here, ($T_{ad}=4$), the outer modes are slightly less unstable than the center mode at $M_c=0$; this situation reverses at higher heat release. The growth rate of the outer modes falls off much more slowly with increasing Mach number, and for the heat release used here, they are the dominant modes for $M_c > 0.5$. At $M_c > 1$, there is a single pair of outer modes of the heated flow; they can be regarded as the extension of either the unheated supersonic flow or low-speed reacting flow reacting modes. Perhaps the most significant point to note is that the growth rate of the outer mode in the reacting supersonic flow is approximately twice that of the corresponding non-reacting flow. Thus, in contrast to the low speed case, heat release due to chemical

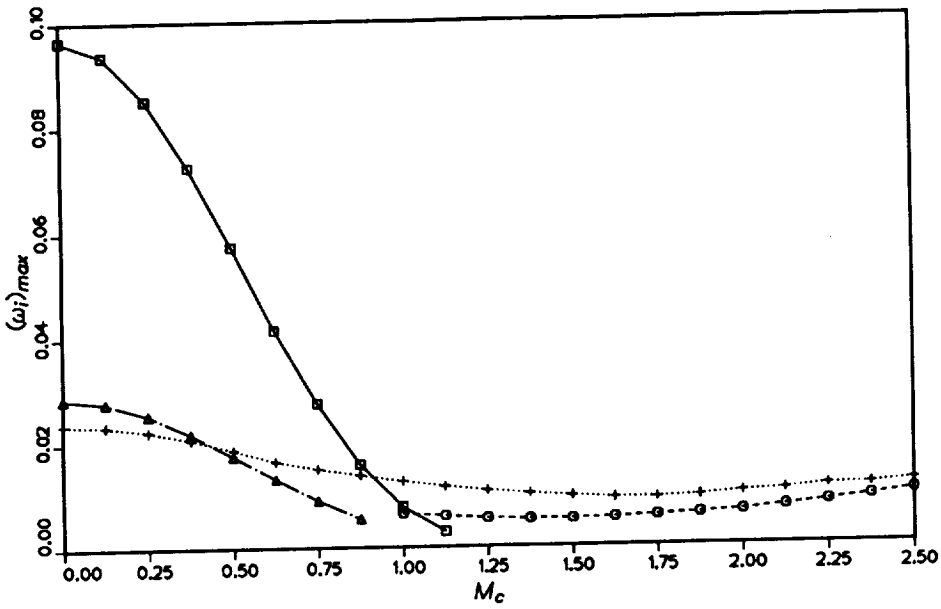

FIGURE 2. Maximum growth rate versus convective Mach number. □ , T_{ad}=1 (center mode); ○ , T_{ad}=1 (outer mode); △ , T_{ad}=4 (center mode); +, T_{ad}=4 (outer mode).

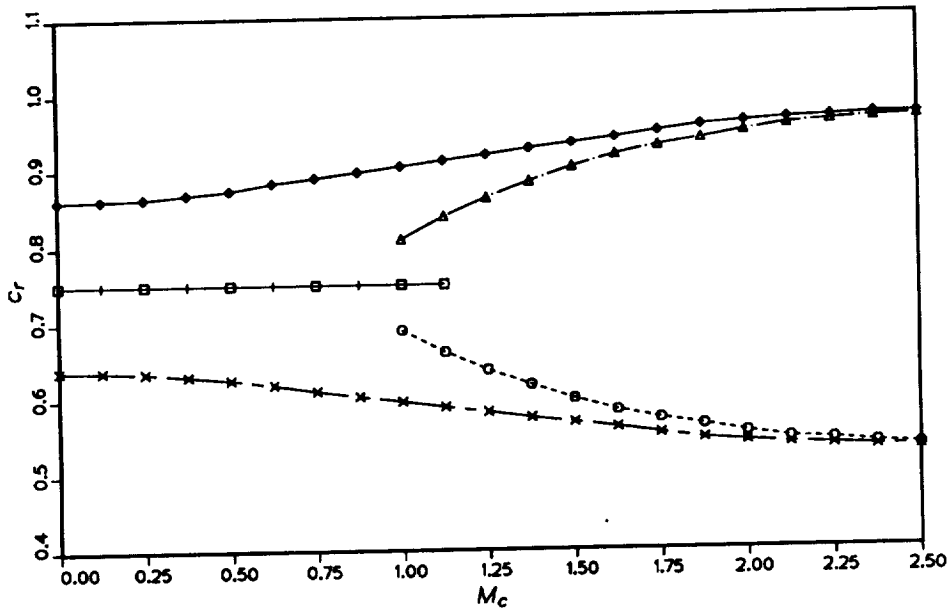

FIGURE 3. Phase speed corresponding Maximum growth rate versus convective Mach number. □ , T_{ad}=1 (center mode); ○ , T_{ad}=1 (slow mode); △ , T_{ad}=1 (fast mode); +, T_{ad}=4 (center mode); ×, T_{ad}=4 (slow mode); ◇ , T_{ad}=4 (fast mode).

reaction is destabilizing in supersonic flow. At higher heat release, these effects would be even larger. Again, the growth rates of the outer modes increase with increasing Mach number in the high Mach number regime.

Figure 3 gives the corresponding phase speeds. The center mode always travels at the average speed of two streams, whereas the fast mode travels faster than the average speed and the slow mode, slower. The phase speeds of the outer modes approach the free stream velocities as the Mach number increases. Increasing the adiabatic flame temperature raises the speed of the fast mode and reduces the speed of the slow mode in the outer modes at any Mach number. At very high Mach number, the speed of the outer modes becomes independent of the heat release.

We now study these modes in more detail. Figures 4-5 show the amplification rates and phase velocities as functions of wavenumber for convective Mach number 0.5 and 1.25, respectively. The corresponding upper-stream Mach numbers are 2 and 5 respectively. For M_c=0.5 and no reaction, only the center mode is unstable. As Mach number or heat release increases, the outer modes become unstable. The maximum growth rate of the outer modes at M_c=1.25 without reaction are only about one-tenth the maximum growth rate of the center mode at M_c=0.5 and T_{ad}=1; the wavenumber corresponding to maximum growth is half that at M_c=0.5. The T_{ad}=4, M_c=0.5 case has three distinct unstable modes, the center, fast, and slow modes. The amplification rate for this case has two maxima, one at α=0.15 due to the center mode and the other at α=0.58 due to the outer modes. The maximum growth rates of the two sets of modes are almost equal, but the other peak is much broader. The maximum growth rate is about one-third of the maximum for the corresponding case with zero heat release. Thus, heat release stabilizes the flow at M_c=0.5 and causes outer modes to appear. At M_c=1.25 and T_{ad}=4, as in the corresponding non-reacting flow, only the outer modes are unstable. The wavenumber is almost twice the non-reacting value, so heat release decreases the wavelength of maximum growth rate. The maximum growth rate is twice that of the T_{ad}=1 case, a trend opposite that found in the M_c=0.5 case.

Due to the symmetry of the mean profiles, the amplification rates of the two outer modes are the same, but the phase velocities are different. The phase velocity of the fast mode, which ranges from 0.8 to 0.9 at M_c=1.25 and T_{ad}=1, approaches the speed of upper stream as wavenumber increases, while that of slow mode approaches the speed of lower stream. At M_c=0.5 and T_{ad}=4, the phase speeds lie in the range of 0.75 to 0.92 for fast mode and 0.58 to 0.75 for slow mode. As the Mach number increases (M_c=1.25), the phase speed of the fast mode lies in the range of 0.81 to 0.95 and that of the slow mode in the range of 0.55 to 0.69.

2.4 Effect of heat release, variable properties, and reaction

In Section 2.1, we showed that heat release due to chemical reaction and the variation of properties through the reacting shear layer influence the mean flow profiles significantly. In this section, we study the effect of heat release, chemical reaction, and property variation on the stability of spatial layers. In the spatial case, the growth rates of the two outer modes are not equal. Figure 6 shows the effect of heat release on the maximum growth rate. At M_c=0.25 (M_1=1), as the

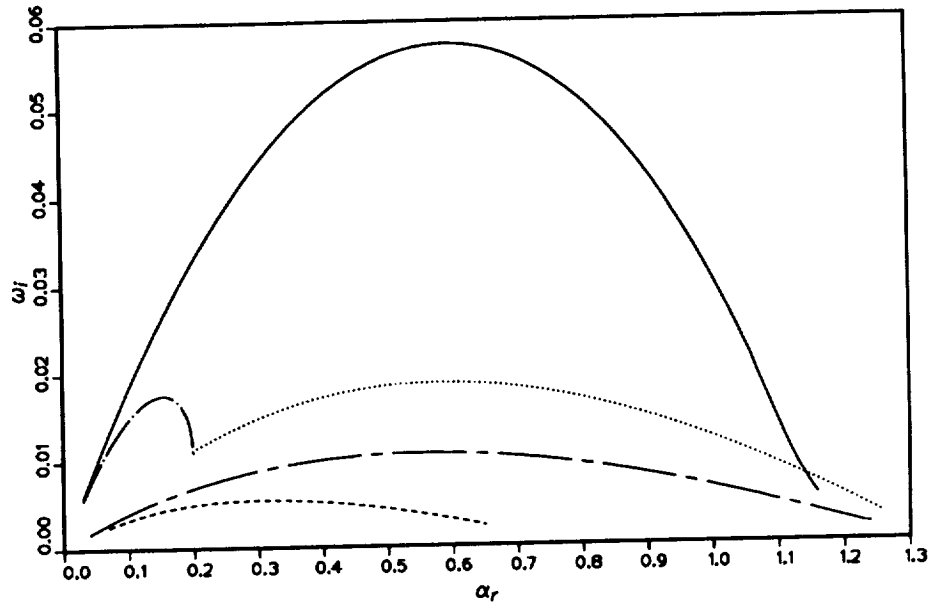

FIGURE 4. Growth rate versus wavenumber. ——— , T_{ad}=1 (M_c=0.5, center mode); - - - - , T_{ad}=1 (M_c=1.25, outer mode); —·— , T_{ad}=4 (M_c=0.5, center mode); ····· , T_{ad}=4 (M_c=0.5, outer mode); —·—·— , T_{ad}=4 (M_c=1.25, outer mode).

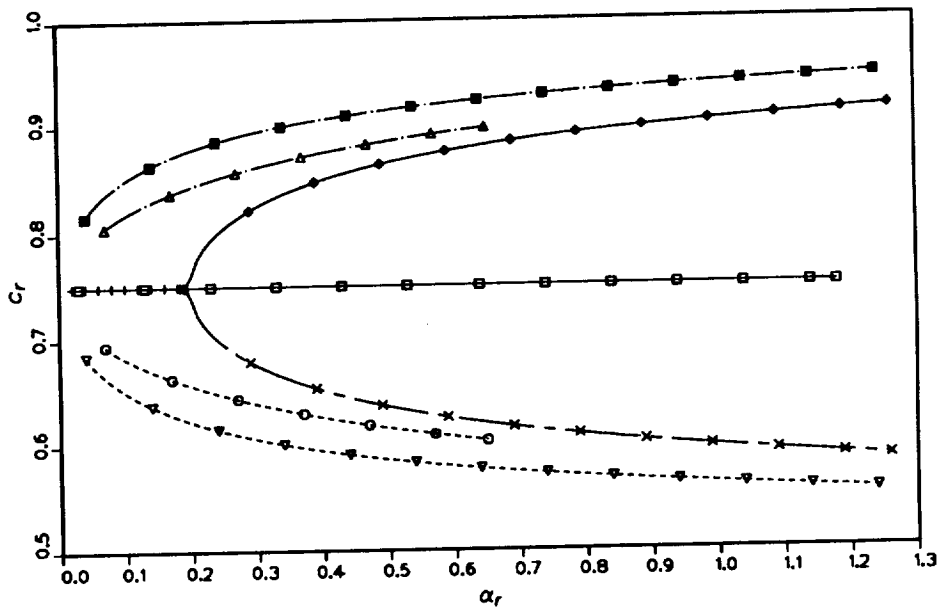

FIGURE 5. Phase speed versus wavenumber. □ , T_{ad}=1 (M_c=0.5, center mode); ○ , T_{ad}=1 (M_c=1.25, slow mode); △ , T_{ad}=1 (M_c=1.25, fast mode); +, T_{ad}=4 (M_c=0.5, center mode); ×, T_{ad}=4 (M_c=0.5, slow mode); ◇ , T_{ad}=4 (M_c=0.5, fast mode); ▽ , T_{ad}=4 (M_c=1.25, slow mode); ⊠ , T_{ad}=4 (M_c=1.25, fast mode).

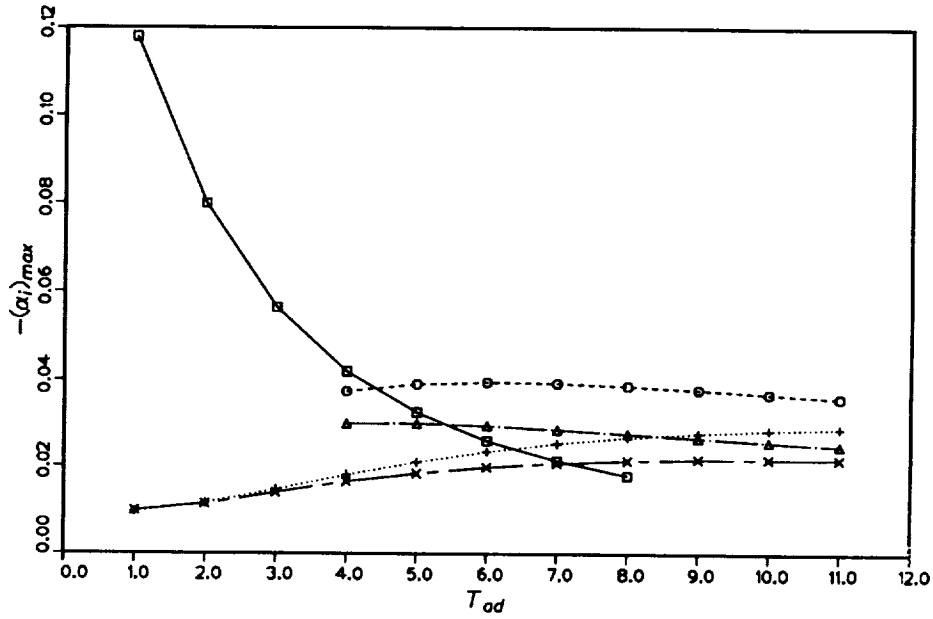

FIGURE 6. Maximum growth rate versus adiabatic flame temperature. □, M_c=0.25 (center mode); ○, M_c=0.25 (slow mode); △, M_c=0.25 (fast mode); +, M_c=1.25 (slow mode); ×, M_c=1.25 (fast mode).

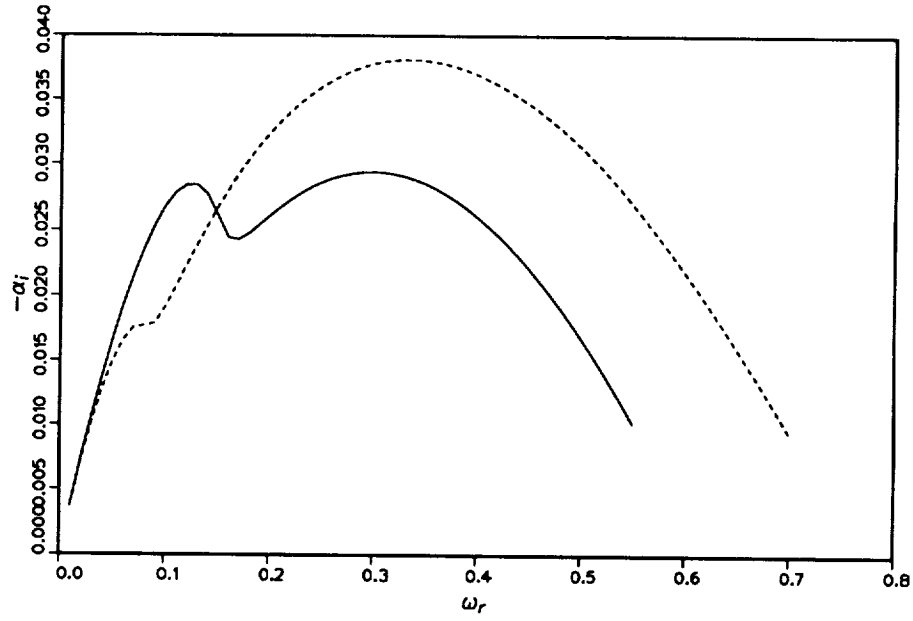

FIGURE 7. Effect of variation of properties on the growth rate at T_{ad}=8, M_c=0.25. ——, constant property; - - - -, variable property.

heat release increases, the maximum amplification rate of the center mode decreases rapidly. The maximum amplification rate in the cold flow is 0.118, while for T_{ad}=8 it is 0.018, or 15% the cold flow value. The amplification rates of the outer modes change very little as the heat release increases. The slow mode is more amplified than the fast mode. Consequently, at high heat release, the outer modes have larger amplification rates than the center mode, and the slow mode should dominate. For T_{ad}=8, the outer modes have almost twice the amplification rate of the center mode. Flows with high heat release should be unstable to the slow mode, but heat release stabilizes the flow at M_c=0.25 (M_1=1).

At M_c=1.25 (M_1=5), only the outer modes are unstable. As the heat release increases, the maximum growth rates increase. The maximum growth rate of slow mode for the non-reacting flow is 0.0095, while for T_{ad}=8 it is 0.027, or about three times as much. The fast mode grows more slowly than the slow mode, but at T_{ad}=11 it has twice the growth rate of most unstable mode in the non-reacting flow. Consequently, at high Mach number, the only outer modes are unstable and their growth rates increase with heat release.

Figure 7 shows the effect of variable properties on the stability characteristics when T_{ad}=8 and M_c=0.25 (M_1=1). The variable property center mode growth rate is two thirds the center mode growth rate of the constant property case; however, the maximum growth rate of the outer mode is almost 30% higher. The constant property profile gives center and outer modes with comparable amplification rates, but with the variable property profile, the outer modes dominate.

In low-speed flow, density variation in the laminar flow has a more significant effect than chemical reaction that occurs during the instability. Figure 8 shows that including the chemical reaction during the instability hardly changes the amplification rate in compressible flow. These results suggest that chemical reaction can be ignored in linear stability analysis.

2.5 Three-dimensional instability

In compressible flow, the obliquity of the most amplified wave increases as Mach number increases (Sandham & Reynolds 1989; Clemens & Mungal 1990). In this section, the effect of heat release on the obliquity of the most amplified mode is studied. Since maximum obliquity occurs at the high Mach number, we consider only the M_c=1.25 (M_1=5) case. Figure 9 shows the maximum amplification rates for various angles of propagation. In Figure 9, only the slow mode growth rates are plotted for readability; the fast modes have almost same growth rates. In a non-reacting mixing layer, for angles less than 30°, the outer modes are dominant and the maximum growth rates change little with angle. However, when the angle is greater than 40°, the outer modes disappear and the center mode begins to dominate. Its maximum amplification rate occurs at about 60° and is much greater than the growth rate of the outer modes at θ=0. Therefore, the most unstable mode is oblique at M_c=1.25. Clemens and Mungal (1990) reported that the flow is highly three-dimensional when $M_c > 0.6$, consistent with our predictions.

The reacting flow has very different behavior. At T_{ad}=2, the three modes behave as they do in the non-reacting flow but the center mode dominates only for angles

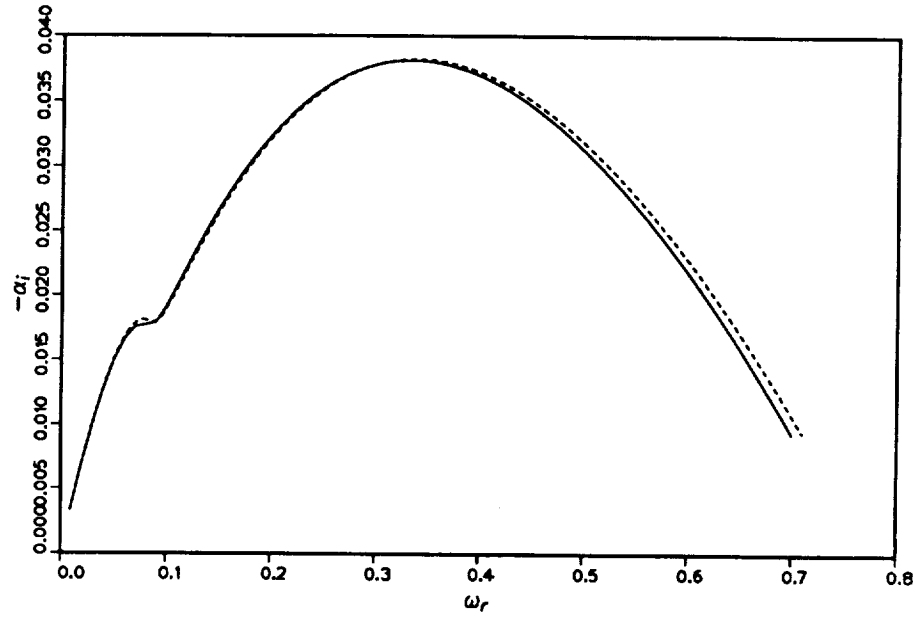

FIGURE 8. Effect of reaction during instability on the growth rate at $T_{ad}=8$, $M_c=0.25$. ——— , with chemical reaction; - - - - , without chemical reaction.

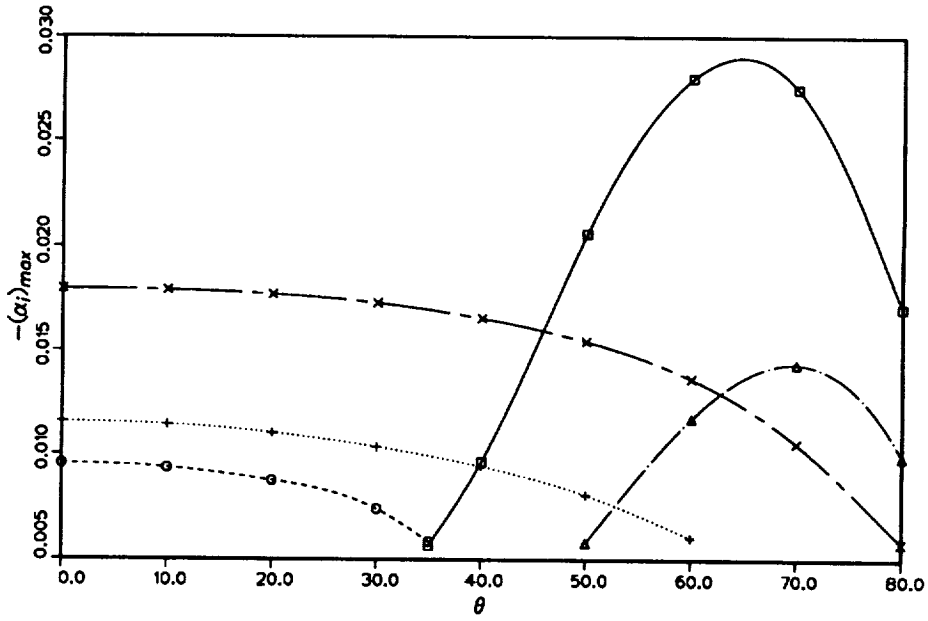

FIGURE 9. Maximum growth rate versus oblique angle at $M_c=1.25$. □ , $T_{ad}=1$ (center mode); ○ , $T_{ad}=1$ (slow mode); △ , $T_{ad}=2$ (center mode); +, $T_{ad}=2$ (slow mode); ×, $T_{ad}=4$ (slow mode).

above 55°; its maximum growth rate occurs at about 70°. As the heat release increases further (T_{ad}=4), the center mode disappears and only the outer modes are amplified. The maximum amplification rates of the outer modes decrease slightly as the obliquity increases. Therefore, heat release makes the dominant mode two-dimensional, even in the highly compressible regime. The three-dimensional modes which dominate in the non-reacting case are stable. In Section 2.4, we showed that the maximum amplification rate of the outer modes increases as heat release increases. For the conditions represented in Figure 9, the maximum amplification rate of the outer modes is about 1.4 times the rate in the non-reacting case. The phase velocities of outer modes approach the average velocity of the two streams as the angle increases.

3. Future plans

3.1 Effect of nonuniform density, stoichiometric ratio and finite chemistry

We have considered only the case of equal free stream densities. To be more realistic, we need to consider a flow in which the fuel and the oxidizer have different initial temperatures. We will study the characteristics of this flow and compare it with the uniform density flow. The stoichiometric ratio in the diffusion flame is defined by

$$\phi = \frac{(Y_F/Y_O)_{real}}{(Y_F/Y_O)_{ideal}} \tag{6}$$

where Y_F, Y_O represent the mass fractions of fuel and oxidizer, respectively. If $\phi > 1$, fuel is rich, while if $\phi < 1$ it is fuel lean. Changing ϕ changes mean flow profiles and the stability characteristics. We will look into this case. Finite rate chemistry is more realistic than the infinite rate chemistry of the flame sheet model. We will study the difference between two cases and establish the importance of using finite rate chemistry.

3.2 The effect of walls on a supersonic reacting mixing layer

Until now, we assumed the shear layers are free and unconfined. However, the situation is quite different in the supersonic mixing layers in a ramjet combustor. There is a coupling between the flow and acoustic modes through reflection of acoustic waves by the walls. This coupling will alter the stability of the shear layer. We will put the mixing layer in a channel to investigate this coupling. The mean flow will include chemical reaction. The stability equation will be derived. We will check the effects of all parameters such as heat release, Mach number, frequency, wavenumber, density ratio, stoichiometric ratio of fuel and oxidizer, thickness of shear layer, the height between walls and the direction of propagation of the disturbance wave. We will compare the results with and without walls. We hope this study will show the validity of using free shear flow.

Acknowledgements

The authors wish to acknowledge Mr. Olivier Planché for helpful discussions.

REFERENCES

BROWN, G. L. & ROSHKO, A. 1974 On density effects and large structure in turbulent mixing layers. *J. Fluid Mech.* **64**, 775–816.

BLUMEN, W., DRAZIN, P. G. & BILLINGS, D. F. 1975 Shear layer instability of an inviscid compressible fluid. Part 2. *J. Fluid Mech.* **71**, 305–316.

CLEMENS, N. T. & MUNGAL, M. G. 1990 Two- and three-dimensional effects in the supersonic mixing layer. *AIAA 90-1978.*

GROPPENGIESSER, H. 1970 Study on the stability of boundary layers in compressible fluids. *NASA TT-F-12.* rm **786**,

PAPAMOSCHOU, D. & ROSHKO, A. 1988 The compressible turbulent shear layer: an experimental study. *J. Fluid Mech.* **197**, 453–477.

SANDHAM, N. D. & REYNOLDS, W. C. 1989 A numerical investigation of the compressible mixing layer. Stanford University, Department of Mechanical Engineering, Thermosciences Division Report TF-45.

SHIN, D. S. & FERZIGER, J. H. 1990 Linear stability of the reacting mixing layer. *AIAA 90-0286.*

Center for Turbulence Research
Annual Research Briefs - 1990

Numerical simulations of turbulent thermal convection with differential rotation

By W. Cabot

1. Motivation and objectives

The solar nebula, from which the planets in our solar system formed, featured a disk of gas and dust grains in rapid, differential rotation, and at some stage was likely to have been unstable to thermal convection. This situation is suspected by many to lead to significant turbulent Reynolds stress production and angular momentum transport in such systems, and estimates of transport rates have been attempted from unsubstantiated phenomenological models (cf. Ruden & Lin 1986; Cabot *et al.* 1987). In order to determine the circumstances and physical conditions under which our own planetary system formed and to explain recent observations of young stellar systems, it is necessary to develop realistic models of heat and angular momentum transport for such flows. Developing an understanding of complicated flows featuring thermal convection, rotation, and shear is also of wide interest in stellar astrophysics and in planetary and terrestrial atmospheric studies.

In order to determine the nature of Reynolds stress production under localized solar nebula conditions, we have performed direct numerical simulations of channel flow (Cabot 1990a, Cabot *et al.* 1990b, Cabot & Pollack 1990c) that include Boussinesq thermal convection (incompressible except for buoyant density fluctuations) with linearly varying gravity and centrifugally stable differential rotation whose axis is aligned with gravity and whose gradient is perpendicular thereto (see Figure 1). These simulations are unrealistic in their near-incompressibility and uniformity of density, in their too high Prandtl number Pr and too low Reynolds number Re (required to resolve the flow fully), and in their impermeable "wall" vertical boundary conditions, although these have been relaxed to no-stress conditions. These simulations do, however, reveal that the turbulent Reynolds stress has a very complex behavior that is sensitive to the rotation and shear rates as well as the Reynolds number.

Our ultimate objective is to develop workable models based on the numerical simulations for constructing global solar nebula models; viz., we want to characterize, quantify, and develop relatively simple prescriptions for heat and angular momentum fluxes from given system parameters (e.g., ratios of rotation, shear, and convective lapse rates). Toward this end, our program has been (1) to attempt to understand the behavior of the direct numerical simulations of Boussinesq convection, which, despite the complexity of the results, is still an overly simplified approximation to the real system and should be more amenable to analysis. These results are also intended to be tested against turbulence models, especially those designed for atmospheric boundary layers, and may provide a basis for subgrid-scale models. (2) In order to make the numerical simulations more realistic with regard

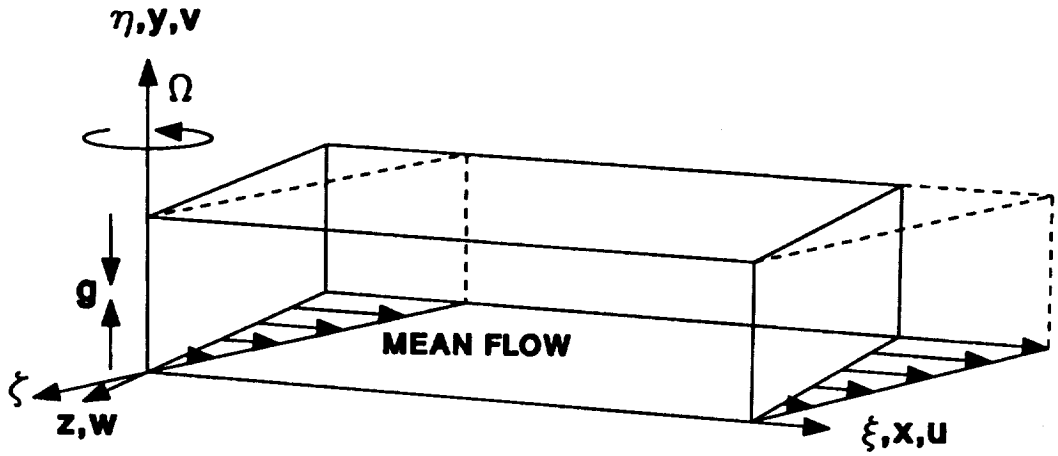

FIGURE 1. Local Cartesian coordinates of the numerical domain with the orientation of gravity (g) and rotation ($\mathbf{\Omega}$): co-rotating coordinates (x, y, z) and velocity components (u, v, w) correspond to azimuthal (streamwise), vertical, and radial (spanwise) coordinates in the solar nebula (channel flow). The co-moving coordinates (ξ, η, ζ) follow the mean flow, as illustrated by the dashed box.

to the solar nebula problem, our goal has been to develop a fully compressible code that will allow us to incorporate large density stratifications and realistic thermodynamic and radiative properties. (3) In order to explore the properties of these flows at the very high values of Re found in natural systems and the very low values of Pr found in most astrophysical contexts, we will need to employ large-eddy simulations for which we want to determine the most appropriate subgrid-scale model to incorporate.

2. Accomplishments

2.1 Direct numerical simulation results for Boussinesq convection

Sequences of direct numerical simulations with Boussinesq thermal convection subjected to centrifugally stable differential rotation (described in Cabot 1990a and Cabot & Pollack 1990c) were completed and their turbulence statistics were compiled. Most sequences used Keplerian rotation, which is typical of centrifugally balanced solar nebula disks. The simulation was carried out with a channel code (Kim, Moin & Moser 1987) that was modified to follow the sheared flow (Rogallo 1981). The key results were: (1) The vertical convective heat flux is largely independent of the horizontal shear *per se*, though it does depend indirectly on it through the epicyclic frequency κ (where $\kappa^2 \equiv 2\Omega[2\Omega + S]$ for a rotation rate Ω

and horizontal shear rate S), which measures the effects of Coriolis forces; (2) the net shear production rate for Keplerian rotation is positive (as expected) at low κ but becomes negative at higher critical values of κ (which increase for increasing Re); and (3) very long streamwise structures develop at high κ nearly independent of Re for fixed Péclét number Pe.

The relative insensitivity of the vertical heat flux to details of horizontal shearing suggests that this can be approximated in physical systems with models that take account of suppression of convection by centrifugally stable rotation. For example, a simple mixing length model for the heat flux with uniform rotation was suggested by Cabot *et al.* (1990b); one would merely need to generalize the rotational vorticity 2Ω to κ in this model.

The behavior of the shear production rate at rapid rotation and shear rates has yet to be understood or modeled adequately. A crude model by Kichatinov (1986), based on linearized equations, appears to reproduce the negative shear production rate at rotation rates comparable to an unspecified turbulence time τ. However, the assumptions that go into the model ($|S| \ll \Omega \ll \tau$) are all violated in our flow. Moreover, Kichatinov's model is constructed for infinite Re, whereas our results apply to low Re, and the trend for our shear production rates to become negative shows signs of disappearing asymptotically at high Re.

Inhomogeneous features of the Reynolds stress $-\overline{uw}$ and shear production rate $-S\overline{uw}$ also need to be explained. Negative shear production at high κ is mostly generated in the outer wall regions (see Figure 2). There are regions around $|y| = 0.6$ that always have positive shear production; these roughly coincide with regions of maximal buoyancy production. The interior regions develop less significant negative shear production rates in low-Re, high-κ simulations, and tend even more to zero at higher Re. The degree of correlation between u and w is never very large, varying between ± 0.3. A sequence of simulations was also performed with heat sinks in the exterior regions so that the outer half of the channel is convectively stable. This better approximates the stable radiative exterior that exists in solar nebula disks and reduces the direct effects of the impermeable walls on the interior convection. Reynolds stress production in the interior of these simulations (see Figure 3) is similar to that across the full width of the fully convective channel (cf. Figure 2). The "splatting" effect at the impermeable walls (ascribed to pressure effects or kinematic blocking) that was seen in the fully convective channel simulations is also present to a lesser degree near the convectively stable-unstable boundary ($|y| \approx 0.5$). This is also near where the most negative correlations between u and w (and the most negative shear production) occur, suggesting a possible link.

The asymptotic behavior with respect to Re cannot be determined conclusively at rapid Keplerian rotation rates due to the appearance of "quasi-two-dimensionality" (Q2D) in which very long streamwise wavelengths develop in one or more of the fluctuating quantities such that the turbulent field cannot be resolved numerically. Linear analysis (cf. Knobloch 1984, 1985) predicts that shear will reduce fluctuations with streamwise variations through the direct action of shearing and indirectly by contracting spanwise wavelengths (in the co-moving frame) such that they are

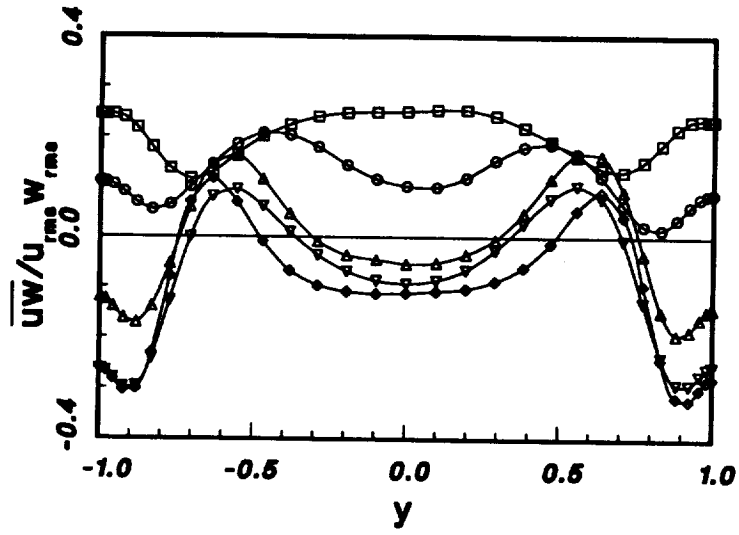

FIGURE 2. Vertical profiles of Reynolds stress correlation coefficients for the fully convective Keplerian rotation sequence with $Re = 559$ for different κ: □ 0.141, ○ 0.253, △ 0.447, ◇ 0.612, and ▽ 0.707.

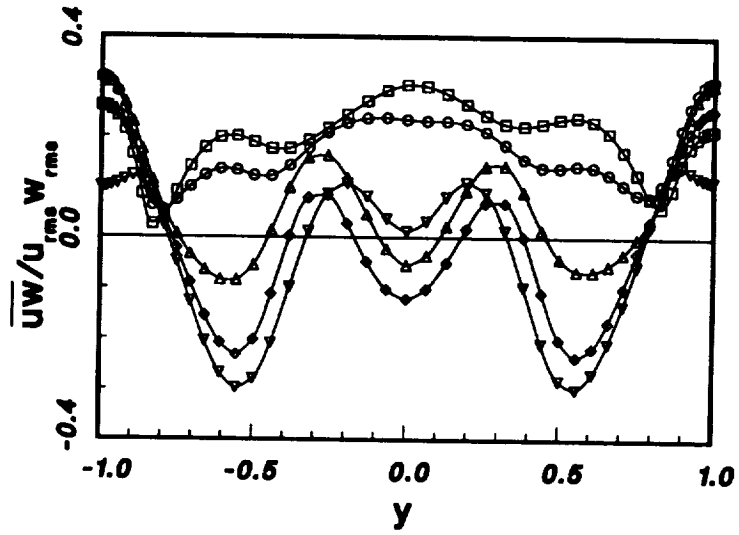

FIGURE 3. Same as Figure 2, but with convectively stable exterior regions ($|y| > 0.5$).

preferentially dissipated. In the long-time limit, all streamwise variations vanish and the shear production is negative perforce for centrifugally stable flows (Cabot & Pollack 1990c). It appears — qualitatively — that nonlinear redistribution of turbulence energy between wavevectors can proceed efficiently at low κ where there is

little stabilization due to Coriolis forces, but that at higher κ, the nonlinear redistribution is hindered sufficiently to allow the linear tendencies to prevail. This picture has some resemblance to the effects that rapid uniform rotation is found to have on nonlinear transfer in turbulence (e.g., through EDQNM analysis by Cambon & Jacquin 1989). However, little progress has been made yet in positively identifying and quantifying the factors that control the onset of Q2D. Both the vertical inhomogeneity and the nonseparability induced by the shear make the problem largely unamenable to spectral analyses, such as EDQNM. Though linear analysis can be applied, it fails to give useful or reliable information about the final turbulence statistics.

For given Pe, Q2D sets at high critical epicyclic frequency κ_c with little (and perhaps inverse) dependence on Re. Q2D sets in between $\kappa = 0.612$ and 0.707 for $Re = 559$ (based on the basal convective lapse rate and channel halfwidth); preliminary results from a very high Reynolds number simulation with $Re = 3200$ indicate that Q2D has marginally set in at $\kappa = 0.612$. This suggests that $\kappa_c \sim Re^{-\alpha}$ with $0 \leq \alpha \leq 1/12$. Also note that oscillatory convection becomes the most rapidly growing disturbance in linear perturbation analysis at values of κ lower by about half, but also depending weakly and inversely on Re ($\kappa_c \sim Re^{-1/6}$). This also suggests that Q2D is associated with strong inertial wave production.

2.2 Direct numerical simulations with full compressibility

A fully compressible channel code (Thompson 1990) has been developed and direct numerical simulations for thermal convection with linearly varying gravity and moderate density stratification have been performed. The results are found to agree very well with the Boussinesq simulations. The r.m.s. Mach number of the turbulence was found for moderate convection ($Pe \sim 100$) to be about 0.3, which is too low for significant compressibility effects. The turbulence kinetic energy was found to be distributed relatively evenly across the channel, as for the corresponding Boussinesq cases, despite a decline in density by a factor of about 3 from midchannel to wall, indicating a tendency for turbulence intensities to vary as the inverse square root of the density. This suggests that highly stratified flows may exhibit very high turbulence intensities in the exterior regions, perhaps leading to shock(let?) formation.

The compressible code at present follows acoustic waves explicitly, which puts a limit on the timestep to achieve numerical stability. For situations in which convective motions are highly subsonic — which may well be the case for rapidly rotating convection —, this limit is overly restrictive in terms of computational costs. We are presently exploring alternative systems of equations that filter sound waves (widely known as "anelastic" or "soundproofed" equations); or implicit time-stepping of acoustic modes ("muffling"?) whereby long timesteps can be used that are numerically stable but inaccurate. The latter alternative is more operationally flexible in terms of treating full or filtered compressibility, but it remains to be seen if it is the most cost-effective.

2.3 Subgrid-scale modeling for large-eddy simulations

The Smagorinsky model for the subgrid-scale (SGS) Reynolds stress is purely dissipative: it extracts energy from the resolved turbulent field. However, the residual SGS Reynolds stress dissipation was computed by Piomelli *et al.* (1990) from direct numerical simulations of channel flow, *inter alia*, with a variety of filters, and it was found that the mean dissipation is generally a small residual of positive and negative terms. At points in transitional flow, energy may actually backscatter into the resolved scales from the unresolved scales. This suggests that more realistic SGS models should include large stochastic terms that allow backscatter.

A model that in principle allows for realistic fore- and backscatter was proposed by Germano *et al.* (1990) based on extrapolating the behavior of SGS stress from the highest resolved wavenumbers in a numerical simulation fitted to a Smagorinsky-esque model. The spatially local version of the model was found to be numerically ill conditioned; thus, well conditioned averages over homogeneous planes were used instead. The advantages of this approach are (1) that no constant need be specified *a priori* for the Smagorinsky model; (2) the new, extrapolated constant can have any sign, so that the SGS model need not be absolutely dissipative in the mean; and (3) the proper wall behavior for the SGS dissipation is predicted without the need for *ad hoc* wall-damping functions. A large-eddy simulation (LES) of channel flow was performed incorporating this model and was followed through transition to turbulence; the new model was found to give comparable or improved results compared with LES's using a standard Smagorinsky model with wall-damping functions. Work was begun incorporating a more general version of this model in a finite-difference channel code.

3. Future plans

3.1 Modeling of Boussinesq convection

We hope to apply one-point closure models to the results from Boussinesq thermal convection with rapid rotation and horizontal shear in order to test their ability to reproduce the observed heat flux properties and the tendency to give net negative shear production at rapid rotation and low Reynolds number. We also want to reproduce the vertical profiles of the observed Reynolds stress profiles. If successful, such a model, modified to include a mean density profile, could be applied to results with density stratification provided other compressibility effects were negligible. Two-point (spectral) closure models are likely to be intractable when applied to these sheared, inhomogeneous flows, but perhaps simpler test situations (e.g., locally homogeneous) can be made tractable to such analyses and made to yield some insight to the long-wavelength behavior associated with rapid rotation and shear.

The Boussinesq simulation code will also likely be used as a testing ground for LES's with large (or infinite) Reynolds numbers and very low (or zero) Prandtl numbers with moderate Péclét numbers. However, it may prove easier to modified extant LES codes to include thermal convection and differential rotation. We will also consider testing SGS Reynolds stress equations, based on one-point closure models, that can readily take account of buoyancy production effects. We wish to

test the possibility, though, that SGS buoyancy models may not be important in low-Pr flows because thermal conductivity preferentially destroys thermal fluctuations at small (subgrid?) scales; if this were the case, the SGS modeling could be greatly simplified for our purposes.

3.2 Compressible simulations

We will proceed with a limited number of fully compressible simulations of turbulent channel convection, largely to assess the importance of acoustic effects in the flow and to test the validity of the assumptions that go into deriving anelastic or soundproofed systems of equations that attempt to approximate low-Mach-number flows. When we believe that we have determined the most efficacious means of sound-filtering, we will modify the existing code and perform some direct numerical simulations in order to validate it numerically as well as physically by comparison with fully compressible results.

The introduction of more realistic thermodynamics, including large density stratification, will lead naturally to a convectively stable exterior region; this may largely mitigate the effects of inaccurate wall boundary conditions. We will also successively introduce uniform rotation and differential rotation. The latter will probably require some significant modifications in the code in order to follow the mean sheared flow. As with the Boussinesq code, we will hope to implement an SGS model in order to perform LES's for high-Re, low-Pr situations; if the Mach numbers in the flow are sufficiently low, then SGS models developed for incompressible cases may be sufficient. We will be keenly interested in learning if long-wavelength behavior develops in the compressible simulations at rapid rotation as it did in the Boussinesq ones. If it does, it may not be possible to construct models in a parameter range useful to solar nebula modeling with these channel simulations; rather, numerical simulations of curved channels with large azimuthal coverage will be necessary.

Acknowledgements

Parts of this work are being done in collaboration with J. B. Pollack and P. Cassen (NASA/Ames) and K. W. Thompson (NASA/Ames and Stanford University).

REFERENCES

CABOT, W. 1990a Turbulent thermal convection in a differentially rotating channel. *CTR Annual Research Briefs - 1989*, 247–259.

CABOT, W., CANUTO, V. M., HUBICKYJ, O., & POLLACK, J. B. 1987 The role of turbulent convection in the primitive solar nebula. I. Theory. *Icarus* **69**, 387–422.

CABOT, W., HUBICKYJ, O., POLLACK, J. B., CASSEN, P., & CANUTO, V. M. 1990b Direct numerical simulations of turbulent convection: I. Variable gravity and uniform rotation. *Geophys. Astrophys. Fluid Dyn.* **53**, 1–42.

CABOT, W. & POLLACK, J. B. 1990c Direct numerical simulations of turbulent convection: II. Variable gravity and differential rotation, preprint.

CAMBON, C. & JACQUIN, L. 1989 Spectral approach to non-isotropic turbulence subjected to rotation. *J. Fluid Mech.* **202**, 295–317.

GERMANO, M., PIOMELLI, U., MOIN, P., & CABOT, W. H. 1990 A dynamic subgrid-scale eddy viscosity model. *CTR Proceedings of the 1990 Summer Program*, 5–17.

KICHATINOV, L. L. 1986 Turbulent transport of angular momentum and differential rotation. *Geophys. Astrophys. Fluid Dyn.* **35**, 93–110.

KIM, J., MOIN, P., & MOSER, R. 1987 Turbulence statistics in fully developed channel flow at low Reynolds number. *J. Fluid Mech.* **177**, 133–166.

KNOBLOCH, E. 1984 On the stability of stratified plane Couette flow. *Geophys. Astrophys. Fluid Dyn.* **29**, 105–116.

KNOBLOCH, E. 1985 The stability of non-separable barotropic and baroclinic shear flows. *Astrophys. Space Sci.* **116**, 149–163.

PIOMELLI, U., CABOT, W. H., MOIN, P., & LEE, S. 1990 Subgrid-scale backscatter in transitional and turbulent flows. *CTR Proceedings of the 1990 Summer Program*, 19–30.

ROGALLO, R. S. 1981 Numerical experiments in homogeneous turbulence. *NASA Tech. Mem.* 81315.

RUDEN, S. P. & LIN, D. N. C. 1986 The global evolution of the primordial solar nebula. *Astrophys. J.* **308**, 883–901.

THOMPSON, K. W. 1990 Turbulent transport in the solar nebula. *CTR Annual Research Briefs - 1989*, 175–184.

Direct simulations of compressible wall-bounded turbulence

By J. C. Buell

Several direct numerical simulations of high-speed turbulent Couette flow have been performed with a new spectral code. Mach numbers up to three and a Reynolds number of 3000 were used. A new time-integration scheme was developed to handle Mach numbers above 1.5, which require greater accuracy and stability than lower Mach numbers. At low Mach number, the large streamwise eddies found by M. J. Lee in his incompressible Couette flow simulations were reproduced. At higher Mach numbers these structures still exist, but they become considerably less organized (although the disorganization may be a function of the spanwise box size). While the same types of vortical structures seen in the incompressible flow are observed at higher Mach numbers, a new structure involving the divergence of the velocity is also observed. This structure is generally associated with low shear areas next to the walls, but it has not been determined whether it is a cause or an effect of the low shear. A "nonphysical" simulation was performed to determine by what mechanism the Mach number affects the flow. It appears that pressure gradient (acoustic) effects are more important than variable viscosity effects in determining the wall shear, but the size of vortical structures is determined more by the local kinematic viscosity. Low-order mean statistics are provided to help quantify these effects.

1. Motivation and objectives

Direct numerical simulations of incompressible turbulence have proven to be invaluable in describing physical mechanisms and quantifying various statistics that are essentially impossible to measure experimentally. For compressible flows, experimental measurements become even more difficult. Skin friction coefficients have been measured in several experiments with adiabatic walls (early results are summarized in Liepmann & Roshko 1957). These show a monotonic decrease with Mach number, but the mechanism is still not understood. Since little is known theoretically, a study was initiated to quantify the effects of compressibility (Mach number) on turbulent boundary layers. Our immediate objective is to be able to describe differences from the incompressible case in the turbulent structures and mean statistics. A longer-term goal is to use this information to improve turbulence models for high Mach-number boundary layers.

Couette flow with isothermal walls was chosen since it is one of the simplest flows in the desired class. The lack of a mean streamwise pressure gradient plus isothermal walls implies that both horizontal directions can be assumed to be homogeneous and that the flow can reach a statistically steady state. Together, these features greatly simplify the calculations and analyses of the results. The scales used for

nondimensionalizing the problem are the channel half-width (b), half the velocity difference between the walls (U_w), average density (ρ_a), wall temperature (T_w), and the fluid viscosity evaluated at the wall temperature (μ_w). In nonconservative form, the continuity, momentum and energy equations are

$$\frac{\partial \rho}{\partial t} + \rho \frac{\partial u_j}{\partial x_j} + u_j \frac{\partial \rho}{\partial x_j} = 0, \tag{1}$$

$$\frac{\partial u_i}{\partial t} + u_j \frac{\partial u_i}{\partial x_j} + \frac{1}{\gamma M^2} \frac{\partial T}{\partial x_i} + \frac{T}{\gamma M^2 \rho} \frac{\partial \rho}{\partial x_i} - \frac{1}{\rho Re} \frac{\partial \tau_{ij}}{\partial x_j} = 0, \tag{2}$$

$$\frac{\partial T}{\partial t} + u_j \frac{\partial T}{\partial x_j} + (\gamma - 1) T \frac{\partial u_j}{\partial x_j} - \frac{\gamma(\gamma - 1) M_d^2}{Re} \frac{\tau_{ij}}{\rho} \frac{\partial u_i}{\partial x_j} + \frac{\gamma}{\rho \, Re \, Pr} \frac{\partial q_j}{\partial x_j} = 0, \tag{3}$$

where

$$\tau_{ij} = \mu \left(\frac{\partial u_i}{\partial x_j} + \frac{\partial u_j}{\partial x_i} - \frac{2}{3} \delta_{ij} \frac{\partial u_k}{\partial x_k} \right), \qquad q_j = -\mu \frac{\partial T}{\partial x_j}.$$

The ideal gas relation $\rho T = \gamma M^2 p$ was used and the Reynolds and Mach numbers are defined by $Re = \rho_a U_w b / \mu_w$ and $M^2 = U_w^2 / \gamma R T_w$. The Prandtl number $Pr = c_p \mu^* / k^*$ and c_p are assumed to be constant throughout the flow (an asterisk is used to distinguish dimensional quantities). Note that in the dissipation term of (3), M is replaced with M_d. A "physical" simulation is obtained when $M_d = M$, but setting $M_d \neq M$ allows us to investigate the relative importance of the pressure gradient term in (2) and the energy dissipation term in (3). The main effect of the latter is to produce mean viscosity and conductivity profiles across the layer. Thus the two most important effects of M are acoustic and variable-property effects.

2. Accomplishments

2.1. Numerical method

The numerical method was described in Buell (1990a). Here we present a brief review of the spatial approximation and a short analysis of the time integration scheme needed for higher Mach numbers.

A classical Galerkin method is implemented in all three spatial dimensions. Thus the expansion functions and "test" functions are identical and satisfy all of the boundary conditions. Since the streamwise and spanwise directions are homogeneous, Fourier methods can be easily used. The implementation is similar to the incompressible direct simulation codes at NASA-Ames in that time advancement is performed in wave space which allows the Galerkin integrals to be performed more accurately (*i.e.*, dealiasing is done in physical space). This is unlike nearly all compressible codes; these typically use collocation methods and do not have any dealiasing at all. The complexity of the compressible equations prevents full dealiasing here, but the use of 30 to 50% more collocation points than modes comes close to eliminating aliasing errors since the strongest nonlinearity is still quadratic.

Because of the small grid size near the wall, an implicit treatment is needed for both the acoustic and diffusive terms. A straightforward implementation of

a spectral method requires that all implicit terms be constant-coefficient linear. The acoustic and diffusive terms are decomposed into a constant-coefficient linear part and a residual. This decomposition is given by Buell (1990a). It amounts to rewriting equations of the form

$$\frac{du}{dt} = \lambda u$$

as

$$\frac{du}{dt} = \lambda_0 u + (\lambda - \lambda_0)u,$$

where λ represents an eigenvalue of a spatial operator that one wants to treat implicitly. Since λ varies in space, a constant numerical parameter λ_0 is introduced so that the first term on the RHS above may be treated implicitly while the second term is treated explicitly. The appropriate value of λ_0 is determined by the range of λ and the time-integration scheme. For large $|\lambda|$, there is a maximum range over which λ can vary and still maintain stability for a single λ_0. This range is about $\lambda_{max}/\lambda_{min} = 2.4$ for the three-substep scheme described in Spalart *et al.* (1990), which is good enough for simulations using Mach numbers up to about 1.5. Motivated by the desire to simulate higher Mach numbers, a new four-substep scheme was developed. The coefficients were optimized so that absolute stability was obtained for $\lambda_{max}/\lambda_{min}$ up to at least 4.5, as well as achieving full third-order accuracy (previous schemes were second order for the implicit part). The new scheme is also stiffly stable (Gear 1971) for higher $\lambda_{max}/\lambda_{min}$, so that it appears that the algorithm will be stable for any Mach number. Details of the derivation and analysis of this scheme are given in Buell (1990b). The problem is that the above decomposition yields an increasing inaccurate time integration when $\lambda_{max}/\lambda_{min} > 5$. A new time integration scheme is still needed for hypersonic Mach numbers that does not require the implicit operator to be constant-coefficient linear.

Several different tests were used to check out the code. The best one consists of using eigenfunctions from a linear stability analysis (Buell 1990a) to verify that the growth rate can be reproduced by the nonlinear code. Many different 2-D and 3-D cases have been tried, and the numerical and linear stability results are always within 0.01 to 1% of each other. Even at $M = 8$, where the time integration is expected to be inaccurate, the results are very close. However, when random numbers or any profile other than an eigenfunction is used as an initial condition, the conclusions are not as clear. After the transient, the numerical growth (or decay) rate is close to linear theory, but only if the rate is averaged in time. Instantaneously, the growth rate oscillates around the average and the oscillations die out very slowly, if at all. We believe this behavior is physical, but do not have an explanation for it as yet.

2.2. Results

Shown in Table I are the four cases for which results are presented here. The Reynolds number is 3000 in all cases. Nx, Ny, and Nz are the number of modes in the three directions, and Lx and Lz are the periodic lengths in the two horizontal directions. The $M = 0.2$ case is marginally resolved, but the statistics compare very well with the better-resolved simulations of Lee (1990). The fluid is assumed

TABLE I

Numerical and physical parameters

case	Nx	Ny	Nz	Lx	Lz	M	M_d
1	60	48	90	12	8	0.2	0.2
2	110	64	60	12	4	1.5	1.5
3	110	64	60	12	4	1.5	0.2
4	90	90	60	10.6	4	3.0	3.0

TABLE II

Statistical properties

case	$\frac{d\bar{u}}{dy}\Big\|_w$	K.E.	$\bar{\rho}_w$	$\bar{\rho}(y=0)$	$\bar{T}(y=0)$
1	11.05	0.0147	1.0058	0.9996	1.0060
2	9.66	0.0130	1.3220	0.9767	1.3399
3	9.50	0.0127	1.0157	0.9974	1.0048
4	9.60	0.0135	2.2298	0.9294	2.3425

to be air with $Pr = 0.7$, $\gamma = 1.4$ and $\mu = T^{.7}$. The wall quantities (subscript w) are averages over time, the homogeneous directions, and both walls. K. E. is the average kinetic energy density over all three directions and time. Even at $M = 3$, the difference between standard and Favre averaging is negligible. The $M = 3$ case is the only one that is linearly unstable (Buell 1990a). Since only a very narrow range of wavelengths around the most unstable wavelength of 2.649 are unstable, we decided to use a box length that is an integral multiple (4) of this length. This guarantees that the flow cannot relaminarize. The spanwise box lengths were chosen based on the incompressible Couette flow results of Lee (1990). He found that large streamwise eddies form that scale on the channel height. With our nondimensionalization, a pair of these would have a width of about four. Since these structures are so large, it is impractical to use box sizes large enough so that the correlations become zero, as is usually the practice in direct simulations. The question of what is the appropriate box size (based on a "preferred" spanwise wavelength) and how it varies with the Reynolds and Mach numbers remains open.

2.2.1. Instantaneous fields

Shown in Figure 1 are representative contour plots of the streamwise velocity u at the midplane $y = 0$ for the three physical cases ($M = 0.2$, 1.5, 3). In all three cases, we see large streamwise structures dominating the flow. At $M = 0.2$, the flow is extremely close to being incompressible and the structures compare very well with the corresponding ones in the incompressible Couette flow simulations of Lee (1990). They are also similar to the structures at late time in homogeneous shear flow simulations (Lee, private communication). This indicates that walls are

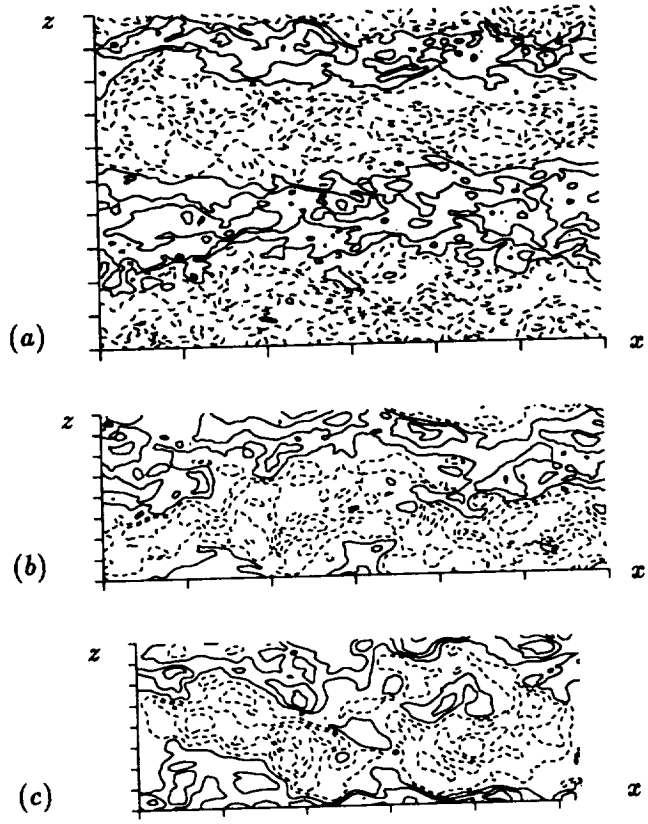

FIGURE 1. Streamwise velocity at $y = 0$ for (a) $M = 0.2$, (b) $M = 1.5$, and (c) $M = 3$. The contour interval is 0.1. Dashed lines denote negative values.

not necessary for their development. Higher Mach numbers appear to cause these structures to become less distinct. The dependence on Mach number appears to be related to boundary-layer effects, but it may be due to a change in the "preferred" spanwise wavelength. Also, the reduction in spanwise box size may allow the large structures to be less organized. This can be tested by performing a low M simulation with Lz = 4.

Figure 2 shows x–y cuts of ω_z through typical shear-layer structures for all four cases. We see that although the average shear at the wall is only about 13% smaller for $M = 3$ than for $M = 0.2$, the dominant vortical structures are about three times larger (extending up to $1 - |y| = 0.5$ instead of $1 - |y| = 0.15$ to 0.2). The vorticity magnitude in the shear layers and the peak values at the wall are correspondingly two to three times lower. Together with the qualitative appearance of the flow, this indicates that the global Reynolds number Re does not characterize the flow in the core of the channel. If the kinematic viscosity evaluated at the channel centerline is used instead of μ_w/ρ_a, then Re would be half as large for the $M = 3$ case as for the $M = 0.2$ case. This would be consistent with the appearances of the vortical structures, but not with the wall shear. Using wall variables to construct a Re_τ

does not provide a better overall scaling. Thus, it appears that there is no single definition of a Reynolds number that characterizes the entire flow. Data is given in Table II that can be used to construct other Reynolds numbers (the overbar represents a time and horizontal-space average).

We conjecture that the larger boundary-layer structures at $M = 3$ tend to break up the jet-like core flow. Increasing the Reynolds number so that the kinematic viscosity in the core matches that of the $M = 0.2$ case would verify this. A more precise comparison is given by the plots in Figure 2 and the data in Table II for the two $M = 1.5$ cases. The fact that the wall shear is independent of M_d indicates that the wall shear depends only on acoustic effects (M). However, the similarity of the vortical structures in the $M = 1.5$, $M_d = 0.2$ case to the $M = 0.2$ case indicates that these structures depend on the viscosity distribution, which is almost entirely dependent on M_d.

Shown in Figure 3 are organized structures of the divergence of velocity on the lower wall for the $M = 3$ case. These take the form of streamwise waves. x–y cuts (not plotted) show that the vertical extent is much smaller than the horizontal dimensions of each structure. Typically, they extend up to about $1 - |y| = 0.1$ with the core of the channel being nearly incompressible. Also shown are areas of low wall shear. The very good correlation with the divergence indicates that the two are related. It may be possible that the "divergence structures" cause the low shear; this would help explain the dependence of wall shear on M. On the other hand, they may be more passive, *i.e.*, a mode that is unstable under certain conditions but does little to affect the rest of the flow. Further investigation is needed to determine the cause and effect.

2.2.2. Statistics

The large length scales in turbulent Couette flow lead to large time scales and increased difficulty in obtaining converged statistics. The time scales are evident in Figure 4, where the average (in x and z) shear on both walls is plotted over the time interval in which statistics are gathered. Although the longest time scales are not well resolved, 300–500 time units is enough for the low-order statistics to be reliable. In particular, this is long enough for the total shear to be constant to within 2% across the channel.

Shown in Figure 5 are the mean profiles for u, ρ and T for the $M = 3$ case. Note that $\bar{\rho}$ and $\bar{T}$ are scaled with $K = \frac{1}{2}PrM^2(\gamma - 1) = 1.26$. This makes the profiles nearly independent of M (except near the walls, where the $M = 0.2$ case has slopes about 15% greater). This is especially true for temperature in the core: $(\bar{T}(y=0)-1)/K = 1.0660$ and 1.0656 for the $M = 0.2$ and $M = 3$ cases, respectively (the difference is not statistically significant).

The variance of each of the velocity components is shown in Figure 6 for the $M = 0.2$ and $M = 3$ cases. As was noted for the integrated kinetic energy, standard and Favre averaging yield the same results, at least up to $M = 3$. The $M = 0.2$ profiles are very close to the incompressible results of Lee (1990). In wall variables, the peak in the streamwise component is $u^+_{\mathrm{rms}} = 2.7$ and it occurs at $y^+ = 12$. There are two important differences between the two cases. First, the drop in the streamwise

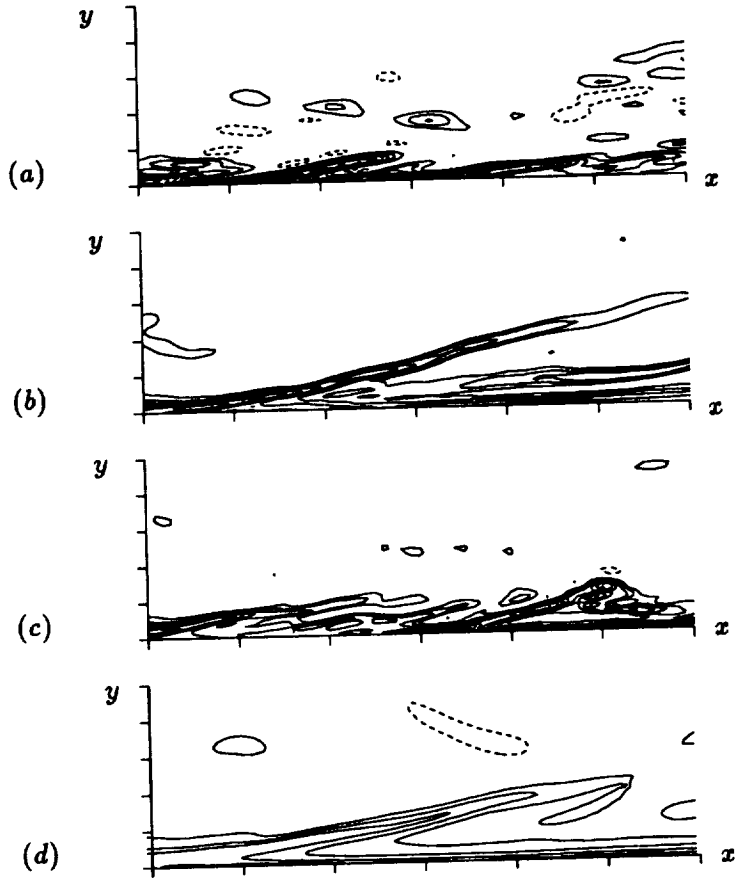

FIGURE 2. Spanwise vorticity $(-\omega_z)$ through typical shear layer structures for (a) $M = 0.2$, (b) $M = 1.5$, $M_d = 1.5$, (c) $M = 1.5$, $M_d = 0.2$, and (d) $M = 3$. The bottom half of the channel $-1 \leq y \leq 0$ and three units along the x-axis is shown in each case. The contour interval is 2.

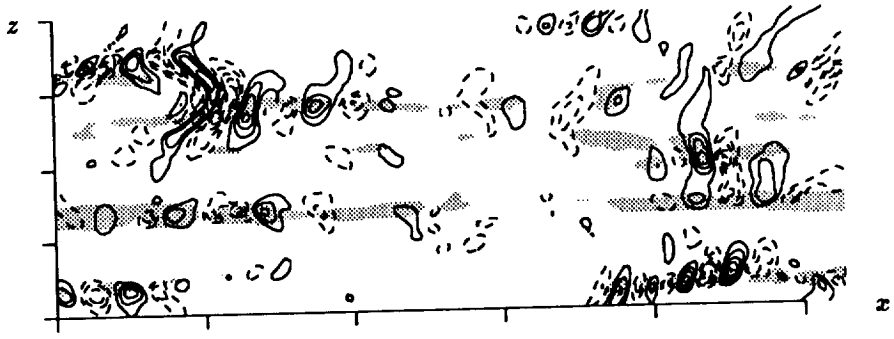

FIGURE 3. Divergence of the velocity at the lower wall for the $M = 3$ case. Contour interval is 0.2. Shaded areas denote low wall shear: $\frac{\partial u}{\partial y} < 5$.

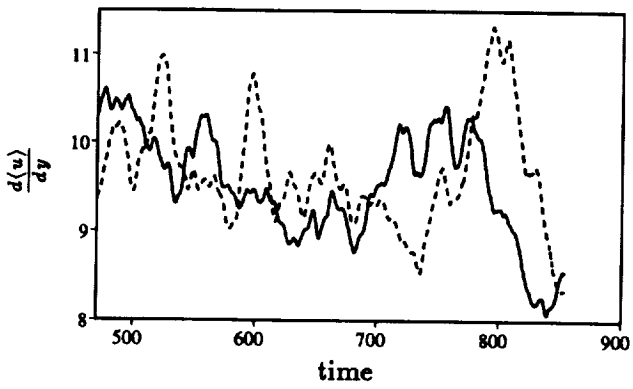

FIGURE 4. Horizontal average of $\frac{\partial u}{\partial y}$ on the lower wall (solid line) and upper wall (dashed line) for $M = 3$.

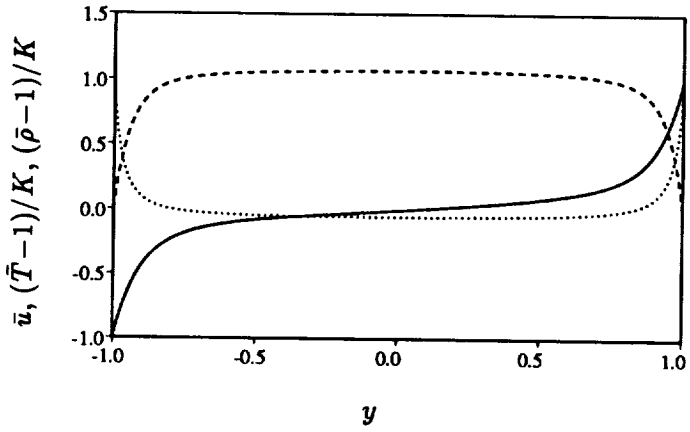

FIGURE 5. Mean profiles for u (solid), T (dashes) and ρ (dots) for $M = 3$. $K = \frac{1}{2}PrM^2(\gamma - 1)$.

component from its peak to its value at the channel center is much greater at the higher Mach number, while the other two components are qualitatively unchanged. This increased isotropy is apparently related to the break-up of the streamwise jets in the core. Second, the peak in the intensity occurs at $1 - |y| = 0.162$ for $M = 3$, but at $1 - |y| = 0.072$ for low Mach numbers. Unlike the relatively small differences in the absolute levels of the turbulence intensities, this difference cannot be scaled by any reasonable choice of the kinematic viscosity and velocity scale.

3. Future plans

We have presented here some results for compressible turbulent flow in a channel, but much work remains to be done in order to achieve our objectives. First, a higher Reynolds number $M = 3$ simulation should be performed where the kinematic

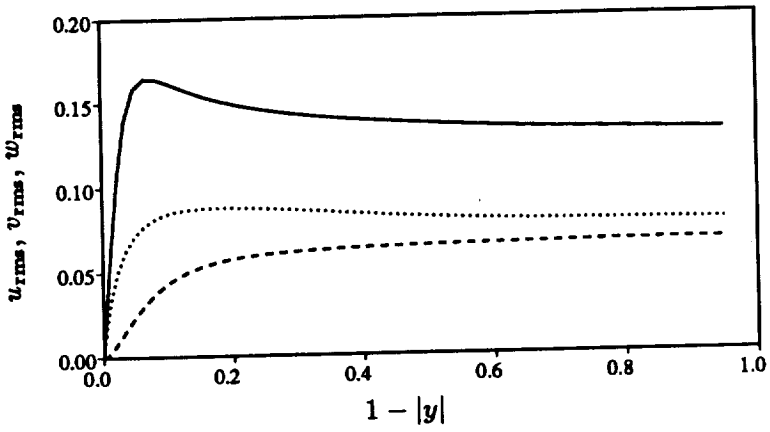

(a)

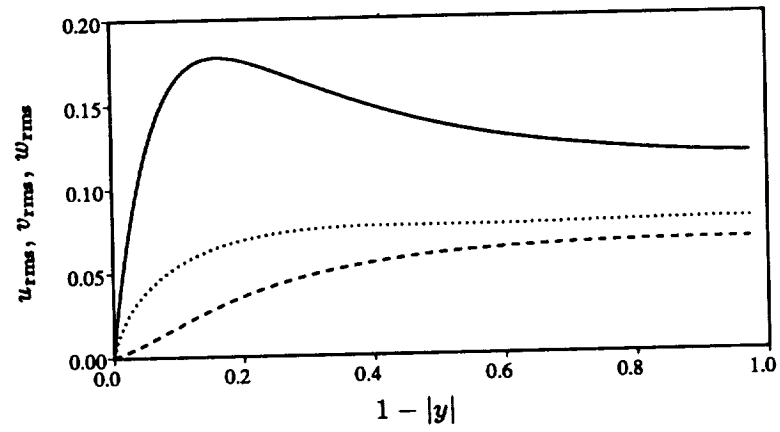

(b)

FIGURE 6. Profiles of the turbulence intensities for u (solid), v (dashes) and w (dots) for (a) $M = 0.2$, and (b) $M = 3$.

viscosity in the core matches that of the low Mach number simulations. This should be straightforward since the $M = 3$ simulation presented here was over-resolved, and since the temperature and density in the core appear to be easily predicted. Next, more realistic adiabatic or mixed boundary conditions need to be implemented for the temperature equation. This increases the implicit-operator bandwidth since the appropriate basis functions require three Legendre polynomials instead of just two. The computational cost of this will be minimal since linear algebra accounts for only about 10% of the run time now. Finally and most importantly, the simulation of higher Mach-number flows requires a different time integration scheme. The best way to do this is to generalize the decomposition (4) so that λ_0 is a low-order polynomial instead of just a constant. This will very effectively reduce the

magnitude of $(\lambda - \lambda_0)/\lambda_0$ and thus increase both the accuracy and stability of the time-integration scheme. The cost will be an increase in the matrix bandwidth by an amount proportional to the order of this polynomial. Fortunately, it appears that all of the x and z derivative operators may be treated explicitly, so that this matrix needs to be inverted only once per substep, at most.

REFERENCES

BUELL, J. C. 1990a Direct simulations of wall-bounded compressible turbulence. in *Annual Research Briefs - 1989*. Center for Turbulence Research.

BUELL, J. C. 1990b Third-order low-storage A-stable time integration schemes. submitted to *J. Comp. Phys.*

GEAR, C. W. 1971 *Numerical Initial Value Problems in Ordinary Differential Equations*. Prentice Hall.

LEE, M. J. 1990 The large-scale structures in turbulent plane Couette flow. in *Annual Research Briefs - 1989*. Center for Turbulence Research.

LIEPMANN, H. W. & ROSHKO, A. 1957 *Elements of Gasdynamics*. J. Wiley & Sons.

SPALART, P. R., MOSER, R. D. & ROGERS, M. R. 1990 Spectral methods for the Navier-Stokes equations with one infinite and two periodic directions. submitted to *J. Comput. Phys.*

Appendix

NAME/TERM		AREA OF INTEREST
POSTDOCTORAL FELLOWS		
BELCHER, Dr. Stephen E. 10/90-present	(Ph.D. DAMTP, 1990 Univ. of Cambridge)	Modeling turbulent boundary layers near separation.
BUELL, Dr. Jeffrey C. 1/89-12/90	(Ph.D. Mech. Engr., 1986, UCLA)	Physics and modeling of 3-D spatially developing mixing layer/physics of compressible wall-bounded flows.
CABOT, Dr. William H. 3/88-present	(Ph.D. Physics, 1983 Univ. of Rochester)	Turbulence in the early solar nebula and turbulence in compressible flows.
GAO, Dr. Feng 9/90-present	(Ph.D. Mech. Engr., 1990, SUNY-Stony Brook)	Investigations of turbulent scalar fields using probability density function approach.
HUANG, Dr. George 3/88-present	(Ph.D. Mech. Engr., 1986, Univ. of Manchester)	Modeling hypersonic boundary layer flows with second-moment closure.
LEE, Dr. Moon J. 12/87-10/90	(Ph.D. Mech. Engr., 1985, Stanford)	Turbulence physics and modeling.
LUND, Dr. Thomas S. 11/90-present	(Ph.D. Aero-Astro, 1987, Stanford)	Large eddy simulation of complex flows.
MENEVEAU, Dr. Charles 9/89-8/90	(Ph.D. Mech. Engr., 1989, Yale)	Study of structure and dynamics of turbulence using the wavelet transform.

POINSOT, Dr. Thierry 9/88-8/90	(Docteur es Sciences, Mech. Engr., 1987, Univ. d'Orsay, France)	Direct simulation of turbulent reacting flows.
SAMUELS, Dr. David C. 10/90-present	(Ph.D. Physics, 1990, Univ. of Oregon)	High Reynolds number flows in superfluid helium II.
SHEN, Dr. Hubert 1/90-present	(Ph.D. Physics, 1988, Univ. of Illinois)	Turbulence theory.
SMITH, Dr. Leslie M. 9/88-present	(Ph.D. Applied Math., 1988, MIT)	Renormalization group theory of turbulence.
SQUIRES, Dr. Kyle D. 7/90-present	(Ph.D. Mech. Engr., 1990, Stanford)	Turbulence model development using a Lagrangian data base and examination of sub-grid scale models for compressible turbulence.
STRETCH, Dr. Derek D. 1/89-1/91	(Ph.D. Engineering, 1986, Cambridge)	Conditional sampling and organized structures in turbulent boundary layers.
THOMPSON, Dr. Kevin W. 6/87-6/90	(Ph.D. Physics, 1985, Princeton)	Direct numerical simulation of compressible turbulent flows with application to the early evolution of solar nebula.
TROUVE, Dr. Arnaud 4/90-present	(Ph.D. Mech. Engr., 1989, Ecole Centrale de Paris)	Direct simulation of turbulent reactive flows.
VASTANO, Dr. John A. 9/88-8/90	(Ph.D. Physics, 1988, Univ. of Texas at Austin)	Low dimensional chaos in turbulence.
VEERAVALLI, Dr. Srinivas 9/89-present	(Ph.D. Mech. Engr., 1989, Cornell Univ.)	Effect of rotation turbulence, and experiments in high Reynolds number turbulence.
VEGT, Dr. J. J. W. van der 9/88-present	(Ph.D. Math., 1988, Delft Univ. of Tech., The Netherlands)	Transition to turbulence at hypersonic speeds.

WALEFFE, Dr. Fabian A. 9/89-1/91	(Ph.D. Applied Math., 1989, MIT)	Hydrodynamic stability and non-linear analysis.
WATMUFF, Dr. Jonathan H. 11/87-11/90	(Ph.D. Mech. Engr., 1979, Univ. of Melbourne, Australia)	Experimental investigation of turbulent boundary layers with adverse pressure gradient.
ZHOU, Dr. Ye 10/90-present	(Ph.D. Physics 1987, College of William & Mary)	Recursive renormalization group based on sub-grid modeling.

SENIOR RESEARCH FELLOWS

DURBIN, Dr. Paul 1/90-present	(Ph.D. DAMTP, 1979, Univ. of Cambridge)	Turbulence modeling.
ZEMAN, Dr. Otto 3/89-present	(Ph.D. Aerospace Engr., 1975, Pennsylvania State Univ.)	Modeling high Mach number turbulent flows.

SENIOR VISITING FELLOWS

CAMBON, C. 3/90-8/90	Professor of Fluid Mech., Ecole Centrale de Lyon	Effect of rotation on turbulence and rapid distortion theory; two point and single point closures.
CRIMINALE, William O. 3/90-6/90	Professor, Applied Math., University of Washington	Initial-value problems in shear flows.
GOTOH, Toshiyuki 11/90-12/90	Professor, Nagoya Inst. of Technology	Lagrangian turbulence modeling.
JIMENEZ, Javier 7/90-11/90	Professor, University of Madrid	Fractal interfaces and product generation in mixing layers.
MATHIEU, Jean 9/90-12/90	Professor, Ecole Centrale de Lyon-PEPIT	Turbulence theory.

ORLANDI, Paolo 6/90-9/90	Professor, Dept. of Mech. & Aero., Univ. of Rome	Numerical simulation of incompressible flow in complex geometry.
OTTINO, Julio M. 12/89-4/90	Professor, Chem. Engr., University of Massachusetts-Amherst	Mixing and chaos.
YAVUZKURT, Savash 9/90-present	Professor, Pennsylvania State University	Characterization of length and velocity scales of free stream turbulence and their effect on surface heat transfer.

GRADUATE STUDENTS

BEAUDAN, Patrick 10/87-present	Large eddy simulation of flow over a cylinder.
BLAISDELL, Gregory 7/90-11/90	Direct numerical simulation of compressible turbulent shear flow.
KARASSO, Paris 7/89-present	Experimantal investigation of a curved shear layer.
KASSINOS, Stavros 10/88-present	Reynolds averaged turbulence modeling.
LE, Hung 4/88-9/90	Direct numerical simulation of flow over a backward facing step.
LIN, Tony Y.-C. 10/89-9/90	3D and unsteady geophysical flows.
SHIN, Dongshin 10/90-present	Linear stability analysis for chemically reacting high Mach number flows.

1990 ADVISORY COMMITTEE

Dr. Dennis M. Bushnell
NASA Langley Research Center

Prof. Robert Dibble
Univ. of California at Berkeley

Dr. Marvin E. Goldstein
NASA Lewis Research Center

Prof. Fazle Hussain
University of Houston

Dr. Robert H. Kraichnan
Los Alamos Laboratories

Prof. Paul A. Libby
Univ. of California at San Diego

Prof. Hans W. Liepmann
California Institute of Technology

Prof. John L. Lumley (Chairman)
Cornell University

Dr. James M. McMichael
Air Force Office of Scientific Research

Prof. Mark V. Morkovin
University of Illinois

Dr. Jack N. Nielsen (Ex-Officio)
NASA Ames Research Center

Dr. Michael Reischmann
Office of Naval Research

Dr. Ronald Smelt
Lockheed

Dr. Michael J. Werle
United Technologies Corporation

Dr. Robert Whitehead
NASA Headquarters

Dr. Louis J. Williams (Ex-officio)
NASA Headquarters

1990 STEERING COMMITTEE

Prof. Dean R. Chapman
Dept. of Aeronautics & Astronautics
and Mechanical Engineering,
Stanford University

Prof. William O. Criminale
Senior Visiting Fellow, 3/90-6/90,
Center for Turbulence Research
Professor, Applied Mathematics,
University of Washington

Dr. Terry L. Holst
Chief, Applied Computational
Fluids Branch
NASA Ames Research Center

Prof. Javier Jimenez
Senior Visiting Fellow, 7/90-11/90,
Center for Turbulence Research
Professor, Fluid Mechanics,
University of Madrid

Dr. John J. Kim
Ames Coordinator,
Center for Turbulence Research
Head, Turbulence Physics Section,
NASA Ames Research Center

Prof. Joseph G. Marvin
Chief, Experimental Fluid
Dynamics Branch,
NASA Ames Research Center

Prof. Parviz Moin
Director, Center for Turbulence Research
Professor, Department of Mechanical
Engineering, Stanford
Senior Staff Scientist,
NASA Ames Research Center

Prof. Julio Ottino
Senior Visiting Fellow, 12/90-5/90,
Center for Turbulence Research
Professor, Chemical Engineering,
Univ. of Massachusetts at Amherst

Prof. William C. Reynolds
Program Coordinator,
Center for Turbulence Research
Professor and Chairman,
Department of Mechanical
Engineering, Stanford
Senior Staff Scientist,
NASA Ames Research Center